

Condition Assessment of Cemented Materials Using Ultrasonic Surface Waves

by

Ahmet Serhan Kırdoğan

A thesis
presented to the University of Waterloo
in fulfillment of the
thesis requirement for the degree of
Doctor of Philosophy
in
Civil Engineering

Waterloo, Ontario, Canada, 2013

© Ahmet Serhan Kırdoğan 2013

Author's Declaration

Hereby declare that I am the sole author of this thesis. This is a true copy of the thesis, including any required final revisions, as accepted by my examiners.

I understand that my thesis may be made electronically available to the public.

Ahmet Serhan Kırlangıç

Abstract

Mechanical waves provide information about the stiffness and the condition of a medium; thus, changes in medium conditions can be inferred from changes in wave velocity and attenuation. Non-destructive testing (NDT) methods based on ultrasonic waves are often more economical, practical and faster than destructive testing. Multichannel analysis of surface waves (MASW) is a well-established surface wave method used for determination of the shear-wave profile of layered medium. The MASW test configuration is also applicable to assess the condition of concrete elements using appropriate frequency range. Both attenuation and dispersion of ultrasonic waves can be evaluated by this technique.

In ultrasonic testing, the characterization of a medium requires the precise measurement of its response to ultrasonic pulses to infer the presence of defects and boundary conditions. However, any ultrasonic transducer attached to a surface affects the measured response; especially at high frequencies. On the other hand, ultrasonic transducers available for engineering application are mostly used to measure wave velocities (travel time method). Therefore, these transducers do not have a flat response in the required frequency range. Moreover, in the case of full-waveform methods, the recorded signals should be normalized with respect to the transfer functions of the transducers to obtain the real response of the tested specimen.

The main objective of this research is to establish a comprehensive methodology based on surface wave characteristics (velocity, attenuation and dispersion) for condition assessment of cemented materials with irregular defects. To achieve the major objective, the MASW test configuration is implemented in the ultrasonic frequency range. The measured signals are subjected to various signal processing techniques to extract accurate information. In addition, a calibration procedure is conducted to determine the frequency response functions (FRF) of the piezoelectric accelerometers outside their nominal frequency range. This calibration is performed using a high-frequency laser vibrometer.

This research includes three main studies. The first study introduces the calibration approach to measure the FRFs of the accelerometers outside of their flat frequency range. The calibrated

accelerometers are then used to perform MASW tests on a cemented-sand medium. The original signals and the corrected ones by eliminating the effect of the FRFs are used to determine material damping of the medium. Although, the damping ratios obtained from different accelerometers are not same, the values from the corrected signals are found closer to the characteristic damping value compared to those from the uncorrected signals.

The second study investigates the sensitivity of Rayleigh wave velocity, attenuation coefficient, material damping and dispersion in phase velocity to evaluate the sensitivity of these characteristics to the damage quantity in a medium. The soft cemented-sand medium is preferred as the test specimen so that well-defined shaped defects could be created in the medium. MASW test configuration is implemented on the medium for different cases of defect depth. The recorded signals are processed using different signal processing techniques including Fourier and wavelet transforms and empirical mode decomposition to determine the surface wave characteristics accurately. A new index, ‘dispersion index’, is introduced which quantifies the defect based on the dispersive behaviour. All surface wave characteristics are found capable of reflecting the damage quantity of the test medium at different sensitivity levels.

In the final study, the condition assessment of six lab-scale concrete beams with different void percent is performed. The beam specimens involving Styrofoam pellets with different ratios are tested under ultrasonic and mechanical equipment. The assessment produce established in the second study with well-defined defects is pursued for the beams with irregular defects. Among the characteristics, attenuation, P and R-wave velocities and dispersion index are found as the promising characteristics for quantifying the defect volume.

Acknowledgements

First and foremost, I express my sincerest gratitude to Dr. Giovanni Cascante and Dr. Marianna Polak for their guidance and suggestions. I greatly appreciate their kind understanding towards me through this research work.

I appreciate the support from Natural Sciences and Engineering Research Council of Canada which provide the opportunity to realize this research.

I would like to acknowledge Dr. Eihad Abdel-Rahman for providing the laser equipment to calibrate the accelerometers used in the research and Dr. Mahmoud Khater for assisting me with the equipment.

My special thanks to John Boldt, Rick Forgett and Jorge Cruz from the Engineering Machine Shop for their assistance and willingness to help and Richard Morrison, Douglas Hirst and Anne Allen from the Department of Civil Engineering for their valuable recommendations in laboratory works and hands on help.

My gratitude is extended to all my fellows for easing the research life: Special thanks to Hassan Ali and Dritan Topuzi for making themselves always available when help is needed; Yanjun Yang and Fernando Tallavo for the change to discuss technical problems; Yen Wu and Soheil Moayerian for creating an enjoyable work environment; and Bijan Mahbaz and Alireza Masnavi for helping me with the laboratory tasks.

I would like to thank my friends; Yelda Türkan, Keivan Ahmedi and Güneş Aluç for their support; Özlem Karadeniz and Hasan Tonak for hosting me and providing a comfortable study environment during my stay in Istanbul.

And of course, none of this would have come true without the support and patience of my family. It could not have been achieved without their deep understanding.

Dedication

Dedicated to my parents.

Aileme itaf edilmiştir.

Table of Contents

Author's Declaration.....	ii
Abstract.....	iii
Acknowledgements.....	v
Dedication.....	vi
Table of Contents.....	vii
List of Figures.....	xi
List of Tables.....	xix
Chapter 1 Introduction.....	1
1.1 Problem Statement.....	1
1.2 Current Methods for Non-destructive Testing of Concrete.....	1
1.3 Objectives.....	3
1.4 Research Methodology.....	4
1.5 Thesis Organization.....	6
Chapter 2 Wave Motion.....	7
2.1 Introduction.....	7
2.2 Equation of motion in elastic medium.....	7
2.3 Dilatational and distortional waves - P and S waves.....	10
2.4 Rayleigh Waves.....	11
2.5 Lamb waves.....	16
2.6 Attenuation of Surface Waves and Material Damping.....	21
2.7 Summary.....	23
Chapter 3 Signal Processing Techniques.....	28
3.1 Introduction.....	28
3.2 1D Fourier Transform.....	28
3.3 2D Fourier Transform.....	32
3.4 Short Time Fourier Transform.....	33
3.5 Continuous Wavelet Transform.....	34
3.5.1 Introduction.....	34
3.5.2 Wavelet Energy.....	36
3.5.3 Requirements for wavelets.....	38
3.5.4 Morlet Wavelet.....	38

3.5.5	Instantaneous Phase from Wavelet Transform	39
3.6	Discrete Wavelet Transform	40
3.7	Empirical Mode Decomposition	41
3.8	Summary	42
Chapter 4	Literature Review on NDT of Concrete.....	46
4.1	Introduction.....	46
4.2	Ultrasonic Pulse Velocity (UPV) Test.....	46
4.3	Impact-Echo (IE) Test.....	47
4.3.1	Spectral C-scan	49
4.3.2	Surface Rendering Method	49
4.4	Fourier Transmission Coefficient (FTC) Method.....	49
4.5	Spectral Analysis of Surface Waves (SASW) and Multi- channel Analysis of Surface Waves (MASW) Methods	52
4.6	Material Damping from Wavelet Transform	54
4.7	Summary	55
Chapter 5	Calibration of Accelerometers	61
5.1	Problem Statement	61
5.2	Background	62
5.3	Calibration Tests	65
5.3.1	Test setup and procedure.....	65
5.3.2	Results of Tests	67
5.3.2.1	Results of Tests for Accelerometer A1	69
5.3.2.2	Results of Tests for Accelerometer A2	71
5.3.2.3	Results of Tests for Accelerometer A3	72
5.3.3	Conclusion and Discussions.....	73
5.4	Summary	75
Chapter 6	Evaluation of Condition Assessment Methodology.....	117
6.1	Introduction.....	117
6.2	Experimental Methodology.....	117
6.3	Phase I: Investigation on Surface Wave Characteristics Using Different Accelerometers.....	118
6.3.1	Laboratory Setup and Test Configurations	118
6.3.2	Data Analyses	120
6.3.2.1	Rayleigh Wave Velocity	120

6.3.2.2	Attenuation and Material Damping Ratio	121
6.3.2.2.1	Frequency Magnitudes.....	121
6.3.2.2.2	Peak to Peak Amplitude of Acceleration and Displacement Traces.....	123
6.3.2.2.3	Decomposed Signals from Discrete Wavelet Transform.....	123
6.3.2.2.4	Decomposed Signals from Empirical Mode Decomposition.....	124
6.3.2.2.5	Continuous Wavelet Transform.....	124
6.3.2.3	Frequency - Wavenumber Plots and Dispersion Curve	125
6.3.3	Characterization of the Cemented-Sand based on the Calibrated	127
	Accelerometers	127
6.3.4	Conclusions.....	129
6.4	Phase II: Investigation on Coupling.....	132
6.4.1	Data Analyses	132
6.4.2	Conclusions.....	134
6.5	Phase III: Investigation on Damage Assessment	136
6.5.1	Data Analyses	136
6.5.1.1	R-wave Velocity	136
6.5.1.2	Attenuation.....	138
6.5.1.3	Material Damping Ratio.....	138
6.5.1.4	Dispersion curve (phase velocity).....	139
6.5.2	Conclusions.....	140
6.6	Summary.....	141
Chapter 7	Condition Assessment of Concrete Beams	188
7.1	Introduction.....	188
7.2	Production of Concrete Beams	188
7.3	Mechanical tests.....	189
7.4	Laboratory Setup and Configuration for Ultrasonic Tests.....	190
7.5	The Results of Data Analyses	191
7.5.1	P-wave and R-wave Velocities	191
7.5.2	Attenuation.....	192
7.5.3	Material Damping Ratio.....	193
7.5.4	Dispersion curve (phase velocity).....	194
7.6	Summary and Conclusions.....	195
Chapter 8	Conclusions and Recommendations	227

8.1	Calibration of Accelerometers	227
8.2	Evaluation of the Condition Assessment Method.....	228
8.2.1	Phase I: Investigation on Surface Wave Characteristics	229
8.2.2	Phase II: Investigation on Coupling.....	230
8.2.3	Phase III: Investigation on Damage Assessment	230
8.3	Condition Assessment for Beams	231
	Bibliography	232
	Appendix A: Summary of ISO 16063 Standards.....	237
	Appendix B: Additional Figures for Chapter 5.....	239
	Appendix C: Matlab Code for Signal Processing Procedure	274
	Appendix D: Additional Figures for Section 6.4	293

List of Figures

Figure 2.1: Stresses acting on an infinitesimal solid in x-direction.	24
Figure 2.2: Compressional wave (P-wave) propagation (Bolt, 1978).	25
Figure 2.3: Shear wave (S-wave) propagation (Bolt, 1978).	25
Figure 2.4: Normalized horizontal, \mathbf{u} , and vertical, \mathbf{w} , displacements vs. normalized depth, $\mathbf{z}\lambda\mathbf{R}$ for different Poisson's ratios (Yang, 2009).	26
Figure 2.5: Rayleigh wave propagation (Bolt, 1978).	26
Figure 2.6: (left) Symmetric and (right) anti-symmetric Lamb modes in a plate (Yang, 2009). .	27
Figure 2.7: Dispersion curves for a cemented-sand medium for the given parameters: $d = 45$ cm, $V_p = 2000$ m/s and $V_s = 1200$ m/s.	27
Figure 3.1: A wavelet superposing with a harmonic signal to illustrate the regions providing positive or negative contribution to the integral.	43
Figure 3.2: Morlet function of $f_0 = 52$ kHz and $\tau = 1.12 \times 10^{-5}$: (a) in time domain (b) in frequency domain.	43
Figure 3.3: (upper) Series of wavelet spectra (lower) decomposition process by filter bank (Valens, 2004).	44
Figure 3.4: Sifting procedure for EMD.	45
Figure 4.1: UPV test setup (Jiang, 2007).	57
Figure 4.2: IE test procedure (Sansalone and Streett, 1997).	57
Figure 4.3: The Fourier spectrum at the top, wavelet marginal spectrum at the middle and the enhanced Fourier spectrum at the bottom (Po-Liang et al., 2008).	58
Figure 4.4: (a) Model of the specimen at the left (b) its 3D image after surface rendering at the right (Po-Liang et al., 2008).	58
Figure 4.5: (a) Experimental setup at the left (b) normalized transmitted amplitudes of the surface waves obtained from the experimental and numerical tests versus the normalized crack depth respect to wavelength (Aggelis, 2009).	59
Figure 4.6: FTC test configurations: (a) non-equal spacing configuration at the left (Popovics, 2000) (b) equal spacing configuration is at the right (Yang, 2009).	59
Figure 4.7: (a) SASW test setup at the top (b) MASW setup at the bottom (Park et al., 1997). ..	60
Figure 5.1: Schematic of the ultrasonic transmitter used in the tests (Tallavo et al., 2009).	76
Figure 5.2: Physical model of an accelerometer.	76
Figure 5.3: The calibration test setup with the laser-scanner.	77
Figure 5.4: Accelerometers (a) A1 at left, (b) A2 at the middle, and (c) A3 at right.	77
Figure 5.5: Locations where the signals are acquired.	78

Figure 5.6: Scheme for data processing procedure: FRFs are computed for acceleration, velocity and displacement.....	79
Figure 5.7: Excitation pulse for transmitter in time and frequency domains.....	80
Figure 5.8: Scan locations for no mass case.	80
Figure 5.9: Velocity on the top of the transmitter in time (COV = 6.9%) and frequency domains. Twenty velocity signals (each one is recorded after two hundred signals are averaged), which are measured on a length of 7 mm at the center of the transmitter's top face, are averaged.	81
Figure 5.10: Time history and Fourier spectrum of acceleration, velocity and displacement at the top of the transmitter under transient excitation of 125 Volt for no mass case. Velocity is computed by averaging twenty readings. Acceleration and displacement are computed from the filtered velocity.	82
Figure 5.11: Acceleration time histories (derivative of the average velocity) and corresponding Fourier spectra at normalized radius of -0.5, 0 and 0.5 respectively under transient excitation of 125 Volt.	83
Figure 5.12: Velocity time histories (average of two hundred measured signals) and corresponding Fourier spectra at normalized radius of -0.5, 0 and 0.5 respectively under transient excitation of 125 Volt.	84
Figure 5.13: Displacement time histories (integration of the average velocity) and corresponding Fourier spectra at normalized radius of -0.5, 0 and 0.5 respectively under transient excitation of 125 Volt.	85
Figure 5.14: Velocity Fourier spectra along the diameter of the transmitter under transient excitation of 125 Volt.	86
Figure 5.15: Displacement time history along the diameter of the transmitter under transient excitation of 125 Volt.	87
Figure 5.16: Effect of the added mass of the accelerometers on the response of the transmitter: (a) Maximum variation with respect to no mass case is observed for A3 with a reduction of 45% in velocity amplitude (each velocity time trace is computed by using 20 signals), (b) Fourier transform of the velocity time traces, (c) Frequency responses that are normalized with respect to no mass case.....	88
Figure 5.17: Comparison of normalized velocities under transient and sinusoidal excitations at the top of transmitter for no mass case. The continuous line represents the Fourier spectrum of velocity under transient excitation and the markers in the dashed line represent the maximum amplitudes in time domain under the corresponding frequency of sinusoidal excitation.....	89
Figure 5.18: Scan locations for Accelerometer A1.....	90
Figure 5.19: Time history and Fourier spectrum of the measured acceleration and the derived velocity and displacement under transient excitation of 2.5 Volt for A1. Velocity and displacement are computed from the filtered acceleration. Acceleration is computed using a sensitivity factor of 102.9 mV/g before computing the velocity and displacement.	91
Figure 5.20: Velocity on the top of the transmitter in time (COV = 9.9%) and frequency domains for A1 is mounted. Twenty velocity signals (each one is recorded after two hundred signals are	

averaged), which are measured on a length of 7 mm (3.5 mm on each side of the accelerometer), are averaged.	92
Figure 5.21: Time history and Fourier spectrum of acceleration, velocity and displacement at the top of the transmitter under transient excitation of 125 Volt for A1 is on the transmitter. Velocity is computed by averaging twenty readings. Acceleration and displacement are computed from the filtered velocity.	93
Figure 5.22: Velocity on the top of A1 in time (COV = 14%) and frequency domains. Twenty-one velocity signals (each one is recorded after two hundred signals are averaged), which are measured at a different location on the top of A1, are averaged.	94
Figure 5.23: Time history and Fourier spectrum of acceleration, velocity and displacement at the top of A1 under transient excitation of 125 Volt. Velocity is computed by averaging twenty one signals measured on the scan area shown in Figure 5.18. Acceleration and displacement are computed from the filtered velocity.	95
Figure 5.24: Acceleration time histories and Fourier spectra of (a,b) output, (c,d) input, and (e,f) vibration on the top of accelerometer A1. Input and top signals are divided by 50 (125V/2.5V) to ensure the same excitation voltage.	96
Figure 5.25: (a) Comparison of normalized velocities under transient and sinusoidal excitations at the top of transmitter for accelerometer A1 is on the transmitter. The continuous line represents the Fourier spectrum of velocity under transient excitation and the markers in the dashed line represent the maximum amplitudes in time domain under the corresponding frequency of sinusoidal excitation. (b) Comparison of normalized output accelerations of accelerometer under transient and sinusoidal excitations. The continuous line represents the Fourier spectrum of acceleration under transient excitation and the markers in the dashed line represent the maximum amplitudes in time domain under the corresponding frequency of sinusoidal excitation.	97
Figure 5.26: From top to bottom, the magnitudes and phases of (a, b) output acceleration, (c, d) input acceleration, and (e, f) frequency response function for A1.	98
Figure 5.27: Scan locations for Accelerometer A2 (a) top view, (b) side view.	99
Figure 5.28: Time history and Fourier spectrum of the recorded acceleration and the derived velocity and displacement under transient excitation of 125 Volt for A2. Velocity and displacement are computed from the filtered acceleration. Acceleration is computed using a sensitivity factor of 9.98 mV/g before computing the velocity and displacement.	100
Figure 5.29: Velocity on the top of the transmitter in time (COV = 13.9%) and frequency domains for A2 is mounted. Twenty velocity signals (each one is recorded after two hundred signals are averaged), which are measured on a length of 7 mm (3.5 mm on each side of the accelerometer), are averaged.	101
Figure 5.30: Time history and Fourier spectrum of acceleration, velocity and displacement at the top of the transmitter under transient excitation of 125 Volt for A2 is on the transmitter. Velocity is computed by averaging twenty readings. Acceleration and displacement are computed from the filtered velocity.	102

Figure 5.31: Velocity on the top of A2 in time (COV = 16.1%) and frequency domains. Thirty-five velocity signals (each one is recorded after two hundred signals are averaged), which are measured on the four sides of accelerometer's top case, are averaged. 103

Figure 5.32: Time history and Fourier spectrum of acceleration, velocity and displacement at the top of A2 under transient excitation of 125 Volt. Velocity is computed by averaging 4x13 signals measured on the scan areas (Fig. 5.27). Acceleration and displacement are computed from the filtered velocity. 104

Figure 5.33: Acceleration time histories and Fourier spectra of (a,b) output, (c,d) input, and (e,f) vibration on the top of accelerometer A2. 105

Figure 5.34: (a) Comparison of normalized velocities under transient and sinusoidal excitations at the top of transmitter for accelerometer A2 is on the transmitter. The continuous line represents the Fourier spectrum of velocity under transient excitation and the markers in the dashed line represent the maximum amplitudes in time domain under the corresponding frequency of sinusoidal excitation. (b) Comparison of normalized output accelerations of accelerometer under transient and sinusoidal excitations. The continuous line represents the Fourier spectrum of acceleration under transient excitation and the markers in the dashed line represent the maximum amplitudes in time domain under the corresponding frequency of sinusoidal excitation. All measurements are taken for A2 with the spacer on top. 106

Figure 5.35: From top to bottom, the magnitudes and phases of (a, b) output acceleration, (c, d) input acceleration, and (e, f) frequency response function for A2..... 107

Figure 5.36: Scan locations for Accelerometer A3..... 108

Figure 5.37: Time history and Fourier spectrum of the measured acceleration and the derived velocity and displacement under transient excitation of 25 Volt for A3. Velocity and displacement are computed from the filtered acceleration. Acceleration is computed using a sensitivity factor of 504.1 mV/g before computing the velocity and displacement. 109

Figure 5.38: Velocity on the top of the transmitter in time (COV = 28.3%) and frequency domains for A3 is mounted. Twenty velocity signals (each one is recorded after two hundred signals are averaged), which are measured on a length of 7 mm (3.5 mm on each side of the accelerometer), are averaged. 110

Figure 5.39: Time history and Fourier spectrum of acceleration, velocity and displacement at the top of the transmitter under transient excitation of 125 Volt for A3 is on the transmitter. Velocity is computed by averaging twenty readings. Acceleration and displacement are computed from the filtered velocity. 111

Figure 5.40: Velocity on the top of A3 in time (COV = 22.7%) and frequency domains. Thirty-six velocity signals (each one is recorded after two hundred signals are averaged), which are measured on the four sides of accelerometer's top case, are averaged. 112

Figure 5.41: Time history and Fourier spectrum of acceleration, velocity and displacement at the top of A3 under transient excitation of 125 Volt. Velocity is computed by averaging nine signals measured on the center scan area (Fig. 5.36). Acceleration and displacement are computed from the filtered velocity. 113

Figure 5.42: Acceleration time histories and Fourier spectra of (a,b) output, (c,d) input, and (e,f) vibration on the top of accelerometer A3. Input and top signals are divided by 5 ($I_{25V}/25V$) to ensure the same excitation voltage.	114
Figure 5.43: (a) Comparison of normalized velocities under transient and sinusoidal excitations at the top of transmitter for accelerometer A3 is on the transmitter. The continuous line represents the Fourier spectrum of velocity under transient excitation and the markers in the dashed line represent the maximum amplitudes in time domain under the corresponding frequency of sinusoidal excitation. (b) Comparison of normalized output accelerations of accelerometer under transient and sinusoidal excitations. The continuous line represents the Fourier spectrum of acceleration under transient excitation and the markers in the dashed line represent the maximum amplitudes in time domain under the corresponding frequency of sinusoidal excitation.....	115
Figure 5.44: From top to bottom, the magnitudes and phases of (a, b) output acceleration, (c, d) input acceleration, and (e, f) frequency response function for A3.....	116
Figure 6.1: Schema for the testing instruments.	142
Figure 6.2: Testing configurations for (a) Test I and II, (b) Test III.....	143
Figure 6.3: Normalized time histories for Test (a) I, (b) II and (c) III.....	144
Figure 6.4: Normalized wavelet magnitudes for Test (a) I, (b) II and (c) III.	145
Figure 6.5: Normalized Fourier spectra for Test (a) I, (b) II and (c) III.	146
Figure 6.6: Attenuation trend of frequencies from non-windowed time signals for Test III. Fourier magnitudes for each frequency are normalized by the maximum value of that frequency obtained from the whole set of spectra.	147
Figure 6.7: The R^2 values for attenuation of frequencies computed after windowing the Fourier spectra with window widths ranging from 1 to 10 kHz. The R^2 is 0.7 for 52 kHz after a frequency window width of 1 kHz.....	148
Figure 6.8: Attenuation trend for spectral magnitude of 52 kHz: experimental and estimated trends from non-windowed time signals.....	149
Figure 6.9: Normalized windowed time histories and corresponding Fourier spectra of Test (a,b) I, (c,d) II and (e,f) III.....	150
Figure 6.10: Attenuation trend of frequencies from windowed time signals for Test III. Fourier magnitudes for each frequency are normalized by the maximum value of that frequency obtained from the whole set of spectra.	151
Figure 6.11: The R^2 values for attenuation of frequencies computed after windowing the Fourier spectra with window widths ranging from 1 to 10 kHz. The R^2 is 0.83 for 52 kHz for a frequency window width of 1 kHz. Time histories are windowed before FT.	152
Figure 6.12: Attenuation trend for spectral magnitude of 52 kHz: experimental and estimated trends from windowed time signals.....	153
Figure 6.13: Normalized (a,b) acceleration, (c,d) velocity, (e,f) displacement time histories and corresponding Fourier spectra for Test III. Red dots mark the pit and black ones mark the peak of R-wave arrival.....	154

Figure 6.14: Attenuation trends of PTP values from acceleration and displacement time histories for Test III.	155
Figure 6.15: Normalized (a) decomposed time signals and (b) associated Fourier spectra for Test III.	156
Figure 6.16: (a) Normalized level 4 (frequency bandwidth of 31.25-62.5 kHz) for all receivers from Test III and (b) associated Fourier spectra.	157
Figure 6.17: Attenuation trend for the spectral areas of level 2, 3, 4 and 5 from Test III.	158
Figure 6.18: Normalized (a) IMFs and (b) associated Fourier spectra for Test III.	159
Figure 6.19: (a) Normalized 1 st IMF for all receivers from Test III and (b) associated Fourier spectra.	160
Figure 6.20: Attenuation trends based on the spectral areas of the first three IMFs from Test III.	161
Figure 6.21: (a) Wavelet magnitude, (b) Damped frequency at arrival of R-wave, (c) Material damping at each receiver location for Test III.	162
Figure 6.22: (a) Material damping ratios from wavelet transform determined using different sets of receivers from Test III, and (b) the associated R ² values.	163
Figure 6.23: Fundamental Lamb Modes for the test medium.	164
Figure 6.24: The f-k plots transformed from the non-windowed time histories and dispersion curves extracted from the f-k plots for Test (a,b) I, (c,d) II and (e,f) III.	165
Figure 6.25: The f-k plots transformed from the windowed time histories and dispersion curves extracted from the f-k plots for Test (a,b) I, (c,d) II and (e,f) III.	166
Figure 6.26: Wrapped phases from (a) non-windowed and (b) windowed time histories.	167
Figure 6.27: Dispersion curves and R ² values computed from unwrapped phase spectra of (a) non-windowed and (b) windowed time histories.	168
Figure 6.28: Time histories and Fourier spectra of the selected original and normalized signals respect to FRF for A1.	169
Figure 6.29: Time histories and Fourier spectra of the selected original and normalized signals respect to FRF for A2.	169
Figure 6.30: Time histories and Fourier spectra of the selected original and normalized signals respect to FRF for A3.	170
Figure 6.31: Comparison of attenuation trends from Test I, II and III: based on (a) Total area of Fourier spectra for windowed time signals, (b) Wavelet magnitudes for a Morlet wavelet of 52 kHz central frequency, (c) Spectral area of decomposed signals form DWT (Level-4), (d) Spectral area of decomposed signals from EMD (IMF 1).	171
Figure 6.32: Attenuation trends of different quantities: Area, total area of Fourier spectra; 52 kHz, Fourier magnitude of 52 kHz; DWT, spectral area of decomposed signal Level-4; WT, wavelet magnitudes for a Morlet wavelet of 52 kHz central frequency; EMD, spectral area of the 1 st IMF. Total spectral area and magnitude of 52 kHz are obtained from non-windowed time signals.	172

Figure 6.33: Attenuation trends for different couplings.	173
Figure 6.34: Attenuation trends obtained from the receiver array (Test5-S2) and the reference receiver (Test6-S2).....	173
Figure 6.35: Attenuation trends obtained under different excitation pulse.	174
Figure 6.36: Waveform captured along the receiver array under 5 kHz steady-state sinusoidal excitation.....	174
Figure 6.37: The damaged section consists of 7 holes at the center of the receiver array.....	175
Figure 6.38: Signal processing algorithm.....	175
Figure 6.39: Comparison of the cases D0 and D12 (a) time histories, (b) Fourier spectra. A Tukey window is applied to the time signals prior to FT.	176
Figure 6.40: Reflection due to the defects (case D12) (a) time histories, (b) Fourier spectra. ...	177
Figure 6.41: R-wave velocity respect to the damage case: $\sigma = 120$ m/s, COV = 11% and $R^2 = 0.73$	178
Figure 6.42: Attenuation trends for (b) wavelet magnitudes and (c) spectral area of decomposed signal (level 4) from DWT.....	179
Figure 6.43: Attenuation coefficients, α , normalized respect to the minimum value in the trend, vs. the damage case; α is calculated from FT (spectral area), CWT (wavelet magnitudes) and DWT (spectral area of level 4).....	180
Figure 6.44: The attenuation coefficient, α , obtained from the spectral area of level 4 from DWT respect to the damage case: $\sigma = 0.5$ m ⁻¹ , COV = 5.6% and $R^2 = 0.83$ for negative exponential model.....	181
Figure 6.45: The material damping ratio, ζ respect to the damage case: $\sigma = 0.6\%$, COV = 12% and $R^2 = 0.87$ for negative exponential model.....	181
Figure 6.46: The reference phase velocity curve obtained from undamaged (0 cm) case; the curve is fitted using a high order polynomial model to ensure continuity for the frequencies from 0 to 50 kHz.....	182
Figure 6.47: Dispersion (phase velocity) curve for damage depth of (l) 10, (k) 11 and (m) 12 cm.	186
Figure 6.48: Dispersion index, DI, respect to the damage case: COV = 22% and $R^2 = 0.92$ for linear model.	187
Figure 7.1: The beams and the associated cones from the compression tests of cylinders.	198
Figure 7.2: Beams' density vs. design void volume (blue curve) and void volume computed based on the density vs. design void volume (red curve). Red curve represent the relative void volume respect to Beam 1, actual values should be larger than the ones provided in the plot... ..	199
Figure 7.3: The prisms cut out from the beams.	200
Figure 7.4: The selected cross-sections of the beams.	201
Figure 7.5: Compressive strength for the cylinders and the rectangular prisms samples cut out from the beams vs. void volume. Outliners are excluded.....	202

Figure 7.6: Ultrasonic testing instrumentation.....	203
Figure 7.7: Lateral excitation configuration.	203
Figure 7.8: (a) Time histories and (b) frequency spectra for Beam 1 (no-void case).....	204
Figure 7.9: (a) Time histories and (b) frequency spectra for Beam 2 (%5 void).....	205
Figure 7.10: (a) Time histories and (b) frequency spectra for Beam 3 (%10 void).....	206
Figure 7.11: (a) Time histories and (b) frequency spectra for Beam 4 (%15 void).....	207
Figure 7.12: (a) Time histories and (b) frequency spectra for Beam 5 (%20 void).....	208
Figure 7.13: (a) Time histories and (b) frequency spectra for Beam 6 (%30 void).....	209
Figure 7.14: P-wave velocity computed for Beam 1.	210
Figure 7.15: P-wave velocity computed from time histories vs. void volume of beam.	211
Figure 7.16: Rayleigh wave velocity computed from PTP magnitudes vs. void volume of beam.	211
Figure 7.17: Attenuation trend for all frequencies (a) Beam 1, (b) Beam 2.	212
Figure 7.18: Attenuation trends for each beam obtained from DWT (Level 4).	215
Figure 7.19: The measured and curve-fitted attenuation trends; α is computed from the curve- fitted trend.	215
Figure 7.20: Attenuation coefficients vs. void ratio.	216
Figure 7.21: Material damping ratio computed from WT vs. void volume of beam.....	216
Figure 7.22: Windowed time signals and associated frequency spectra from Beam 1 for phase velocity calculations.....	217
Figure 7.23: Frequency and wavenumber plots from windowed signals (a) Beam 1, (b) Beam 2.	218
Figure 7.24: The reference curve from Beam 1.	221
Figure 7.25: Experimental dispersion curves (two maximum points in the f-k plots (Figs. 7.23) are picked for each frequency) along with the theoretical Lamb modes that are obtained from the Rayleigh-Lamb frequency equation (Eq. 2.35a).....	222
Figure 7.26: The selected portions of the dispersion curves (Fig. 7.25) to be used for the DI calculation.	223
Figure 7.27: Dispersion index (DI_v) vs. void volume for vertical excitation.	223
Figure 7.28: Dispersion curves attained under horizontally oriented transmitter. Theoretical Lamb modes are also shown.	224
Figure 7.29: Dispersion index (DI_h) vs. void volume for horizontal excitation.	225
Figure 7.30: Signal processing algorithm for the beam.	226

List of Tables

Table 5.1 Nominal properties of accelerometers	66
Table 5.2 Calibration measurements.....	67
Table 5.3 Maximum vibration measurements	69
Table 5.4 Maximum vibration measurements	70
Table 5.5 Maximum vibration measurements	72
Table 5.6 Maximum vibration measurements	73
Table 5.7 Coefficient of Variations for Input Signal	74
Table 5.8 Displacements	74
Table 6.1 Summary of the test data	119
Table 6.2 Summary of velocities	121
Table 6.3 Material damping ratios	128
Table 6.4 Summary of attenuation coefficients	129
Table 6.5 Summary of the tests.....	132
Table 6.6 Summary of Statistics of Attenuation Coefficients	140
Table 6.7 Summary of statistics for surfaces wave characteristics.....	141
Table 7.1 The concrete recipe.....	189
Table 7.2 The properties of beams.....	190
Table 7.3 Summary of the statistics for characteristics	196

Chapter 1 Introduction

1.1 Problem Statement

The condition assessment of concrete structures is at the forefront of public agenda in order to allow for rational decisions regarding what action should be taken for the renewal of aging infrastructures. Deterioration of concrete structures may be caused by many reasons (e.g. corrosion, overloading, aging, temperature effects, ground shaking) that produce cracks at either the micro or macro scale. Methods based on surface wave propagation have been used for evaluating the degradation in concrete. Monitoring variations in the surface wave characteristics, such as attenuation and dispersion, makes it possible to infer the material conditions. Previous studies utilizing the surface wave methods to detect the surface-breaking cracks have provided satisfactory results (Yang et al. 2009, Yang et al. 2010, Angelis et al. 2009, Zerwer et al. 2005, Popovics et al. 2000). However, a complete damage assessment of whole element is not available. The previously proposed procedures have to be repeated for different cracks along the structural element; this limits its applicability in the field. Also, cracks may not be visible; for instance in the case of corrosion, delamination may be initiated along the reinforcements which cannot be observed until spalling occurs on the surface. Therefore, instead of evaluating crack depth, a comprehensive approach for damage detection is proposed in this study based on the multi-channel analysis of surface waves (MASW) method.

1.2 Current Methods for Non-destructive Testing of Concrete

The condition assessment of construction materials either be destructive or non-destructive. The search for innovative non-destructive testing (NDT) methods has been accelerated in the past decade due to the physical and economical constraints of destructive tests. Conventional inspection methods for concrete are either not qualitative or time consuming, such as core sampling. Although destructive testing is straightforward, it causes further damage on the structure. Moreover, to determine the dynamic characteristics of construction materials, complex

test laboratory equipments is required, such as dynamic testing frames and shaking tables which is only applicable for large strain deformations. Because of the drawbacks of destructive tests, non-destructive methods are becoming more needed in practice.

Different NDT methods are commercially available for specific applications, such as acoustic emission (AE), ground penetrating radar (GPR), infrared thermography and ultrasound, (ACI 228.2R-98, RILEM TC 212-ACD, IAEA-TCS-17, Goueygou et al. 2008, Daniels 2004). Each of these methods has different levels of reliability and efficiency; therefore, the use of hybrid methods is the new trend in NDT (Keel et al., 2012). Ultrasonic tests have widespread usage because of their fast execution, low cost, and practicability. Some common ultrasonic tests available are ultrasonic pulse velocity (UPV), impact echo (IE), and spectral analysis of surface waves (SASW) (ASTM C597 2002, ASTM C1383-98a, Heisey et al. 1982). Although, the last one is a seismic method using low frequencies, ultrasonic waves can be also utilized by employing ultrasonic transducers and selecting proper receiver spacing (Kalinski et al., 1994). The first two methods are preferred for thickness evaluation and flaw detection. Both methods are based only on the measurement of wave velocities. However, in the case of a crack with contacting faces, these methods are not capable of detecting the crack even it is a deeper one (Aggelis et al. 2009). On the other hand, the SAWS method is superior among all since a depth profile of the material is obtained. Nevertheless, all three methods may be time-consuming because the testing procedure has to be repeated many times to cover a structural element completely. Therefore, a comprehensive approach to assess the condition of structural elements is needed. Multi-channel analysis of surface waves (MASW) testing is convenient to assess larger portion of an element at once. MASW was originally developed for determination of the shear-wave profile of shallow soil layers (Park et al., 1997). However, additional information about the surface waves, such as primary (P-wave) and Rayleigh (R-wave) wave velocities, attenuation, phase velocity and material damping, can be assessed using the MASW test configuration. All of these characteristics are affected by defects or degradation in the material.

Apart from the chosen test configuration, the characteristics of the transducer employed in the test setup also affects significantly the test results. In UPV testing, ultrasonic transducers are used to measure wave velocities only (travel time method); on the other hand, full-waveform

methods use the whole time signal to extract important information, such as phase velocity and material damping (Yang et al., 2011). Since the ultrasonic signals are affected by the characteristics of the transducers, the measured signals should be normalized with respect to the frequency response function of the transducer to obtain the real response of the tested specimen.

1.3 Objectives

The main objective of this research is to establish a comprehensive methodology for condition assessment of cemented materials based on the use of surface wave characteristics (velocity, attenuation and dispersion). To achieve the major objective, the MASW test configuration is implemented at ultrasonic frequency range and the recorded signals are subjected to various signal processing techniques to extract the most relevant information. In addition, a new calibration procedure is developed to determine the frequency response functions of the piezoelectric accelerometers in a frequency range beyond their flat response. The ISO 16063 "Methods for the calibration of vibration and shock transducers" standards have a upper frequency limit of 10 kHz for the transducer calibration. However, the current laser technology allows to measure high frequencies with displacements in the order of nanometer. Therefore, the new procedure is based on the use of a high-frequency laser scanner which allows to measure frequencies up to 1 MHz. This research includes three main studies:

Study I - Calibration of ultrasonic accelerometers beyond their flat response: A new calibration procedure, which is based on the ISO 16063-13:2001 recommendations, is introduced to measure the frequency response function (FRF) of the piezoelectric accelerometers beyond the flat response. A microscopic laser scanner is employed to measure the output response generated by a piezoelectric transmitter when the accelerometer is attached on top of the transmitter. The FRFs of three different accelerometers are determined for a frequency range from 10 to 70 kHz. The calibrated accelerometers are then used for the characterization of an intact cemented-sand medium.

Study II - Evaluation of the new condition assessment method on a medium with well-defined defect sizes: The new condition assessment methodology is first evaluated on a half-space

medium made of cemented-sand containing defects of well-defined size and shape. This study includes three experimental phases to determine: (i) a reliable signal processing procedure to extract the main surface wave characteristic using different accelerometers, (ii) a consistent coupling mechanism for the transducers, and (iii) the sensitivity of the main surface wave characteristic with respect to the damage level.

Study III - Testing of the proposed assessment procedure on lab-scale concrete beams with distributed defects: Ultrasonic and mechanical tests are conducted for six lab-scale concrete beams with different damage levels simulated by different percentages of void space. The relationships between the damage volume and the wave characteristics, P-wave and Rayleigh-wave velocities, attenuation coefficients, material damping ratios, and the dispersion index along with the compression strength are evaluated.

1.4 Research Methodology

The proposed condition assessment methodology is based on the measurement of surface waves in the ultrasonic frequency range. For these measurements, an array of piezoelectric transducers calibrated beyond their nominal frequency range is needed. The recorded signals must be analyzed using different signal processing techniques such as one-dimensional and two dimensional Fourier transforms, wavelet transform, and the empirical mode decomposition method. The proposed methodology, including the new transducer calibration procedure using a nano-laser interferometer, is first tested on a lightly cemented material representing a half-space. Then, a pilot study is performed using concrete beams with different levels of soft aggregates is performed to show the potential of the new methodology to identify distributed damage in concrete members.

The first step of this research is the development of a new calibration procedure for the determination of the transfer functions of piezoelectric transducers. These transducers are commonly used for velocity measurements where only the time of the first arrival is needed. However for the new condition assessment methodology, which is based on time and frequency domains calculations, the full waveform is needed. Hence, the high frequency response of the

transducers beyond their nominal frequency range is required. The new calibration procedure employs a laser vibrometer; which is capable of measuring frequencies up to 1 MHz and displacements in the order of nanometer. This laser vibrometer is a state-of-the-art equipment has been commercially available only in recent years. With this new laser system, it is possible to precisely measure the vibrations occurring on the top of the ultrasonic transmitter; which is used to generate the mechanical perturbation in the tested material. The measurement of the actual response of the transmitter is critical to compute the transfer functions of the receivers.

After the new calibration procedure is developed, the new condition assessment methodology is used on a laboratory scale model of a semi-infinite half-space medium of lightly cemented sand. This geometry is selected to minimize the effects of the wave reflections from boundaries. The surface waves recorded on this sandbox are used to test different signal processing techniques for the extraction of key signal properties such as wave velocity, attenuation coefficient, material damping and phase velocities. Many signal processing techniques including windowing, filtering, one and two dimensional Fourier transforms, continuous and discrete wavelet transforms (CWT and DWT) and empirical mode decomposition (EMD) are used to process the recorded signals.

After the ultrasonic tests on the cemented-sand with weak surface conditions, the effect of the coupling on the results is investigated. Therefore, a sub-study is presented using different coupling conditions for the receivers. To ensure a high level of repetition of the tests, the set of receivers permanently fixed on the specimen. The soft cemented-sand specimen is damaged by drilling regular-shaped holes along the area under investigation. The ultrasonic tests are repeated for different depths of holes to study the sensitivity of the selected wave characteristics (velocity, attenuation, damping and dispersion) with respect to the damage depth. Finally, a pilot study is conducted on lab-scale concrete beams in order to evaluate the damage level of the distributed defects. The signal processing procedure developed for the half-space medium is modified for the beam geometry.

1.5 Thesis Organization

Chapter 1 introduces the research.

Chapter 2 explains the fundamentals of wave propagation in elastic materials including body, Rayleigh and Lamb waves. The wave equations for different boundary conditions and associated solutions are presented.

Chapter 3 summarizes the most common signal processing techniques: 1D and 2D Fourier transforms, short time Fourier transform, continuous and discrete wavelet transforms, and empirical mode decomposition.

Chapter 4 reviews the literature on non-destructive techniques for concrete including ultrasonic pulse velocity (UPV), impact echo (IE), Fourier transmission coefficient (FTC), the spectral analysis of surface waves (SASW), and the multi-channel version (MASW).

In *Chapter 5*, the new calibration procedure for piezoelectric transducers is explained and evaluated on three different accelerometers. The limitations and applicability of the procedure are discussed.

Chapter 6 presents the experimental work conducted on the cemented-sand in three main sections: (i) development of the signal processing procedure, (ii) investigation of coupling conditions, and (iii) evaluation of the new condition assessment method on cemented-sand. The chapter also includes the characterization of the cemented-sand by using the calibrated accelerometers.

Chapter 7 covers the experimental work conducted on the concrete beams; which includes the construction of the beams, and the mechanical and ultrasonic tests. The effect of the damage on the surface wave characteristic are discussed, and the modifications needed on the signal processing procedure (developed in Chapter 6) for the beams are explained.

Chapter 8 summarizes the conclusion for all three studies with recommendations for future study.

Chapter 2 Wave Motion

2.1 Introduction

In this chapter the fundamentals of wave propagation in elastic materials are reviewed. Depending on the boundary conditions, different types of waves exist in a concrete member. In the case of infinite medium, two types of waves are observed: dilatational and distortional waves. While in the former one the particle motion is along the direction of the wave propagation, in the latter the particle motion is perpendicular to the distortion of the wave. In a finite medium with free surfaces, surface waves are generated due to the interaction of the body waves and the medium boundaries. The particle motion of the surface waves is elliptical. In case of only one traction-free boundary, Rayleigh waves occur. Meanwhile, two traction-free boundaries produce Lamb (Plate) waves.

Firstly, the wave equation is developed from the equation of motion of an elastic infinitesimal element. The solutions regarding different boundary conditions are derived in the order of infinite (unbounded) medium, semi-finite (one traction-free surface) medium and the plate with two traction-free surfaces.

2.2 Equation of motion in elastic medium

The derivations presented next are taken mostly from Kolsky (2003). Figure 2.1 shows stresses acting on an infinitesimal body in x direction of which the resulting force, F_R is:

$$F_R = \left(\sigma_{xx} + \frac{\partial \sigma_{xx}}{\partial x} \delta x \right) \delta y \delta z - \sigma_{xx} \delta y \delta z + \left(\sigma_{xy} + \frac{\partial \sigma_{xy}}{\partial y} \delta y \right) \delta x \delta z - \sigma_{xy} \delta x \delta z + \left(\sigma_{xz} + \frac{\partial \sigma_{xz}}{\partial z} \delta z \right) \delta x \delta y - \sigma_{xz} \delta x \delta y \quad (2.1)$$

The simplified form for the above equations is:

$$F_R = \left(\frac{\partial \sigma_{xx}}{\partial x} + \frac{\partial \sigma_{xy}}{\partial y} + \frac{\partial \sigma_{xz}}{\partial z} \right) \delta x \delta y \delta z \quad (2.2)$$

Regarding Newton's second law, the resulting force is equal to:

$$\left(\frac{\partial \sigma_{xx}}{\partial x} + \frac{\partial \sigma_{xy}}{\partial y} + \frac{\partial \sigma_{xz}}{\partial z} \right) \delta x \delta y \delta z = (\rho \delta x \delta y \delta z) \frac{\partial^2 u}{\partial t^2} \quad (2.3)$$

where ρ is density and u is the displacement in axis x . Likewise, Eq. 2.3 can be written for the y and z axes as:

$$\rho \frac{\partial^2 u}{\partial t^2} = \left(\frac{\partial \sigma_{xx}}{\partial x} + \frac{\partial \sigma_{xy}}{\partial y} + \frac{\partial \sigma_{xz}}{\partial z} \right) \quad (2.4a)$$

$$\rho \frac{\partial^2 v}{\partial t^2} = \left(\frac{\partial \sigma_{yx}}{\partial x} + \frac{\partial \sigma_{yy}}{\partial y} + \frac{\partial \sigma_{yz}}{\partial z} \right) \quad (2.4b)$$

$$\rho \frac{\partial^2 w}{\partial t^2} = \left(\frac{\partial \sigma_{zx}}{\partial x} + \frac{\partial \sigma_{zy}}{\partial y} + \frac{\partial \sigma_{zz}}{\partial z} \right) \quad (2.4c)$$

where v and w are displacements in axes y and z respectively. The stress parameters in Eqs. 2.4 can be replaced with the elastic relations for an isotropic material derived from Hooke's law:

$$\sigma_{xx} = \lambda \Delta + 2\mu \varepsilon_{xx} \quad (2.5a) \quad \sigma_{yz} = \mu \varepsilon_{yz} \quad (2.5d)$$

$$\sigma_{yy} = \lambda \Delta + 2\mu \varepsilon_{yy} \quad (2.5b) \quad \sigma_{zx} = \mu \varepsilon_{zx} \quad (2.5e)$$

$$\sigma_{zz} = \lambda \Delta + 2\mu \varepsilon_{zz} \quad (2.5c) \quad \sigma_{xy} = \mu \varepsilon_{xy} \quad (2.5f)$$

where $\Delta = \frac{\partial u}{\partial x} + \frac{\partial v}{\partial y} + \frac{\partial w}{\partial z}$ is the dilatation (volumetric) strain and λ and μ are the elastic constants (Lame's constants). The relationships between Lamé's constants and the engineering constants, namely Young's modulus E , the shear modulus G , Poisson's ratio ν , the bulk modulus k , and the constrained modulus M are given as:

$$E = \frac{\mu(3\lambda + 2\mu)}{\lambda + \mu} \quad (2.6a)$$

$$G = \mu \quad (2.6b)$$

$$\nu = \frac{\lambda}{2(\lambda + \mu)} \quad (2.6c)$$

$$k = \lambda + \frac{2\mu}{3} \quad (2.6d)$$

$$M = \lambda + 2\mu \quad (2.6e)$$

Substituting the elastic stress-strain relations (Eqs. 2.6) into Newton's second law for axis x (Eq. 2.4a) results in Navier's equation:

$$\rho \frac{\partial^2 u}{\partial t^2} = \frac{\partial}{\partial x} (\lambda \Delta + 2\mu \varepsilon_{xx}) + \frac{\partial}{\partial y} (\mu \varepsilon_{xy}) + \frac{\partial}{\partial z} (\mu \varepsilon_{xz}) \quad (2.7)$$

Since strains are defined as:

$$\varepsilon_{xx} = \frac{\partial u}{\partial x} \quad \varepsilon_{xz} = \frac{\partial w}{\partial x} + \frac{\partial u}{\partial z} \quad \varepsilon_{xy} = \frac{\partial v}{\partial x} + \frac{\partial u}{\partial y} \quad (2.8)$$

Eq. 2.7 can be written for axis x as:

$$\rho \frac{\partial^2 u}{\partial t^2} = (\lambda + \mu) \frac{\partial \Delta}{\partial x} + \mu \nabla^2 u \quad (2.9a)$$

where $\nabla^2 = \frac{\partial^2}{\partial x^2} + \frac{\partial^2}{\partial y^2} + \frac{\partial^2}{\partial z^2}$, is Laplacian operator. As for the other two directions:

$$\rho \frac{\partial^2 v}{\partial t^2} = (\lambda + \mu) \frac{\partial \Delta}{\partial y} + \mu \nabla^2 v \quad (2.9b)$$

$$\rho \frac{\partial^2 w}{\partial t^2} = (\lambda + \mu) \frac{\partial \Delta}{\partial z} + \mu \nabla^2 w \quad (2.9c)$$

Eqs. 2.9 are called one-dimensional wave equations.

2.3 Dilatational and distortional waves - P and S waves

The wave equations given Eqs. 2.9 represent the motion of an isotropic elastic body without any body force and involve two types of wave propagation. To identify the velocities of these two waves, manipulation of the wave equations is needed. If both sides of Eqs. 2.9 are differentiated respect to x , y and z successively and added up, the following expression is obtained:

$$\rho \frac{\partial^2 \Delta}{\partial t^2} = (\lambda + 2\mu) \nabla^2 \Delta \quad (2.10)$$

This equation implies that the dilatation, Δ , propagates with a velocity of $\sqrt{(\lambda + 2\mu)/\rho}$, which is the velocity of compressional wave:

$$V_p = \sqrt{\frac{\lambda + 2\mu}{\rho}} = \sqrt{\frac{M}{\rho}} \quad (2.11)$$

To find out the velocity of the second wave, volumetric quantity, Δ , should be eliminated from the wave equations. Therefore, Eq. 2.9b and 2.9c are differentiated respect to y and z successively and then subtracted. Hence:

$$\rho \frac{\partial^2}{\partial t^2} \omega_x = \mu \nabla^2 \omega_x \quad (2.12a)$$

is obtained where $2\omega_x = \frac{\partial w}{\partial y} - \frac{\partial v}{\partial z}$ is the rotation about the axis x . Similarly for the axes y and z are written as:

$$\rho \frac{\partial^2}{\partial t^2} \omega_y = \mu \nabla^2 \omega_y \quad (2.12b)$$

$$\rho \frac{\partial^2}{\partial t^2} \omega_z = \mu \nabla^2 \omega_z \quad (2.12c)$$

This set of equations reveals the velocity of the rotation of the body, in other words the transverse wave:

$$V_s = \sqrt{\frac{\mu}{\rho}} \quad (2.13)$$

Eq. 2.11 and 2.13 are the velocities of the dilatation and rotation of a body within an infinite medium. The dilatational and rotational velocities are also called P-wave (primary, longitudinal, compressional) and S-wave (secondary, transverse, and shear) velocities. Figures 2.2 and 2.3 show the compressional and shear wave propagations respectively.

2.4 Rayleigh Waves

In the case of a traction-free surface, surface waves emerge. For a 2D solution of the wave equation, xy plane can be assumed as the traction-free surface with axis z is positive through the interior of the solid. So that, the 2D displacements can be defined with the potential functions, ϕ and ψ defined as:

$$u = \frac{\partial \phi}{\partial x} + \frac{\partial \psi}{\partial z} \quad \text{and} \quad w = \frac{\partial \phi}{\partial z} - \frac{\partial \psi}{\partial x} \quad (2.14)$$

Then dilation and rotation may be written as:

$$\Delta = \frac{\partial u}{\partial x} + \frac{\partial w}{\partial z} = \nabla^2 \phi \quad (2.15)$$

$$2\omega_x = \frac{\partial u}{\partial z} - \frac{\partial w}{\partial x} = \nabla^2 \psi \quad (2.16)$$

In Eq. 2.15 and 2.16, ϕ and ψ correspond to dilation and rotation respectively. This representation allows to separate these two movements.

Substituting Eqs. 2.14 and 2.15 into the wave equation (Eq. 2.9a and 2.9c) results in:

$$\rho \frac{\partial}{\partial x} \left(\frac{\partial^2 \phi}{\partial t^2} \right) + \rho \frac{\partial}{\partial z} \left(\frac{\partial^2 \psi}{\partial t^2} \right) = (\lambda + 2\mu) \frac{\partial}{\partial x} (\nabla^2 \phi) + \frac{\partial}{\partial z} (\nabla^2 \psi) \quad (2.17a)$$

$$\rho \frac{\partial}{\partial z} \left(\frac{\partial^2 \phi}{\partial t^2} \right) - \rho \frac{\partial}{\partial x} \left(\frac{\partial^2 \psi}{\partial t^2} \right) = (\lambda + 2\mu) \frac{\partial}{\partial z} (\nabla^2 \phi) - \frac{\partial}{\partial x} (\nabla^2 \psi) \quad (2.17b)$$

Adding and subtracting these equations (Eqs. 2.17) give the following Helmholtz equations:

$$\frac{\partial^2 \phi}{\partial t^2} = \left(\frac{\lambda + 2\mu}{\rho} \right) \nabla^2 \phi = V_p^2 \nabla^2 \phi \quad (2.18a)$$

$$\frac{\partial^2 \psi}{\partial t^2} = \left(\frac{\mu}{\rho} \right) \nabla^2 \psi = V_s^2 \nabla^2 \psi \quad (2.18b)$$

Since a plane harmonic solution is sought in axis x to Eq. 2.18a and 2.18b, ϕ and ψ can be defined as:

$$\phi = F(z) e^{i(\kappa x - \omega t)} \quad (2.19a)$$

$$\psi = G(z) e^{i(\kappa x - \omega t)} \quad (2.19b)$$

which represent a sinusoidal wave traveling in axis x with a frequency of $f = \omega/2\pi$ and velocity of $c = \omega/\kappa$. κ is the wave number, $i = \sqrt{-1}$, F and G are the functions of amplitudes in axis z . Substituting ϕ and ψ into Eqs. 2.18a and 2.18b respectively gives:

$$-\frac{\omega^2}{V_p^2}F(z) = -\kappa^2F(z) + \frac{d^2F(z)}{dz^2} \quad (2.20a)$$

$$-\frac{\omega^2}{V_s^2}G(z) = -\kappa^2G(z) + \frac{d^2G(z)}{dz^2} \quad (2.20b)$$

After rearrangement:

$$\frac{d^2F(z)}{dz^2} - \left(\kappa^2 - \frac{\omega^2}{V_p^2}\right)F(z) = 0 \quad (2.21a)$$

$$\frac{d^2G(z)}{dz^2} - \left(\kappa^2 - \frac{\omega^2}{V_s^2}\right)G(z) = 0 \quad (2.21b)$$

The general solutions of Eqs. 2.21 are:

$$F(z) = A_1e^{-\alpha z} + A_2e^{\alpha z} \quad (2.22a)$$

$$G(z) = B_1e^{-\beta z} + B_2e^{\beta z} \quad (2.22b)$$

where $\alpha^2 = \kappa^2 - \omega^2/V_p^2$ and $\beta^2 = \kappa^2 - \omega^2/V_s^2$. The first terms of solutions (Eqs. 2.22) correspond to the motion decreasing with depth, which apply to surface waves. Hence, the potential functions become:

$$\phi = Ae^{-\alpha z}e^{i(\kappa x - \omega t)} \quad (2.23a)$$

$$\psi = Be^{-\beta z}e^{i(\kappa x - \omega t)} \quad (2.23b)$$

σ_{zz} and σ_{zx} from Hooke's Law (Eq. 2.5c and 2.5e) can be restated in terms of the potential functions as:

$$\sigma_{zz} = \lambda\Delta + 2\mu \frac{\partial w}{\partial z} = (\lambda + 2\mu) \frac{\partial^2 \phi}{\partial z^2} + \lambda \frac{\partial^2 \phi}{\partial x^2} - 2\mu \frac{\partial^2 \psi}{\partial x \partial z} \quad (2.24a)$$

$$\sigma_{zx} = \mu \left(\frac{\partial u}{\partial z} + \frac{\partial w}{\partial x} \right) = \mu \left(2 \frac{\partial^2 \phi}{\partial x \partial z} - \frac{\partial^2 \psi}{\partial x^2} + \frac{\partial^2 \psi}{\partial z^2} \right) \quad (2.24b)$$

Substituting the potential functions (Eqs. 2.23) into these stress components (Eqs. 2.24) at $z = 0$ should give zero since $\sigma_{zz} = \sigma_{zx} = 0$ for a medium with one traction-free surface. Therefore:

$$A[(\lambda + 2\mu)\alpha^2 - \lambda\kappa^2] - 2B\mu i\beta\kappa = 0 \quad (2.25a)$$

$$2A i\alpha\kappa + (\beta^2 + \kappa^2)B = 0 \quad (2.25b)$$

Taking the ratio of Eq. 2.25a and Eq. 2.25b, eliminates A and B:

$$4\mu\alpha\beta\kappa^2 = [(\lambda + 2\mu)\alpha^2 - \lambda\kappa^2](\beta^2 + \kappa^2) \quad (2.26)$$

If Eq. 2.26 is manipulated first by taking square of both sides and then substituting $\alpha^2 = \kappa^2 - \omega^2/V_p^2$ and $\beta^2 = \kappa^2 - \omega^2/V_s^2$, and finally dividing by $\mu^2\kappa^8$, it becomes:

$$16 \left(1 - \frac{\omega^2}{V_p^2} \frac{1}{\kappa^2} \right) \left(1 - \frac{\omega^2}{V_s^2} \frac{1}{\kappa^2} \right) = \left[2 - \frac{(\lambda + 2\mu)\omega^2}{\mu} \frac{1}{V_p^2 \kappa^2} \right]^2 \left(2 - \frac{\omega^2}{V_s^2} \frac{1}{\kappa^2} \right)^2 \quad (2.27)$$

By remembering $(\lambda + 2\mu)/\mu = (V_p/V_s)^2$ and $c = \omega/\kappa = V_R$, which is the surface (Rayleigh) wave velocity denoted as V_R , Eq. 2.27 can be restated as:

$$16 \left[1 - \left(\frac{V_R}{V_p} \right)^2 \right] \left[1 - \left(\frac{V_R}{V_s} \right)^2 \right] = \left[2 - \left(\frac{V_R}{V_s} \right)^2 \right]^4 \quad (2.28)$$

Eq. 2.28 is the Rayleigh frequency equation. Substituting $V_p = \gamma V_s$, where $\gamma = \sqrt{(\lambda + 2\mu)/\mu}$, into the Rayleigh frequency equation gives:

$$\left(\frac{V_R}{V_S}\right)^6 - 8\left(\frac{V_R}{V_S}\right)^4 + (24 - 16\gamma^{-2})\left(\frac{V_R}{V_S}\right)^2 + (16\gamma^{-2} - 16) = 0 \quad (2.29)$$

Since the above equation is a cubic one in $(V_R/V_S)^2$, the solution must have three roots which only one of them satisfies the precondition $V_R/V_S < 1$ as β^2 has to be a positive value. Eq. 2.28 reveals that the surface wave velocity depends on dilatational and distortional velocities which are governed by the elastic properties of the medium. Hence, Rayleigh wave is non-dispersive or independent of frequency.

In order to derive the vertical and horizontal displacements, potential functions (Eqs. 2.23) should be substituted into Eq. 2.14:

$$u = -(A\kappa i e^{-\alpha z} + B\beta e^{-\beta z})e^{i(\omega t - \kappa x)} \quad (2.30a)$$

$$w = -(A\alpha e^{-\alpha z} + B\kappa i e^{-\beta z})e^{i(\omega t - \kappa x)} \quad (2.30b)$$

and then if B from Eq. 2.25b is substituted into Eqs. 2.30, displacements are given as:

$$u = A\kappa i \left[-e^{-\alpha z} + \frac{2\alpha\beta}{\beta^2 + \kappa^2} e^{-\beta z} \right] e^{i(\omega t - \kappa x)} \quad (2.31a)$$

$$w = A\kappa \left[-\frac{\alpha}{\kappa} e^{-\alpha z} + \frac{2\alpha\kappa}{\beta^2 + \kappa^2} e^{-\beta z} \right] e^{i(\omega t - \kappa x)} \quad (2.31b)$$

The expressions in the brackets represent the attenuation of displacements within the depth of medium. As it can be seen in Eqs. 2.31, attenuation is a function of frequency which means high frequencies attenuate more than the low ones. Figure 2.4 displays the horizontal and vertical displacements, u and w , normalized with respect to the displacements at the surface, u_0 and w_0 , vs. the depth, z , normalized respect to the Rayleigh wavelength, λ_R for different Poisson's ratios. Near the subsurface, the particle movement is elliptical with a retrograde rotation generated due to positive vertical displacements, $w > 0$, and negative horizontal displacements, $u < 0$. This

motion reverses with increasing depth where the horizontal displacements become positive. This phenomenon is shown in Figure 2.5.

2.5 Lamb waves

Wave propagation in a bounded medium is more complicated compared to a semi-infinite medium due to multiple reflections of waves between the boundary surfaces and mode conversions of body waves. In the case of a plate, the interaction of waves generates a new kind of wave modes which is called Lamb. The solution procedure followed for the semi-infinite medium can also be applied for the plates as long as the new boundary conditions of two parallel traction-free surfaces are taken into account.

The potential functions representing the wave propagation in a plate are chosen as (Viktorov, 1967):

$$\phi = A_s \cosh(\alpha z) e^{i\kappa x} + B_a \sinh(\alpha z) e^{i\kappa x} \quad (2.32a)$$

$$\psi = C_s \cosh(\beta z) e^{i\kappa x} + D_a \sinh(\beta z) e^{i\kappa x} \quad (2.32b)$$

When compared to Rayleigh wave formulation in Eq. 2.23, term $e^{-i\omega t}$ is dropped for simplicity. The parameters α and β are same as the ones for Rayleigh waves. Employing these potential functions in the stress expression given in Eqs. 2.24 and introducing the new boundary conditions for the plate, which $\sigma_{xz} = \sigma_{zz} = 0$ at $z = \pm d$, provides the following set of equations:

$$\begin{aligned} (\kappa^2 + \beta^2) \cosh(\alpha d) A_s + (\kappa^2 + \beta^2) \sinh(\alpha d) B_a + 2i\kappa\beta \sinh(\beta d) C_a \\ + 2i\kappa\beta \cosh(\beta d) D_s = 0 \end{aligned} \quad (2.33a)$$

$$\begin{aligned} (\kappa^2 + \beta^2) \cosh(\alpha d) A_s - (\kappa^2 + \beta^2) \sinh(\alpha d) B_a - 2i\kappa\beta \sinh(\beta d) C_a \\ + 2i\kappa\beta \cosh(\beta d) D_s = 0 \end{aligned} \quad (2.33b)$$

$$2i\kappa\alpha \sinh(\alpha d)A_s + 2i\kappa\alpha \cosh(\alpha d)B_a - (\kappa^2 + \beta^2) \cosh(\beta d)C_a - (\kappa^2 + \beta^2) \sinh(\beta d)D_s = 0 \quad (2.33c)$$

$$-2i\kappa\alpha \sinh(\alpha d)A_s + 2i\kappa\alpha \cosh(\alpha d)B_a - (\kappa^2 + \beta^2)\cosh(\beta d)C_a + (\kappa^2 + \beta^2)\sinh(\beta d)D_s = 0 \quad (2.33d)$$

After rearranging and putting Eqs. 2.33 in a matrix form, two sets of equations are obtained:

$$\begin{bmatrix} (\kappa^2 + \beta^2) \cosh(\alpha d) & 2i\kappa\beta \cosh(\beta d) \\ 2i\kappa\alpha \sinh(\alpha d) & -(\kappa^2 + \beta^2) \sinh(\beta d) \end{bmatrix} \begin{bmatrix} A_s \\ D_s \end{bmatrix} = 0 \quad (2.34a)$$

$$\begin{bmatrix} (\kappa^2 + \beta^2) \cosh(\alpha d) & 2i\kappa\beta \cosh(\beta d) \\ 2i\kappa\alpha \sinh(\alpha d) & -(\kappa^2 + \beta^2) \sinh(\beta d) \end{bmatrix} \begin{bmatrix} B_a \\ C_a \end{bmatrix} = 0 \quad (2.34b)$$

The determinants of Eqs. 2.34 give the Rayleigh-Lamb frequency equation which is the mathematical equivalent of the Eigen-values of wave number, κ . The first matrix (Eq. 2.34a) represents the symmetrical wave modes, denoted by s , while the latter one (Eq. 2.34b) is for the anti-symmetrical modes, denoted by a . The Rayleigh-Lamb frequency equation for the symmetrical and the anti-symmetrical waves are then:

$$\frac{\tanh(\beta d)}{\tanh(\alpha d)} + \frac{4\alpha\beta\kappa^2}{(\kappa^2 - \beta^2)^2} = 0 \quad (2.35a)$$

$$\frac{\tanh(\beta d)}{\tanh(\alpha d)} + \frac{(\kappa^2 - \beta^2)^2}{4\alpha\beta\kappa^2} = 0 \quad (2.35b)$$

The symmetric Lamb modes (Eq. 2.35a) generate displacements symmetrical respect to the plane located at the middle thickness of plate; while the anti-symmetric Lamb modes (Eq. 2.35b) cause bending deformation of the plate (Fig. 2.6). Eqs. 2.35 are given in one expression as:

$$\frac{\tanh(\beta d)}{\tanh(\alpha d)} + \left[\frac{4\alpha\beta\kappa^2}{(\kappa^2 - \beta^2)^2} \right]^{\pm 1} = 0, \quad \begin{cases} +1 = \text{symmetrical} \\ -1 = \text{antisymmetrical} \end{cases} \quad (2.36)$$

Depending on whether $\kappa^2 \lesseqgtr \omega^2/V_p^2, \omega^2/V_s^2$, parameters: α and β are real, zero or imaginary. For propagating waves, only real roots are considered. Using the identity $\tanh(\alpha d) = -i \tan(i\alpha d)$, for $\kappa^2 < \omega^2/V_p^2, \omega^2/V_s^2$, $\tanh(i\alpha d) = -i \tan(-\alpha d)$ where $i \tan(-\alpha d) = -i \tan(\alpha d)$, Eq. 2.36 can be expressed as:

$$\frac{\tan(\beta d)}{\tan(\alpha d)} + \left[\frac{4\alpha\beta\kappa^2}{(\kappa^2 - \beta^2)^2} \right]^{\pm 1} = 0, \quad \begin{cases} +1 = \text{symmetrical} \\ -1 = \text{antisymmetrical} \end{cases} \quad (2.37)$$

For any given frequency, ω , there are a finite number of symmetrical and anti-symmetrical Lamb wave modes with a specific phase and group velocity. As $\omega \rightarrow 0$, Eq. 2.37 has only one root corresponding to the zeroth (fundamental) symmetrical or anti-symmetrical Lamb mode denoted by S_0 or A_0 . On the other hand, as ω increases, Eq. 2.37 leads to more roots which represent higher Lamb modes. The critical frequencies where a higher Lamb mode appears can be given in terms of plate thickness, and wavelengths of P and S waves (Viktorov, 1967):

For symmetrical modes:

$$2d = \frac{\lambda_p}{2}, \frac{3\lambda_p}{2}, \frac{5\lambda_p}{2}, \dots \quad (2.38a)$$

$$2d = \lambda_s, 2\lambda_s, 3\lambda_s, \dots \quad (2.38b)$$

For anti-symmetrical modes:

$$2d = \lambda_p, 2\lambda_p, 3\lambda_p, \dots \quad (2.38c)$$

$$2d = \frac{\lambda_s}{2}, \frac{3\lambda_s}{2}, \frac{5\lambda_s}{2}, \dots \quad (2.38d)$$

The total number of symmetrical and anti-symmetrical Lamb modes is given respectively:

$$N_s = 1 + \text{round} \left[\frac{2d}{\lambda_s} \right] + \text{round} \left[\frac{2d}{\lambda_p} + \frac{1}{2} \right] \quad (2.39a)$$

$$N_a = 1 + \text{round} \left[\frac{2d}{\lambda_p} \right] + \text{round} \left[\frac{2d}{\lambda_s} + \frac{1}{2} \right] \quad (2.39a)$$

By performing numerical solution of the Rayleigh-Lamb frequency equation (Eq. 2.37), the variation of phase or group velocities with respect to frequency (dispersion) for each Lamb mode can be calculated. In Figure 2.7, the dispersion curves for a medium made of cement and sand mixture with a thickness of 45 cm and having P and S wave velocities of 2000 m/s and 1200 m/s, respectively are shown. For high frequencies, S_0 and A_0 converge to the velocity of Rayleigh wave, since the corresponding wavelengths become sufficiently short compared to the thickness of the medium. Hence, the interaction of waves with two traction-free surfaces is not significant. This phenomenon can be also proofed within Eq. 2.37. A high frequency or a wavelength short enough, $\tan(\alpha d) \approx \tan(\beta d) \approx 1$; therefore, the Rayleigh-Lamb frequency equation simplifies to Rayleigh frequency equation (Eq. 2.26). On the other hand, low frequencies have the following approximations:

$$\tan(\alpha d) \approx \alpha h \left(1 + \frac{1}{3} \alpha^2 d^2 \right) \quad (2.40a)$$

$$\tan(\beta d) \approx \beta h \left(1 + \frac{1}{3} \beta^2 d^2 \right) \quad (2.40b)$$

Substituting the above relations (Eqs. 2.40) into the Rayleigh-Lamb frequency equation (Eq. 2.37) gives the velocities for the fundamental Lamb modes at low frequencies:

$$V_{ext} = \sqrt{\frac{\lambda + 2\mu}{(1 - \nu^2)}} = \sqrt{\frac{M}{(1 - \nu^2)}} \quad (2.41a)$$

$$V_{flx} = \kappa d \sqrt{\frac{\lambda + 2\mu}{3\rho(1 - \nu^2)}} = \kappa d \sqrt{\frac{M}{3\rho(1 - \nu^2)}} \quad (2.41b)$$

$$\frac{V_{ext}}{V_p} = \sqrt{\frac{\rho}{(1-v^2)}} \quad (2.41c)$$

$$\frac{V_{flx}}{V_s} = \kappa d \sqrt{\frac{\mu}{3\rho(1-v^2)}} \quad (2.41d)$$

The velocity of the fundamental symmetrical Lamb mode, V_{ext} , which is accepted as the velocity for the global extensional mode, depends only on material properties. On the other hand, the velocity of the fundamental anti-symmetrical Lamb mode, V_{flx} , which is the global flexural mode of the plate, varies with the wave-number.

To determine the displacements, the potential functions (Eqs. 2.32) should be rearranged. If terms D_s and C_a from Eqs. 2.33 are defined in terms of A_s and B_a successively, the potential functions look like:

$$\phi = A_s \cosh(\alpha_s z) e^{i\kappa_s x} + B_a \sinh(\alpha_a z) e^{i\kappa_a x} \quad (2.42a)$$

$$\begin{aligned} \psi = & \frac{2i\kappa_s \alpha_s \sinh(\alpha_s d)}{(\kappa_s^2 + \beta_s^2) \sinh(\beta_s d)} A_s \sinh(\beta_s z) e^{i\kappa_s x} \\ & + \frac{2i\kappa_a \alpha_a \cosh(\alpha_a d)}{(\kappa_a^2 + \beta_a^2) \cosh(\beta_a d)} B_a \cosh(\beta_a z) e^{i\kappa_a x} \end{aligned} \quad (2.42b)$$

where $\alpha_{s,a}^2 = \kappa_{s,a}^2 - \omega^2/V_p^2$ and $\beta_{s,a}^2 = \kappa_{s,a}^2 - \omega^2/V_p^2$. Since the potential functions are defined as the sum of symmetrical and anti-symmetrical motions in Eqs. 2.32, then the displacements can be shown in this manner:

$$u = u_s + u_a \quad (2.43a)$$

$$w = w_s + w_a \quad (2.43b)$$

Substituting the potentials (Eqs. 2.42) into displacement expressions (Eqs. 2.14) with the help of the above relations (Eqs. 2.43), the symmetrical and anti-symmetrical displacement components may be written as:

$$u_s = A\kappa_s \left[\frac{\cosh(\alpha_s z)}{\sinh(\alpha_s d)} - \frac{2\alpha_s \beta_s}{\kappa_s^2 + \beta_s^2} \cdot \frac{\cosh(\beta_s z)}{\sinh(\beta_s d)} \right] e^{i(\kappa_s x - \omega t - \frac{\pi}{2})} \quad (2.44a)$$

$$w_s = -A\alpha_s \left[\frac{\sinh(\alpha_s z)}{\sinh(\alpha_s d)} - \frac{2\kappa_s^2}{\kappa_s^2 + \beta_s^2} \cdot \frac{\sinh(\beta_s z)}{\sinh(\beta_s d)} \right] e^{i(\kappa_s x - \omega t)} \quad (2.44b)$$

$$u_a = B\kappa_a \left[\frac{\sinh(\alpha_a z)}{\cosh(\alpha_a d)} - \frac{2\alpha_a \beta_a}{\kappa_a^2 + \beta_a^2} \cdot \frac{\sinh(\beta_a z)}{\cosh(\beta_a d)} \right] e^{i(\kappa_a x - \omega t - \frac{\pi}{2})} \quad (2.44c)$$

$$w_a = -B\alpha_a \left[\frac{\cosh(\alpha_a z)}{\cosh(\alpha_a d)} - \frac{2\kappa_a^2}{\kappa_a^2 + \beta_a^2} \cdot \frac{\cosh(\beta_a z)}{\cosh(\beta_a d)} \right] e^{i(\kappa_a x - \omega t)} \quad (2.44d)$$

where A and B are arbitrary constants. Eqs. 2.44 reveal a phase difference of $\pi/2$ between the horizontal and vertical displacements for both the symmetric and the anti-symmetric Lamb modes.

2.6 Attenuation of Surface Waves and Material Damping

Energy dissipation of waves is caused by geometric radiation and deformation. The first one is related to increasing surface area of the propagating wave-front and the latter one represents the material damping. The total attenuation of a propagating wave is defined as (Graff, 1975):

$$\frac{A_1}{A_2} = \left(\frac{x_1}{x_2} \right)^\beta e^{\alpha_x(x_1 - x_2)} \quad (2.45)$$

where A_1 and A_2 are the amplitudes at distances x_1 and x_2 from the source, β is the geometric attenuation constant which is -0.5 for surface waves (cylindrical wave fronts), α_x is the spatial coefficient of wave attenuation caused by material damping. Rearranging Eq. 2.45:

$$\alpha_x = \frac{1}{x_2 - x_1} \left[\ln \left(\frac{A_2}{A_1} \right) - \beta \ln \left(\frac{x_2}{x_1} \right) \right] \quad (2.46)$$

The relation between α_x and the material damping ratio, D , is given as a function of frequency:

$$D = V \frac{\alpha_x}{\omega} \quad (2.47)$$

where V is the wave velocity, in this case it is the velocity of Rayleigh wave and ω is the angular frequency. α_x may be calculated from different parameters, such as peak-to-peak (PTP) amplitude in the time domain, maximum magnitudes in the frequency domain, spectrum area, etc. If it is rewritten in terms of spectral magnitudes of wave signals obtained at different distances from the source, Eq. 2.45 becomes:

$$\frac{|G(\omega, x_1)|}{|G(\omega, x_2)|} = \left(\frac{x_1}{x_2} \right)^\beta e^{\alpha_x(x_1 - x_2)} \quad (2.48)$$

After rearranging Eq. 2.48 in the form of Eq. 2.46:

$$\alpha_x = \frac{1}{x_2 - x_1} \left[\ln \left(\frac{|G(\omega, x_2)|}{|G(\omega, x_1)|} \right) - \beta \ln \left(\frac{x_2}{x_1} \right) \right] \quad (2.49)$$

which provides frequency dependent attenuation.

2.7 Summary

In this chapter, solutions of the wave equation for different boundary conditions are reviewed. This theoretical knowledge is used to interpret the experimental results in the next chapters. In Chapter 6, the recorded waves are assumed propagating as Rayleigh waves without any dispersive behaviour since the wavelengths generated are small enough compared to the thickness of the specimen. On the other hand, for beam samples in Chapter 7, the Lamb wave solution is pursued to have a better understanding of the test results since the utilized frequencies are suspected to generate Lamb waves.

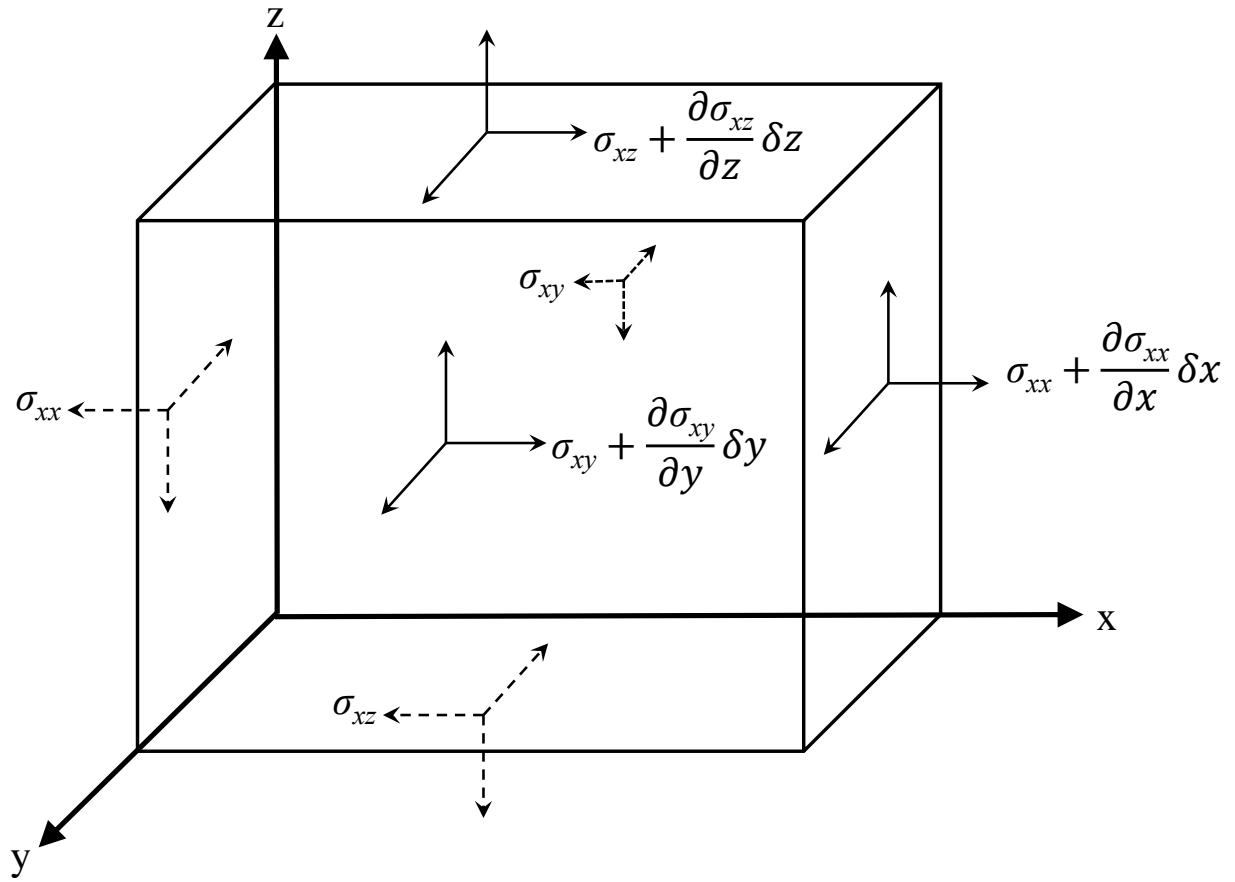


Figure 2.1: Stresses acting on an infinitesimal solid in x-direction.

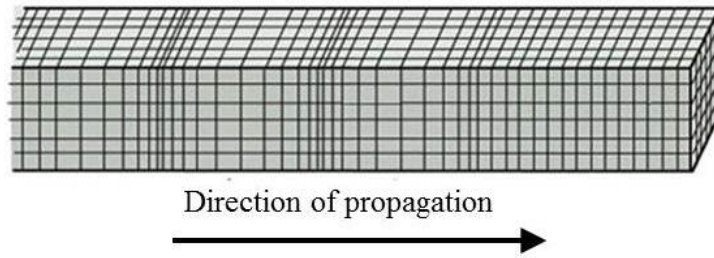


Figure 2.2: Compressional wave (P-wave) propagation (Bolt, 1978).

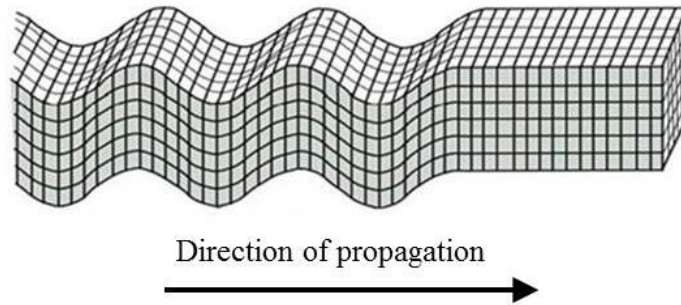


Figure 2.3: Shear wave (S-wave) propagation (Bolt, 1978).

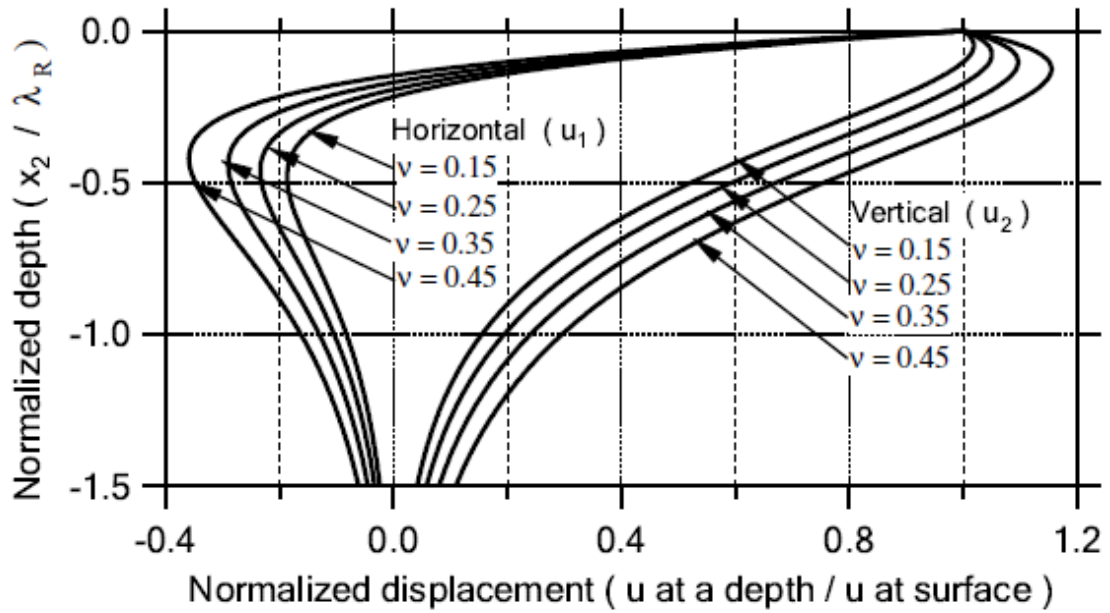


Figure 2.4: Normalized horizontal, \mathbf{u} , and vertical, \mathbf{w} , displacements vs. normalized depth, z/λ_R for different Poisson's ratios (Yang, 2009).

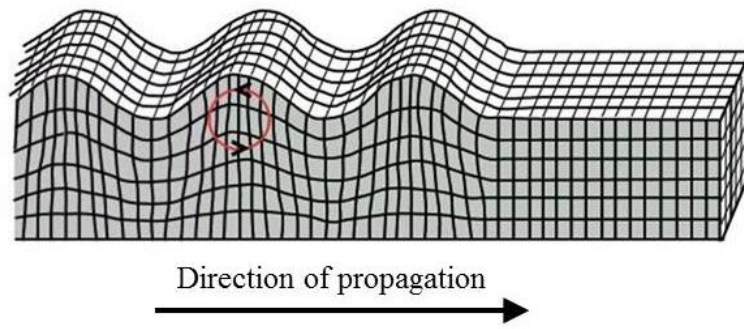


Figure 2.5: Rayleigh wave propagation (Bolt, 1978).

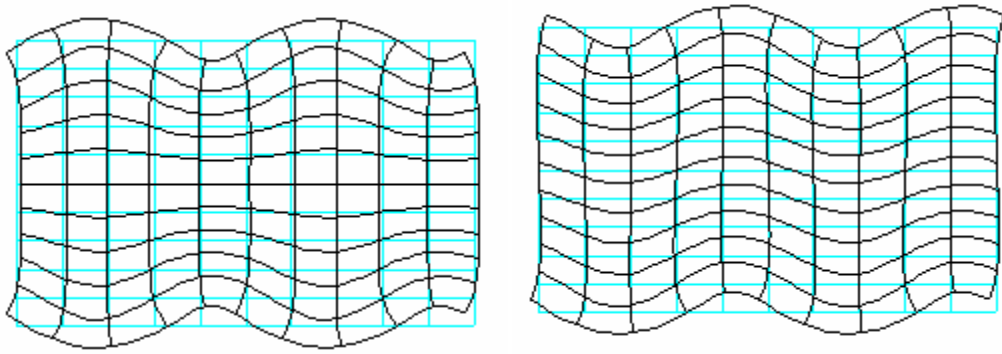


Figure 2.6: (left) Symmetric and (right) anti-symmetric Lamb modes in a plate (Yang, 2009).

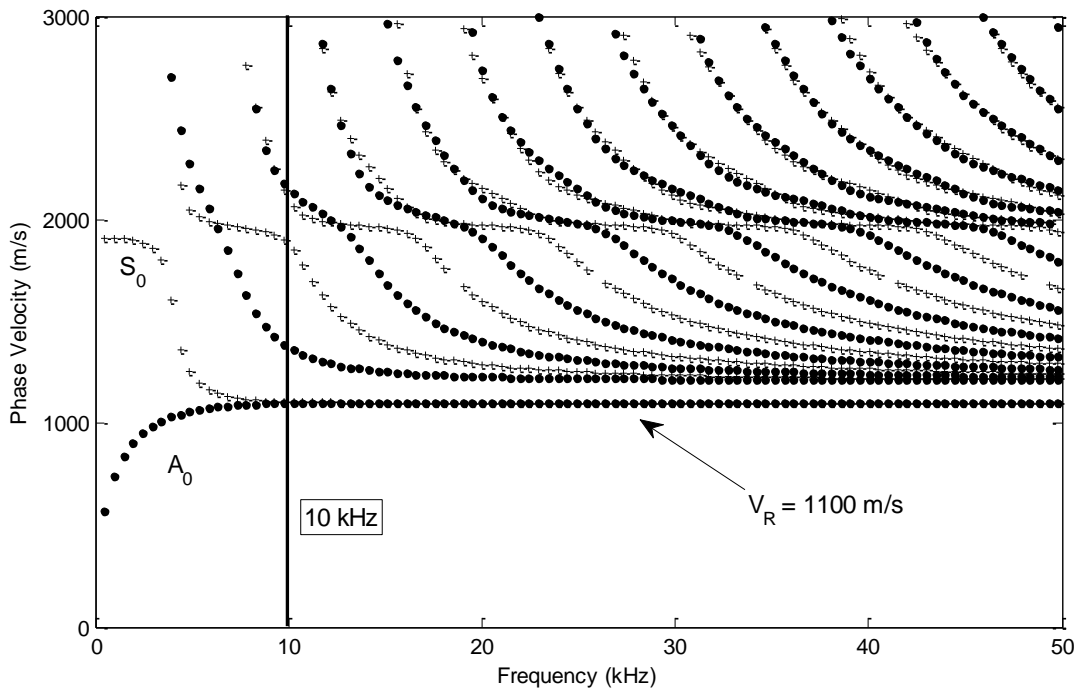


Figure 2.7: Dispersion curves for a cemented-sand medium for the given parameters: $d = 45$ cm, $V_P = 2000$ m/s and $V_S = 1200$ m/s.

Chapter 3 Signal Processing Techniques

3.1 Introduction

Various signal processing techniques are available that are used to analyse the measured signals. In this chapter, the most common transforms used for non-destructive testing are reviewed. First, Fourier transform is covered including its one-dimensional (transition from time domain into frequency domain) and two-dimensional (transition from time-space domain into frequency-wave number domain) versions. Then, the short-time Fourier transform (windowed Fourier transform) is presented. It is followed by continuous and discrete wavelet transforms; which are capable of holding time and frequency information simultaneously. Lastly, the empirical mode decomposition technique as an alternative to discrete wavelet transform, is explained.

3.2 1D Fourier Transform

A time signal can be considered as combination of harmonic waves. Hence, it is possible to decompose it into basic harmonic components using the complex Fourier series:

$$p(t) = \sum_{j=-\infty}^{\infty} P_j e^{i(j\omega_0 t)} \quad (3.1)$$

where the first harmonic has the circular frequency $\omega_0 = 2\pi/T_0$ and j th harmonic has $\omega_j \equiv j\omega_0$. P_j represents the j th Fourier coefficient; which can be expressed in terms of $p(t)$ since the exponential functions are orthogonal:

$$P_j = \frac{1}{T_0} \int_0^{T_0} p(t) e^{-i(j\omega_0 t)} dt \quad j = 0, \pm 1, \pm 2, \dots \quad (3.2)$$

The average value of $p(t)$ can be given by the first Fourier coefficient. So that, for $j = 0$:

$$P_0 = \frac{1}{T_0} \int_0^{T_0} p(t) dt \quad (3.3)$$

The complex Fourier represents periodic signals. On the other hand, the Fourier integral represents non-periodic signals as:

$$p(t) = \frac{1}{2\pi} \int_{-\infty}^{\infty} P(\omega) e^{i\omega t} d\omega \quad (3.4)$$

where

$$P(\omega) = \int_{-\infty}^{\infty} p(t) e^{-i\omega t} dt \quad (3.5)$$

Eq. 3.5 is known as Fourier transform (FT) whereas Eq. 3.4 is called inverse Fourier transform (IFT). The FT decomposes the time signal, $p(t)$, in a set of complex exponentials, $e^{i\omega t}$, through convolution. Thus, the frequency spectrum $P(\omega)$ reveals the energy of a given complex exponential function in the original time signal. Eqs. 3.4 and 3.5 are called the Fourier transform pair.

Since the analytical solution for all non-periodic signal is not possible, numerical evaluation is required. Therefore, the Fourier transform pair is performed in discrete form:

$$p(t) = p(n\Delta t) = \frac{1}{N\Delta t} \sum_{j=0}^{N-1} P(j2\pi\Delta f) e^{i2\pi j \frac{n}{N}} \quad (3.6)$$

$$P(\omega) = P(n2\pi\Delta f) = \Delta t \sum_{j=0}^{N-1} p(j\Delta t) e^{-i2\pi j \frac{n}{N}} \quad (3.7)$$

where $n = 0, 1, 2, \dots, N - 1$. N is the total number of sampled points; Δt and Δf are time and frequency intervals, respectively. Eqs. 3.6 and 3.7 constitute the Discrete Fourier transform (DFT) pair. Since $\Delta f = 1/T_0 = 1/N\Delta t$, the relation between time and frequency intervals is:

$$\Delta t = \frac{1}{N\Delta f} \quad (3.8)$$

In the DFT, only positive frequencies are taken into account contrary to the FT (Eqs. 3.4 and 3.5). The frequencies corresponding to $N/2 < j \leq N - 1$ do not have any physical importance in DFT, just as negative frequencies in FT. Therefore, the highest meaningful frequency, f_{max} , existing in DTF equals to $f_{N/2} = (N/2)\Delta f$, which is also called the Nyquist frequency, $f_{Nyquist}$:

$$f_{Nyquist} = \frac{N\Delta f}{2} = \frac{f_{sampling}}{2} \quad (3.9)$$

The following Nyquist criterion should be satisfied to retain the interested frequency range in the Fourier spectrum:

$$f < f_{Nyquist} \quad (3.10)$$

Otherwise, a phenomenon called aliasing, which causes folding of some frequencies around some others, occurs. The DFT of a time signal has the following complex valued numbers:

$$P(j\Delta\omega) = Re[P(j\Delta\omega)] + iIm[P(j\Delta\omega)] \quad (3.11)$$

where Re is the function to extract the real part and Im is for the imaginary component. For each frequency, the spectral amplitude, Am , and the phase angle, Ph , are obtained by:

$$Am(j\Delta\omega) = \sqrt{Re^2[P(j\Delta\omega)] + Im^2[P(j\Delta\omega)]} \quad (3.12)$$

$$Ph(j\Delta\omega) = \arctan \left[\frac{Im(j\Delta\omega)}{Re(j\Delta\omega)} \right] \quad (3.13)$$

The j th harmonic of the time signal can be defined as:

$$p_j(t) = Am(j\Delta\omega) \cos[j\Delta\omega t + Ph(j\Delta\omega)] \quad (3.14)$$

Therefore, the original signal can be reconstructed by superposition of the harmonics given in Eq. 3.14:

$$p(t) \approx \sum_{j=0}^{N-1} p_j(t) = A_0 + \sum_{j=0}^{N-1} \{Am(j\Delta\omega) \cos[j\Delta\omega t + Ph(j\Delta\omega)]\} \quad (3.15)$$

where A_0 is the DC component.

The spectral energy of a frequency involved in a time signal is defined as square of the spectral amplitude. Hence, the cumulative spectral energy of the time signal is:

$$E_{total} = \int_{-\infty}^{\infty} |P(\omega)|^2 d\omega \quad (3.16)$$

If only a portion of the frequency range is considered, then the corresponding energy:

$$E_{partial} = \int_{\omega_1}^{\omega_2} |P(\omega)|^2 d\omega \quad (3.17)$$

For a time signal with finite energy, it is possible to define the following localization parameters (Stark, 2005):

$$t_p = \frac{1}{E_{total}} \int_{-\infty}^{\infty} t |p(t)|^2 dt \quad (3.18)$$

$$\Delta t_p = \sqrt{\frac{1}{E_{total}} \int_{-\infty}^{\infty} (t - t_p)^2 |p(t)|^2 dt} \quad (3.19)$$

$$\omega_p = \frac{1}{2\pi E_{total}} \int_{-\infty}^{\infty} \omega |P(\omega)|^2 d\omega \quad (3.20)$$

$$\Delta\omega_p = \sqrt{\frac{1}{E_{total}} \int_{-\infty}^{\infty} (\omega - \omega_p)^2 |P(\omega)|^2 d\omega} \quad (3.21)$$

t_p represents the location on time axis where the signal $p(t)$ is accumulated and Δt_p implies how $p(t)$ is distributed around t_p . Similar parameters, ω_p and $\Delta\omega_p$, are also available in frequency domain as given in Eqs. 3.20 and 3.21.

Another commonly used parameter in signal processing is the cross power spectrum which represents the cross correlation of two time signals $p_1(t)$ and $p_2(t)$ in frequency domain:

$$P_{12}(\omega) = P_1(\omega)P_2^*(\omega) \quad (3.22)$$

where $P_1(\omega)$ and $P_2(\omega)$ are the frequency spectra of $p_1(t)$ and $p_2(t)$, respectively, while $P_2^*(\omega)$ is the complex conjugate of $P_2(\omega)$.

3.3 2D Fourier Transform

One-dimensional Fourier transform can be generalized to higher dimensions. In case, a set of signals is a function of both time and space, the two-dimensional FT (2D FT) can be used for the representation of temporal and spatial information, $p(t, x)$ into frequency and wave number domain, $P(\omega, \kappa)$, respectively as follows:

$$P(\omega, \kappa) = \int_{-\infty}^{\infty} \int_{-\infty}^{\infty} p(t, x) e^{-i(\omega t - \kappa x)} dt dx \quad (3.23)$$

For numerical analyses, the discrete 2D FT may be given as:

$$P(u\Delta\omega, v\Delta\kappa) = \sum_{n=0}^{N-1} \sum_{m=0}^{N-1} p(n\Delta t, m\Delta x) e^{-i(u\Delta\omega n\Delta t - v\Delta\kappa m\Delta x)} \quad (3.24)$$

where Δt , Δx , $\Delta\omega$ and $\Delta\kappa$ are time, space, frequency and wave number intervals respectively, while u, v, m and n are the counters. If the 2D FT spectrum is plotted in frequency-wave number domain ($\omega - \kappa$), the incident, reflected and transmitted events generated during the wave propagation can be identified. A specific event among all can be extracted by first windowing the 2D transformed data, and then applying an inverse 2D FT on the selected event. A typical 2D window in frequency domain utilizing a Hanning window is defined as (Oppenheim, 2006):

$$W(\omega, \kappa) = \begin{cases} 0.5 + 0.5 \cos\left(\frac{\omega - \omega^{(event)}(\kappa)}{BW}\right) & \text{if } \omega - \omega^{(event)}(\kappa) \leq \frac{BW}{2} \\ 0 & \text{if } \omega - \omega^{(event)}(\kappa) > \frac{BW}{2} \end{cases} \quad (3.25)$$

where BW is a frequency bandwidth and $\omega^{(event)}(\kappa)$ is the relation between frequency and wave number for the event. After windowing the data in $\omega - \kappa$ domain and performing the inverse 2D FT, the single event in time-space domain is obtained:

$$p^{(event)}(t, x) = \int_{-\infty}^{\infty} \int_{-\infty}^{\infty} P(\omega, \kappa) W(\omega, \kappa) e^{i(\omega t - \kappa x)} d\omega d\kappa \quad (3.26)$$

3.4 Short Time Fourier Transform

The transformation of a signal from time domain into frequency domain causes time information to be lost; therefore, determining the arrival time of a particular event is impossible. For this reason, the idea of applying a time window within Fourier transform emerges. By shifting the time window, the frequency content of the signal for different time intervals can be obtained. This modified Fourier transform, namely the short-time (windowed) Fourier transform (STFT), is defined as:

$$P(\omega, b) = \int_{-\infty}^{\infty} p(t) w(t - b) e^{-i(\omega t)} dt \quad (3.27)$$

where b is the shift time used in translating the window function $w(t - b)$ in time axis. In the STFT, the window width is kept same. However, the resolution of time and frequency is related to the width of window: a wide window provides better frequency resolution but poor time resolution and vice versa. The second moment of time and frequency data (Eqs. 3.19 and 3.21) can be used to define an uncertainty condition (Qian, 2002):

$$\frac{1}{2} \leq \Delta t_p \Delta \omega_p \quad (3.28)$$

Eq. 3.28 shows a trade-off between time and frequency resolutions. Only if the Gaussian function is chosen as time window, then the equality, $1/2 = \Delta t_p \Delta \omega_p$, holds (Qian, 2002).

3.5 Continuous Wavelet Transform

3.5.1 Introduction

The wavelet transform (CWT) is a signal processing technique to convert a signal into a more appealing form to be interpreted with respect to specific needs of a study (Addison 2002, Qian 2002, Stark 2005). A wavelet function, $\psi(t)$, is needed as “mother wavelet” to perform the transform. The mother wavelet can be considered as a band-pass filter which lets the components of a signal pass within a certain range of frequencies proportional to its energy spectrum. Wavelets can be manipulated in terms of dilation and translation. In other words, a wavelet can be stretched or squeezed by introducing a dilation parameter (scale), a , and shifted at the same time by help of a location parameter, b . The dilated and shifted version of the wavelet function is denoted by $\psi((t - b)/a)$. The wavelet transform of a continuous signal, $p(t)$, is:

$$WT(a, b) = w(a) \int_{-\infty}^{\infty} p(t) \psi^* \left(\frac{t - b}{a} \right) dt \quad (3.29)$$

where ψ^* is the complex conjugate of the wavelet. WT (Eq. 3.29) can be seen as a cross correlation of a signal with a set of wavelets having various widths. To ensure energy conservation at each scale, $w(a)$ is set to $1/\sqrt{a}$. So that, Eq. 3.29 can be stated as:

$$WT(a, b) = \frac{1}{\sqrt{a}} \int_{-\infty}^{\infty} p(t) \psi^* \left(\frac{t-b}{a} \right) dt \quad (3.30)$$

Eq. 3.30 is called continuous wavelet transform (CWT). Basically CWT is the integration of the product of a signal and a given wavelet over the signal range, which is mathematically called convolution. A more compact expression of wavelet function is:

$$\psi_{a,b}(t) = \frac{1}{\sqrt{a}} \psi \left(\frac{t-b}{a} \right) \quad (3.31)$$

Thus, Eq. 3.30 can be written as:

$$WT(a, b) = \int_{-\infty}^{\infty} p(t) \psi_{a,b}^*(t) dt \quad (3.32)$$

The continuous wavelet transform given in Eq. 3.30 may be expressed in a discrete form (DCWT) to be used in numerical computations:

$$WT(a, b) = \frac{1}{\sqrt{a}} \sum_{n=0}^{N-1} p(n\Delta t) \psi \left(\frac{n\Delta t - b}{a} \right) \Delta t \quad (3.33)$$

where N is the total number of sampled points. The DCWT should not be confused with the discrete wavelet transform (DWT) which will be introduced later. CWT can also be expressed in frequency domain as:

$$WT(a, b) = \frac{1}{C_g} \int_{-\infty}^{\infty} P(f) \hat{\psi}_{a,b}^*(f) df \quad (3.34)$$

where C_g is called admissibility coefficient, will be explained in Section 3.5.3, and $\hat{\psi}_{a,b}(f)$ is the Fourier transform of the wavelet:

$$\hat{\psi}_{a,b}(f) = \frac{1}{\sqrt{a}} \int_{-\infty}^{\infty} \psi\left(\frac{t-b}{a}\right) e^{-i(2\pi f)t} dt \quad (3.35)$$

The idea of wavelet transform is illustrated in Figure 3.1: a wavelet with given parameters a and b is superimposed with a harmonic signal, showing the positive and negative contributions to the overall integral. The value of positive contribution depends on how well the wavelet and the signal match each other. For instance, at the locations where the wavelet is in phase with the signal will provide a big positive magnitude. Therefore, CWT should be performed over a continuous range of scale, a , and shift time, b to ensure a complete investigation.

As like Fourier transform, WT can also be performed inversely. When WT is integrated over all scales and locations, the original signal can be recovered:

$$p(t) = \frac{1}{C_g} \int_{-\infty}^{\infty} \int_0^{\infty} WT(a,b) \psi_{a,b}(t) \frac{da db}{a^2} \quad (3.36)$$

If the integration given in above equation is performed over a limited scale, an adapted signal can be reconstructed with the frequencies wanted.

3.5.2 Wavelet Energy

The energy of a signal in time domain is its integration of squared magnitude:

$$E(t) = \int_{-\infty}^{\infty} |p(t)|^2 dt \quad (3.37)$$

Energy can also be defined as function of WT:

$$E(a, b) = |WT(a, b)|^2 \quad (3.38)$$

This equation is used to calculate energy contribution of each scale and location of the signal. The plot associated with this energy equation is known as scalogram. A scalogram can be integrated over a and b to recover the total energy in a signal as follows:

$$E = \frac{1}{C_g} \int_{-\infty}^{\infty} \int_0^{\infty} |WT(a, b)|^2 \frac{da db}{a^2} \quad (3.39)$$

If integration is performed only over shift time, then the relative energy contribution of each scale, a , can be determined:

$$E(a) = \frac{1}{C_g} \int_{-\infty}^{\infty} |WT(a, b)|^2 db \quad (3.40)$$

This scale dependent energy function, $E(a)$, can be converted into a frequency dependent function, $E(f)$. To do so, the parameter, a , should be defined based on one of the so-called wavelet frequency: the central, f_0 , the peak, f_p , or the band-pass center, f_c . Since the scale, a , is inversely proportional to frequency, it can be written as:

$$f = \frac{f_c}{a} \quad (3.41)$$

Substituting Eq. 3.41 into Eq. 3.39 results in:

$$E = \frac{1}{C_g f_c} \int_{-\infty}^{\infty} \int_0^{\infty} |WT(f, b)|^2 df db \quad (3.42)$$

This makes it possible to compare the wavelet energy directly with the Fourier energy spectrum.

3.5.3 Requirements for wavelets

A function is classified as wavelet if the following mathematical criteria are satisfied (Addison, 2002):

1. The wavelet should have finite cumulative spectral energy, E_{total} (Eq. 3.16).
2. The wavelet should have zero mean, in other words null DC. For this reason, the following condition, named admissibility condition, must hold:

$$C_g = \int_0^{\infty} \frac{|\hat{\psi}(f)|^2}{f} df < \infty \quad (3.43)$$

3. As for the complex valued wavelets - such as Morlet wavelet which will be given next - the Fourier transform must be real and vanish for negative frequencies.

Utilizing a wavelet satisfying the above criteria will let the time-signal be reconstructed without missing any information from the original signal.

3.5.4 Morlet Wavelet

Morlet function is a complex wavelet, therefore using it as mother wavelet for the transform allows us to separate the amplitude and phase components of a signal. Besides, it represents the output force of an ultrasonic piezoelectric transmitter used in this research (Yang, 2009). It is defined as a harmonic complex function in time enveloped by a Gaussian function (Lardies, 2007):

$$\psi(t) = e^{-i(2\pi f_0)t} e^{-t^2/\tau^2} \quad (3.44)$$

where f_0 is the central frequency and τ is the modulation parameter to arrange bandwidth. Since Eq. 3.44 is modulated by a Gaussian function, it has good resolution both in time and frequency domain according to the uncertainty principle (Section 3.4). The amplitude of the Fourier transform of the Morlet wavelet is:

$$|\psi(f)| = \sqrt{\pi\tau} e^{-\frac{\tau^2}{4}(2\pi f - 2\pi f_0)^2} \quad (3.45)$$

A Morlet function for $f_0 = 52$ kHz and $\tau = 1.12 \times 10^{-5}$ in time and frequency domains is shown in Figure 3.2.

3.5.5 Instantaneous Phase from Wavelet Transform

A damped harmonic oscillation is described as:

$$p(t) = A e^{-\xi\omega_n t} \cos(\omega_d t + \theta) \quad (3.46)$$

where A , the amplitude; ξ , the viscous damping ratio; ω_n , the undamped natural frequency; $\omega_d = \omega_n \sqrt{1 - D^2}$, the damped natural frequency; and θ , the initial phase. If $\xi < 1$, it means the system is underdamped - for many practical cases $\xi \ll 1$, thus $\omega_d \approx \omega_n$. Hence, the signal $x(t)$ is asymptotical respect to zero. The wavelet transform for this case is (Lardies, 2007):

$$WT(a, b) = \frac{\sqrt{a}}{2} A e^{-\xi\omega_n b} \psi(a\omega_d) e^{-i(\omega_d b + \theta)} \quad (3.47)$$

and the phase of this expression is:

$$Ph[WT(a, b)] = \omega_d b + \theta \quad (3.48)$$

whose derivative will provide the damped frequency:

$$\frac{d}{db} Ph[WT(a, b)] = \omega_d \quad (3.49)$$

In summary, using above procedure, the instantaneous damped frequency in a time signal can be determined.

3.6 Discrete Wavelet Transform

If one prefers to investigate all frequencies existing in an arbitrary signal instead of looking for a specific frequency, continuous wavelet transform is not compatible tool due to three difficulties. The first one is the redundancy problem caused by continuous shifting of a continuously scalable wavelet over a signal. Secondly, the infinite number of wavelets in the transform is required which is not computationally possible. Lastly, a fast algorithm is needed to decompose a time signal into its sub-signals; each associated with different frequency resolution. To overcome these difficulties, DWT is proposed by the researches (Mallat, 1989).

Firstly, to get rid of the high redundancy problem, the wavelets are defined with discrete translation and scale steps:

$$\psi_{j,k}(t) = \frac{1}{\sqrt{a_0^j}} \psi\left(\frac{t - k\tau_0 a_0^j}{a_0^j}\right) \quad (3.50)$$

This presentation of wavelets is called discrete wavelets where j and k are integers and a_0 is a fixed dilation step and τ_0 is the translation factor. To get the advantage of dyadic sampling in the frequency and time axes, these parameters are set as $a_0 = 2$ and $\tau_0 = 1$.

The next step is to estimate how many different scales is needed to cover all frequency components. Since a wavelet works as a band-pass filter, it is possible to generate a series of dilated wavelets derived from a primary wavelet. Figure 3.3a displays such a wavelet series where each wavelet has half of the spectrum width of its right neighbour. This kind of a wavelet series is built by compressing the wavelet in time domain by a factor of two, so that the frequency spectrum can be stretched to its double size with shifting all frequencies upwards by a factor of two. Shortly, all spectrum of the signal can be covered with the spectra of the dilated wavelets.

Lastly, the lack of a fast algorithm to perform multi-resolution decomposition of a time signal is satisfied by Mallat (1998). The wavelet series introduced above constitutes a filter bank for the

decomposition by splitting the frequency spectrum of the signal in two parts, a low-pass and a high-pass part. A sequence of splitting process is pursued as depicted in Figure 3.3b. Designing only two filters is enough for the transform; a band-pass band to be doubled and low-pass filter which is called as the scaling function. Output of the each step represents a decomposed signal component that is called “level”. The levels are numbered starting from -1 to $n + 1$, where $N = 2^n$ is the number of points in the signal. In this study, decomposition of the signals is realized by Matlab[®] wavelet toolbox which performs Mallat’s pyramid algorithm using Daubechies wavelets.

3.7 Empirical Mode Decomposition

Empirical mode decomposition (EMD) is a powerful tool to decompose a signal into its simple oscillatory modes which are named as intrinsic mode functions (IMF) (Huang et al., 1998). Unlike wavelet transform where a mother wavelet is employed, in EMD the original signal is utilized for decomposition procedure. The following steps constitute the sifting procedure to extract the IMFs (Fig. 3.4):

- identify upper and lower envelopes of the original signal,
- curve-fit the envelopes using a cubic spline,
- take the average of two envelopes to calculate the mean curve,
- subtract the mean curve from the original signal,
- repeat the procedure until the mean curve becomes efficiently zero (stoppage criteria),
- fulfil a certain stoppage criteria to obtain the first IMF,
- run the sifting produce until the residue becomes monotonic.

As a counterpart to the decomposed levels in DWT, each IMF is associated with specific frequency bands. The first IMF represents the highest frequencies of the original signal, whereas it lowers with subsequent IMFs. However, differently than DWT, the frequency bandwidths of the sub-signals are not governed by the original signal’s resolution or length, but the content of

it. Therefore, the energy carried by the same frequency ranges might be separated into more than a single IMF.

3.8 Summary

Fourier transform is the most commonly used technique to compute the frequency content of a signal. If the arrival time of a specific frequency is also required, short time Fourier transform should be performed. However, a fine resolution of time and frequency cannot be achieved with this method. On the other hand, continuous wavelet transform combines the frequency and time information at the same time without losing any information. Discrete wavelet transform is an improved version of CWT which makes computation to be more efficient and reduce the redundancy of CWT. Lastly, EMD is capable of decomposing a signal into its basic oscillatory modes; however, this technique requires more computation effort compared to the others. In this study, all of these techniques are used; except STFT, to analyze different wave characteristics of the measured signals.

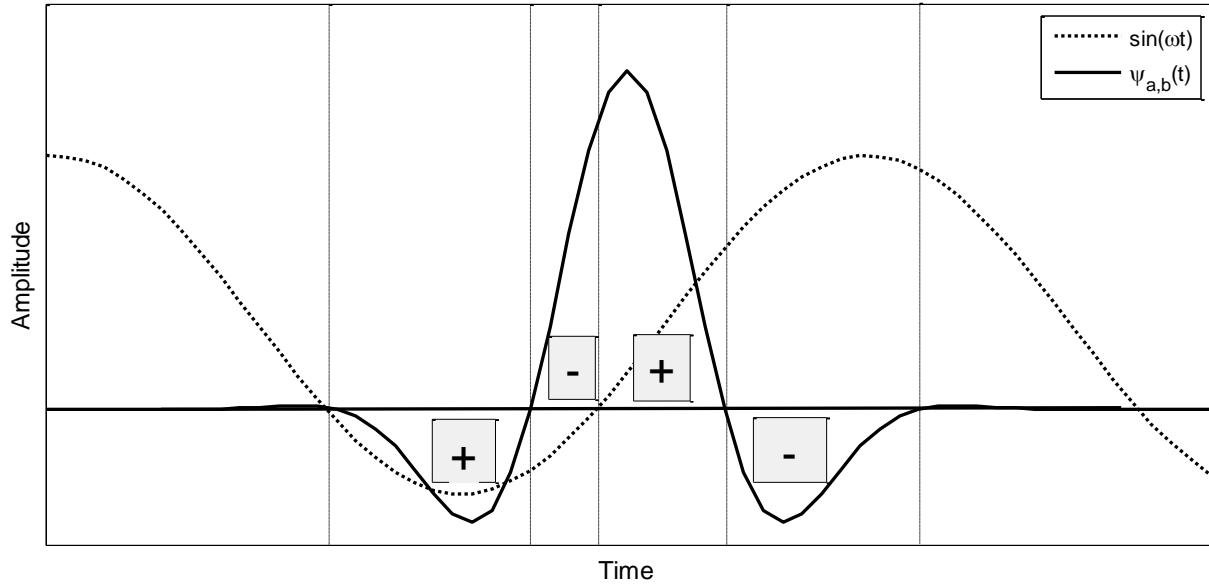


Figure 3.1: A wavelet superposing with a harmonic signal to illustrate the regions providing positive or negative contribution to the integral.

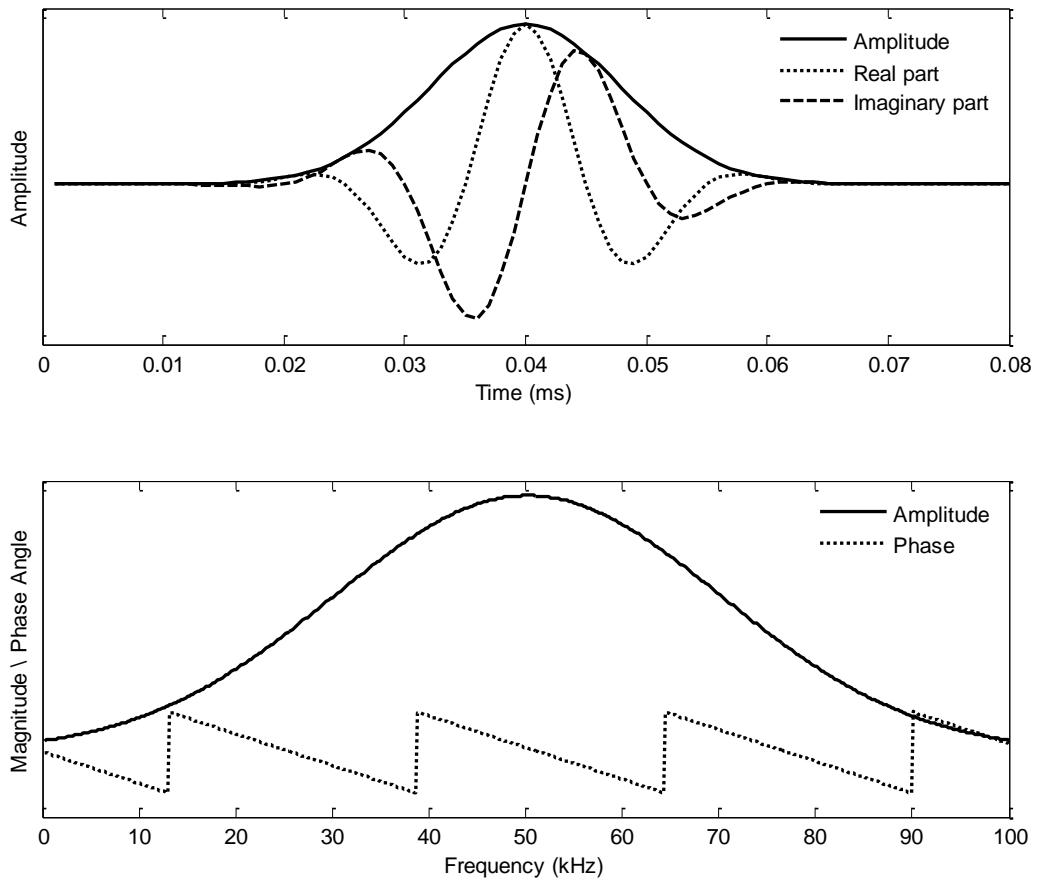


Figure 3.2: Morlet function of $f_0 = 52$ kHz and $\tau = 1.12 \times 10^{-5}$: (a) in time domain (b) in frequency domain.

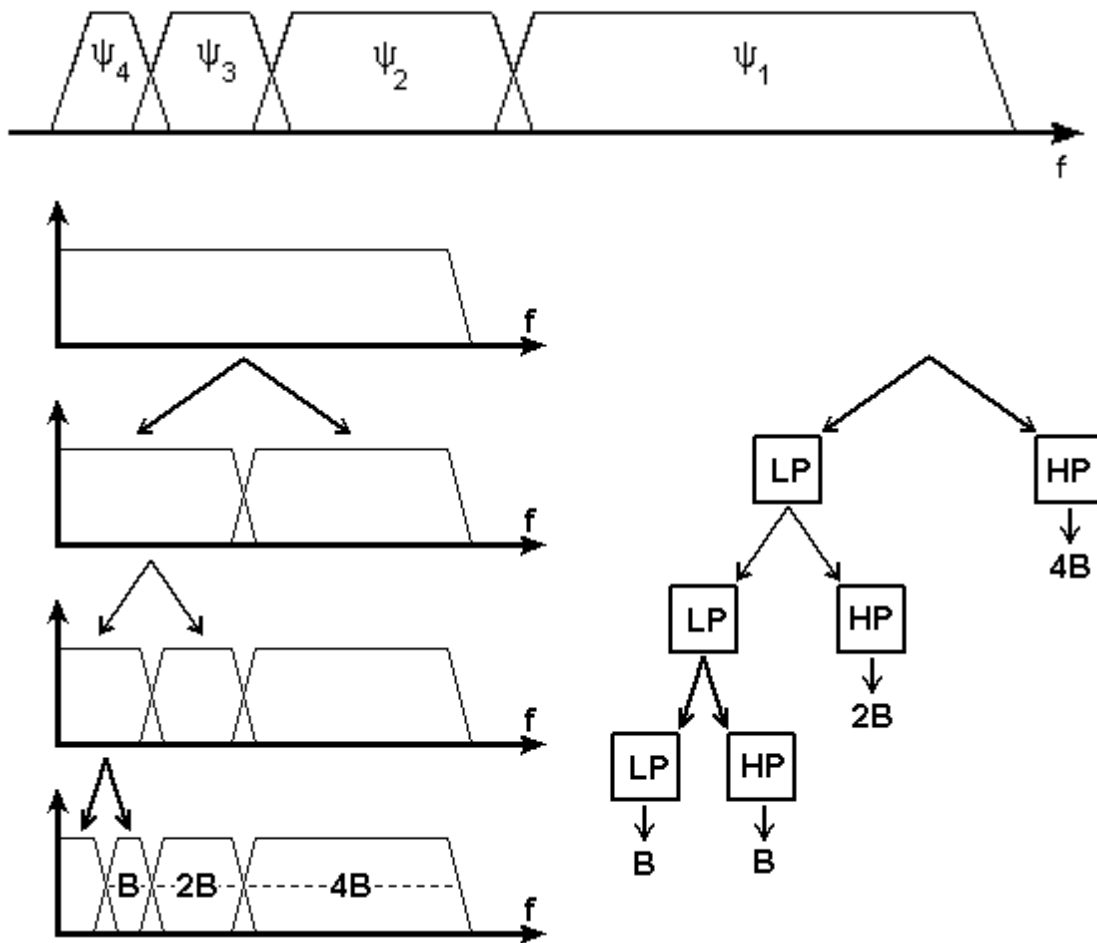


Figure 3.3: (upper) Series of wavelet spectra (lower) decomposition process by filter bank (Valens, 2004).

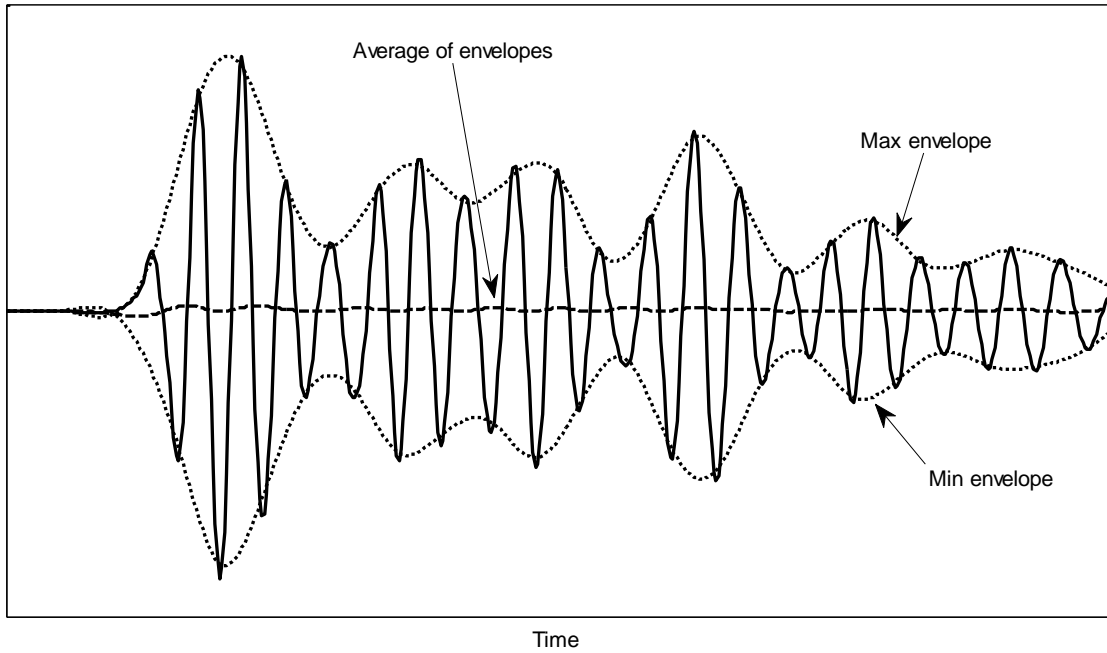


Figure 3.4: Sifting procedure for EMD.

Chapter 4 Literature Review on NDT of Concrete

4.1 Introduction

Non-destructive testing methods have roots back in 1930's; however, it was the 80's that NDT has become more applicable thanks to the developments in digital data acquisition and signal processing techniques. In this chapter, NDT techniques based on propagation of ultrasonic waves are reviewed. These wave-based methods provide information about the internal condition and elastic properties of materials. Depending on the problem investigated, the required technique may base on one of two different types of mechanical waves; either P-waves or surface waves. For instance, if one would like to determine the thickness of a concrete plate, techniques based on P-waves should be employed, whereas working on surface waves may be more appropriate for evaluation of depth of a surface-breaking crack. The most commonly known wave-based techniques: Ultrasonic Pulse Velocity (UPV), Impact Echo (IE), Fourier Transmission Coefficient (FTC) and Spectral Analysis of Surface Waves (SASW) are explained in the proceeding sections; the first two techniques measure the velocity of the waves, while the last two utilize other wave characteristics, such as attenuation or dispersion. In addition to these conventional techniques, determination of material damping from multi-channel analysis of surface waves (MASW) test data using wavelet transform is explained.

4.2 Ultrasonic Pulse Velocity (UPV) Test

Ultrasonic pulse velocity (UPV) test allow measuring the velocity of a transient wave passing through a medium (ASTM C597, 2002). By using the measured velocity, the elastic modulus of material can be then calculated as given in Eq. 2.11 and 2.13. The test is conducted by applying a pulse through a mechanical impact on the medium surface, so that a pulse travelling through the specimen is generated. This pulse develops longitudinal (P-wave), shear (S-wave) and surface waves that are shaped by the morphology, elastic modulus, density, microstructure and boundary conditions of the medium. The P-waves are the first ones reaching to the receiver transducer,

where the mechanical wave is converted into an electrical signal to be displayed on an oscilloscope (Fig. 4.1). Thereby, the P-wave velocity, V_p , can be calculated by:

$$V_p = l/t \quad (4.1)$$

where l is the length of the specimen, and t is the measured arrival time of the wave. Detection of voids and flaws are also possible with UPV. In the case of a void in the medium, waves arrive with delays causing lower velocities. However, if the voids are small enough, they do not lower the velocity but cause higher frequencies attenuate.

The UPV test has some significant drawbacks. First of all, the wave velocities may not always be an accurate indicator of the strength of concrete. It was shown that concrete specimens with lower strength caused by porosity do not display any remarkable decrease in wave velocity (Popovics, 1969). Moreover, the insensitivity of the pulse velocity to the presence of an opening cut in a concrete slab was demonstrated by Schickert (1984). Most of the time, a frequency range between 20 and 150 kHz is preferred to conduct the test. However, the small voids and micro-cracking that are smaller than the signal wavelength cannot be detected by the frequency range (Suaris et al., 1987). Lastly, this method assumes that wave velocity is constant with respect to frequency despite the fact that dispersion occurs in concrete. Because of all these limitations, UPV is not always reliable in determination of the conditions of concrete specimens.

4.3 Impact-Echo (IE) Test

Impact-echo (IE) test is based on measurement of stress waves travelling through a medium which are reflected by internal flaws and external surfaces (ASTM C1383-98a). IE test makes it possible to measure thickness of concrete plates or to locate voids, internal flaws and delaminations for the structures accessible only on one side. The test configuration differs from UPV test since the receiver transducer is placed next to the source of impact. During the test, a mechanical impact is applied to the surface of a plate like medium to generate stress waves propagating radially into the medium. Since back and forth reflections occur between the top surface and the internal defects or the bottom of the medium, multiple reflected waves are

detected by the receiver. Then, the detected waveform is recorded in time-domain and transformed into frequency-domain. Repeated reflections due to the bottom edge or any other reflector appear as a large peak in the frequency spectrum. All testing procedure is depicted in Fig. 4.2. The thickness of the plate medium or the distance from the reflecting interface is calculated by:

$$h = V_p/2f \quad (4.2)$$

where h is the distance to the reflector, V_p is the P-wave velocity and f is the frequency of P-wave reflections.

The limitation of this method is that it is hard to detect small defects in inhomogeneous materials due to the relatively low frequency range used (Popovics and Rose, 1994). On the other hand, preferring high frequencies above 100 kHz limits the investigation due to the scattering. In some cases, multiple peaks can be observed in the Fourier spectrum due to reflections from other interferences which preventing the depth of a crack to be calculated easily. To overcome this difficulty, Po-Liang et al. (2008) has suggested enhancing the Fourier spectrum by multiplying it with the wavelet marginal spectrum (WMS) of the signal. WMS is obtained by integrating the scalogram of the signal respect to time. Scalogram is the density plot of square of the wavelet transform of the signal which reveals the energy distribution along frequencies in time. As an example, Fourier, wavelet marginal and enhanced Fourier spectrums of a signal are shown in Fig. 4.3. The echo peak in the wavelet marginal spectrum is not as sharp as in the Fourier spectrum, but it exposes the dominant frequency in the whole time signal. The WMS works as a band-pass filter when multiplied with the Fourier spectrum, so that the echo peak is exposed precisely. The enhanced Fourier spectrum takes the advantages of both FT and WT: high frequency resolution from FT and temporal information from WT.

The following imaging techniques are also developed to visualize the data obtained from IE testing:

4.3.1 Spectral C-scan

A series of impact echo tests are performed at the grids of a square mesh drawn on the surface of a medium (Liu and Yiu, 2002). The tests are followed by the Fourier transform of the measured signals. Then, the spectral echo amplitude for each test location is represented in a given color scale. By plotting the density plot of these echo amplitudes, a 2D image of the horizontal cross-section of the tested area is constructed. The final image is called “spectral C-scan”. In the case of no interface on the test area, no color variation is observed on the image.

4.3.2 Surface Rendering Method

A surface rendering technique is proposed by Po-Liang et al. (2009) to upgrade the 2D C-scan to a 3D image. The echo frequencies are transformed into spatial manner to locate the defect depth in the third axis. The other two axes are set by the coordinates of the tested area. To achieve the transformation of the third axis, a constant depth interval, Δd , is chosen. Then, the depth of defect is determined by Eq. 4.2 where $i\Delta d$ ($i = 1, 2, \dots$) is substituted to find the corresponding frequency, f_i . Lastly, plotting the amplitude for each f_i versus $i\Delta d$ yields the depth spectrum of the signal. While this transform provides a spectrum for constant depth interval, it is possible that a peak in the original spectrum can be omitted if it falls between f_i and f_{i+1} . So, the maximum amplitudes in any interval (f_i, f_{i+1}) should be determined before plotting the depth spectrum of the signal. Fig. 4.4a and 4.4b show the model of a medium with an internal defect and its 3D image after surface rendering respectively. A hole appears beneath the void which provides supplementary information about the defect’s size and location.

4.4 Fourier Transmission Coefficient (FTC) Method

The penetration depth of the surface waves depends on the wavelength; while high frequencies travel at the shallow depth, lower ones go deeper thanks to their large wavelengths. The penetration is disturbed when the wave encounters with a surface-breaking crack. Depending on the crack depth, the relatively large wavelengths are transmitted to the other side, whereas the smaller wavelengths are filtered by the crack. Hevin (1998) found that if the crack is deeper than

one third of the wavelength, the associated frequency is not allowed to pass. Therefore, the cut-off wavelength, λ_{cut} , is three times larger than the crack depth, d :

$$\lambda_{cut} = 3d \quad (4.3)$$

Aggelis (2009) demonstrated this relation by carrying out experimental and numerical tests illustrated in Fig. 4.5a. The graph given in Fig. 4.5b shows the normalized transmitted amplitudes of the surface waves versus the crack depth normalized respect to the wavelength. The results revealed that the cracks having a depth of 0.3 of the wavelength could be detected.

A practical test configuration was developed by Popovics et al. (2000) to determine the depth of surface-breaking cracks: Fourier transmission coefficient (FTC). FTC is basically the ratio of the spectral amplitudes of the transmitted and incident surface waves, which is correlated with the crack depth. FTC method requires two sources and two receivers placed along a line at both sides of the crack as shown in Fig. 4.6a. The sources are mounted at points A and D, whereas the receivers are placed at points B and C. Force applied at point A generates transient waves recorded at point B and C, which are denoted as f_{AB} and f_{AC} respectively. Then, the measurement is repeated by applying the identical force at point D, so that the resulting signals f_{DC} and f_{DB} can be captured at points C and B respectively. Such a configuration allows to eliminate the unknown characteristics of the receivers, transmitters and couplings that exist between the transducers and the medium. The four recorded signals can be expressed in frequency domain as:

$$F_{AB}(\omega) = S_A(\omega)C_A(\omega)M_{AB}(\omega)C_B(\omega)R_B(\omega) \quad (4.4a)$$

$$F_{AC}(\omega) = S_A(\omega)C_A(\omega)M_{AC}(\omega)C_C(\omega)R_C(\omega) \quad (4.4b)$$

$$F_{DC}(\omega) = S_D(\omega)C_D(\omega)M_{DC}(\omega)C_C(\omega)R_C(\omega) \quad (4.4c)$$

$$F_{DB}(\omega) = S_D(\omega)C_D(\omega)M_{DB}(\omega)C_B(\omega)R_B(\omega) \quad (4.4d)$$

where $F_{AB}(\omega)$, $F_{AC}(\omega)$, $F_{DC}(\omega)$ and $F_{DB}(\omega)$ are the Fourier transforms of the time signals f_{AB} , f_{AC} , f_{DB} and f_{DC} ; $S_i(\omega)$, $C_i(\omega)$ and $R_i(\omega)$ are the transfer functions of the transmitters, the couplings and the receivers at point i respectively, whereas $M_{ij}(\omega)$ is the transfer function of the

medium between points i and j . Using these relations, the transmitted energy between points B and C is defined by Popovics et al. (2000) as:

$$FTC(\omega) = \sqrt{\frac{F_{AC}(\omega)F_{DB}(\omega)}{F_{AB}(\omega)F_{DC}(\omega)}} \quad (4.5)$$

Substituting Eqs. 4.4 in Eq. 4.5 and simplifying the unknown effects of the source, receiver and coupling, we have:

$$FTC(\omega) = \sqrt{\frac{M_{AC}(\omega)M_{DB}(\omega)}{M_{AB}(\omega)M_{DC}(\omega)}} \quad (4.6)$$

In the case of no crack, the FTC will be equal to one indicating transmission of all wave energy, while a zero value will reveal a complete attenuation.

The most significant benefit of this method is that the determination of wave velocity analysis is not required; therefore, the result is free of the unknown effects of source, receiver and coupling. On the other side, since the receivers are located unequally from the source, the contribution of the geometric attenuation to the total attenuation will be higher for the farthest receiver. To overcome this disadvantage, the equal spacing configuration shown in Fig. 4.6b was proposed by Yang (2009). In this configuration, two receivers are placed equally spaced from the sources, such that a square configuration forms. So that, the attenuation caused only by the crack can be determined. Another issue needed to be considered for both non-equal and equal spacing configurations is the interaction of the surface waves with the reflected P-waves from the bottom of the medium or from the crack. The decision of the appropriate source-receiver-crack spacing should be made carefully to reduce this interaction.

FTC can also be modified by employing other parameters, such as maximum amplitude of wavelet transform (Yang, 2009) or the spectral energy of a specific frequency range (Shin et al., 2008) other than the Fourier amplitudes. Regardless of the parameter preferred, the procedure to determine the transmission coefficient remains same.

4.5 Spectral Analysis of Surface Waves (SASW) and Multi-channel Analysis of Surface Waves (MASW) Methods

The SASW method, developed by Heisey et al. (1982), determines the shear modulus and thickness of the layers in a soil medium. This method bases on the calculation of dispersion of the surface waves in a layered medium. The test is performed with two receivers placed at a distance of Δx . The difference of phase, $\Delta\varphi(f)$ as a function of frequency, between the receivers is calculated from the phase of the cross-power spectrum of the corresponding signals as:

$$\Delta\varphi(f) = \varphi_2(f) - \varphi_1(f) = \text{phase}\langle Y_1(f)Y_2^*(f) \rangle \quad (4.7)$$

where $Y_1(f)$ and $Y_2(f)$ are the Fourier transform of the signals recorded at the corresponding locations and * represents the complex conjugate. Knowing the phase shift, $\Delta\varphi(f)$, and the distance, Δx , provides the phase velocity for a given frequency as:

$$V_{ph}(f) = 2\pi f \Delta x / \Delta\varphi(f) \quad (4.8)$$

This equation allows the dispersion curve to be computed from the experimental data, which is followed by an inversion process of the curve, so that the corresponding shear wave velocity profile, elastic moduli, and layer thicknesses can be calculated. For the inversion process, firstly a theoretical dispersion curve is constructed for an assumed shear wave velocity profile and the layer thicknesses, and then the theoretical curve is matched with the experimental one by iterating until a threshold is achieved. At the end, the shear wave velocity profile is obtained.

Figure 4.7a illustrates the test configuration where a mechanical impact generates the propagating waves captured by an array of receivers on the surface. The receiver spacing should be decided based on the following factors (Nazarian et al. 1983, Hiltunen et al. 1988, Stokoe et al. 1983): the wave velocity in the specimen, the expected depth, the frequency range of the transmitter, and the attenuation behaviour of the specimen. Mostly, it is kept short for shallow depths and large for the deeper layers of the medium. There are two phenomena that should be taken into consideration during the test: i) the near-field effect occurring when the distance

between the source and receiver is not long enough to let the waves fully form. ii) the far-field effect occurring when the spacing is relatively larger than the wavelengths. To overcome these concerns, the following criteria relating the receiver spacing with the wavelength is recommended (Heisey et al., 1982):

$$\lambda_R/3 \leq \Delta x \leq 2\lambda_R \quad (4.9)$$

where λ_R denotes wavelength of the Rayleigh wave. The configuration of the source and receivers has a direct effect on the recorded data (Hiltunen, 1988). The largest wavelength that can be recorded is determined by the source - first receiver distance, while the shortest one is determined by the distance between the receivers.

SASW method uses only two receivers, therefore the repetitions of the test are needed for different source-receiver spacings, so that different depths of the medium can be investigated. The test should also be performed in two opposite directions to check any internal phase shift due to the receivers or instrumentation (Nazarian et al., 1983). To reduce the test repetitions, the multi-channel analysis of surface waves (MASW) was developed (Park et al., 1997), in which multiple receivers spaced equally and a multi-channel seismograph are employed (Fig. 4.7b).

When the data captured during MASW test is analysed using a 2D spectrum analysis, the phase angle of each frequency can be evaluated as a function of distance. A horizontally uniform medium will display a phase function varying linearly with distance, whereas a non-uniform one will have a phase function deviating from a linear trend. Using a fine spacing between the receivers will increase the ability to detect the smaller anomalies in the horizontal properties of the medium. Although SASW and MASW were developed to determine the near surface soil profile, utilizing transmitters at ultrasonic range enables to assess the condition of concrete elements as well.

4.6 Material Damping from Wavelet Transform

A methodology to determine the material damping, based on the magnitude and phase information extracted from the wavelet transform of the surface waves, is proposed by Yang (2011). A travelling wave can be defined as:

$$g(t, x) = Ae^{-\alpha_t \omega_n(x)(t-t_x)} e^{-\alpha_x x} \cos(\omega_d(x)t + \theta(x)) \quad (4.10)$$

where A is the amplitude; α_t and α_x are temporal and spatial coefficients respectively; $\omega_n(x)$ and $\omega_d(x)$ are the natural and damped frequencies at distance x , respectively, for small values of damping, it can be assumed that $\omega_n(x) \approx \omega_d(x)$, t_x is the arrival time at distance x ; and $\theta(x)$ is the initial phase. For flaw detection, Su (2009) suggests to use Morlet function to perform wavelet transform due to the similarity between Morlet function and Lamb wave signals. Other wavelet functions, such as Mexican hat can also be investigated; however, in this thesis Morlet function is chosen for damage detection. The wavelet transform of Eq. 4.10, using Morlet function, $\phi(t)$, as the wavelet is expressed by:

$$G(a, b, x)^{\langle WT \rangle} = \frac{\sqrt{a}}{2} Ae^{-\alpha_t \omega_n(x)(b-t_x)} e^{-\alpha_x x} |\Phi(a\omega_d(x))| e^{i\omega_d(x)b + \theta(x)} \quad (4.11)$$

where $\Phi(\omega)$ is the frequency spectrum for the Morlet function. The phase spectrum can be extracted from Eq. 4.11:

$$Ph[G(a, b, x)^{\langle WT \rangle}] = \Theta(a, b, x) = \omega_d(x)b + \theta(x) \quad (4.12)$$

The amplitude of wavelet transform, $G(a, b, x)^{\langle WT \rangle}$, is maximum for $b = t_x$ for a distance x from the source. Therefore, the maximum amplitude, $G(1, t_x, x)^{\langle WT \rangle}$, simplifies to:

$$G(1, t_x, x)^{\langle WT \rangle} = Y(x) = \frac{A}{2} e^{-\alpha_x x} |\Phi(\omega_d(x))| \quad (4.13)$$

If the derivative of the phase spectrum of wavelet transform (Eq. 4.12) with respect to the shift time, b , is taken, the damped frequency, $\omega_d(x)$, is obtained:

$$\frac{\partial}{\partial b} [\Theta(a, b, x)] = \omega_d(x) \quad (4.14)$$

To determine the spatial attenuation coefficient, α_x , two maximum magnitudes at two distances are required: $Y(x_1)$ and $Y(x_2)$ are first normalized with respect to the corresponding mother wavelet magnitude, and then are substituted in Eq. 2.48; thus, α_x can be obtained as:

$$\alpha_x = -\frac{1}{x_2 - x_1} \left[\ln \left(\frac{Y(x_2)}{|\Phi(\omega_d(x_2))|} \right) - \ln \left(\frac{Y(x_1)}{|\Phi(\omega_d(x_1))|} \right) \right] \quad (4.15)$$

For $(x_2 - x_1) \rightarrow 0$, Eq. 4.15 can be written as a derivative:

$$\alpha_x = -\frac{d}{dx} \ln \left(\frac{Y(x)}{|\Phi(\omega_d(x))|} \right) \quad (4.16)$$

Substituting $\omega_d(x)$ from Eq. 4.14 and α_x from Eq. 4.16 into Eq. 2.47 gives:

$$D(x) = V \frac{\alpha_x(x)}{\omega_d(x)} \quad (4.17)$$

which is the material damping ratio varying with distance. This equation makes it possible to calculate material damping for different locations, and the average of these calculated values provides a mean damping ratio representing the whole medium.

4.7 Summary

The NDT techniques explained in this chapter mostly focus on detection of a single defect/ flaw/ crack. Hence, any preferred test has to be repeated for all cracks existing in a medium, which reduces the practicability of the method in the field. Among all methods

described above, MASW appears as a prominent method since larger portions of an element can be investigated by selecting appropriate receiver spacing and frequency range. Moreover, in-depth knowledge about the medium, including attenuation, damping and dispersion characteristics can be obtained from MASW. Therefore, in this study, MASW test configuration is utilized with various signal processing techniques to establish a reliable and practical procedure for the condition assessment of concrete elements.

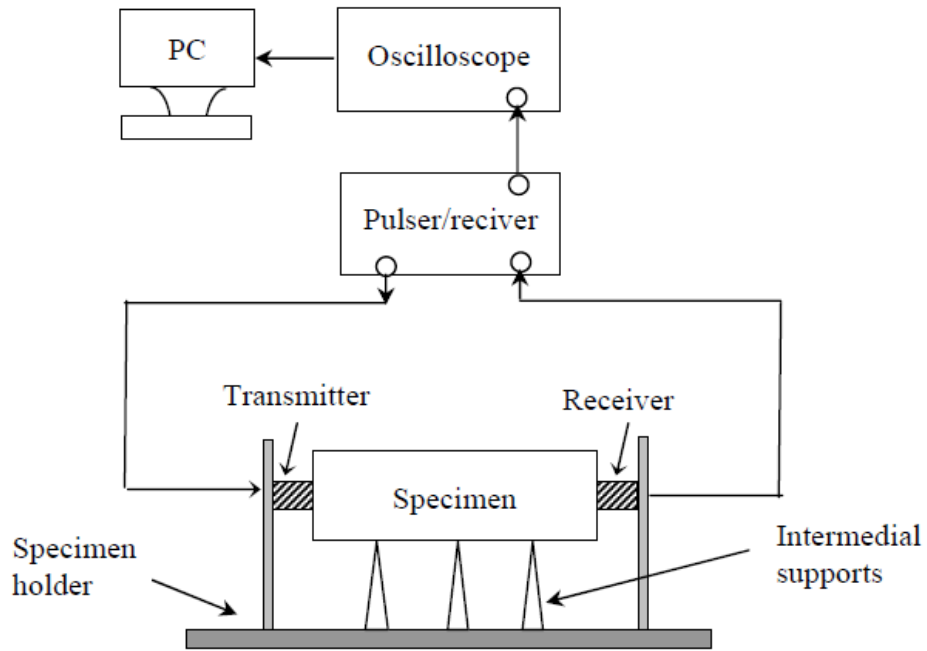


Figure 4.1: UPV test setup (Jiang, 2007).

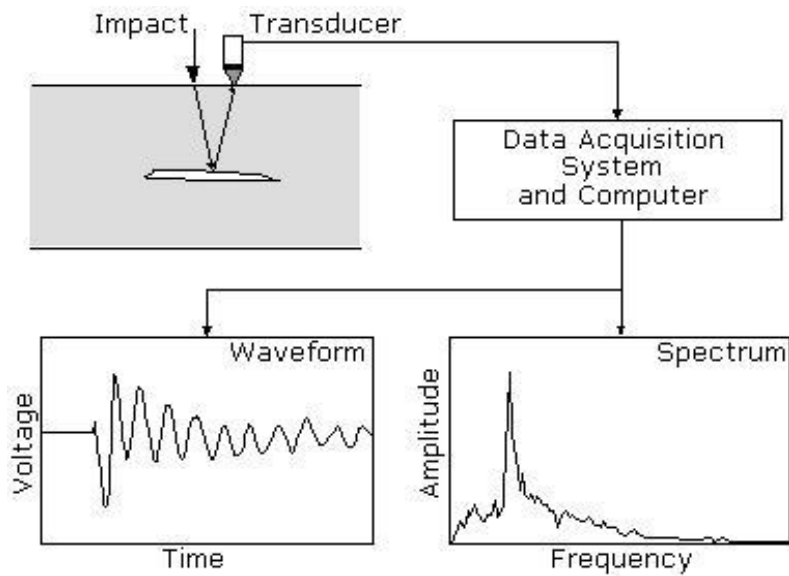


Figure 4.2: IE test procedure (Sansalone and Streett, 1997).

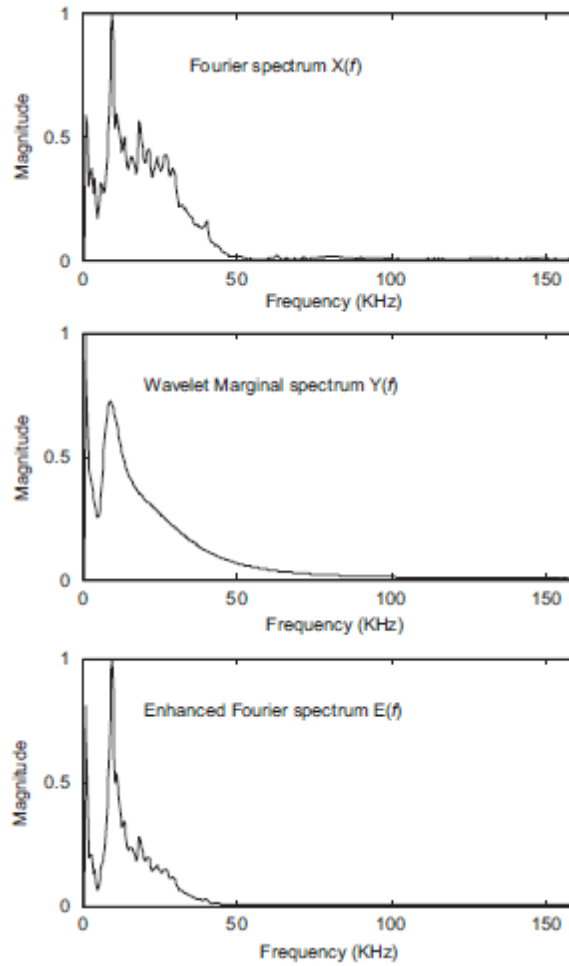


Figure 4.3: The Fourier spectrum at the top, wavelet marginal spectrum at the middle and the enhanced Fourier spectrum at the bottom (Po-Liang et al., 2008).

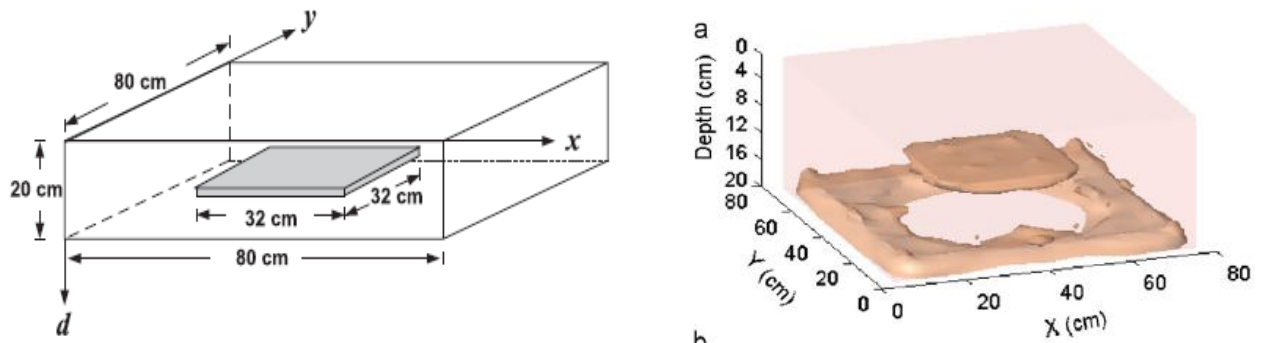


Figure 4.4: (a) Model of the specimen at the left (b) its 3D image after surface rendering at the right (Po-Liang et al., 2008).

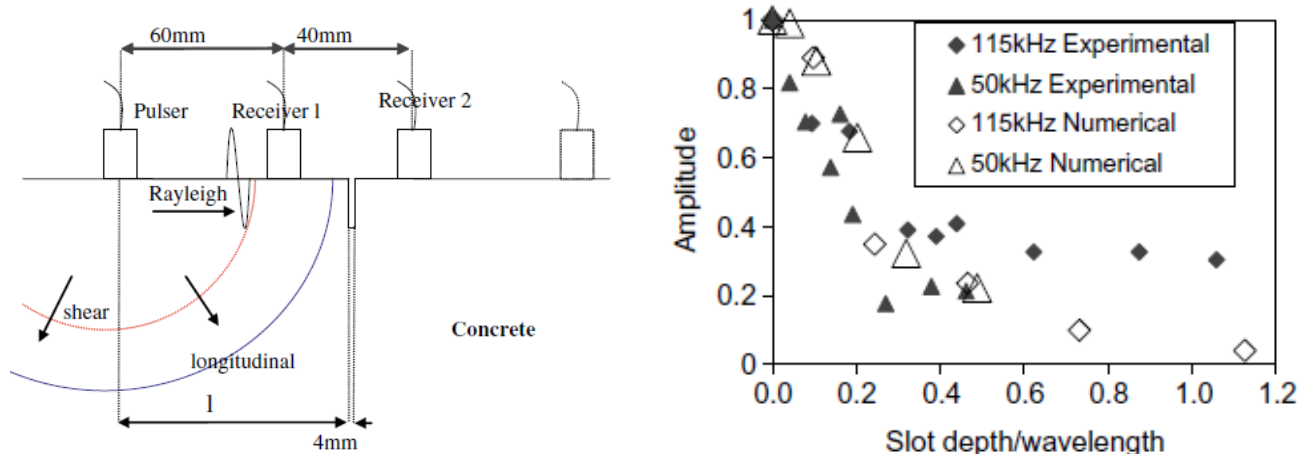


Figure 4.5: (a) Experimental setup at the left (b) normalized transmitted amplitudes of the surface waves obtained from the experimental and numerical tests versus the normalized crack depth respect to wavelength (Aggelis, 2009).

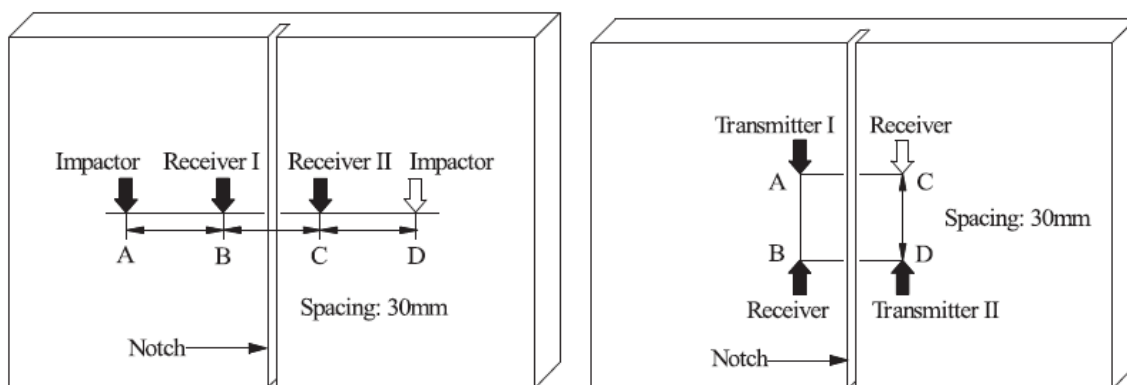


Figure 4.6: FTC test configurations: (a) non-equal spacing configuration at the left (Popovics, 2000) (b) equal spacing configuration is at the right (Yang, 2009).

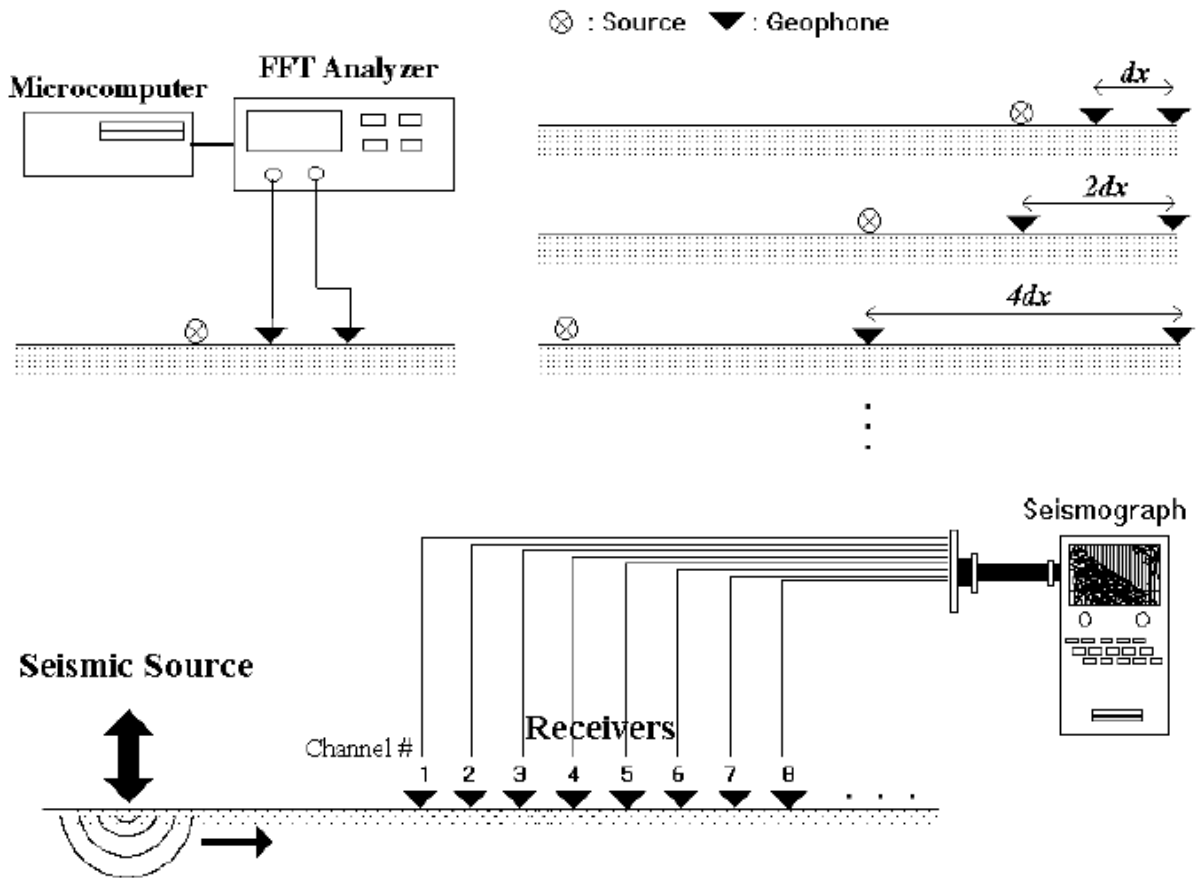


Figure 4.7: (a) SASW test setup at the top (b) MASW setup at the bottom (Park et al., 1997).

Chapter 5 Calibration of Accelerometers

5.1 Problem Statement

Ultrasonic tests based on pulse velocity, as described in Chapter 4, are preferred for the condition assessment of materials mainly because of their fast execution, low cost, and simplicity (ASTM C597 2002). In the pulse velocity testing, the first arrival of the wave is the only parameter that needs to be obtained; however, full-waveform methods use the whole time signal to provide additional information, such as phase velocity and material damping, as functions of frequency (Yang, 2009). These kinds of analyses are rarely performed in practice because of difficulties in characterization of transducers and their coupling with the specimen (Tallavo et al., 2009). If frequency response functions (FRF) of transducers are known, it is possible to calculate the actual response of a specimen. Any signal measured by a transducer includes responses from the medium and transducer itself. Therefore, the measured signal can be expressed in the frequency domain as:

$$Y(\omega) = X(\omega)H_S(\omega)H_{CS}(\omega)H_M(\omega)H_{CR}(\omega)H_R(\omega) \quad (5.1)$$

where Y is the signal recorded via the receiver, X is the electrical input excitation, H_S and H_R are the transfer functions of transmitter and the receiver, respectively; while H_{CS} and H_{CR} refer to the coupling characteristics between the transducers and the medium, and finally H_M is the transfer function representing the response of the medium. Therefore, the measured signal should be normalized respect to the frequency response function of the accelerometer to uncover the actual material response. In this chapter, three different piezo-electric accelerometers are calibrated by pursuing a procedure inspired from ISO 16063-13:2001 recommendations, where a laser Doppler scanner is employed. The accelerometers calibrated in this chapter are then used for the material characterization of a material made of cement and sand mixture as explained in Chapter 6.

5.2 Background

A piezoelectric transducer is a device that employs a piezoelectric crystal to convert electric signals into mechanical waves (transmitter) or vice versa (receiver). It generates voltage when a mechanical force is applied, and deforms mechanically when its faces are subjected to a voltage (Gautschi, 2002). The structure of an ultrasonic transmitter is shown in Figure 5.1. The output vibration of the transmitter can be modelled as a Morlet function in time domain (Yang, 2009) which is derived from an approximate model of the transfer function of the transmitter (Fitting, 1981). On the other hand, Figure 5.2 illustrates the physical model of a typical accelerometer (receiver), which basically consists of a mass, m , supported by a linear spring with stiffness, k , and damping element, c . The equation of motion for this single degree of freedom system is expressed by:

$$m \frac{d^2 r(t)}{dt^2} + c \frac{dr(t)}{dt} + kr(t) = m \frac{d^2 s(t)}{dt^2} \quad (5.2)$$

where $s(t)$ is the displacement at the base of the accelerometer and $r(t)$ is the displacement of the dynamic mass. The charge of a piezoelectric accelerometer, $q(t)$, can be expressed as a quantity proportional to the force $\gamma r(t)$, where γ represents a piezoelectric constant to convert the mechanical vibration of the mass into the charge (Link et al., 2004). So that, the output signals is:

$$z(t) = \kappa q(t) = \kappa \gamma r(t) = \rho r(t) \quad (5.3)$$

where κ is a preamplifier gain factor which transforms the charge into the accelerometer output signal and ρ is called as sensitivity factor of the accelerometer which combines both constants; κ and γ . Using Eq. 5.3 and the expressions $2\delta = c/\sqrt{km}$ and $\omega_0^2 = k/m$, Eq. 5.2 can be expressed as:

$$\ddot{z} + 2\delta\omega_0\dot{z} + \omega_0^2 z = \rho\ddot{s}(t) \quad (5.4)$$

where ω_0 and δ are the resonant angular frequency and damping ratio of the accelerometer, respectively. The analytical transfer function between the base acceleration and the mass acceleration given in Eq. 5.4 is expressed by (Link et al., 2006):

$$H(\omega) = \frac{\rho}{(\omega_0^2 - \omega^2) + 2j\delta\omega\omega_0} \quad (5.5)$$

In practise, it is difficult to determine the analytical frequency response function of a transducer because the details of the material properties of the transducer are usually not provided by the manufacturer. Even if the initial properties are known, transducer properties may change within time. The response of a transducer can be, however; determined by means of experimental measurements. There is a series of calibration standards for accelerometers published by the International Organization of Standardization (ISO), under the title of ISO 16063 to guide the experimental methods. The main goal in these codes is to determine the sensitivity of the transducers, which is defined as the ratio of the electrical output to the mechanical input applied along a specified axis. In most of the cases, it a complex quantity including both amplitude and phase information given in terms of millivolt, mV per acceleration of gravity, g . The frequency response function of the transducer is calculated by normalizing the response respect to the sensitivity at a reference frequency within the flat range (Harris, 2002). The ISO standards can be categorized based on two types of properties:

- i) The type of excitation used for calibration: sinusoidal vibration or shock impact. The excitation type is selected according to the usage of the accelerometer. If a full frequency response function is needed, the calibration should be carried out using a sinusoidal sweep excitation. Thus, the complex sensitivity factor, covering the frequency range of interest, is obtained. On the other hand, if the response of the accelerometer against high amplitude acceleration is required, a shock pulse should be used. In this case, a single sensitivity value corresponding to that particular shock pulse identified by a specific shape, amplitude and frequency bandwidth is obtained. A complex sensitivity function may be calculated from the information obtained from the shock calibration measurement (ISO 16063-13 Annex C), which is valid only for that particular shock pulse. These methods are also limited for frequencies up to 10 kHz.
- ii) The type of test configuration: absolute calibration of the receiver (primary) or relative calibration respect to a primarily calibrated receiver (comparison or secondary): Here, the

term “primary” refers to absolute measurement of the transducer’s sensitivity by measuring the motion applied to the transducer following one of the methods given in ISO 16063-13. Laser interferometry technique is the one preferred among the others for this study. A laser beam is split into two, one beam travelling along a reference path and the other one striking a moving target causing the frequency of the reflected beam modulated by a phase shift. Then, interference of these two reflected beams is captured by a photodetector, and is consequently encoded (demodulation) in the output signal of the photodetector in both magnitude and phase (Harris, 2002, ISO 16063-1:1998). If it is not possible to measure the input motion directly, then ISO 16063-22 recommends comparative calibration methods respect to a reference transducer calibrated by the mean of primary calibration. A summary of the methods given in ISO 16063-13 & 22 are tabulated in Appendix A.

The ISO standards do not provide the parameters of the SDOF system given in Eq. 5.5. To overcome this drawback, Link et al (2004) proposed an accelerometer identification method based on the back calculation of the resonant frequency and damping ratio of a transducer from the experimental data. The procedure includes acquisition of input and output accelerations as described in ISO 16063 series, then the equation of motion of the SDOF system (Eq. 5.4) is represented as a first order differential equation using the state-space model and finally the model parameters are estimated using a prediction error method.

The limitations of the calibration procedures followed within this research are discussed next. The first limitation arises due to the frequency range of the transmitter. The transmitter is capable of generating energy over a frequency range of 10 to 70 kHz with a resonant frequency at 54 kHz. ISO 16023-22 requires that the resonant frequency of the accelerometer should be at least five times higher than the resonant of the transmitter. However, the transmitter used in this work has a nominal resonance at 54 kHz which overlaps with the resonant frequencies of the test accelerometers (see section 5.3). Moreover, contrary to mechanical vibrators or air bearing electro-dynamic shakers, the piezoelectric transmitter used in this study does not provide a uniform axial force, as recommended in ISO 16063 standards. Instead of an uniaxial wavefront, a superposition of different flexure modes of a circular plate is generated (Tallavo et al., 2009). Jones (1968) manipulated the resonance and the damping of particular frequencies by mounting

resonance masses and damping layers on the top of a piezoelectric transmitter, so that a desired uniform flat response may be achieved. However, in this work a transmitter without any modification is employed. The objective of this study is to calibrate the receivers for specific ultrasonic tests which are performed to evaluate material damping of the specific test material (Chapter 6). Considering these limitations, the approach imitates the primary calibration methods as explained in the next section.

5.3 Calibration Tests

5.3.1 Test setup and procedure

The frequency response function of an accelerometer can be determined if the output displacement generated by the transmitter is known. Therefore, first the vibration at the top of the transmitter is measured using a laser-scanner (Polytec MSV-400) with a built-in microscope. The objective (Mitutoyo M Plan Apo 2X) mounted on the microscope enabled a scan area of $3 \times 3 \text{ mm}^2$. Compared to the surface area of the 2.5-cm-radius transmitter, the scan area of the microscope was small. Therefore, the top surface of the transmitter was meshed by squares of $3 \times 3 \text{ mm}^2$ to guide the scanning process. The complete test setup (Fig. 5.3) includes a 54 kHz piezoelectric transmitter, the pulse generator to drive the transmitter, the function generator integrated oscilloscope (Aligent DSO-X 3014A) to generate the input excitation and also to acquire accelerometer output, and the laser scanner.

After capturing the vibration at the top of transmitter, three different accelerometers are mounted at the center of transmitter (Fig. 5.4). The first one (PCB 353B65) has a resonant frequency of 52 kHz with a flat response from 10 Hz to 10 kHz ($\pm 3 \text{ dB}$) and a sensitivity of 102.9 mV/g. The second one (PCB 352A60) has a resonant frequency above 95 kHz and a flat response between 5 Hz and 60 kHz at ($\pm 3 \text{ dB}$) with a sensitivity of 9.98 mV/g. The last one (Dytran 3055B3) has a resonant frequency of 35 kHz and a flat response between 1 Hz and 10 kHz with a sensitivity of 504.1 mV/g. The nominal properties of the accelerometers are summarized in Table 5.1. For simplicity, PCB 353B65, PCB 352A60 and Dytran 3055B3 will be denoted as A1, A2 and A3

respectively in the rest of this chapter. Each accelerometer is mounted using a nut that is glued on the transmitter.

Table 5.1 Nominal properties of accelerometers

Accelerometer	A1	A2	A3
Model	PCB 353B65	PCB 352A60	Dytran 3055B3
Serial no	44352	70329	5622
Sensitivity	102.9 mV/g	9.98 mV/g	504.1 mV/g
Frequency range	10-10,000 Hz	5-60,000 Hz	1-10,000 Hz
Resonant frequency	≥ 52 kHz	≥ 95 kHz	≥ 35 kHz
Measurement range	± 50 g	± 500 g	± 500 g
Mass^[1]	1.72 (2.64) gr	5.76 (7.00) gr	8.63 (10.66) gr

[1] Masses given in the parenthesis are the total masses including the required nut, screw and spacer.

All accelerometers are subjected transient and sinusoidal excitations during the calibration tests:

1. **Transient excitation:** The calibration is performed by exciting the ultrasonic transmitter with a square pulse of 4 ms duration. The vibration at the base of the accelerometer is measured along the radius of the transmitter while the accelerometer is attached on it. The input velocity to the accelerometer is computed by averaging the velocities captured at the base. The velocity at the top of accelerometer is measured to check if the accelerometer moves rigidly respect to the transmitter surface. To summarize, three kinds of data are captured for transient excitation (Fig. 5.5):
 - Electrical output signal of the accelerometer, “output signal”,
 - Velocity measured at the top surface of transmitter (base of the accelerometer) while the accelerometer is attached, “input velocity”,
 - Velocity measured at the top of the accelerometer to check the rigid body motion, “top velocity”.
2. **Steady-state sinusoidal excitation:** Sinusoidal excitations covering a range of frequencies from 10 kHz to 100 kHz are also used in this study.

The calibration measurements are summarized in Table 5.2. As for the laser measurements under transient excitation, the transmitter is excited by 125V to provide as large vibration amplitudes as possible so that a stronger interferometric signal can be ensured for the laser scanner. On the other hand, in order to acquire the accelerometers' output signals, a different excitation voltage for each accelerometer is used since higher voltages cause saturation in the response. It is possible to use different excitation voltages to measure the output and input signals because of the linear response of the transmitter respect to voltage.

Table 5.2 Calibration measurements

Excitation	Measured Signals	Signal Type	Input Voltage (V)				Acquisition Resolution
			No mass	A1	A2	A3	
Square Pulse	Input(Base) ^{[1][2]}	Velocity	125	125	125	125	1.024 MHz
	Top ^[1]	Velocity	N/A	125	125	125	1.024 MHz
	Output	Acceleration	N/A	2.5	125	25	1 MHz
Sinusoidal Wave	Input(Base) ^[3]	Velocity	25	25	25	25	1.024 MHz
	Output	Acceleration	N/A	2.5	25	2.5	400 kHz

[1] The velocity signals are acquired by the laser scanner after taking average of two hundred signals, so that the high noise ratio due to poor reflective surface could be decreased. [2] Three data sets are recorded by the laser scanner from three different lines parallel to the radius of top surface of the transmitter, when the accelerometer is attached at the top. For each scan location the average of associated three signals from the data sets are taken to improve the quality of the signal in the case of a poor reflective point on the top surface. [3] Readings taken on nine scan points close to the center of the transmitter's diameter for each frequency.

5.3.2 Results of Tests

This section first presents the test result for the response of the transmitter with no mass on top; and then, the test results for the accelerometers A1, A2 and A3. Before computing the FRFs, the signal processing procedure depicted in Figure 5.6 - where a digital 6th order recursive band-pass Butterworth filter with the cut-off frequencies of 5 and 100 kHz - is used for output and input signals. It is followed by computation of the empirical TFs, which is simply the conventional frequency response function estimator defined as the cross input-output spectrum divided by the input auto-spectrum in frequency domain (Maia, 1997). The input and output signals are

normalized with respect to the excitation voltages before computing the FRFs. The velocity and displacement FRFs are also computed.

A square excitation is used to excite the transmitter. The effect of this type of excitation can be assumed as a spike with a duration equal to the time-lag between the arrival and the first peak of the vibration measured at the top of transmitter. The corresponding frequency content of the spike is broad enough to cover the frequency range of interest (Fig. 5.7). The first set of measurements includes 140 signals recorded on 20 scan areas along the diameter of the transmitter without any mass on top (Fig. 5.8). The maximum value of the measured velocity on the top of the transmitter under the excitation pulse of 125 V is 0.0072 m/s and the derived acceleration and displacement are 215 *g* (2107 m/s²) and 28.5 μ m respectively. Twenty velocity signals, ten signals on each side of the center of diameter, are selected to compute the average velocity and its variation along the portion of the diameter which overlaps with the diameter of the receivers to be calibrated. Before averaging the signals, each one is filtered and then normalized respect to its maximum peak-to-peak (PTP) value. Linear regression analysis for the PTP values of these signals respect to the distance to the center of the transmitter is performed. The value in the linear trend that is corresponding to the center of the diameter is picked for each pair, and then the average of these two values is taken to be multiplied with the normalized velocity signal. Table 5.3 summarizes the maximum values for measured and computed vibrations. The coefficient of variance (COV) is mostly found as smaller than 10% between 10 and 70 kHz for the signals taken into account for averaging (Fig. 5.9). Acceleration and displacement computed from the average velocity are displayed in Figure 5.10. Three signals representing the motion on the center and quarters of the diameter are given in Figures 5.11-5.13 for acceleration, velocity and displacement; all of which reveal the symmetrical vibration respect to the center of the diameter. However, this symmetrical behaviour declines with the further distance from the center as shown in the contour plot of the frequency content of the measured velocities in Figure 5.14. Also, the displacement traces integrated from the velocities along the diameter of the transmitter exposes the first mode of vibration of the transmitter's face, and then the contribution of higher modes causing fluctuations as shown in Figure 5.15. Additional plots for acceleration and velocity traces are also presented in Appendix B (Figs. B.1 and B.2).

As expected, mass of the accelerometer affects the vibration occurring on the transmitter. The mass effects on the vibrations because of A1, A2 and A3 are compared to the case of no mass in Figure 5.16. Since the mass of the accelerometer alters the vibrations, input signals are measured for each accelerometer separately so that the associated FRFs can be calculated. As a complementary analysis, the normalized velocities under transient and sinusoidal excitations are compared in Figure 5.17. The maximum amplitudes of responses in time domain upon the standing sinusoidal waves of frequencies from 10 to 100 kHz are displayed along with the Fourier spectrum of response under the transient excitation. Responses under these two types of excitations show good agreement.

Table 5.3 Maximum vibration measurements

Signal	Acceleration (m/s ²)	Velocity (x10 ⁻³ m/s)	Displacement (η m)
Input ^{[1][2]}	2107.0	7.2	28.48
Input ^[3]	1929.8	6.8	27.28
Δ Input ^[4]	8.4%	5.5%	4.2%

[1] Velocity is measured by the laser scanner; acceleration and displacement are derived from the measured velocity. [2] Values before regression analysis. [3] Values after regression analysis. [4] Difference between the measured and computed input values over the measured input value.

5.3.2.1 Results of Tests for Accelerometer A1

The input and top velocities for A1 are measured at the scan areas shown in Figure 5.18. The acquired output of A1 is normalized respect to its sensitivity factor of 102.9 mV/g before integrating it into velocity and displacement (Fig 5.19). The normalized input velocity is calculated by taking the average of 20 readings as it is explained in the previous section; however, more variation in frequency content is observed (Fig. 5.20) compared to the no mass case. Next, the maximum peak-to-peak values are selected for these 20 signals, as pairs of 10, to perform regression analyses respect to the distance as it is performed for no mass case to compute the input signal for the accelerometer (Fig. 5.21). The computed input signal is later used to compute the FRF. All measured velocities along the diameter and its derived accelerations and displacements, along with some selected signals can be seen in Appendix B (Figs. B.3 to B.9). On the other hand, ‘Top’ velocity is computed by taking the average of the normalized signals captured on the top of receiver’s case (Fig. 5.22), and then multiplied with the

maximum amplitude of the signal obtained at the center, before deriving the acceleration and displacement (Fig. 5.23). Although compared to the input acceleration, the top acceleration trace reveals that the case of A1 vibrates completely different than the active material (Fig. 5.24a,b), it still satisfies that no tilting affect occurs on the accelerometer since all signals captured on the top varies from the mean velocity slightly (Fig. 5.22).

Figure 5.24 displays the output, input and top accelerations for A1 together. The same type of plot for velocity and displacement can also be seen in Appendix B (Figs. B.10, B.11). The measured and computed maximum vibration values for acceleration, velocity and displacement are all summarized in Table 5.4 along with the maximum values of input signals before the regression analysis which are taken from Appendix B (Figs. B.3, B.5 and B.7). The difference between the computed and measured input signal over the measured value is the least for displacement, due to the fact that integration has a smoothing effect which reduces the variations of spikes in the input signal. All signals presented in this section are filtered by a digital 6th order recursive 5-100 kHz band-pass Butterworth filter. As the last analysis, the output accelerations and the input velocities for A1 under transient and sinusoidal excitations are compared in Figure 5.25. The peak amplitudes obtained under sinusoidal excitations are also normalized respect to the input voltage (output voltage of piezo-driver) since it varies by changing the sinusoidal frequency. The responses of transmitter and A1 under these two different excitations present close trends. To conclude, the frequency response functions, both gain and phase shift, for acceleration are computed for a frequency band between 10 and 70 kHz as shown in Figure 5.26. The FRF for velocity and displacement are also determined as given in Appendix B (Figs. B.12 and B.13).

Table 5.4 Maximum vibration measurements

Signal	Excitation Voltage (V)	Acceleration (m/s²)	Velocity (x10⁻³ m/s)	Displacement (nm)
Output ^[1]	2.5	112.1	0.36	1.60
Input ^{[2][3]}	125	1713.7	5.9	25.50
Input ^{[2][4]}	125	1571.6	5.4	24.79
ΔInput ^[5]	N/A	8.3%	8.5%	2.8%
Top ^[2]	125	12539	34.2	105.10

[1] Acceleration is acquired; velocity and displacement are integrated from the measured acceleration. [2] Velocity is measured by the laser scanner; acceleration and displacement are derived from the measured velocity. [3] Values before regression analysis. [4] Values after regression analysis; these values are used

for computing FRF. [5] Difference between the measured and computed input values over the measured input value.

5.3.2.2 Results of Tests for Accelerometer A2

The data and analyses for the calibration of A2 (Fig. 5.27) are presented in the same order as A1. The output signal (Fig. 5.28) is obtained by dividing the recorded signal by the sensitivity factor of 9.98 mV/g. The measured input velocities (Fig. 5.29) exhibit less variation compared to A1. The input velocity (Fig. 5.30) is computed in the same manner with A1. Additional plots of acceleration, velocity and displacement traces and spectra are provided in Appendix B (Figs. B.14-B.19). The contour plot given in Figure B.20 indicates that the energy is mostly concentrated in the same frequency bandwidth as in the cases of no mass and A1.

To measure the motion at the top of A2, an aluminum spacer was manufactured to provide a flat reflection surface for the laser. The laser beam is aimed to four scan areas; each on one side of the spacer (Fig. 5.27). For each scan area, 13 signals are captured and averaged to represent the motion on each side (Fig. 5.31). Unlike the results for A1, variation is observed in frequency content between the sides of the receiver indicating a non-rigid motion respect to the base. This is most probably caused because of larger height of A2. Nevertheless, the average of these four signals is taken to represent the top signal (Fig. 5.32) which features the same peaks in frequency spectrum as the output signal (Fig. 5.33) indicating the accelerometer's active element and case vibrates somehow closer unlike A1.

Output, input and top signals are compared in terms of acceleration in Figure 5.33 (see Figs. B.21 and B.22 for velocity and displacement). The maximum values for each vibration type are summarized in Table 5.5. The difference between the computed and measured input signals is the smallest for displacement like as A1. However, compared to A1, the differences are larger for all signals. This indicates that the laser scanner readings are scattered more compared to the case of A1. The reliability of the signals obtained under transient excitation is confirmed by those captured under the steady-state sinusoidal excitations as given in Figure 5.34. The computed FRF for acceleration (Fig. 5.35) exposes a peak at 20 kHz with a relative flat response beyond that (see Figs. B.23 and B.24 for the FRFs of velocity and displacement).

Table 5.5 Maximum vibration measurements

Signal	Excitation Voltage (V)	Acceleration (m/s ²)	Velocity (x10 ⁻³ m/s)	Displacement (η m)
Output ^[1]	125	533.4	2.2	19.77
Input ^{[2][3]}	125	1751.2	6.1	24.19
Input ^{[2][4]}	125	1390.5	5.0	22.61
ΔInput ^[5]	N/A	20.6%	18.0%	6.5%
Top ^[2]	125	1331.8	4.7	34.34

[1] Acceleration is acquired; velocity and displacement are integrated from the measured acceleration. [2] Velocity is measured by the laser scanner; acceleration and displacement are derived from the measured velocity. [3] Values before regression analysis. [4] Values after regression analysis; these values are used for computing FRF. [5] Difference between the measured and computed input values over the measured input value.

5.3.2.3 Results of Tests for Accelerometer A3

The last calibrated accelerometer is A3 (Fig. 5.36). Response of the accelerometer reveals two peaks; 15 and 48 kHz (Fig. 5.37). The second peak at 48 kHz is due to the resonance of the transmitter (Fig. 5.38). The measured signals along the diameter of the transmitter as well as their derived accelerations and displacements are presented in Appendix B (Figs. B.25 - B.31) in the same order as those given for the previous accelerometers. Compared to A1 and A2, similar frequency content for the input vibrations are attained (Fig. 5.39). However, the maximum values of computed and measured input signals (Table 5.6) are smaller compared to A1 and A2. The reason is because the diameter of A3 is almost twice larger than A2 which prevents to take readings close to the center of the transmitter.

The vibrations at the top of A3 are measured at five scan areas shown in Figure 5.36. The average of the measurements taken at the four edges of the top is shown in Figure 5.40. The variations in the vibrations at the different edges indicate that the rigid body motion could not be achieved most likely due to the large height of A3. However, the velocity signals read at the center of the accelerometer are used to compute the top signal shown in Figure 5.41. As observed for A1, the case of A3 introduces multiple resonant frequencies. Figure 5.42 presents the acceleration for output, input and top signals to expose the resonant frequencies caused by each component of the system; transmitter, piezoelectric material and case of A3 (see Figs. B.32 and B.33 for velocity and displacement).

The maximum vibration values are given in Table 5.6. The difference between the computed and measured input signals, compared to other two accelerometers, is quite large for all signals. As mentioned earlier, because of the large diameter of A3, the readings could not be taken at the closer distances to the transmitter's center. Hence, the signals scanned have less STN ratio causing larger variation in neighbour readings. As like A1 and A2, A3 also provides similar responses under so called sinusoidal sweep and transient excitations (Fig. 5.43). Finally, the frequency response function for acceleration is computed (Fig. 5.44, see Figs. B.34 and B.35 for the FRFs in velocity and displacement) which exhibits a flat-like response between 20 and 60 kHz, despite the fact that it has been advised as having a resonant frequency beyond 35 kHz.

Table 5.6 Maximum vibration measurements

Signal	Excitation Voltage (V)	Acceleration (m/s ²)	Velocity (x10 ⁻³ m/s)	Displacement (μ m)
Output ^[1]	25	103.8	0.49	3.88
Input ^{[2][3]}	125	1470.7	5.5	23.02
Input ^{[2][4]}	125	1089.9	3.8	19.95
ΔInput ^[5]	N/A	%25.9	%30.9	%13.3
Top ^[2]	125	4101.4	13.1	41.71

[1] Acceleration is acquired; velocity and displacement are integrated from the measured acceleration. [2] Velocity is measured by the laser scanner; acceleration and displacement are derived from the measured velocity. [3] Values before regression analysis. [4] Values after regression analysis; these values are used for computing FRF. [5] Difference between the measured and computed input values over the measured input value.

5.3.3 Conclusion and Discussions

The variation in the amplitude of the measured velocity increases with respect to the larger accelerometer size and mass (Table 5.7). The maximum values of the input velocity change between 5.5 and 6.1 m/s due to the fact that the scan locations are constrained by the size of the accelerometer. The bigger the size, the further from the center of transmitter could be scanned which results in recording smaller amplitudes of vibrations. Moreover, the velocities computed using the regression analysis of the measured ones have maximum values from 3.8 to 5.4 m/s. The difference between the measured and the computed velocities is largest for A3. Because the readings could not be taken at the closer distances to the transmitter's center compared to A1, the signals measured for A3 have less STN ratio. Regarding the outputs of the accelerometers, A2

and A3 resonance at multiple frequencies whereas, all of three expose clearly the resonant frequency of the transmitter in the neighbourhood of 48 kHz.

Table 5.7 Coefficient of Variations for Input Signal

Signal	No Mass	A1	A2	A3
Input	6.9%	9.9%	13.9%	28.3%
Top	N/A	14.0%	16.1%	22.7%

On the other hand, the vibrations recorded at the top of the accelerometers reveals two facts. The first one is that as the mass and size of the accelerometer increases, the variation in vibrations at the top of the accelerometer increases indicating that rigid body motion of the accelerometer respect to the base is jeopardized (Table 5.7). Secondly, the accelerometer case vibrates differently with respect to the accelerometer’s active element and the base. The variation between the responses of the active element and the case is significant for A1 and A3 whereas it is less significant for A2. Moreover, the displacements at the top of the accelerometers are larger in amplitude compared to the vibrations measured at the base as given in Table 5.8. Therefore, in the case of a back-to-back calibration configuration the output signal of the reference accelerometer cannot be used as the input excitation for the one to be calibrated.

Table 5.8 Displacements

Signal	No Mass (ηm)	A1 (ηm)	A2 (ηm)	A3 (ηm)
Input	27.28	25.50	24.19	23.02
Top	N/A	105.10	34.34	41.71

Another main limitation of the test configuration is the fact that the excitation source is capable of transmitting energy for the frequencies between 10 and 70 kHz. Hence, as for all three accelerometers, the computed FRFs are not accurate for the frequencies out of this range. It is recommended to use transmitters with different frequency band-widths to extent the calibration for a broader frequency range. In consequent, the real dynamic behaviour of the medium under investigation can be approximated closer. Also, the calibrated accelerometer should be reasonably smaller in size than the transmitter to ensure the uniaxial excitation during the calibration test. Nevertheless, the FRF of the transducers determined in this chapter will be used

for material characterization in the next chapter. Normalizing the response captured on the test specimen respect to the computed FRF of the accelerometer will provide the real dynamic behaviour of the sample under investigation, as long as the type of excitation pulse is kept same.

5.4 Summary

A calibration approach is explained to determine the experimental frequency response function (FRF) of the accelerometers that are used for frequencies out of their flat responses. For the procedure, a microscopic laser scanner is employed to measure the output response generated by a piezoelectric transmitter when the piezoelectric accelerometer is mounted on top of the transmitter. The FRFs of three different accelerometers are determined for a frequency range from 10 to 70 kHz. These accelerometers are used to perform multi-channel analysis of surface wave (MASW) test on a cemented-sand medium in Chapter 6 to determine its material damping.

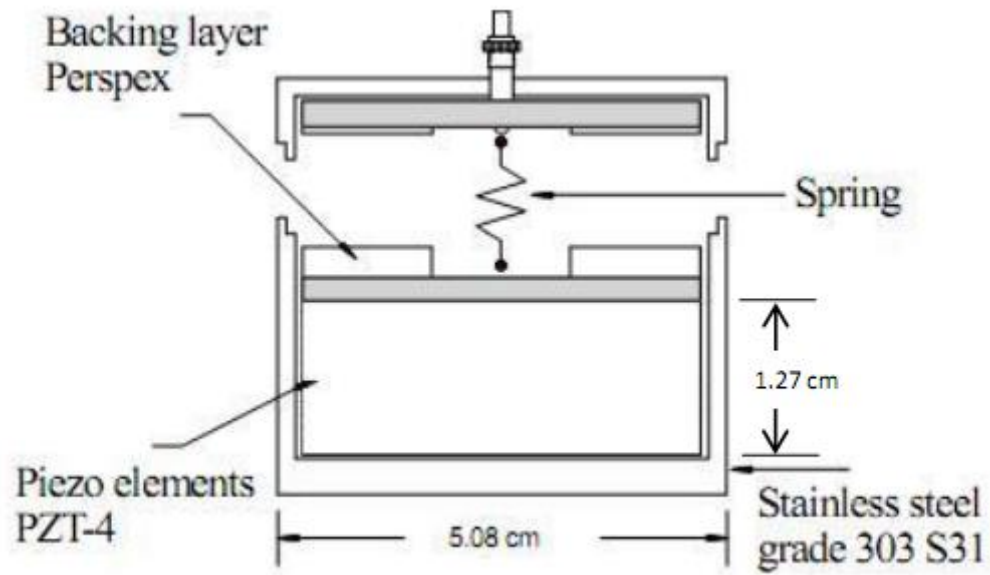


Figure 5.1: Schematic of the ultrasonic transmitter used in the tests (Tallavo et al., 2009).

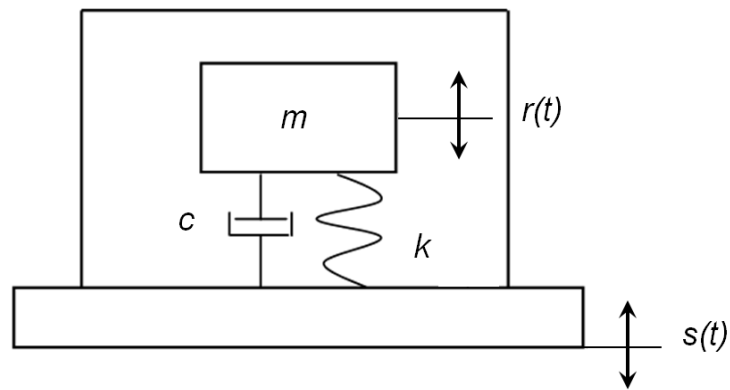


Figure 5.2: Physical model of an accelerometer.



Figure 5.3: The calibration test setup with the laser-scanner.

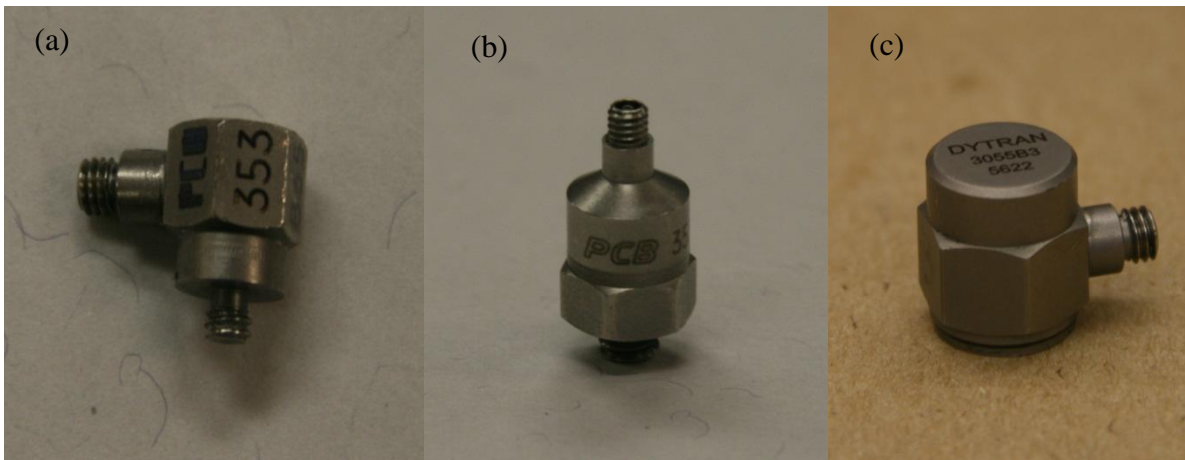


Figure 5.4: Accelerometers (a) A1 at left, (b) A2 at the middle, and (c) A3 at right.

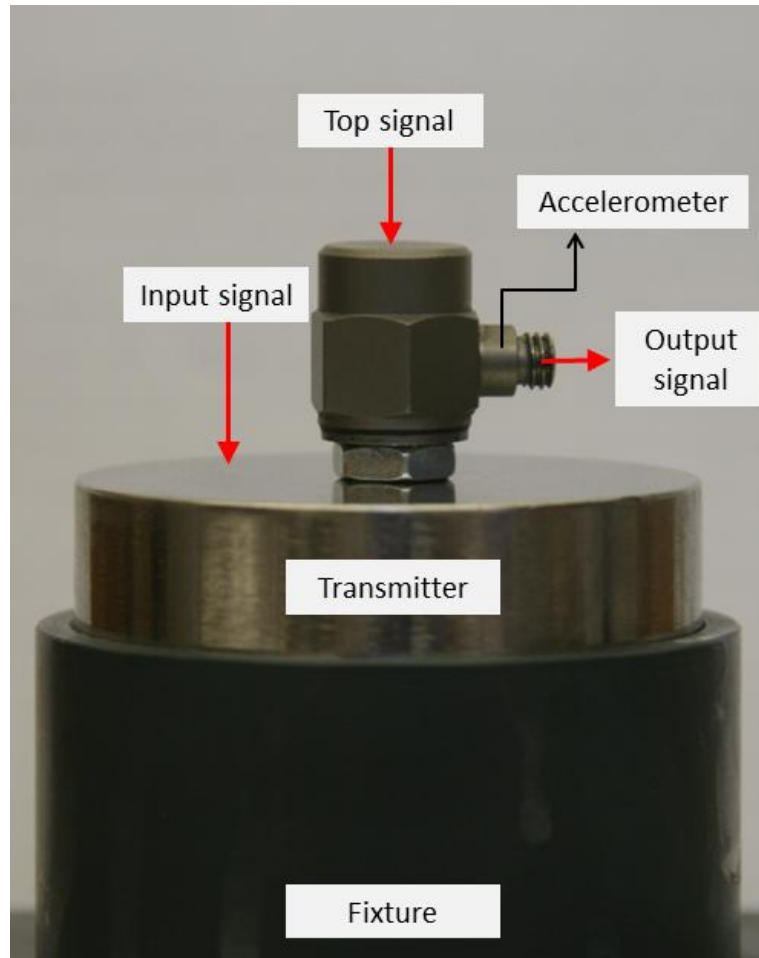
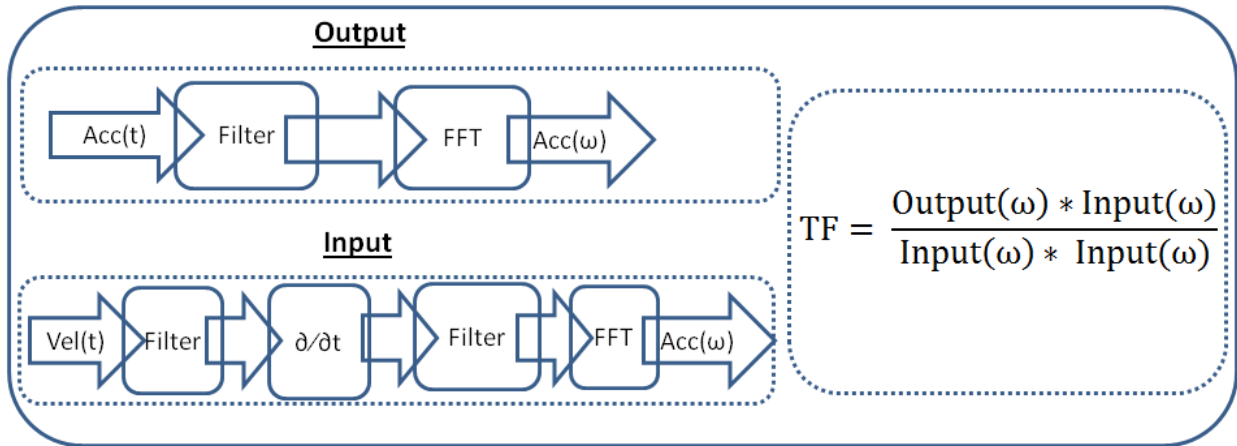
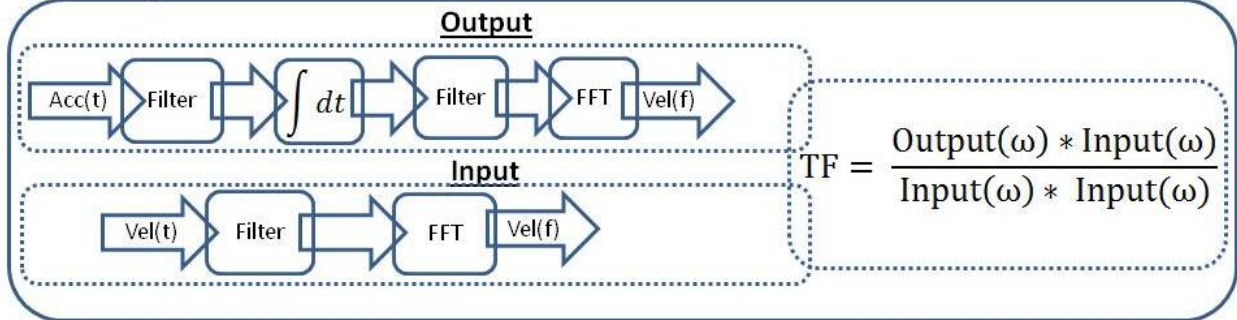


Figure 5.5: Locations where the signals are acquired.

Acceleration



Velocity



Displacement

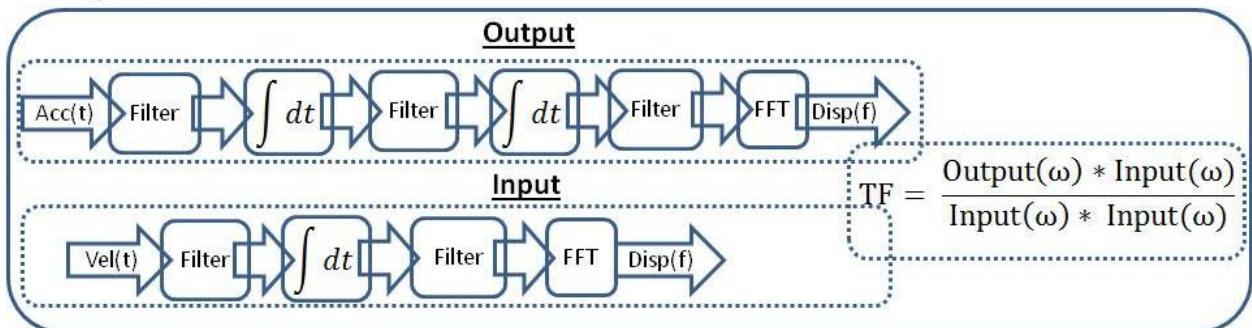


Figure 5.6: Scheme for data processing procedure: FRFs are computed for acceleration, velocity and displacement.

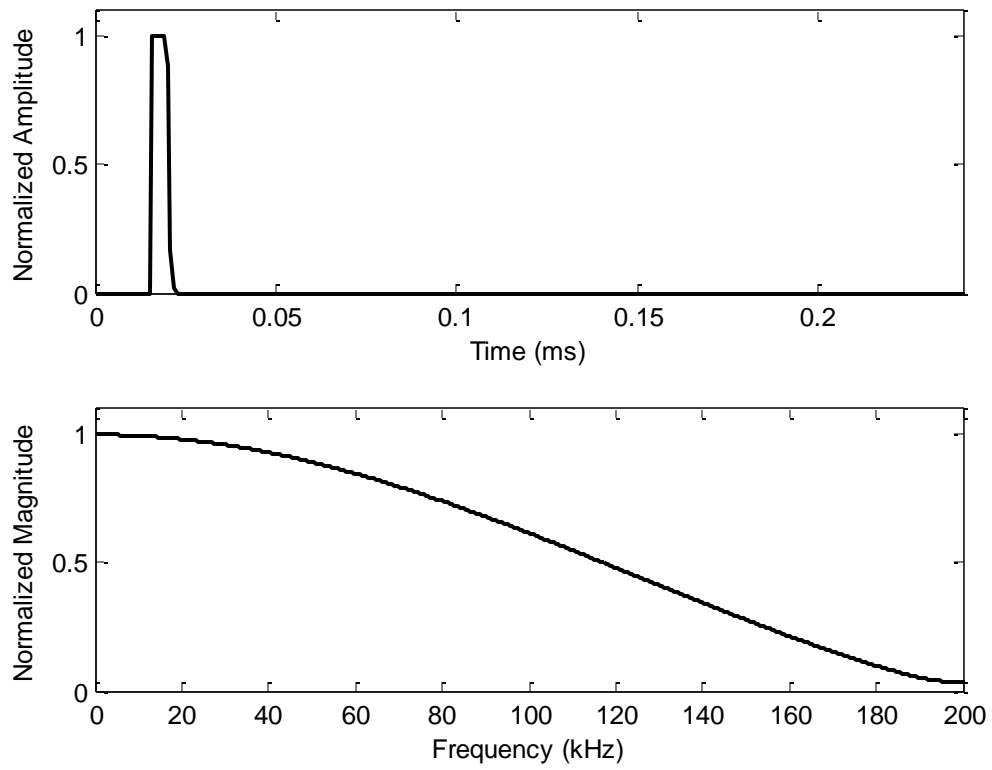


Figure 5.7: Excitation pulse for transmitter in time and frequency domains.

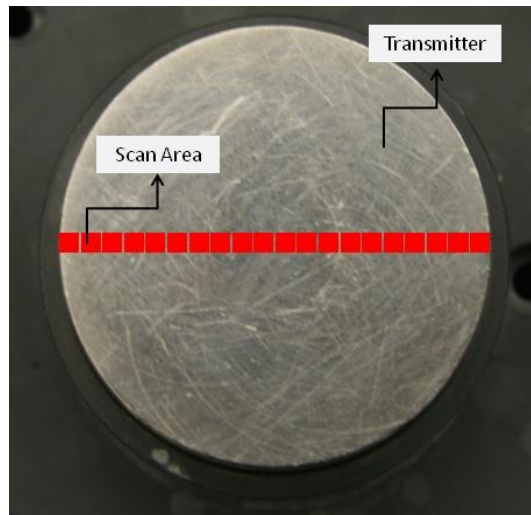


Figure 5.8: Scan locations for no mass case.

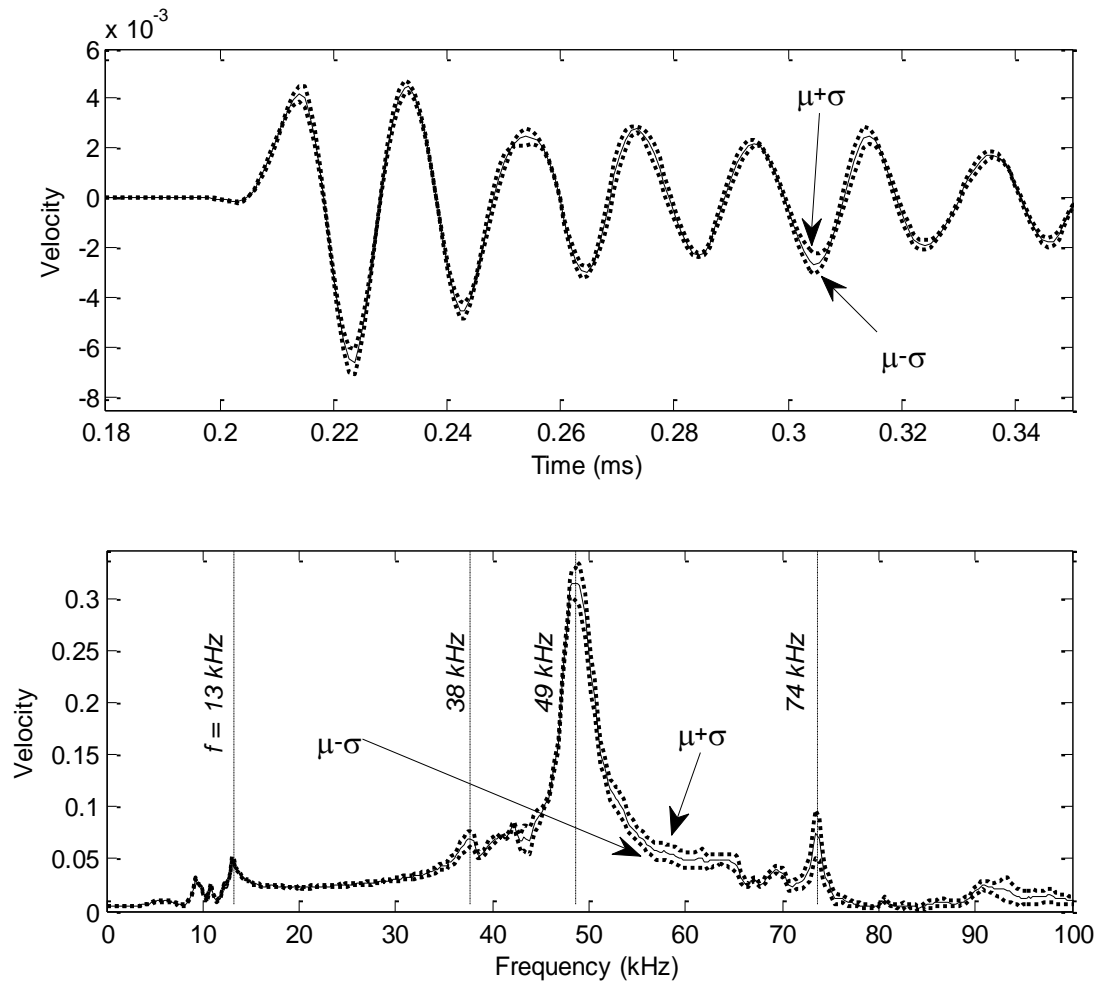


Figure 5.9: Velocity on the top of the transmitter in time (COV = 6.9%) and frequency domains. Twenty velocity signals (each one is recorded after two hundred signals are averaged), which are measured on a length of 7 mm at the center of the transmitter's top face, are averaged.

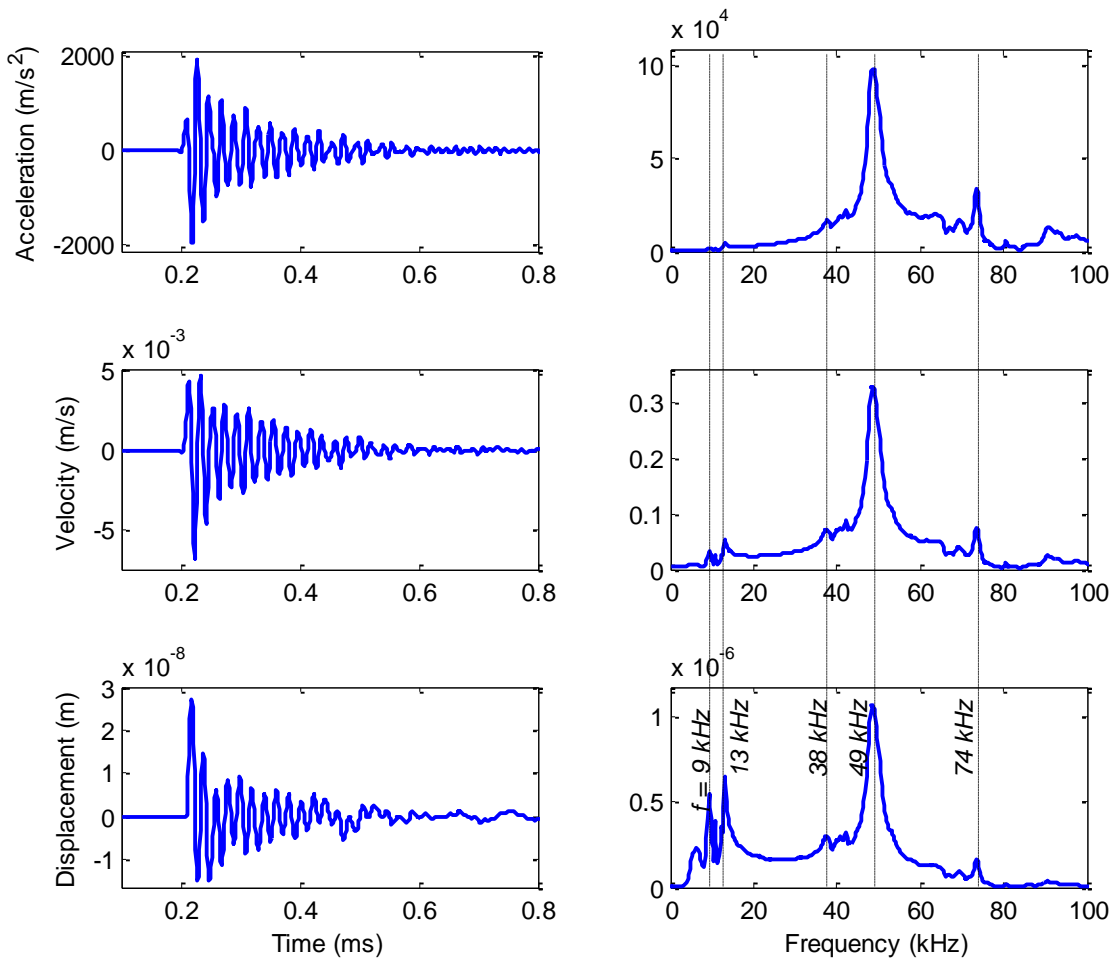


Figure 5.10: Time history and Fourier spectrum of acceleration, velocity and displacement at the top of the transmitter under transient excitation of 125 Volt for no mass case. Velocity is computed by averaging twenty readings. Acceleration and displacement are computed from the filtered velocity.

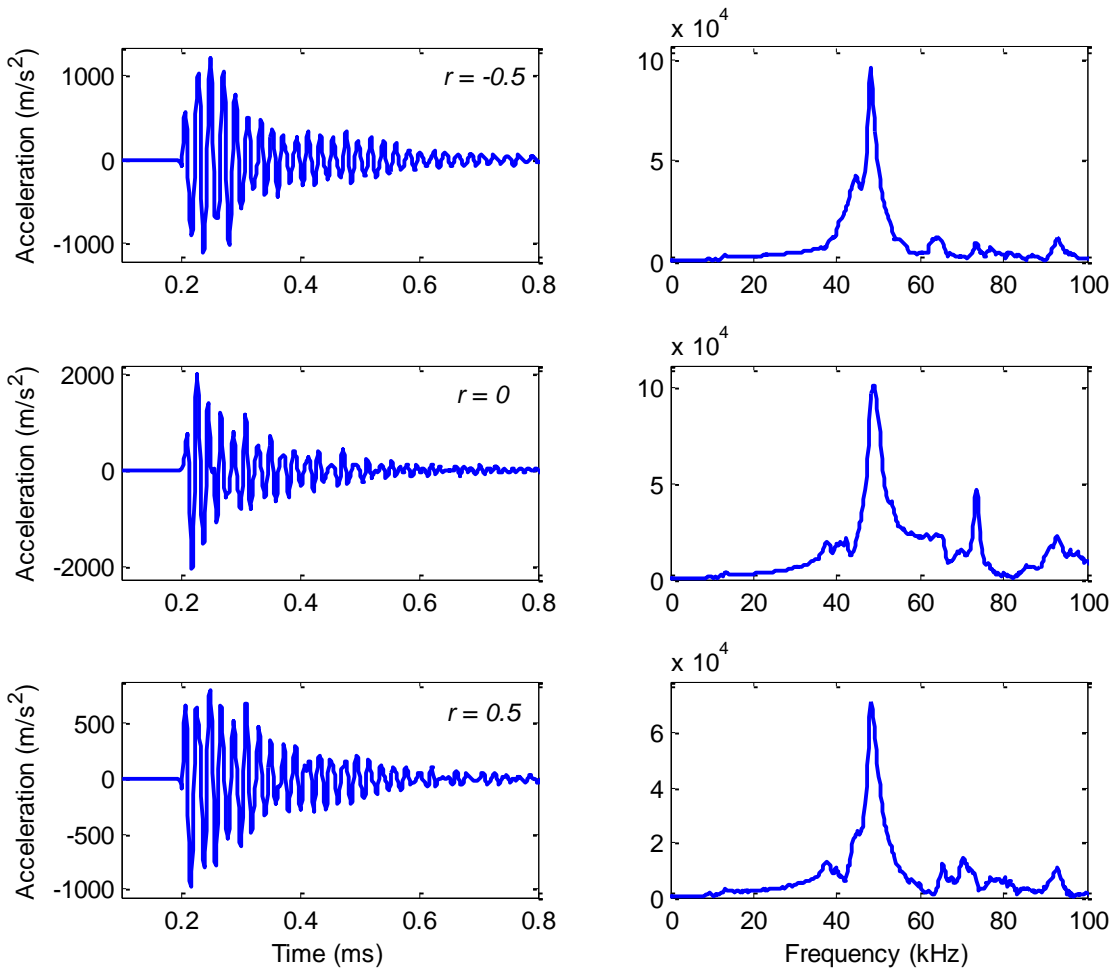


Figure 5.11: Acceleration time histories (derivative of the average velocity) and corresponding Fourier spectra at normalized radius of -0.5, 0 and 0.5 respectively under transient excitation of 125 Volt.

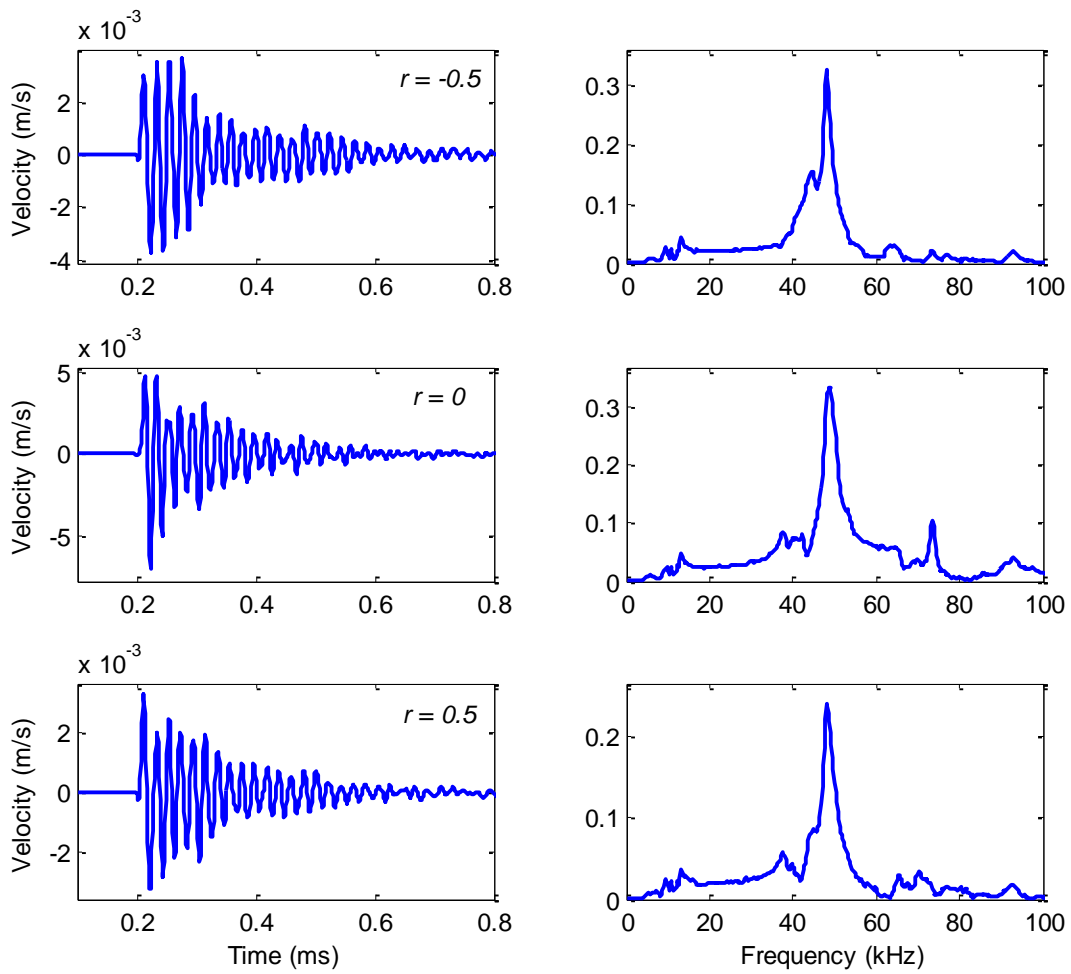


Figure 5.12: Velocity time histories (average of two hundred measured signals) and corresponding Fourier spectra at normalized radius of -0.5, 0 and 0.5 respectively under transient excitation of 125 Volt.

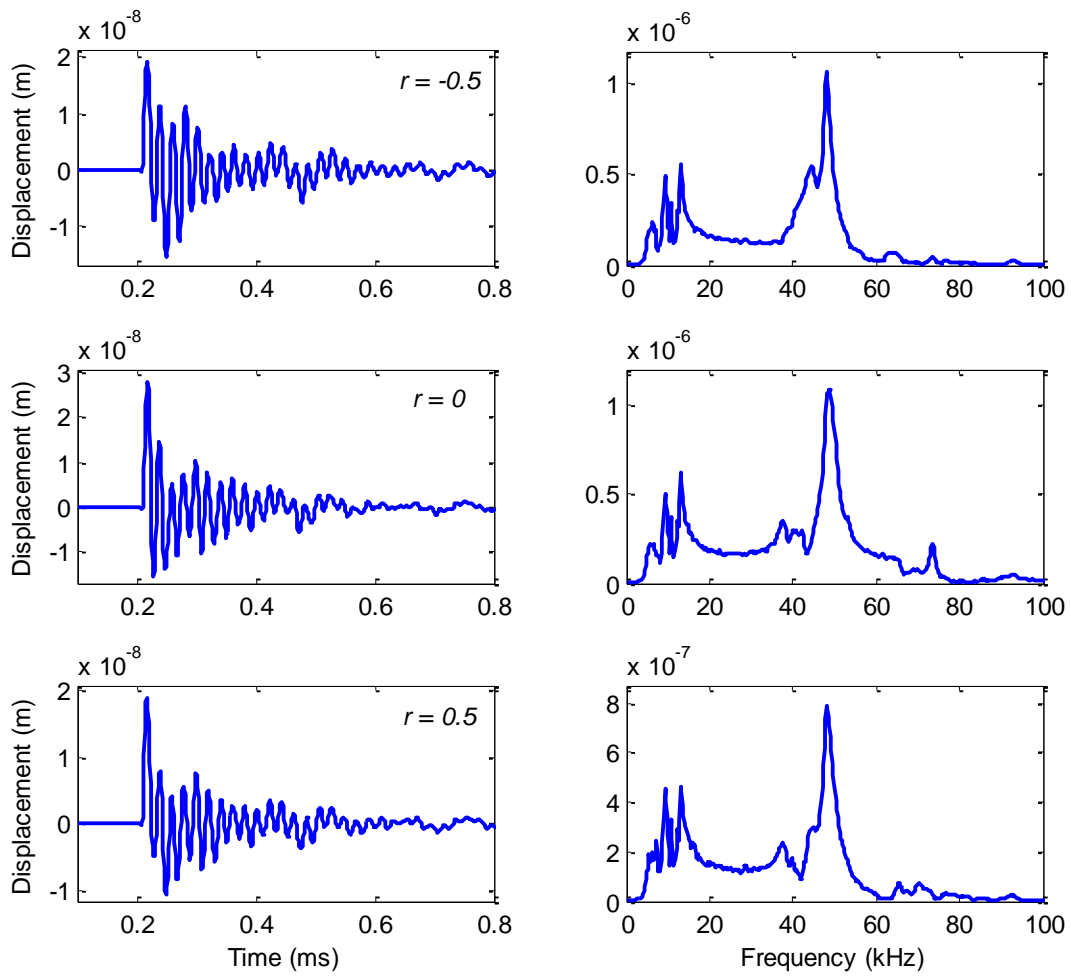


Figure 5.13: Displacement time histories (integration of the average velocity) and corresponding Fourier spectra at normalized radius of -0.5, 0 and 0.5 respectively under transient excitation of 125 Volt.

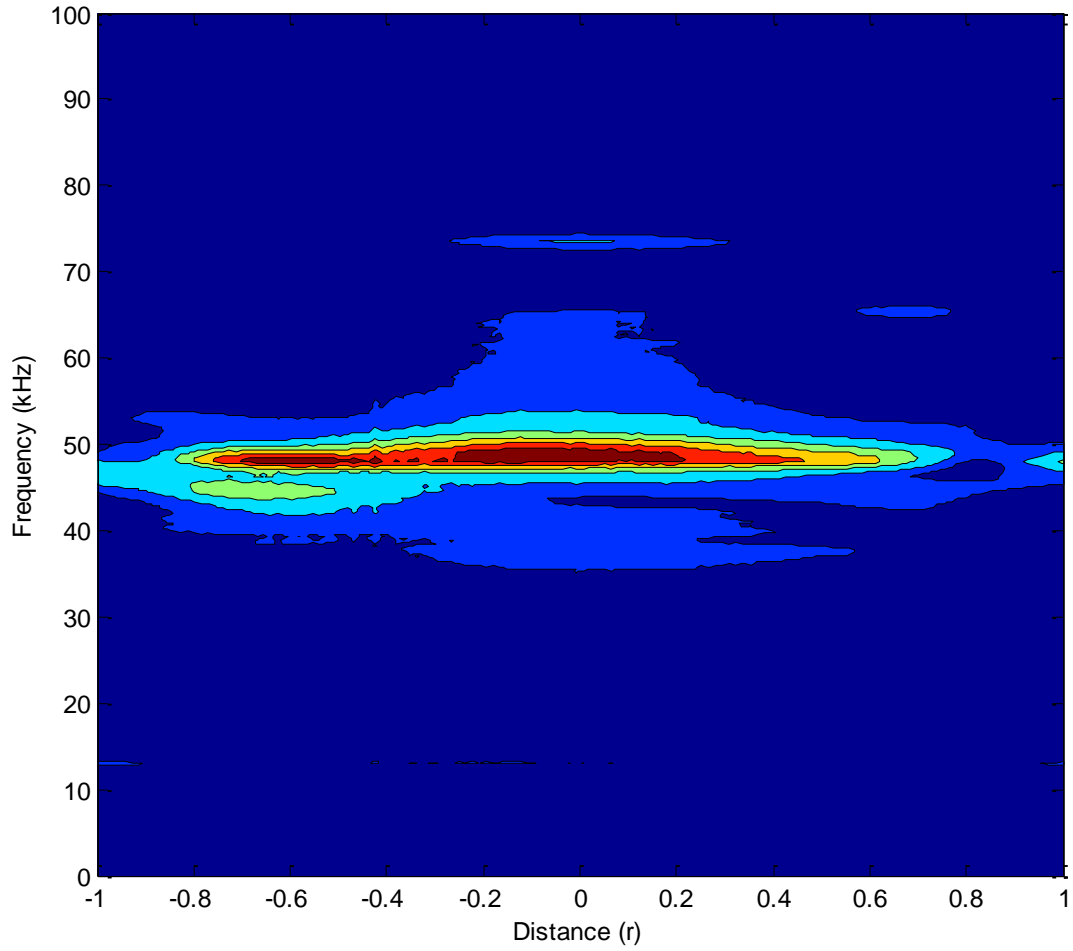


Figure 5.14: Velocity Fourier spectra along the diameter of the transmitter under transient excitation of 125 Volt.

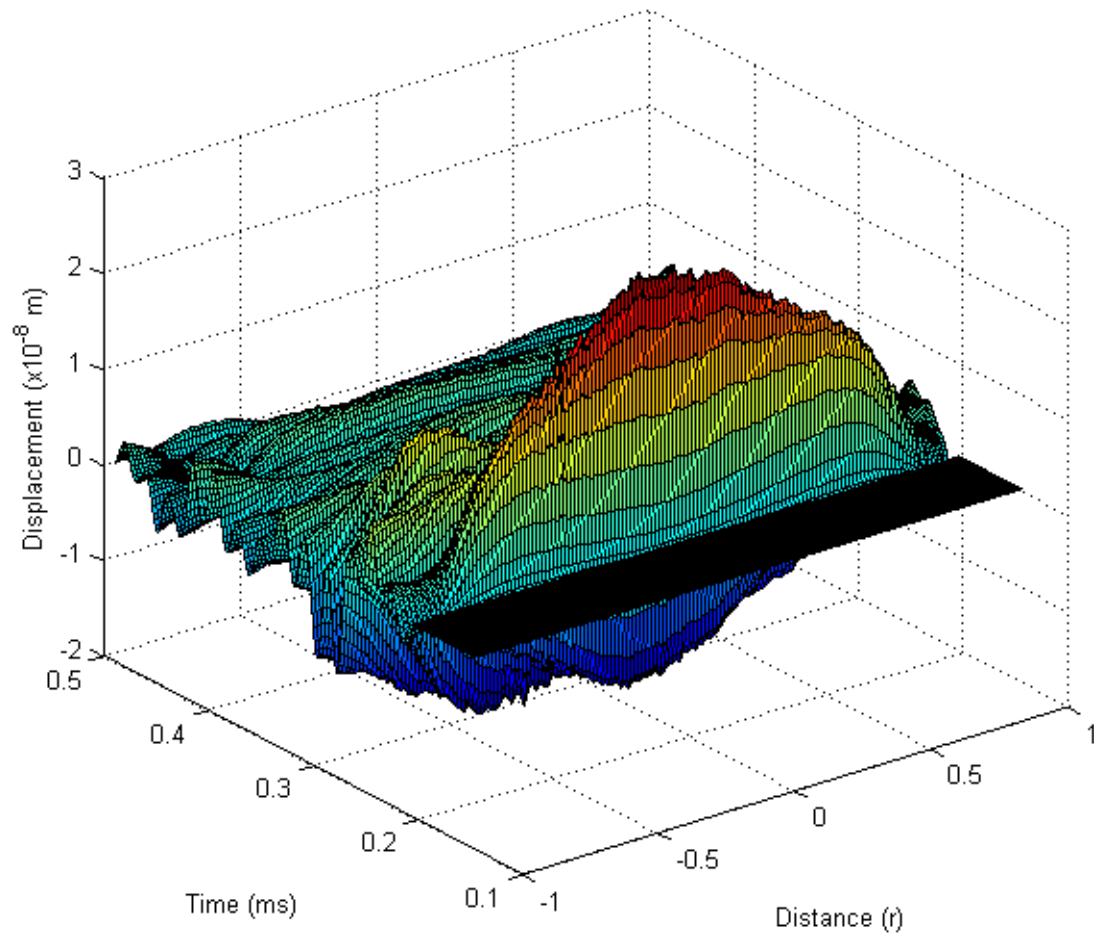


Figure 5.15: Displacement time history along the diameter of the transmitter under transient excitation of 125 Volt.

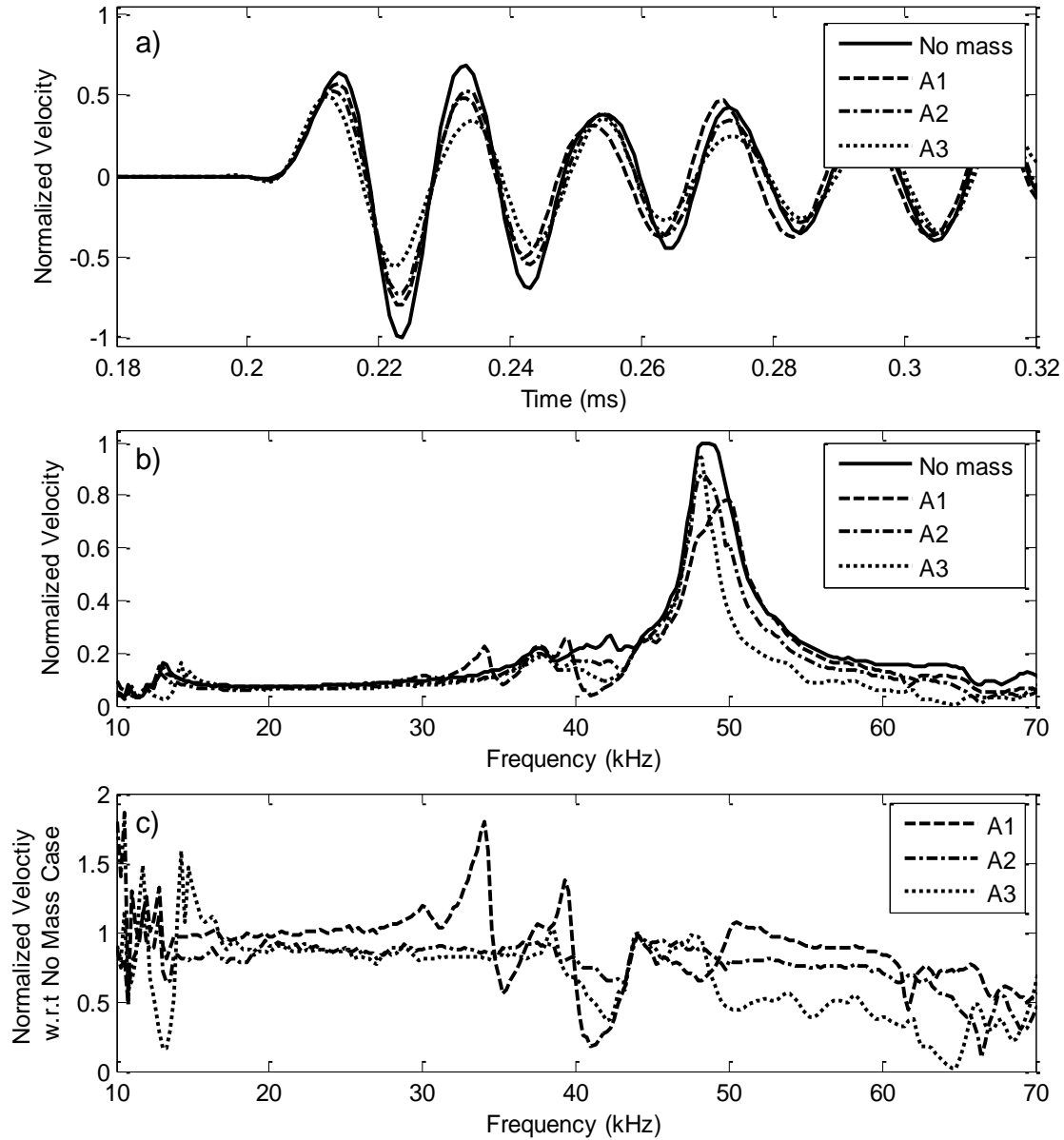


Figure 5.16: Effect of the added mass of the accelerometers on the response of the transmitter: (a) Maximum variation with respect to no mass case is observed for A3 with a reduction of 45% in velocity amplitude (each velocity time trace is computed by using 20 signals), (b) Fourier transform of the velocity time traces, (c) Frequency responses that are normalized with respect to no mass case.

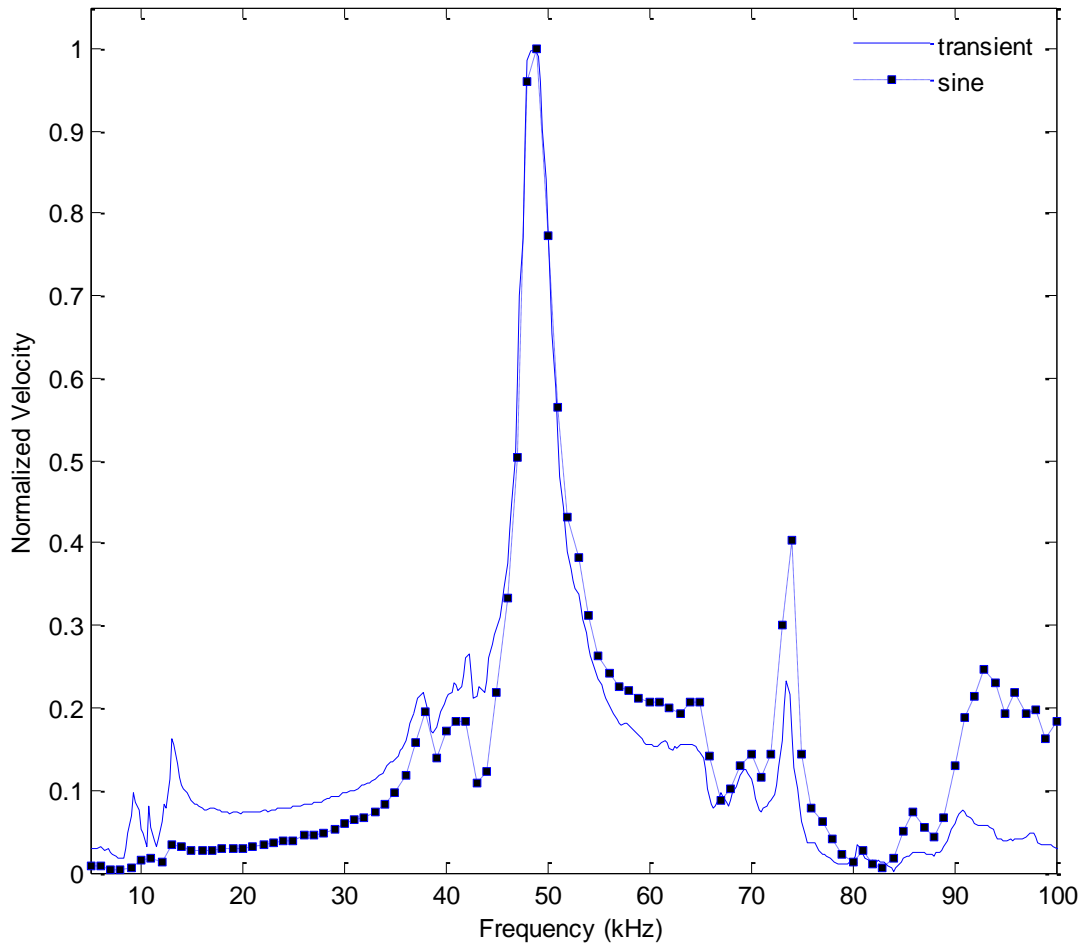


Figure 5.17: Comparison of normalized velocities under transient and sinusoidal excitations at the top of transmitter for no mass case. The continuous line represents the Fourier spectrum of velocity under transient excitation and the markers in the dashed line represent the maximum amplitudes in time domain under the corresponding frequency of sinusoidal excitation.

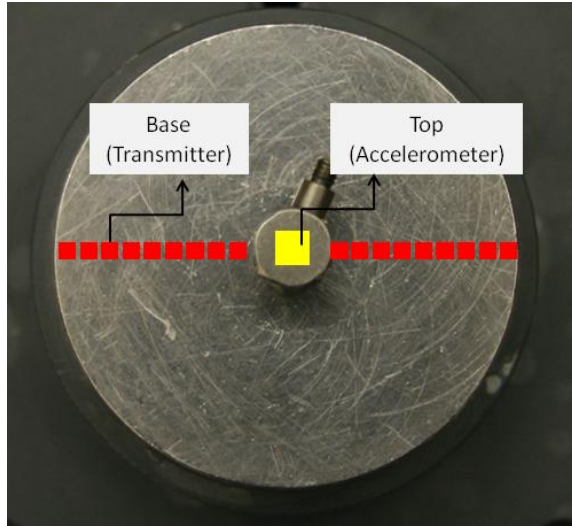


Figure 5.18: Scan locations for Accelerometer A1.

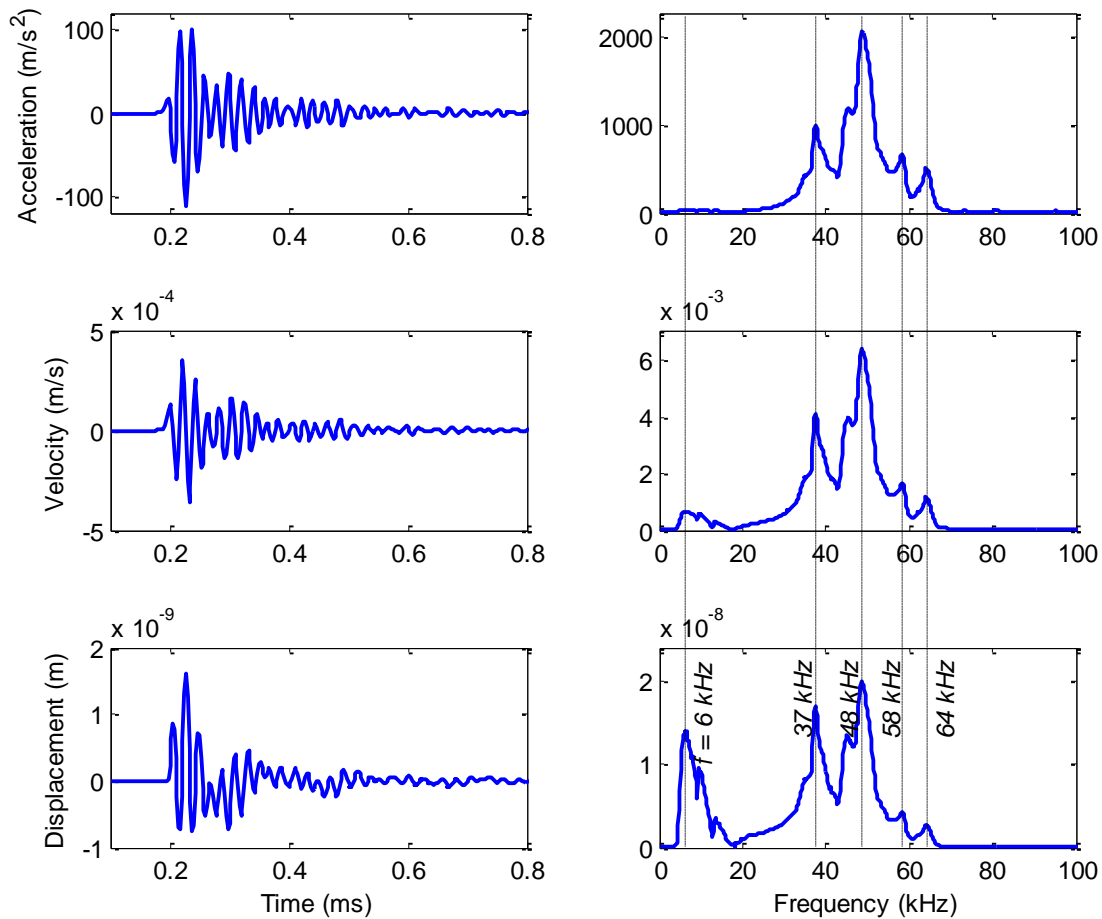


Figure 5.19: Time history and Fourier spectrum of the measured acceleration and the derived velocity and displacement under transient excitation of 2.5 Volt for A1. Velocity and displacement are computed from the filtered acceleration. Acceleration is computed using a sensitivity factor of 102.9 mV/g before computing the velocity and displacement.

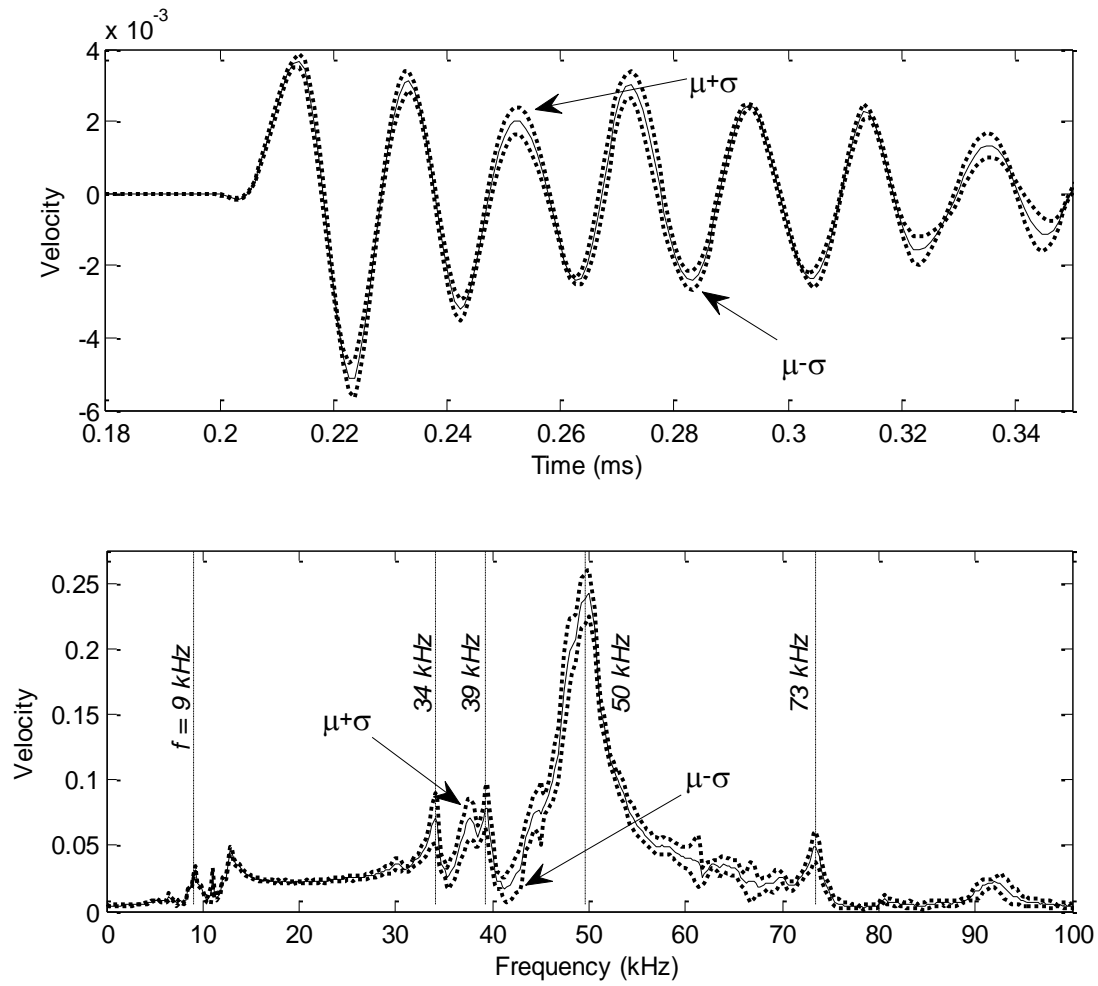


Figure 5.20: Velocity on the top of the transmitter in time (COV = 9.9%) and frequency domains for A1 is mounted. Twenty velocity signals (each one is recorded after two hundred signals are averaged), which are measured on a length of 7 mm (3.5 mm on each side of the accelerometer), are averaged.

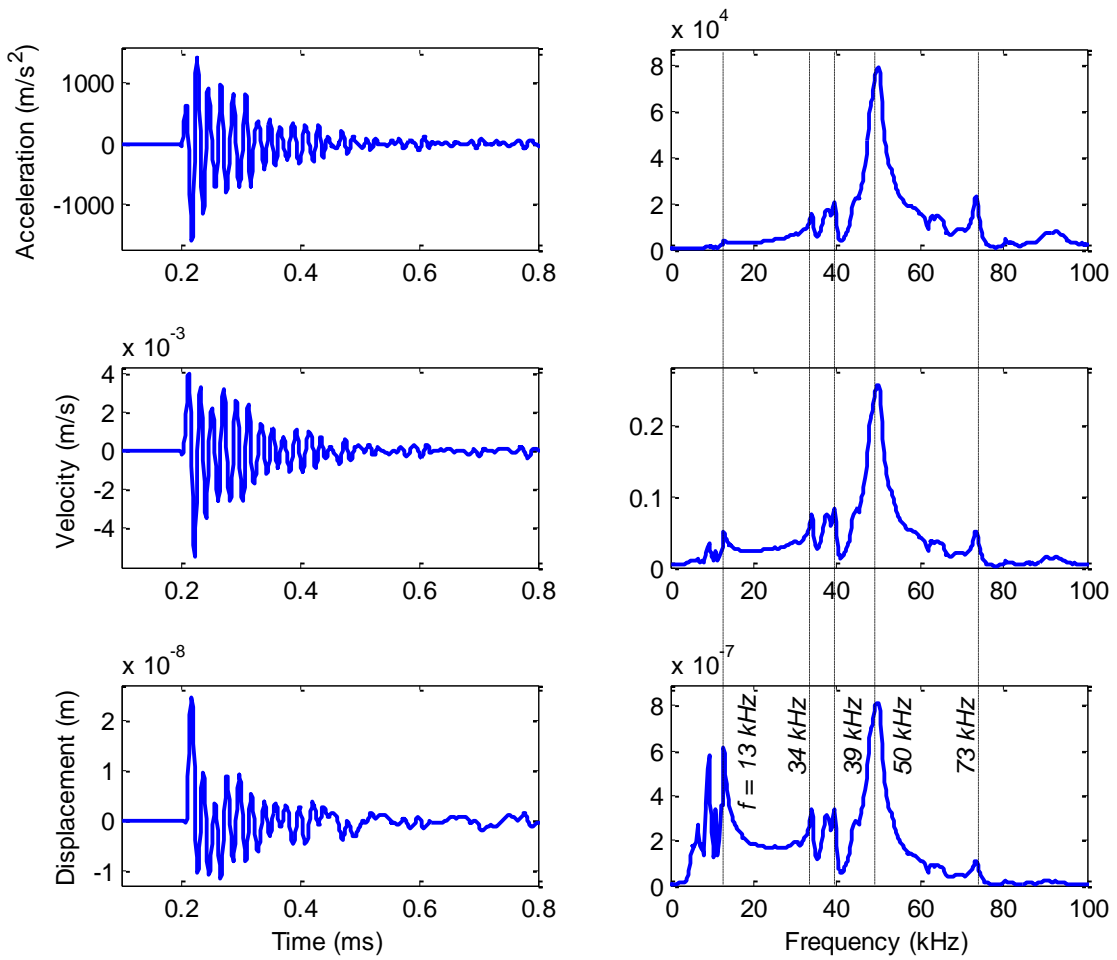


Figure 5.21: Time history and Fourier spectrum of acceleration, velocity and displacement at the top of the transmitter under transient excitation of 125 Volt for A1 is on the transmitter. Velocity is computed by averaging twenty readings. Acceleration and displacement are computed from the filtered velocity.

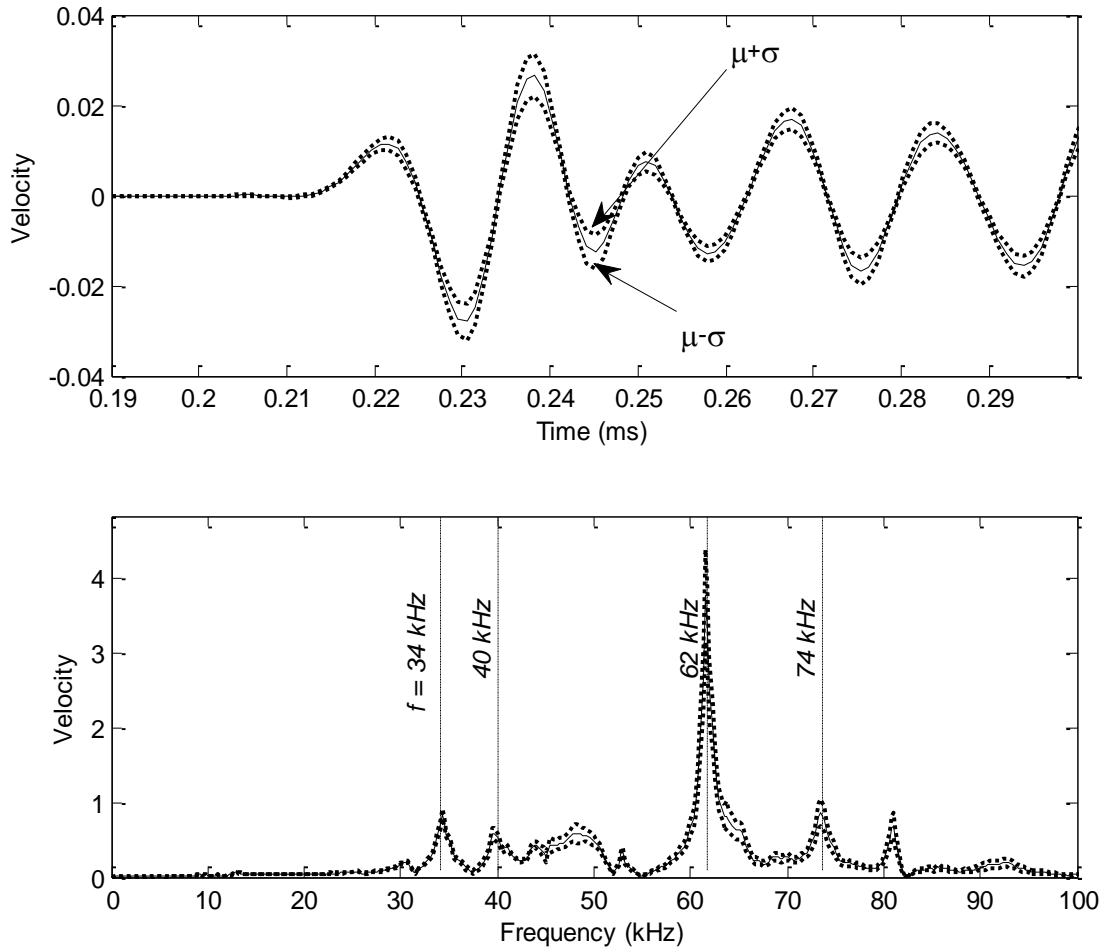


Figure 5.22: Velocity on the top of A1 in time (COV = 14%) and frequency domains. Twenty-one velocity signals (each one is recorded after two hundred signals are averaged), which are measured at a different location on the top of A1, are averaged.

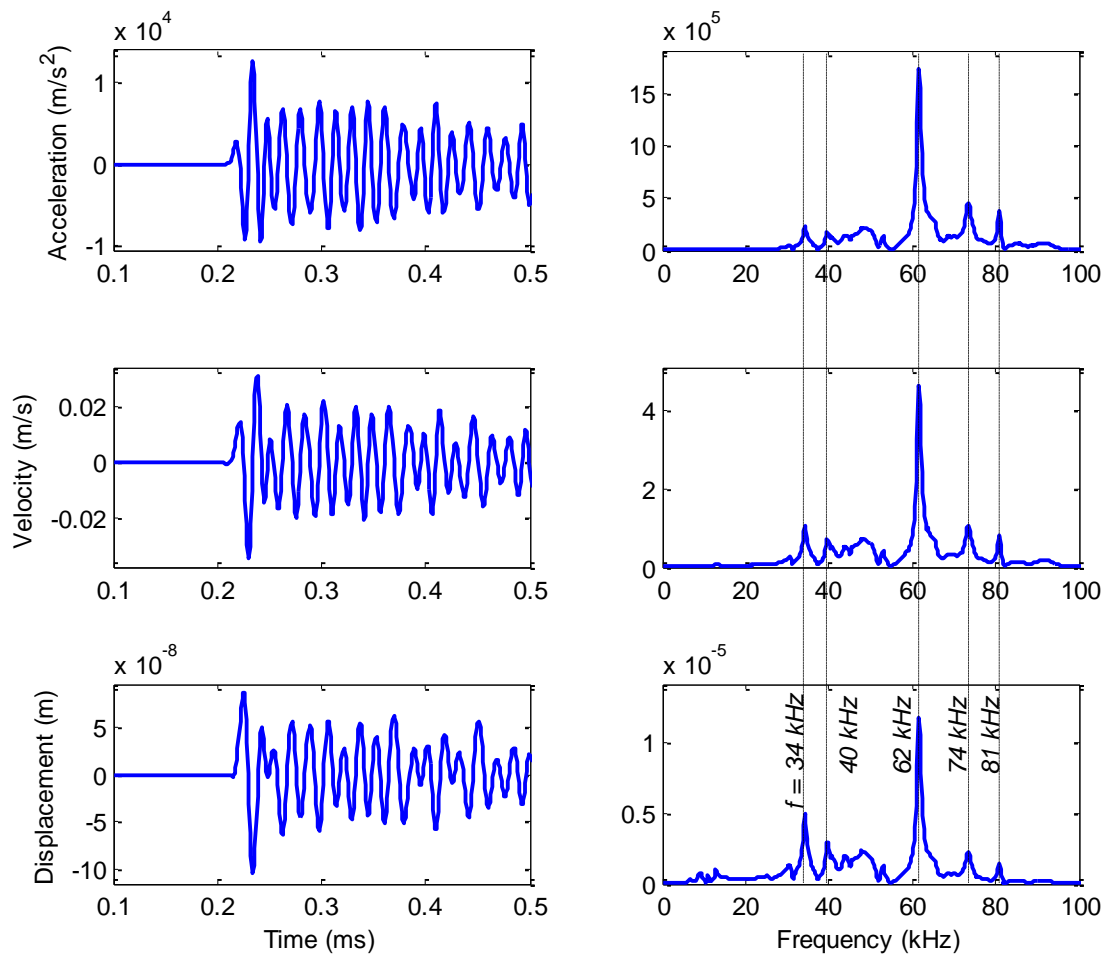


Figure 5.23: Time history and Fourier spectrum of acceleration, velocity and displacement at the top of A1 under transient excitation of 125 Volt. Velocity is computed by averaging twenty one signals measured on the scan area shown in Figure 5.18. Acceleration and displacement are computed from the filtered velocity.

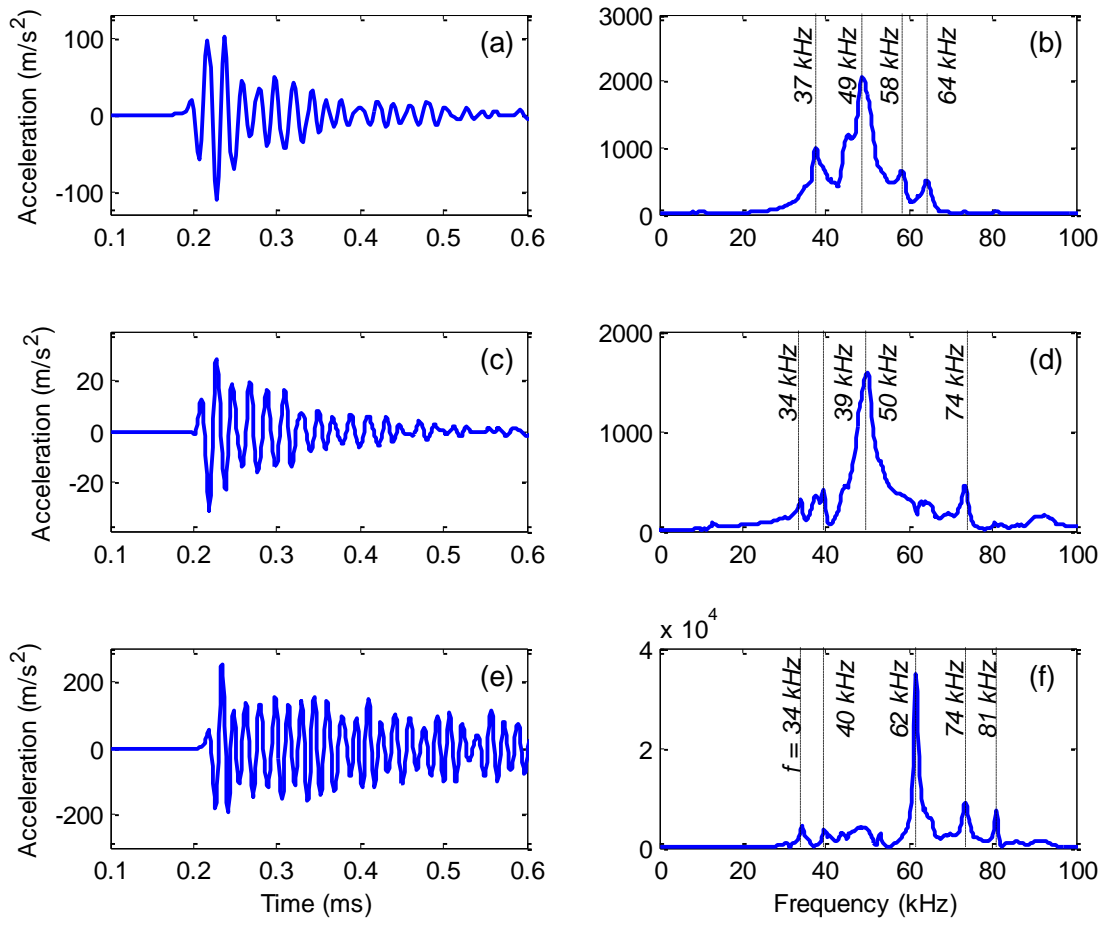


Figure 5.24: Acceleration time histories and Fourier spectra of (a,b) output, (c,d) input, and (e,f) vibration on the top of accelerometer A1. Input and top signals are divided by 50 ($125V/2.5V$) to ensure the same excitation voltage.

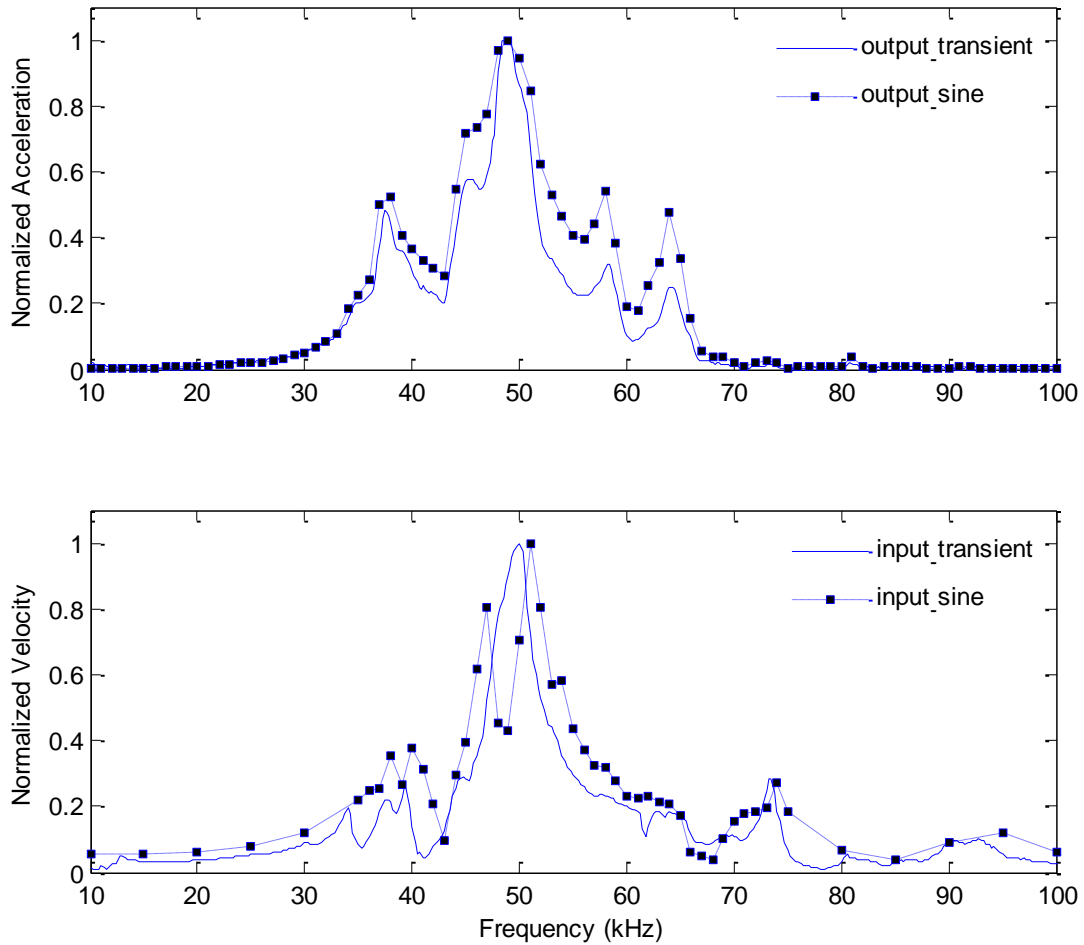


Figure 5.25: (a) Comparison of normalized velocities under transient and sinusoidal excitations at the top of transmitter for accelerometer A1 is on the transmitter. The continuous line represents the Fourier spectrum of velocity under transient excitation and the markers in the dashed line represent the maximum amplitudes in time domain under the corresponding frequency of sinusoidal excitation. (b) Comparison of normalized output accelerations of accelerometer under transient and sinusoidal excitations. The continuous line represents the Fourier spectrum of acceleration under transient excitation and the markers in the dashed line represent the maximum amplitudes in time domain under the corresponding frequency of sinusoidal excitation.

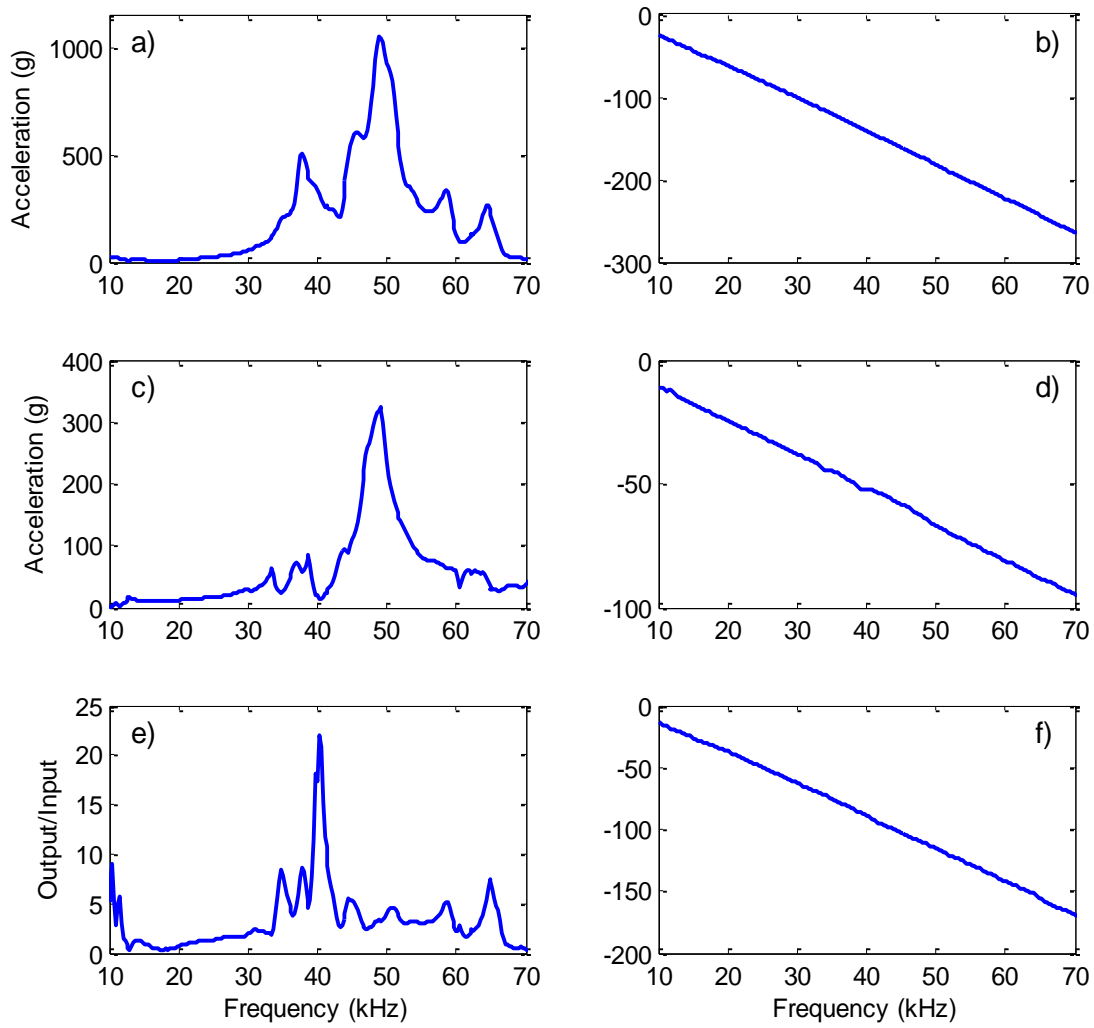


Figure 5.26: From top to bottom, the magnitudes and phases of (a, b) output acceleration, (c, d) input acceleration, and (e, f) frequency response function for A1.

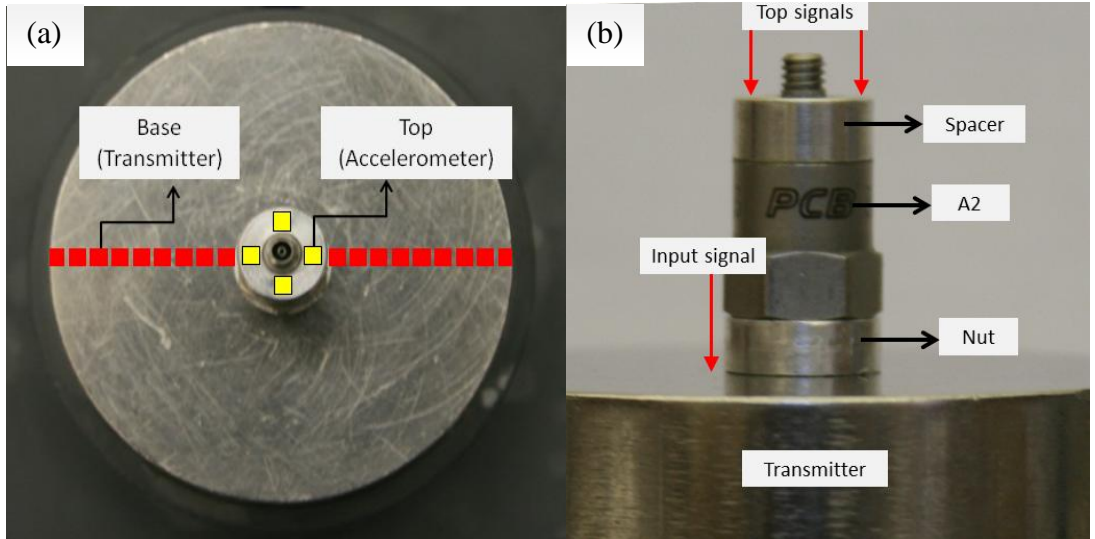


Figure 5.27: Scan locations for Accelerometer A2 (a) top view, (b) side view.

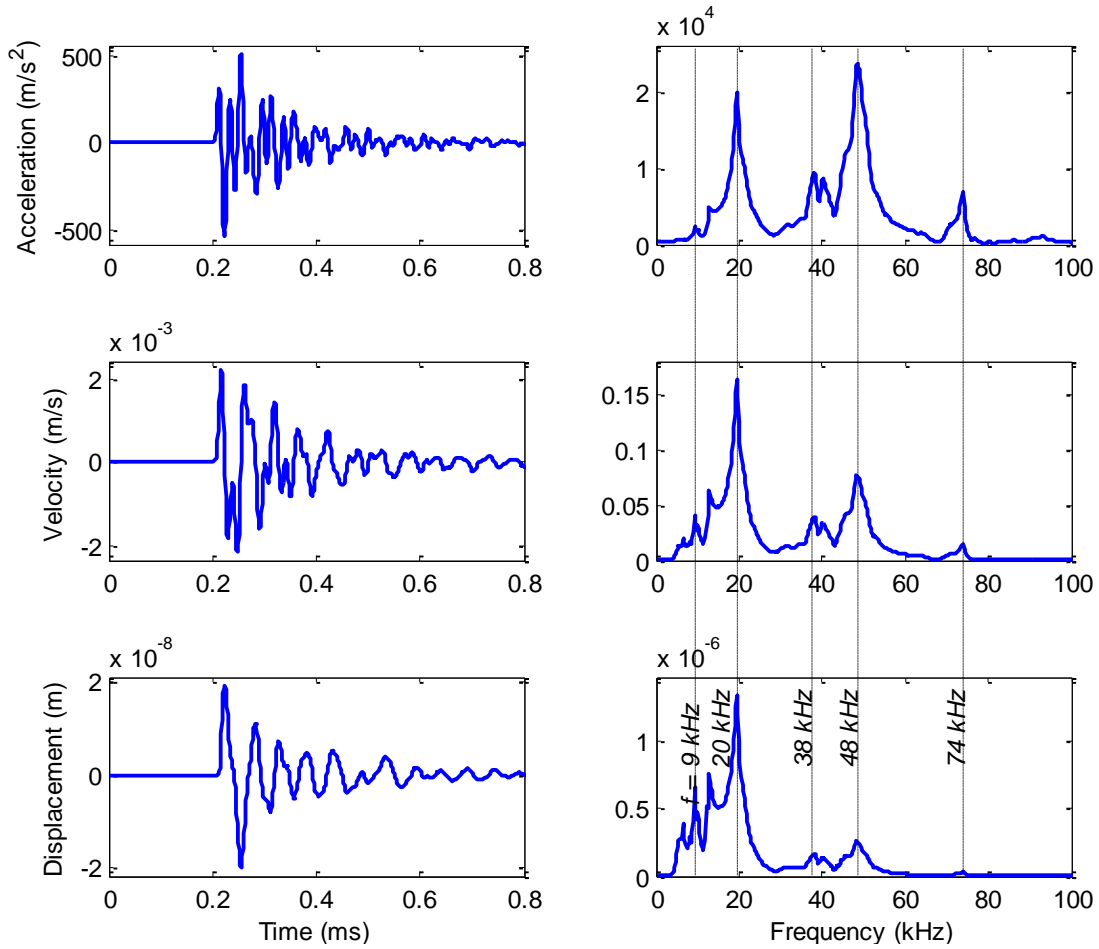


Figure 5.28: Time history and Fourier spectrum of the recorded acceleration and the derived velocity and displacement under transient excitation of 125 Volt for A2. Velocity and displacement are computed from the filtered acceleration. Acceleration is computed using a sensitivity factor of 9.98 mV/g before computing the velocity and displacement.

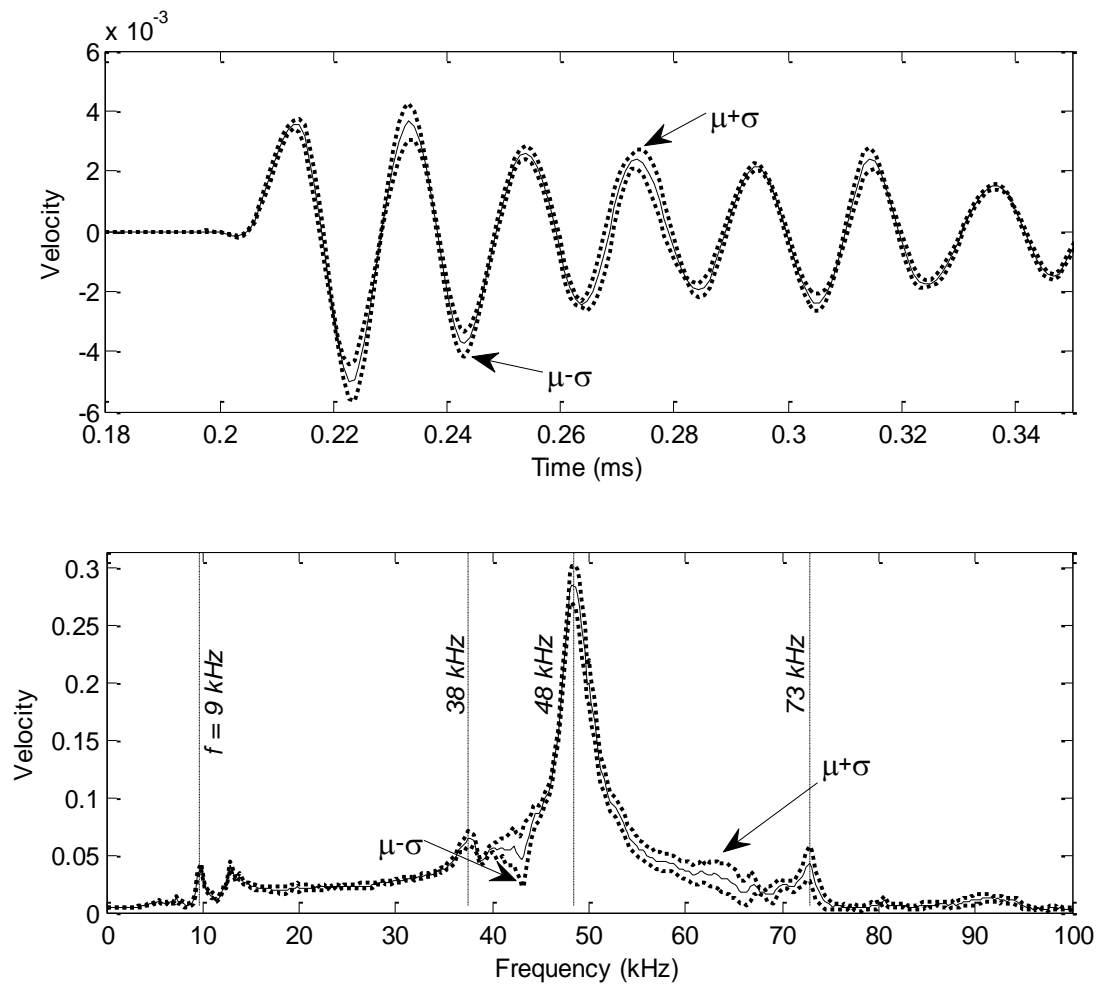


Figure 5.29: Velocity on the top of the transmitter in time (COV = 13.9%) and frequency domains for A2 is mounted. Twenty velocity signals (each one is recorded after two hundred signals are averaged), which are measured on a length of 7 mm (3.5 mm on each side of the accelerometer), are averaged.

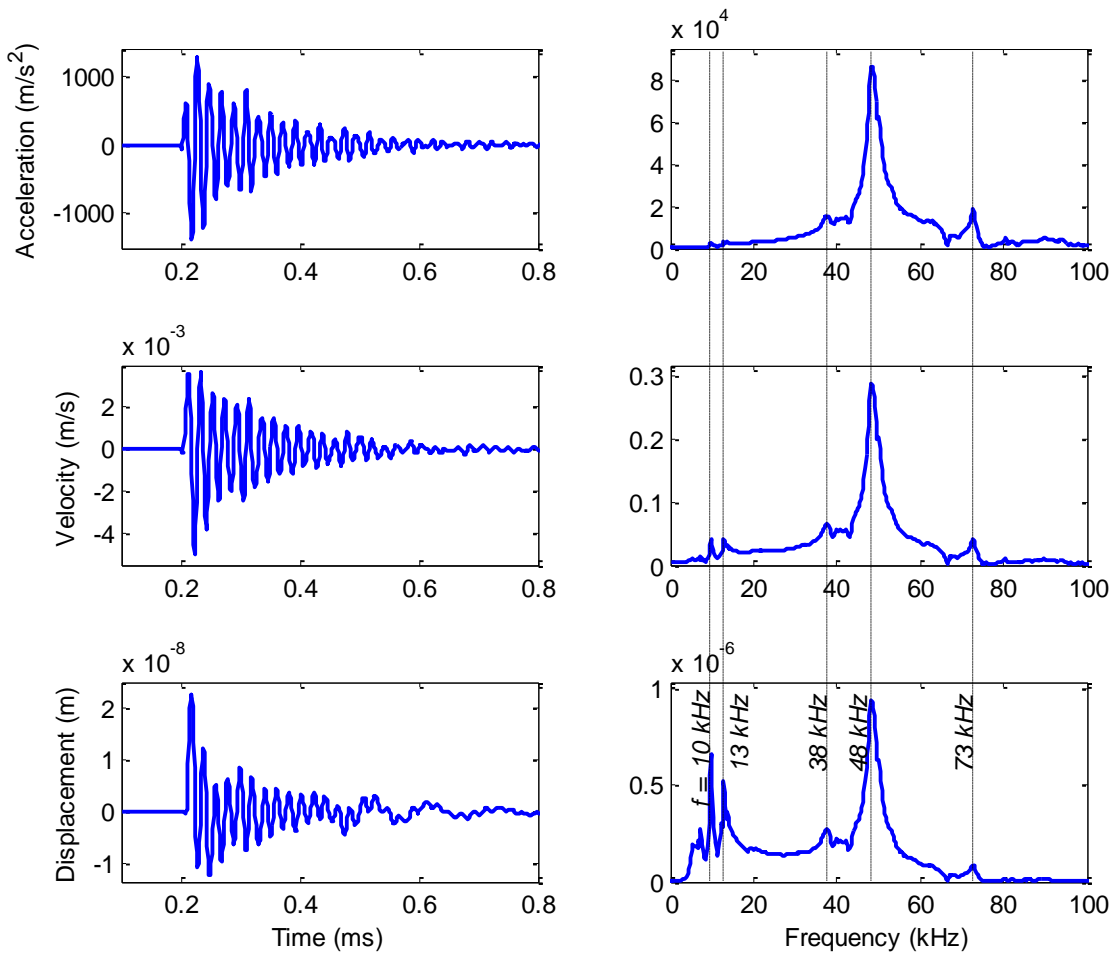


Figure 5.30: Time history and Fourier spectrum of acceleration, velocity and displacement at the top of the transmitter under transient excitation of 125 Volt for A2 is on the transmitter. Velocity is computed by averaging twenty readings. Acceleration and displacement are computed from the filtered velocity.

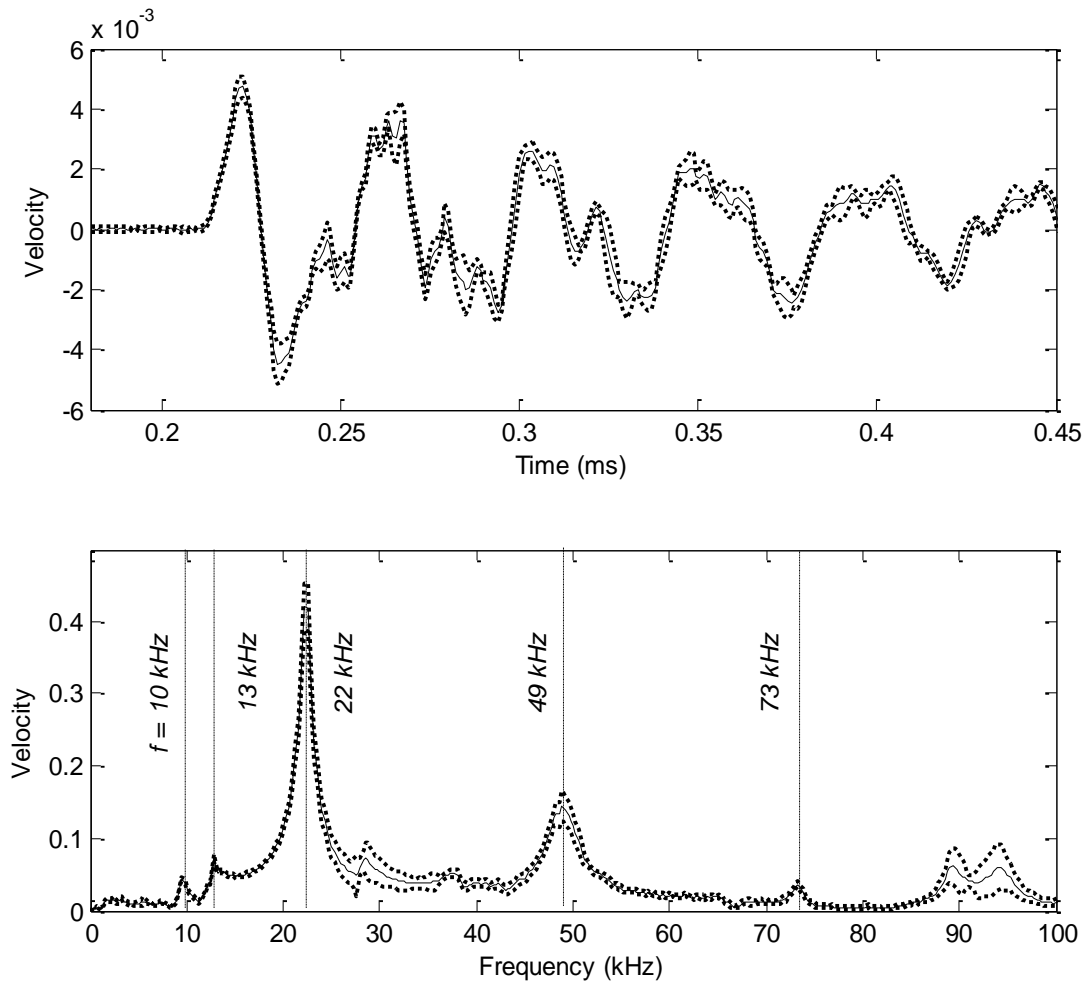


Figure 5.31: Velocity on the top of A2 in time (COV = 16.1%) and frequency domains. Thirty-five velocity signals (each one is recorded after two hundred signals are averaged), which are measured on the four sides of accelerometer's top case, are averaged.

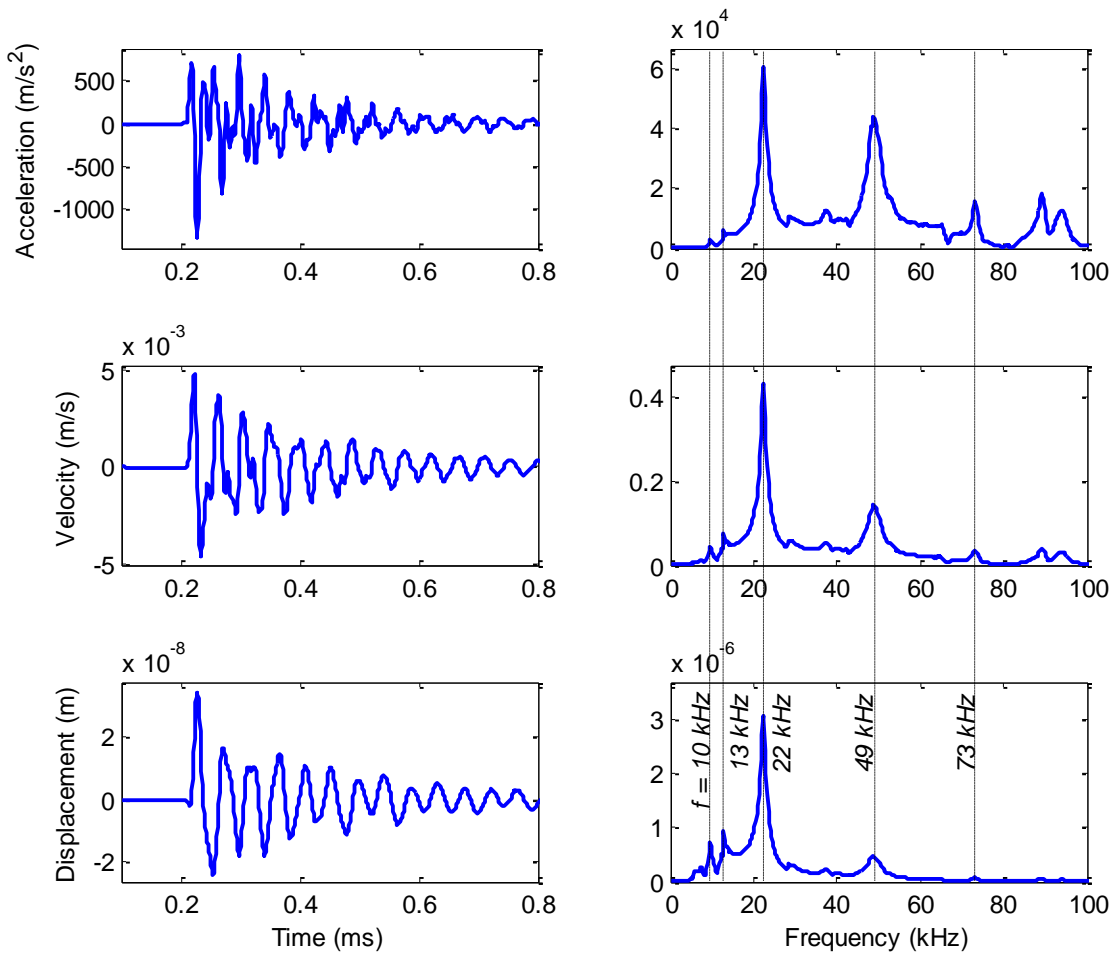


Figure 5.32: Time history and Fourier spectrum of acceleration, velocity and displacement at the top of A2 under transient excitation of 125 Volt. Velocity is computed by averaging 4x13 signals measured on the scan areas (Fig. 5.27). Acceleration and displacement are computed from the filtered velocity.

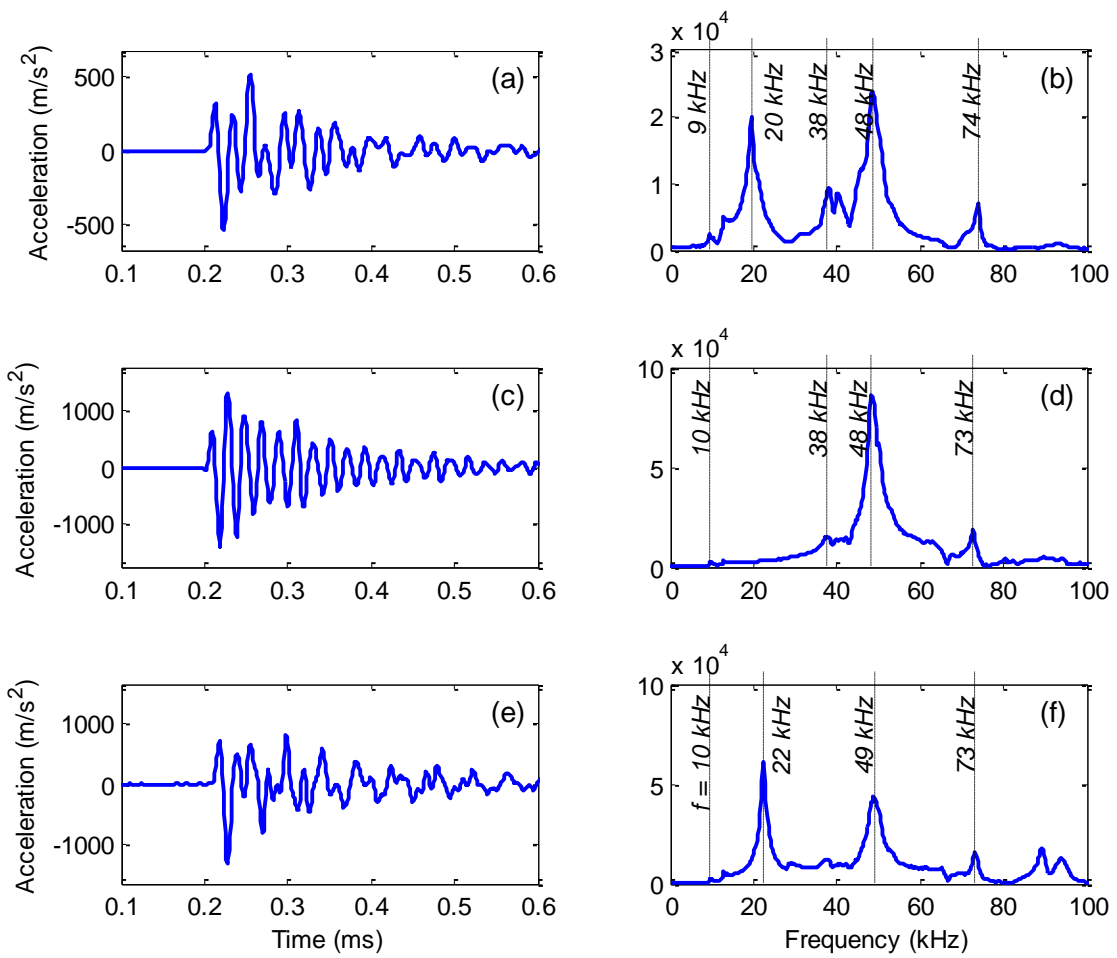


Figure 5.33: Acceleration time histories and Fourier spectra of (a,b) output, (c,d) input, and (e,f) vibration on the top of accelerometer A2.

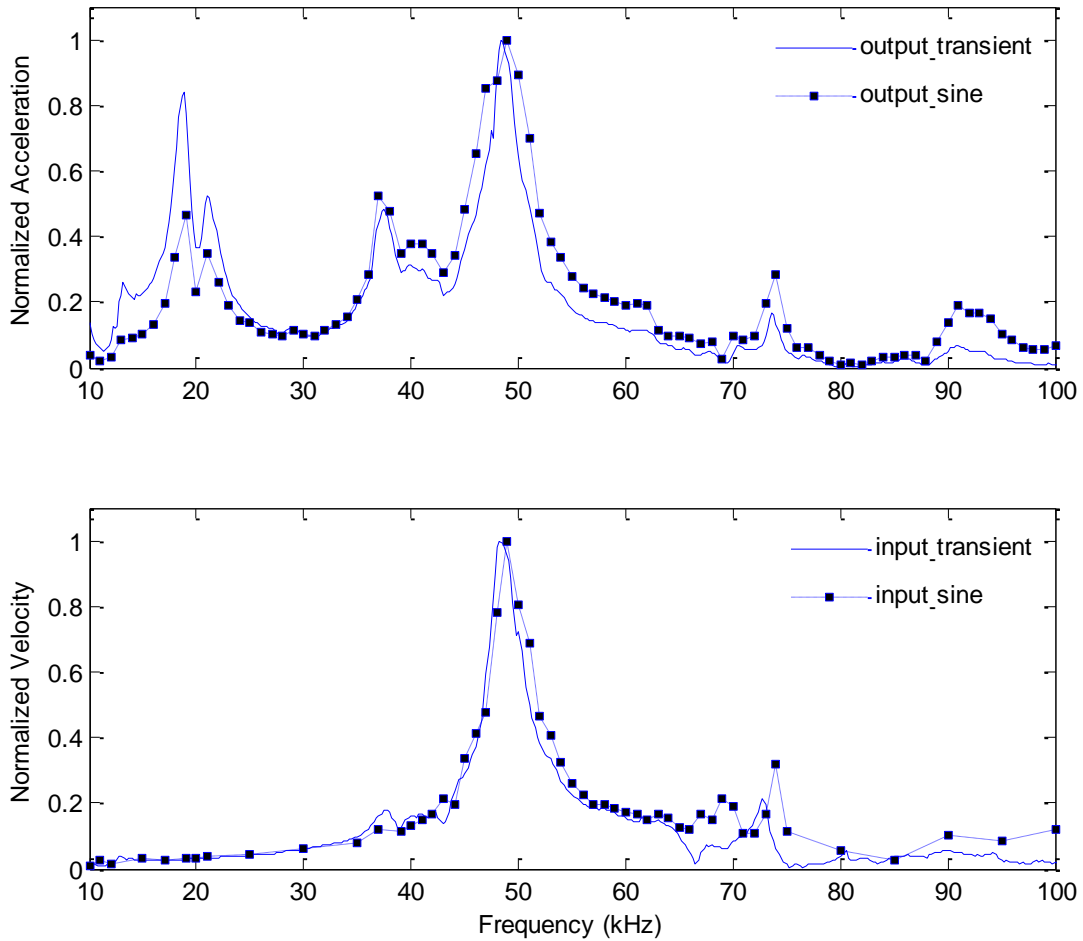


Figure 5.34: (a) Comparison of normalized velocities under transient and sinusoidal excitations at the top of transmitter for accelerometer A2 is on the transmitter. The continuous line represents the Fourier spectrum of velocity under transient excitation and the markers in the dashed line represent the maximum amplitudes in time domain under the corresponding frequency of sinusoidal excitation. (b) Comparison of normalized output accelerations of accelerometer under transient and sinusoidal excitations. The continuous line represents the Fourier spectrum of acceleration under transient excitation and the markers in the dashed line represent the maximum amplitudes in time domain under the corresponding frequency of sinusoidal excitation. All measurements are taken for A2 with the spacer on top.

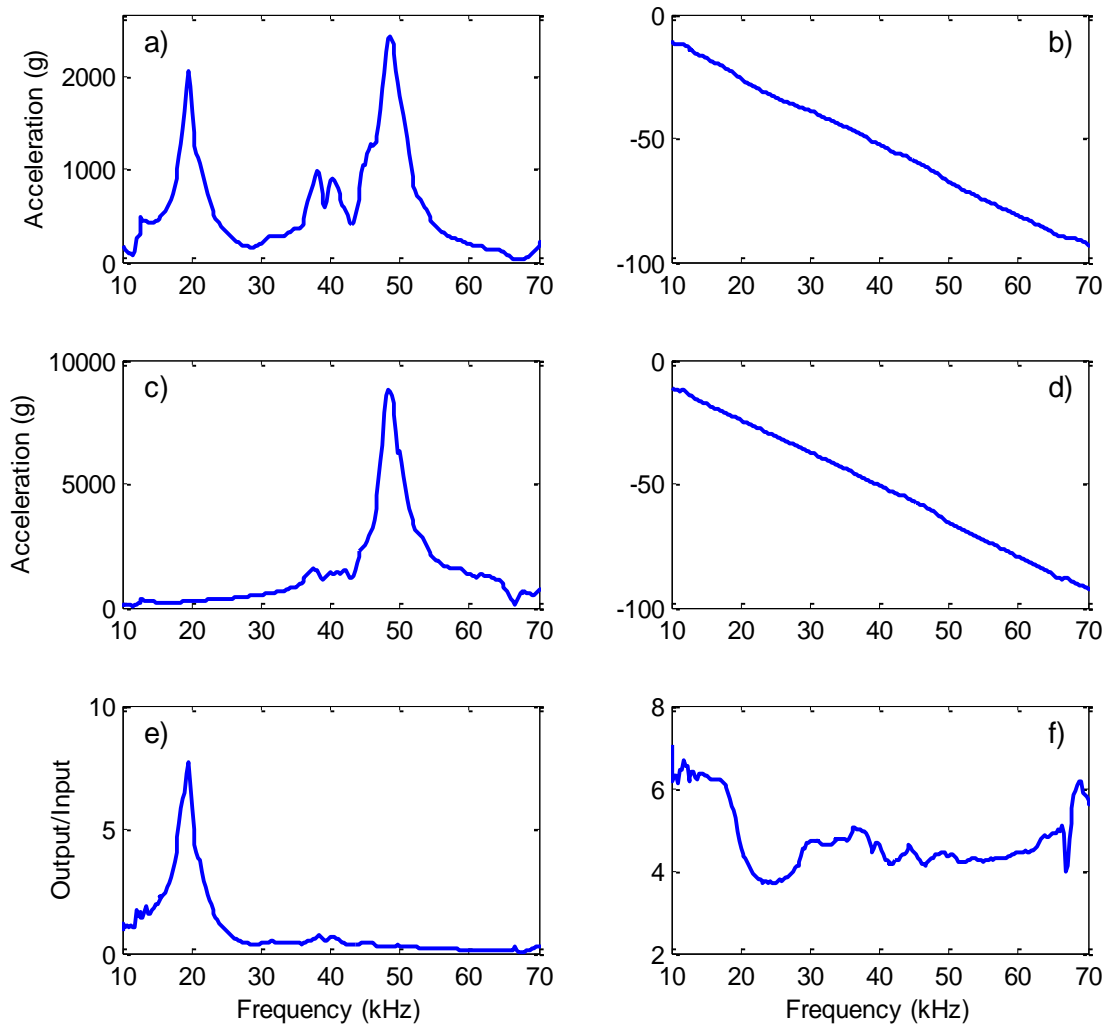


Figure 5.35: From top to bottom, the magnitudes and phases of (a, b) output acceleration, (c, d) input acceleration, and (e, f) frequency response function for A2.

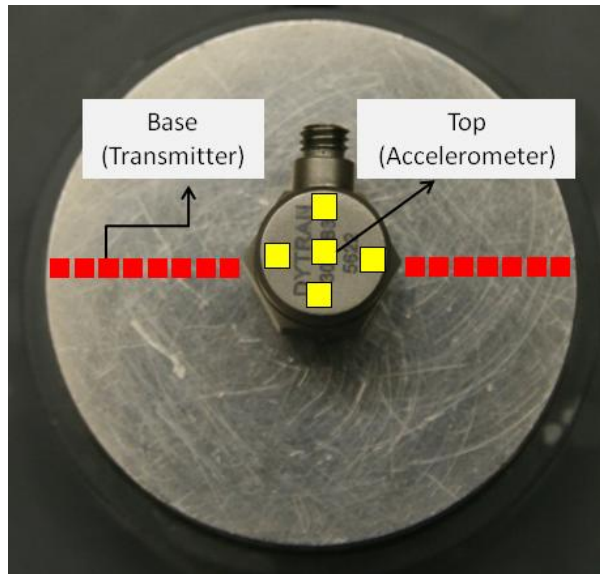


Figure 5.36: Scan locations for Accelerometer A3.

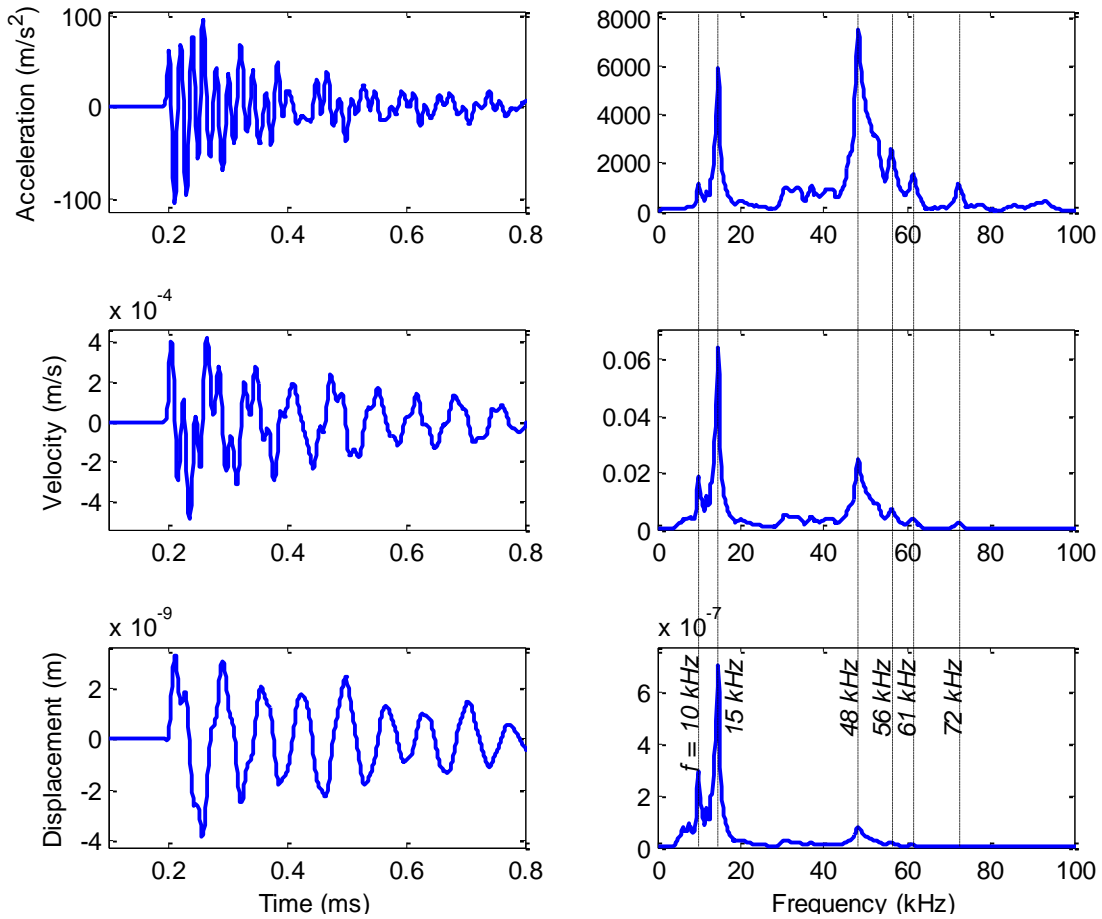


Figure 5.37: Time history and Fourier spectrum of the measured acceleration and the derived velocity and displacement under transient excitation of 25 Volt for A3. Velocity and displacement are computed from the filtered acceleration. Acceleration is computed using a sensitivity factor of 504.1 mV/g before computing the velocity and displacement.

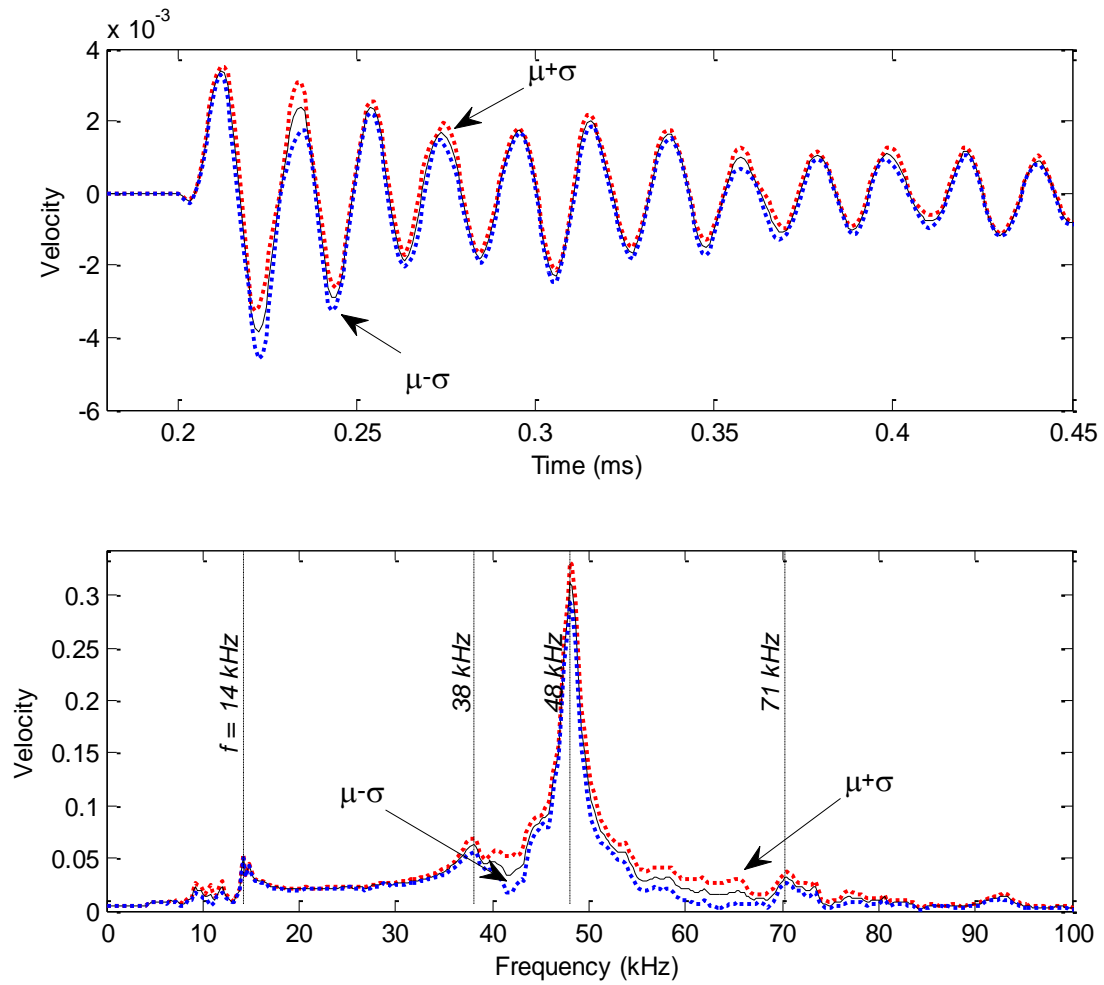


Figure 5.38: Velocity on the top of the transmitter in time (COV = 28.3%) and frequency domains for A3 is mounted. Twenty velocity signals (each one is recorded after two hundred signals are averaged), which are measured on a length of 7 mm (3.5 mm on each side of the accelerometer), are averaged.

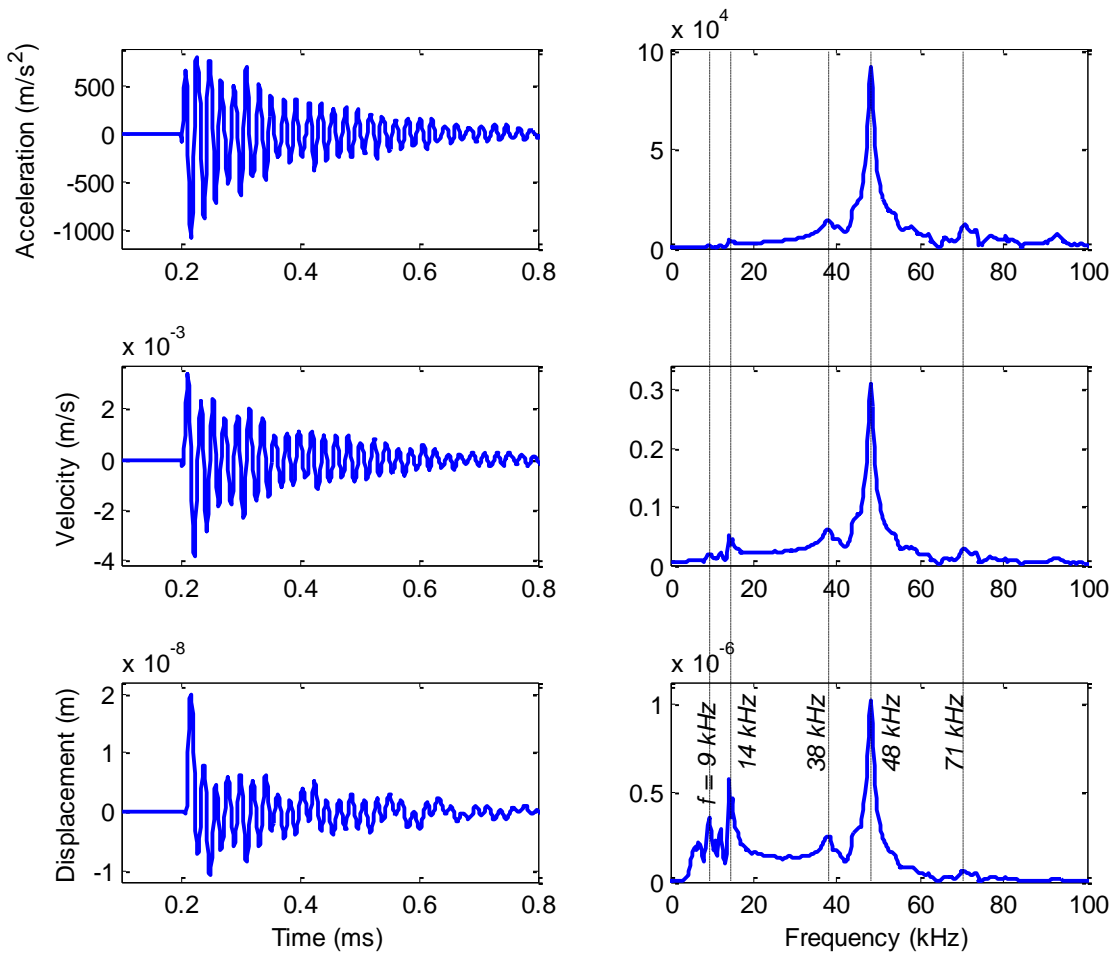


Figure 5.39: Time history and Fourier spectrum of acceleration, velocity and displacement at the top of the transmitter under transient excitation of 125 Volt for A3 is on the transmitter. Velocity is computed by averaging twenty readings. Acceleration and displacement are computed from the filtered velocity.

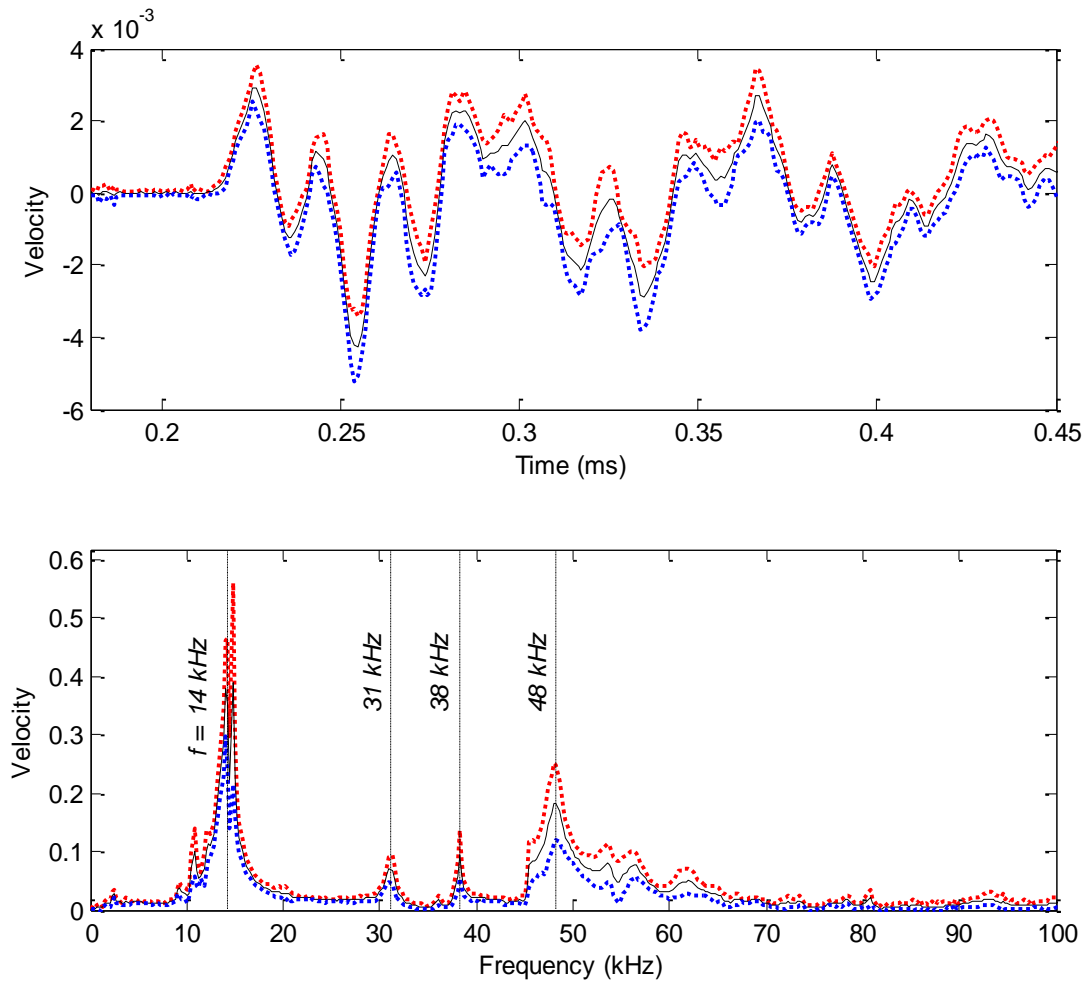


Figure 5.40: Velocity on the top of A3 in time (COV = 22.7%) and frequency domains. Thirty-six velocity signals (each one is recorded after two hundred signals are averaged), which are measured on the four sides of accelerometer's top case, are averaged.

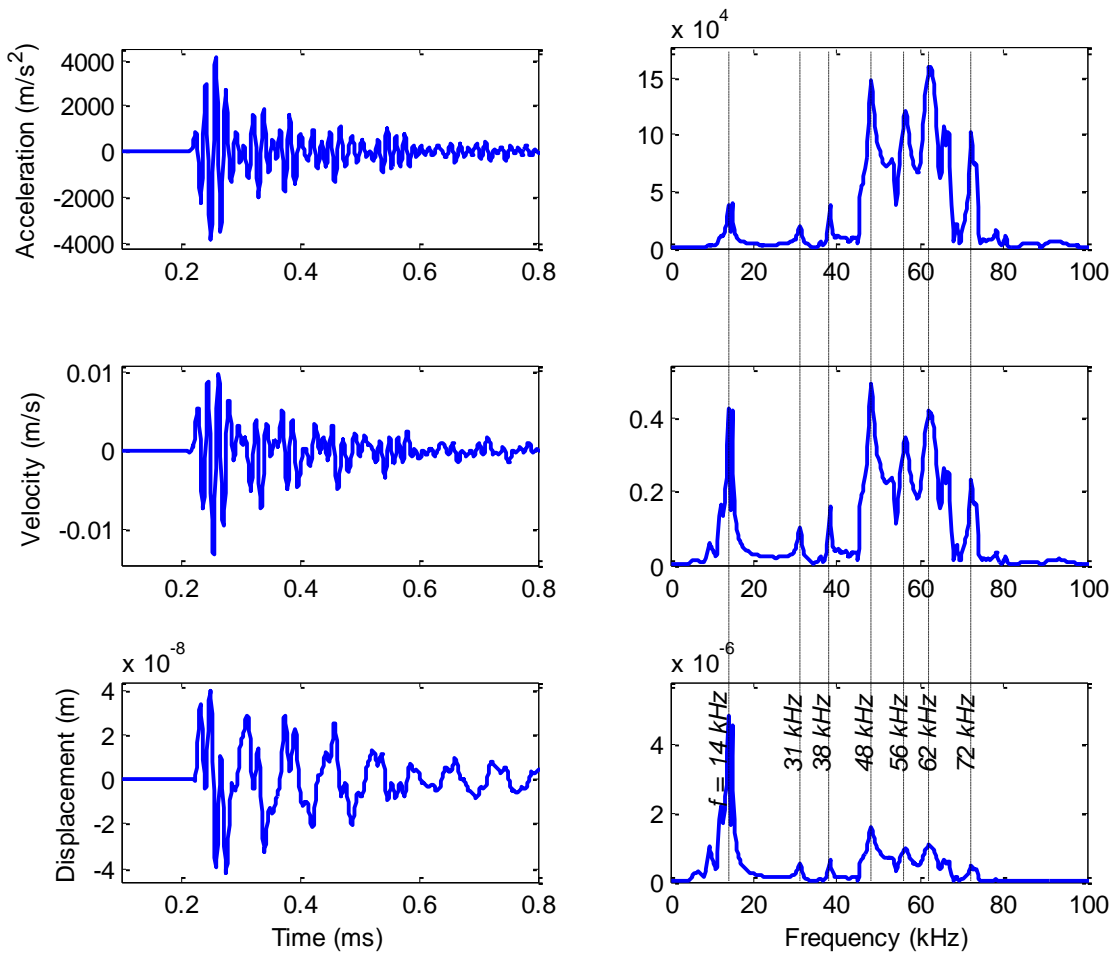


Figure 5.41: Time history and Fourier spectrum of acceleration, velocity and displacement at the top of A3 under transient excitation of 125 Volt. Velocity is computed by averaging nine signals measured on the center scan area (Fig. 5.36). Acceleration and displacement are computed from the filtered velocity.

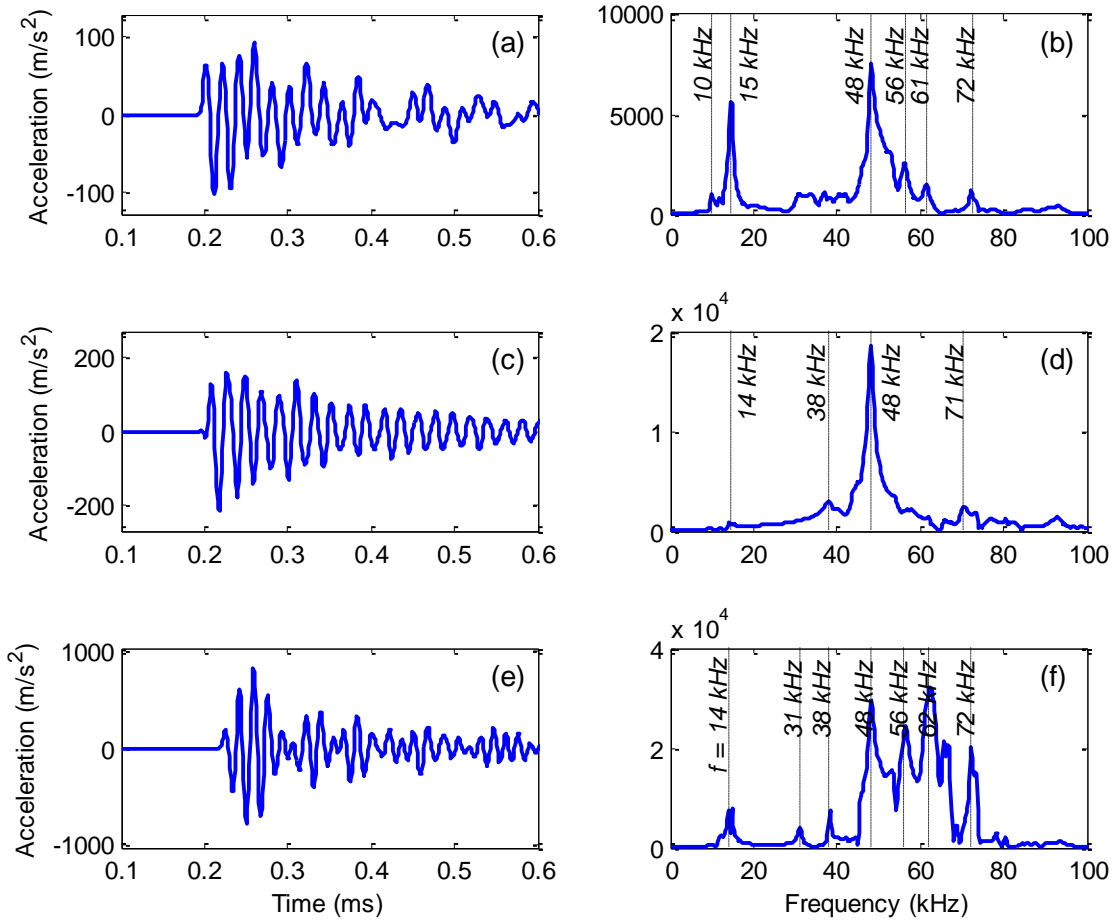


Figure 5.42: Acceleration time histories and Fourier spectra of (a,b) output, (c,d) input, and (e,f) vibration on the top of accelerometer A3. Input and top signals are divided by 5 ($125V/25V$) to ensure the same excitation voltage.

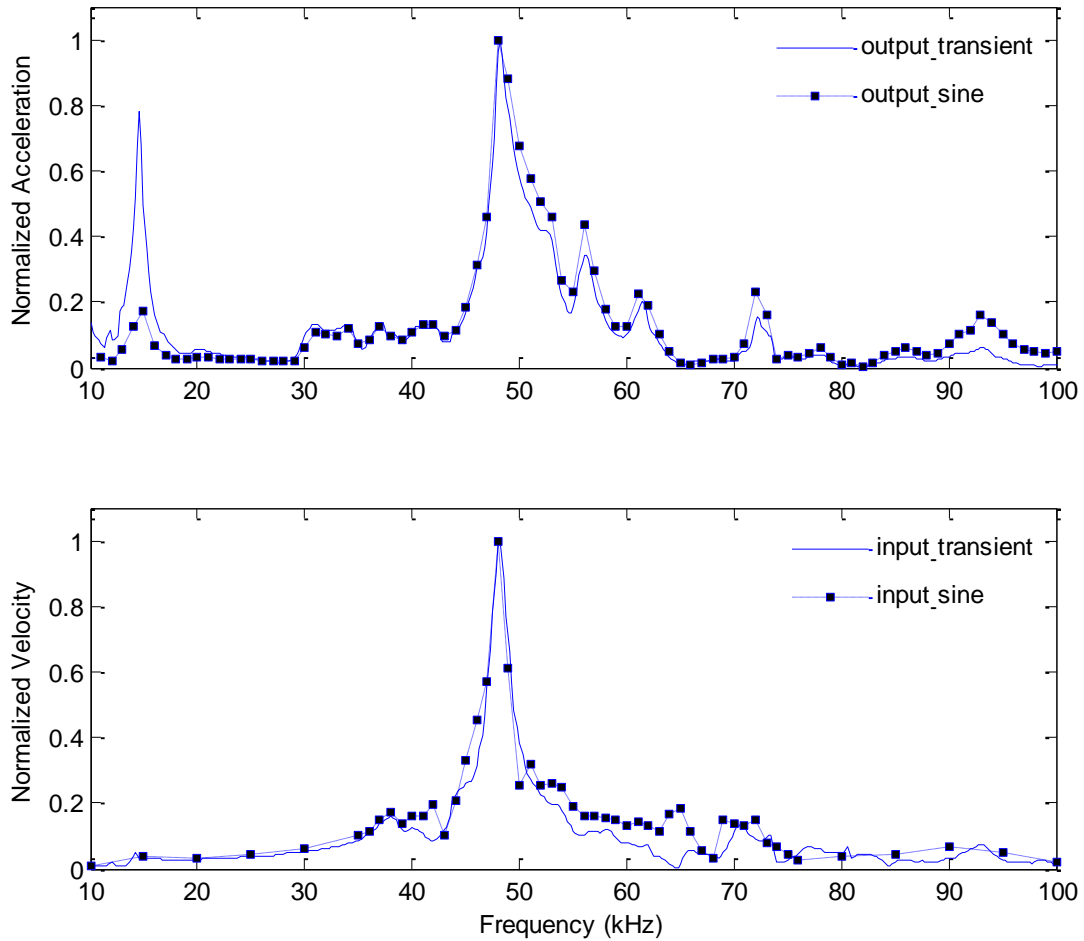


Figure 5.43: (a) Comparison of normalized velocities under transient and sinusoidal excitations at the top of transmitter for accelerometer A3 is on the transmitter. The continuous line represents the Fourier spectrum of velocity under transient excitation and the markers in the dashed line represent the maximum amplitudes in time domain under the corresponding frequency of sinusoidal excitation. (b) Comparison of normalized output accelerations of accelerometer under transient and sinusoidal excitations. The continuous line represents the Fourier spectrum of acceleration under transient excitation and the markers in the dashed line represent the maximum amplitudes in time domain under the corresponding frequency of sinusoidal excitation.

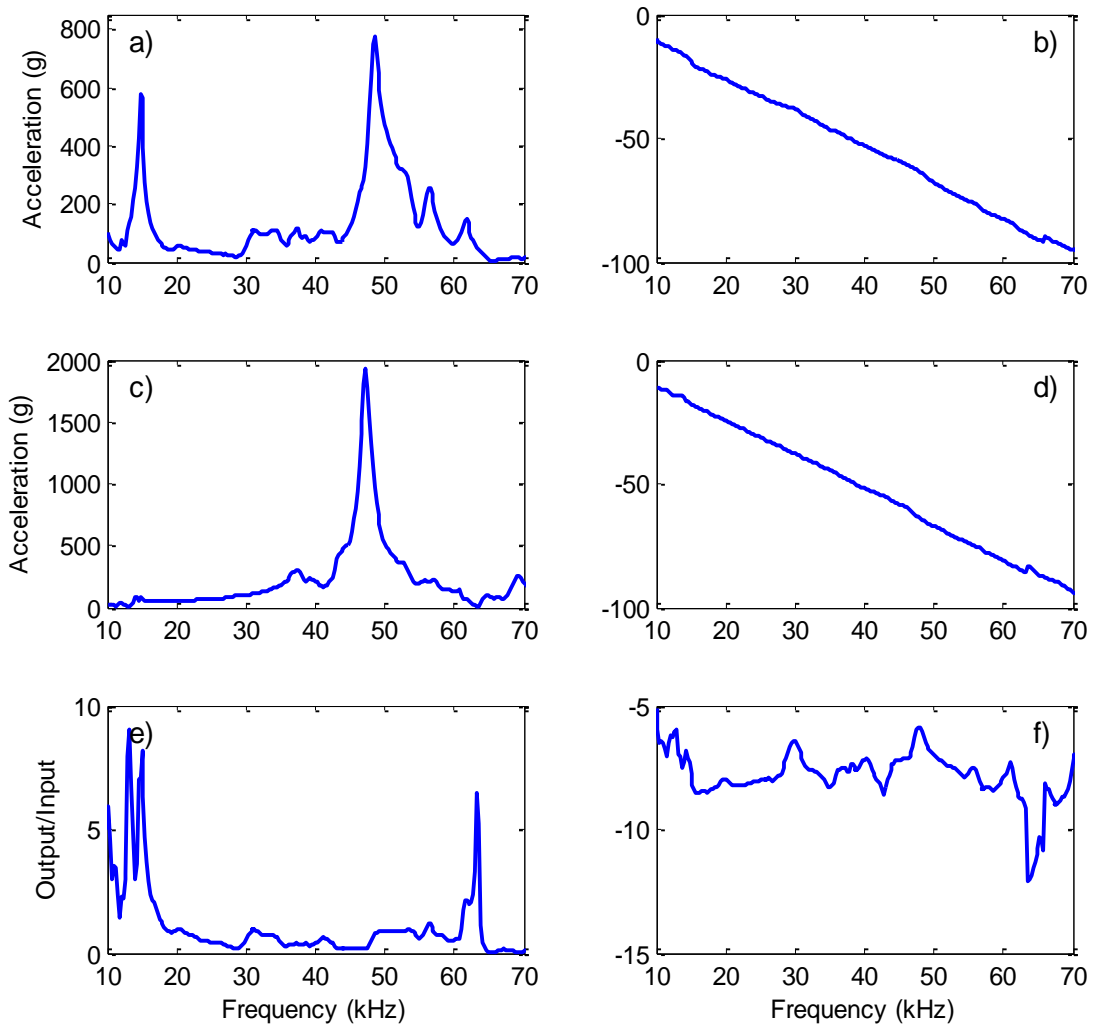


Figure 5.44: From top to bottom, the magnitudes and phases of (a, b) output acceleration, (c, d) input acceleration, and (e, f) frequency response function for A3.

Chapter 6 Evaluation of Condition Assessment Methodology

6.1 Introduction

Prior to the experimental studies conducted on concrete beams (Chapter 7), the proposed damage assessment methodology is investigated on a half-space medium made of cemented sand. Cemented sand is preferred as the test material since it is soft enough to introduce defects with well-defined shapes. This chapter covers three experimental phases conducted on the cemented sand. Each phase addresses a specific problem: The first phase investigates different surface wave characteristics by employing different accelerometers. The second phase looks into the coupling conditions of the transducers, whereas the third one is on evaluation of damage condition of the medium.

6.2 Experimental Methodology

The first phase of the experimental study includes three ultrasonic tests; each is conducted using a different accelerometer: A1, A2 and A3 which are introduced in Chapter 5. The main purpose of Phase I is to evaluate surface wave characteristics; namely, Rayleigh wave velocity, attenuation coefficient, material damping ratio and phase velocity (dispersion behaviour) based on different parameters and signal processing techniques and to reveal the most reliable ones. Moreover, the signals measured by A1, A2 and A3 are normalized respect to the associated FRF for material characterization. During the first phase, it is observed that coupling between the transducer and medium has a significant effect than it was initially thought. Thus, the second phase of experiments is initiated to investigate the coupling conditions of the transducers. In this phase, firstly different adhesive couplings; such as, glue and epoxy are used to mount the receiver ‘A1’ on the material surface to check which type of coupling has less effect on the response. Then, a set of receivers, all are same type as ‘A3’, are fixed on the test medium instead of shifting a single receiver along the array. A set of reference signals is obtained from this

receiver array whose coupling conditions are controlled to be compared to the damaged cases acquired during Phase III. The third phase consists of 13 data sets including the intact case. Each data set represents a different defect depth. The selected parameters from Phase I are computed for each data set in Phase III to constitute a correlation between the wave characteristics and the level of defect.

6.3 Phase I: Investigation on Surface Wave Characteristics Using Different Accelerometers

The first phase includes three sets of data each measured using an accelerometer with a different range of linear response (Table 5.1). The test results obtained in the first phase are valuable to investigate the following concerns:

- Which parameter to be used for evaluation of surface wave characteristics: Parameters obtained from different signal processing techniques; such as, Fourier transform, empirical mode decomposition, continuous and discrete wavelet transforms have been compared to reveal which one is more reliable to determine R-wave velocity, attenuation, material damping ratio and phase velocity.
- Effect of accelerometer's response on determination of surface wave characteristics: The signals captured by three different types of receivers are analyzed and compared to reveal the effect of the acceleration type on material characterization.
- What distance source offset should be: The source-receiver spacing is crucial to avoid near and far field effects. The material damping is evaluated for different source offsets to examine its dependency on the test configuration.

6.3.1 Laboratory Setup and Test Configurations

The experimental tests are conducted on a sand-box (Fig. 6.1) with two layers; the top layer is made of cemented sand which has a depth of 30 cm, and the bottom layer is filled with dry sand with a depth of 45 cm. The horizontal dimensions of the sand-box are 106 and 87 cm. An

underground void having a size of 15 x 10 cm is embedded in the box. The void is located at the center that is 8 cm below the surface.

Three data sets are acquired at different locations on the medium each using a different accelerometer. Table 6.1 gives the general information of the test configurations. The first and second tests consist of 18 time signals received along an array with a spacing of 2 cm (Fig. 6.2a). The transmitter is 25 and 21 cm away from the boundaries of the sand box. This location minimizes the reflections caused by the void and the boundaries. The transmitter is mounted 4 cm away from the first receiver. Test I and II are performed by moving a single receiver - that is A1 for Test I and A2 for Test II - along a straight path. However, as for the third test, 14 receivers, all of whom are same type of receiver as A3, are fixed on the medium surface. The configuration for Test III is depicted in Figure 6.2b.

Table 6.1 Summary of the test data

Test No	Accelerometer	Transmitter	# of receivers	Receiver spacing (cm)	Source offset (cm)
I	$f_R = 52 \text{ kHz}$	$f_R = 50 \text{ kHz}$	18	2.0	4.0
II	$f_R = 95 \text{ kHz}$	$f_R = 50 \text{ kHz}$	18	2.0	4.0
III	$f_R = 35 \text{ kHz}$	$f_R = 50 \text{ kHz}$	14	2.5	5.5

The instrumentation used for the tests (Fig. 6.1) includes an ultrasonic piezoelectric transmitter with a resonant frequency of 54 kHz which is driven by a pulser. Three different kinds of accelerometer A1, A2 and A3, whose properties are given in Table 5.1, are used as receivers for each test. The receivers are mounted on the surface through nuts; a commercial glue is used as coupling between the specimen and nuts. The accelerometers are powered with an external power supply (PCB 483A). As for Test I and II, the signals are filtered with a 200 kHz low-pass filter/amplifier (KH 3384), and recorded with WaveBook/516E (16 bits resolution, 1 MHz sampling rate) data acquisition system. Whereas, for Test III the signals are captured by a 24-channel data acquisition system with a 1 MHz sampling rate (LDS Nicolet Genesis). A 100 kHz low-pass Bessel filter available within the acquisition unit is applied prior to acquisition.

6.3.2 Data Analyses

Different signals process techniques are utilized to determine the following parameters for each data set (See Appendix C for the Matlab code):

1. Rayleigh wave velocity based on:
 - Arrival time of the first peak in time domain
 - Arrival time of wavelet magnitudes
2. Spatial attenuation coefficient and material damping ratio based on:
 - Peak to peak (PTP) amplitude in time domain (Acceleration and displacement)
 - Magnitudes in frequency domain (Including the total area of Fourier spectrum)
 - Decomposed signals (Discrete wavelet transform - DWT)
 - Decomposed signals (Empirical mode decomposition - EMD)
 - Magnitudes of continuous wavelet transform (CWT)
3. Dispersion curve (phase velocity) based on:
 - 2D Fourier transform (Frequency-wave number plot)
 - Unwrapped phase spectrum

6.3.2.1 Rayleigh Wave Velocity

The Rayleigh wave velocity is calculated by first selecting arrival times in time signals and then fitting them into a linear line whose slope gives the velocity (Fig. 6.3). For regression analysis, the time signals of those which do not suffer from either near or far field effects are used to determine the velocities. Same threshold for each data set is used to peak the arrival times. The computed R-wave and P-wave velocities for three of the data sets are summarized in Table 6.2. P-wave value differs within a range of 5%, whereas 10% variation is observed for R-wave velocity. In the case of a defect within the test medium, the wavefront is distorted in a way that it becomes less visible which makes the arrival time selection harder. Therefore, R-wave velocity is also determined using the arrival times of wavelet magnitudes (Fig. 6.4), which requires less manual selection of the peaks. The R-wave velocities obtained from time signals and those from wavelet magnitudes varies only less than 6.5%. For these reasons, as for the damage assessment

phase (Section 6.5), the R-wave velocities obtained from wavelet magnitudes are compared for different damage cases.

Strictly speaking, the R-waves obtained from wavelet magnitudes look faster than the ones from time signals. The reason most likely lies in the center frequency of mother wavelet function employed in wavelet transform; it is 52 kHz for this case. Hence, the R-wave from wavelet transform mostly represents the group velocity of the frequencies within the neighbourhood of 52 kHz, while those obtained from time domains correspond to a larger frequency bandwidth.

Table 6.2 Summary of velocities

Test No	Accelerometer	P-wave ^[1] (m/s)	R-wave ^[1] (m/s)	R-wave ^[2] (m/s)
I	$f_R = 52 \text{ kHz}$	1913	1101	1070
II	$f_R = 95 \text{ kHz}$	2015	1098	1136
III	$f_R = 35 \text{ kHz}$	1904	1220	1299

[1] Computed from time histories, [2] Computed from wavelet magnitudes.

6.3.2.2 Attenuation and Material Damping Ratio

Spatial attenuation coefficient, α , is determined by substituting different parameters such as peak to peak amplitudes or frequency magnitudes into Eq. 2.49. The following parameters are investigated to find out the most reliable one for the determination of attenuation.

6.3.2.2.1 Frequency Magnitudes

The frequency spectra for each data set are shown in Figure 6.5. As discussed in Chapter 5, each measured signal contains the frequency response functions of the receiver, transmitter, coupling and the material tested. Hence, decision of which frequency to rely on for attenuation calculations requires additional care. The contour plot shown in Figure 6.6 displays the attenuation trends of frequencies along the distance for Test III. Selection of a reliable frequency from Figure 6.6 can be managed by performing regression analysis for attenuation of magnitudes of each frequency. Prior to regression analysis, the Fourier spectra are windowed with a square window which is shifted along the frequency axis so that the attenuation of a sub-spectral area

representing a central frequency is calculated. Considering a portion of spectral area instead of single frequency magnitude reduces the inconsistency in the attenuation trend. Different window widths ranging from 1 to 10 kHz are applied. A linear regression analysis is carried out to fit the logarithm of sub-spectral areas into a straight line. Figure 6.7 displays the coefficient of determination (R^2) values determined for different window widths. All resolutions expose relatively higher correlation between 45 and 70 kHz. Within this range, 52 kHz provides a R^2 value of 0.7 after windowing the spectra using a window width of 1 kHz. However, no reliable frequency can be observed around 10 kHz which is one of the main two frequencies in the Fourier spectra (Fig. 6.5c). The reason is mostly likely because of the near-field effect; the corresponding wavelength, 12.5 cm, does not form fully along the first part of the receiver array. Also, considering the transmitter's frequency range, which is between 10 and 75 kHz (Fig. 5.9), the frequencies lower than 10 kHz are not reliable. As conclusion, 52 kHz appeals as the most appropriate frequency for attenuation calculation since it doesn't only provide a higher R^2 value but also stands within the neighbourhood of the transmitter's resonance frequency of 54 kHz. A nonlinear curve-fitting is also performed for the attenuation trend of 52 kHz (Fig. 6.8); regression results in $\alpha = 7.04$ with $R^2 = 0.71$, whereas α and R^2 are found 4.97 and 0.70 respectively from the linear regression of logarithm of 52 kHz magnitudes.

So far, the attenuation is determined using the whole waveform; however, windowing the traces in time domain has a potential to increase the quality of calculations. The signals are windowed such that the portions that most likely represent the R-wave motion are aimed to be subtracted from the raw signals. Hence, the effect of reflections could be minimized. Tukey windows, with increasing width for further receivers, are chosen for subtracting the primary event in the wave propagations. The windowed signals with associated Tukey windows and corresponding Fourier spectra are shown in Figure 6.9. As it can be seen in the frequency spectra, windowing results in eliminating the ripples, and reveal the shift of energy concentration from high frequencies to low frequencies. In Figure 6.10, the contour plot derived from windowed signals clearly exposes the frequency dependence of attenuation; low frequencies keep their existence almost along the whole receiver array, whereas high frequencies die out by distance. The improvement in attenuation calculation is observed when R^2 values for non-windowed (Fig. 6.7) and windowed

cases (Fig. 6.11) are compared. For instance, regarding the attenuation based on 52 kHz, R^2 increases from 0.70 to 0.83 after windowing (Fig. 6.12).

6.3.2.2.2 Peak to Peak Amplitude of Acceleration and Displacement Traces

The attenuation coefficient is also computed based on peak to peak (PTP) amplitudes of recorded accelerations and computed velocities and displacements. The time signals and Fourier spectra of acceleration, velocity and displacement traces for Test III are given in Figure 6.13. The velocities and displacements are integrated from the acceleration time histories. It is clearly seen in the Fourier spectra, acceleration is better in representing the high frequencies, whereas displacement are more convenient to observe the low frequencies. The computed attenuation coefficients are 7.23 and 1.56 for acceleration and displacement respectively (Fig. 6.14). In the figure, the PTP values from velocity traces are not given since the signals from the first receivers are dominated by the high frequencies while the rest of the signals are mostly consist of the lower frequencies. Therefore, the attenuation of PTP from velocities does not provide any meaningful information. On the other hand, displacements are dominated by lower frequencies whose the computed attenuation value is smaller compared to the one from accelerations. In the case of accelerations, high frequencies stronger in first cycle of the signals; however, for the further receivers low frequencies becomes more apparent, which makes it harder to correlate the computed attenuation coefficient with a specific frequency. Therefore, attenuation based on magnitudes in Fourier spectrum is more appropriate for defect detection.

6.3.2.2.3 Decomposed Signals from Discrete Wavelet Transform

Discrete wavelet transform (DWT) based on Mallat's algorithm (Mallat, 1989) provides a general picture of the frequency distribution of a signal over time that cannot be given by the Fourier transform. As an example of the Mallat's algorithm for wavelet transform, a Daubechies wavelet (dbn18) is used to decompose signals for the second receiver from Test III as shown in Figure 6.15a; where only six levels carrying the most of the energy are displayed. Each signal in the figure labelled with a level number representing the associated frequency range (Fig. 6.15b). Energy contribution is obtained mostly from Level-4 which has a frequency bandwidth of 31.25 and 62.5 kHz. For this level, the decomposed time signals and corresponding frequency spectra

for all receivers are displayed in Figure 6.16. The energy dissipation based on the spectral area for each level can be used to determine the attenuation coefficient related to that specific frequency bandwidth. The attenuation trends for 4 levels are shown in Figure 6.17; it is justified again by DWT that lower frequencies have smaller attenuation coefficients. Level 4 (31.25-62.5 kHz) provides the highest R^2 with 0.85 since it has the most of the spectral energy cumulated within that range.

6.3.2.2.4 Decomposed Signals from Empirical Mode Decomposition

As an alternative to DWT, empirical mode decomposition (EMD) is performed to seek any possible improvement in data interpretation. A Matlab code modified from Clifford's routine is used for the decomposition. The intrinsic mode functions (IMFs), decomposed from the signal captured by the second receiver from Test III, (Fig. 6.18a) seem similar to those obtained from DWT (Fig. 6.15a). An analogy can be affirmed between the 1st IMF and Level-4 from DWT thanks to the matching spectra of both (Fig. 6.18b). By theory, the IMFs are not decomposed based on any predefined frequency range due to EMD's empirical characteristic. Yet, in this practice, the first mode is associated with the significant frequencies; hence, it looks like Level 4 from DWT. While with the higher modes, the spectral energy decreases. The first modes presented in Figure 6.19 for all receivers are used to compute the spectral areas, so that the attenuation trend can be determined. In Figure 6.20, the trends obtained from the first three modes are displayed. Since the first and second modes share the main energy transmitted, both expose close behaviour with high correlations. However, compared to Level-4 from DWT, any IMF obtained from EMD could not provide a better correlation. Since DWT explicitly decomposes a signal within well-defined frequency ranges, the main energy cumulated is not divided between the decomposed signals as like EMD does. In EMD, some of the main energy is presented by the second mode decreasing the reliability of the first mode.

6.3.2.2.5 Continuous Wavelet Transform

The damped frequency at the arrival time of R-wave and associated attenuation of that frequency and consequently the material damping can be calculated by utilizing continuous wavelet transform (CWT) as explained in Section 4.7. A Morlet function with 52 kHz central frequency,

only because to be consistent with Section 6.3.2.2.1, is used as the mother wavelet to transform data set from Test III (Fig. 6.4c). The maximum wavelet magnitudes and the associated damped frequencies at the arrival times, along with the material damping ratios for each signal are plotted in Figure 6.21. The variation in the damped frequency, computed from the phase spectra of wavelet transformed signals, is limited between 42 and 52 kHz (Fig. 6.21b). Since the Morlet wavelet itself works as a window, no prior windowing is applied. Utilizing CWT eases the difficulties encountered in the selection of proper frequencies. However, selecting the most reliable receiver set that is representing the material damping is another issue. Therefore, damping ratio is computed for different sets of receivers by selecting different numbers and locations of the receivers. It starts with a set including all receivers - 14 of them - and then is followed by reducing one receiver in the set for the next step. For each step, the receiver set is shifted along the receiver sequence. For instance, for a set having 8 receivers, it is moved 7 times to cover all locations tested on the medium. In Figure 6.22, the mean damping ratios - the average of damping values computed for each receiver - and associated R^2 values computed for different sets of receivers are plotted. This figure reveals two facts: (i) Smaller the source offset better the correlation since the signal to noise ratio (SNR) is stronger for this distance. Energy dissipation along the distance reduces SNR which decreases the reliability of the signals. (ii) Decreasing the number of receiver increases R^2 values; however, on the other side smaller regions of the medium are taken into account missing the approach to make a global assessment. The computed damping results (3.24% based on whole array) are higher compared to the literature value, 0.4%, which was obtained from a cemented-sand specimen tested with UPV (Khan, 2006). Nevertheless, these damping results can provide beneficial information when a comparative study including tests results from non-damaged and damaged materials is pursued. Therefore, 14 receivers from Test III are taken into account to determine the mean material damping. It also enables the largest area for investigation.

6.3.2.3 Frequency - Wavenumber Plots and Dispersion Curve

The dispersion phenomenon is explained in Chapter 2; large wavelengths which are compatible with the depth of a medium cause vibrations at higher Lamb modes. In this study, considering the frequency range preferred for the ultrasonic tests and thickness of the test material, dispersion

due to the plate behaviour is ignored. The theoretical dispersion for the test medium is determined using Eq. 2.37. Two fundamental Lamb modes computed from the analytical solution are shown in Figure 6.23. Both fundamental modes, symmetrical and anti-symmetrical, converge to a constant R-wave velocity for the frequencies higher than 10 kHz, which is the frequency interest of this study.

On the other hand, experimental dispersion curves can be obtained utilizing two dimensional Fourier transform (2D FT) of time histories. Thus, a frequency-wave number domain (f-k) plot, which exposes incident, reflected and transmitted events occurring during the propagation of waves, is generated. Rayleigh wave occurs in homogenous half space medium; therefore, it is non-dispersive and appears as a straight line in the f-k plot whose slope gives the R-wave velocity. The medium subjected to testing - the top layer of the sand box which is made of cemented sand - is assumed homogenous half space. The f-k plots generated from three of the tests are shown in Figure 6.24. No significant reflection is observed since the receivers are located off the void and efficiently far away from the boundaries. For all three tests, high magnitudes of wave energy appear within the range of 10 and 20 kHz; where a consistent R-wave mode can be pointed out. On the other hand, dispersive behaviour is observed for the frequencies lower than 10 kHz, due to large wavelengths that interfering with the boundary between the cemented and dry sand layers. Meanwhile, another high energy region arises around the neighbourhood of 55 kHz. Unfortunately, no constant phase velocity could be determined, because of spatial aliasing caused by insufficient space between the receivers. Frequency of 55 kHz has approximately 2 cm wavelength which is smaller than the recommended receiver spacing in Eq. 4.9. The red dots on the f-k plots mark the maximum peaks. By selecting the frequencies and wave-numbers associated with these peaks, phase velocities, in other words dispersion curves, can be plotted. Figures 6.24b-d-f depict the dispersion curve extracted from the f-k plot for each data set. The curves for all tests approach to a constant R-wave velocity of approximately 1100 m/s which is close to those obtained from the arrival times in time signals (Section 6.3.2.1). Another interesting information interpreted is that all test data exhibit the anti-symmetrical mode clearly; this mode represents the flexural mode of a plate. Acknowledging the vertical excitation transmitted by the source transducer, the strong appearance of the anti-symmetrical mode is expected.

The phase velocity curves given in Figure 6.24 lose their convergent trend above 20 kHz due to the numerical dispersion having no physical meaning. The ripples in the f-k plots jeopardize selection of the maximum peaks and consequently the associated frequencies. For this reason, the same type of window used in attenuation calculations (Section 6.3.2.2.1) is employed, prior to 2D Fourier transform. As a result, the numerical error is reduced and the accurate frequencies carrying the energy are exposed. Figure 6.25 give the f-k plots and associated dispersion curves for the windowed signals. Interestingly, utilizing windows provides to extract the symmetrical mode which is related to the extensional mode govern by the compression waves. Windowing reduces the dominance of anti-symmetrical mode and gives the compression mode a change to be detected. As like attenuation calculations, windowing improves the consistency of the data which provides us making better interpretation. Hence, for the damage detection (Section 6.5), dispersion curves that are properly windowed are taken into account.

Another method to compute phase velocity is based on phase spectra using Eq. 4.8. First, the unwrapped phase for all signals are computed and then a linear regression analysis is performed to fit the unwrapped phase values respect to distance; the slope of the fitted line provides the phase velocity. Procedure is repeated for each frequency. However, this method may be erroneous due to the spurious cycles in the phase spectra (Al-Hunaidi, 1993). On the other hand, windowing the time signals improves the phase spectra which leads us obtain more accurate values that are closer to the expected Rayleigh wave velocity. Figure 6.26 show the wrapped phases of windowed and raw signals as an example, and Figure 6.27 is given to display the computed phase velocities for each case. R^2 values obtained from regression analyses are the evident of improvement achieved by windowing especially for lower frequencies. Nevertheless, for the rest of this study, the phase velocity curves obtained from 2D Fourier transform are preferred for the analyses.

6.3.3 Characterization of the Cemented-Sand based on the Calibrated Accelerometers

The accelerometers' FRFs determined in Chapter 5 are used to characterize the cemented-sand specimen. The signals captured by each accelerometer are normalized respect to corresponding

FRF to determine the material damping. The effect of the accelerometer's FRF is removed from the original signals in frequency domain and then the impulse response function (IRF) of the medium derived by applying the inverse Fourier transform of these normalized Fourier spectra. The original measured signals are first subjected to a digital 10 - 70 kHz band-pass filter before eliminating the FRF to be consistent with the applicable frequency range of the FRF. Later, the computed IRFs are windowed using a Tukey window to trim out the unreal early arrivals faster than the arrival time of the P-wave (Table 6.2). Some selected time signals recorded by A1, A2 and A3 and the associated frequency spectra are shown in Figures 6.28-6.30. Material damping ratio is calculated for both the original signals and the IRFs of the medium as given by Eq. 2.47 for $V_R = 1220$ m/s and $f = 54$ kHz which is the resonant frequency of the transmitter. The computed damping ratios obtained from the original signals and the normalized signals are summarized in Table 6.3.

Table 6.3 Material damping ratios

	A1	A2	A3
Original Signals ^[1]	0.75%	0.23%	1.74%
Corrected Signals ^[1]	0.58%	0.38%	1.71%

[1] Same distance is used for each test to calculate damping ratio.

The damping ratio is determined as 0.58% and 0.38% based on the corrected signals for A1 and A2 successively. These damping values are closer to the characteristic damping of the tested material, 0.4% (Khan, 2006), rather than the ones obtained from the original signals. Regarding A3, the improvement in the damping ratio is negligible. Apparently, assuming all accelerometers employed in Test III have the same FRF is not correct, even though all of them are same type transducers. To summarize, the FRFs determined in Chapter 5 improve the damping result; therefore, it is recommended to use transmitters with different frequency bandwidths to extent the calibration for a broader frequency range. In consequent, the real dynamic behaviour of the medium under investigation can be approximated closer which will lead to a more accurate characterization.

6.3.4 Conclusions

R-wave Velocity

- The computed P-wave and R-wave velocities for three of the data sets differ within a range of 5% and 10% variation respectively.
- The R-wave velocities obtained from wavelet magnitudes requires less manual selection of the peaks and only differs 6.5% than those from time signals. Hence; R-wave velocities from wavelet transformed signals are used for damage evaluation in Phase III.

Attenuation and Material Damping

- The attenuation trends of different parameters obtained from Test I, II and III are compared in Figure 6.31. Test III in which receiver ‘A3’ is employed provides the highest correlation, due the fact that coupling is more consistent compared to other two tests where the receiver has to be shift along the distance. In terms of parameter, DWT (Level-4) provides higher R^2 value for all tests since it is associated with frequency bandwidth carrying most of the energy compared to other parameters.
- The attenuation trends of different parameters are plotted in the same figure (Fig. 6.32) for comparison. The attenuation coefficients for each trend and associated R^2 values are also tabled in Table. 6.4.

Table 6.4 Summary of attenuation coefficients

Signal Parameter	$\alpha^{[1][2]} (m^{-1})$	R^2
Magnitude of 52 kHz	4.97	0.70
Magnitude of 52 kHz ^[3]	8.95	0.83
Total spectral area	4.15	0.76
Total spectral area ^[3]	6.42	0.87
Spectral area from DWT ^[4]	7.55	0.85
Spectral area from EMD ^[5]	5.81	0.79
Magnitudes from CWT ^[6]	7.66	0.82

[1] Attenuation coefficients are determined using linear regression analysis. [2] All receivers are taken into account for calculations. [3] Obtained after windowed time signals. [4] Spectral areas are calculated from Level-4 (31.25 - 62.5 kHz). [5] 1st IMF is used to compute spectral area. [6] The central frequency of the Morlet function is 52 kHz.

- Windowing the signals improves the reliability of attenuations obtained from the spectral parameters (Table 6.4) since it eliminates the ripples, and exposes the energy concentrated frequencies clearly in the spectra.
- As for frequencies lower than 10 kHz, signals from whole receiver array cannot be used to determine attenuation due to the near-field effects. Appropriate source offset should be selected prior to calculating attenuation for this frequency range.
- 52 kHz appeals as the most appropriate frequency for attenuation calculation from Test III. It doesn't only provide a higher R^2 value (Fig. 6.7) but also stands within the neighbourhood of the transmitter's resonance frequency of 50 kHz. Therefore, it is selected as the central frequency of Morlet function to be used for CWT.
- Displaying magnitudes for all frequencies respect to distance together on a single contour plot (Fig. 6.10) clearly exposes the frequency dependence of attenuation; the low frequencies keep their existence almost along the whole receiver array; while, the high frequencies die out by distance.
- Acceleration is better in representing the high frequencies; whereas, displacement is more convenient to observe the low frequencies.
- The energy dissipation of the decomposed signals from DWT appears as the most reliable parameter to determine attenuation. Because selecting a wide frequency bandwidth instead of a single magnitude from Fourier spectra reduces the inconsistency in the attenuation trend.
- It is clearly justified again by performing DWT that lower frequency bandwidths have smaller attenuation coefficients (Fig. 6.17).
- Compared to DWT, IMFs obtained from EMD does not provide a better correlated attenuation. DWT explicitly decomposes a signal into signals associated with well-defined frequency ranges, unlike EMD which may split the high energy into different decomposed signals.
- CWT provides the instantaneous damped frequency at the arrival time to be determined conveniently since the Morlet wavelet itself is a time window.
- Investigation on material damping reveals that selecting smaller set of receivers that are located closer to transmitter ensures better the correlation since SNR is stronger for this distance. However, damping is calculated using all receivers to allow the largest area to be investigated.

- Although, the determined material damping for 14 receivers from Test III, %3.24, is higher than the literature value, 0.4%, this value can constitute the reference value to be compared to the results that will be obtained from damaged medium.

Dispersion

- The f-k plots reveal a consistent R-wave mode for the range between 10 and 20 kHz without any significant reflection.
- Spatial aliasing caused by insufficient space between the receivers does not let to calculate phase velocities for frequencies above 55 kHz.
- The R-wave velocities, approximately 1100 m/s, exposed by the dispersion curves are within the same range with those obtained from the arrival times.
- The fundamental anti-symmetrical Lamb mode for the frequencies lower than 10 kHz is observed for the experimental data that matches with the theoretical one.
- The ripples in the f-k plots cause numerical dispersion in dispersion curves. Therefore, the time signals are windowed prior to 2D Fourier transform, to obtain the smoothed dispersion curves.
- Windowing provides extraction of the fundamental symmetrical (extensional) mode by reducing the dominance of anti-symmetrical (flexural) mode caused by the vertical excitation generated by the transmitter.

Material characterization from calibrated accelerometers

- The damping ratio is found as 0.58% and 0.38% from the corrected signals acquired via A1 and A2 successively. These damping values are closer to the characteristic damping of the tested material rather than the ones obtained from the original signals.
- It is recommended to extend the calibration for a broader frequency range. So that, the real dynamic behaviour of the medium under investigation can be approximated closer.

6.4 Phase II: Investigation on Coupling

In this section, the investigation on coupling, which is the most common issue encountered in ultrasonic testing, is addressed. Additionally, different types of excitations pulse are also studied. The experimental works introduced in the previous section are first initiated with employing the accelerometer A1 (52 kHz resonant frequency), simply because its resonance frequency matches the transmitter's enhancing SNR of the received signals. However, only a single transducer of this type was available for the tests. For each test session, this single receiver had to be moved along the distance subjected to investigation; thus, applying an equal torque to tighten it up was not possible, which decreases the consistency of the coupling. Moreover, the cemented-sand is a soft material; therefore, to ensure a strong bonding between the nuts and the material without distorting the responses received by the accelerometer is a challenge. For this reason many trial tests have been conducted, the selected ones (Table 6.4) will be discussed here as an attempt to find out the best coupling condition.

Table 6.5 Summary of the tests

Test #	Coupling	Receiver	Excitation	Receiver spacing (cm)	Source offset (cm)
Test1	Adhesive	A1	Square	2.0	4.0
Test2	Embedded	A1	Square	2.0	4.0
Test3	Epoxy	A1	Square	2.0	4.0
Test4	Epoxy discrete	A1	Square	2.0	4.0
Test5-S2 ^[1]	Adhesive	A3	Square	2.5	8
Test6-S2 ^[1]	Vacuum grease	A3	Square	2.5	8
Test5-S1	Adhesive	A3	Square	2.5	5.5
Test7	Adhesive	A3	1 cycle Sine (50 kHz)	2.5	5.5
Test8	Adhesive	A3	Steady-state sine (50 kHz)	2.5	5.5
Test9	Adhesive	A3	Steady-state sine (5 kHz)	2.5	5.5

[1] Transmitter is located at the other side of the receiver array refer to Test5-S1.

6.4.1 Data Analyses

The first four tests listed in Table 6.4 are conducted to find out the coupling with the strongest bonding without compromising the signals' quality. The data sets obtained for each coupling

condition are plotted in Appendix D. The first coupling used (Test1) is the adhesive (Loctite® QuickTite®) which could not provide a strong bonding as a coupling material. Therefore, it is decided to embed the nuts into the medium to increase the bonding area (Test2); however, doing so does not improve the bonding either. Third test is conducted with the epoxy gel (Loctite®) which is applied as a strip along the receiver array. Although, the strongest bonding is achieved with the epoxy, the time histories are altered significantly in an unusual manner (Fig. D.1). Most likely the epoxy strip behaves as the second layer at the top of the medium, despite the fact that the thickness of the epoxy is kept minimal. So, the epoxy layer is discretized (Test4). By doing so eliminated the dispersion effect observed in Test3. The attenuation trends displayed in Figure 6.33 reveals how the coupling affects the PTP amplitudes of the signals. The best correlation is obtained from the epoxy (Test3) with a R^2 of 0.90 thanks to the strong bonding which allowed applying higher torque increasing the energy transfer from the medium to the receiver. Nevertheless, in all cases, the failure of bonding with repeated test could not be avoided even with the epoxy since the torque applied by hand to tighten the accelerometer cannot be kept same each time. For the sake of both reliability and practicability of the tests that will be performed in Phase III, it is decided to fix a set of receivers (14 accelerometers) at once and complete the entire tests without moving any of them (Test5). Hence, the coupling would be consistent during whole assessment procedure.

The next step is an effort to perform in-situ calibration. Test5 is the same test configuration that was introduced as Test III in Phase I. This data set constitutes the reference (no damage case) time histories for the condition assessment that will be discussed in Phase III. All receivers employed for Test5 are the same type of accelerometers which are known to have a flat response between 1 Hz and 10 kHz with a resonance frequency above 35 kHz; however, no information about the frequency function of the receivers is known beyond 10 kHz. On the contrary, as discussed earlier in Phase I, the interested range of frequencies is between 10 and 70 kHz for the assessment procedure. Calibration for 14 accelerometers under laser scanner could not be possible due to time limitation within this study. Therefore, a reference receiver is shifted along the array which is coupled with vacuum grease (Dow Corning®) to realize the in-site calibration. The signals obtained from both reference transducer (Test6-S2) and receiver array (Test-S2) are given in Appendix D. The R-wave velocities obtained from Test5 and Test6 are almost same,

which are 1205 and 1197 m/s respectively. Moreover, the attenuation trends based on the PTP amplitudes are found in good agreement with each other providing correlations higher than 0.90 (Fig. 6.34). Even though, the frequency response functions of each receiver in the array is not available, the comparison of the data from the reference receiver and the set of receivers reveals that using a set of receivers fixed for the damage evaluation in a relative manner would be appropriate for laboratory testing.

All the data presented so far in this section is acquired under a square pulse excitation with a pulse repetition frequency of 50 Hz. As an additional effort, responses of the receivers under different excitation types are investigated by conducting Test7-9. The same configuration as Test5 is used in the following order: one cycle of sinusoidal with a frequency of 50 kHz, individual steady-state sinusoidal waves of 50 and 5 kHz. The attenuation trends based on the PTP amplitudes (Fig. 6.35) for each excitation type confirms the consistency of the receiver set. Test9 is not included in the figure since 5 kHz attenuates insignificantly compared to higher frequencies. However, this low frequency excitation enables to picture the vibration of the test medium along the array thanks to its long wavelength (Fig. 6.36). In Figure 6.36, the waveform is constructed with the amplitudes picked at a certain time for each receiver which perfectly presents a sinusoidal waveform of a period of 1/5000 sec with a decent attenuation trend. Even though, the amplitudes of the voltage recoded are so low, the receivers are capable of capturing the vibration properly confirming that the coupling is appropriate for each receiver. To conclude, as for the next phase, a square excitation is decided to be used to take advantage of a broader frequency range.

6.4.2 Conclusions

- The strongest bonding is achieved with a strip epoxy on test medium; however, it caused serious distortion in the time signals.
- To increase the reliability of the damage evaluation tests in Phase III, a set of receiver is decided to be mounted permanently on the test sample instead of shifting a single accelerometer which causes inconsistent coupling.

- The lack of calibration information for all accelerometers is fulfilled with an in-situ calibration test which is performed via a reference receiver. The calibration data confirms that the investigated surface wave characteristics are in good agreement with the ones obtained from the receiver array.
- The stable coupling respect to frequency content is confirmed under different excitations.

6.5 Phase III: Investigation on Damage Assessment

The third phase covers the ultrasonic tests conducted on the artificially damaged cemented-sand. Different levels of damage ranging from less to severe are introduced to the medium by drilling. A drill with a $\frac{1}{4}$ inch (6.35 mm) bite is used to create vertical inclusions within the medium. The damaged section is created at the center of the receiver array, 20.5 cm away from the first transmitter (Fig. 6.2b); it is consisted of 7 holes with 1 cm spacing (Fig. 6.37). The depth of the inclusions is increased up to 12 cm with an increment of 1 cm. The total number of the test sets is 13 including the undamaged case. The test results from different damage cases are analyzed to constitute a correlation between the parameters selected from the first phase of tests (Section 6.3) and the level of deterioration. The test instrumentation and configuration is same as Test III which is given in Section 6.3.1. Data sets are named in the format of D# in which the number refers the maximum depth of the overall holes.

6.5.1 Data Analyses

The signal processing procedure followed for the data analyses is depicted in Figure 6.38. This procedure is finalized based on the investigation pursued in Phase I and the following parameters are decided to be determined for the damage assessment:

1. R-wave velocity from arrival times based on wavelet magnitudes,
2. Attenuation of spectral area from DWT (Level-4: 31.25-62.5 kHz),
3. Material damping ratio based on continuous wavelet transform,
4. Dispersion curves (phase velocity) based on 2D Fourier transform.

6.5.1.1 R-wave Velocity

Time histories and Fourier spectra from case D0 and D12 (the depths of all holes are 0 and 12 cm successively) are plotted together in Figure 6.39. Signals captured behind the damaged section for case D12 reveal distorted wave-fronts compared to the intact case which makes it harder to select the arrival times (Fig. 6.39a). Therefore, wavelet transform is performed to

determine the R-wave velocity conveniently from the arrival times of the wavelet transformed amplitudes as explained in Section 6.3.2.1. The frequency spectra of the signals for two cases reveal similar frequency peaks for the receivers before the damaged sections, whereas it varies significantly for the rest of the receivers (Fig. 6.39b). The signals for the damaged case can be considered as the combination of the incident event (non-damaged case) and the reflected or diffracted event (it depends on whether the receiver is located before or after the holes) due to the defects. Therefore the signals from the damaged case can be written as:

$$g(t) = f(t) + Af(t - t_o) \quad (6.1)$$

where $f(t)$ is the incident signal and $Af(t - t_o)$ is reflected or diffracted wave defined with the delay time, t_o and the transmission coefficient, A . So, the difference between the damaged and non-damaged signals should provide the second event (Reflection or diffraction):

$$h(t) = g(t) - f(t) = Af(t - t_o) \quad (6.2)$$

In frequency domain it is given as:

$$H(\omega) = AF(\omega)e^{-i\omega t_o} \quad (6.3)$$

The basic outcome of this equation is that the frequency content of the second event due to the defects is just an altered version of the incident event which is scaled in magnitude and shifted in phase. The differences of the time signals for case D0 and D12 are simply computed by subtracting the signals of the non-damaged case from those of the damaged case (Fig. 6.40a). The corresponding Fourier spectra of the second event match firmly to the frequency spectra of the incident event (non-damaged case) in Figure 6.40b justifying Eq. 6.3.

The R-wave velocity is obtained by taking all of 14 receivers into account for each damage case. The computed velocities are shown in Figure 6.41. The velocity varies within a range of 900 and 1350 m/s and displays a declining trend upon the depth of damage with a standard deviation (σ) of 120 m/s and a coefficient of variation (COV) of 11%. The experimental trend is fitted into a linear line; the coefficient of determination (R^2) is found as 0.73 which justifies the linear relationship between the R-wave velocity and the defect depth.

6.5.1.2 Attenuation

The attenuation coefficient, α , is determined using three parameters: whole spectral area, wavelet magnitude determined using a Morlet function with a central frequency of 52 kHz and the spectral area of the decomposed signal from DWT (Level-4: 31-62.5 kHz). The normalized magnitudes for all of these parameters are plotted for all damage cases in Figures 6.42a-b-c. The jump seen at 25 cm in Figure 6.42a is most likely due to the contribution of reflections from the boundaries. However, the effect of reflections is reduced for the parameters obtained from DWT because the decomposed signal obtained from DWT is an outcome of a narrow and high frequency bandwidth. Therefore, the attenuation trends obtained from DWT appear as the most consistent ones (Fig. 6.42c). Differently, Morlet function used in WT has a larger and lower frequency bandwidth; hence, the effect of the reflections due to lower frequencies is still included (Fig. 6.42b). Attenuation coefficients, which are obtained by including all of the receivers, are plotted respect to the damage case in Figure 6.43. The effect of the holes' depth exposes itself as a quick increase in attenuation at the beginning and then converges to a constant for all three parameters. However, it is decided to attain α from the spectral area of Level-4 (31-62.5 kHz) obtained via DWT since it is more reliable to focus on a frequency range which overlaps with the transmitter's effective frequency range. Also, among the curves shown in Figure 6.43, the smallest standard variation is attained as 0.5 m^{-1} with a COV of 5.6% for the DWT parameter. Therefore, a nonlinear regression is performed to curve-fit this selected trend. Since the rate of increase in attenuation becomes smaller and approaches to an asymptote, the experimental data is fitted to a negative exponential model which achieves a R^2 value of 0.83 (Fig. 6.44). The attenuation coefficient increases ultimately up to 25% of its initial value while loses its sensitivity to damage with increasing defect size. The frequency range for Level-4 is corresponding to the wavelengths between 1 and 4 cm. As confirmed by the curve, the attenuation coefficient is a good indicator for the defect depth up to 4 cm; beyond that size, lower frequency ranges should be investigated.

6.5.1.3 Material Damping Ratio

The material damping ratio, ζ , of the distance covered by the complete receiver array is calculated using the wavelet transform as explained in Section 6.3.2.2.5. As expected, the

damping value raises in correlation with the level of damage with a σ of 0.6% with a COV of 12%; the maximum change in damping is found as 35% respect to the initial value (Fig. 6.45). Since material damping is frequency dependent and 52 kHz is taken into consideration for the calculations, this trend represents how significantly the frequencies around 52 kHz fade away with respect to increasing deterioration conditions. The correlation of the damping and the damage depth is fitted to the same model selected for attenuation coefficient; it provides a higher correlation, $R^2 = 0.87$, than the attenuation coefficient does. Although the material damping ratio and attenuation coefficients look like displaying the same trend, ζ is more refined compared to α , since it also takes the damped frequency at the arrival time for each receiver into account.

6.5.1.4 Dispersion curve (phase velocity)

Phase velocities, V_{ph} , are determined from the f-k plots rather than utilizing unwrapped phase spectrum as explained in Section 6.3.2.3. A dispersion index, DI, associated with the severity of the damage is introduced to expose the correlation between the dispersion in phase velocity and the damage depth. As the first step, the dispersion curve for the undamaged case (D0) is determined and curve-fitted to provide continuity in the phase velocity for the frequency range from 0 to 50 kHz (Fig. 6.46). The experimental curve for the no-damage case given in Figure 6.46 exposes the single mode of R-wave; however, dispersive behaviour reveals starting from the case of 1 cm damage depth and exaggerates with increasing depth. Depending on how large the extent of defect is, more frequencies contribute into the dispersion as can be inferred by comparing the dispersion curves given in Figures 6.47a-m. So, the DI is defined as:

$$DI^{(case)} = \sum \Delta V_{ph}^{(case)}(f) / V_{ph}^{(0)}(f) \quad (6.4)$$

where

$$\Delta V_{ph}^{(case)}(f) = \sqrt{\left(V_{ph}^{(case)}(f) - V_{ph}^{(0)}(f)\right)^2} \quad (6.5)$$

DI is basically the summation of the variations in phase velocity normalized respect to the reference phase velocity curve (non-damaged case) for a specified frequency bandwidth; thus it is dimensionless. DI takes the total variation of phase velocities into account such that it reduces the information into one single index which makes it easier to assess the damage. The

normalized dispersion index versus the damage depth is plotted in Figure 6.48 and is fitted to a linear line. The change in DI between the damages cases of 1 and 12 cm depths is almost %100; obviously DI is much more sensitive to damage assessment. Although DI displays more variation with a COV of 22% than the other surface wave characteristics discussed previously; on the other hand, the highest correlation with the damage depth is achieved for DI with $R^2 = 0.92$.

6.5.2 Conclusions

- Attenuation coefficients are determined by performing three different signals processing techniques: FFT, WT and DWT. The one obtained from DWT provides the most reliable correlation with damage (Table 6.6).

Table 6.6 Summary of Statistics of Attenuation Coefficients

Characteristics	σ	COV	Sensitivity ^[1]
α (FT)	0.9 m ⁻¹	10.1%	48%
α (WT)	1.2 m ⁻¹	10.9%	59%
α (DWT)	0.5 m ⁻¹	5.7%	24%

[1] Sensitivity refers the total change over to the initial value.

- The frequency range for Level-4 is corresponding to the wavelengths between 1 and 4 cm. As confirmed by the curve, the attenuation coefficient is a good indicator for the defect depth up to 4 cm; beyond that size, lower frequency ranges should be investigated.
- Correlations of four surface wave characteristics; namely, Rayleigh-wave velocity, attenuation coefficient, material damping ratio and dispersion index respect to the damage depth are determined. Table 6.7 summaries the statistical findings for all of these characteristics.

Table 6.7 Summary of statistics for surfaces wave characteristics

Characteristics	Statistic			
	σ	COV	R ²	Sensitivity ^[3]
V_R	120 m/s	11%	0.73 ^[1]	28%
α	0.5 m ⁻¹	5.6%	0.83 ^[2]	48%
ζ	0.6%	12%	0.87 ^[2]	69%
DI	N/A	22%	0.92 ^[1]	51%

[1] Linear regression, [2] Nonlinear regression, [3] Sensitivity refers the total change over to the initial value.

- Attenuation, damping ratio and DI are positive correlated with the damage quantity, whereas R-wave velocity is negative correlated.
- Attenuation coefficient and damping ratio have limited sensitivity due to the frequency range of the transmitter; therefore, both tend to converge an asymptote after 4 cm of depth while R-wave velocity and DI keep their linear relationship for higher depths of defect.
- Damping ratio reveals as the most sensitive characteristics to the quantity of the damage; it is followed by DI, attenuation coefficient and R-wave velocity.

6.6 Summary

In this chapter, Rayleigh wave velocity, attenuation, material damping and dispersion in phase velocity were investigated to evaluate the sensitivity of these characteristics to the damage quantity in a medium. The test specimen, which is a half-space medium made of cement and sand mixture, was subjected to the ultrasonic testing for different depths of defect. The recorded signals were processed using different signal transformation methods, such as FT, WT and EMD to increase the reliability of the results. All investigated characteristics were found capable of reflecting the damage quantity of the test medium at different sensitivity levels. Additionally, prior to damage evaluation, the same specimen was tested by calibrated accelerometers to perform material characterization. Eliminating the FRFs of the transducers returned with the material damping values closer to the literature value.

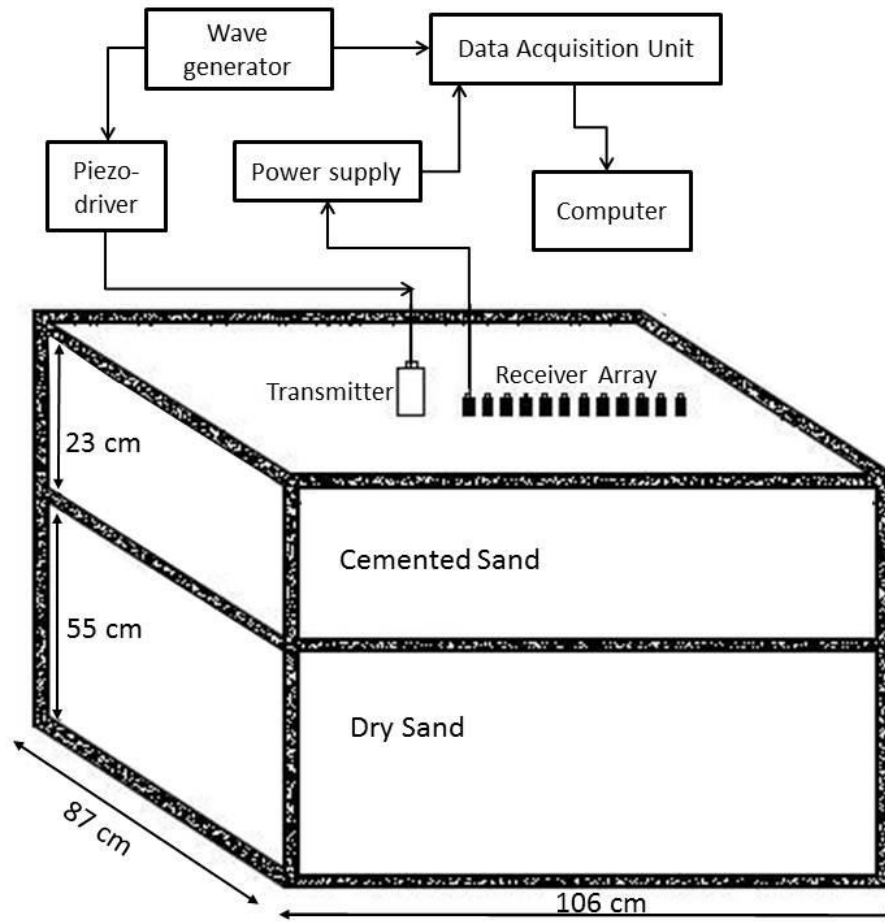


Figure 6.1: Schema for the testing instruments.

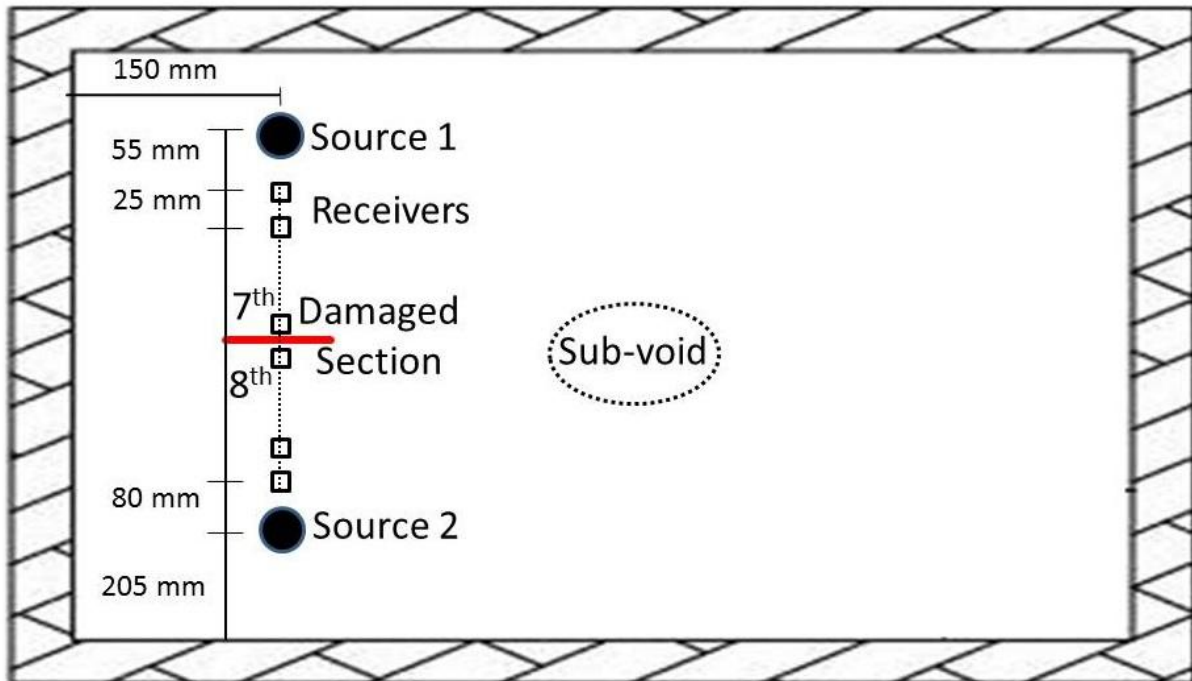
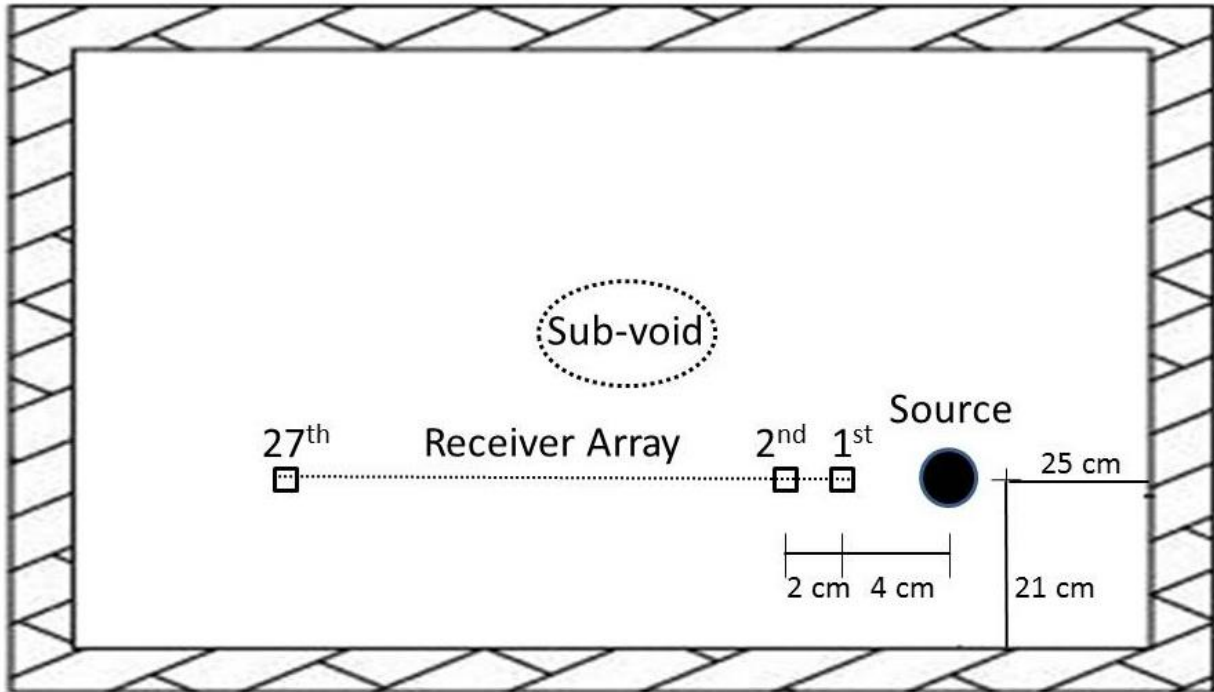


Figure 6.2: Testing configurations for (a) Test I and II, (b) Test III.

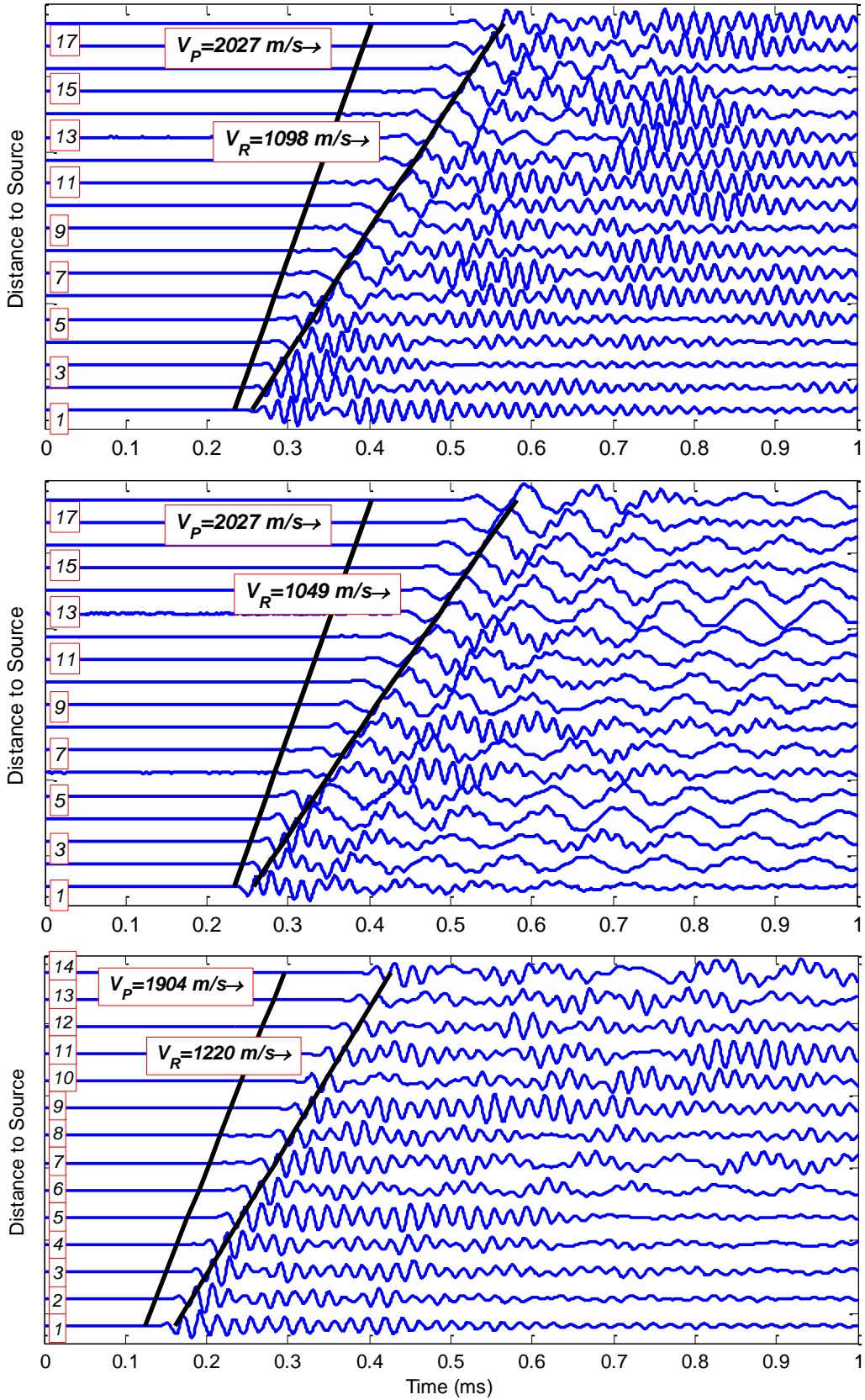


Figure 6.3: Normalized time histories for Test (a) I, (b) II and (c) III.

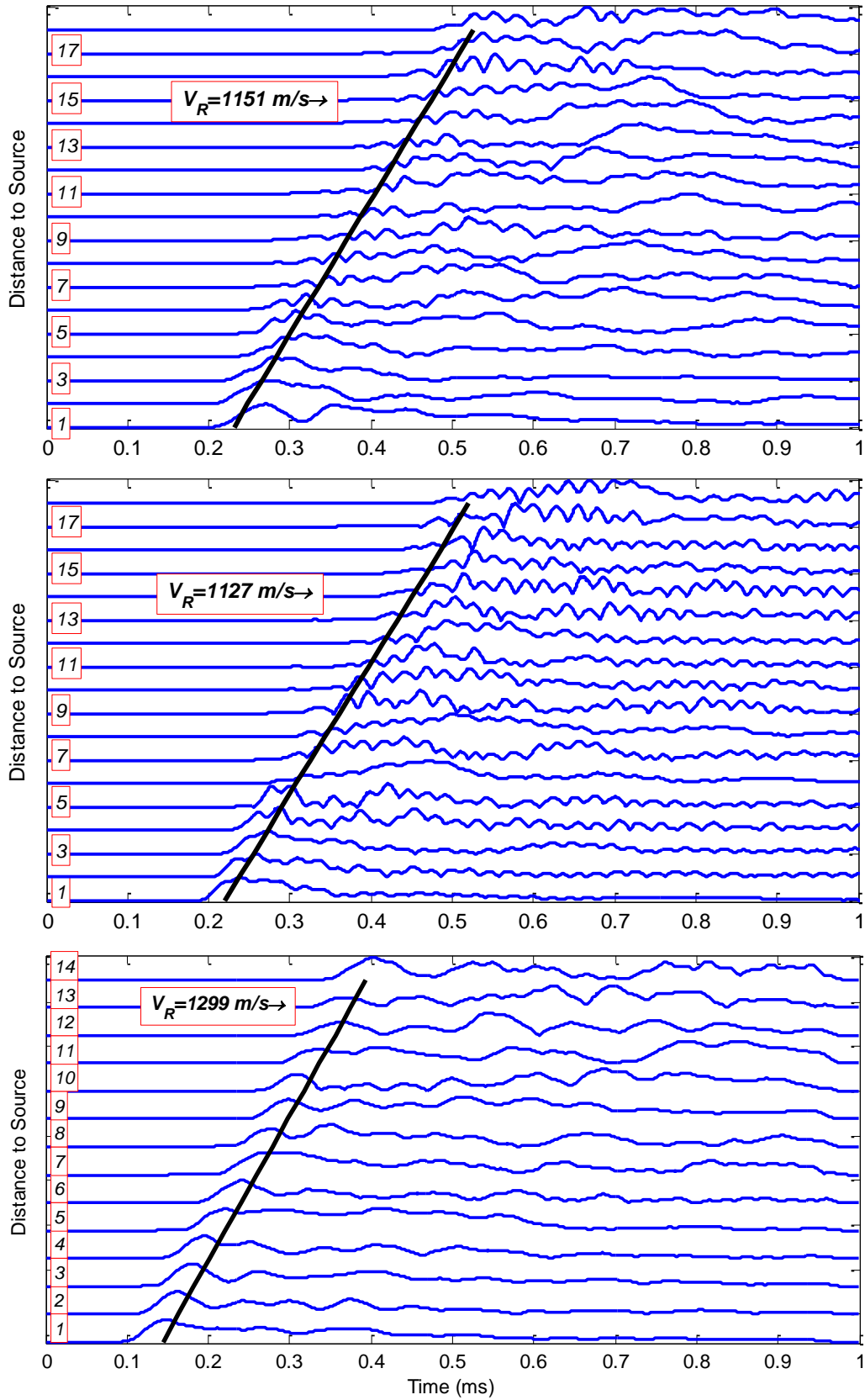


Figure 6.4: Normalized wavelet magnitudes for Test (a) I, (b) II and (c) III.

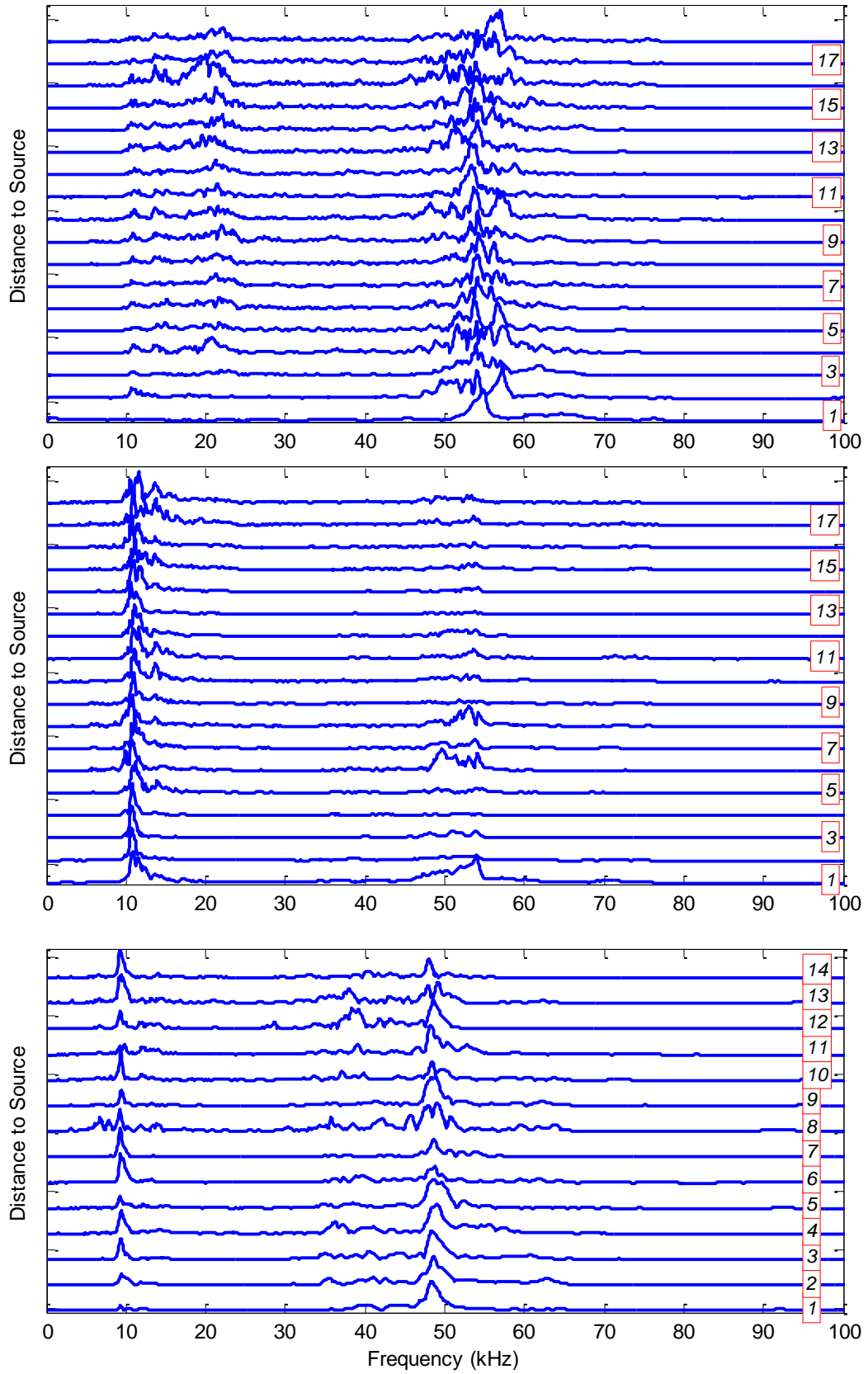


Figure 6.5: Normalized Fourier spectra for Test (a) I, (b) II and (c) III.

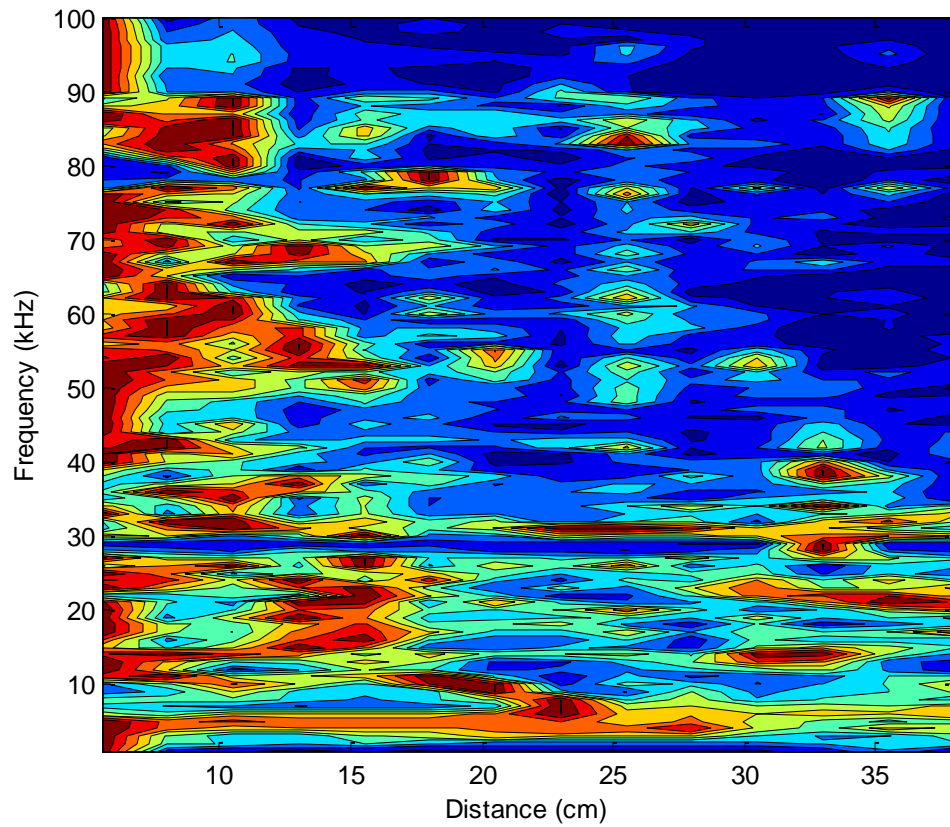


Figure 6.6: Attenuation trend of frequencies from non-windowed time signals for Test III. Fourier magnitudes for each frequency are normalized by the maximum value of that frequency obtained from the whole set of spectra.

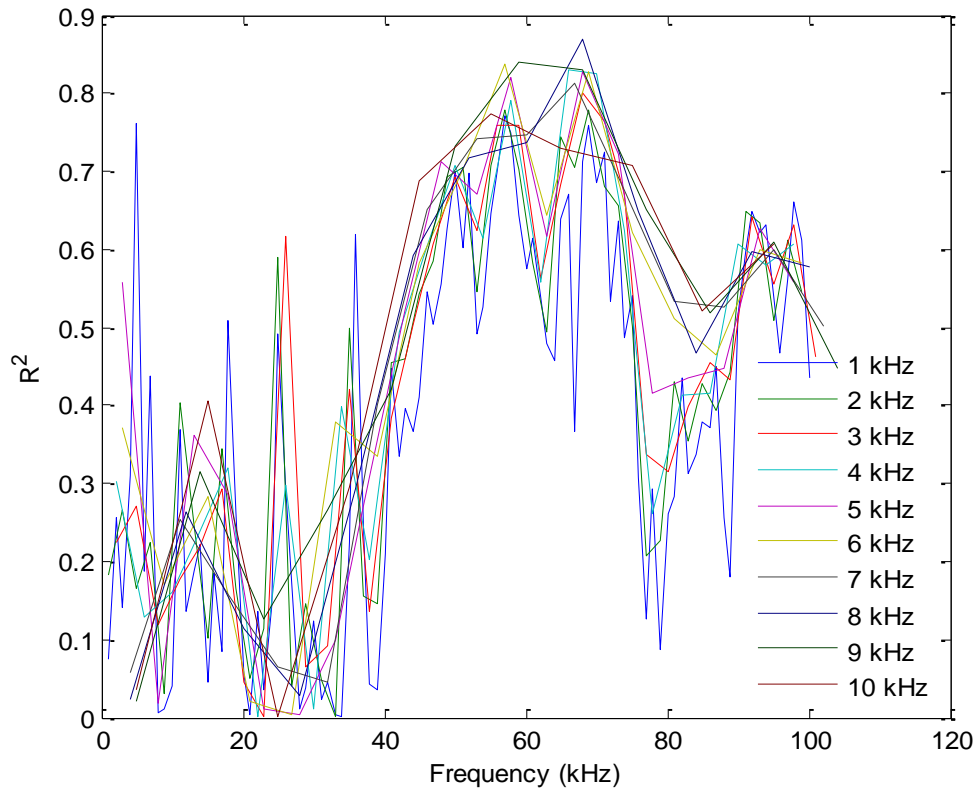


Figure 6.7: The R^2 values for attenuation of frequencies computed after windowing the Fourier spectra with window widths ranging from 1 to 10 kHz. The R^2 is 0.7 for 52 kHz after a frequency window width of 1 kHz.

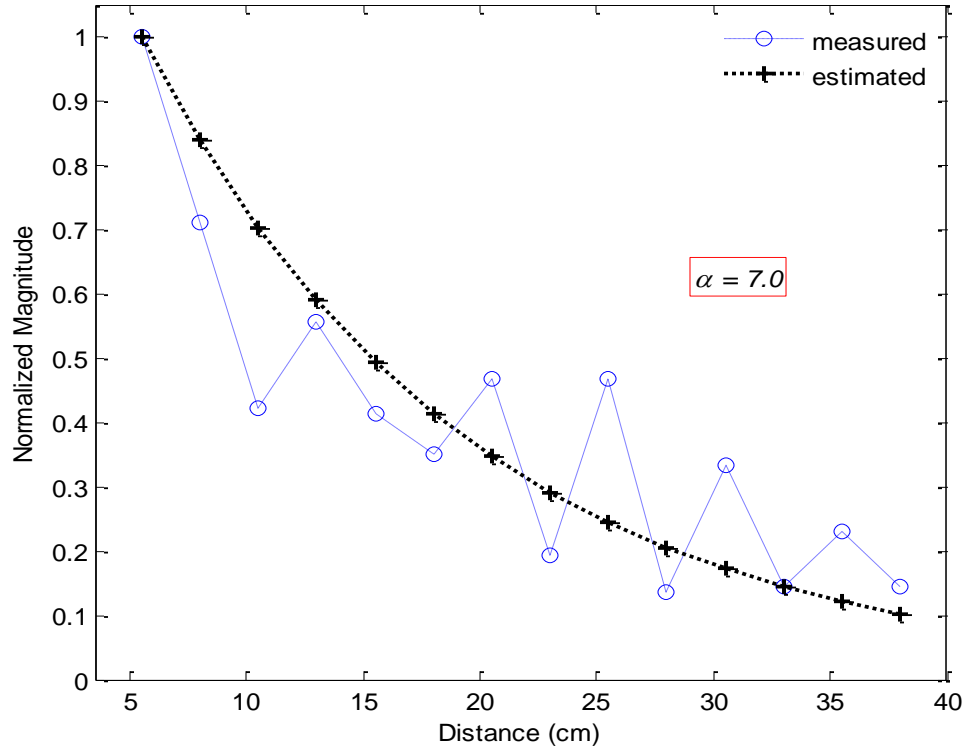


Figure 6.8: Attenuation trend for spectral magnitude of 52 kHz: experimental and estimated trends from non-windowed time signals.

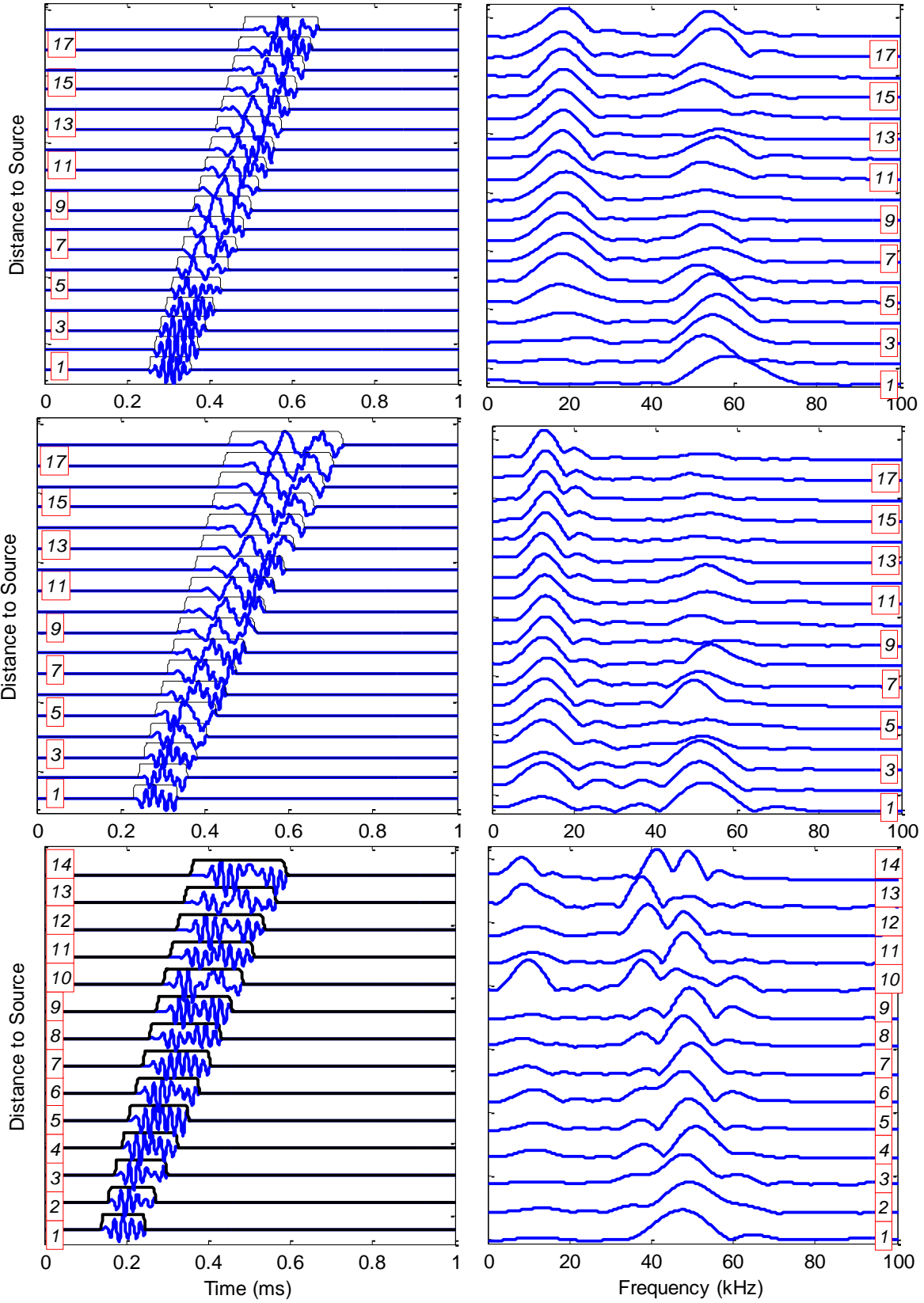


Figure 6.9: Normalized windowed time histories and corresponding Fourier spectra of Test (a,b) I, (c,d) II and (e,f) III.

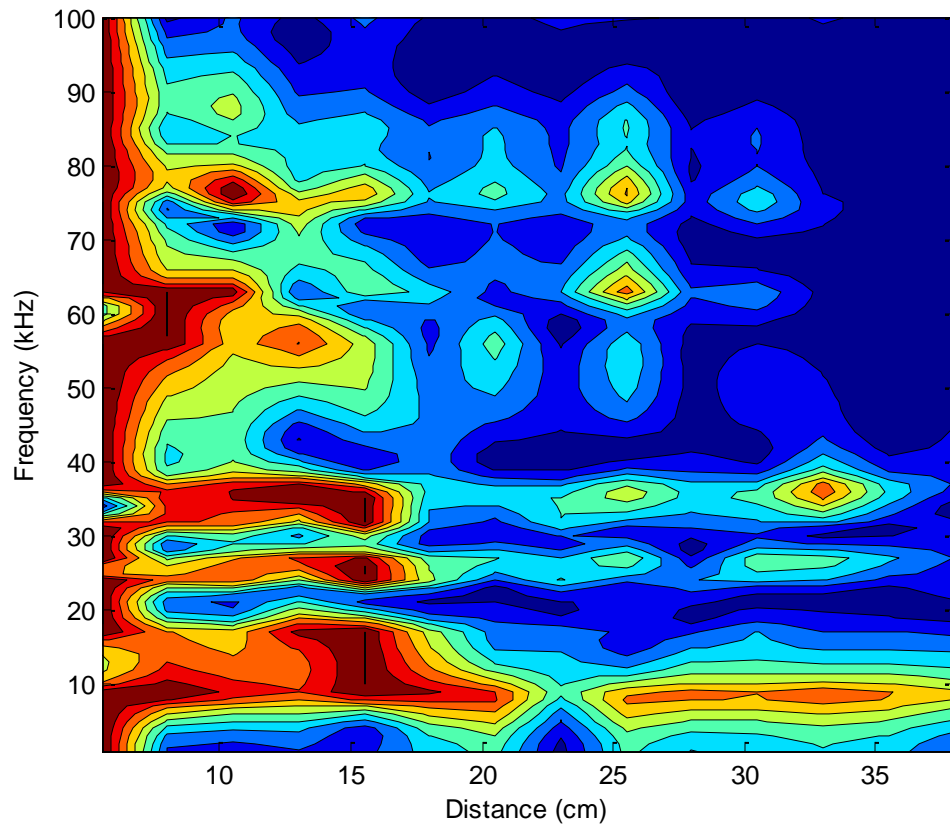


Figure 6.10: Attenuation trend of frequencies from windowed time signals for Test III. Fourier magnitudes for each frequency are normalized by the maximum value of that frequency obtained from the whole set of spectra.

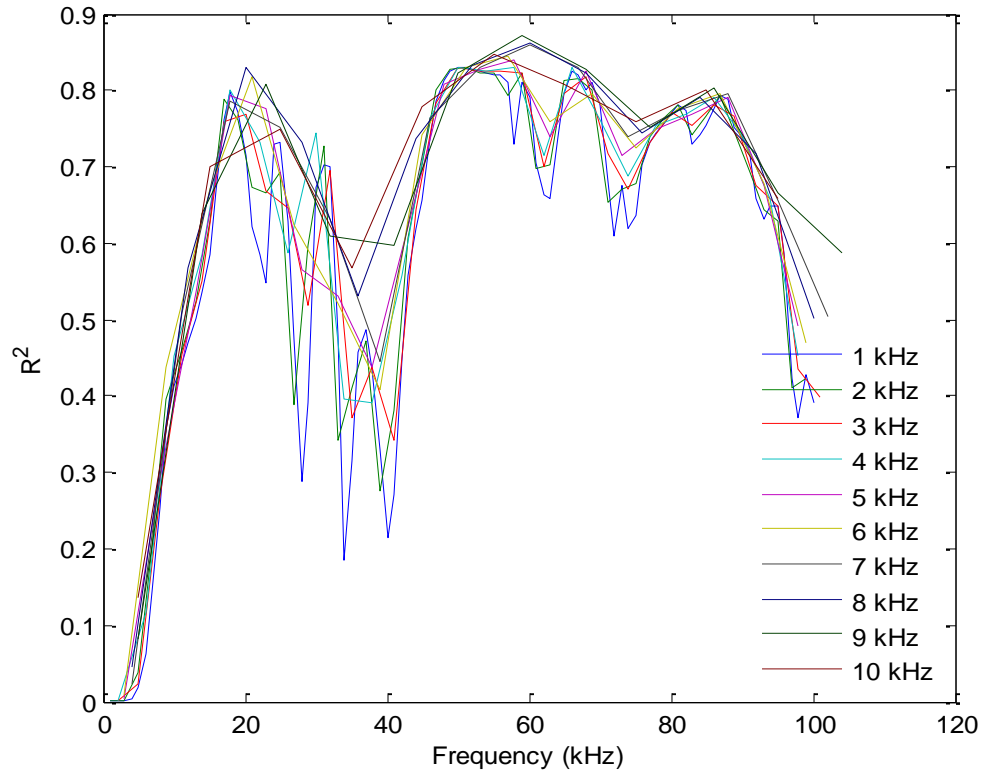


Figure 6.11: The R^2 values for attenuation of frequencies computed after windowing the Fourier spectra with window widths ranging from 1 to 10 kHz. The R^2 is 0.83 for 52 kHz for a frequency window width of 1 kHz. Time histories are windowed before FT.

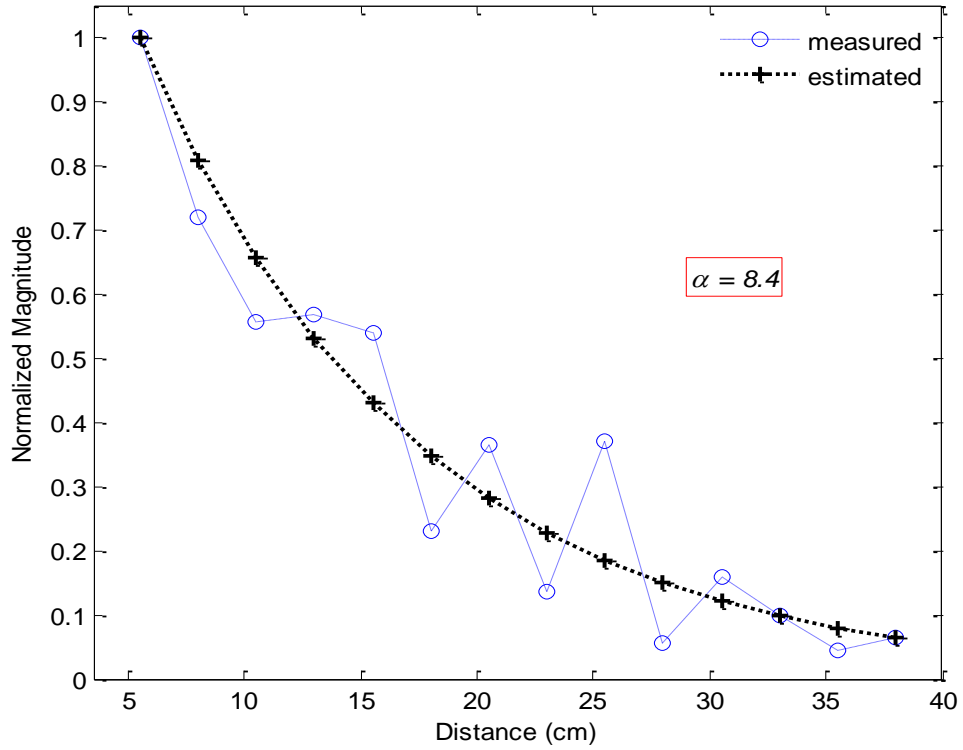


Figure 6.12: Attenuation trend for spectral magnitude of 52 kHz: experimental and estimated trends from windowed time signals.

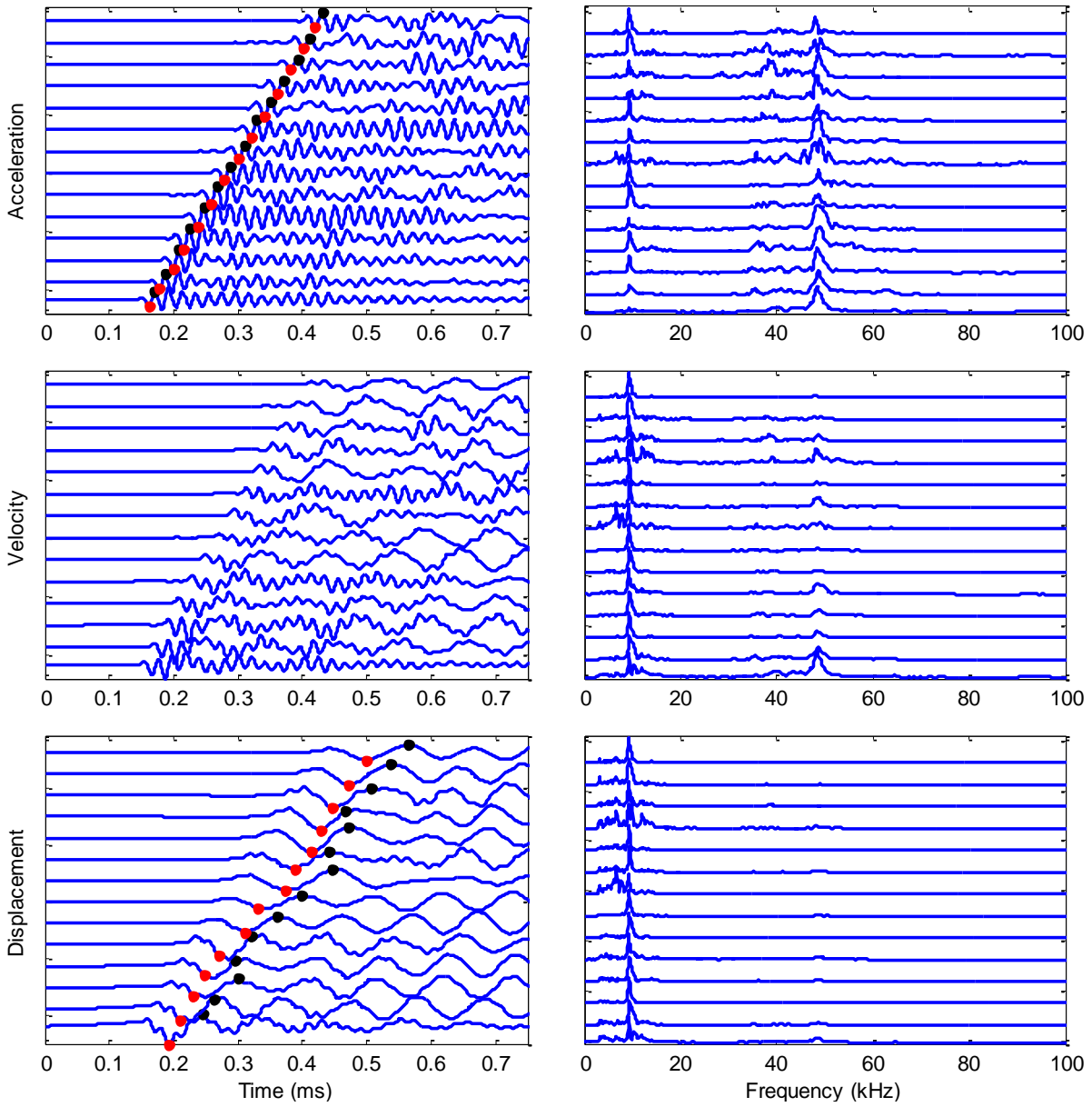


Figure 6.13: Normalized (a,b) acceleration, (c,d) velocity, (e,f) displacement time histories and corresponding Fourier spectra for Test III. Red dots mark the pit and black ones mark the peak of R-wave arrival.

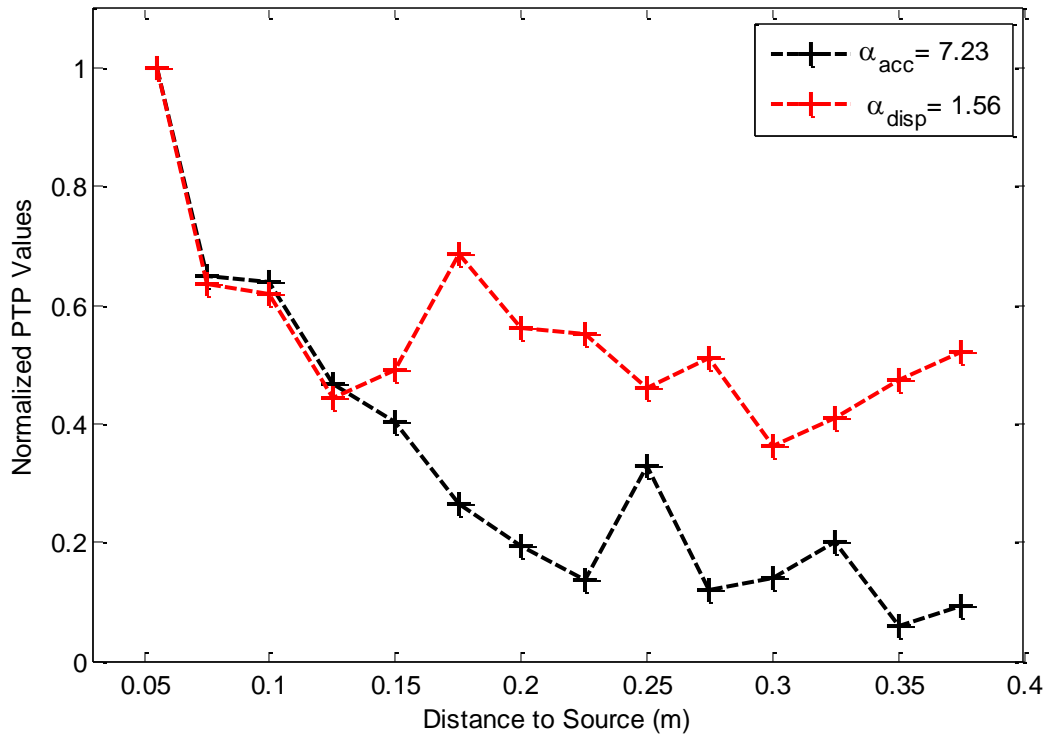


Figure 6.14: Attenuation trends of PTP values from acceleration and displacement time histories for Test III.

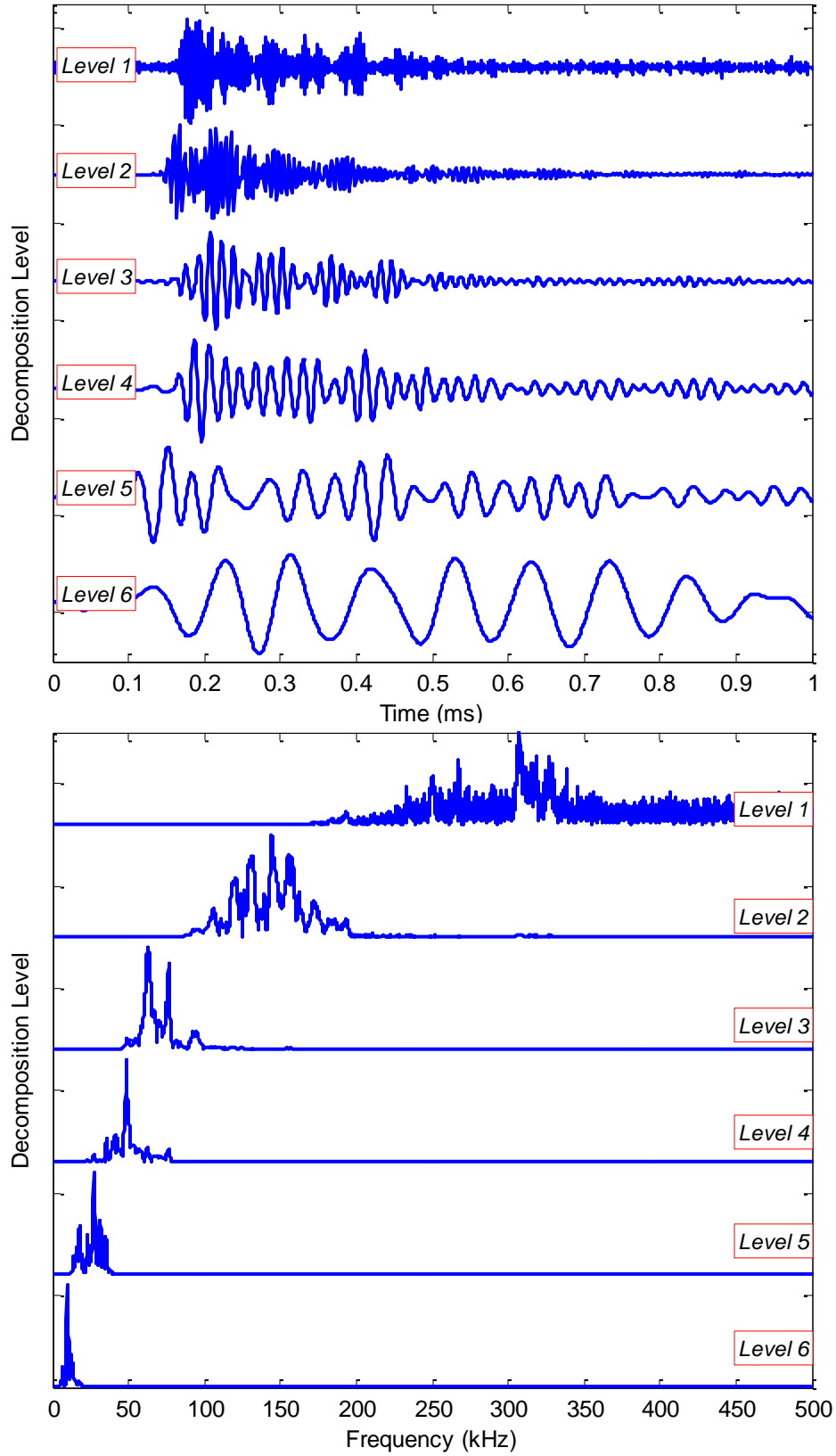


Figure 6.15: Normalized (a) decomposed time signals and (b) associated Fourier spectra for Test III.

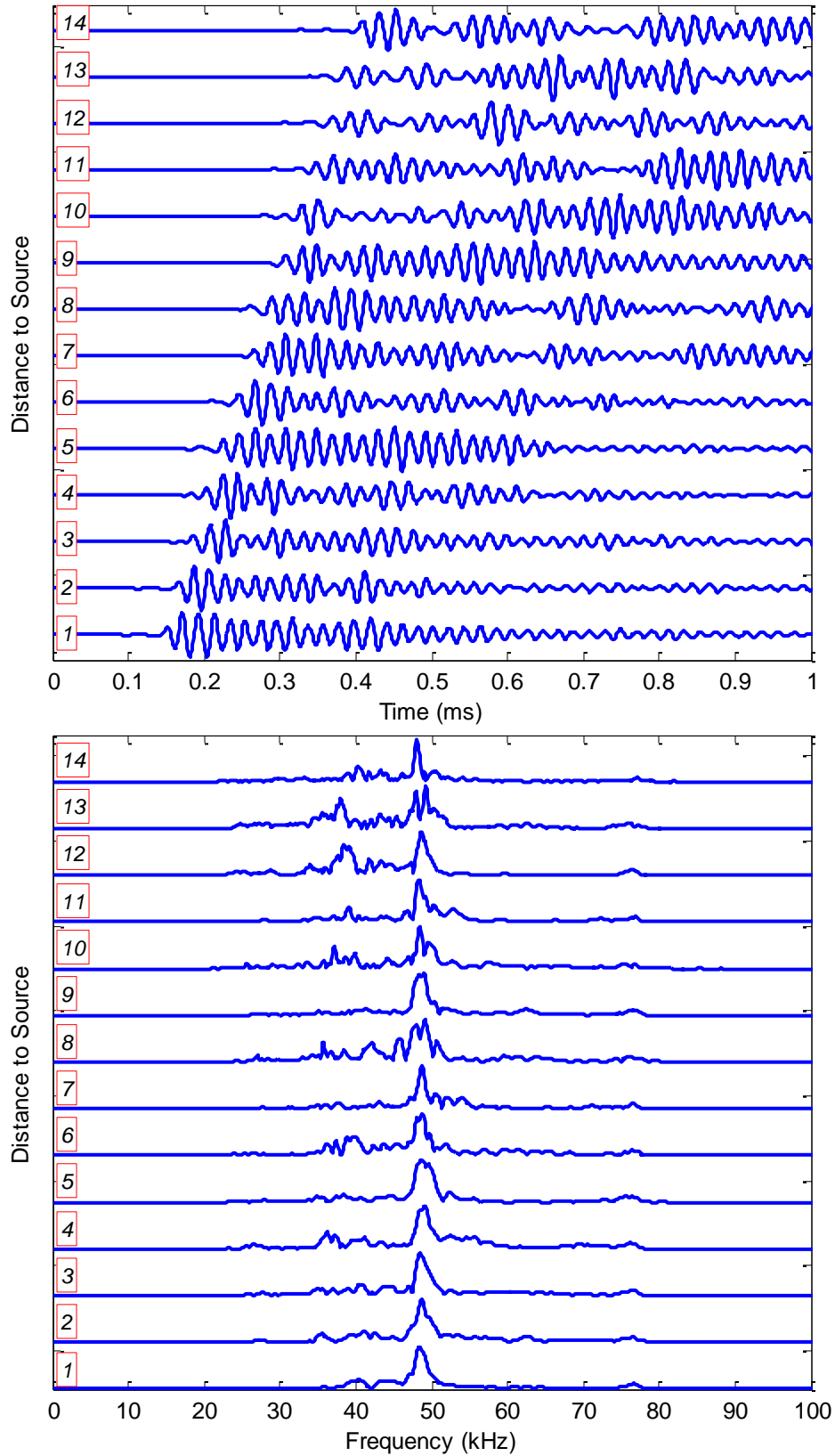


Figure 6.16: (a) Normalized level 4 (frequency bandwidth of 31.25-62.5 kHz) for all receivers from Test III and (b) associated Fourier spectra.

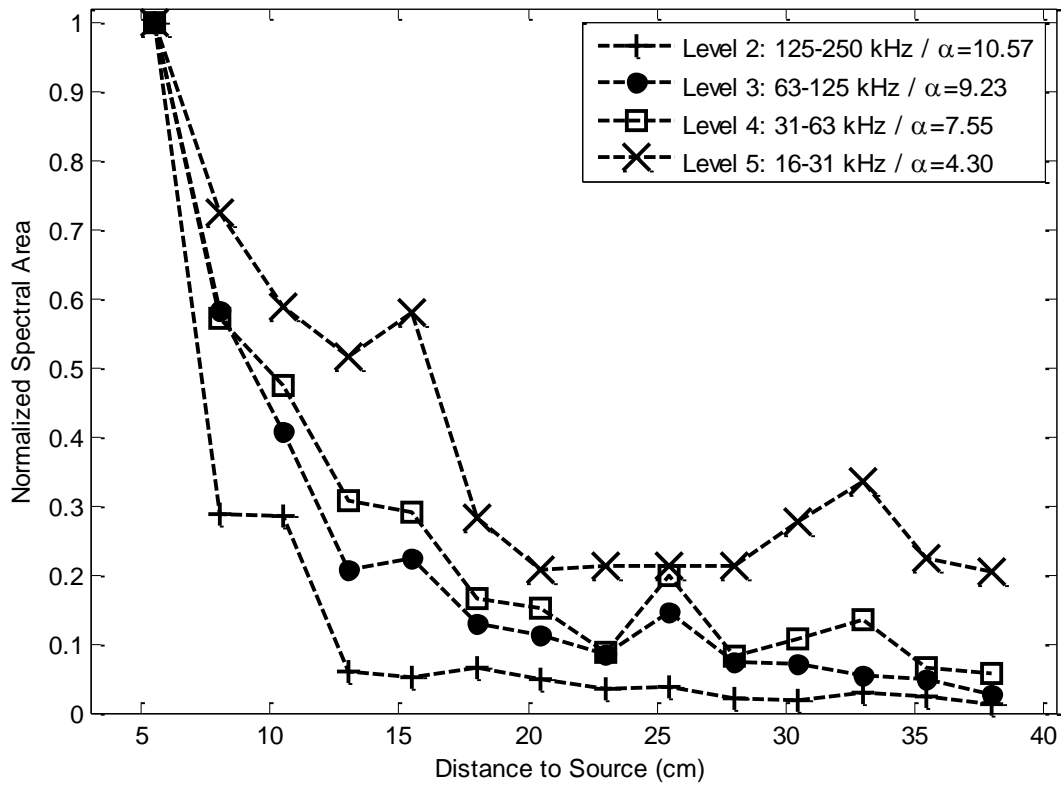


Figure 6.17: Attenuation trend for the spectral areas of level 2, 3, 4 and 5 from Test III.

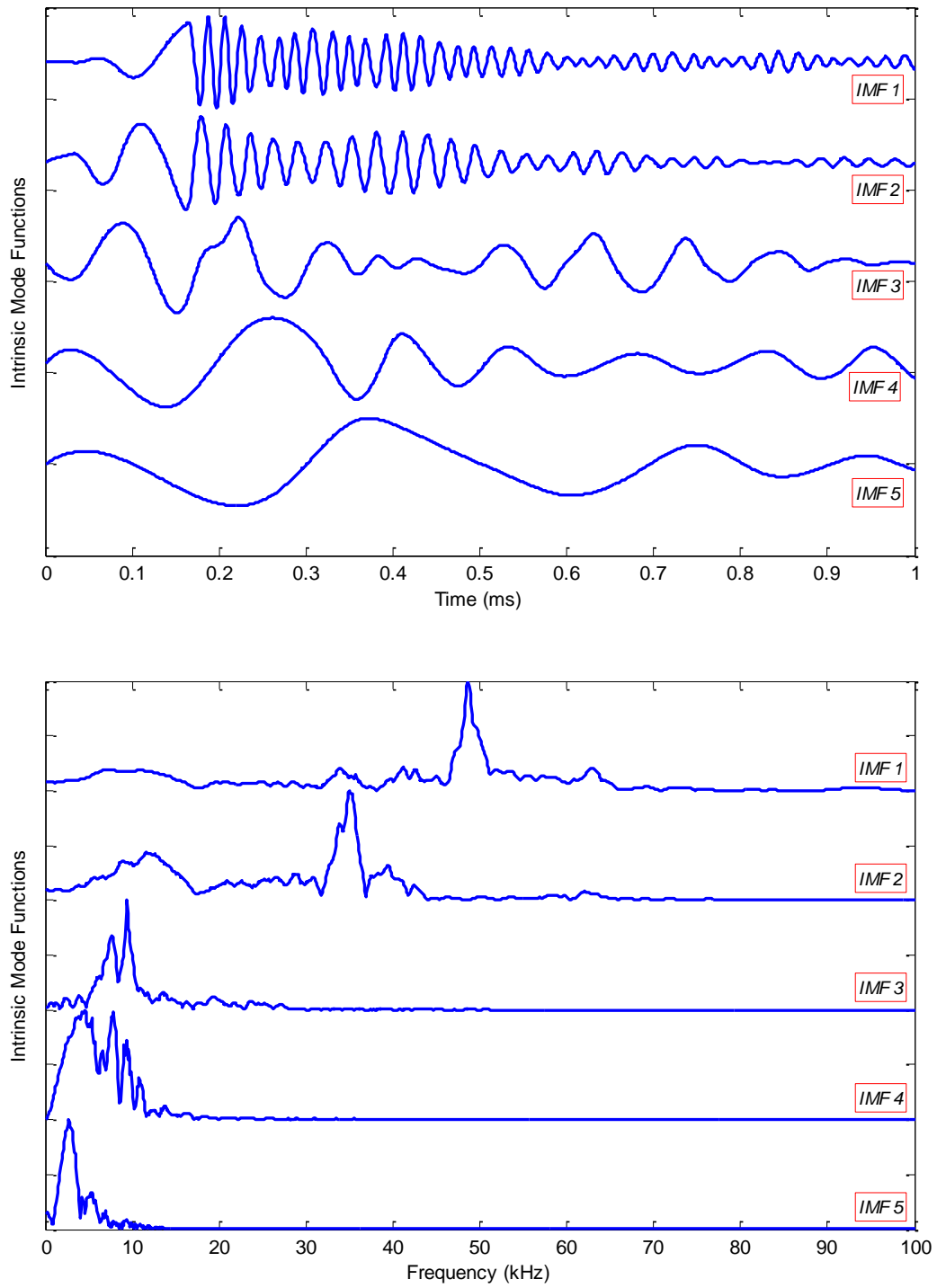


Figure 6.18: Normalized (a) IMFs and (b) associated Fourier spectra for Test III.

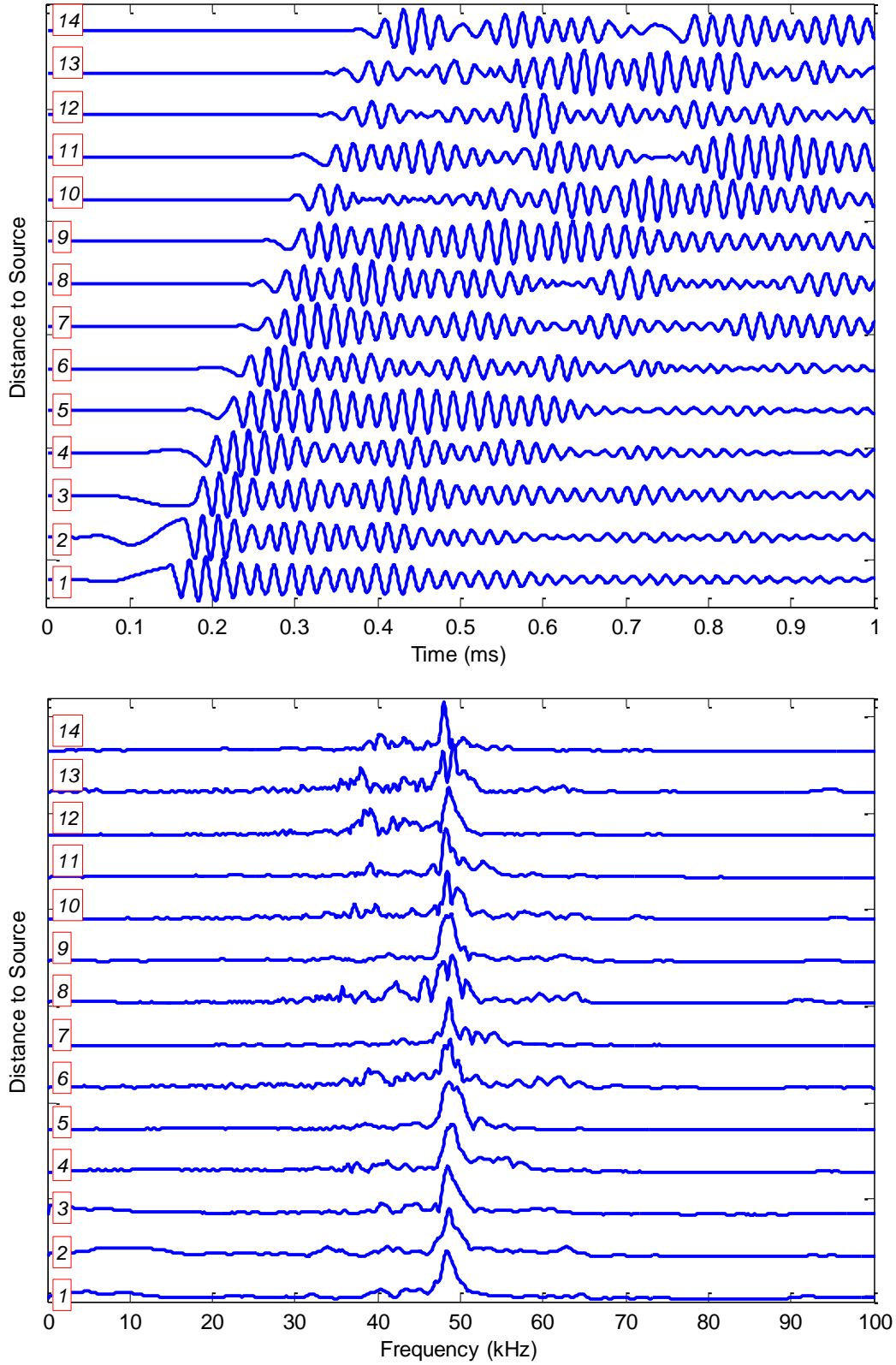


Figure 6.19: (a) Normalized 1st IMF for all receivers from Test III and (b) associated Fourier spectra.

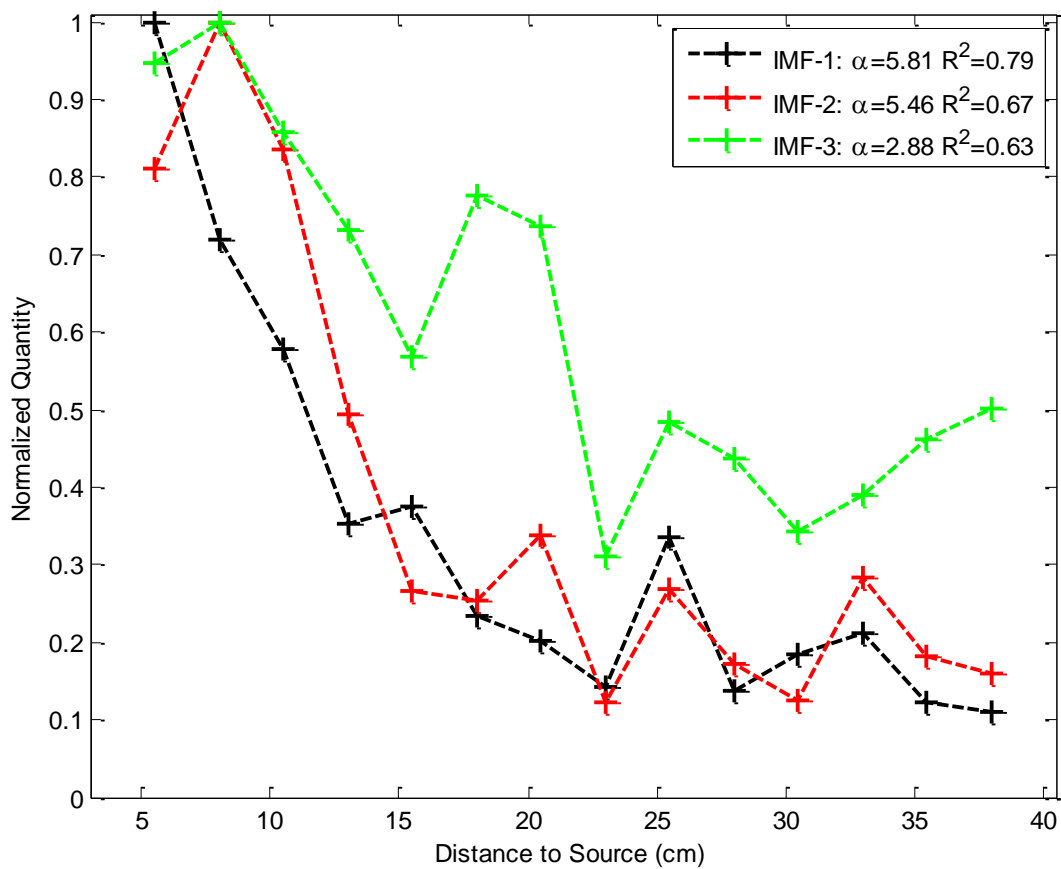


Figure 6.20: Attenuation trends based on the spectral areas of the first three IMFs from Test III.

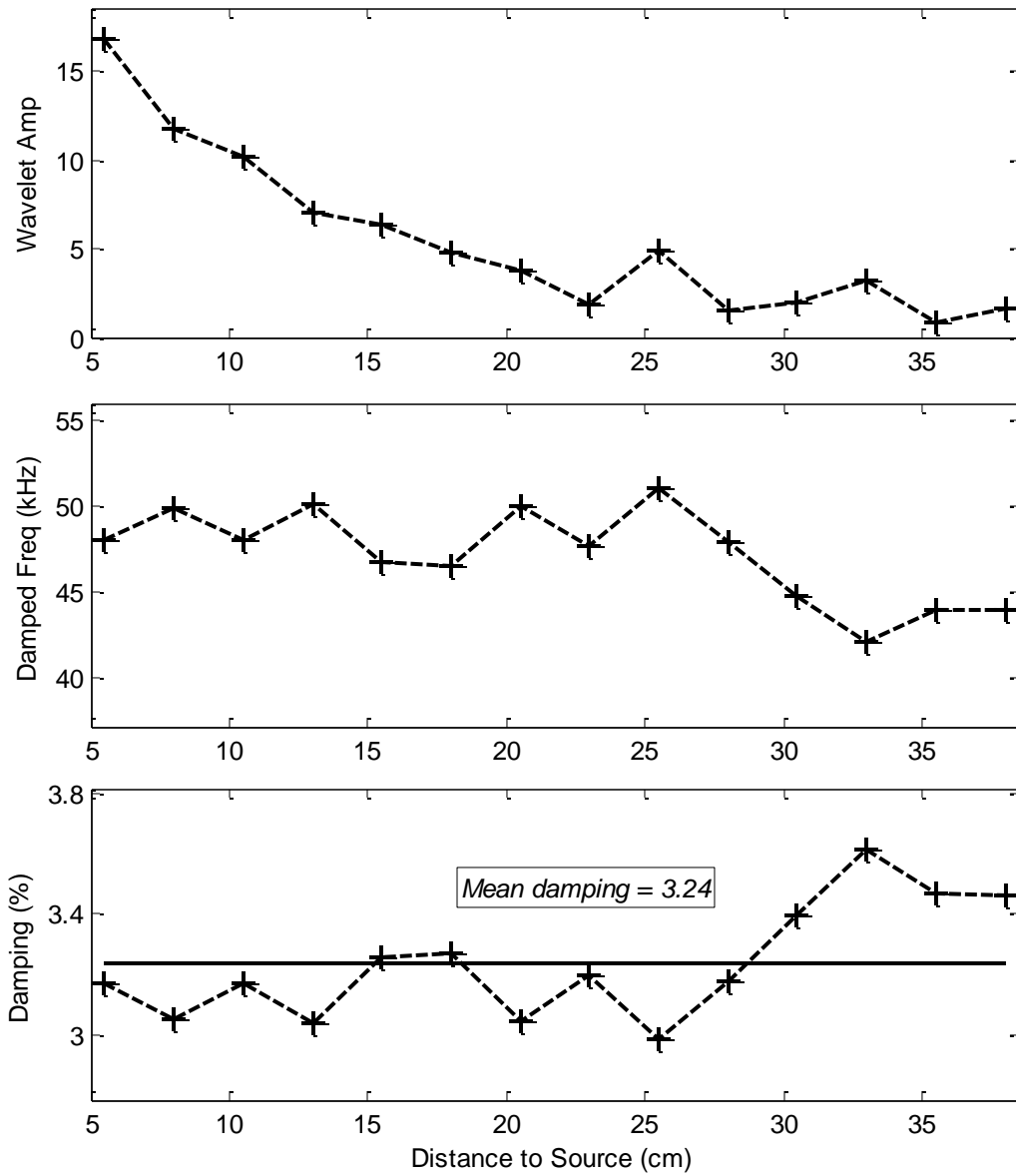


Figure 6.21: (a) Wavelet magnitude, (b) Damped frequency at arrival of R-wave, (c) Material damping at each receiver location for Test III.

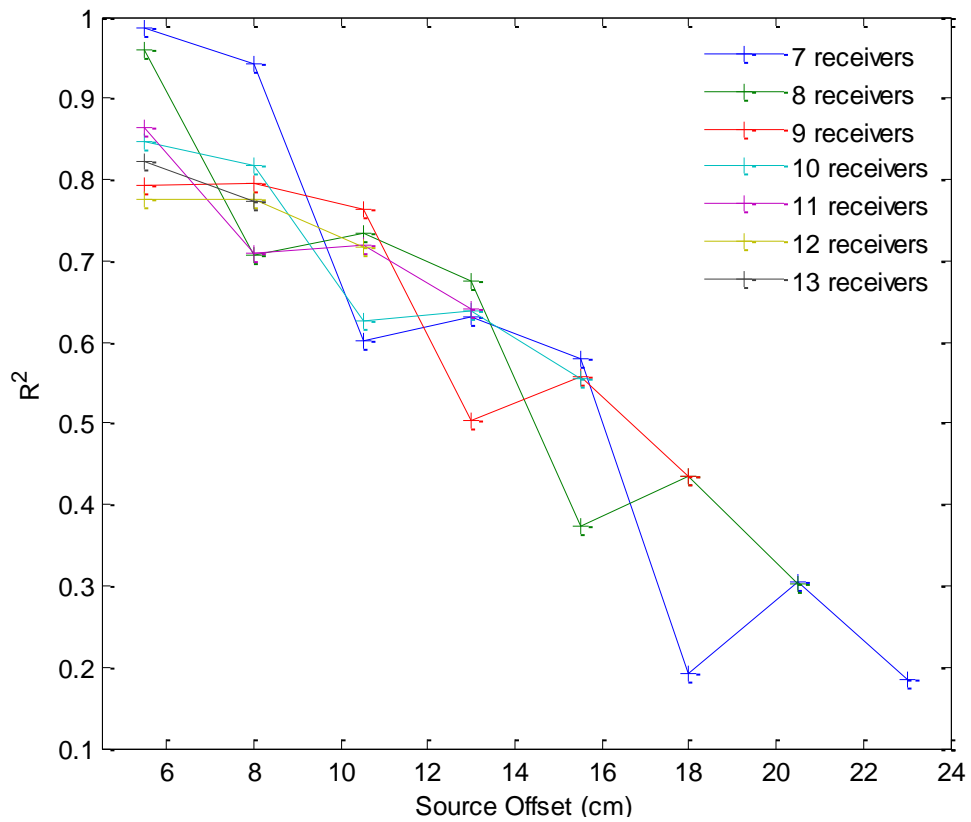
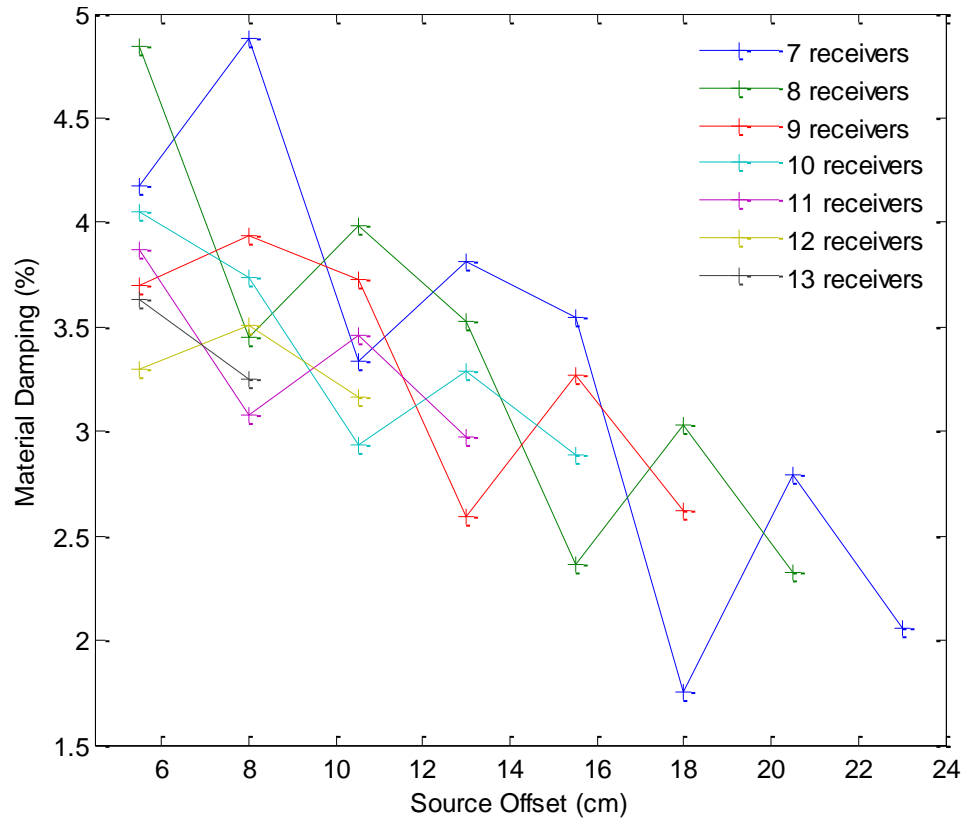


Figure 6.22: (a) Material damping ratios from wavelet transform determined using different sets of receivers from Test III, and (b) the associated R^2 values.

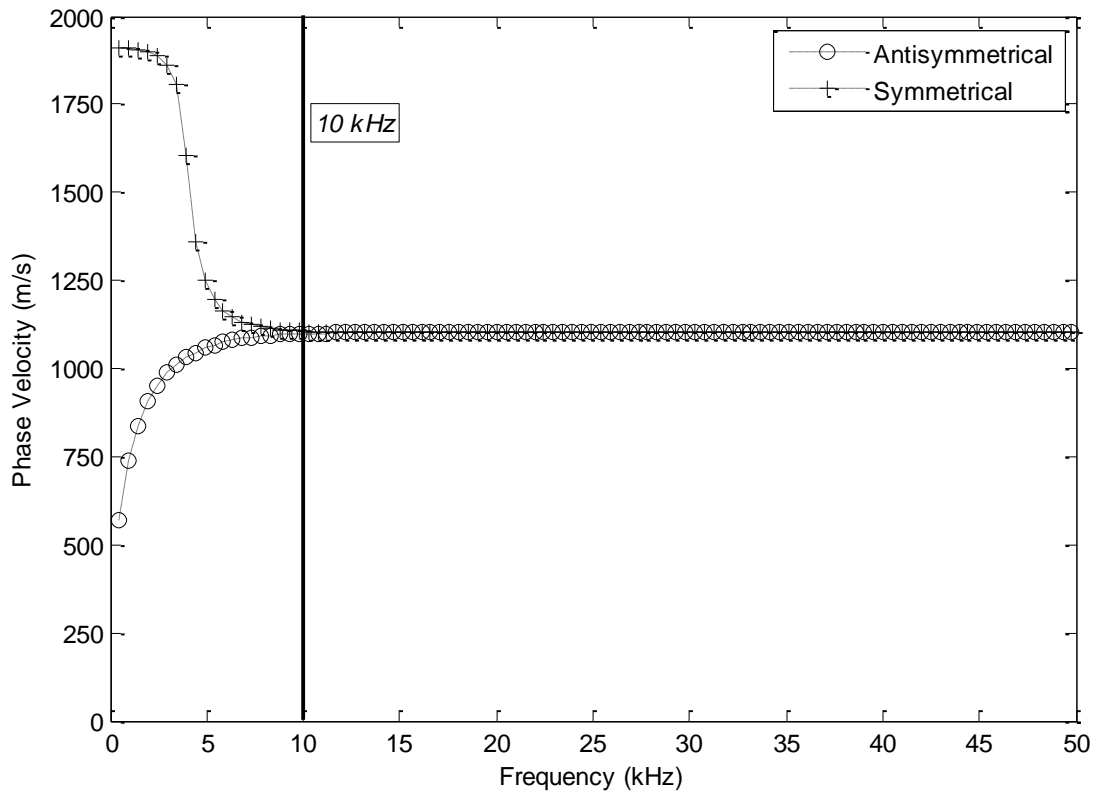


Figure 6.23: Fundamental Lamb Modes for the test medium.

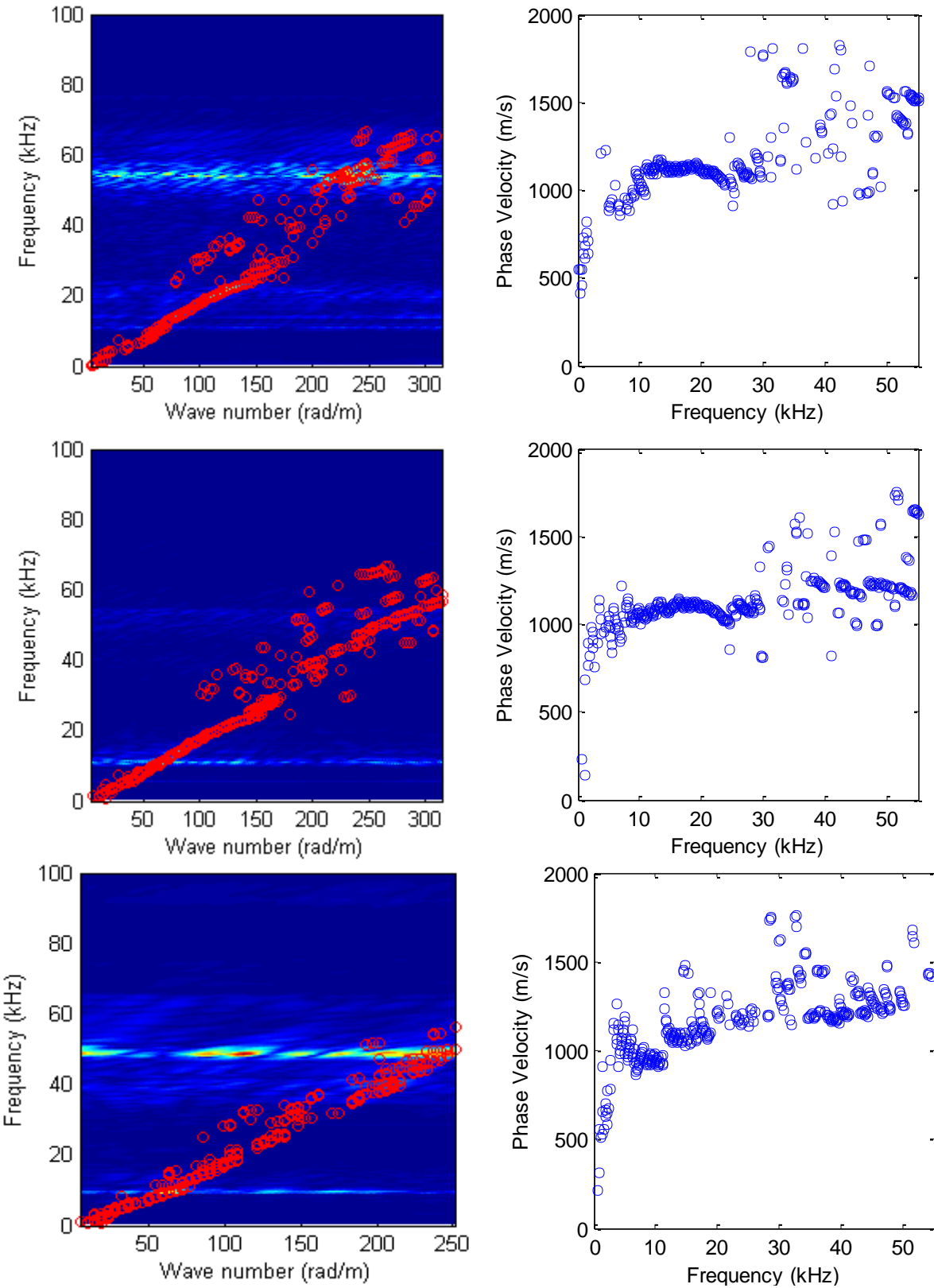


Figure 6.24: The f-k plots transformed from the non-windowed time histories and dispersion curves extracted from the f-k plots for Test (a,b) I, (c,d) II and (e,f) III.

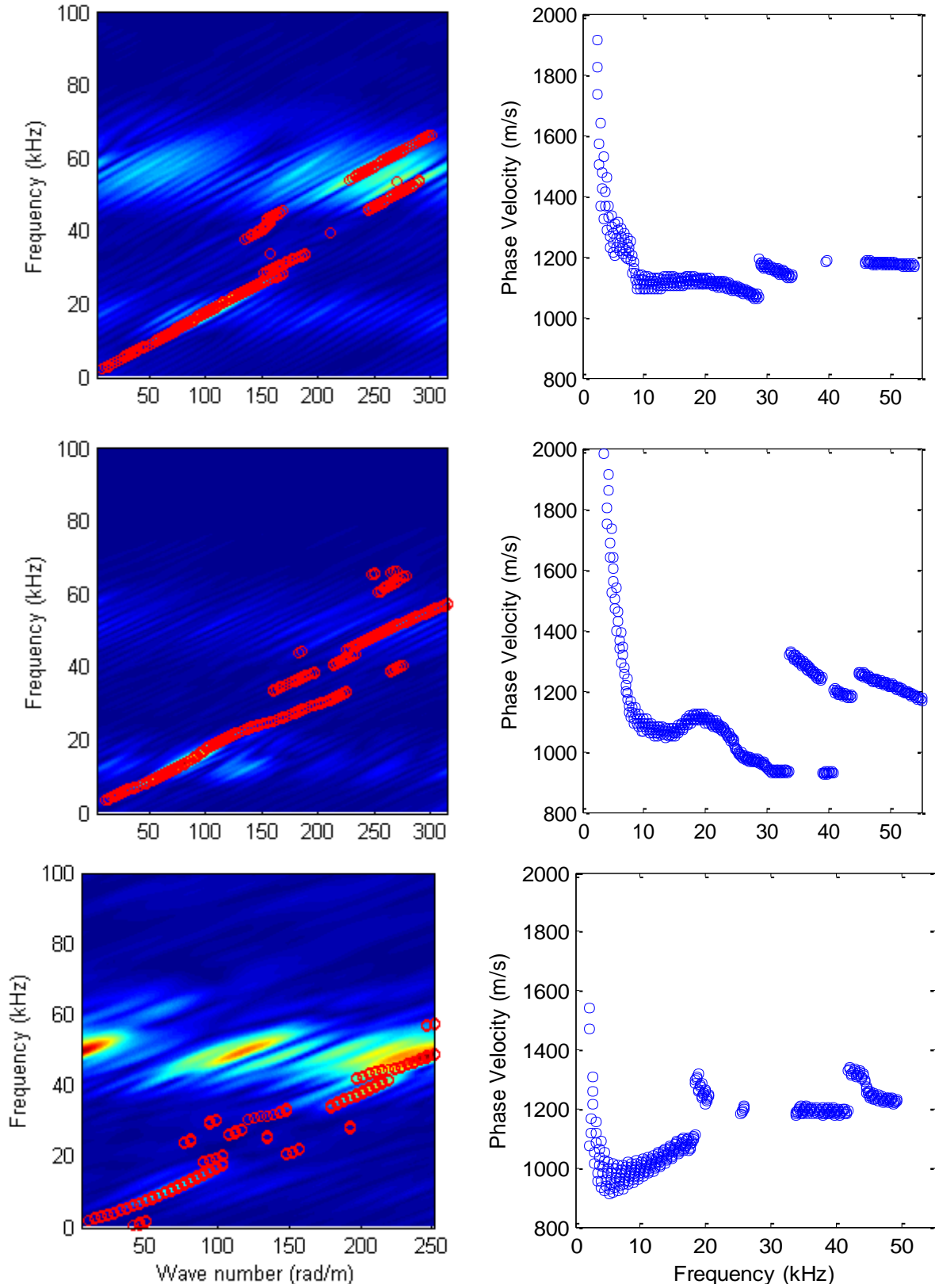


Figure 6.25: The f-k plots transformed from the windowed time histories and dispersion curves extracted from the f-k plots for Test (a,b) I, (c,d) II and (e,f) III.

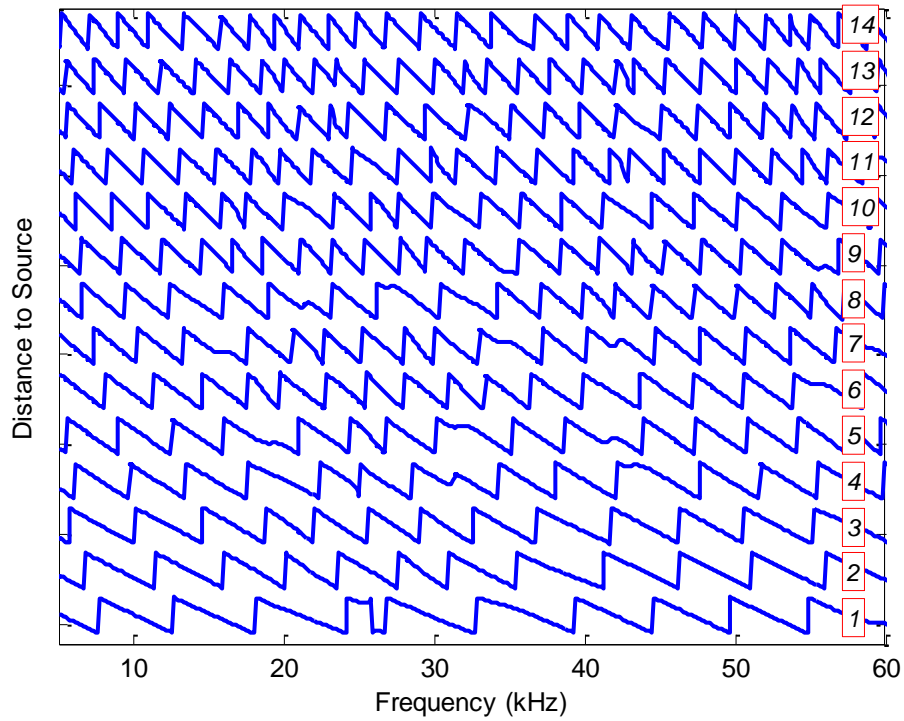
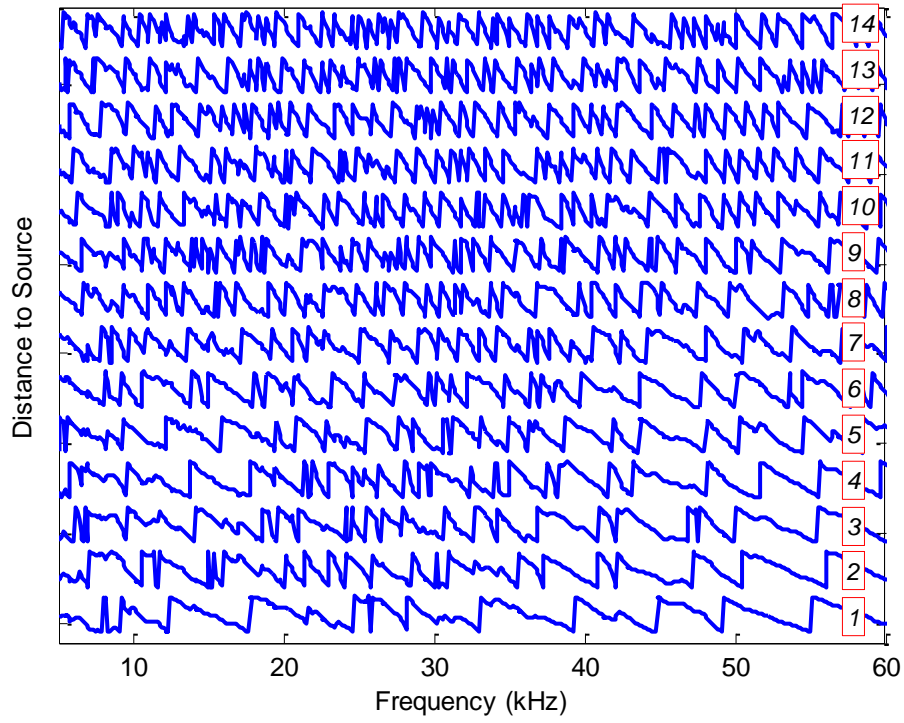


Figure 6.26: Wrapped phases from (a) non-windowed and (b) windowed time histories.

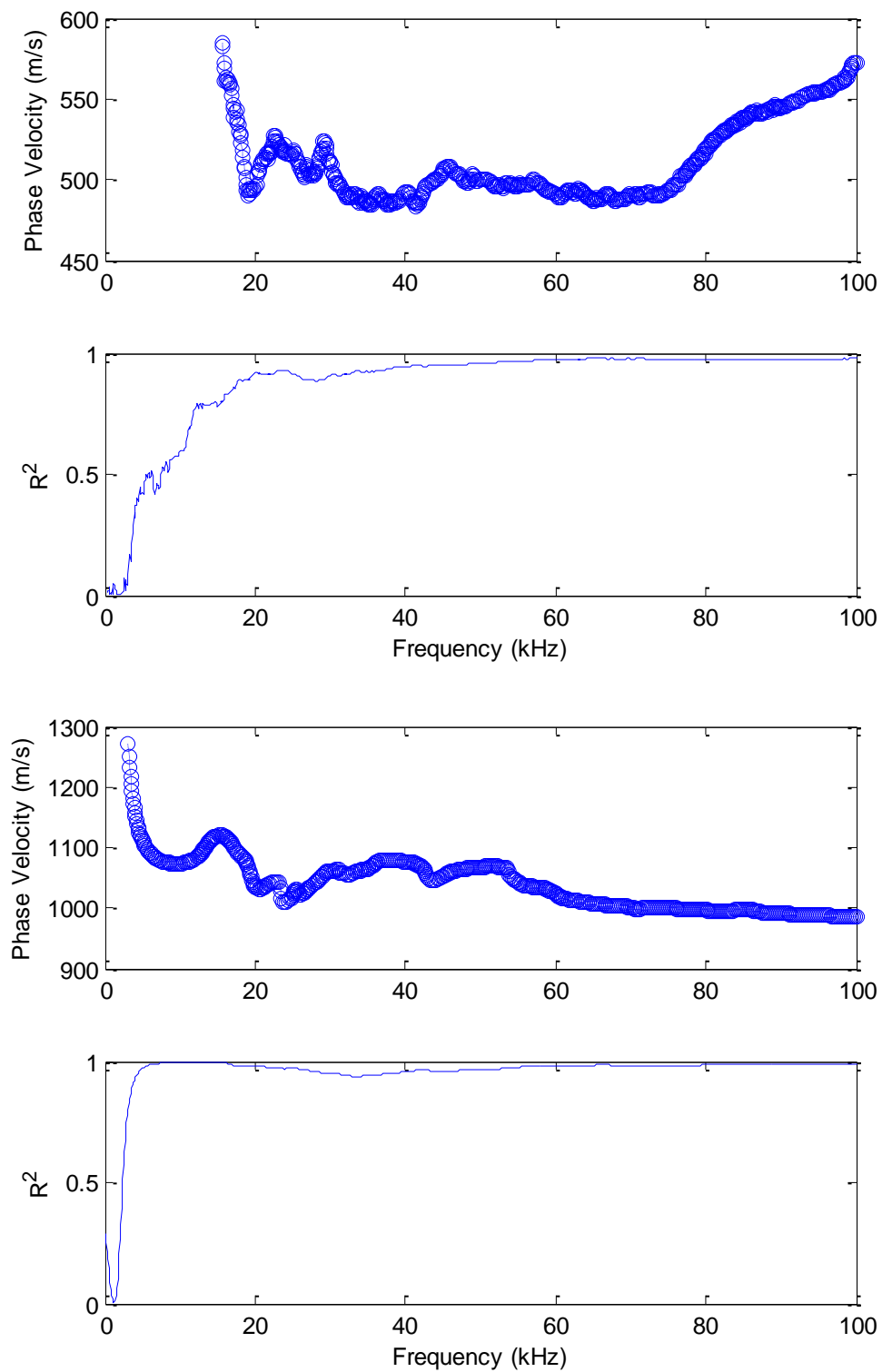


Figure 6.27: Dispersion curves and R^2 values computed from unwrapped phase spectra of (a) non-windowed and (b) windowed time histories.

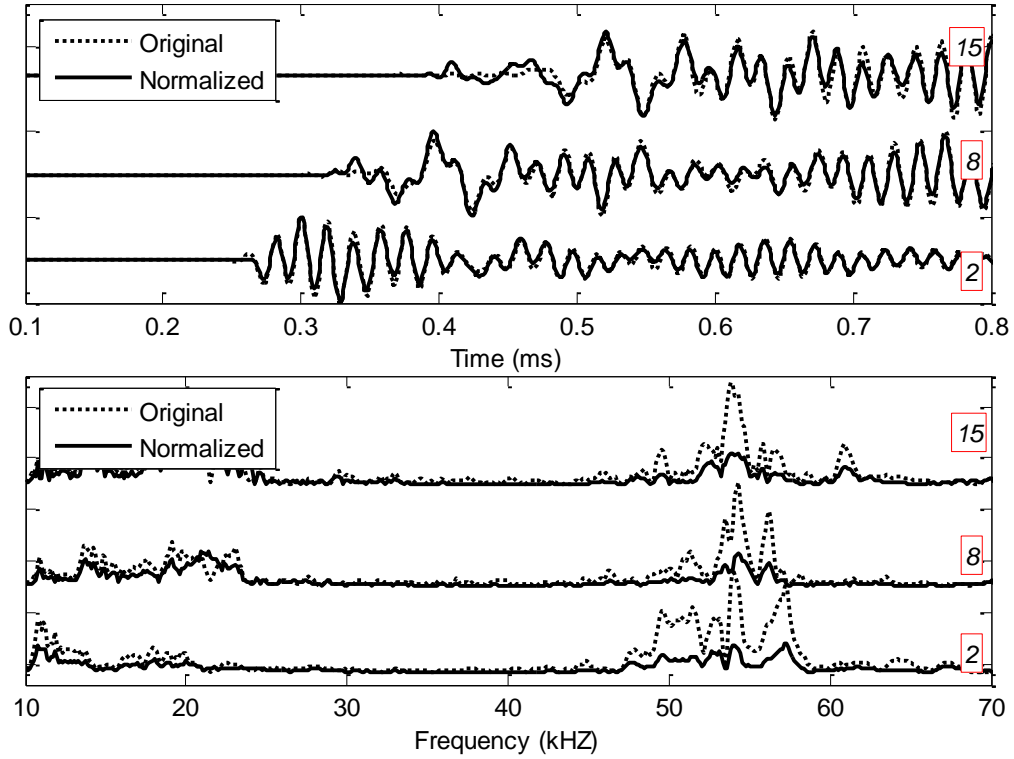


Figure 6.28: Time histories and Fourier spectra of the selected original and normalized signals respect to FRF for A1.

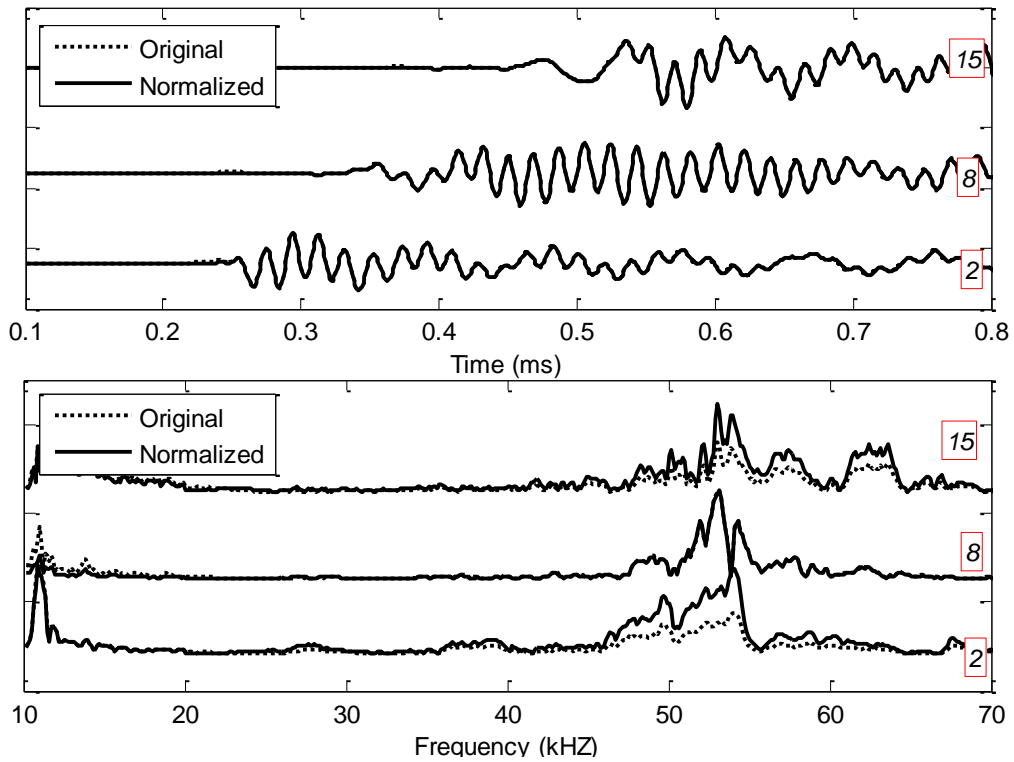


Figure 6.29: Time histories and Fourier spectra of the selected original and normalized signals respect to FRF for A2.

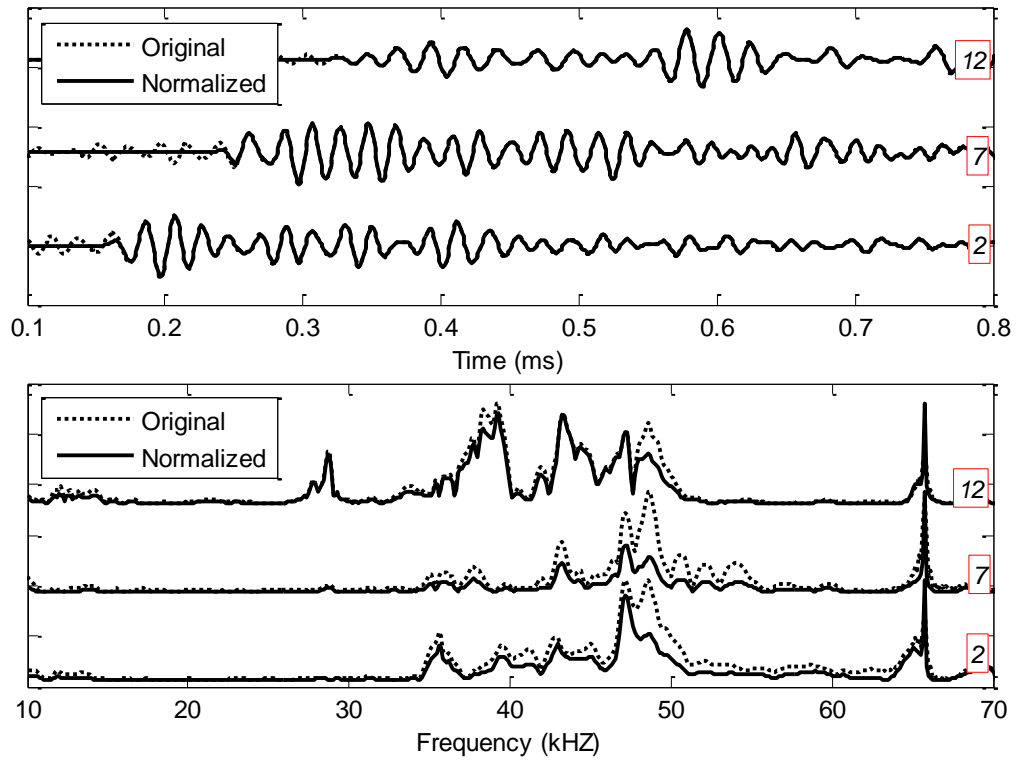


Figure 6.30: Time histories and Fourier spectra of the selected original and normalized signals respect to FRF for A3.

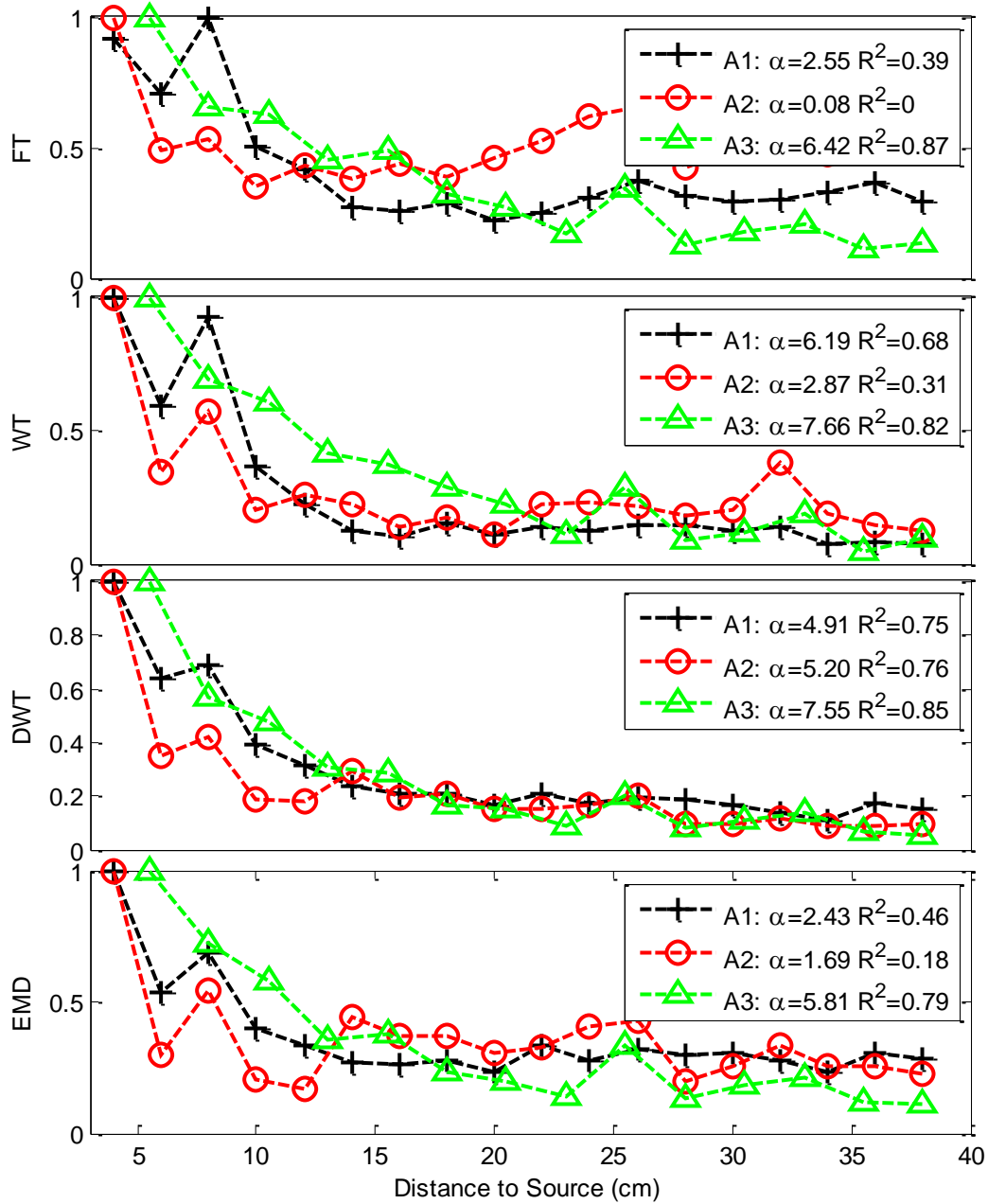


Figure 6.31: Comparison of attenuation trends from Test I, II and III: based on (a) Total area of Fourier spectra for windowed time signals, (b) Wavelet magnitudes for a Morlet wavelet of 52 kHz central frequency, (c) Spectral area of decomposed signals form DWT (Level-4), (d) Spectral area of decomposed signals from EMD (IMF 1).

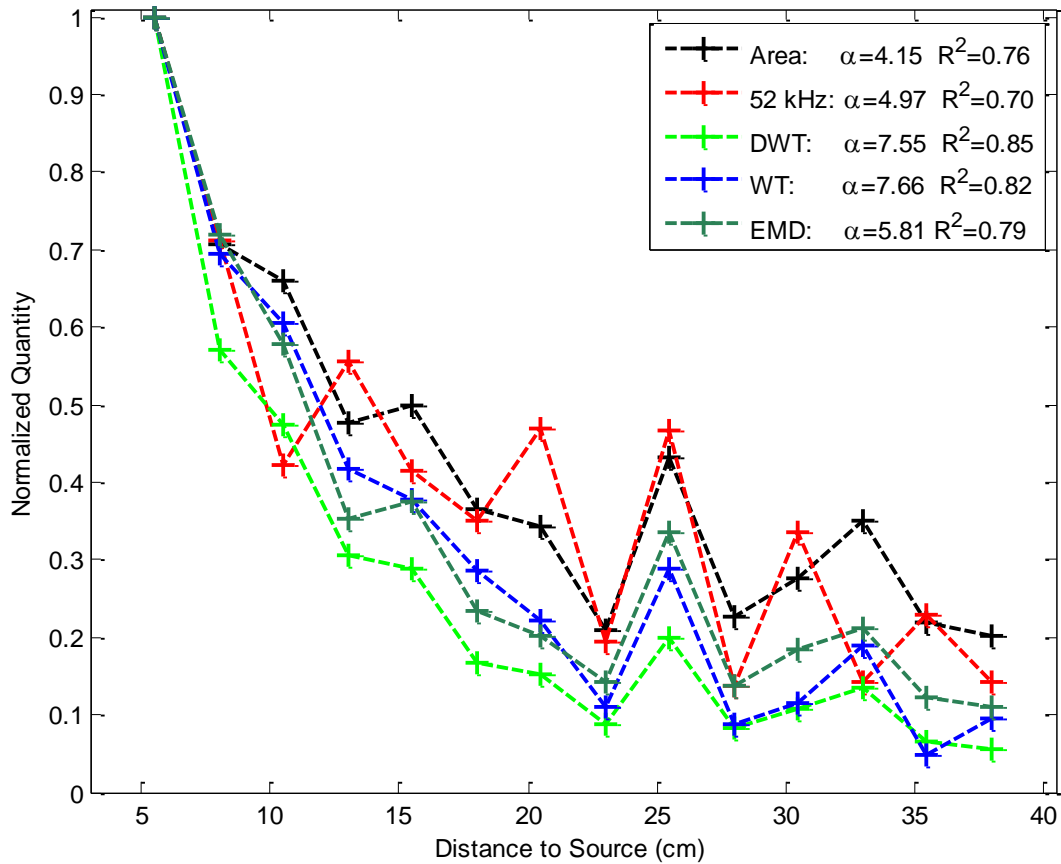


Figure 6.32: Attenuation trends of different quantities: Area, total area of Fourier spectra; 52 kHz, Fourier magnitude of 52 kHz; DWT, spectral area of decomposed signal Level-4; WT, wavelet magnitudes for a Morlet wavelet of 52 kHz central frequency; EMD, spectral area of the 1st IMF. Total spectral area and magnitude of 52 kHz are obtained from non-windowed time signals.

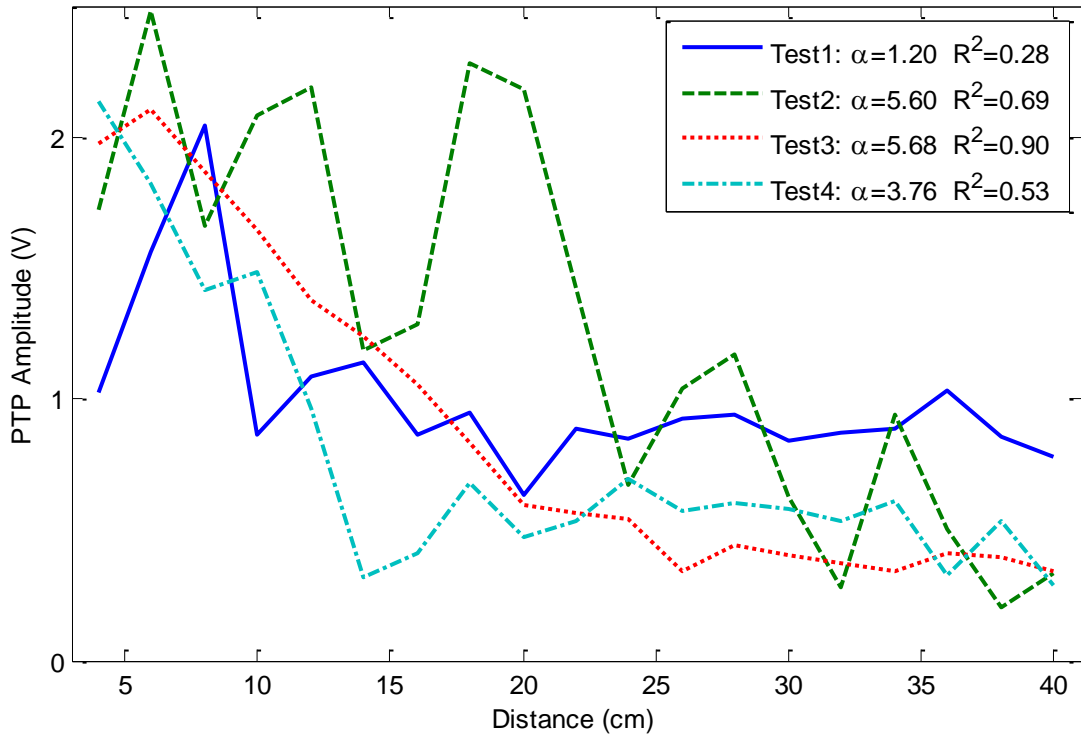


Figure 6.33: Attenuation trends for different couplings.

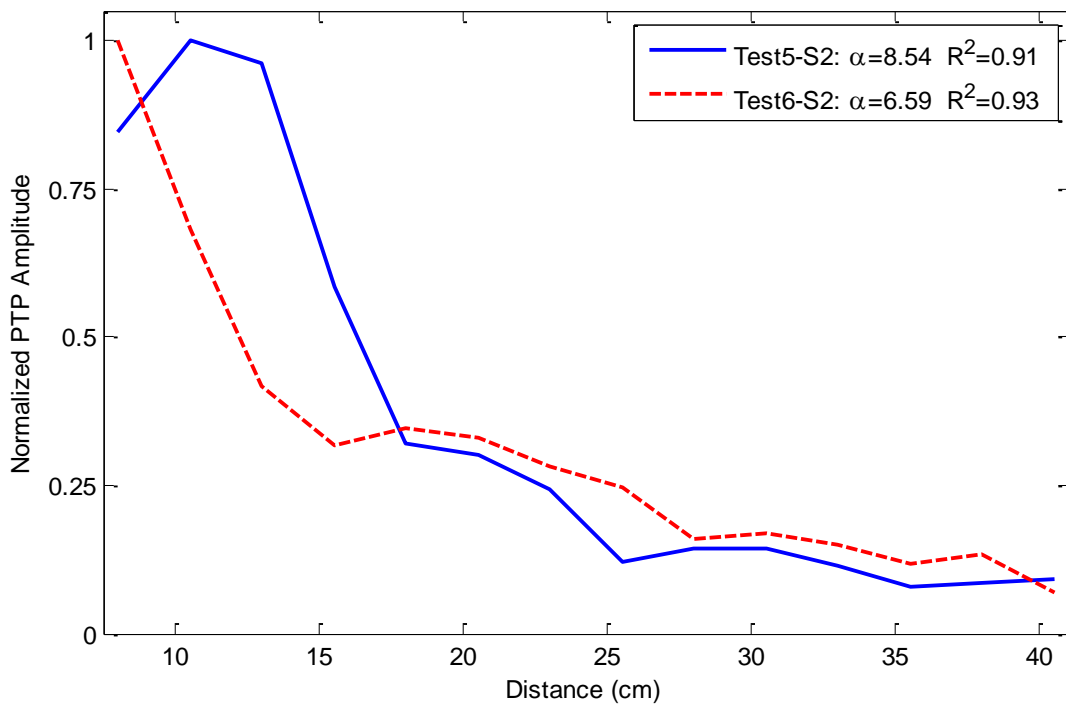


Figure 6.34: Attenuation trends obtained from the receiver array (Test5-S2) and the reference receiver (Test6-S2).

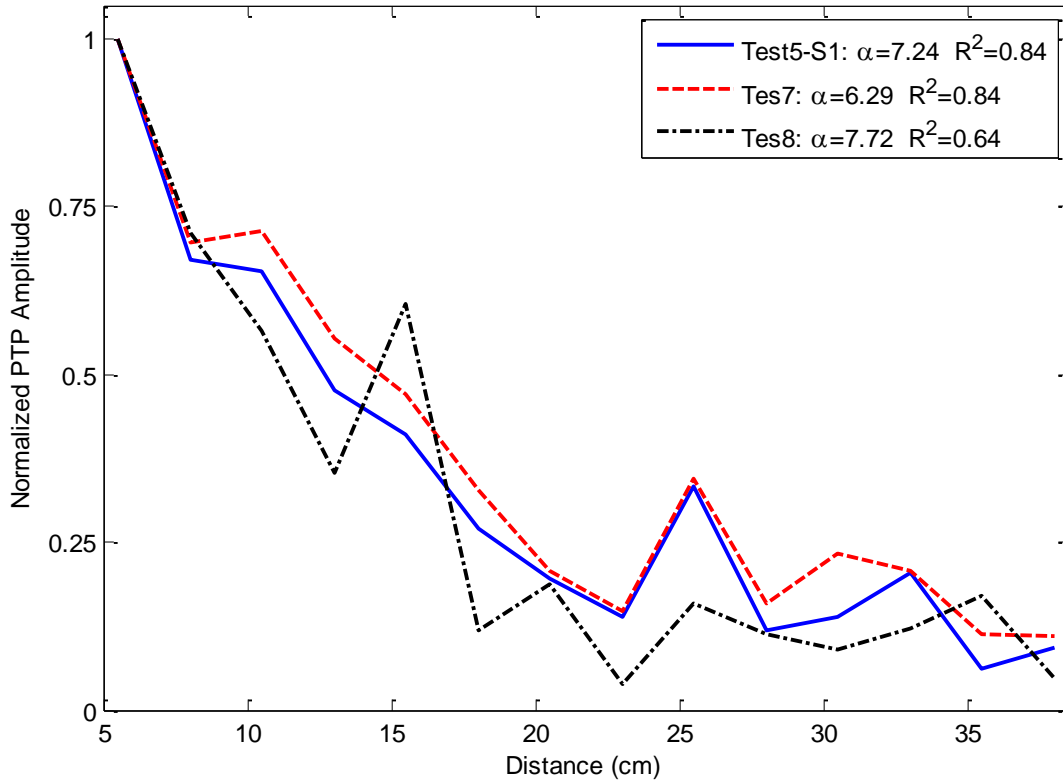


Figure 6.35: Attenuation trends obtained under different excitation pulse.

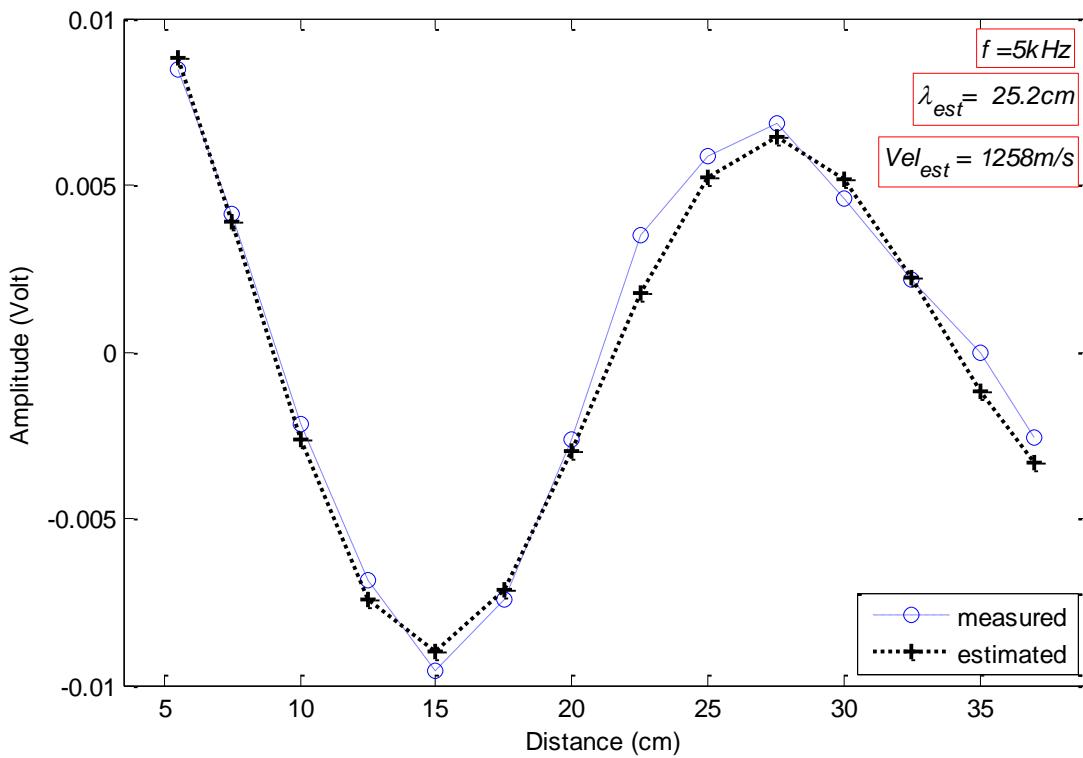


Figure 6.36: Waveform captured along the receiver array under 5 kHz steady-state sinusoidal excitation.

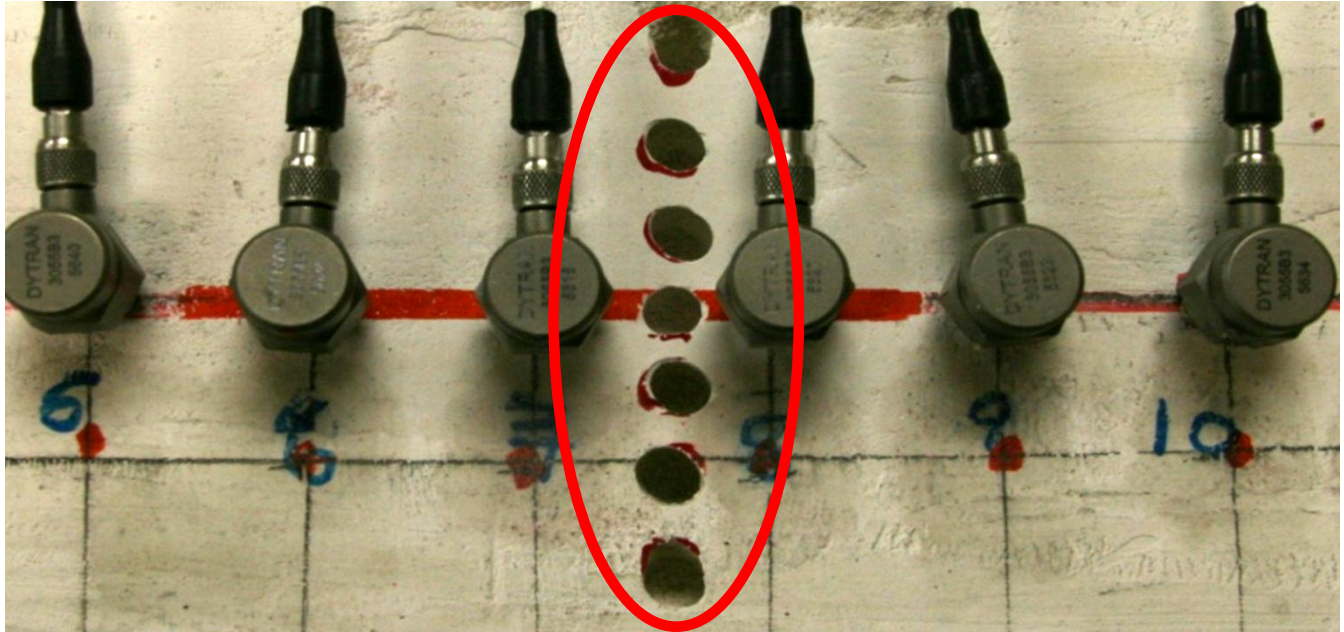


Figure 6.37: The damaged section consists of 7 holes at the center of the receiver array.

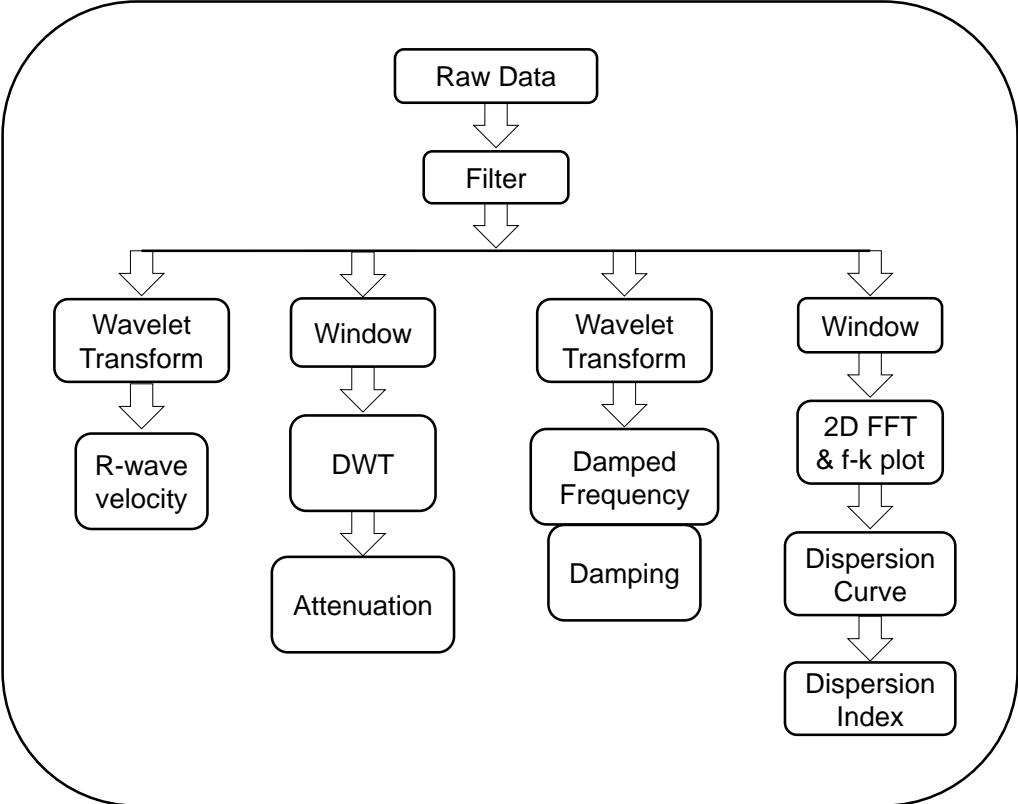


Figure 6.38: Signal processing algorithm

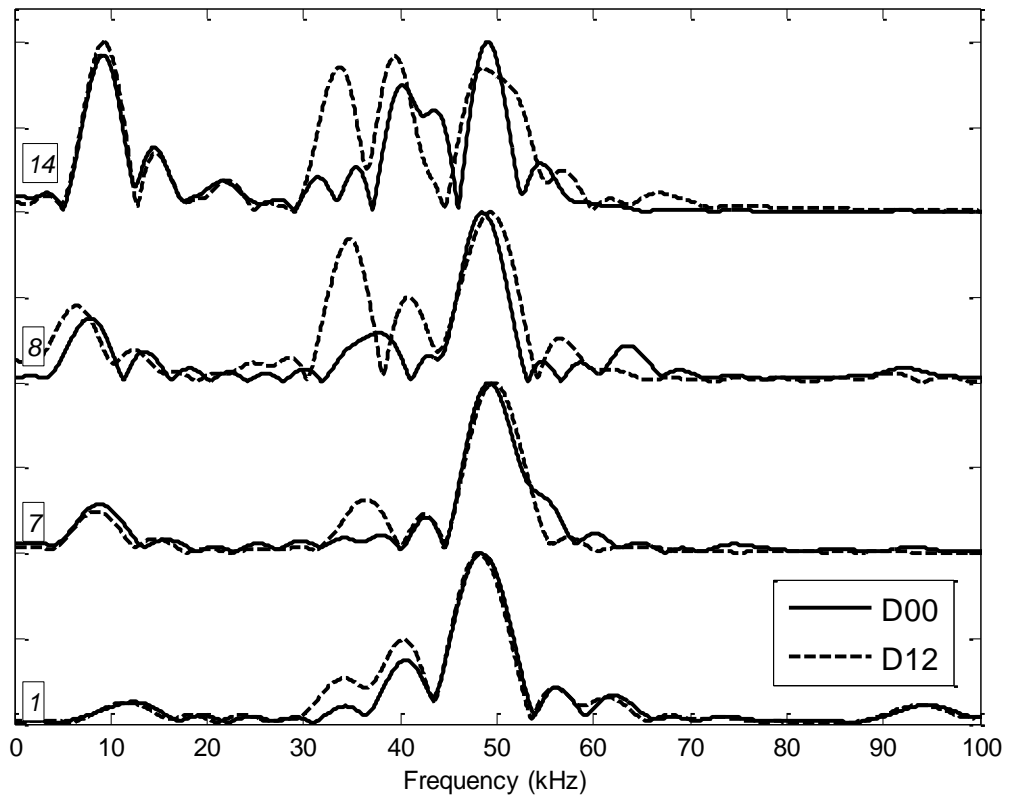
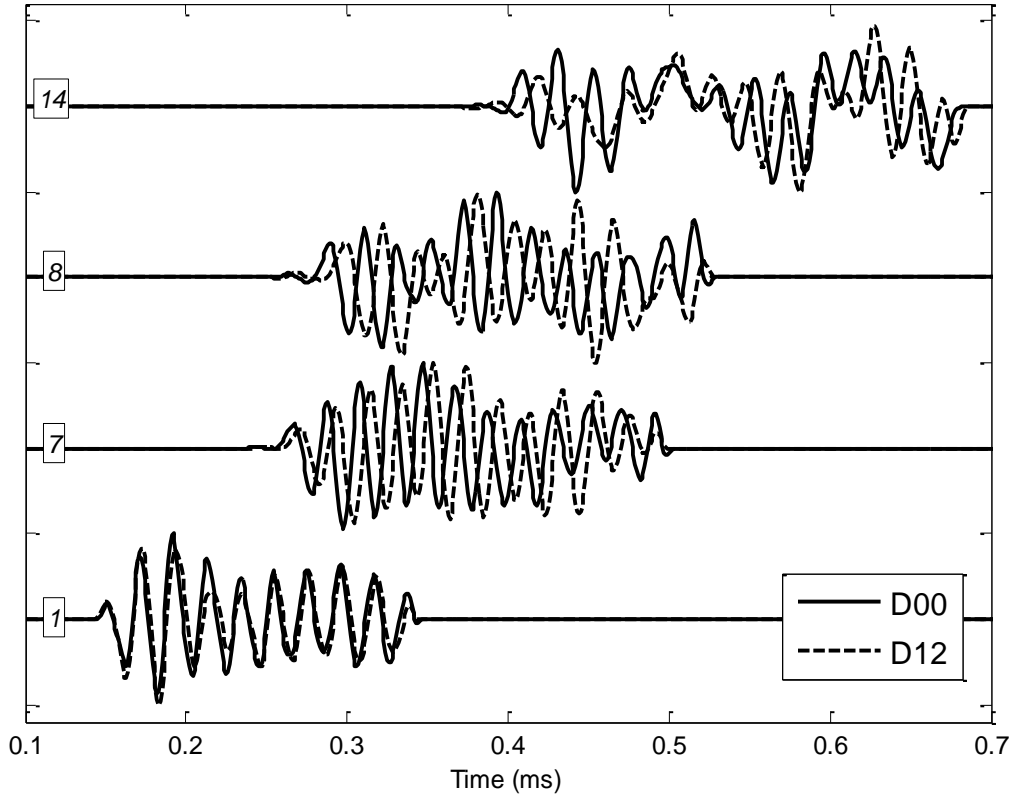


Figure 6.39: Comparison of the cases D0 and D12 (a) time histories, (b) Fourier spectra. A Tukey window is applied to the time signals prior to FT.

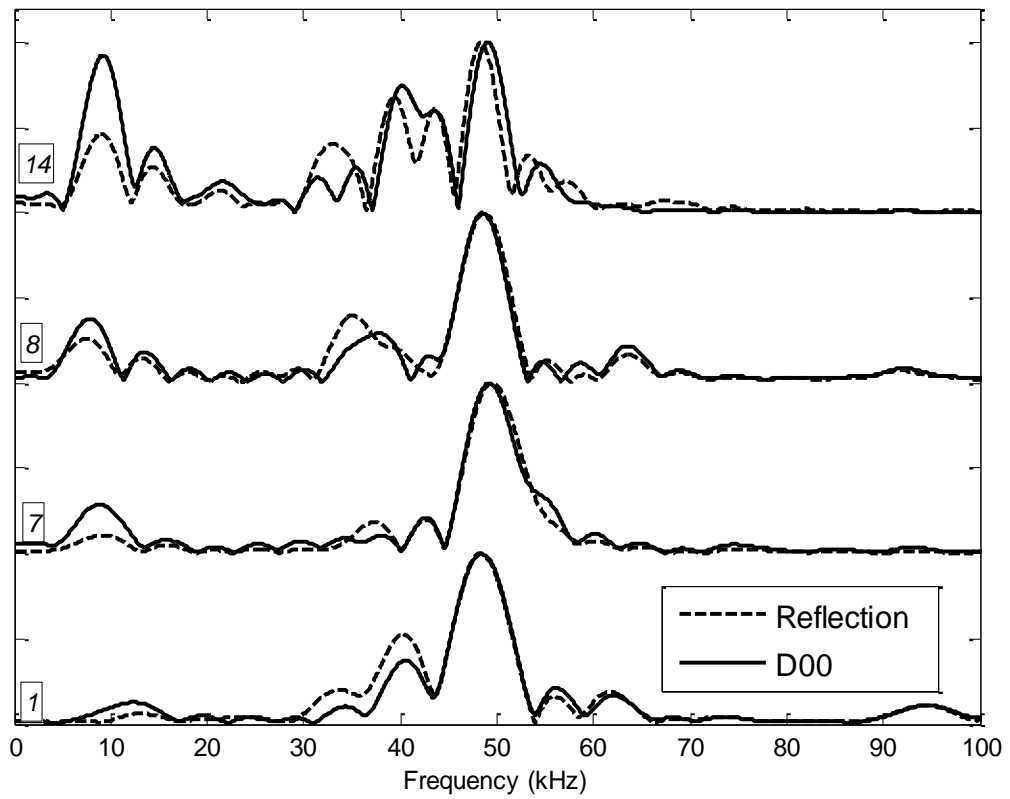
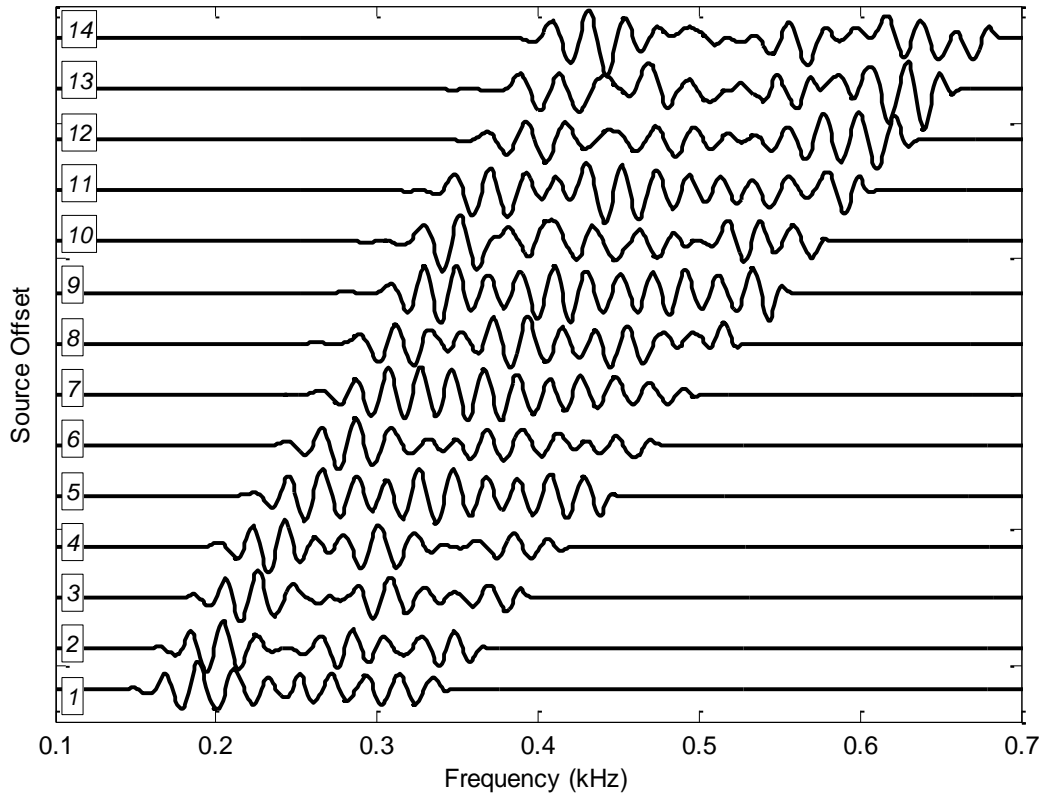


Figure 6.40: Reflection due to the defects (case D12) (a) time histories, (b) Fourier spectra.

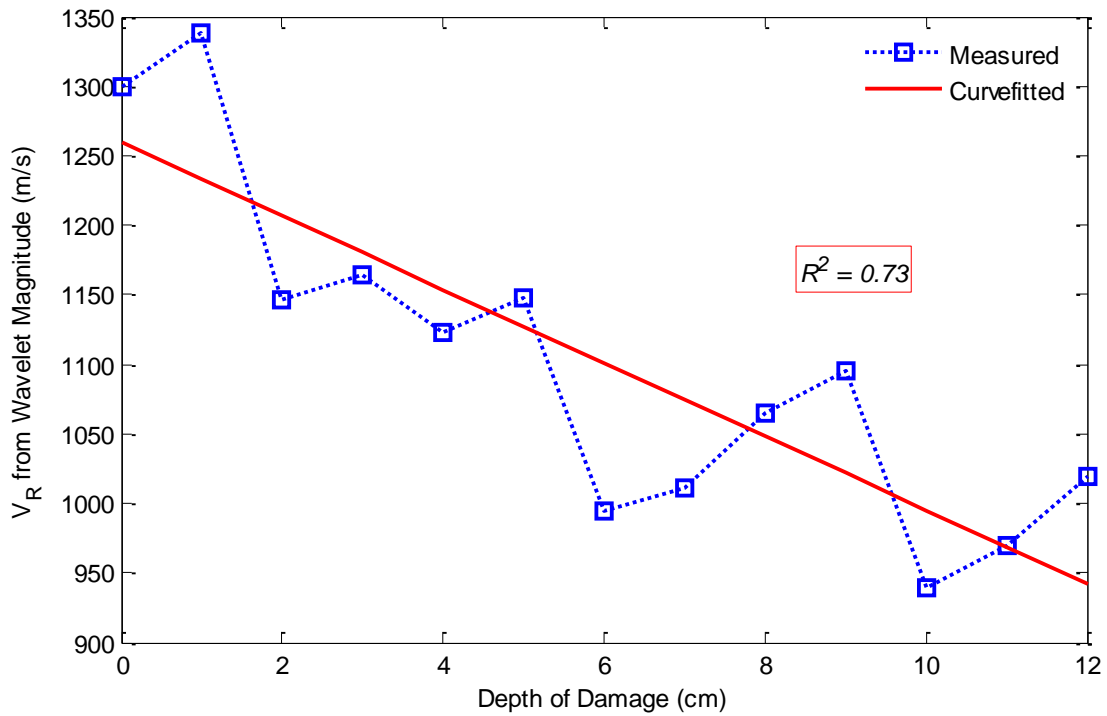


Figure 6.41: R-wave velocity respect to the damage case: $\sigma = 120$ m/s, $COV = 11\%$ and $R^2 = 0.73$.

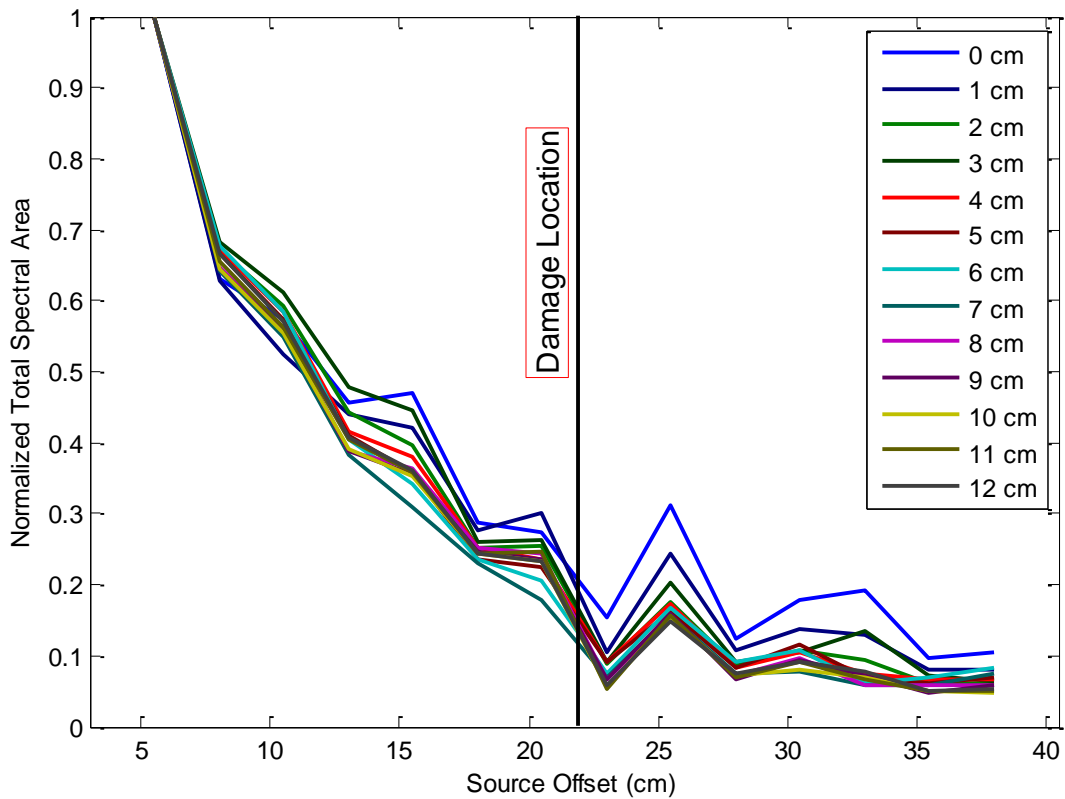


Figure 6.42: (a) Attenuation trend of total spectral area for each damage case.

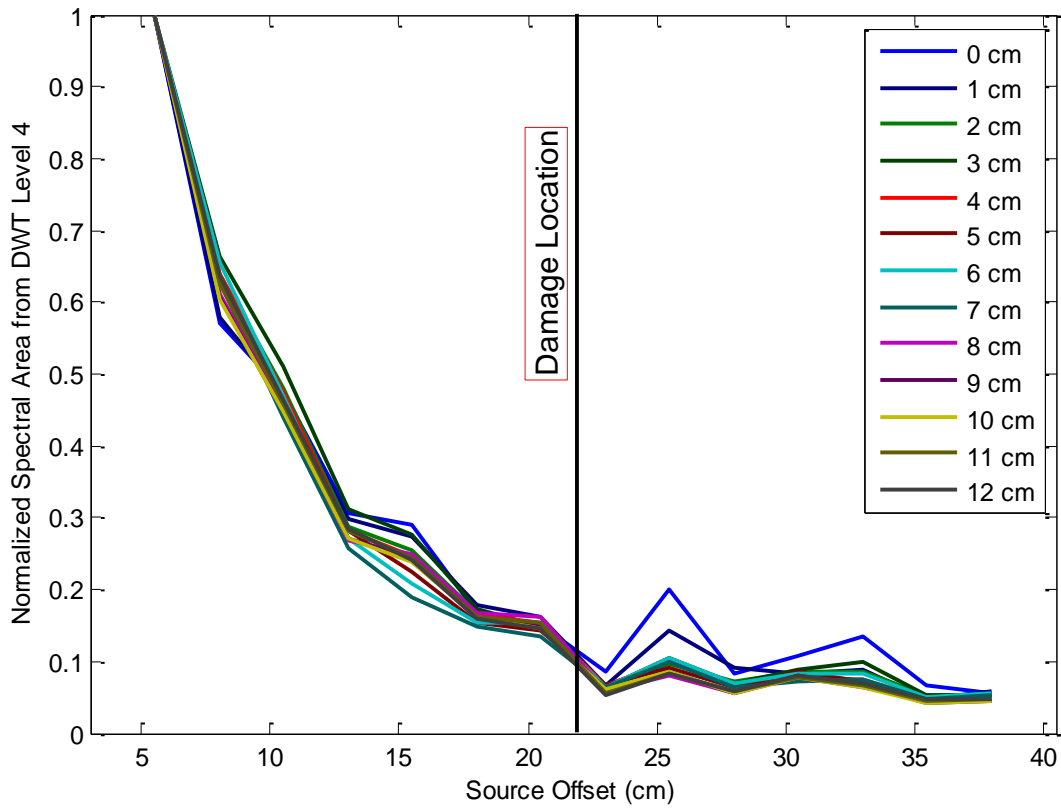
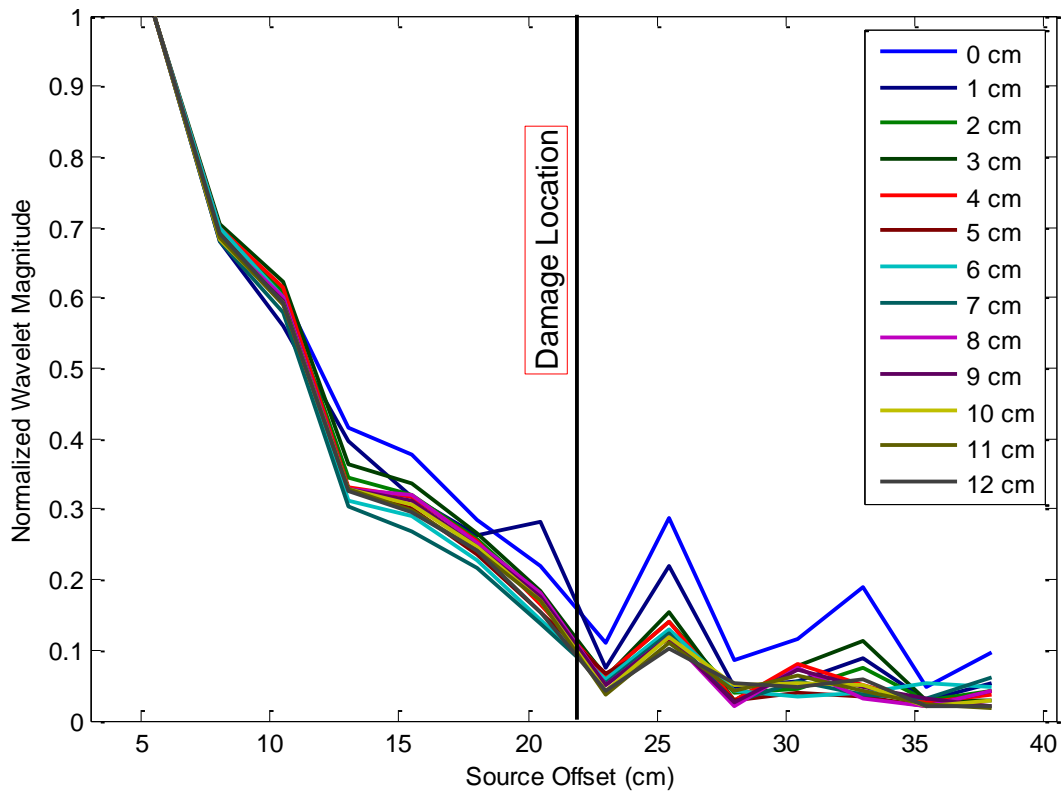


Figure 6.42: Attenuation trends for (b) wavelet magnitudes and (c) spectral area of decomposed signal (level 4) from DWT.

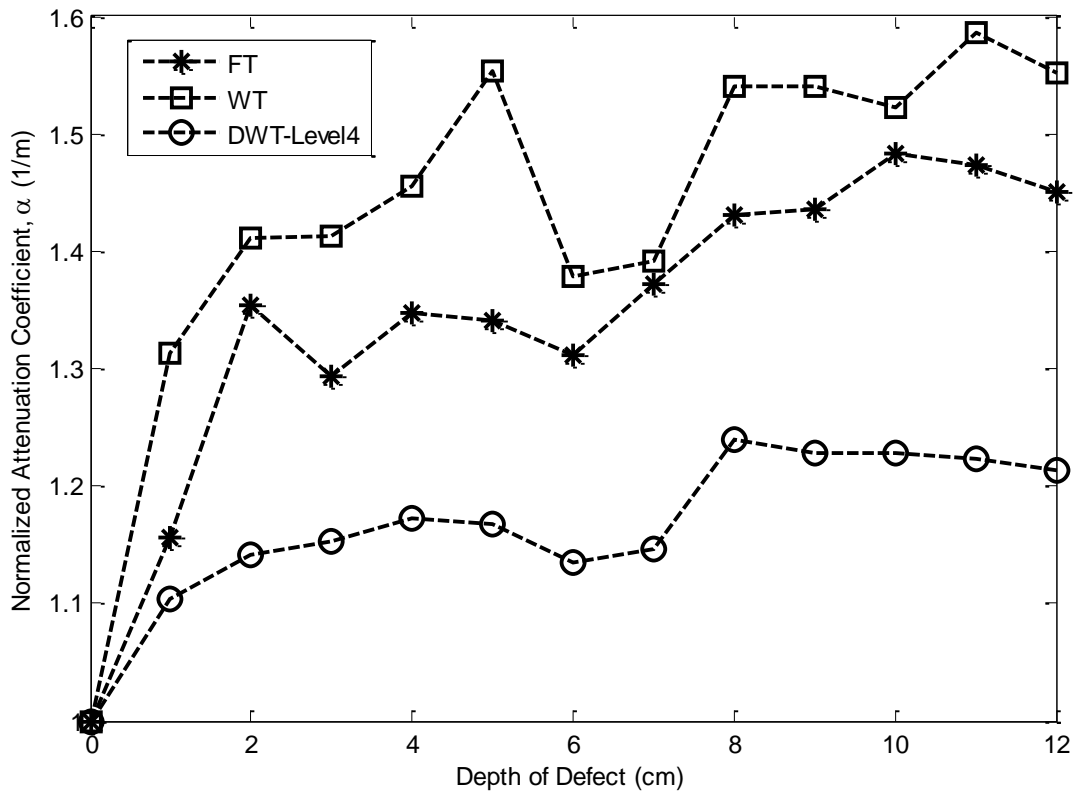


Figure 6.43: Attenuation coefficients, α , normalized respect to the minimum value in the trend, vs. the damage case; α is calculated from FT (spectral area), CWT (wavelet magnitudes) and DWT (spectral area of level 4).

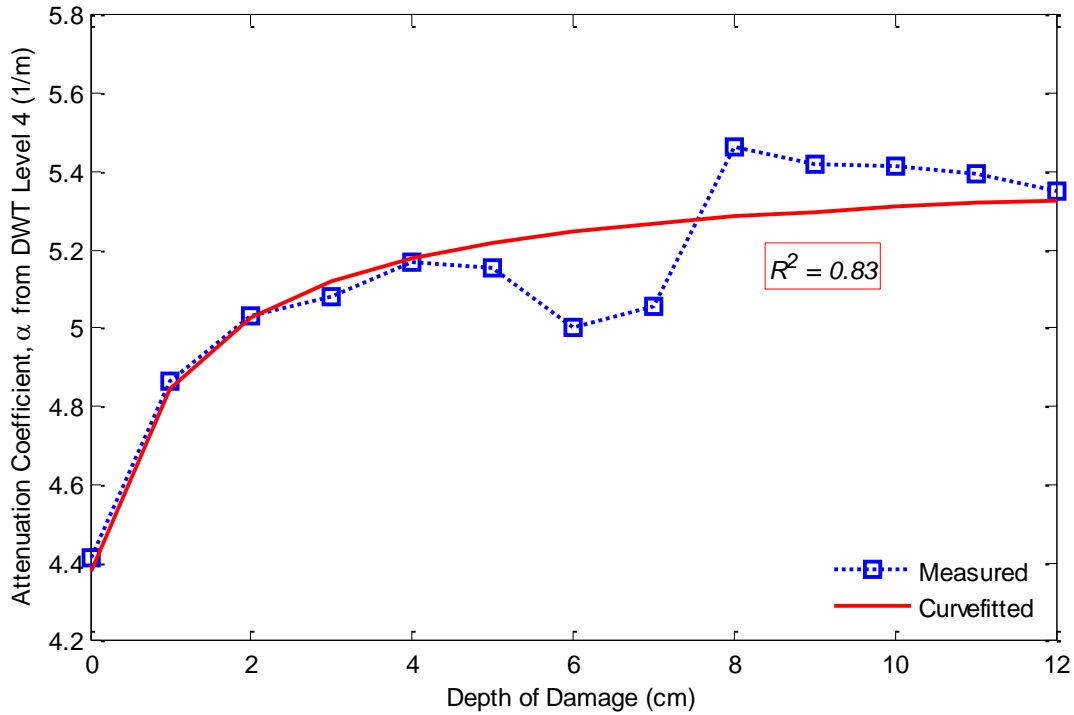


Figure 6.44: The attenuation coefficient, α , obtained from the spectral area of level 4 from DWT respect to the damage case: $\sigma = 0.5 \text{ m}^{-1}$, $\text{COV} = 5.6\%$ and $R^2 = 0.83$ for negative exponential model.

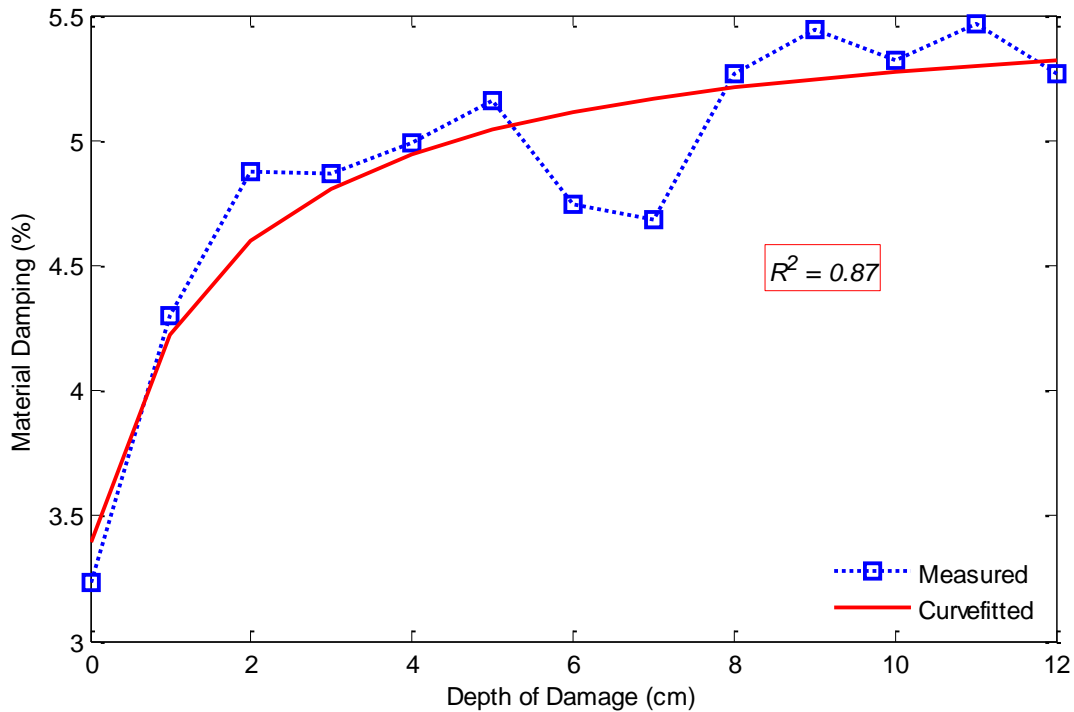


Figure 6.45: The material damping ratio, ζ respect to the damage case: $\sigma = 0.6\%$, $\text{COV} = 12\%$ and $R^2 = 0.87$ for negative exponential model.

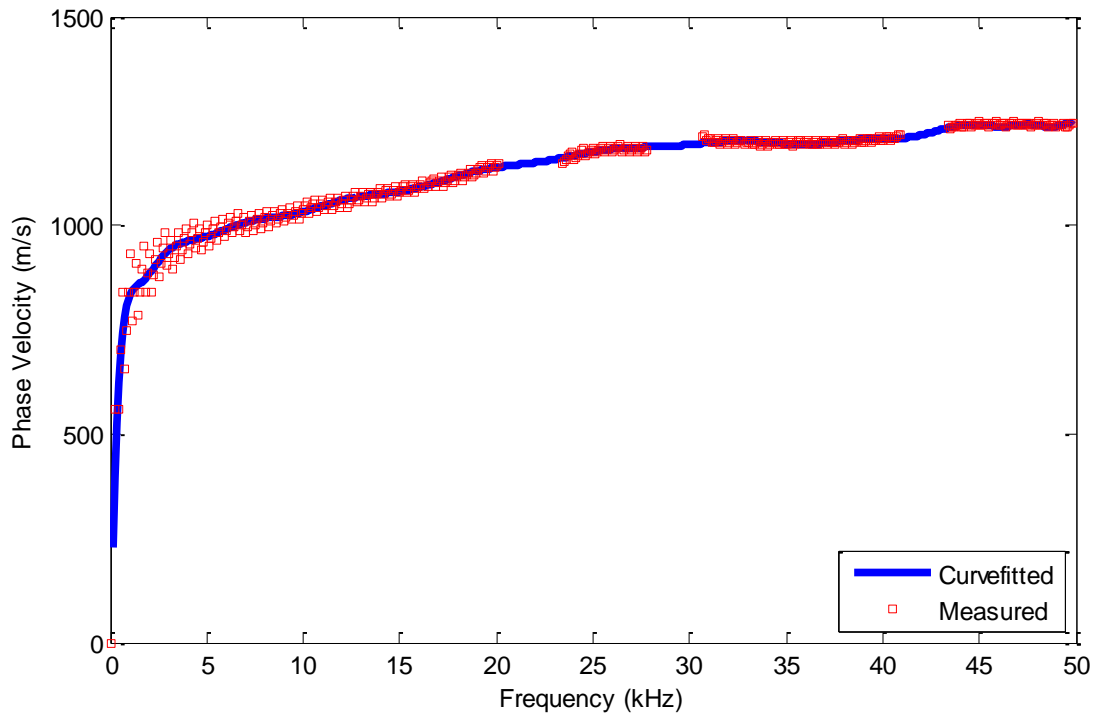


Figure 6.46: The reference phase velocity curve obtained from undamaged (0 cm) case; the curve is fitted using a high order polynomial model to ensure continuity for the frequencies from 0 to 50 kHz.

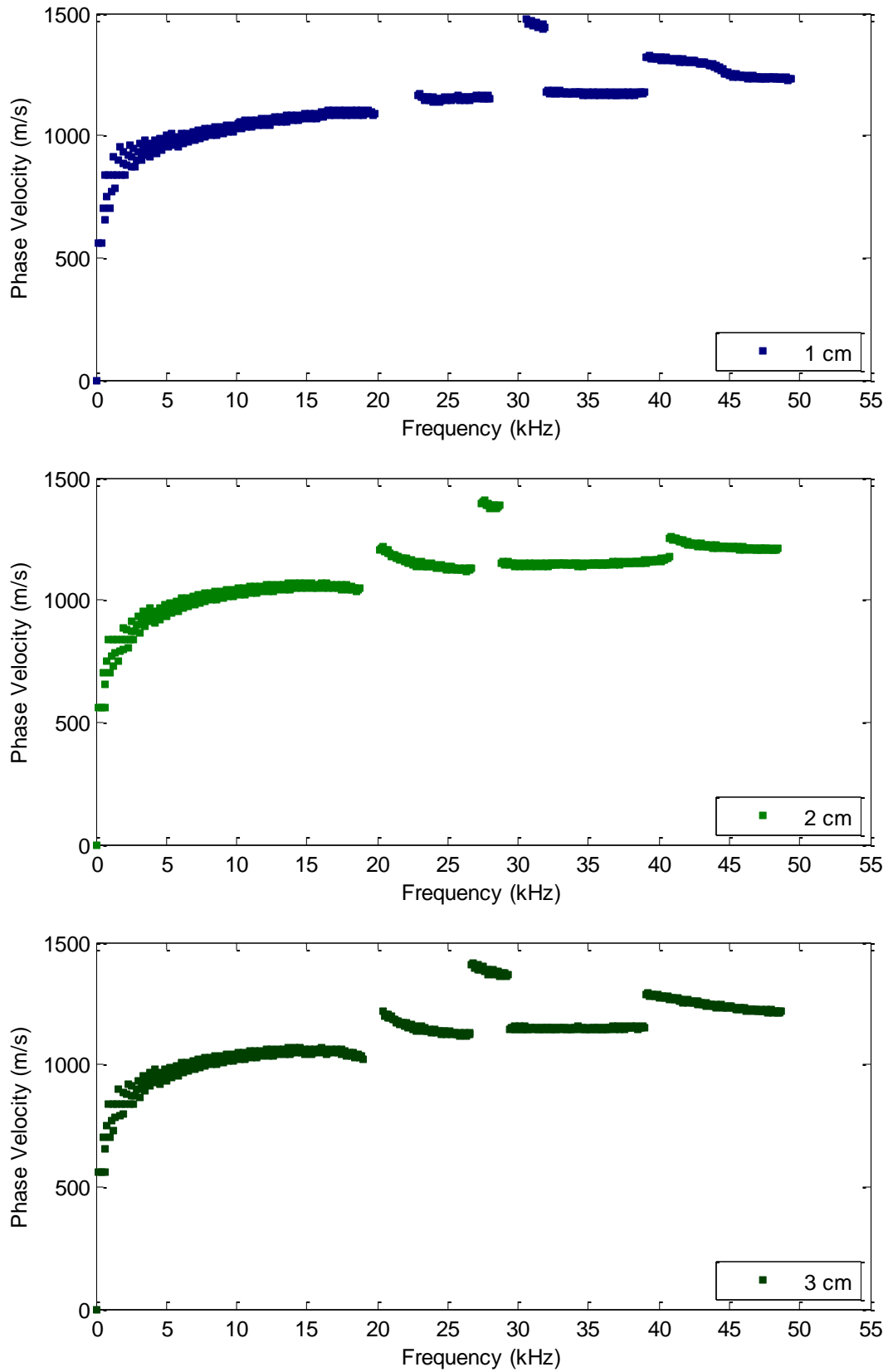


Figure 6.47: Dispersion (phase velocity) curve for the damage depths of (a) 1, (b) 2 and (c) 3 cm.

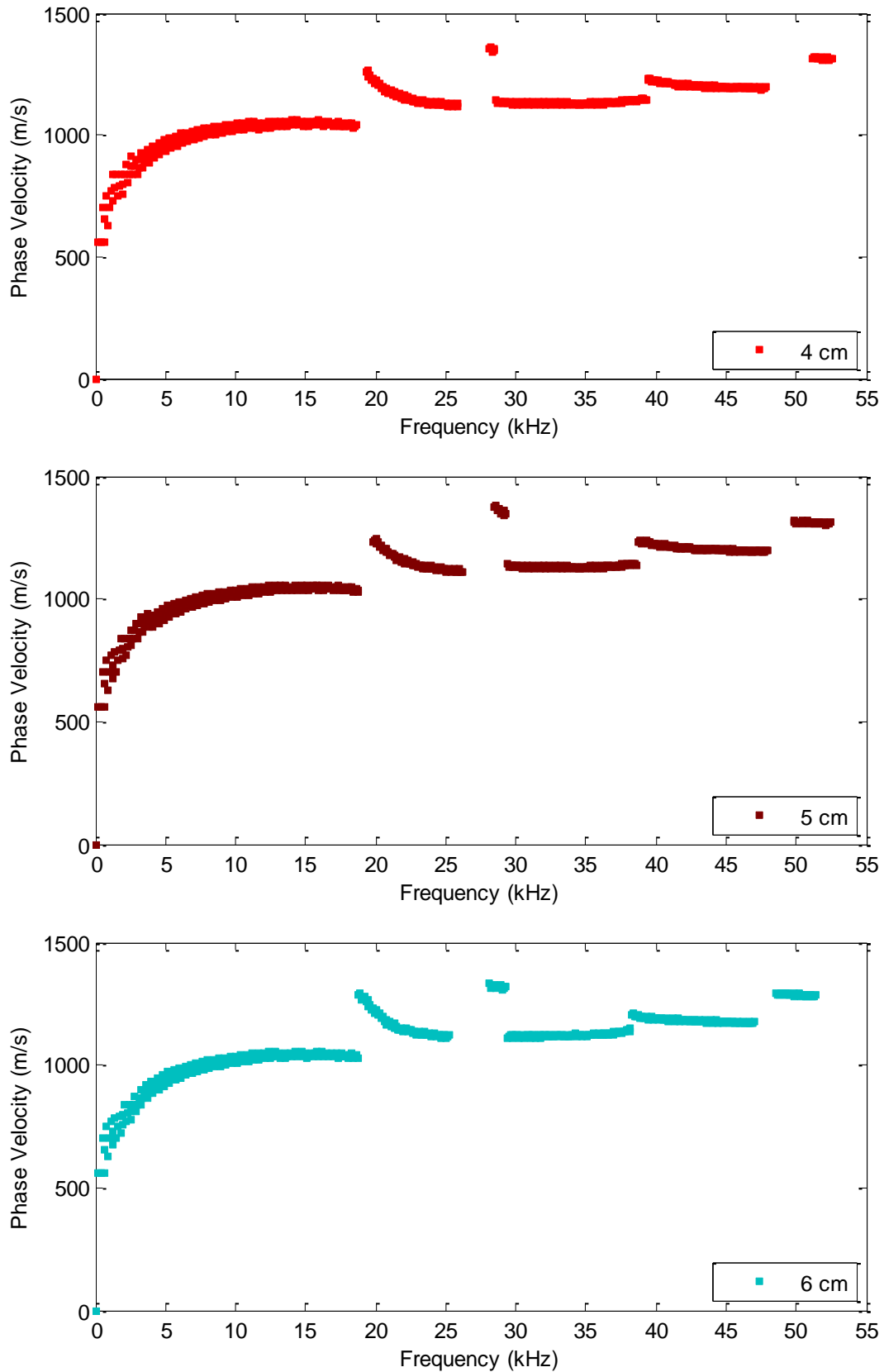


Figure 6.47: Dispersion (phase velocity) curve for the damage depths of (d) 4, (e) 5 and (f) 6 cm.

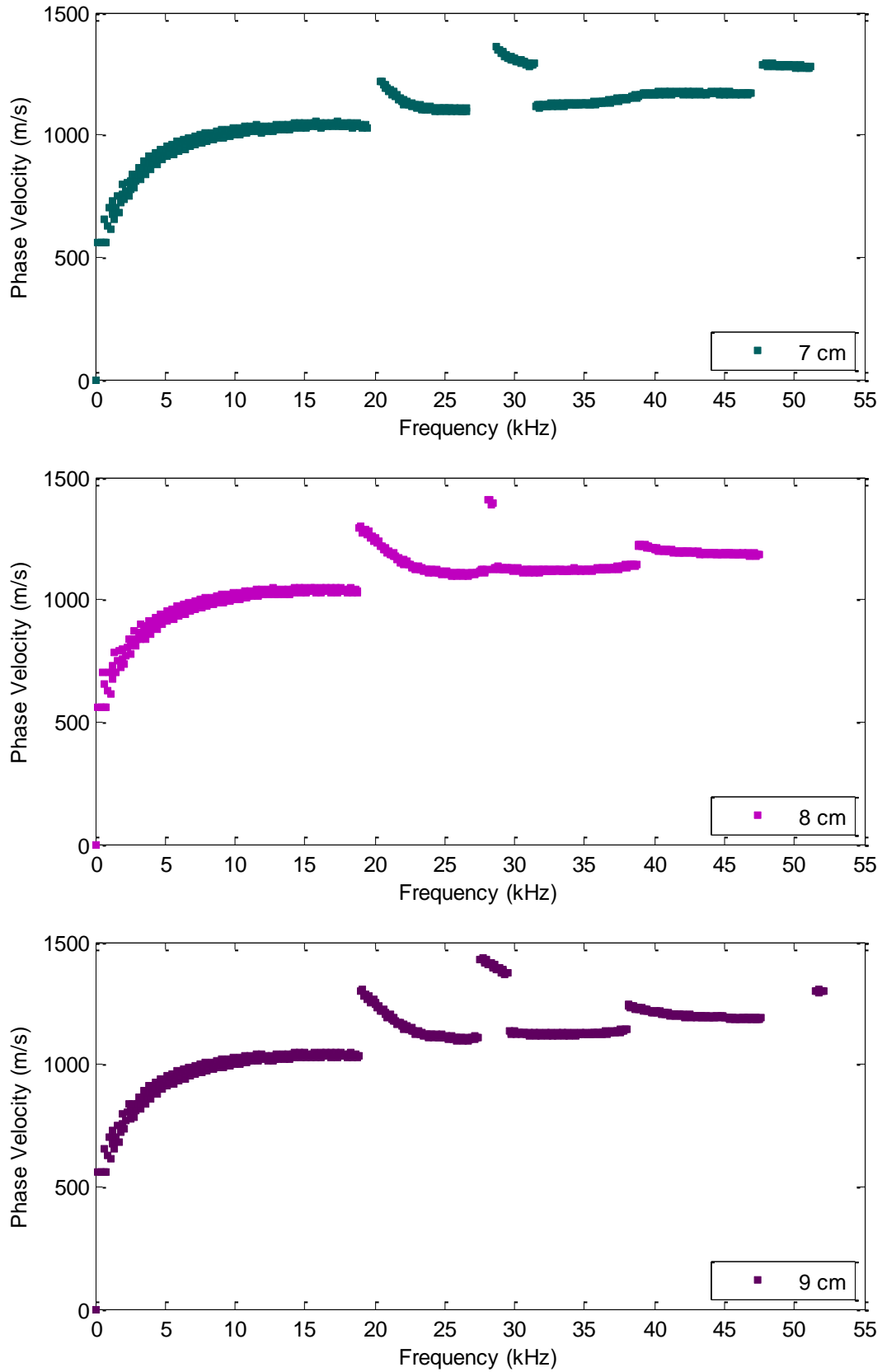


Figure 6.47: Dispersion (phase velocity) curve for the damage depths of (g) 7, (h) 8 and (i) 9 cm.

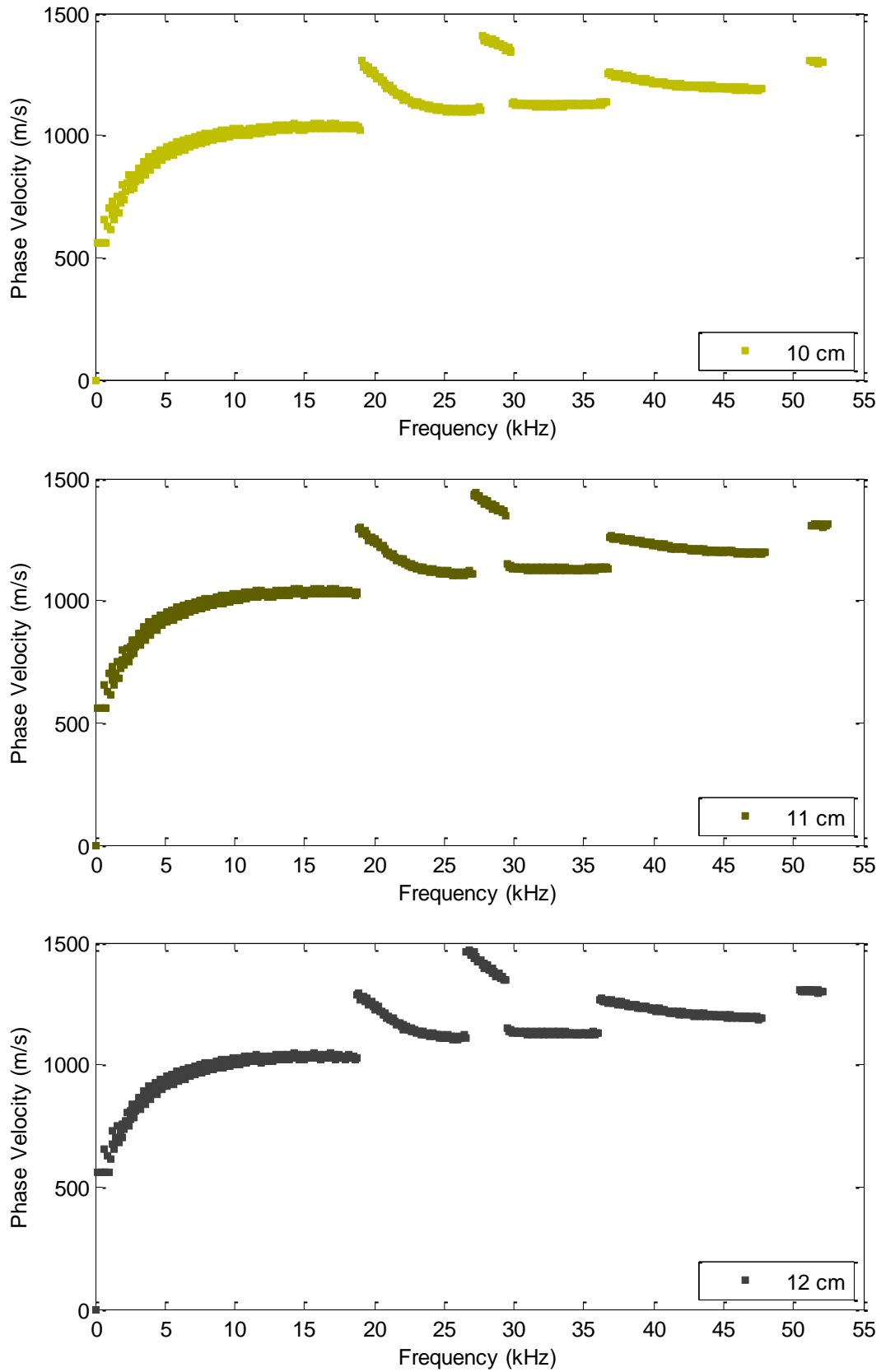


Figure 6.47: Dispersion (phase velocity) curve for damage depth of (l) 10, (k) 11 and (m) 12 cm.

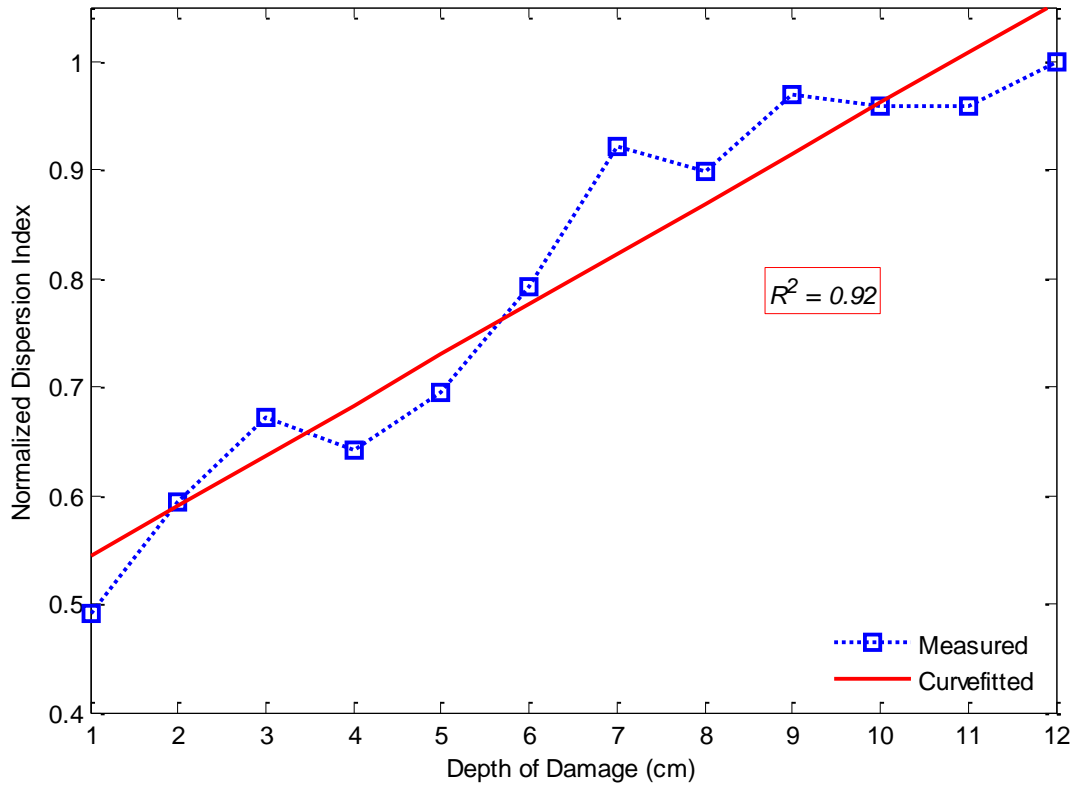


Figure 6.48: Dispersion index, DI, respect to the damage case: COV = 22% and $R^2 = 0.92$ for linear model.

Chapter 7 Condition Assessment of Concrete Beams

7.1 Introduction

In this chapter, the experimental work undertaken for the assessment of six laboratory scale beams is presented. The signal processing procedure introduced in Chapter 6 is implemented for the analyses of beams. The surface wave characteristics are determined to investigate their sensitivities with respect to the deterioration level.

Cracking in concrete may occur due to different reasons such as loading, environmental conditions and weathering. It is hard to present the cracking in structural elements in the laboratory. Therefore, mostly the cracks are reproduced as notches in laboratory works. This study aims at overall structural assessment; instead focusing on a single notch, and thus deterioration in the beams is simulated by distributed voids along the specimens. Void content is created by mixing the concrete paste with Styrofoam[®] pellets. Although, generating voids in the beams is not realistic to represent the damage structure of concrete, this is the only practical way to reproduce damage which could be quantified prior to the experimental tests. The experimental study includes the ultrasonic and mechanical tests of which results are presented in the proceeding sections of this chapter.

7.2 Production of Concrete Beams

Six beams of dimensions $110 \times 15 \times 10 \text{ cm}^3$, containing different void volumes, were produced and cured as advised in CSA A23.2-3C (Fig. 7.1). Voids were created by mixing the concrete batch with Styrofoam pellets of 7 mm diameter. Beam 1 is the control beam with 0% pellets whereas other beams have 5%, 10%, 15%, 20% and 30% volume of pellets. These are called “design void ratios” herein. The concrete batch was mixed using a machine mixer, and casting was completed without using a vibrator to prevent the pellets from rising towards to the surface of the wet concrete. Moreover, a low slump concrete was used to allow for uniform pellet distribution in the mixture. The amounts of ingredients used for a single beam are given in Table 7.1. The round

shaped coarse aggregate with the maximum diameter of 9.5 mm was used which is consistent to the size of Styrofoam pellets.

Table 7.1 The concrete recipe

Stone (kg)	Sand (kg)	Cement (kg)	Water (kg)	W/C
29.729	21.405	7.135	4.281	0.6

The curves in Figure 7.2 show the density and the relative void ratio for each beam. The density, ρ , decreases from 2.56 to 2.12 g/cm³, while the relative void ratio increases from 0 to 17%. The relative void ratio is computed by $1 - \rho/\rho_s$, where ρ_s is the specific unit density of Beam 1. Void ratio for Beam 1 (no pellets) is assumed zero. This plot reveals how the void volume varies among the beams. The design void ratio and relative void ratios differ. Further action is taken by visually checking the interior of the beams. Five rectangular prisms with a width of 10 cm are cut out from each beam (Fig. 7.3) after the ultrasonic testing. These sections of the beams corresponds to the regions where the ultrasonic tests were conducted. Some selected cross sections of the prisms are shown in Figure 7.4 where large air voids are also visible in addition to the pellets. It is evident that the low slump concrete batches casted without using a vibrator caused the beams to be compacted poorly.

In subsequent sections, results are plotted versus design void ratios. This is because the volume of pellets placed in the concrete mix is the only sure number representing damage in the concrete. In reality the percentage volume of total defects in these beams was likely even higher than the percentage volume of the pellets alone.

7.3 Mechanical tests

The compressive strength of the concrete beams is measured in accordance with CSA A23.2-9C for both rectangular prisms cut out from the beams and concrete cylinders which are produced at the time of casting. The individual and average compressive strengths of the specimens are shown in Figure 7.5. Strength of both cylinders and prisms exhibit similar trends, which drops from 50 to 10 MPa with increasing void ratio. The initial 5% void causes approximately 20%

drop in strength, while both of 15% and 20% void volumes reveal same level of strength which is in agreement with 1% difference in the computed effective void ratios for these two beams.

Initially four beams were casted (B1, B3, B4, B5). Two more beams (B2 and B6) are included in addition to the initial four beams. For this reason, not all of the beams could be tested at the same age. The beams casted later (B2 and B6) could be cured for 21 days, whereas the others were kept in the humidity room for 28 days. It is advised that a 21-days cured concrete achieves 96% of its 28-days' strength for cement type I and moist cured specimens (ACI 209R-92). After curing period, all beams were moved to the laboratory environment and kept under normal conditions until all the ultrasonic and mechanical testes were completed. Although, the ages of the beams were different at the testing date since they were all kept in laboratory air, the strength gained during the waiting period is ignored. Taking this information into account, the strength curve given in Fig. 7.5 is corrected as tabulated in Table 7.2.

Table 7.2 The properties of beams

Beam #	Design Void Volume (%)	Relative Void Volume^[1] (%)	Curing Duration^[2] (days)	Age at Testing^[3] (days)	Strength^[4] (MPa)	Corrected Strength^[5] (MPa)
Beam 1	0	0	28	180	46.5	46.5
Beam 2	5	1.1	21	28	37.1	38.6
Beam 3	10	8.8	28	180	33.7	33.7
Beam 4	15	12.3	28	180	25.0	25
Beam 5	20	12.6	28	180	23.5	23.5
Beam 6	30	17.1	21	28	9.8	10.2

[1] The relative void volumes are measured based on the beams' densities; the real void volumes are larger than the relative ones, [2] Beams and cylinders were kept in the humidity room, [3] Ages are approximate; the compression tests were performed two days later than the ultrasonic tests, [4] Measured from the prisms, [5] Corrected based on the curing duration.

7.4 Laboratory Setup and Configuration for Ultrasonic Tests

The instrumentation used for the tests (Fig. 7.6) consists of an piezoelectric transmitter (50 kHz resonant frequency) which is driven by a pulser, 18 accelerometers (Dytran 3055B3, 35 kHz resonant frequency, 1 Hz - 10 kHz flat response, 504.1 mV/g sensitivity) as receivers, two external power supplies (PCB 483A) to run all of the accelerometers at once, and a data

acquisition system (Genesis, 24 channel, 1 MHz sampling rate) to capture the signals. A 100 kHz low-pass Bessel filter available within the acquisition unit is applied prior to recording the signals. All of the receivers are fixed at once along the center line of the beams through nuts; a commercial glue is used as coupling between the specimens and nuts. The receiver array covers a length of 40 cm on the beams. The source transmitter is located 30 cm away from the edge of the beam while the receivers have a spacing of 2 cm and 6 cm source offset. As an additional configuration, the source is mounted horizontally on the edge of the beam to excite the longitudinal waves as well (Fig. 7.7). The transmitter is supported with a ratchet strap in this position where vacuum grease is used as coupling.

7.5 The Results of Data Analyses

7.5.1 P-wave and R-wave Velocities

The recorded time histories and their associated Fourier spectra for all of the beams are plotted in Figures 7.8-7.13. It should be noted that the waveforms are consistent for the first couple of receivers within all beams. This indicates that the arrival times of frequencies are similar for these locations. However, further the receiver's location from the source, especially for the beams with less void ratio, the effect of the reflections become much stronger; hence, larger amplitudes are recorded for these locations than the magnitudes of the wave-front. This may be explained with the constructive behavior of incident and reflected events. An automated code, developed in Matlab[®], is used to calculate the R-wave velocity, in which the same threshold value is defined for all time histories to peak the PTP amplitudes and the corresponding arrival times. In the code, prior to the velocity computation, the arrival of the wave-front is extracted by windowing. This is done in order for the first arriving peak representing the surface wave arrival to be selected. The selection of wavelet magnitude's arrival, as described in Chapter 6, is not chosen for the beams because the pre-windowing is still needed to magnify the amplitudes at arrival, which makes performing wavelet transform redundant.

The P-wave velocity is determined using the 'pseudo-color' plots generated by Matlab with the preference of 'lines' color-map, which exposes the P-wave arrival clearly even if its amplitude is

small (Fig. 7.14). The trend shown in Figure 7.15 exhibits a negative correlation between the void ratio and the P-wave velocity. It drops from around 4530 to 3630 m/s in a linear fashion with a standard deviation (σ) of 305 m/s and a coefficient of variation (COV) of 7.4%. When the experimental trend is fitted into a linear line; the coefficient of determination (R^2) is found as 0.97 which justifies the linear relationship between the P-wave velocity and the void volume. On the other hand, the computed R-wave velocities vary within a range of 1600 and 2400 m/s and displays a declining trend upon the void ratio with a standard deviation of 260 m/s and COV of 12.6% (Fig. 7.16). Although, the R^2 is attained as high as 0.92 indicating the linear relationship, the R-wave velocity is not as sensitive to the void ratio as the P-wave velocity, especially for the beams with intermediate void ratios. This can be attributed to the fact that the real void ratio is not that much different between these beams as given in Table 7.2.

7.5.2 Attenuation

Each frequency spectrum displayed throughout Figures 7.8 to 7.13 is normalized with respect to its maximum magnitude in the spectrum. This kind of presentation is useful to expose the significant frequencies existing within a signal; however, if the attenuation trend for each frequency component is needed, the contour plots as given in Figures 7.17 are more practical. In these contour plots, each frequency component is normalized with respect to its maximum magnitude obtained within all spectra set; so that, the frequencies that die out along the distance can be visually detected. The dark blue colored region which gets larger with the increasing void volume indicates the higher frequency components, especially the ones above 60 kHz fade away significantly. However, the focus in this study is for the frequency band between 30 and 60 kHz because of the central frequency of the transmitter employed in the tests.

The attenuation coefficient, α , is determined from the spectral area of the decomposed signals utilizing DWT (level 4: 31-62.5 kHz) as it has been found as the most reliable parameter in Chapter 6. The attenuation trends for all beams (Fig. 7.18) are fitted to $\exp(\alpha(x_1 - x_i))$ to estimate α , where x_i is the location of the receiver with respect to the source. As an example, the measured and curve-fitted trends are plotted for Beam 1 in Figure 7.19. The geometric attenuation (Eq. 2.45) is not eliminated from the signals prior to regression analyses; which is different to the cemented-sand tests (Chapter 6). Because the attenuation in concrete is much less

than in the cemented-sand, it is more difficult to capture the trend experimentally. Moreover, a geometric attenuation coefficient of -0.5 is not valid for the beam geometry since the incident event is contaminated by the reflections of the recorded signals. Therefore, unless the reflections are decomposed, the effect of geometric spreading cannot be eliminated. However, the deterioration level can be evaluated based on the total attenuation, α , which represents the combined effect of material and geometric attenuations.

In Figure 7.20, the variation in α is displayed with respect to the void volume. The increase in attenuation with the increasing void volume is visible. It is observed that α increases by a factor of 2 with respect to its initial value, for a void ratio of 20%. A big jump is apparent for 30% void ratio; makes the sensitivity of α with respect to the damage level questionable. Therefore, a Tukey window is applied to signals before determining attenuation. Compared to calculations without windowing, applying a window reduces the level of jumps observed earlier (Fig. 7.20); moreover R^2 and COV are improved from 0.88 and 57% to 0.89 and 32% successively. It is evident that eliminating the reflections improves the results simply because the dual effect caused by the reflected waves is omitted in the attenuation calculation. For instance, in the case of Beam 1 (no void), the reflected event may be as strong as the incident event; on the other hand, in the case of Beam 6 (30% void), both incident and reflected waves are attenuated faster due to large void content. Therefore, the computed attenuation is correlated with the square of the real attenuation. In summary, windowing reveals a more realistic correlation; however, selection of the window size is subjective and it can influence the obtained results.

7.5.3 Material Damping Ratio

The material damping ratio, ζ , is evaluated for the region covered by the receiver array (a length of 40 cm) using Eq. 4.17. Damping is computed based on the energy dissipation of the decomposed signals (DWT level 4). Time histories are windowed using a Tukey window prior to decomposition. The decomposed signals are transformed into wavelet domain using the Morlet function with the central frequency of 52 kHz; so that the damped frequencies at the arrival of the surface wave can be determined. The R-wave velocity computed for each beam (Fig. 7.16) is substituted in Eq.4.17. Unlike the case with attenuation, geometric attenuation is eliminated since

only material attenuation is required to evaluate the damping (Eq. 2.46 & 2.47). The computed material damping ratios plotted in Fig.7.21 do not indicate any clear trend of which σ and COV are attained as 1.09% and 32%. As discussed in the previous section, a geometric coefficient of -0.5 does not fit beam geometry; even though, the reflections are intended to be eliminated by applying a window. However, it should be noted that the material damping ratio for Beam 1 (no defects) is determined as 2.22% which is smaller than the value, 3.24%, obtained for the cemented-sand in Chapter 6 which is consistent with less damping for the stiffer material. The material damping ratio although couldn't capture the exact defect volume; however, it still can be used for material characterization for the solid specimens.

7.5.4 Dispersion curve (phase velocity)

Prior to 2D Fourier transform, time signals are subjected to windowing as shown in Figure 7.22; in order for the incident waves to be extracted. Then, phase velocities, V_{ph} , are determined from the f-k plots (Figs. 7.23) by selecting the associated frequencies and wave-numbers of the maximum peaks. Higher frequency resolution was achieved for the beams compared to the cemented-sand due to the higher phase velocities in concrete. To avoid aliasing in a f-k plot, the upper limit frequency should at least have a wavelength, λ , equal to the receiver spacing, Δx . In this case, 120 kHz is attained as the upper frequency for $\Delta x = 2 \text{ cm}$ and $V_R = 2400 \text{ m/s}$. For this reason, the reference dispersion curve obtained from Beam 1 is curve-fitted to provide continuity in the phase velocity for the frequency range from 0 to 120 kHz (Fig. 7.24). The reference curve exposes the first antisymmetrical Lamb mode (A0); which is altered with the increasing void ratio as displayed in Figure 7.25. The larger the total volume of the defects, the larger dispersion can be observed. The theoretical Lamb modes are also shown in the same figure. The Rayleigh-Lamb frequency equation (Eq. 2.35a) is used to compute the theoretical dispersion curves for a concrete plate of 10 cm thickness of which V_P and V_S velocities are 4530 and 2650 m/s respectively. Although, the analytical solution is provided for plates, it is in good agreement with the experimental curves obtained for the beams. The torsional modes that might occur in a beam are omitted since the beam specimen is excited on its symmetrical axis.

Due to the structure of the defects existing within the beams, investigating some specific Lamb modes is not suitable. In other words, in the case of a surface breaking notch or delamination of the concrete due to corrosion, conversion of the modes could be tracked to detect the defect; however, in the case of randomly distributed voids, clear mode conversion cannot be observed. However, the voids capable of disturbing the R-wave travelling with a constant velocity depending on their sizes and the locations. Therefore, the dispersion index, which was introduced in Chapter 6, is found suitable to quantify the defect volume. In Figure 7.26, the selected portions of the curves are shown to assess the DI presented in Figure 7.27. The control beam is presented with zero in the curve, simply because its dispersion behavior is assumed zero due the fact that the reference curve is obtained from it. The trend of DI can be approximated as linear after excluding the control beam (B1). Compared to the attenuation coefficient, the DI displays same level of variation with a COV of 35% and a R^2 of 0.89. The change in DI between Beam 2 and 6 is almost 100%; which emphasizes DI as a promising parameter for evaluation of concrete members.

As a supplementary analysis, the dispersion curves are also obtained under lateral excitation. The horizontal configuration of the source provides the symmetrical (longitudinal) modes amplified as shown in Figure 7.28. In this case, the first symmetrical Lamb mode (S0) for Beam 1 in the dispersion curve plot is extracted to evaluate the dispersion behavior for the rest of the beams. The dispersion index for the horizontal excitation, DI_h , (Fig. 7.29) is not found capable of capturing any linear correlation with $R^2 = 0.58$ unlike the vertical excitation case (Fig. 7.27). However, a linear increase in dispersion is evident among Beam 2, 3 and 4; however, beyond 15% void ratio, the DI_h is not sensitive anymore to the increasing defect volume. Most probably the large distance between the source and the receivers array (30 cm) coupling with the large void content in Beam 5 and 6 makes the DI_h insensitive to the defect amount. It is recommended to repeat the tests for smaller source offset under horizontal excitation.

7.6 Summary and Conclusions

Six lab-scale concrete beams with different void percent were produced and tested using ultrasonic and mechanical equipment. The relationships between the defect volume and the

characteristics, namely P-wave and Rayleigh-wave velocities, attenuation coefficient, material damping ratio and dispersion index along with the compression strength are investigated performing various digital signal processing methods. Based on the presented investigations the following conclusions can be offered.

- The signal processing procedure developed for the half space medium in Chapter 6 is modified for the beams as shown in Figure 7.30.
- 2D Fourier transform is the most common method to expose the incident and reflected events in a data set. However, the experimental data do not always clearly reveal the events separately. For this reason, in this study, the time signals are first windowed and then the transforms are performed.
- Attenuation coefficients are improved by windowing the time signals to allow only the energy dissipation of the incident event to be determined.
- Linear correlations are observed for the P and R wave velocities, attenuation and DI with respect to the defect amount. The statistical findings are tabulated in Table 7.3.

Table 7.3 Summary of the statistics for characteristics

Characteristic	Statistics			
	σ	COV	R^2	Sensitivity ^[3]
Strength	12.7 MPa	43%	0.98	79%
V_P	305 m/s	7.4%	0.97	20%
V_R	260 m/s	12.6%	0.92	32%
α^[1]	2.5 m ⁻¹	32%	0.89	122%
ζ	1.09%	32%	0.26	119%
DI^[2]	N/A	35%	0.88	55%

[1] Determined based on windowed signals, [2] Determined for the vertical excitation, [3] Sensitivity refers the total change over to the initial value.

- α exhibits a sensitivity factor over than 100% as being the most sensitive characteristics for quantifying the damage; it is followed by the velocities, and then the DI.
- Material damping ratio could not capture the damage level due to the fact that the geometric attenuation coefficient given as -0.5 for surface waves does not fit the beam geometry.

- Attenuation, P and R-wave velocities and dispersion index are found as the promising characteristics for quantifying the defect volume.













Beam 1		
Beam 2		
Beam 3		
Beam 4		
Beam 5		
Beam 6		

Figure 7.1: The beams and the associated cones from the compression tests of cylinders.

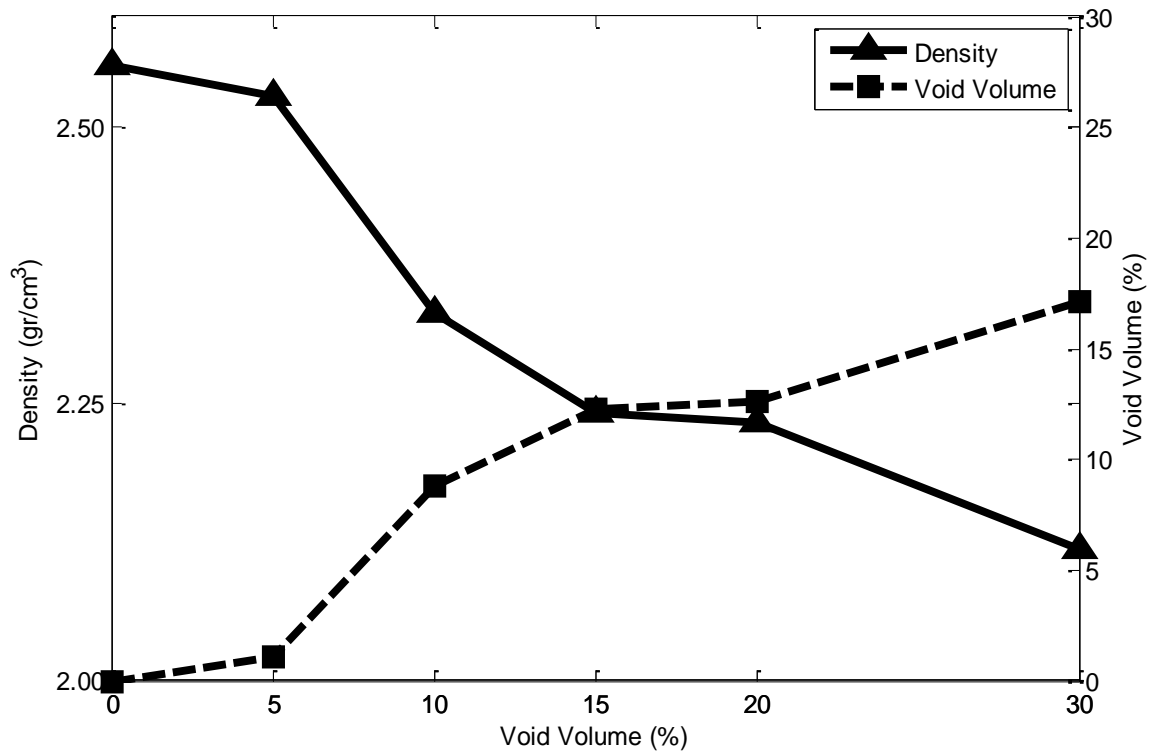


Figure 7.2: Beams' density vs. design void volume (blue curve) and void volume computed based on the density vs. design void volume (red curve). Red curve represent the relative void volume respect to Beam 1, actual values should be larger than the ones provided in the plot.

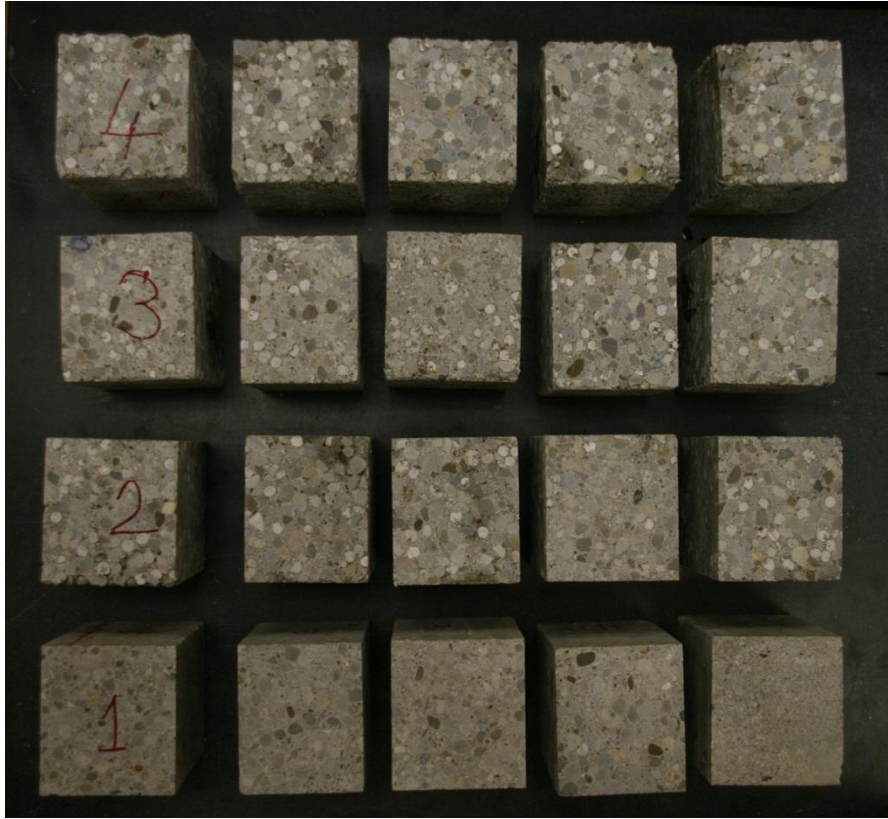


Figure 7.3: The prisms cut out from the beams.




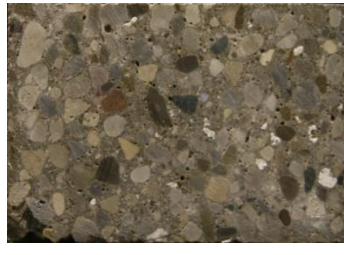



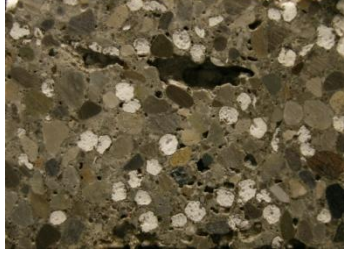




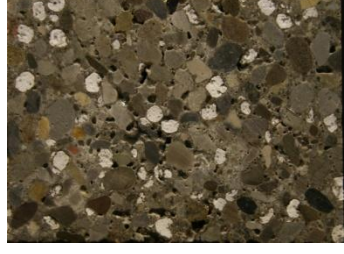



Beam 1			
Beam 2			
Beam 3			
Beam 4			
Beam 5			
Beam 6			

Figure 7.4: The selected cross-sections of the beams.

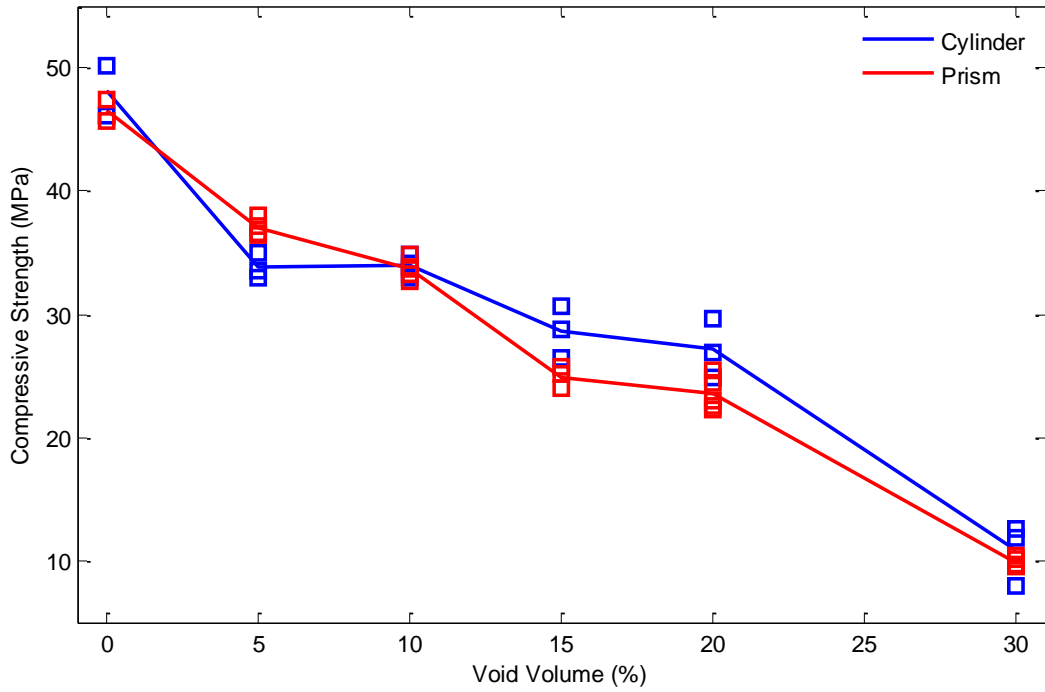


Figure 7.5: Compressive strength for the cylinders and the rectangular prisms samples cut out from the beams vs. void volume. Outliners are excluded.

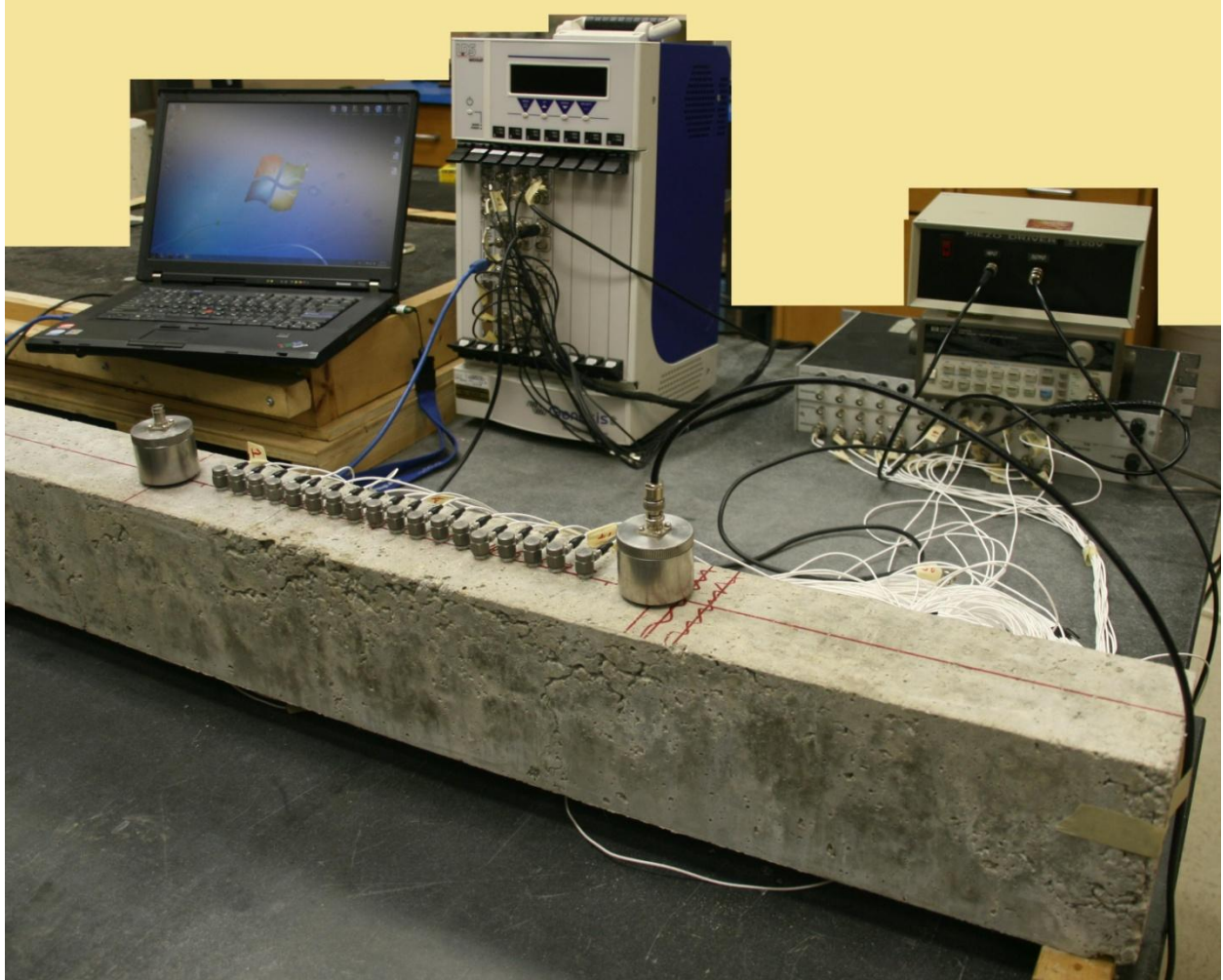


Figure 7.6: Ultrasonic testing instrumentation

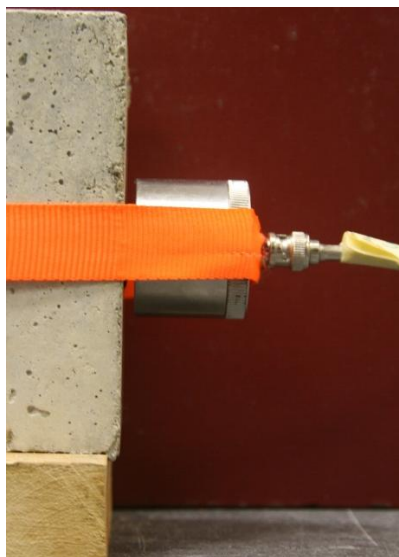


Figure 7.7: Lateral excitation configuration.

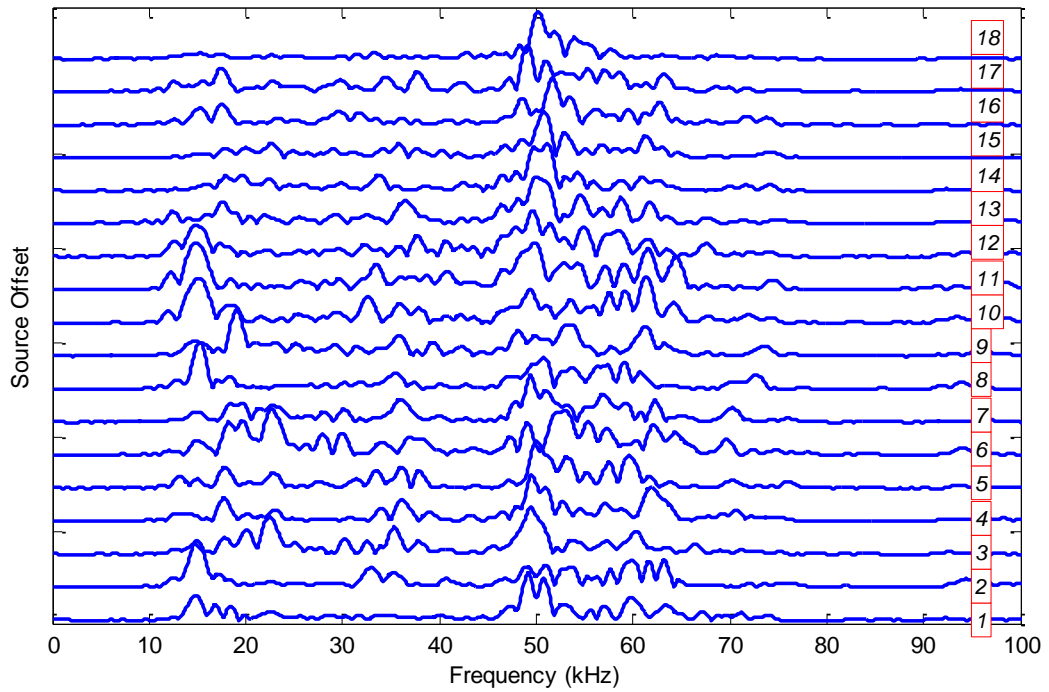
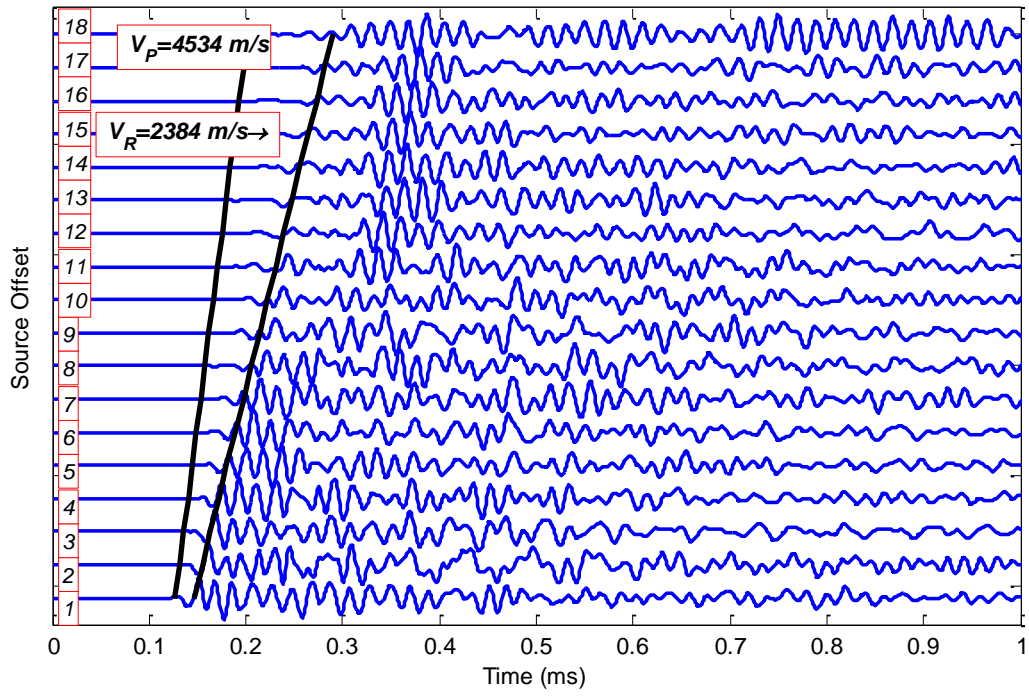


Figure 7.8: (a) Time histories and (b) frequency spectra for Beam 1 (no-void case).

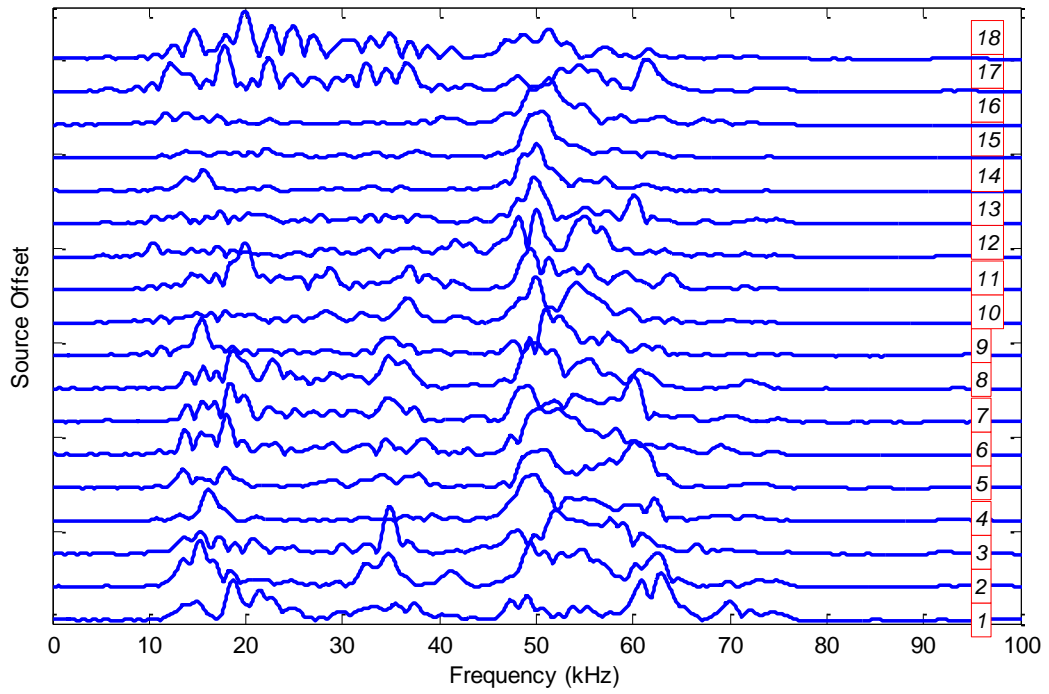
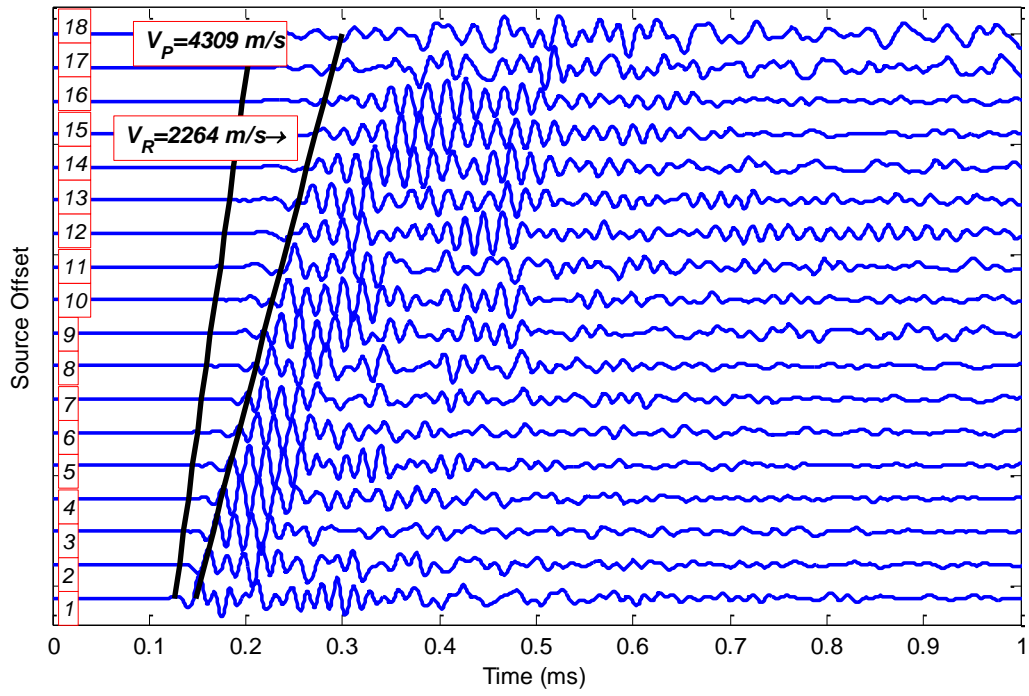


Figure 7.9: (a) Time histories and (b) frequency spectra for Beam 2 (%5 void).

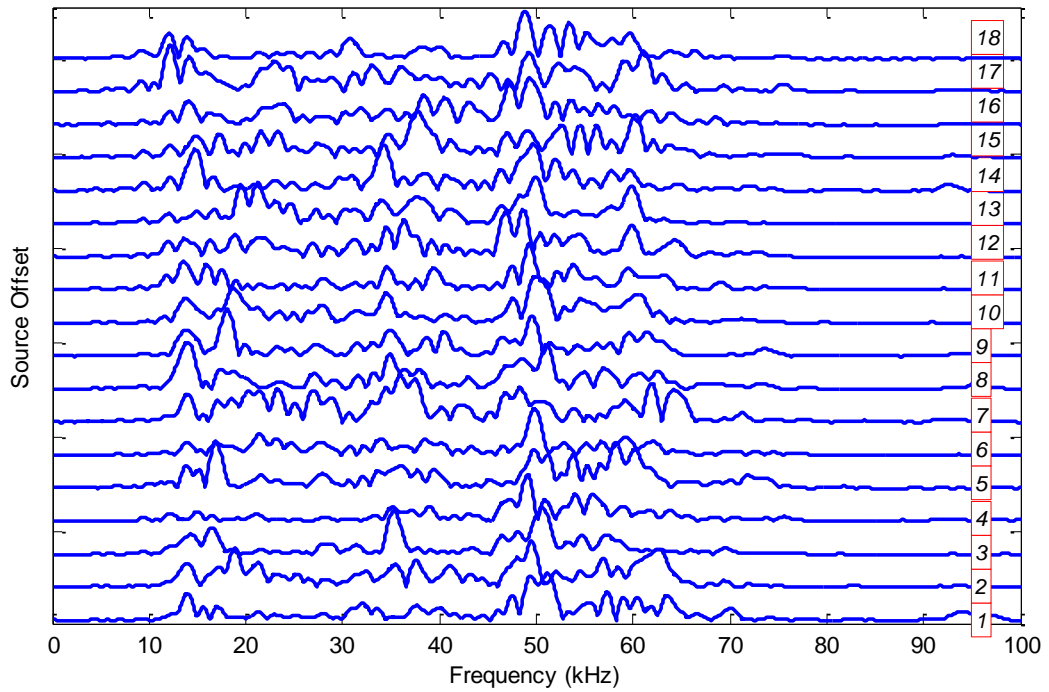
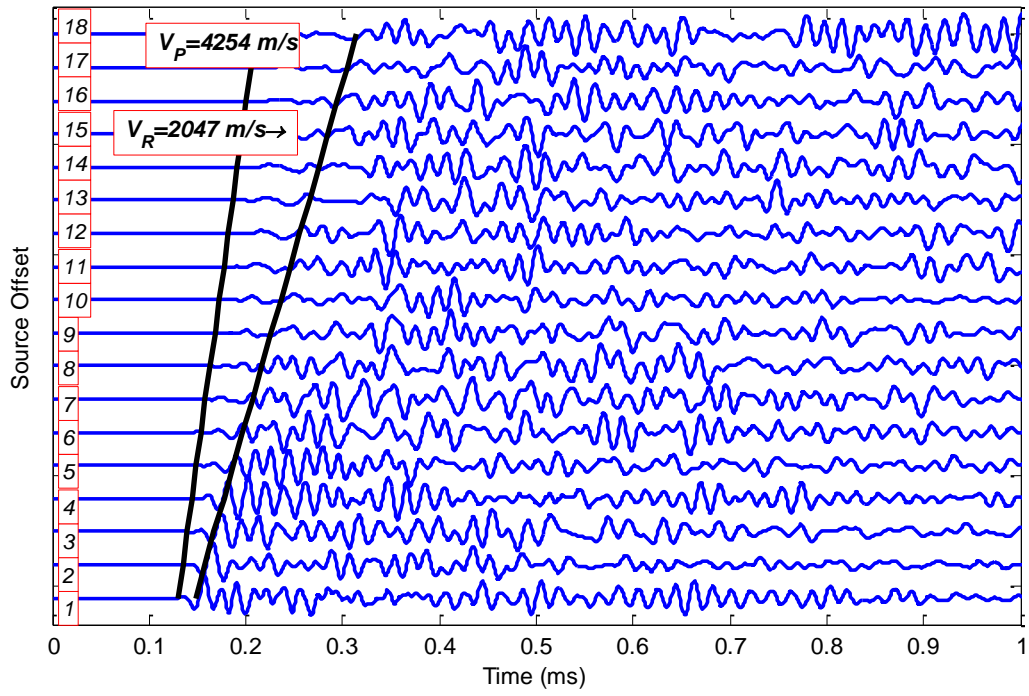


Figure 7.10: (a) Time histories and (b) frequency spectra for Beam 3 (%10 void).

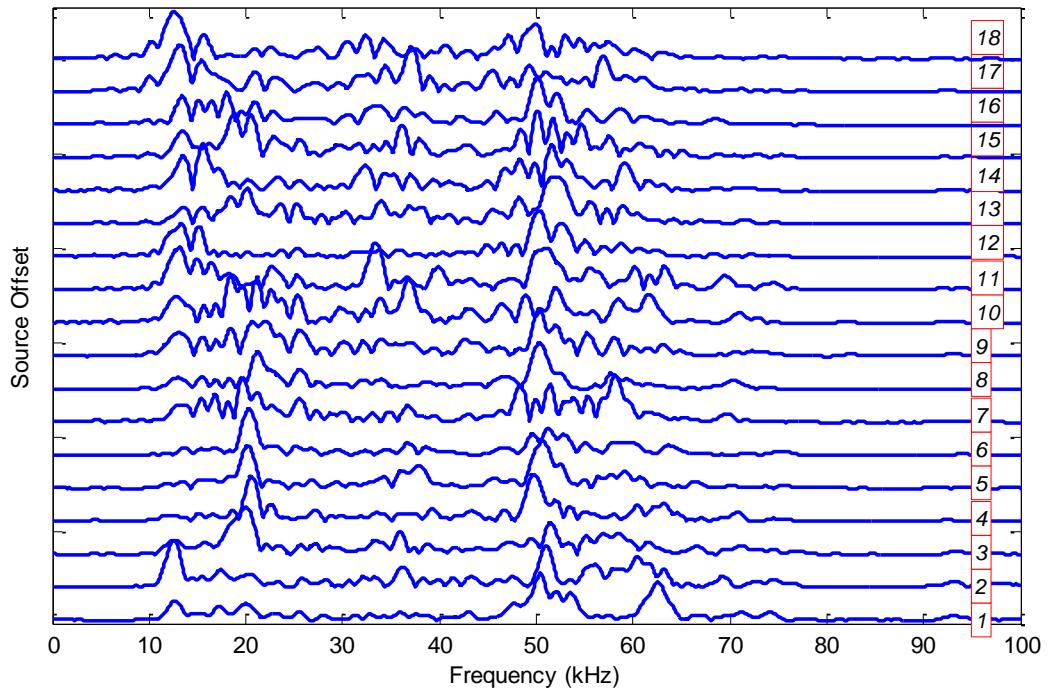
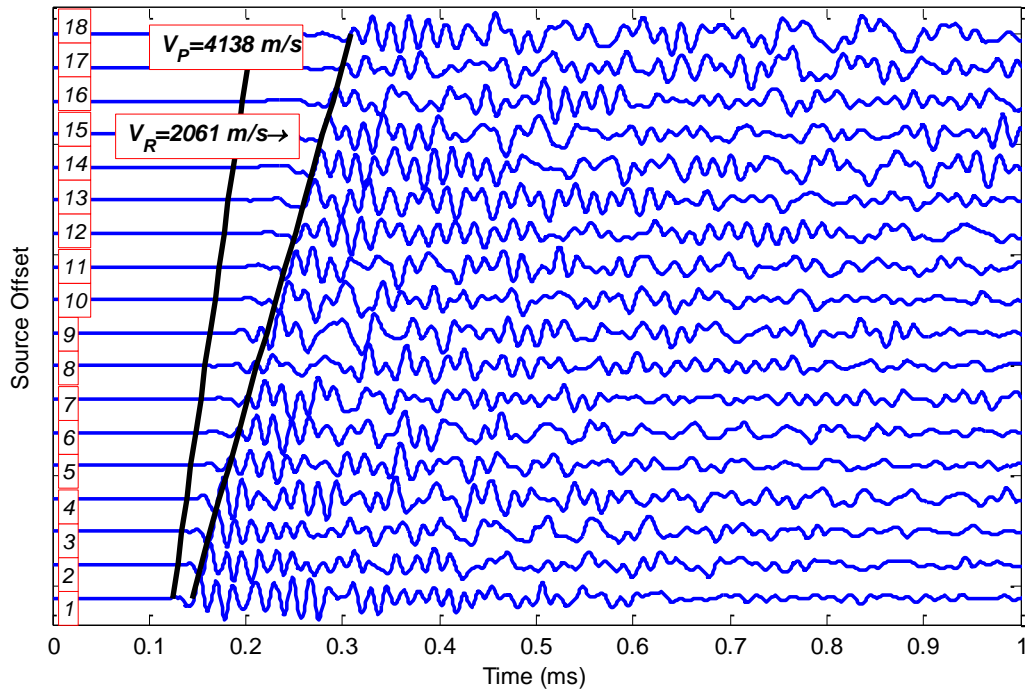


Figure 7.11: (a) Time histories and (b) frequency spectra for Beam 4 (%15 void).

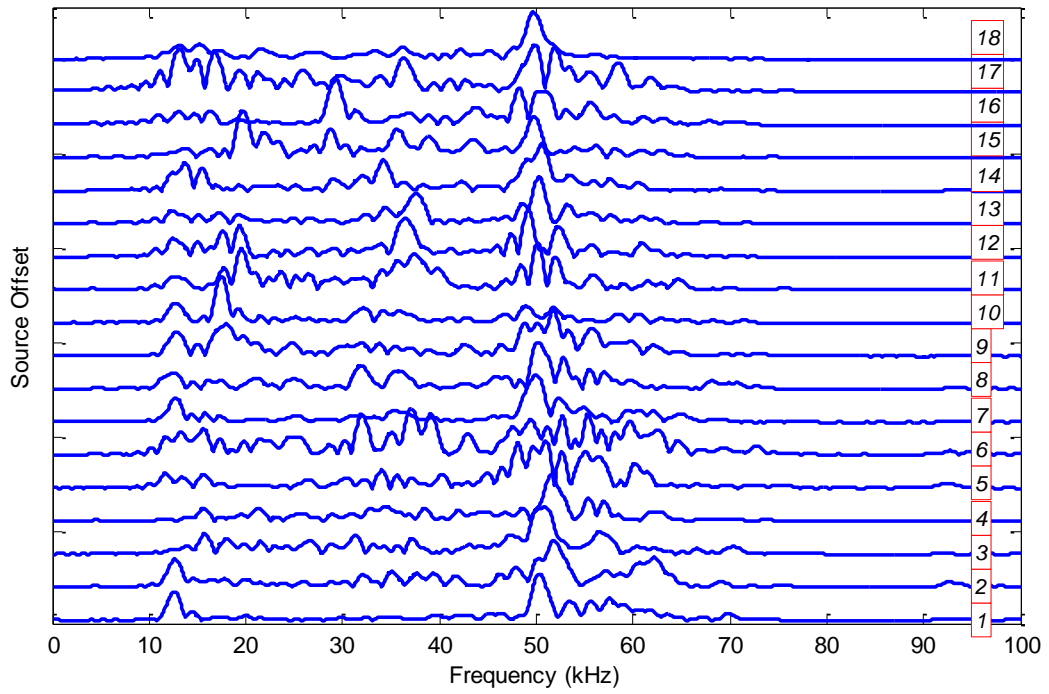
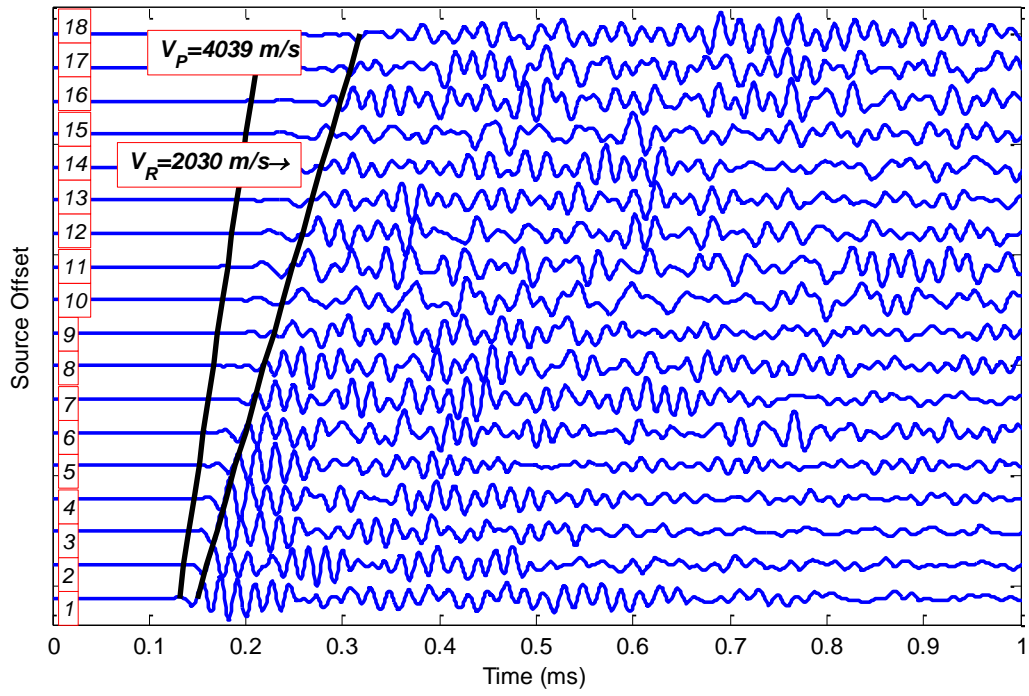


Figure 7.12: (a) Time histories and (b) frequency spectra for Beam 5 (%20 void).

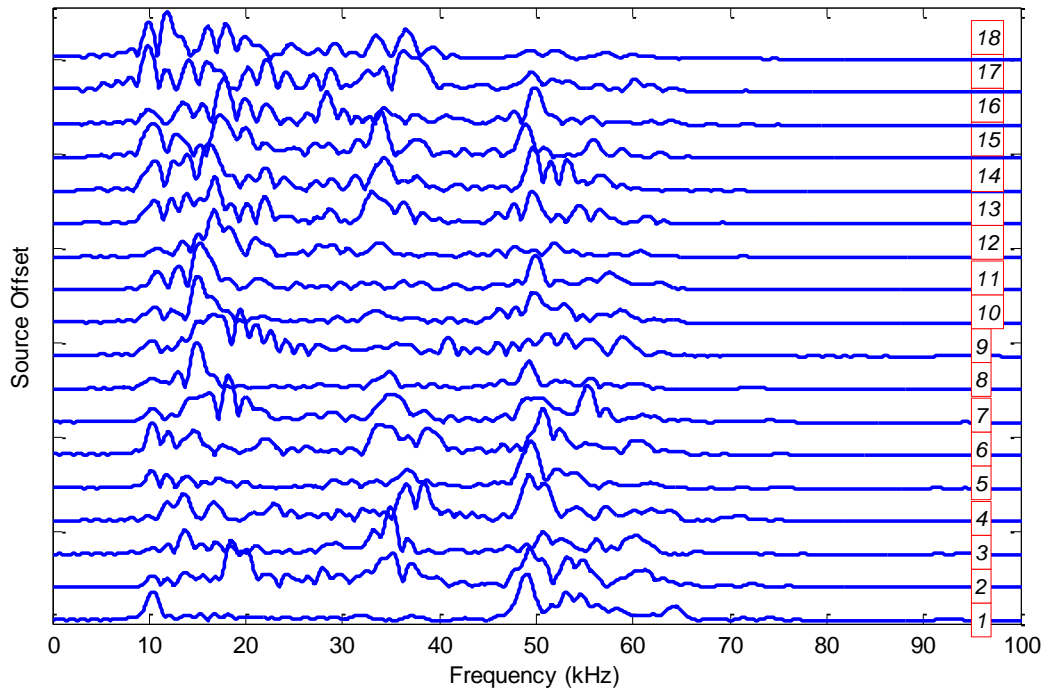
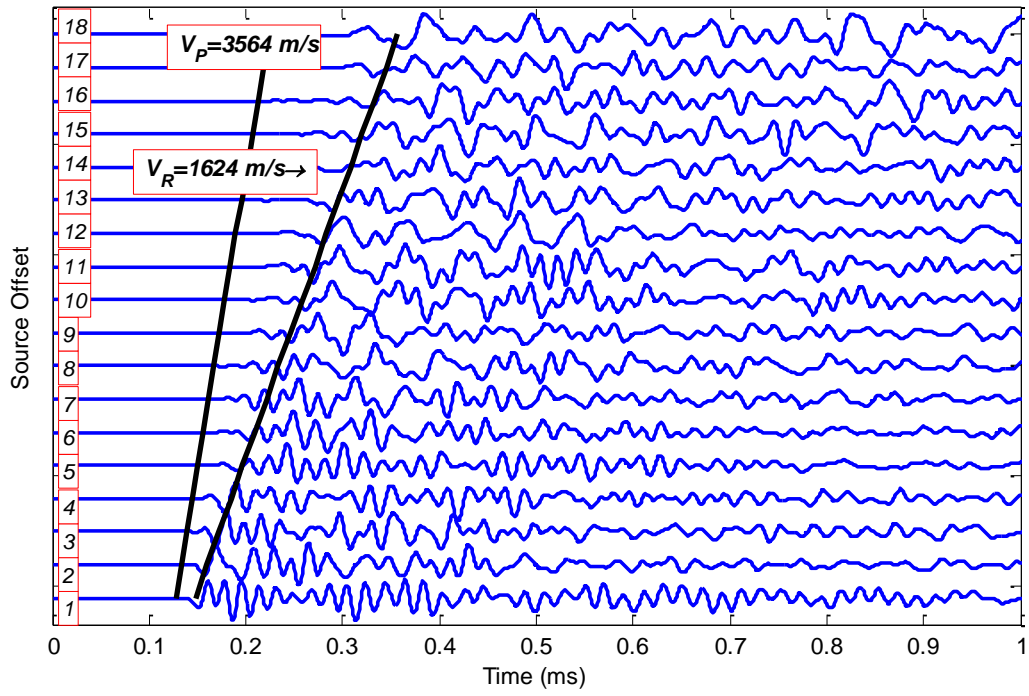


Figure 7.13: (a) Time histories and (b) frequency spectra for Beam 6 (%30 void).

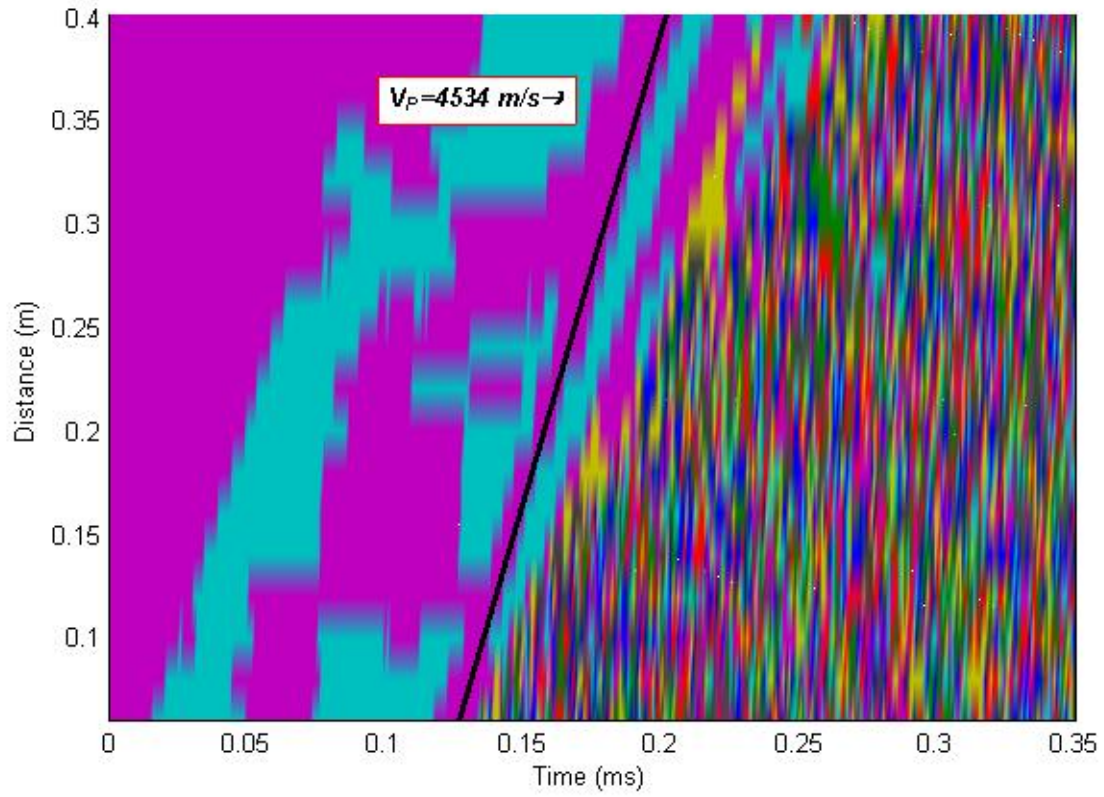


Figure 7.14: P-wave velocity computed for Beam 1.

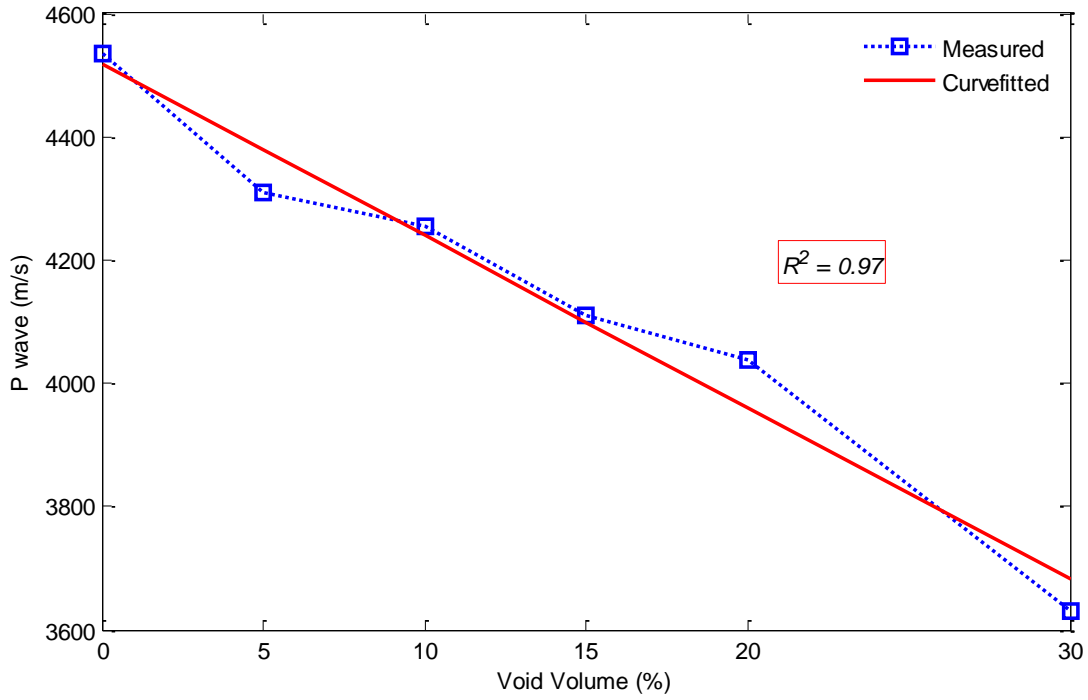


Figure 7.15: P-wave velocity computed from time histories vs. void volume of beam.

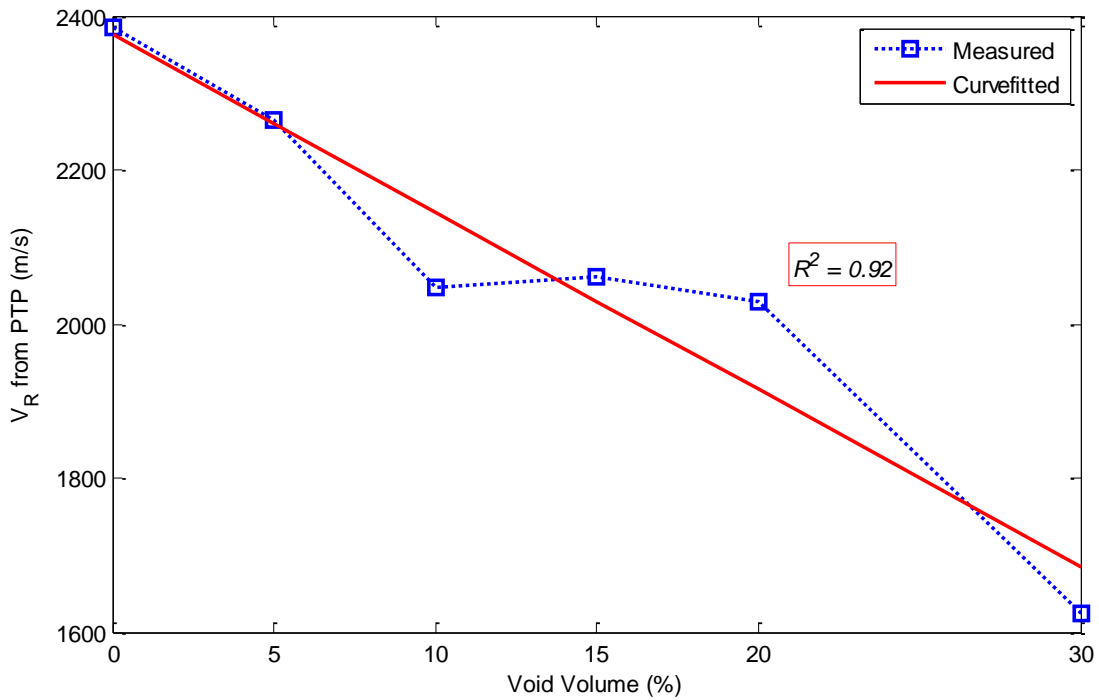


Figure 7.16: Rayleigh wave velocity computed from PTP magnitudes vs. void volume of beam.

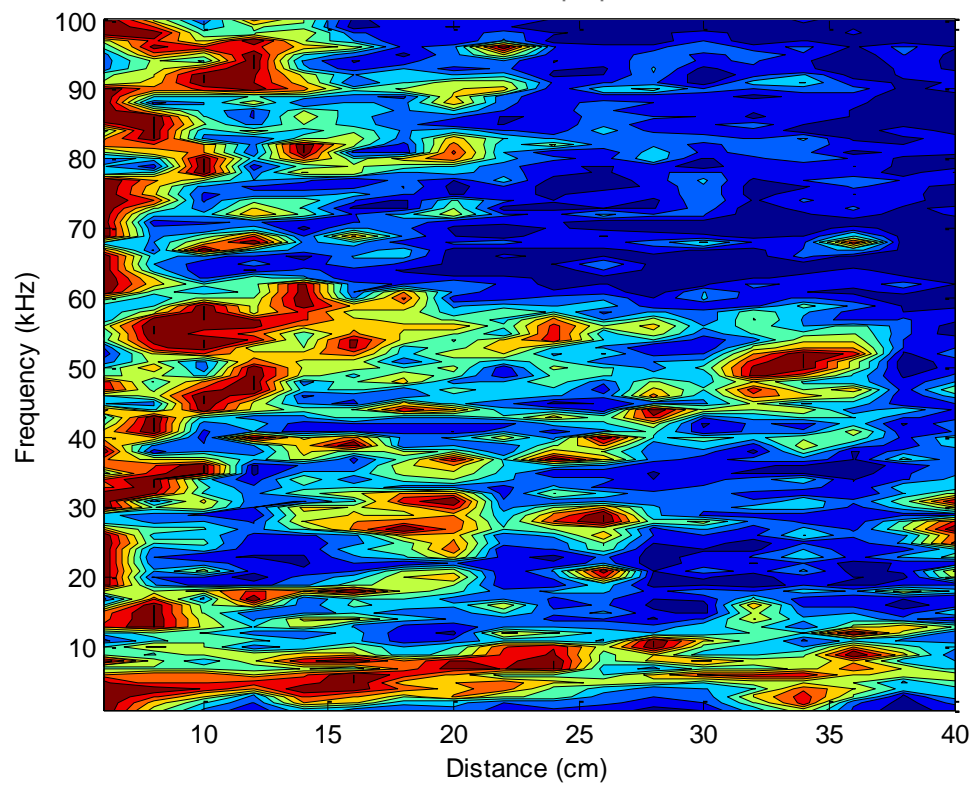
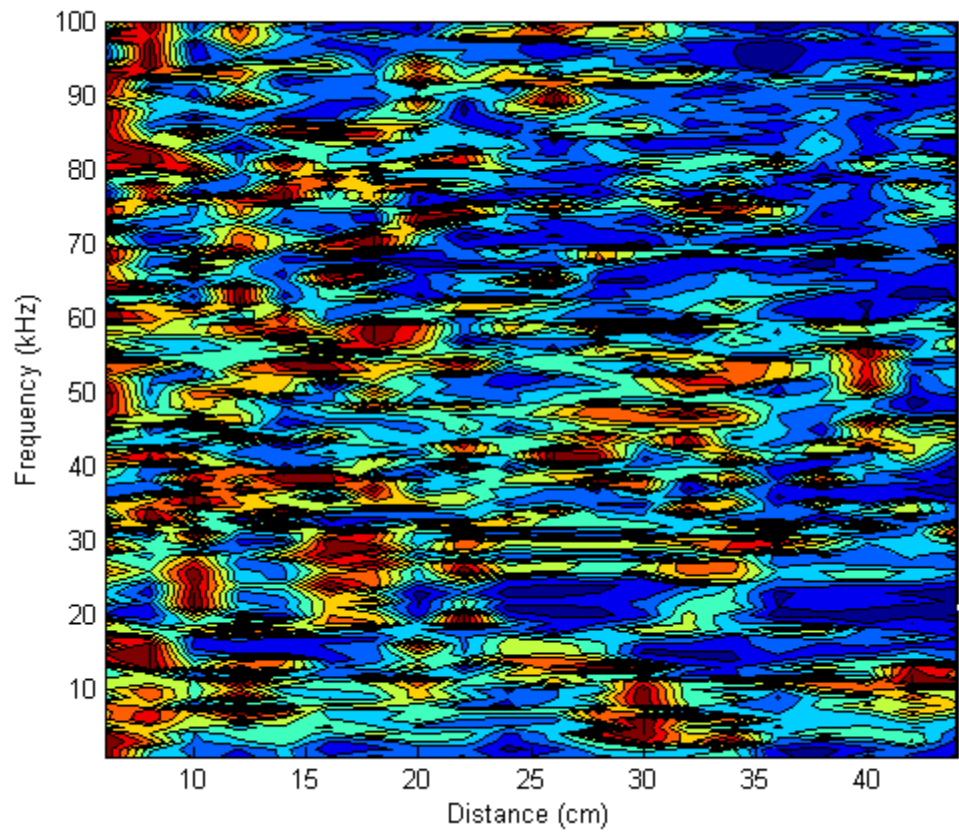


Figure 7.17: Attenuation trend for all frequencies (a) Beam 1, (b) Beam 2.

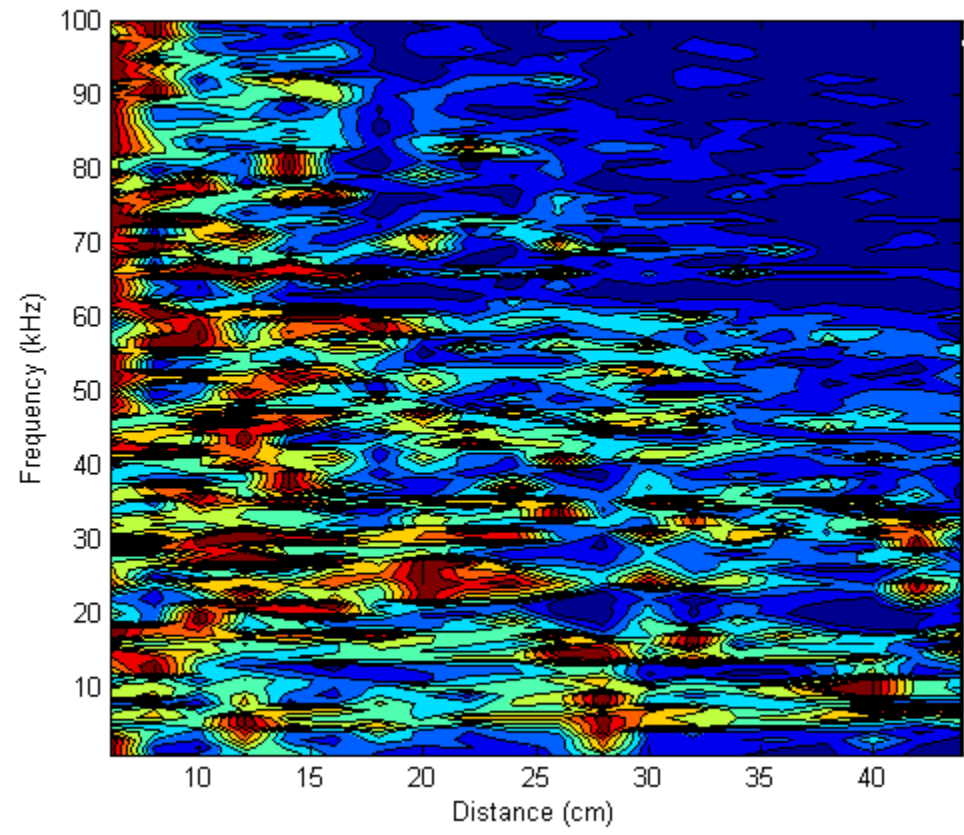
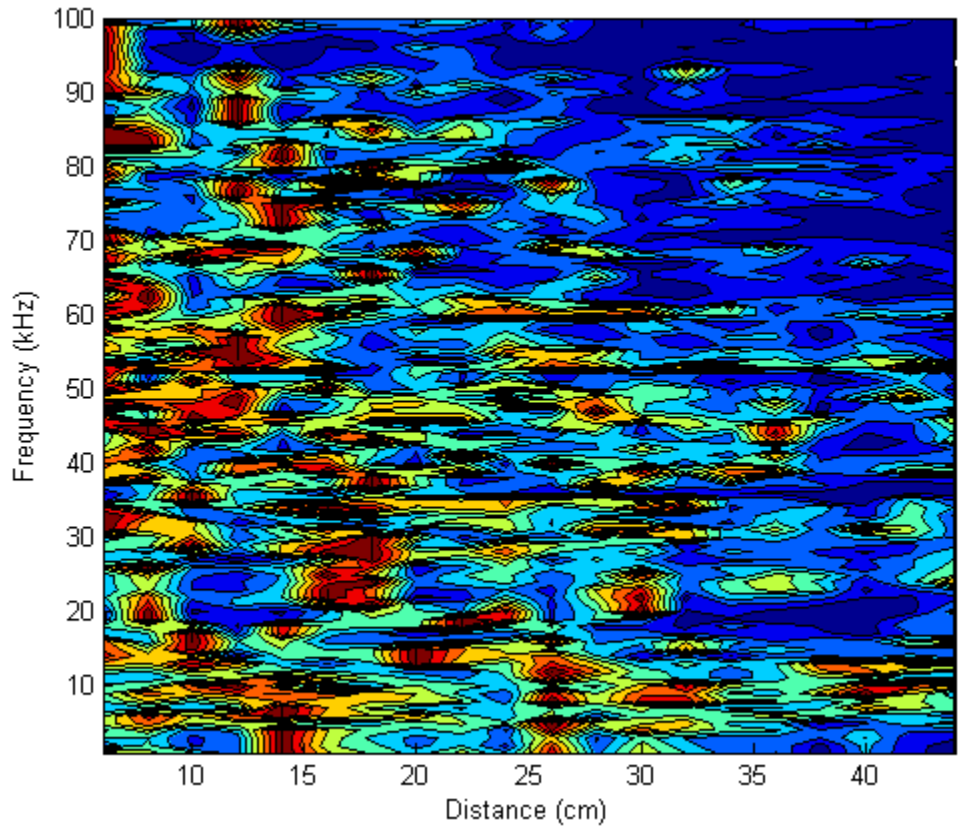


Figure 7.17: Attenuation trend for all frequencies (c) Beam 3, (d) Beam 4.

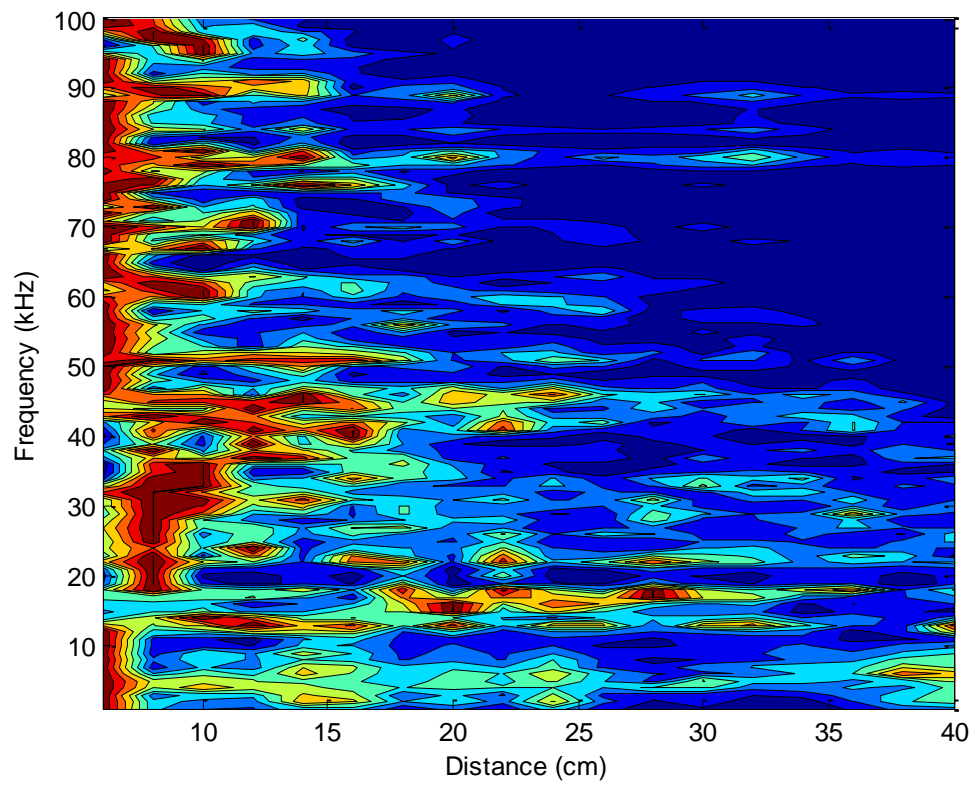
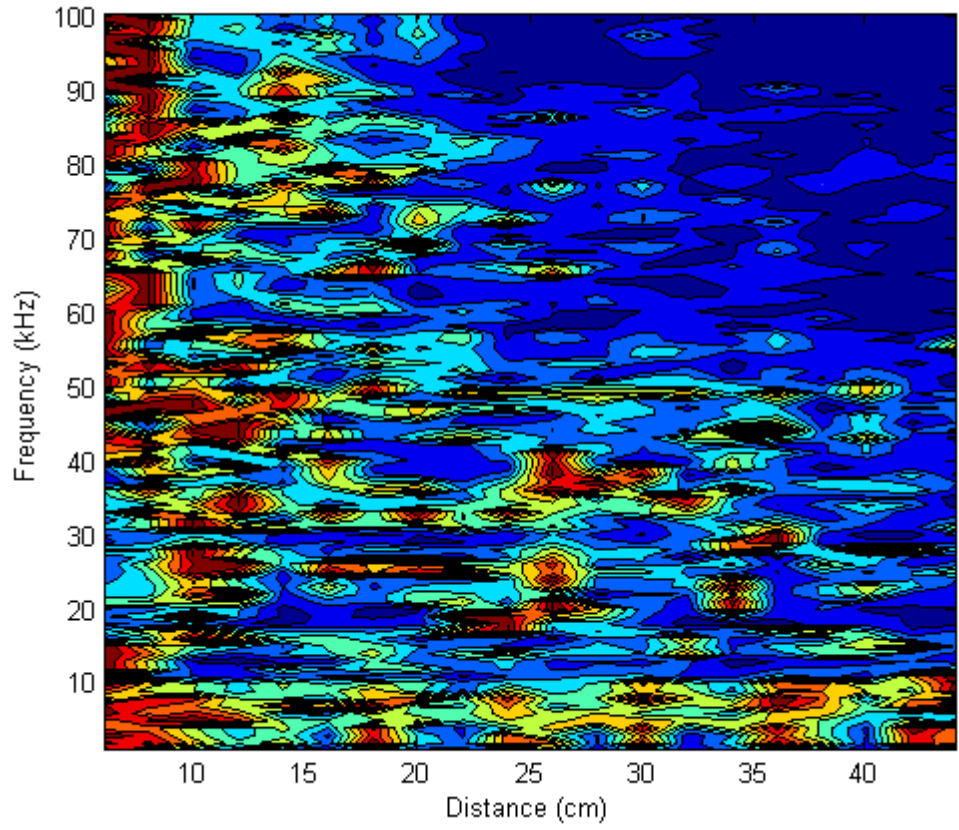


Figure 7.17: Attenuation trend for all frequencies (c) Beam 5, (d) Beam 6.

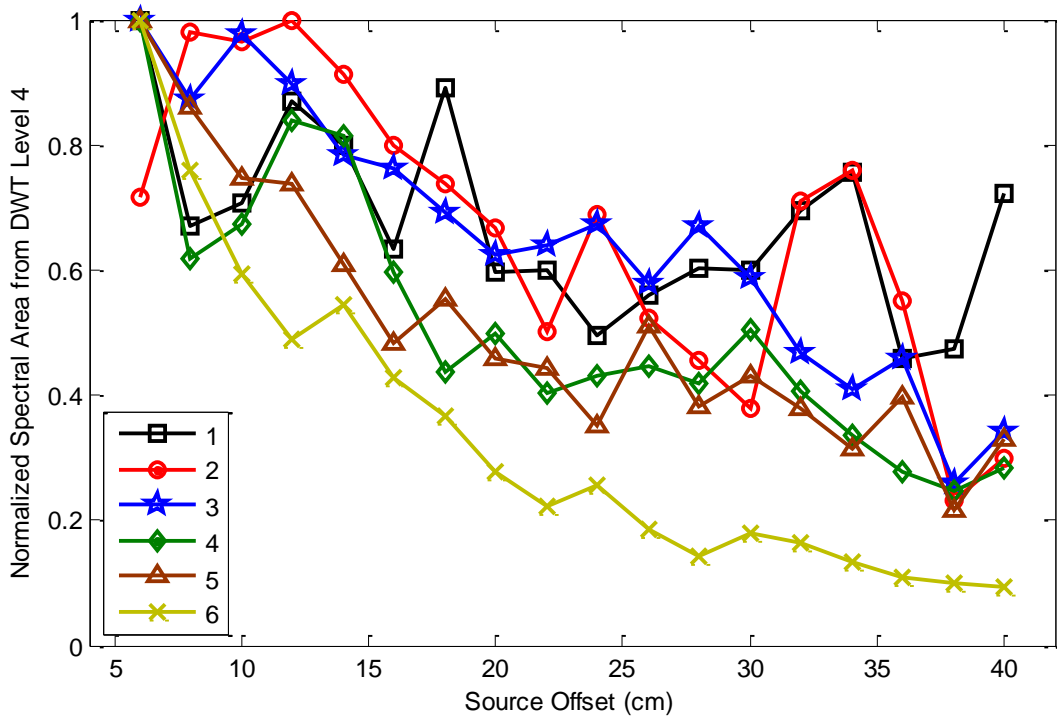


Figure 7.18: Attenuation trends for each beam obtained from DWT (Level 4).

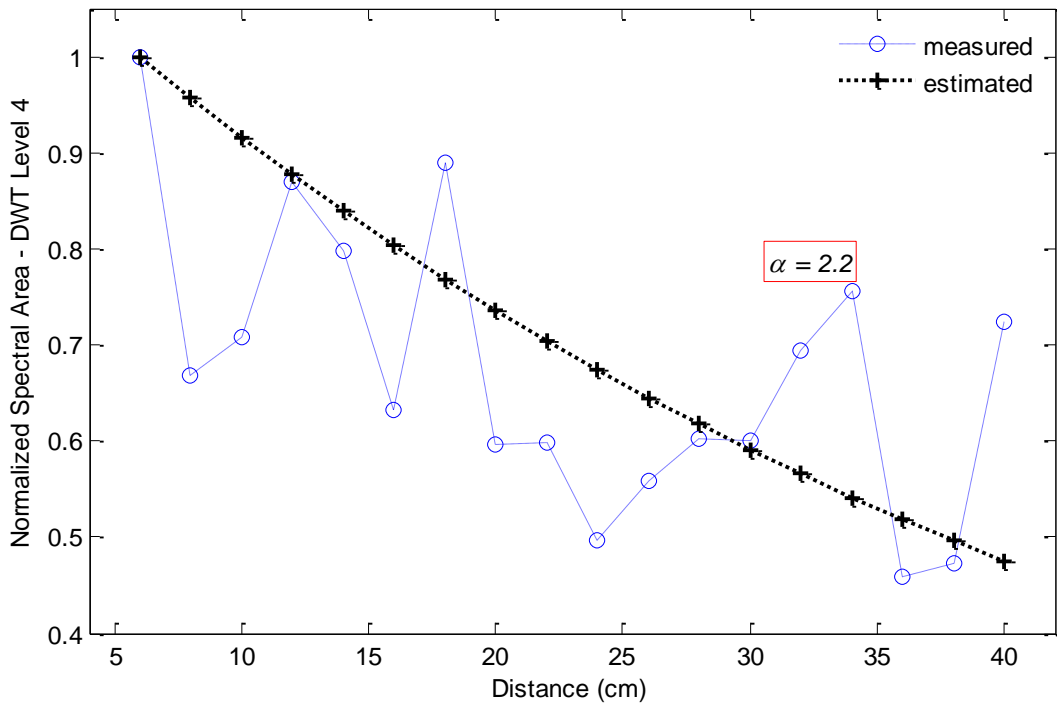


Figure 7.19: The measured and curve-fitted attenuation trends; α is computed from the curve-fitted trend.

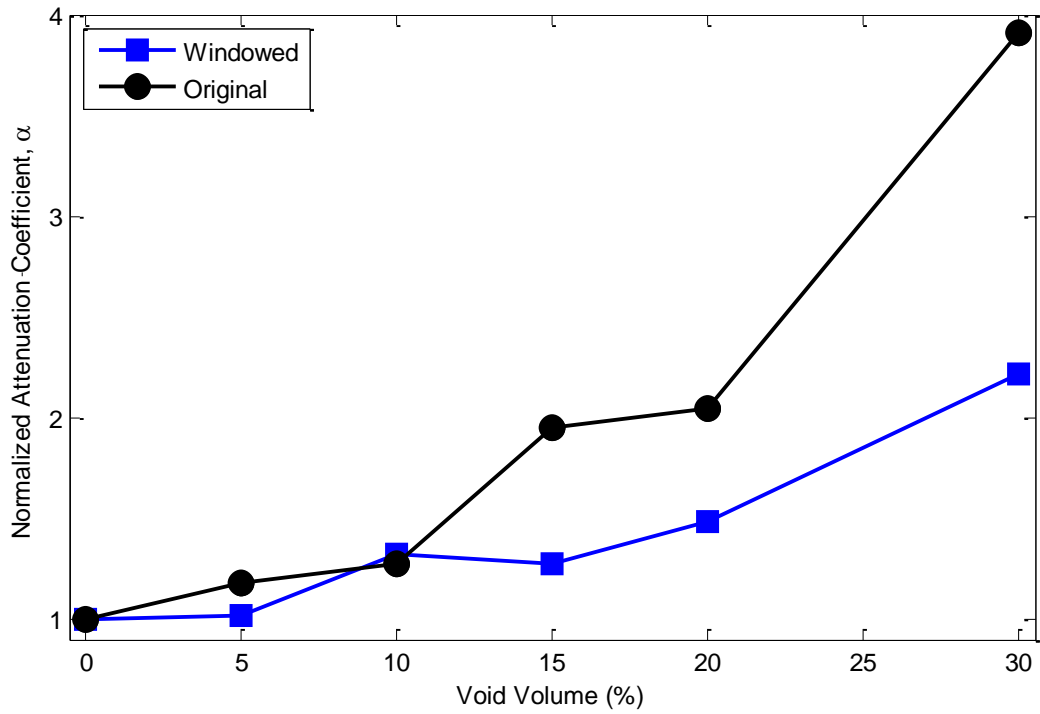


Figure 7.20: Attenuation coefficients vs. void ratio.

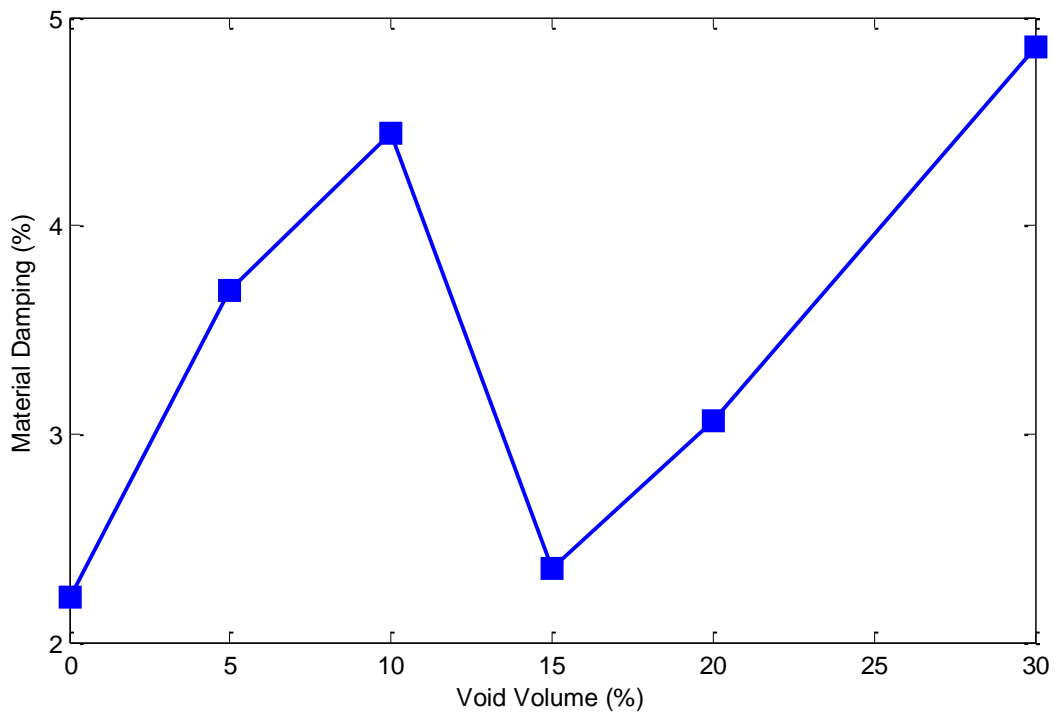


Figure 7.21: Material damping ratio computed from WT vs. void volume of beam.

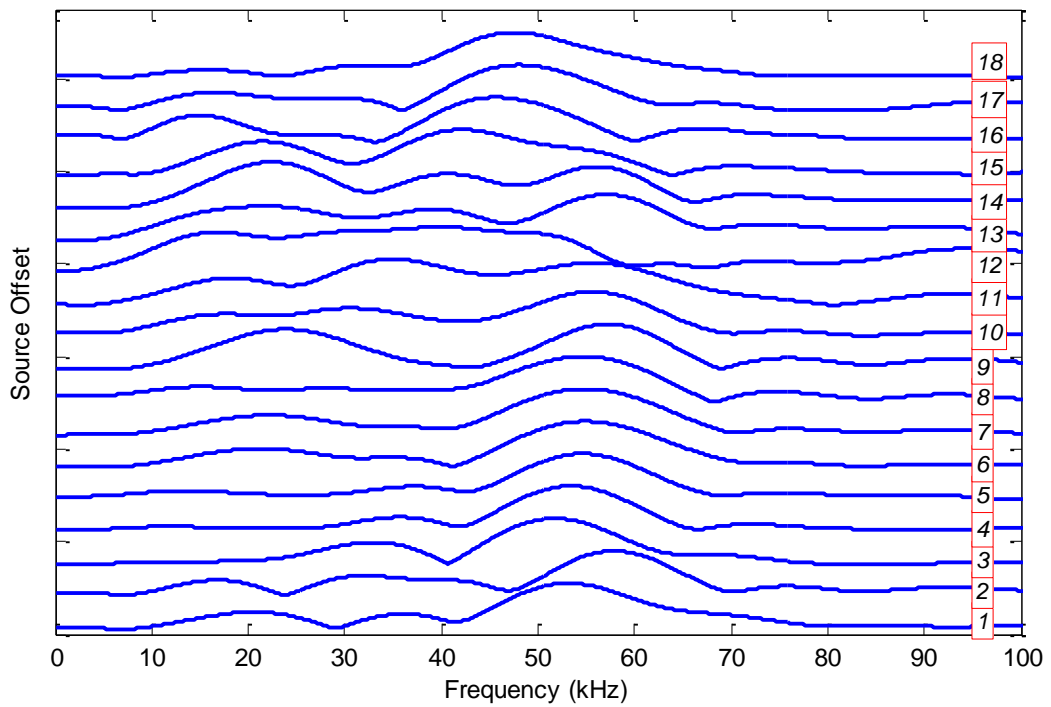
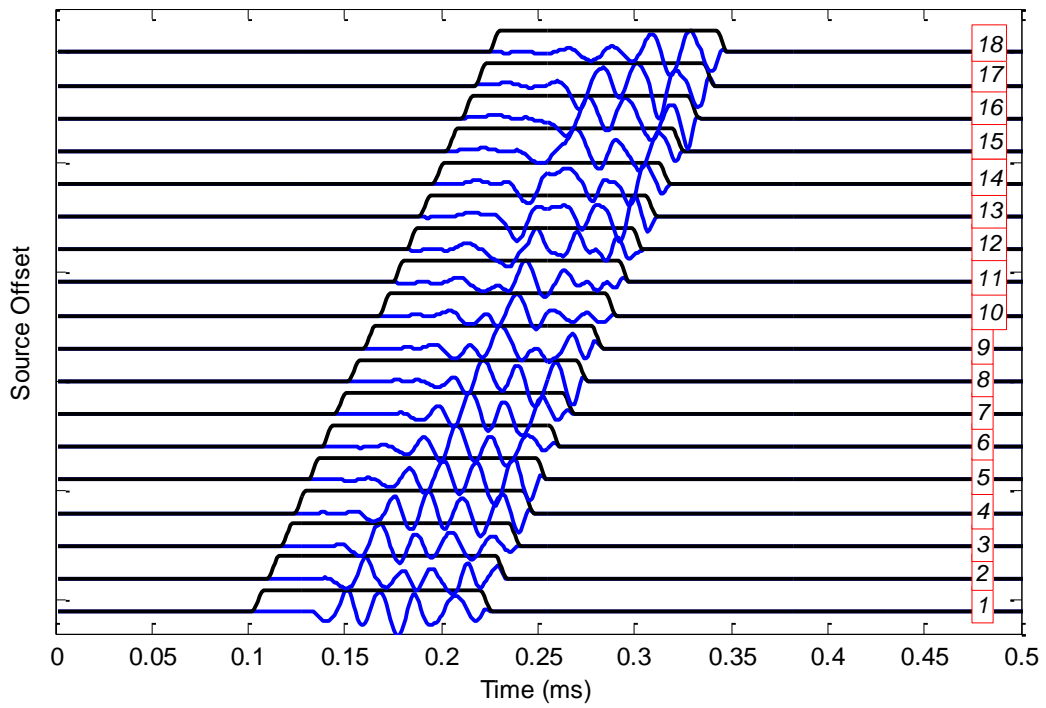


Figure 7.22: Windowed time signals and associated frequency spectra from Beam 1 for phase velocity calculations.

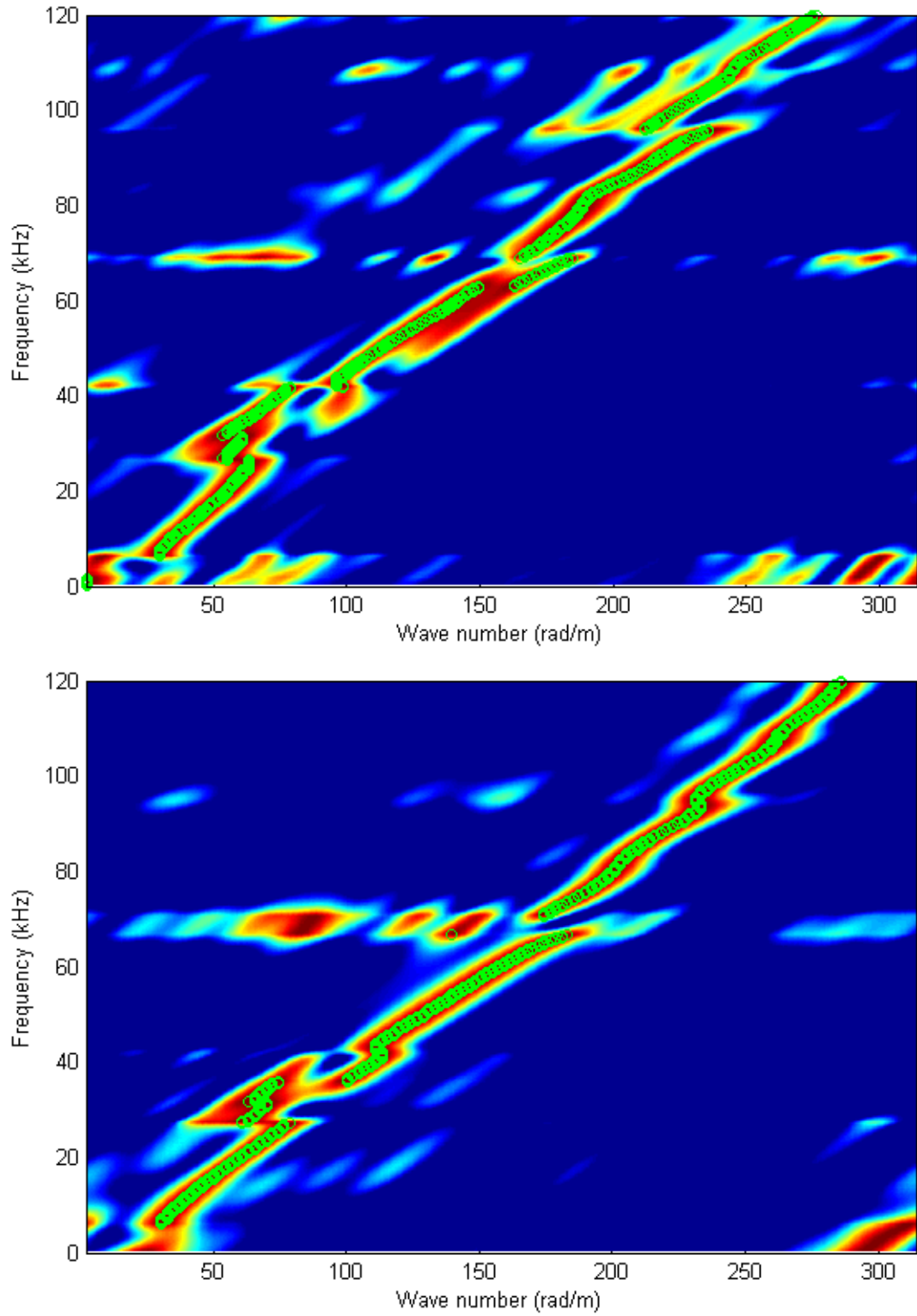


Figure 7.23: Frequency and wavenumber plots from windowed signals (a) Beam 1, (b) Beam 2.

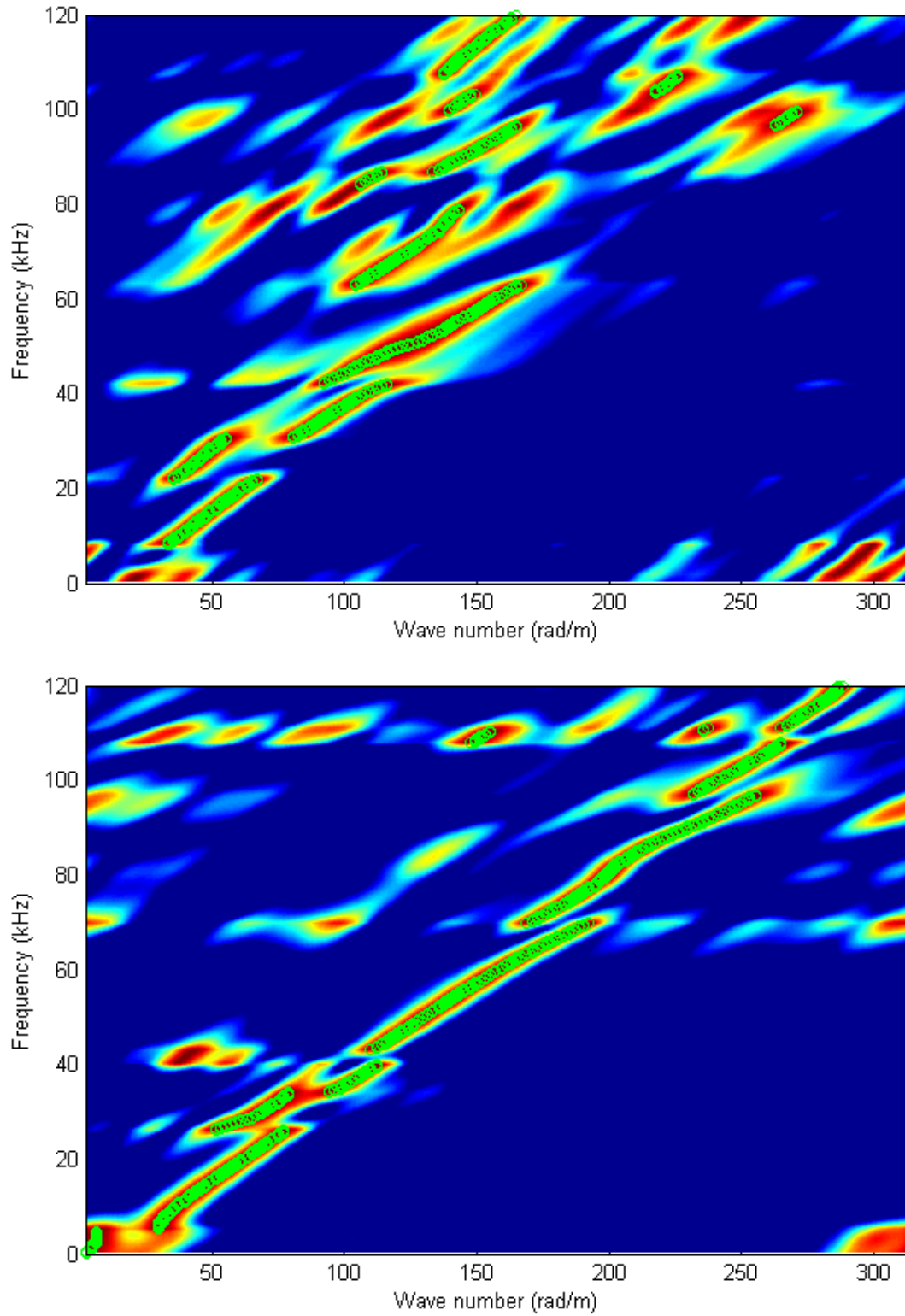


Figure 7.23: Frequency and wavenumber plots from windowed signals (c) Beam 3, (d) Beam 4.

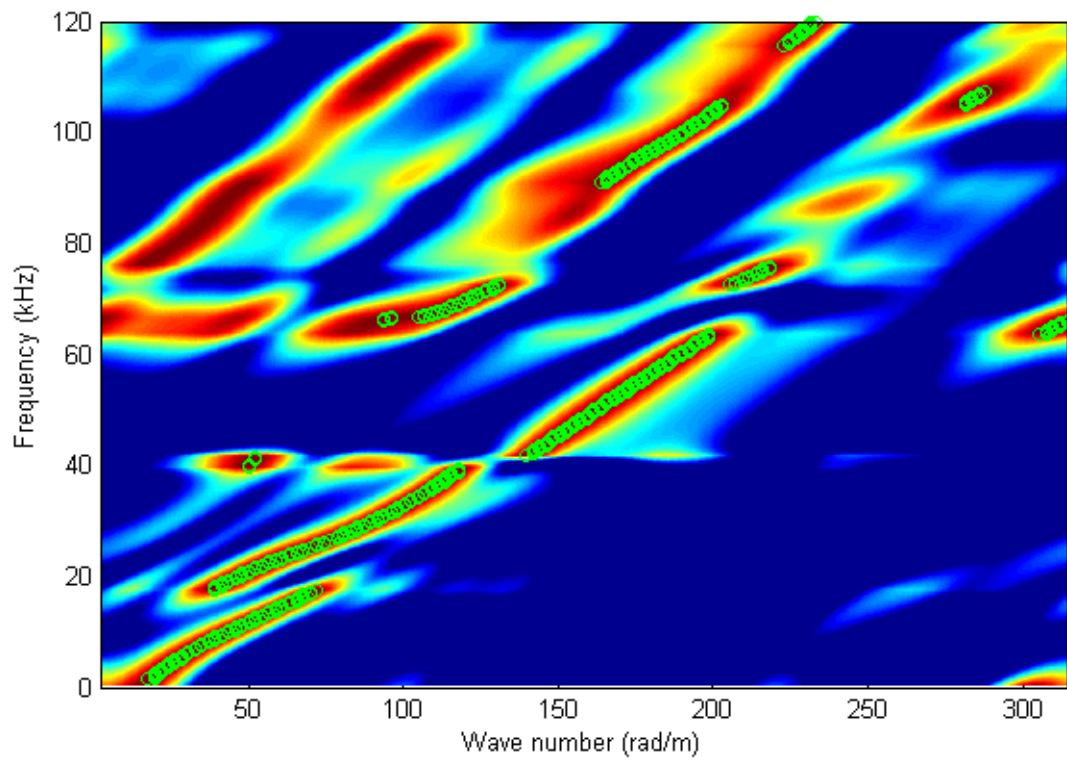
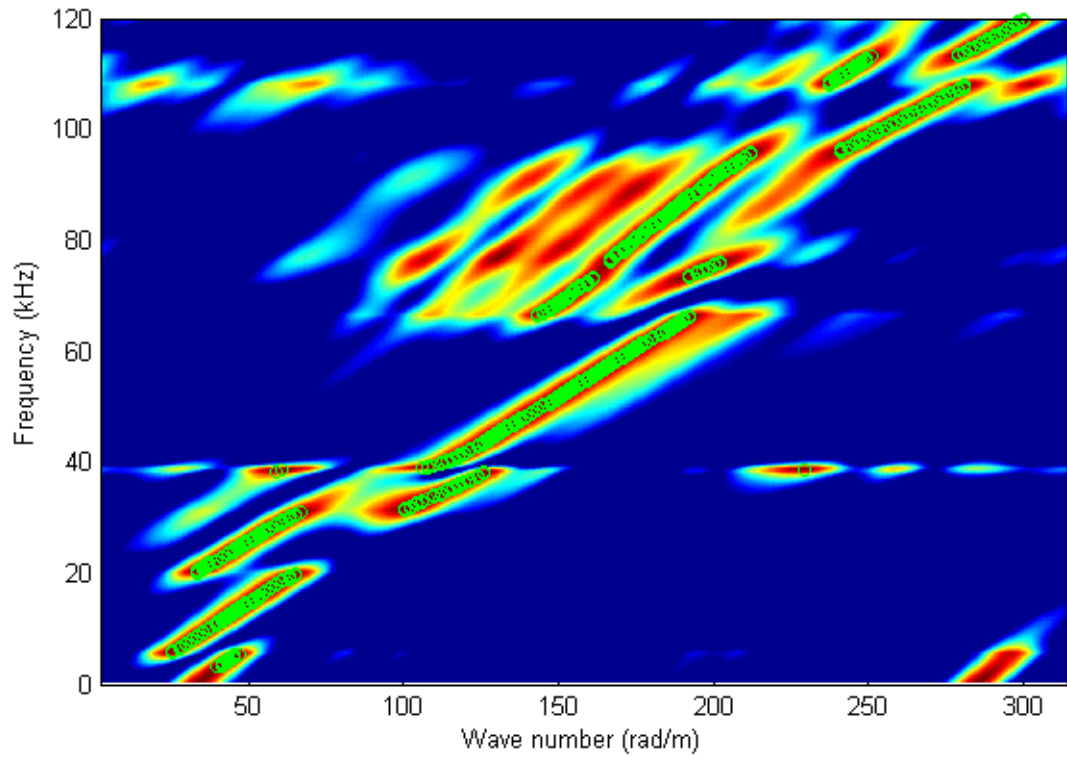


Figure 7.23: Frequency and wavenumber plots from windowed signals (e) Beam 5, (f) Beam 6.

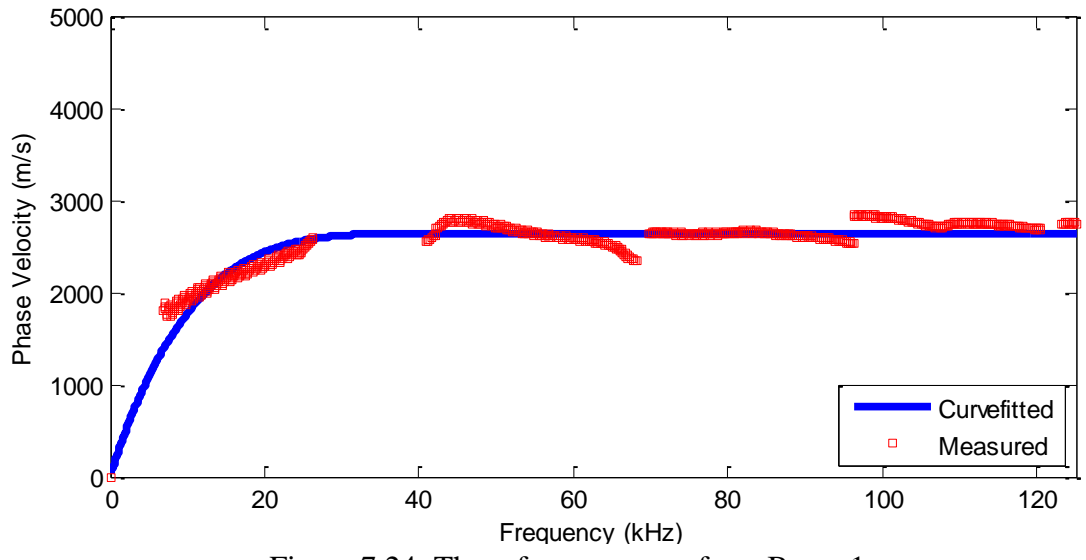


Figure 7.24: The reference curve from Beam 1.

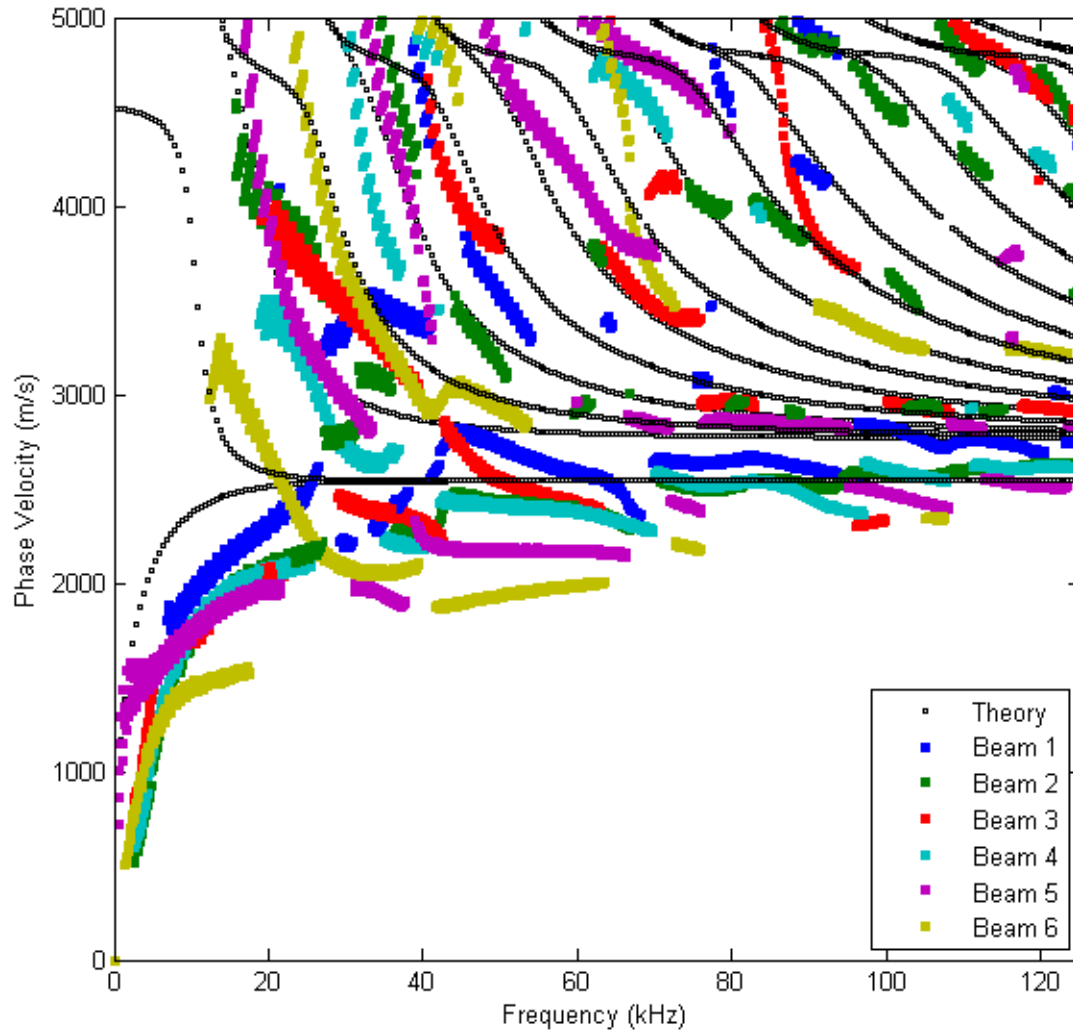


Figure 7.25: Experimental dispersion curves (two maximum points in the f - k plots (Figs. 7.23) are picked for each frequency) along with the theoretical Lamb modes that are obtained from the Rayleigh-Lamb frequency equation (Eq. 2.35a).

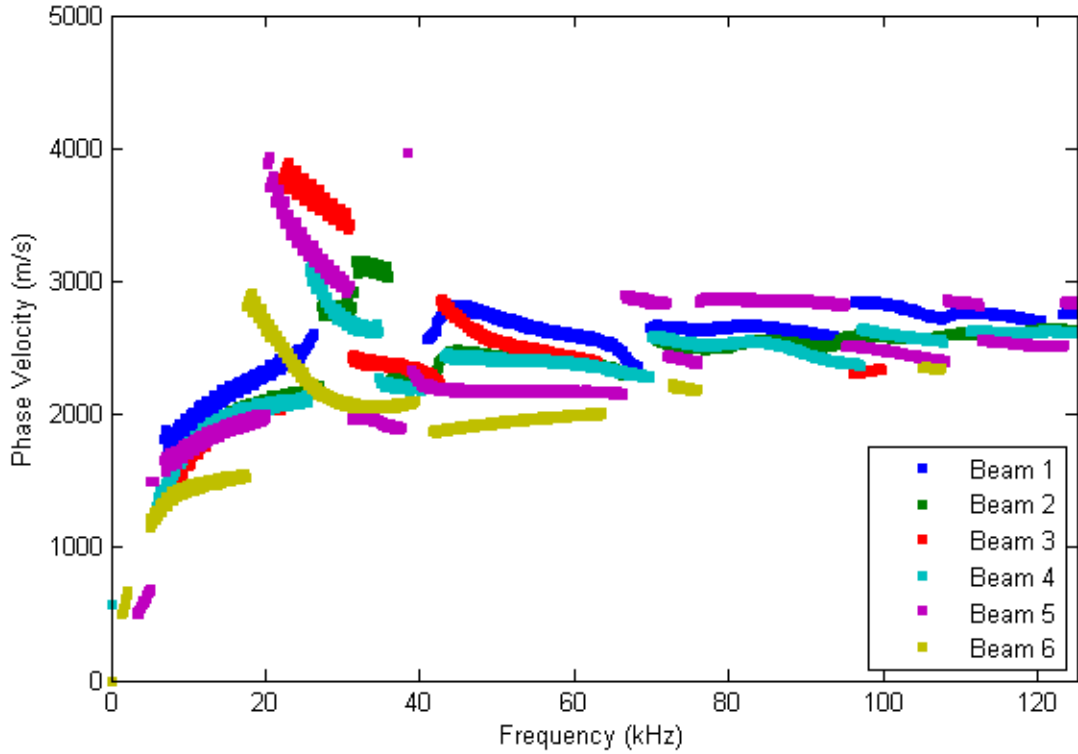


Figure 7.26: The selected portions of the dispersion curves (Fig. 7.25) to be used for the DI calculation.

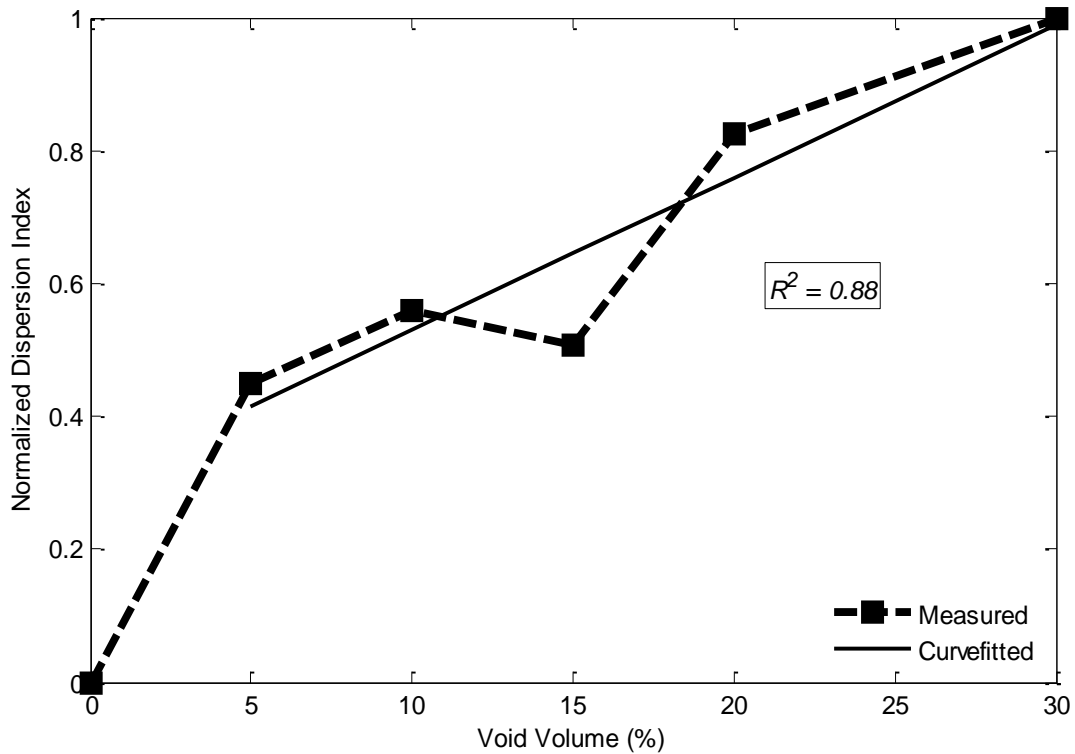


Figure 7.27: Dispersion index (DI_v) vs. void volume for vertical excitation.

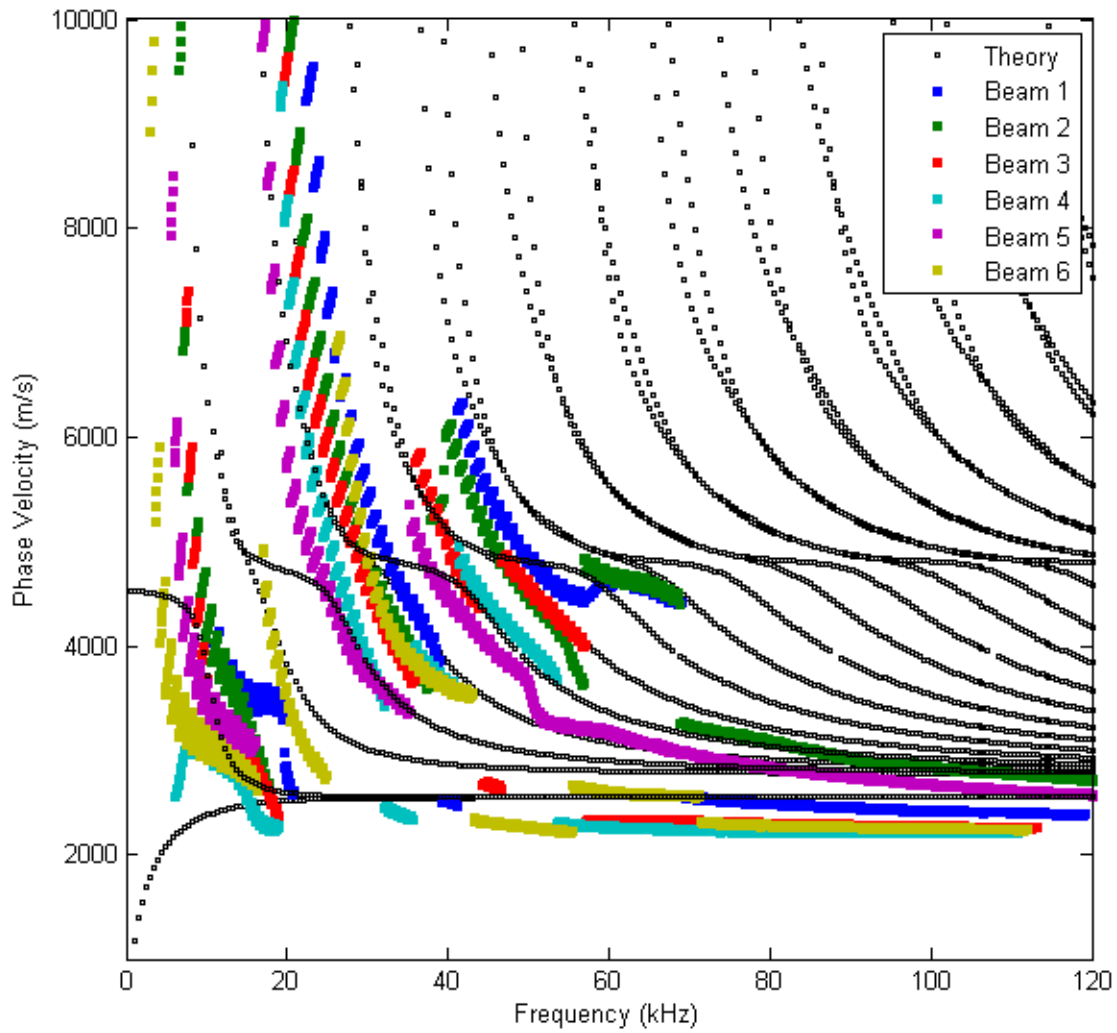


Figure 7.28: Dispersion curves attained under horizontally oriented transmitter. Theoretical Lamb modes are also shown.

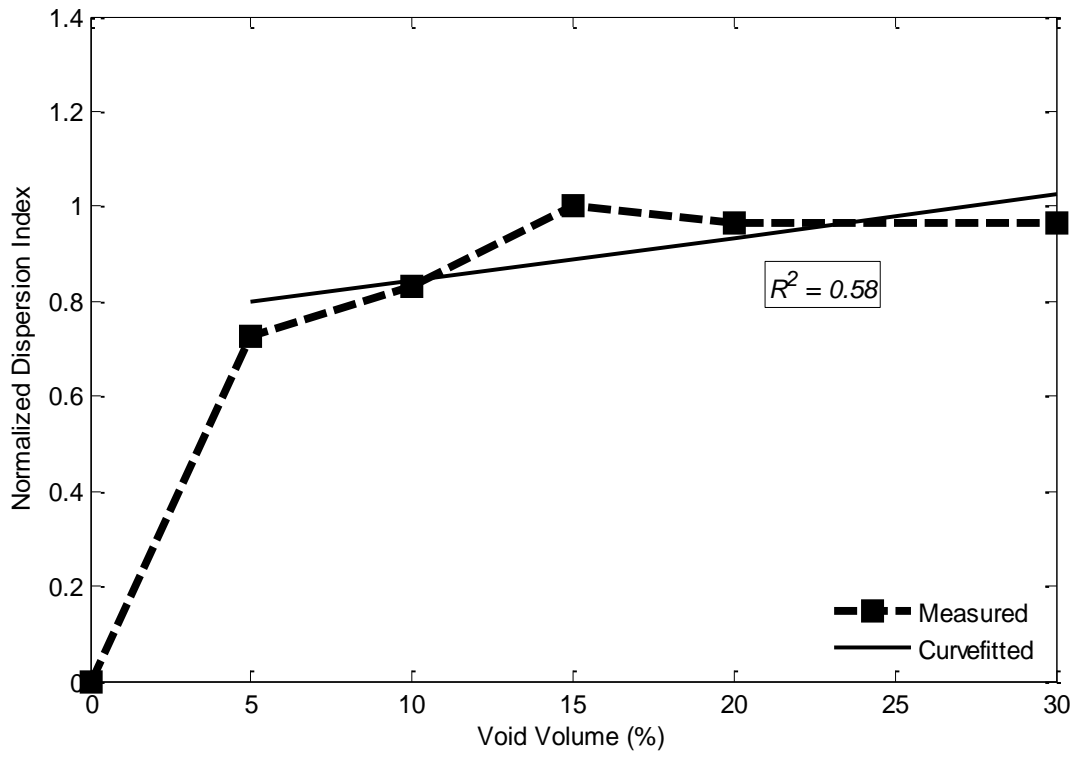


Figure 7.29: Dispersion index (DI_h) vs. void volume for horizontal excitation.

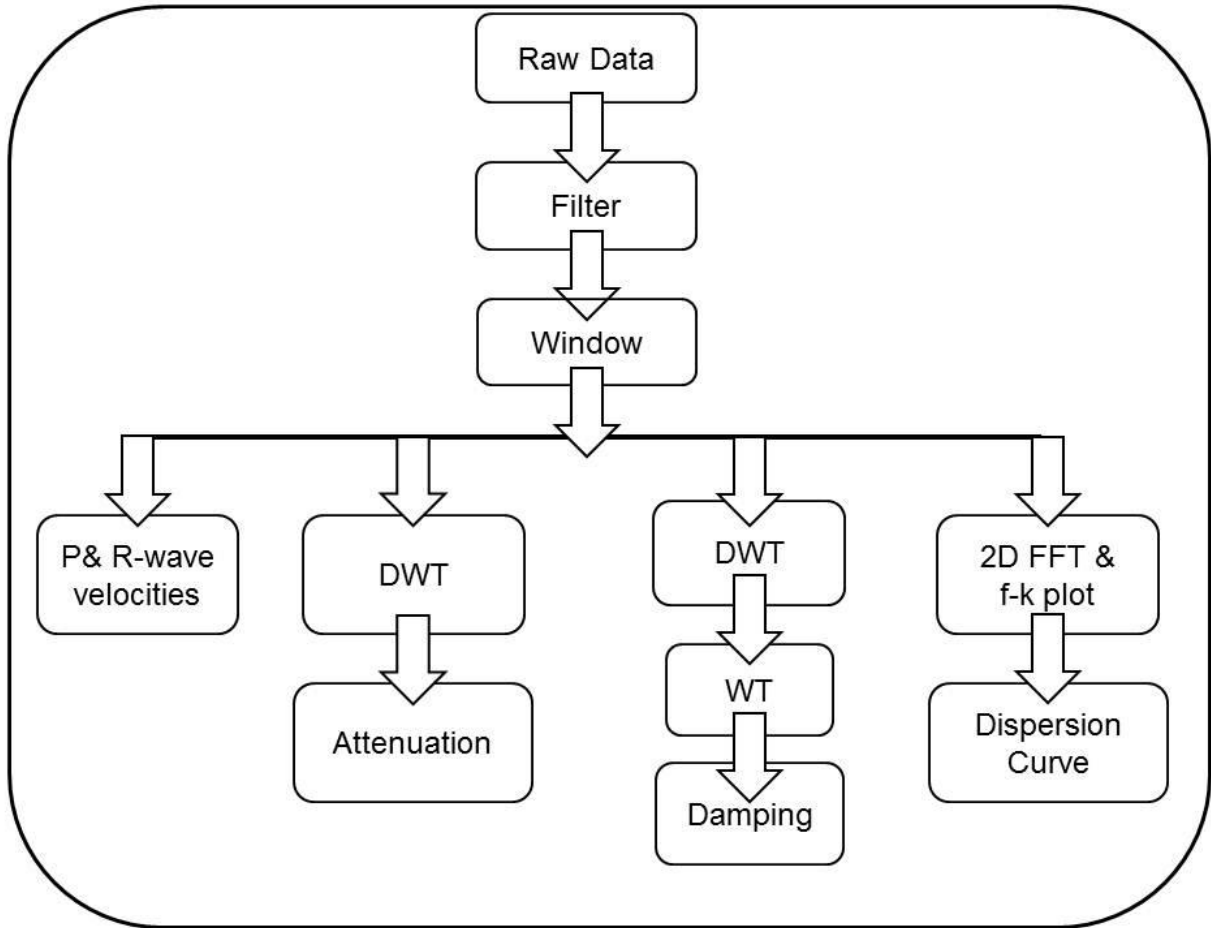


Figure 7.30: Signal processing algorithm for the beam.

Chapter 8 Conclusions and Recommendations

In this research, a comprehensive approach for condition assessment of concrete is introduced. The approach consists of implementation of multi-channel analysis of surface waves (MASW) test configuration at ultrasonic frequency range, calibration of ultrasonic accelerometers beyond their flat response, and various signal processing techniques to interpret the surface wave characteristics. This research includes three separate studies: (i) calibration of transducers, (ii) evaluation of the assessment method on a medium with well-defined defect sizes, and (iii) implementation of the procedure on lab-scale concrete beams with irregular defects. The findings of this research are summarized and recommendations for the future studies are given for each study in the next sections.

8.1 Calibration of Accelerometers

A calibration procedure is introduced to determine the empirical frequency response function of the piezoelectric accelerometers beyond the flat response. A microscopic laser scanner is employed to measure the output response generated by a piezoelectric transmitter when the accelerometer is attached on top of the transmitter. The FRFs of three different accelerometers are determined for a frequency range from 10 to 70 kHz. The calibrated accelerometers are then used for the characterization of the cemented-sand medium. The primary findings are listed as follows:

- Depending on the accelerometer mass, the vibrations occurring at the top of the transmitter vary; therefore, the input signal should be recorded for each accelerometer separately while it is mounted on the source.
- The vibrations recorded at the top of the accelerometers indicated that as the size of the accelerometer increases, its rigid body motion respect to the base is jeopardized. Because the ultrasonic transmitter does not provide uniaxial excitation for comparatively larger accelerometers. Therefore, the accelerometer to be calibrated should be reasonably smaller in size than the transmitter to ensure the rigid motion.

- It is observed that an accelerometer case does not necessarily experience the same vibration as its active element does. Therefore, in the case of a back-to-back calibration configuration, the output signal of a reference accelerometer cannot be used as the input excitation for the one to be calibrated unless the top vibration of the reference accelerometer is controlled with a laser scanner.
- The flat response up to 65 kHz claimed by the manufacturer for A2 could not be verified.
- In the case of non-reflective surfaces, the quality of the interferometric signals should be increased by covering the scan area with reflective tapes. Additionally, instead of a microscopic laser scanner, utilizing one that is capable of scanning larger areas at once will improve the reliability of the measurements.
- The calibration is valid between 10 and 70 kHz due to the transmitter's effective frequency bandwidth. Thus, it is recommended to use transmitters with different frequency bandwidths to extend the calibration for a broader frequency range. So that, the real dynamic behaviour of the medium under investigation can be approximated more accurately.
- The damping ratio of the cemented-sand is found closer to the characteristic value after eliminating the effect of the FRF from the original signals.
- The calibration method conducted in this study is applicable only for this study since it is dependent on a specific source transmitter and excitation type. It is not meant for the generic usage of the accelerometers.

8.2 Evaluation of the Condition Assessment Method

The condition assessment methodology is first evaluated on a half-space medium made of cemented-sand containing defects of well-defined size and shape. This study includes three experimental phases to investigate: (i) a reliable signal processing procedure to determine the surface wave characteristic by employing different accelerometers. (ii) a consistent coupling conditions for the transducers. (iii) the sensitivity of the surface wave characteristic respect to the defect quantity. The findings and recommendations for the second study are as follows:

8.2.1 Phase I: Investigation on Surface Wave Characteristics

- Three of accelerometers provided similar P-wave and R-wave velocities; however, the attenuation trend differs for each one most likely due to the effect of either accelerometer's FRF or coupling. The R-wave velocities obtained from wavelet magnitudes requires less manual selection of the peaks and only differs 6.5% than those obtained from time domain.
- Attenuation coefficient is determined from four different signal processing techniques, namely FT, WT, DWT and EMD. The energy dissipation of the decomposed signals from DWT is found as the prominent parameter to determine attenuation. Because selecting a wide frequency bandwidth instead of a single magnitude from Fourier spectra reduces the inconsistency in the attenuation trend. Compared to DWT, EMD does not provide a better correlated attenuation. DWT explicitly decomposes a signal into sub-signals associated with well-defined frequency ranges unlike EMD; which may split the high energy into different decomposed signals.
- Acceleration traces is better in representing the high frequencies, whereas displacement traces is more convenient to observe the low frequencies.
- CWT allows extracting the instantaneous damped frequency at the arrival time of the surface wave conveniently since the Morlet wavelet itself works as a time window.
- Material damping is computed for various source offsets and from different number of receivers. Although smaller sets located closer to the source ensure better correlation, a longer receiver array enables to investigate larger areas on the medium as preferred in this study.
- The experimental and the analytical dispersion curves matched meaningfully proving the assumption that the frequencies above 10 kHz propagate as surface wave in the test specimen.
- The major drawback of the MASW testing is the spatial aliasing in f-k plots for the frequencies higher than 50 kHz caused by insufficient receiver spacing.
- Windowing the signals improves the reliability of attenuations obtained from the spectral parameters since it eliminates the ripples, and exposes the energy concentrated frequencies clearly in the spectra. Therefore, the time signals are windowed prior to 2D Fourier transform, to obtain the smoothed dispersion curves. Moreover, windowing provides extraction of the first extensional mode by reducing the dominance of flexural mode caused by the vertical excitation.

8.2.2 Phase II: Investigation on Coupling

- The strongest bonding is achieved with epoxy. Nevertheless, a set of receivers is fixed on the test specimen to increase the repeatability of the tests, instead of shifting a single accelerometer which causes inconsistent coupling.
- The lack of calibration information for all accelerometers is fulfilled with a so-called in-situ calibration test which is performed via a reference receiver. The surface wave characteristics obtained from the reference receiver and the fixed receiver array are found in good agreement.
- It is recommended to utilize a laser scanner instead of piezo-electric transducer to measure the vibrations occurring on the specimen; thus, the unknowns in the signals due to the coupling or the accelerometer's FRF can be eliminated at the first place.

8.2.3 Phase III: Investigation on Damage Assessment

- A new index, named as 'dispersion index (DI)', is introduced to quantify the increasing dispersive behaviour of phase velocity with larger defect sizes. This index is computed based on cumulative variation of the frequency dependent velocities respect to the reference R-wave velocity (or the first fundamental antisymmetrical mode) obtained from the intact medium.
- Surface wave characteristics are all found capable of reflecting the defect quantity in the following sensitivity order: material damping ratio, dispersion index, attenuation coefficient, R-wave velocity. Attenuation, damping ratio and DI are positive correlated with the defect size, whereas R-wave velocity is negative correlated.
- Attenuation coefficient determined from DWT provides the most reliable correlation with the defect size compared to those obtained from FT or CWT. It is a good indicator for the defect depth up to 4 cm; beyond that size, lower frequency ranges should be investigated by employing different transmitters.
- Attenuation coefficient and damping ratio have limited sensitivity due to the frequency range of the transmitter. Both approach to a constant value after 4 cm of depth, while R-wave velocity and DI keep their linear relationship for even higher defect depths.

8.3 Condition Assessment for Beams

Ultrasonic and mechanical tests are conducted for six lab-scale concrete beams with different void percent. The relationships between the defect volume and the characteristics, namely P-wave and Rayleigh-wave velocities, attenuation coefficient, material damping ratio and dispersion index along with the compression strength are investigated. The major findings and recommendations are summarized as:

- Attenuation, P and R-wave velocities and dispersion index are found as the promising characteristics; all of which exhibit linear correlation with defect volume.
- Attenuation coefficient has a sensitivity factor over than 100% as being the most sensitive characteristics for quantifying the damage; it is followed by the velocities, and then the DI.
- Existence of the higher lamb modes are observed for beams. Therefore, time traces are subjected to windowing prior to calculate attenuation, so that only the energy dissipation of the incident event can be determined. However, windowing remains as a subjective process.
- Material damping could not capture the damage level due to the fact that the geometric attenuation coefficient given as -0.5 for surface waves is not suitable for the beam geometry.
- The void ratios calculated based on the beams' density do not verify the intended void ratios; therefore, in the future, more than one beam sample should be produced for each void ratio to validate the repetition of the beam production with pellets. Also the number of beams should be increased for different void ratios to fine tune the correlation.
- It is hard to quantify the amount of the cracks or defects within a concrete element physically. Nevertheless, a two-phase experimental program can be pursued where beams are first subjected to different loading condition and then the ultrasonic testing procedure proposed in this study can be conducted. Even though, the absolute crack quantity still cannot be measured, a correlation between the crack amount caused by loading and the evaluated wave characteristics can be constituted; which will indicate the damage level indirectly.

Bibliography

Achenbach, J. D. (1973). *Wave propagation in elastic solid*. Amsterdam: North-Holland Pub. Co.

Addison, P. (2002). *The Illustrated Wavelet Transform Handbook: Introductory Theory and Applications in Science*. Bristol and Philadelphia, USA: Institute of Physics Publishing.

Aggelis, D. G. (2009). Numerical simulation of surface wave propagation in material with inhomogeneity: Inclusion size effect. *NDT and E International* , 42 (6), 558-563.

Aggelis, D. G., & Shiotania, T. (2007). Experimental study of surface wave propagation in strongly heterogeneous media. *Acoustical Society of America* , 122 (5), 151-157.

Aggelis, D. G., Momoki, S., & Chai, H. (2009). Surface wave dispersion in large concrete structures. *NDT&E International* , 42 (4), 304-307.

Aggelis, D. G., Shiotani, T., & Polyzos, D. (2009). Characterization of surface crack depth and repair evaluation using Rayleigh waves. *Cement & Concrete Composites* , 31 (1), 77-83.

Al-Hunaidi, M. O. (1994). Analysis of dispersed multi-mode signals of the SASW method using the multiple filter / cross correlation technique, 1994, Soil Dynamics and Earthquake Engineering. *Soil Dynamics and Earthquake Engineering* , 13 (1), 13-24.

Al-Hunaidi, M. O. (1992). Difficulties with phase spectrum unwrapping in spectral analysis of surface waves nondestructive testing of pavements. *Canadian Journal of Civil Engineering* , 29 (3), 506-511.

Al-Hunaidi, M. O. (1993). Insights on SASW nondestructive testing method. *Canadian Journal of Civil Engineering* , 20 (6), 940-950.

Benmeddour, F., Grondel, S., Assaad, J., & Moulin, E. (2008). Study of the fundamental Lamb modes interaction with asymmetrical discontinuities. *NDT and E International* , 41 (5), 330-340.

Benmeddour, F., Grondel, S., Assaad, J., & Moulin, E. (2008). Study of the fundamental Lamb modes interaction with symmetrical notches. *NDT and E International* , 41 (1), 1-9.

Bolt, B. A. (1978). *Earthquakes: A primer*. San Francisco: W.H. Freeman and Co.

Bruns, T., Link, A., & Elster, C. (2006). Current developments in the field of shock calibration. *XVIII IMEKO World Congress, Metrology for a Sustainable Development*. Rio de Janeiro.

Chopra, A. K. (2001). *Dynamics of structures: Theory and applications to earthquake engineering*. Prentice Hall.

Clifford, G. D. (n.d.). *Open source code*. Retrieved 2012, from <http://www.robots.ox.ac.uk/~gari/code.html>

Daniels, D. J. (2004). *Ground Penetrating Radar*. Institution of Engineering and Technology.

- Fitting, D. W., & Adler, L. (1981). *Ultrasonic spectral analysis for non-destructive evaluation*. New York and London: Plenum Press.
- Gautschi, G. (2006). *Piezoelectric sensorics: Force, strain, pressure, acceleration and acoustic emission sensors, materials and amplifiers*. Springer.
- Goueygou, M., Abraham, O., & Lataste, J. F. (2008). A comparative study of two non-destructive testing methods to assess near-surface mechanical damage in concrete structures. *NDT & E International* , 41 (6), 448-456.
- Graff, K. F. (1975.). *Wave motion in elastic solids*. Belfast: Ohio State University Press.
- Granger, S., Pijaudier, C. G., Loukili, A., Marlot, D., & Lenain, J. C. (2009). Monitoring of cracking and healing in an ultra high performance cementitious material using the time reversal technique. *Cement and Concrete Research* , 39 (4), 296-302.
- Heisey, J. S., Stokoe, K. H., Hudson, W. R., & Meyer, A. H. (1982). *Research Report 256-2: Determination of in situ wave velocities from spectral analysis of surface waves*. University of Texas at Austin. Austin: Centre for Transportation Research.
- Hevin, G., Abraham, O., Pedersen, H. A., & Campillo, M. (1998). Characterization of surface cracks with Rayleigh waves: a numerical model. *NDT & E International* , 31 (4), 289-297.
- Hiltunen, D. R., & Woods, R. D. (1988). SASW and crosshole test results compared. *Earthquake Engineering and Soil Dynamics II: Recent Advances in Ground Motion Evaluation, Geotechnical Special Publication 20* (pp. 279-289). New York: ASCE.
- Huang, N. E., Shen, Z., Long, S., Wu, M. C., Shih, H. H., Zheng, Q., et al. (1998). *The empirical mode decomposition and Hilbert spectrum for nonlinear and non-stationary time series analysis*. Proceedings of the Royal Society of London.
- In, C. W., Kim, J. Y., Kurtis, K. E., & Jacobs, L. J. (2009). Characterization of ultrasonic Rayleigh surface waves in asphaltic concrete. *NDT and E International* , 42 (7), 610-617.
- Jones, E., Yelon, W. B., & Edelman, S. (1969). Piezoelectric Shakers for Wide-Frequency Calibration of Vibration Pickups. *Journal of Acoustic Society of America* , 45 (6), 1556-1559.
- Kalinski, M. E., Stokoe, K. H., Jirsa, J. O., & Roesset, J. M. (1994). Nondestructive identification of internally damaged areas of concrete beam using the SASW method. (1458), 14-19.
- Kee, S. H., Taekeun, O., & Popovics, J. S. (2012). Nondestructive bridge deck testing with air-coupled impact-echo and infrared thermography. *Journal of Bridge Engineering* , 17 (6), 928-939.
- Khan, Z., Cascante, G., & El Naggar, M. H. (2010). Measurement of dynamic properties of stiff specimens using ultrasonic waves. *Canadian Geotechnical Journal* , 48 (1), 1-15.
- Khan, Z., Majid, A., Cascante, G., Hutchinson, D. J., & Pezeshkpour, P. (2006). Characterization of a cemented sand with the pulse-velocity method. *Canadian Geotechnical Journal* , 43 (3), 294-309.

- Kolsky, H. (1963). *Stress waves in solids*. New York: Dover Publications.
- Lardies, J. (2007). Identification of a dynamic model for an acoustic enclosure using the wavelet transform. *Applied Acoustics* , 68 (4), 473-490.
- Lin, C.-C., Liu, P.-L., & Yeh, P.-L. (2009). Application of empirical mode decomposition in the impact-echo test. *NDT and E International* , 42 (7), 589-598.
- Link, A., & Martens, H. J. (2004). Accelerometer identification using shock excitation. *Measurement* , 35 (2), 191-199.
- Link, A., Taubner, A., Wabinski, W., Bruns, T., & Elster, C. (2006). Calibration of accelerometers: determination of amplitude and phase response upon shock excitation. *Measurement of Science and Technology* , 17 (7), 1888-1894.
- Liou, T., Hsiao, C., Cheng, C. C., & Chang, N. (2009). Depth measurement of notches as models for shallow cracks in concrete. *NDT and E International* , 42 (1), 69-76.
- Liu, P. L., & Yeh, P. L. (2010). Vertical spectral tomography of concrete structures based on impact echo depth spectra. *NDT and E International* , 43 (1), 45-53.
- Liu, P. L., & Yiu, C. Y. (2002). Imaging of concrete defects using elastic wave tests. *The Far-East Conference on Nondestructive Testing*. Tokyo.
- M., H. C., & Piersol, A. G. (2002). *Harris' shock and vibration handbook*. McGraw-Hill.
- M Maia, N. M., & Silva, J. M. (1997). *Theoretical and Experimental Modal Analysis*. Research Studies Press Limited.
- Mallat, S. G. (1989). A theory for multiresolution signal decomposition: The wavelet representation. *IEEE Transactions on Pattern Analysis and Machine Intelligence* , 11 (7), 674-693.
- Nasseri-Moghaddam, A., Cascante, G., Phillips, C., & Hutchinson, D. J. (2007). Effects of underground cavities on Rayleigh waves - Field and numerical experiments. *Soil Dynamics and Earthquake Engineering* , 27 (4), 300-313.
- Nazarian, S., Stokoe, K. H., & Hudson, W. R. (1983). Use of spectral analysis of surface waves method for determination of moduli and thicknesses of pavement systems. *Transportation Research Record* (921), 38-45.
- Oppenheim, A., & Schafer, R. (2006). *Discrete-Time Signal Processing*. Pearson Education.
- Ovanosova, A. V., & Suárez, L. E. (2004). Applications of wavelet transforms to damage detection in frame structures. *Engineering Structures* , 26 (1), 39-49.
- Park, C. B., Miller, R. D., & Xia, J. (1997). *Multichannel analysis of surface waves*. Kansas Geological Survey.

- Popovics, J. S., & Rose, J. L. (1994). A survey of developments in ultrasonic NDE of concrete. *IEEE Transactions on Ultrasonics, Ferroelectrics and Frequency Control* , 41 (1), 140-143.
- Popovics, J. S., & Song, W. J. (2000). Application of surface wave transmission measurements for crack depth determination in concrete. *ACI Materials Journal* , 97 (2), 127-135.
- Popovics, S. (1969). Effect of porosity on the strength of concrete. *Journal of Materials* , 4 (2), 356-371.
- Qian, S. (2002.). *Time-frequency and wavelet transforms*. Prentice-Hall Inc.
- Russo, M. (n.d.). *SWAN (Surface waves analysis)* . Retrieved 2010, from Geostier: <http://www.geoastier.com>
- Sansalone, M., & Streett, W. B. (1997). *Impact-echo: nondestructive evaluation of concrete and masonry*. Bullbrier Press.
- Shickert, G. (1984). Critical reflections on nondestructive testing of concrete. *Materials and Structures* , 5 (6), 217-220.
- Shah, A., & Ribakov, Y. (2009). Non-destructive evaluation of concrete in damaged and undamaged states. *Materials and Design* , 30 (9), 3504-3511.
- Shin, S. W., Yun, C. B., Popovics, J. S., & Kim, J. H. (2007). Improved Rayleigh wave velocity measurement for nondestructive early-age concrete monitoring. *Research in Nondestructive Evaluation* , 18 (1), 45-68.
- Shin, S. W., Zhu, J., Min, J., & Popovics, J. S. (2008). Crack depth estimation in concrete using energy transmission of surface waves. *ACI Materials* , 105 (5), 510-516.
- Song, W. J., Popovics, J. S., Aldrin, J. C., & Shah, S. P. (2003). Measurement of surface wave transmission coefficient across surface-breaking cracks and notches in concrete. *Acoustical Society of America Journal* , 113 (2), 717-725.
- Stark, H. G. (2005). *Wavelets and signal processing: an application-based introduction*. Springer.
- Stokoe, K. H., & S., N. (1983). Effectiveness of ground improvement from spectral analysis of surface waves. *Proceedings of the European Conference on Soil Mechanics and Foundation Engineering*, (pp. 91-94).
- Su, Z., & Ye, L. (2009). *Identification of Damage Using Lamb Waves: From Fundamentals to Applications*. Springer-Verlag.
- Suaris, W., & Fernando, V. (1987). Ultrasonic pulse attenuation as a measure of damage growth during cyclic loading of concrete. *Materials Journal* , 84 (3), 185-193.
- Tallavo, F., Cascante, G., & Pandey, M. D. (2009). New methodology for source characterization in pulse velocity testing. *Geotechnical Testing Journal* , 32 (6), 537-552.

- Valens, C. (1999). *A really friendly guide to Wavelets*. Retrieved 2010, from <http://www.robots.ox.ac.uk/~parg/mlrg/papers/arfgtw.pdf>
- Viktorov, I. A. (1967.). *Rayleigh and Lamb waves*. New York: Plenum Press.
- Wang, L., & Yuan, F. G. (2005). Damage identification in a composite plate using Prestack reverse-time migration technique. *Structural Health Monitoring* , 4 (3), 195-211.
- Yang, Y., Cascante, G., & Polak, M. (2009). Depth detection of surface-breaking cracks in concrete plates using fundamental Lamb modes. *NDT & E International* , 42 (6), 501-512.
- Yang, Y., Cascante, G., & Polak, M. (2011). New method for the evaluation of material damping using the wavelet transform. *Journal of Geotechnical and Geoenvironmental Engineering* , 137 (8), 798–808.
- Yang, Y., Cascante, G., & Polak, M. (2010). Nondestructive evaluation of the depth of surface-breaking cracks in concrete pipes. *Tunnelling and Underground Space Technology* , 25 (6), 736-744.
- Yeh, P. L., & Liu, P. L. (2008). Application of the wavelet transform and the enhanced Fourier spectrum in the impact echo test. *NDT and E International* , 41 (5), 382-394.
- Yeh, P. L., & Liu, P. L. (2009). Imaging of internal cracks in concrete structures using the surface rendering technique. *NDT and E International* , 42 (3), 181-187.
- Zerwer, A., Cascante, G., & Hutchinson, J. (2002). Parameter estimation in finite element simulations of Rayleigh waves. *Journal of Geotechnical and Geoenvironmental Engineering* , 128 (3), 250-261.
- Zerwer, A., Polak, M., & Santamarina, J. C. (2005). Detection of surface breaking cracks in concrete members using Rayleigh waves. *Journal of Environmental & Engineering Geophysics* , 10 (3), 295-306.
- Zerwer, A., Polak, M., & Santamarina, J. C. (2002). Effects of surface cracks on Rayleigh wave propagation: an experimental study. *Journal of Structural Engineering* , 128 (2), 240-248.
- Zerwer, A., Polak, M., & Santamarina, J. C. (2003). Rayleigh wave propagation for the detection of near surface discontinuities: finite element study. *Journal of Nondestructive Evaluation* , 22 (2), 39-52.
- Zerwer, A., Polak, M., & Santamarina, J. C. (2000). Wave propagation in thin Plexiglas plates: implication for Rayleigh waves. *NDT & E International* , 33 (1), 33-41.

Appendix A: Summary of ISO 16063 Standards

Standard		Methods	Acceleration peak magnitude (m/s ²)	Shock duration, T (ms)	Shock shape ^[1]
ISO 16063-13	Primary shock calibration by laser interferometry ^{[3][4]}	Shock machine based on rigid motion of an anvil ^[5]	100 – 5000	0.8 – 10 ^{[7][8]}	Half-sin, half-sin squared, Gaussian acceleration
		Shock machine based on wave propagation inside a long thin bar ^[6]	1000 – 100000	0.03 – 0.3 ^{[7][8]}	Gaussian velocity
ISO 16063-22	Shock calibration by comparison to a reference ^[9]	Pendulum shock calibrator ^[10]	100 – 1500	3 – 8	Half-sin
		Drop-ball shock calibrator ^[11]	100 – 100000	0.1 – 10	N/A
		Pneumatically operated piston shock calibrator ^[12]	200 – 100000	0.1 – 3	Half-sin
		Hopkinson bar shock calibrator ^[13]	1000 – 100000 ^[14]	N/A	N/A

[1] Depending on the shock machine, shock pulse will have one of the following shapes.

[2] Total range of acceleration peak magnitude is 0.1 – 1000 m/s².

[3] As for a single ended accelerometer, the laser measurement is taken on the polished surface of the anvil bar. In the case of a back-to-back (BTB) accelerometer that will be used as a reference transducer, a dummy mass (equivalent to the mass of the accelerometer to be calibrated by comparison method given as in ISO 16063-22) shall be mounted at the top of it. The motion may be captured either at the top of the BTB transducer or on the dummy mass. If the motion of the dummy mass departs from a rigid body motion, then the relative motion between the top and bottom surfaces must be taken into account.

[4] Three different signal processing algorithms are given in the standard. Performing one of these processes, the displacement signal measured on the surface of the anvil (input motion for the transducer) is differentiated to acceleration. Then, the shock sensitivity, S_s , is calculated in time domain by taking the ratio of the peak value of the output of the accelerometer, u_{peak} , over the peak value of the acceleration, a_{peak} , derived from the displacement as given by $S_{sh} = u_{peak}/a_{peak}$. It should be noted that this single value of sensitivity is not frequency or phase dependent and only associated with a certain input acceleration identified by the shock amplitude, duration and shape. Yet, an alternative way to calculate the complex sensitivity, $S(f_n)$, from the shock sensitivity is also available within this standard. If one calculates the complex frequency spectrum of both filtered input and output accelerations by applying DFT, and then takes the ratio of this two, the magnitudes and the phase shift of the complex sensitivity shall be calculated from $S(f_n) = X_u(f_n)/j2\pi f_n X_v(f_n)$ where f_n is the discrete frequency values, $X_u(f_n)$ and $X_v(f_n)$ are the complex frequency spectra of the accelerometer output and the velocity signal measured by the laser respectively.

[5] The desired shock duration and shape is obtained by placing crushing pads - made of rubber, paper, etc - between the hammer and anvil.
[6] The desired shock duration is obtained based on the length of the bar which affects the occurrence time of the echo at the mounting surface.
[7] Frequency bandwidth depends on the shock magnitude, duration and shape.
[8] Given by Martens et al. (2000), however, in ISO 16063-13, the shock pulse duration range is given between 0.05 and 10 ms without mentioning the type of shock machine used.
[9] The transducer under test is mounted on the top of the reference one (except pendulum shock calibrators) of which the mass should not be significantly smaller than test transducer and the mounting fixture since the frequency response of the reference transducer will be affected by the attached mass. Also, the natural period of the test transducer should be smaller than 0.2 times the duration of the shock pulse to avoid ringing due to resonance.
[10] The pulse shape and duration is determined by the hardness of rubber pad employed in the test setup.
[11] While the shape and duration of the shock pulse is govern by the diameter and mass of the ball, the desired frequency range of the pulse, which is between 5 and 10 kHz, is determined by the size of anvil.
[12] Different pulse amplitudes and durations are may be achieved by controlling pressure, pad thickness and masses of anvil and additional masses.
[13] Hopkinson bar is a slender bar having a length-to-diameter ratio of 100. The method bases on measuring a reference acceleration / velocity on the bar via either strain gauge or laser doppler vibrometer, instead of employing a reference BTB accelerometer, and comparing this reference input with the output of the test transducer. Two types of Hopkinson bar shock calibrator (HBSC) is available namely, HBSC by comparison in terms of velocity or acceleration and Split-HBSC by comparison with a force transducer. At the first one, the reference velocity measured on the bar is compared with the integrated acceleration of the test transducer, whereas the later one provides the reference acceleration without a need to integrate and compare it to the output of the transducer directly.
[14] Although it is possible to create accelerations up to 200000 m/s ² by using Hopkinson bar, here it is limited to 100000 m/s ² which the reference transducer could be only calibrated up to.
[15] The shock sensitivity, S_{sh} , is calculated by selecting the peak values of input and output accelerations in time domain, after performing proper signal processing (low-pass filtering) by the formula $S_{sh} = S_s(u_{x,peak}/u_{s,peak})$ where S_s is the sensitivity of the reference transducer and $u_{x,peak}$ and $u_{s,peak}$ are the peak values of output and input accelerations respectively. The complex sensitivity may also be calculated by $S_x(j\omega) = S_s(j\omega)[u_x(j\omega)/u_s(j\omega)]$, if the complex sensitivity is available from the primary shock calibrations as given ISO 16063-13.

Appendix B: Additional Figures for Chapter 5

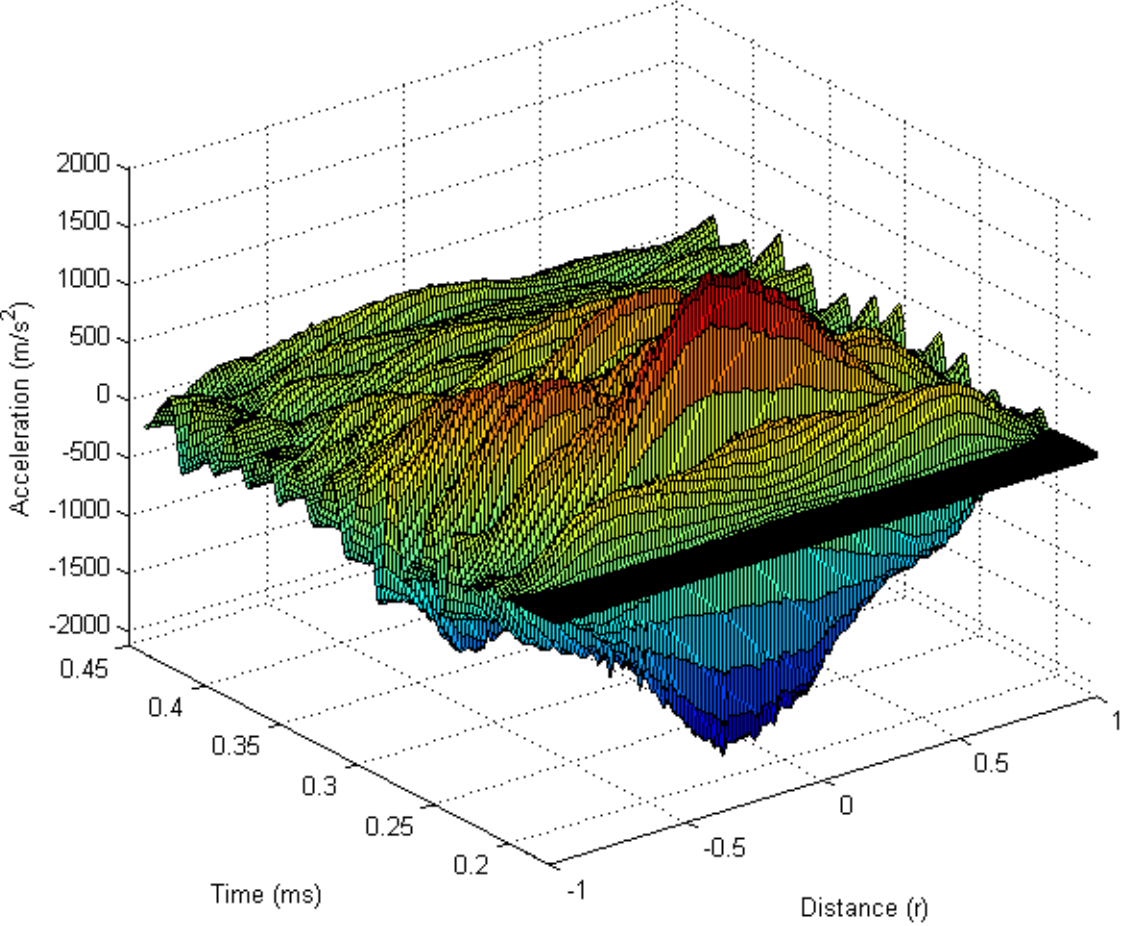


Figure B.1: Acceleration time histories along the diameter of the transmitter under transient excitation of 125 Volt, no mass case.

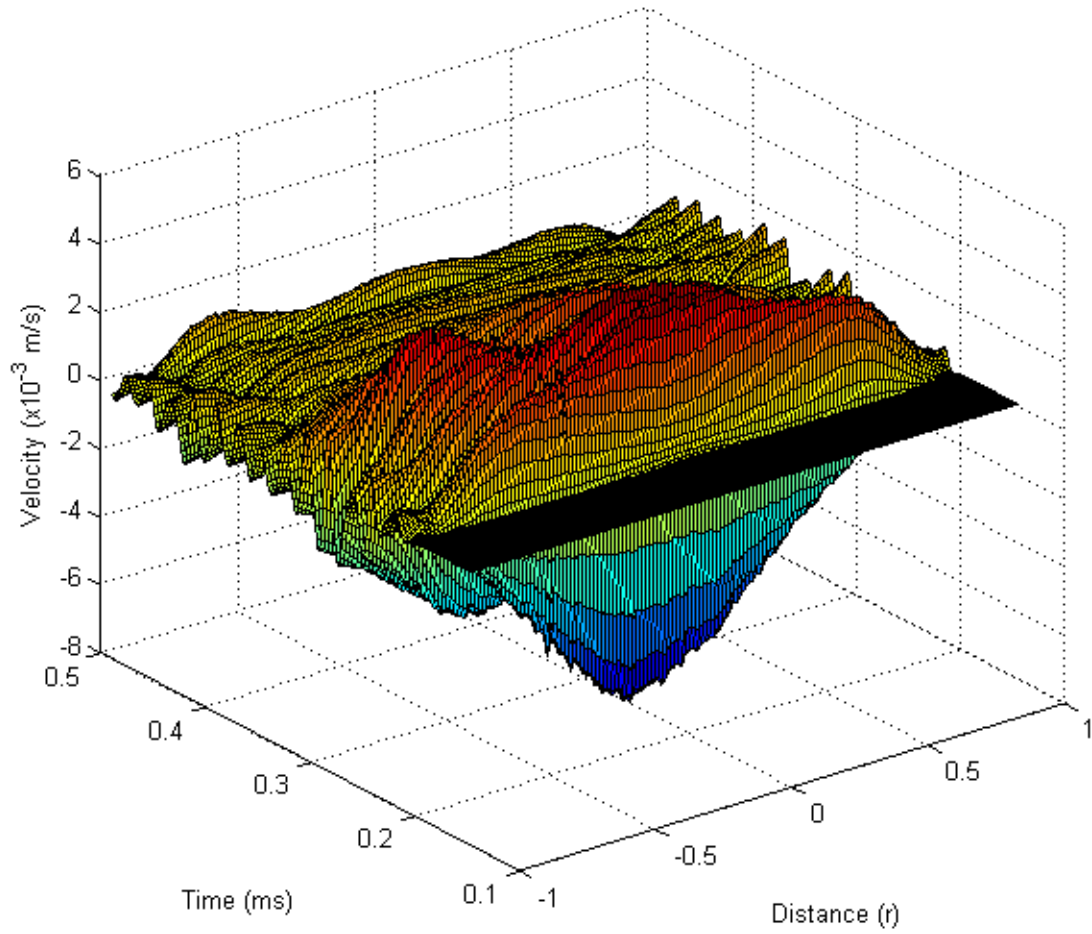


Figure B.2: Velocity time history along the diameter of the transmitter under transient excitation of 125 Volt, no mass case.

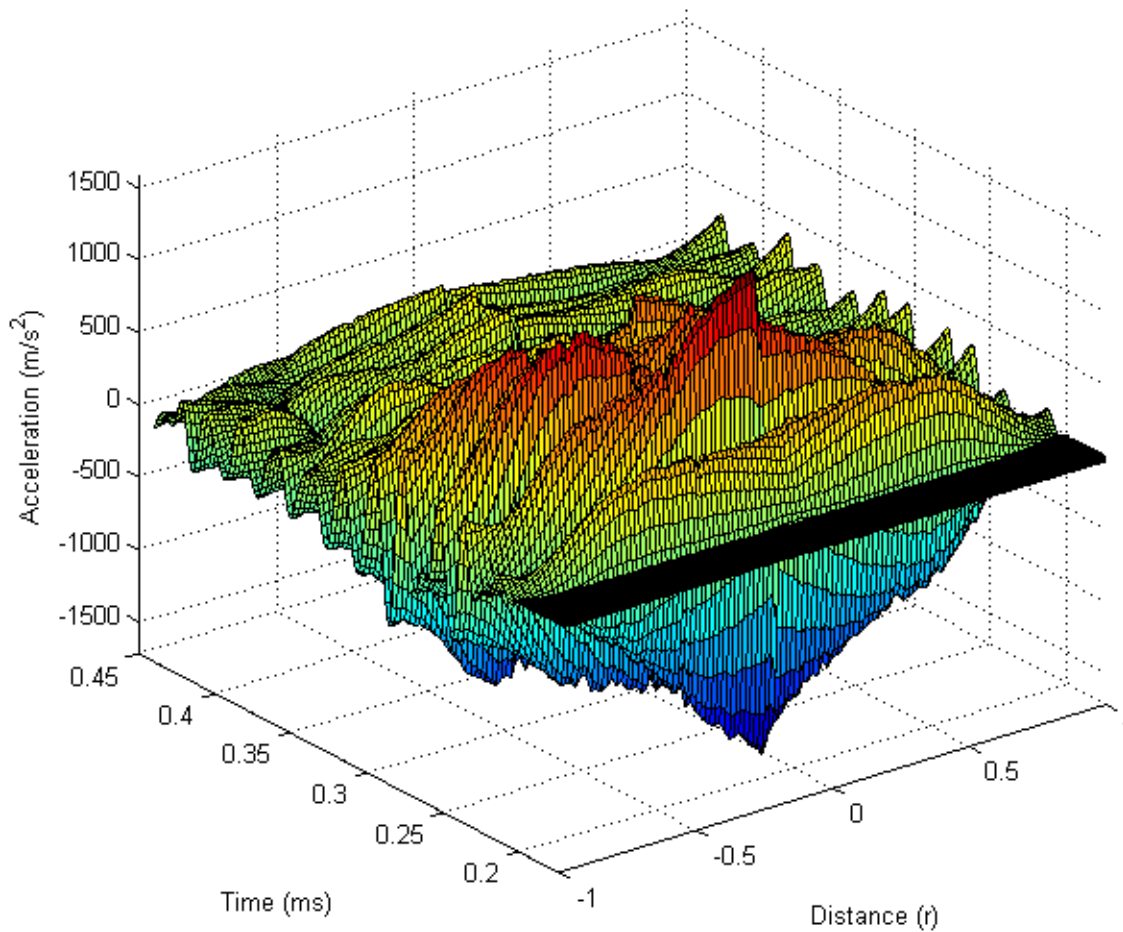


Figure B.3: Acceleration time history along the diameter of the transmitter under transient excitation of 125 Volt. The measurements at the center of the transmitter ($r=0$) corresponds to the scans at the edge of accelerometer A1, since center cannot be measured due to the attached accelerometer.

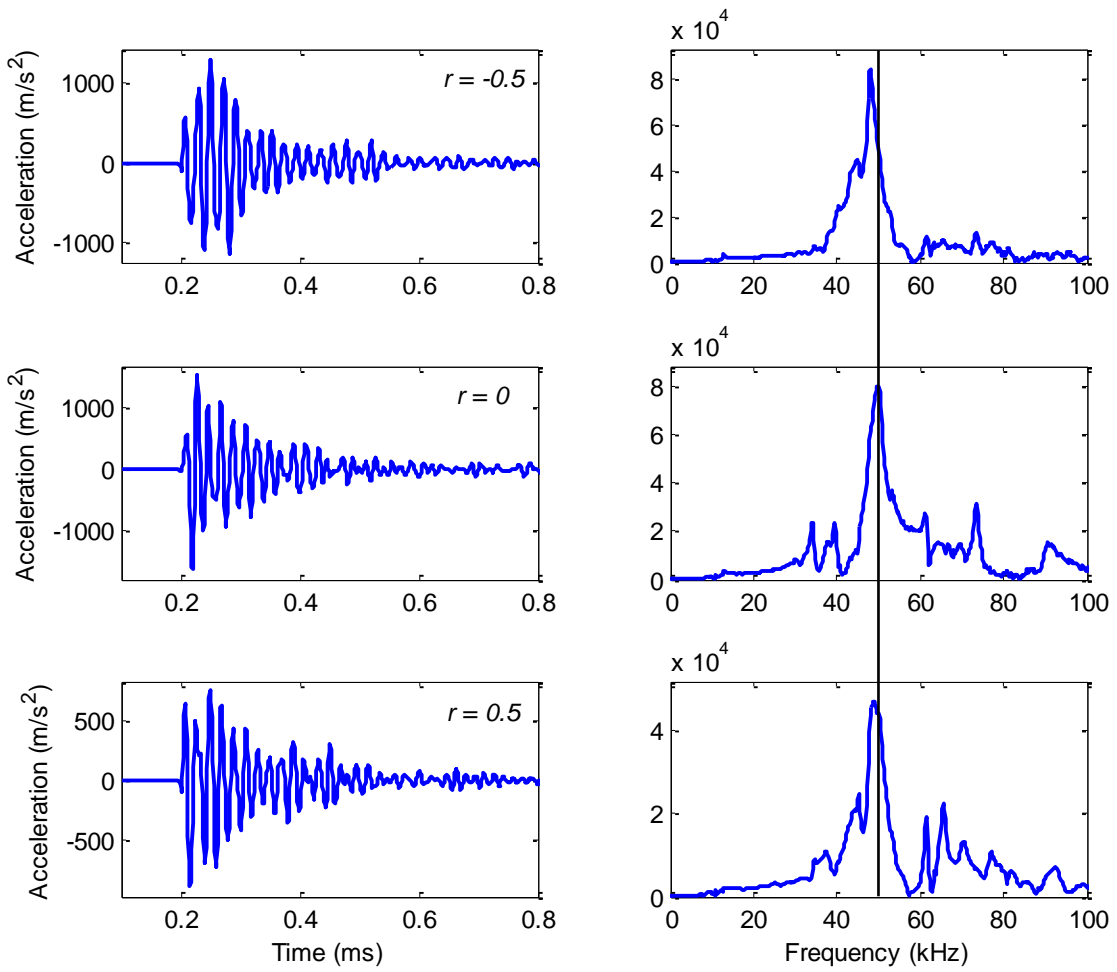


Figure B.4: Acceleration time histories and corresponding Fourier spectra at normalized radius of -0.5, 0 and 0.5 (Fig. B.3) respectively under transient excitation of 125 Volt for A1.

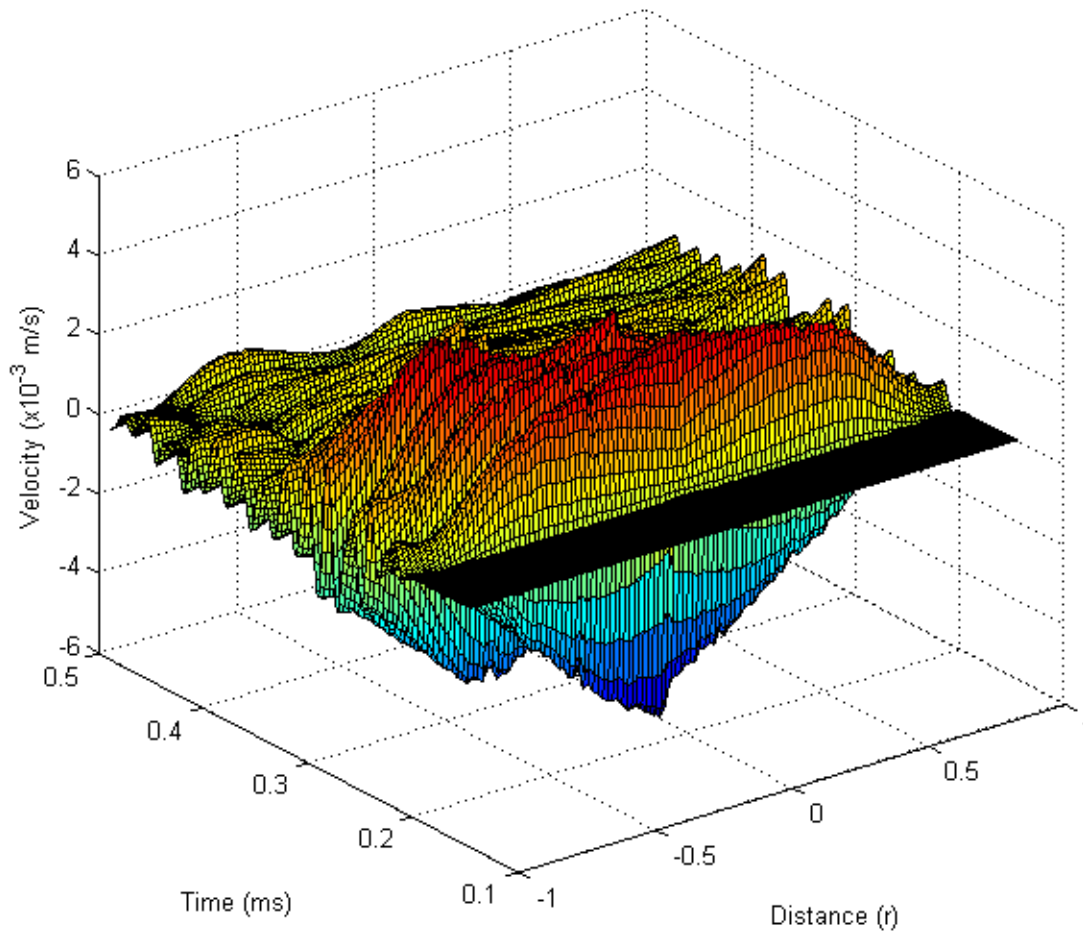


Figure B.5: Velocity time history along the diameter of the transmitter under transient excitation of 125 Volt. The measurements at the center of the transmitter ($r=0$) corresponds to the scans at the edge of accelerometer A1, since center cannot be measured due to the attached accelerometer.

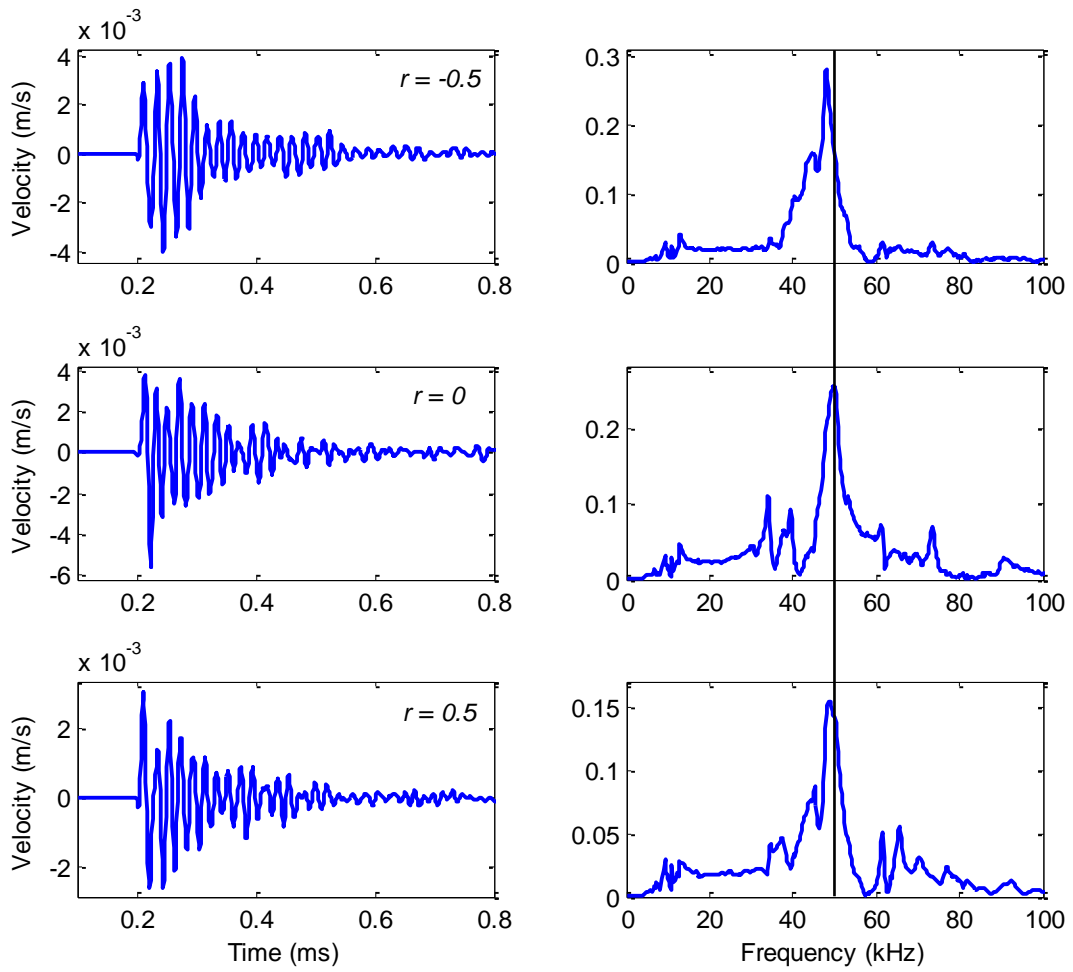


Figure B.6: Velocity time histories and corresponding Fourier spectra at normalized radius of -0.5, 0 and 0.5 (Fig. B.5) respectively under transient excitation of 125 Volt for A1.

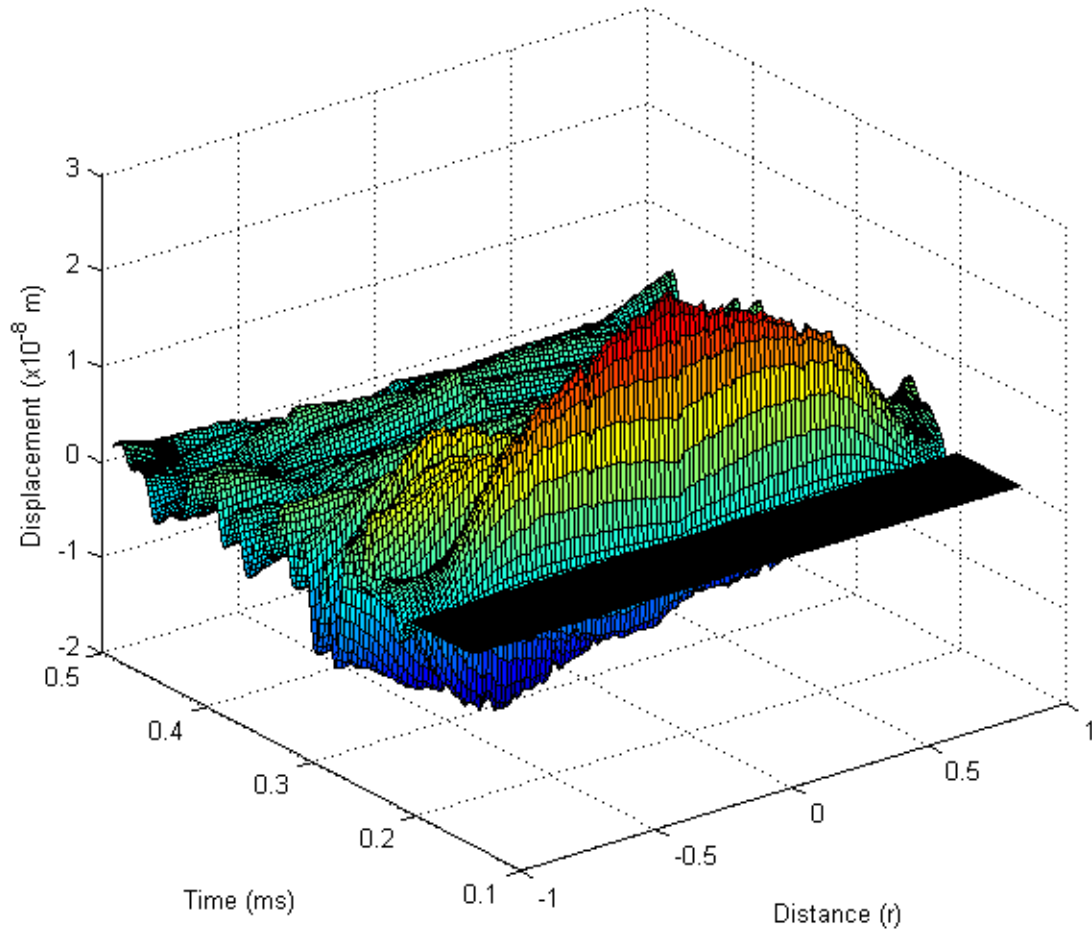


Figure B.7: Displacement time history along the diameter of the transmitter under transient excitation of 125 Volt. The measurements at the center of the transmitter ($r=0$) corresponds to the scans at the edge of accelerometer A1, since center cannot be measured due to the attached accelerometer.

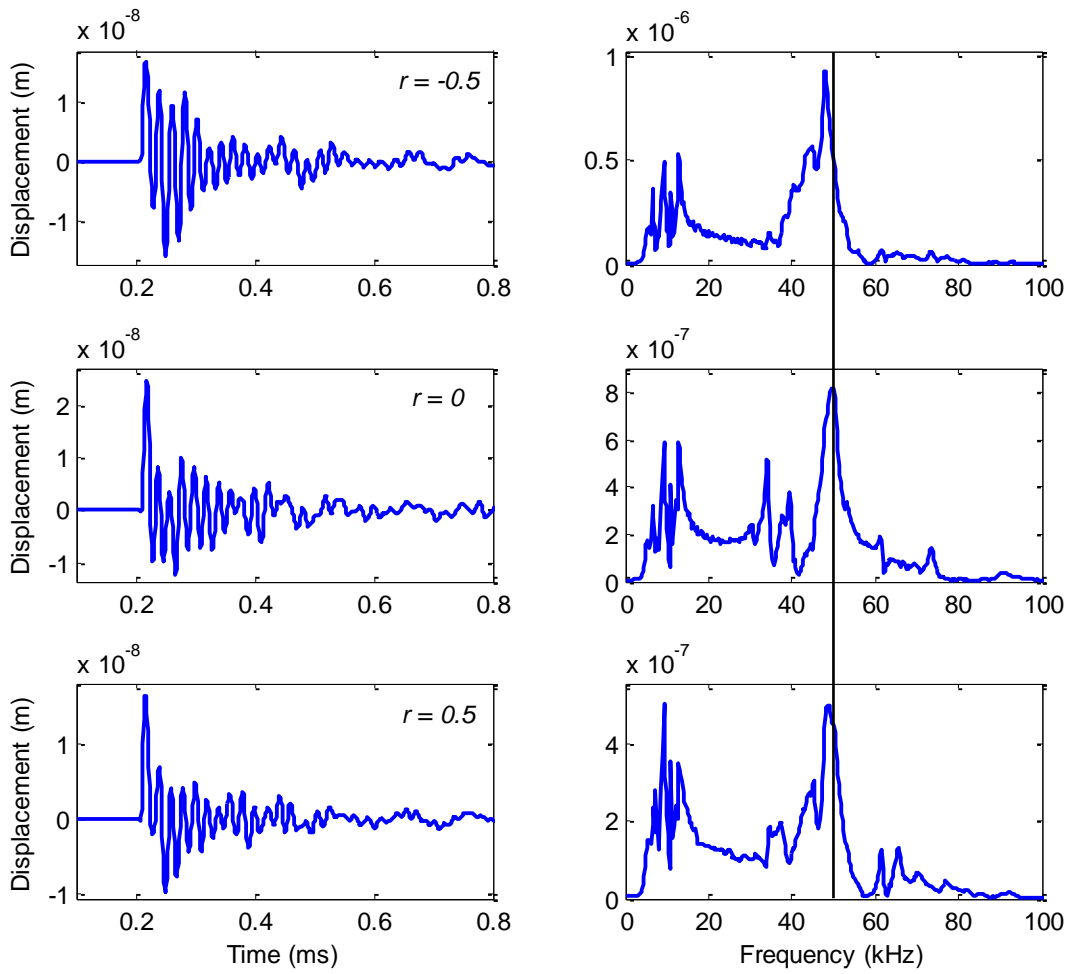


Figure B.8: Displacement time histories and corresponding Fourier spectra at normalized radius of -0.5, 0 and 0.5 (Fig. B.7) respectively under transient excitation of 125 Volt for A1.

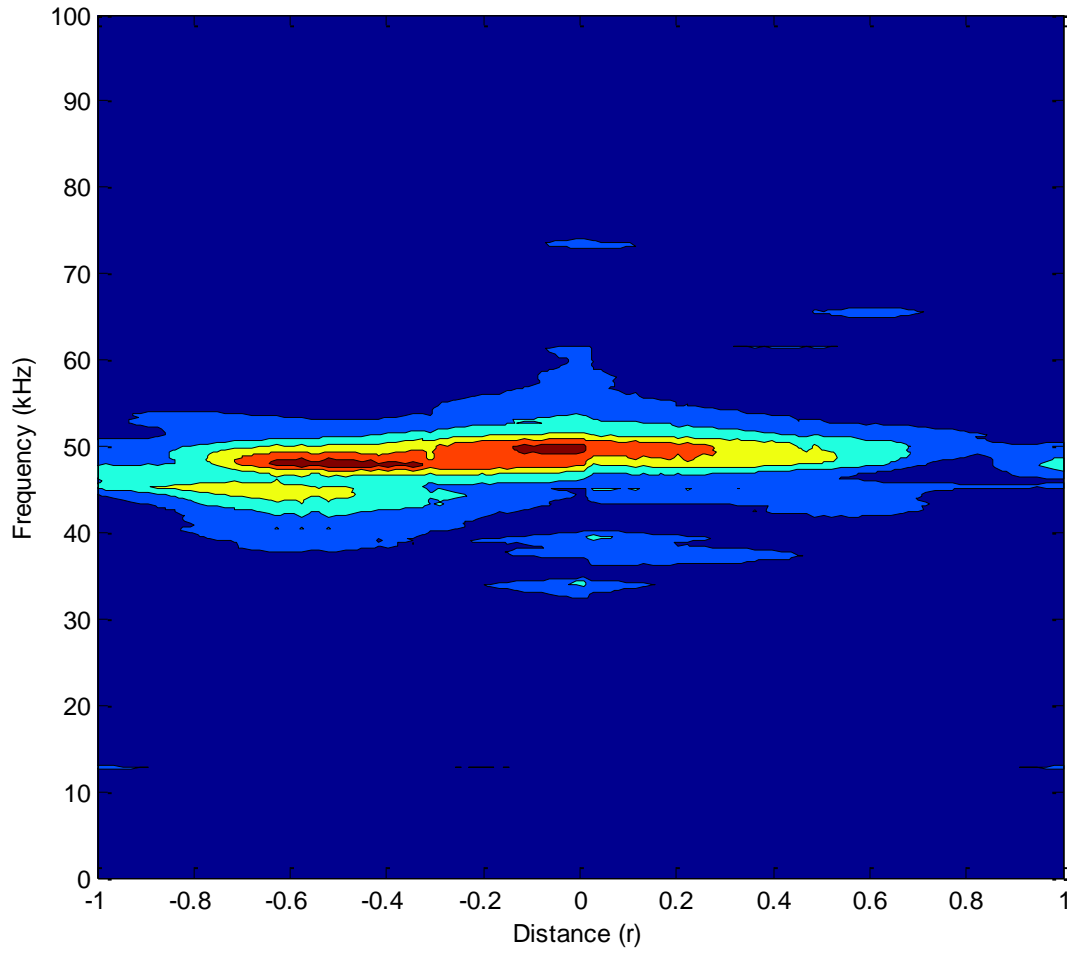


Figure B.9: Velocity Fourier spectra along the diameter of the transmitter under transient excitation of 125 Volt. The measurements at the center of the transmitter ($r=0$) corresponds to the scans at the edge of accelerometer A1, since center cannot be measured due to the attached accelerometer.

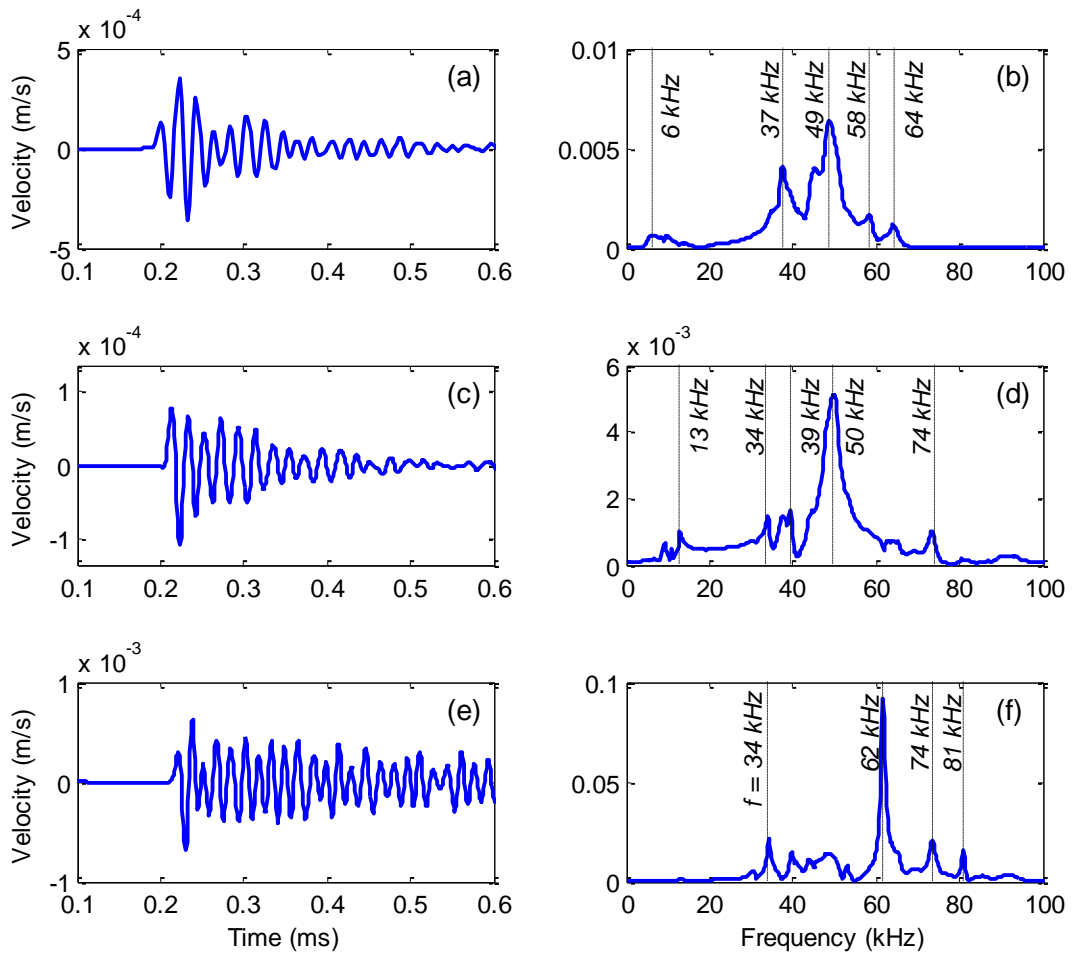


Figure B.10: Velocity time histories and Fourier spectra of (a,b) output, (c,d) input, and (e,f) vibration on the top of accelerometer A1. Input and top signals are divided by 50 ($125V/2.5V$) to ensure the same excitation voltage.

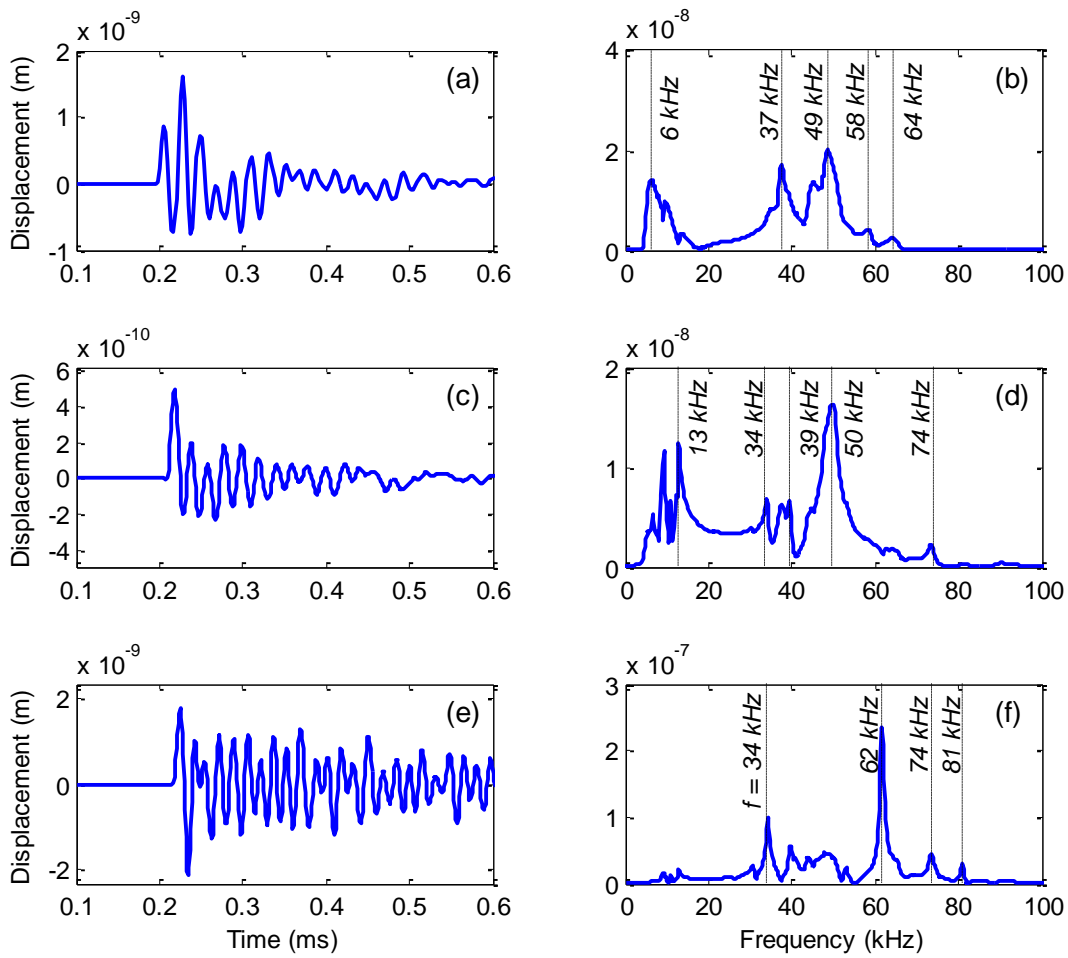


Figure B.11: Displacement time histories and Fourier spectra of (a,b) output, (c,d) input, and (e,f) vibration on the top of accelerometer A1. Input and top signals are divided by 50 ($125V/2.5V$) to ensure the same excitation voltage.

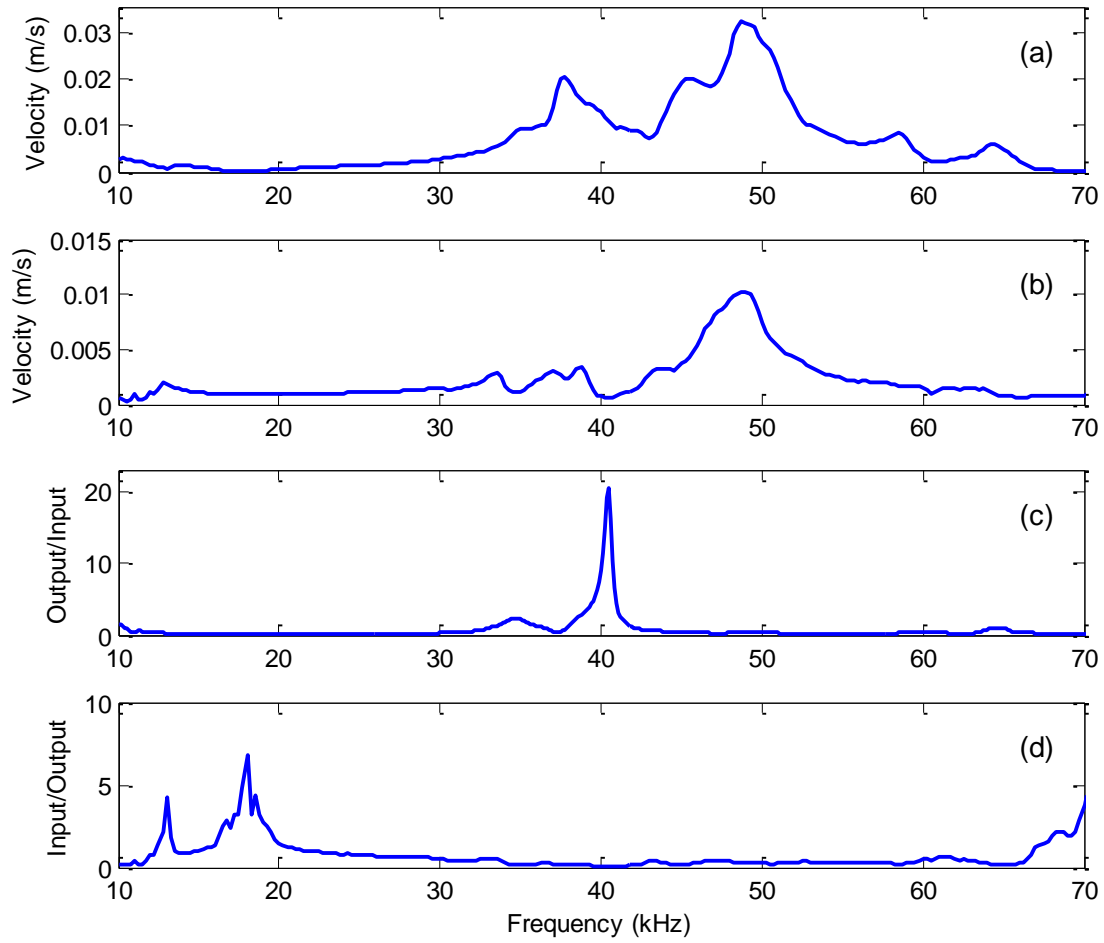


Figure B.12: (a) Input velocity, (b) Output velocity, (c) Frequency response function computed by taking the ratio of output over input, (d) Inverse FRF for A1.

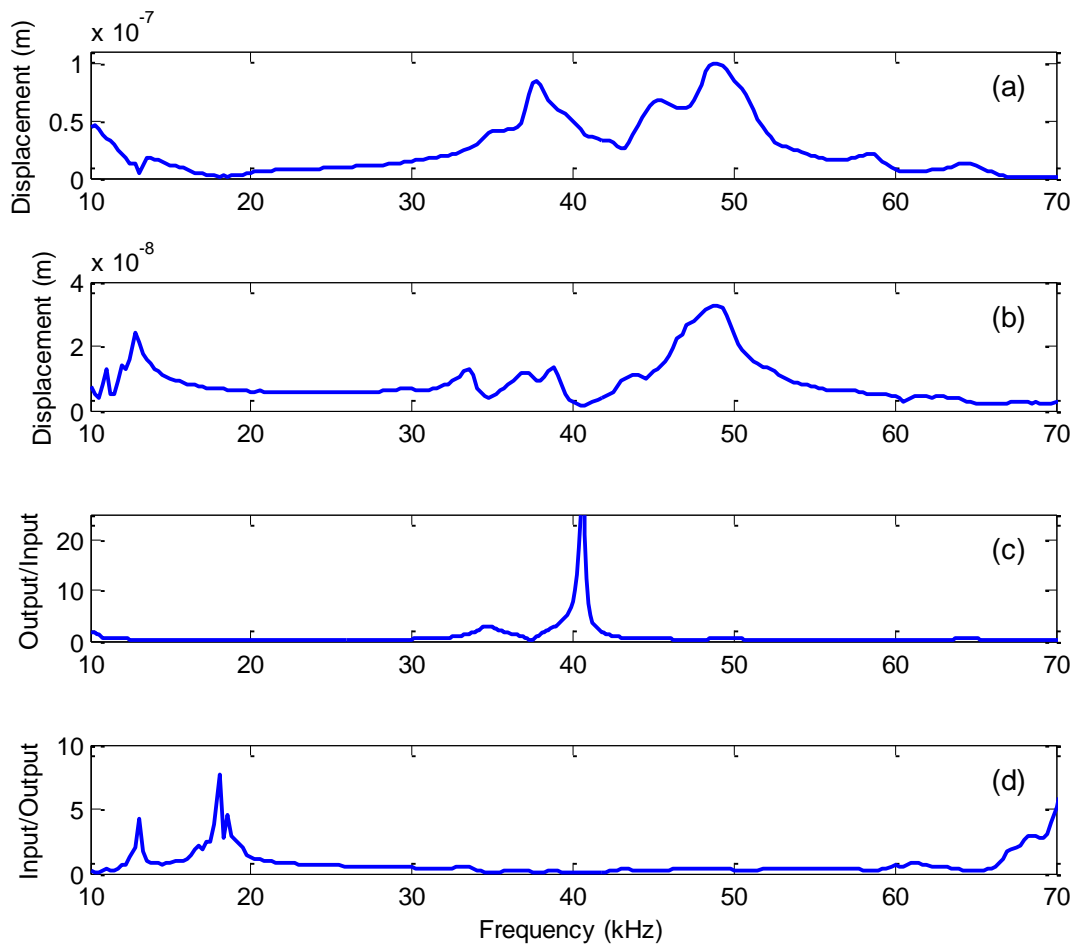


Figure B.13: (a) Input displacement, (b) Output displacement, (c) Frequency response function computed by taking the ratio of output over input, (d) Inverse FRF for A1.

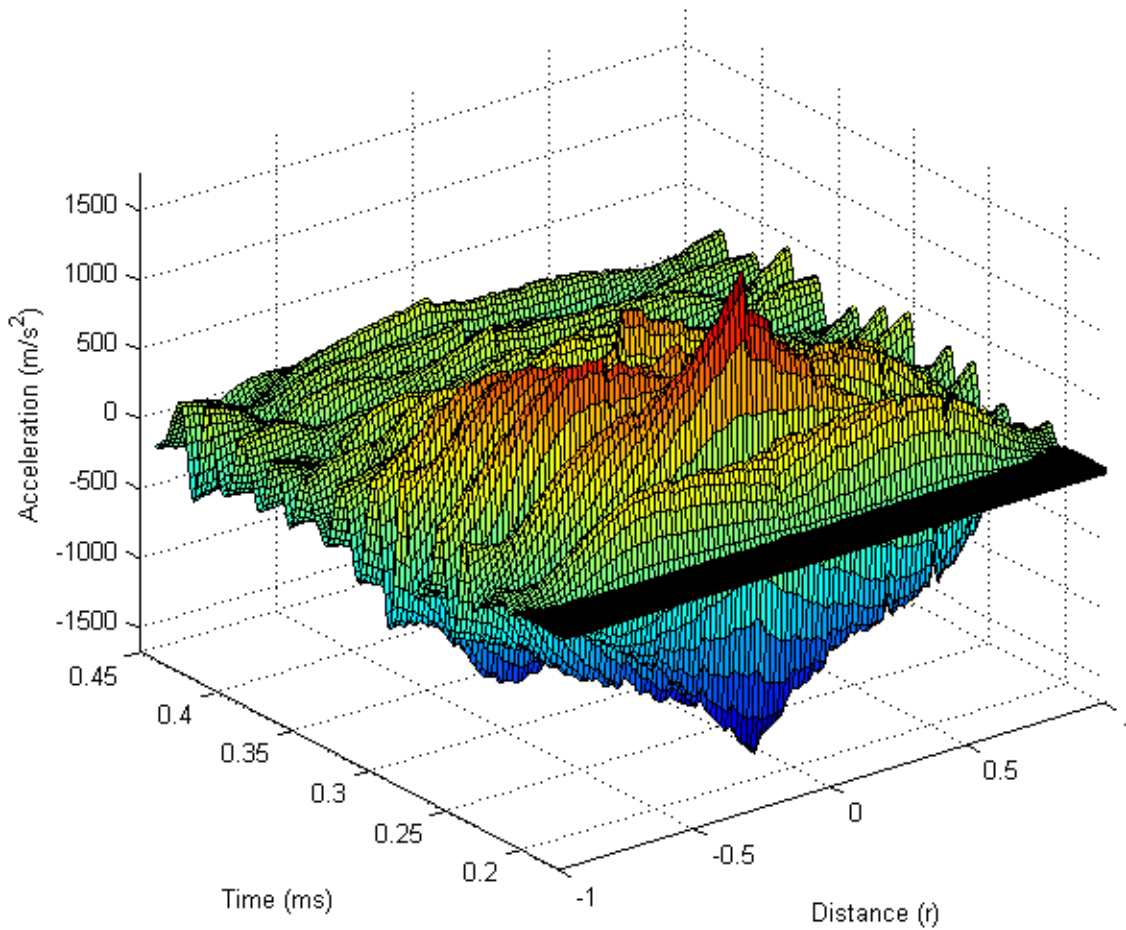


Figure B.14: Acceleration time history along the diameter of the transmitter under transient excitation of 125 Volt. The measurements at the center of the transmitter ($r=0$) corresponds to the scans at the edge of accelerometer A2, since center cannot be measured due to the attached accelerometer.

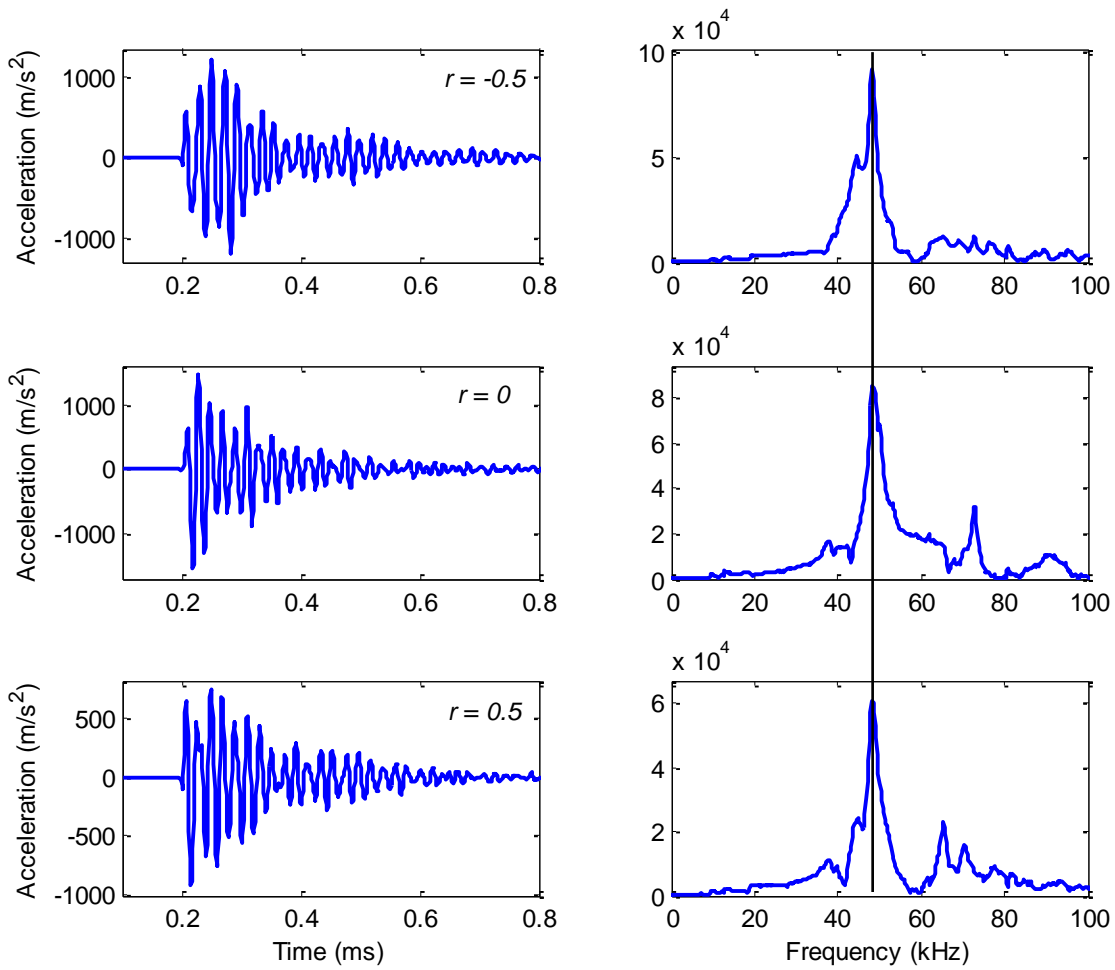


Figure B.15: Acceleration time histories and corresponding Fourier spectra at normalized radius of -0.5, 0 and 0.5 (Fig. B.14) respectively under transient excitation of 125 Volt for A2.

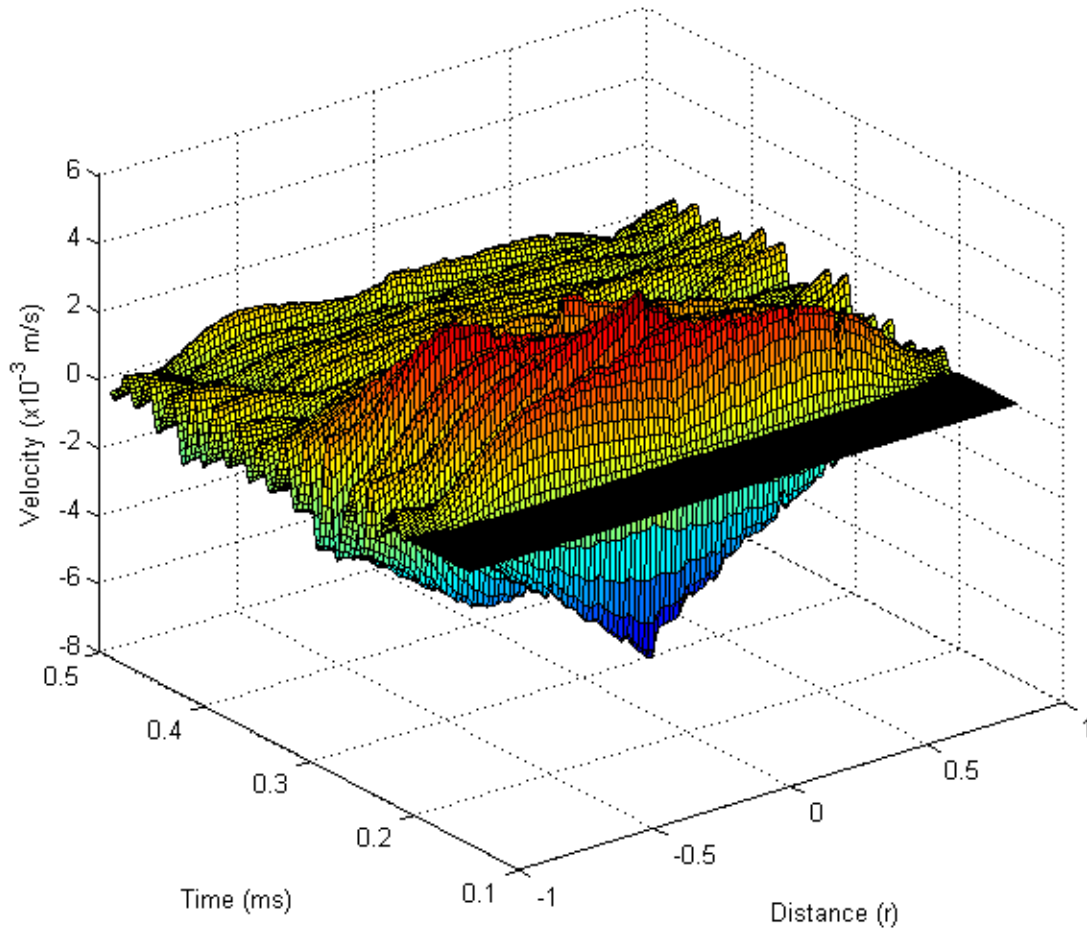


Figure B.16: Velocity time history along the diameter of the transmitter under transient excitation of 125 Volt. The measurements at the center of the transmitter ($r=0$) corresponds to the scans at the edge of accelerometer A2, since center cannot be measured due to the attached accelerometer.

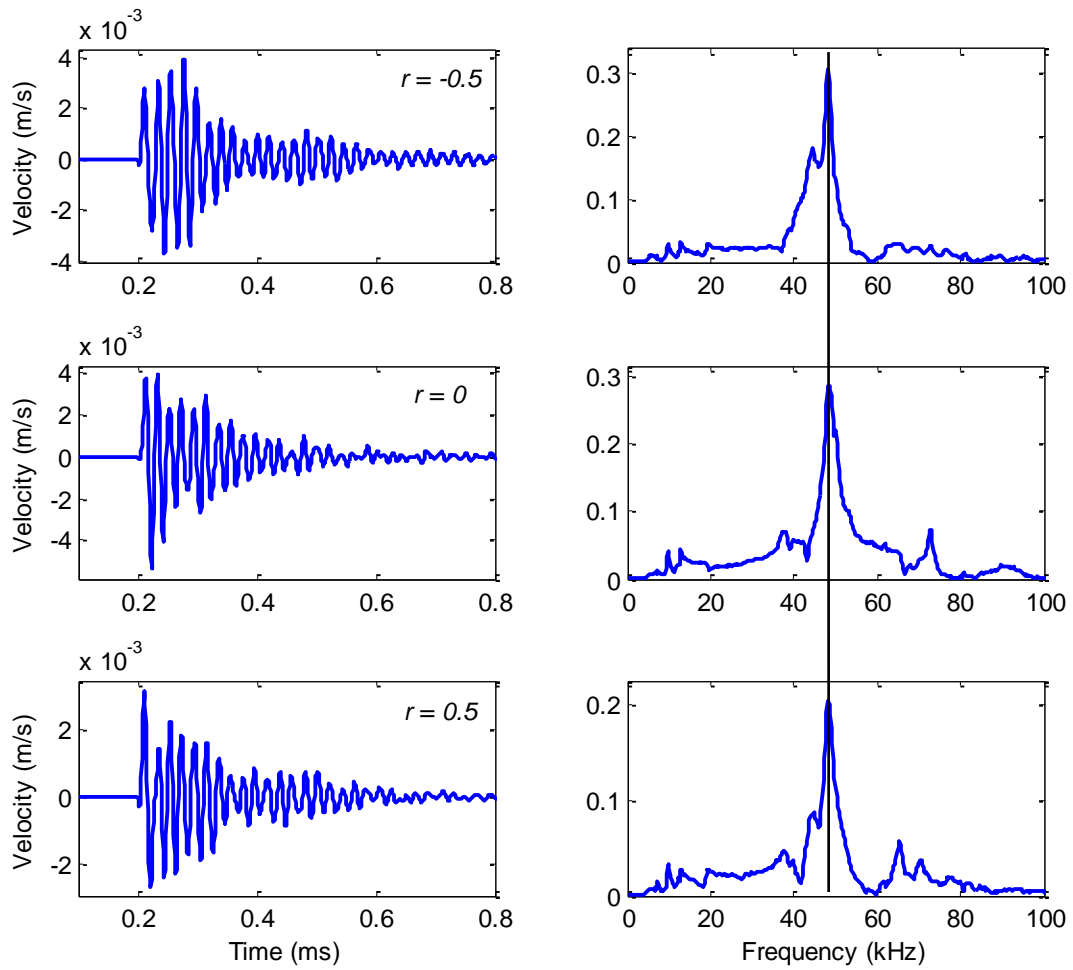


Figure B.17: Velocity time histories and corresponding Fourier spectra at normalized radius of -0.5, 0 and 0.5 (Fig. B.16) respectively under transient excitation of 125 Volt for A2.

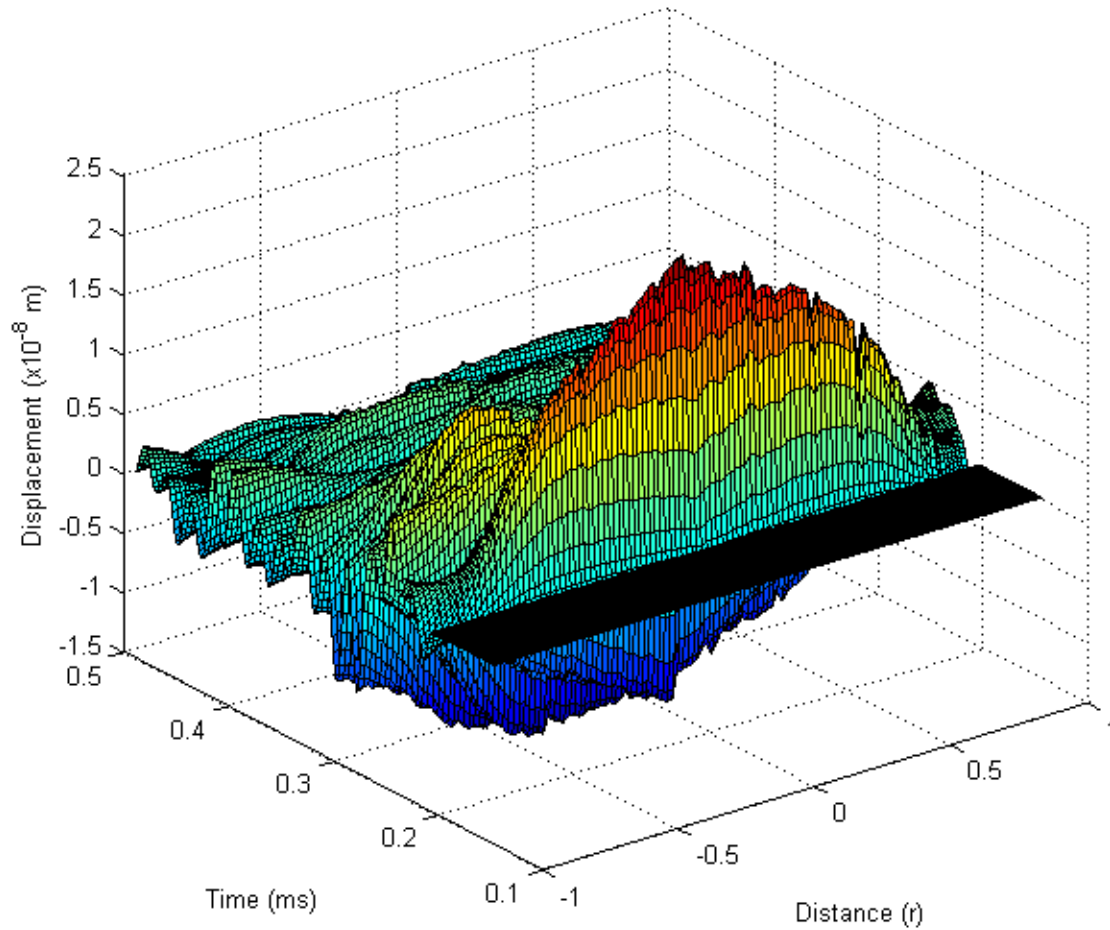


Figure B.18: Displacement time history along the diameter of the transmitter under transient excitation of 125 Volt. The measurements at the center of the transmitter ($r=0$) corresponds to the scans at the edge of accelerometer A2, since center cannot be measured due to the attached accelerometer.

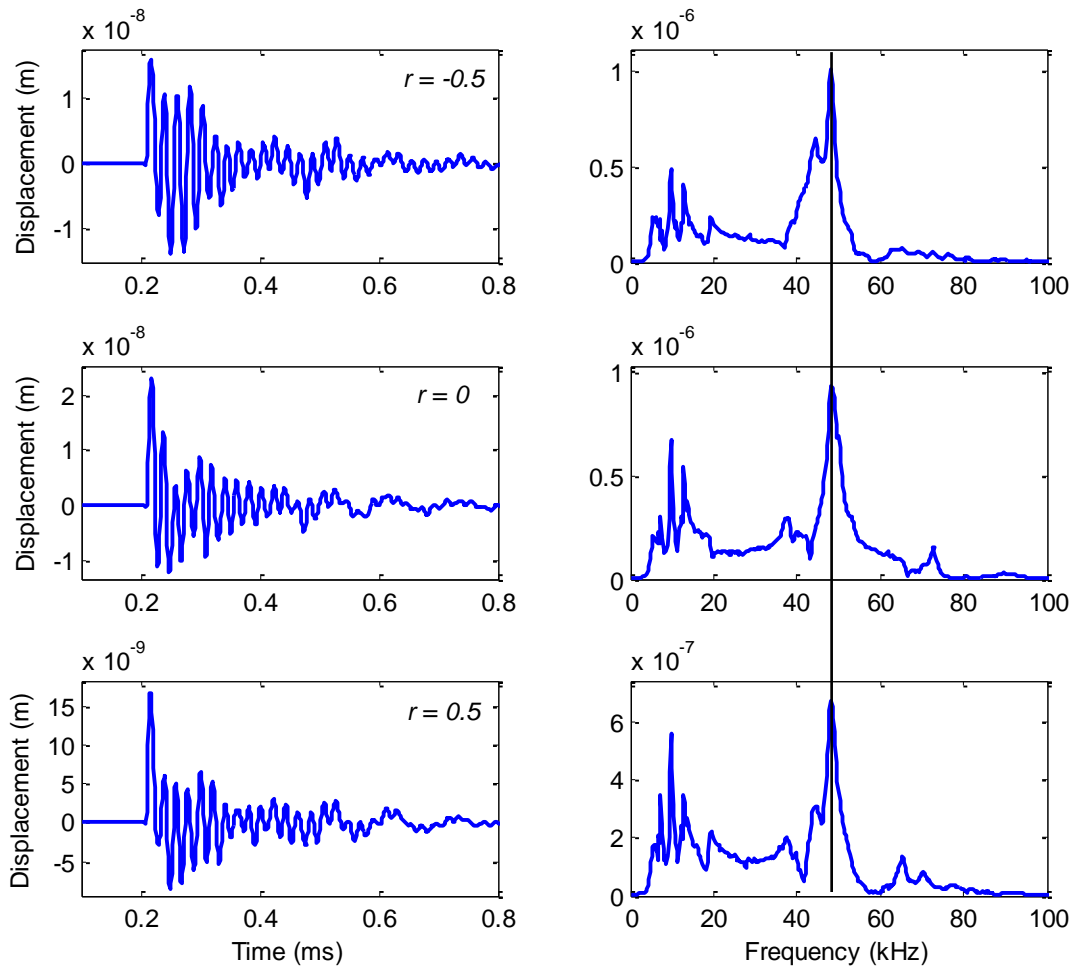


Figure B.19: Displacement time histories and corresponding Fourier spectra at normalized radius of -0.5, 0 and 0.5 (Fig. B.18) respectively under transient excitation of 125 Volt for A2.

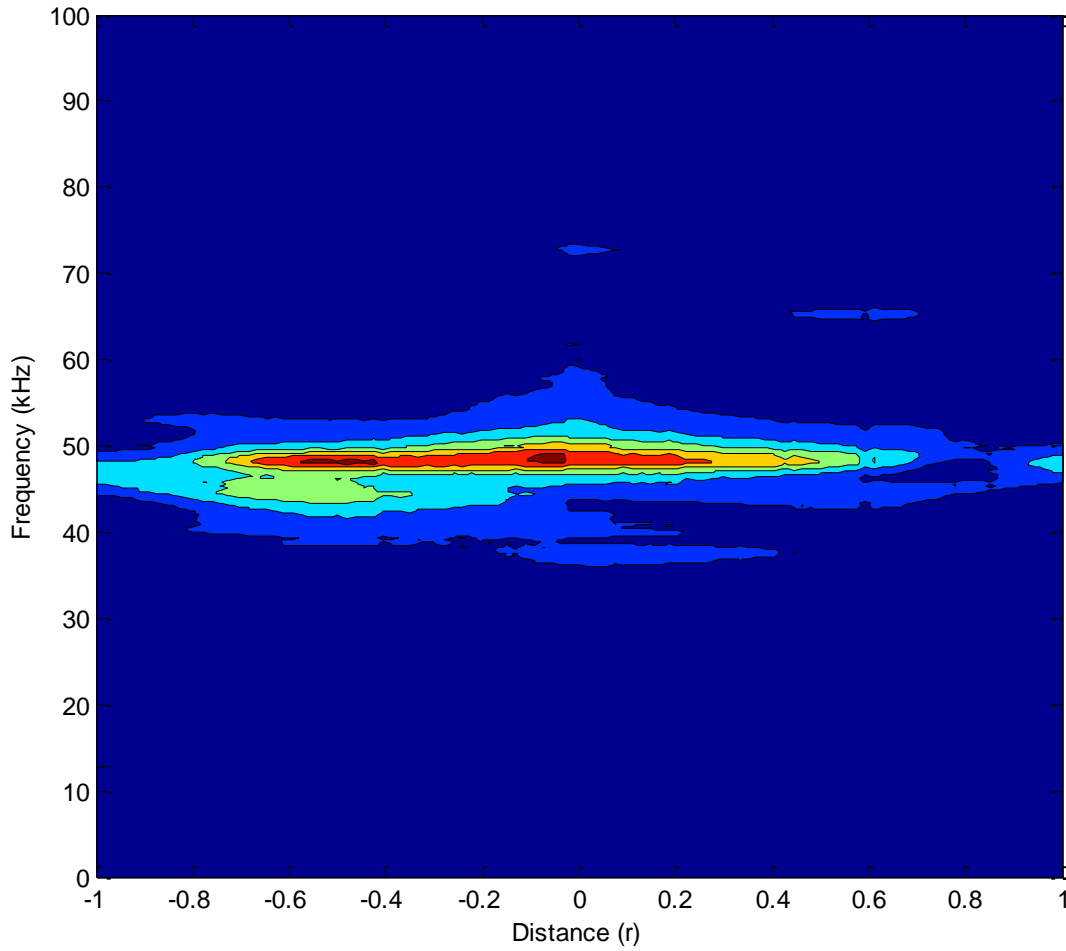


Figure B.20: Velocity Fourier spectra along the diameter of the transmitter under transient excitation of 125 Volt. The measurements at the center of the transmitter ($r=0$) corresponds to the scans at the edge of accelerometer A2, since center cannot be measured due to the attached accelerometer.

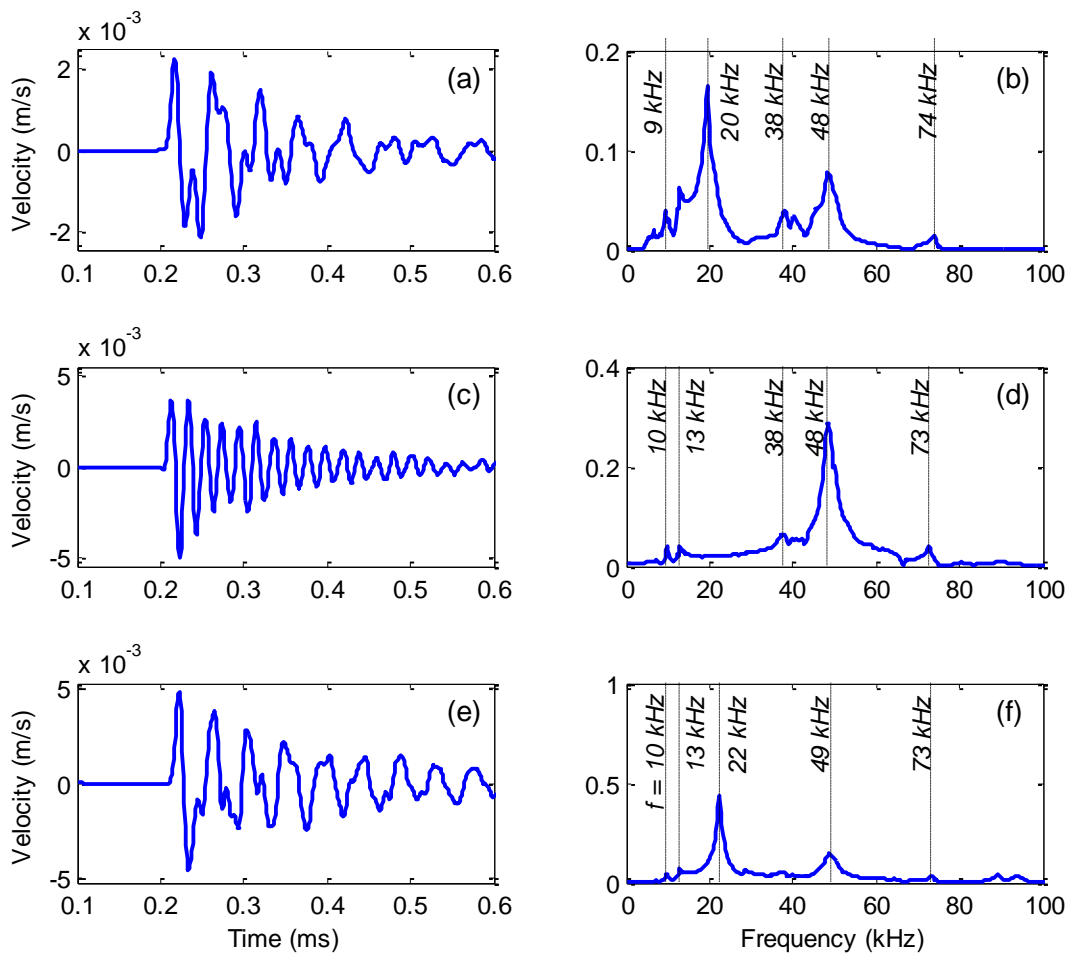


Figure B.21: Velocity time histories and Fourier spectra of (a,b) output, (c,d) input, and (e,f) vibration on the top of accelerometer A2.

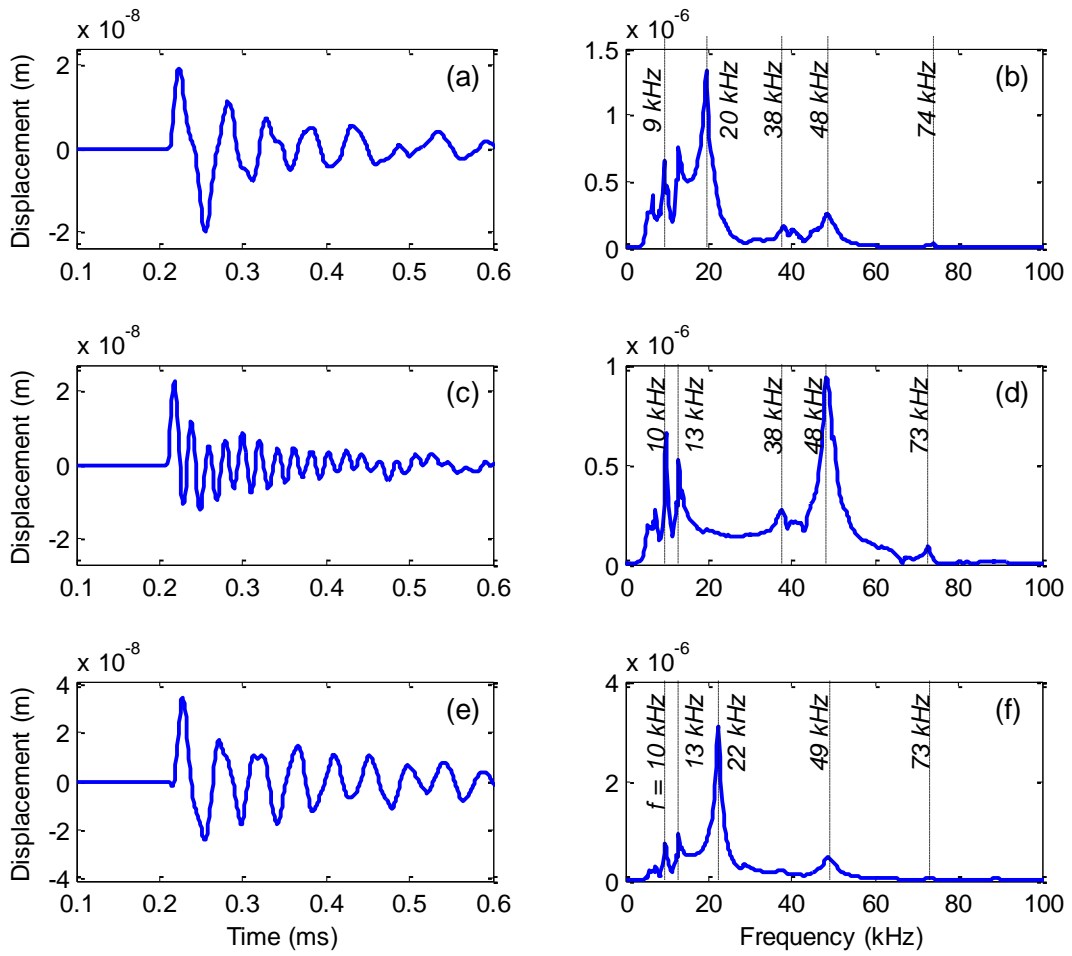


Figure B.22: Displacement time histories and Fourier spectra of (a,b) output, (c,d) input, and (e,f) vibration on the top of accelerometer A2.

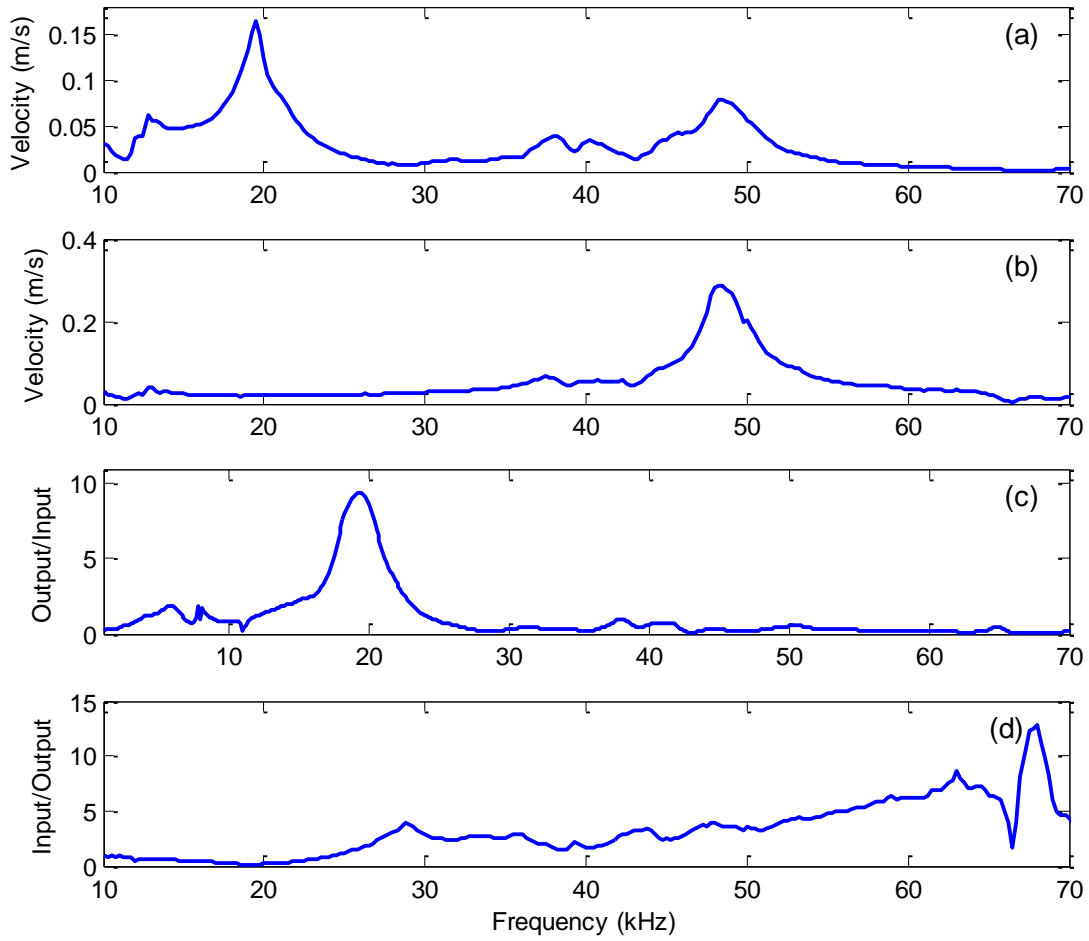


Figure B.23: (a) Input velocity, (b) Output velocity, (c) Frequency response function computed by taking the ratio of output over input, (d) Inverse FRF for A2.

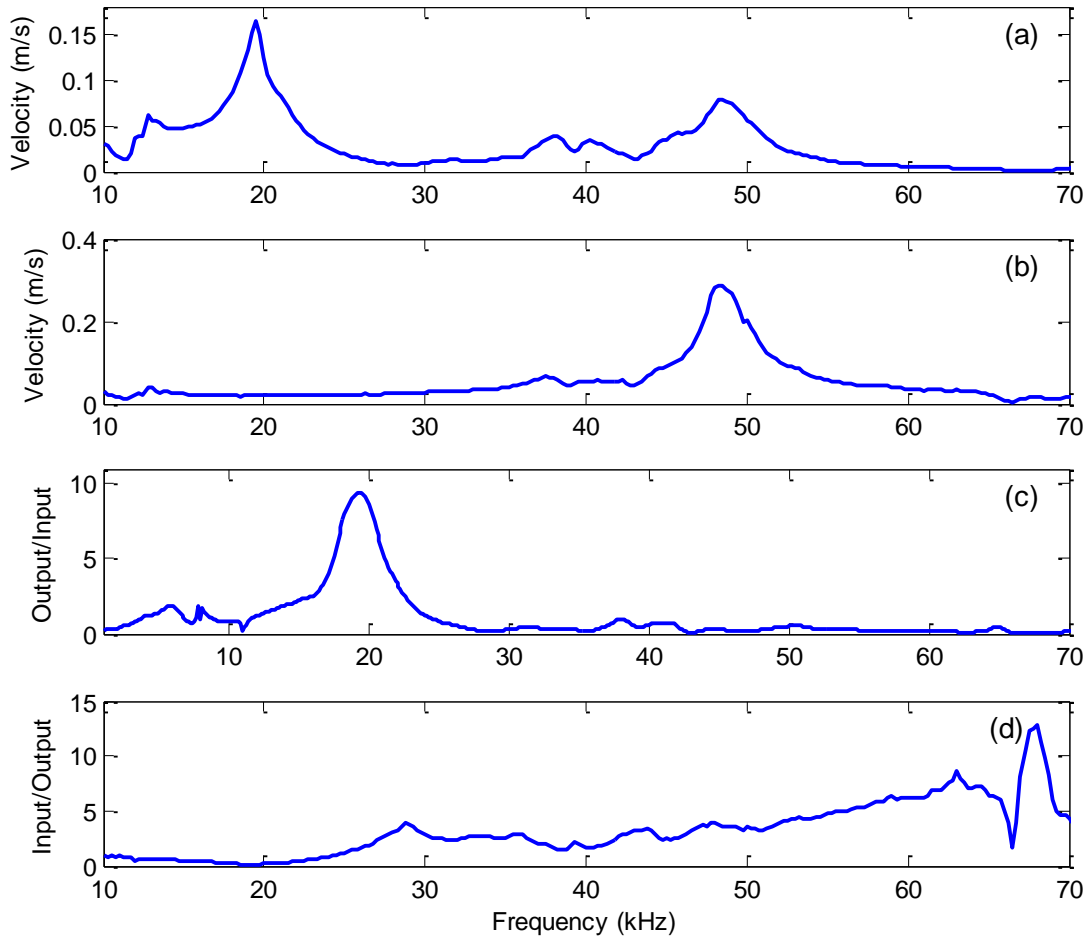


Figure B.24: (a) Input displacement, (b) Output displacement, (c) Frequency response function computed by taking the ratio of output over input, (d) Inverse FRF for A2.

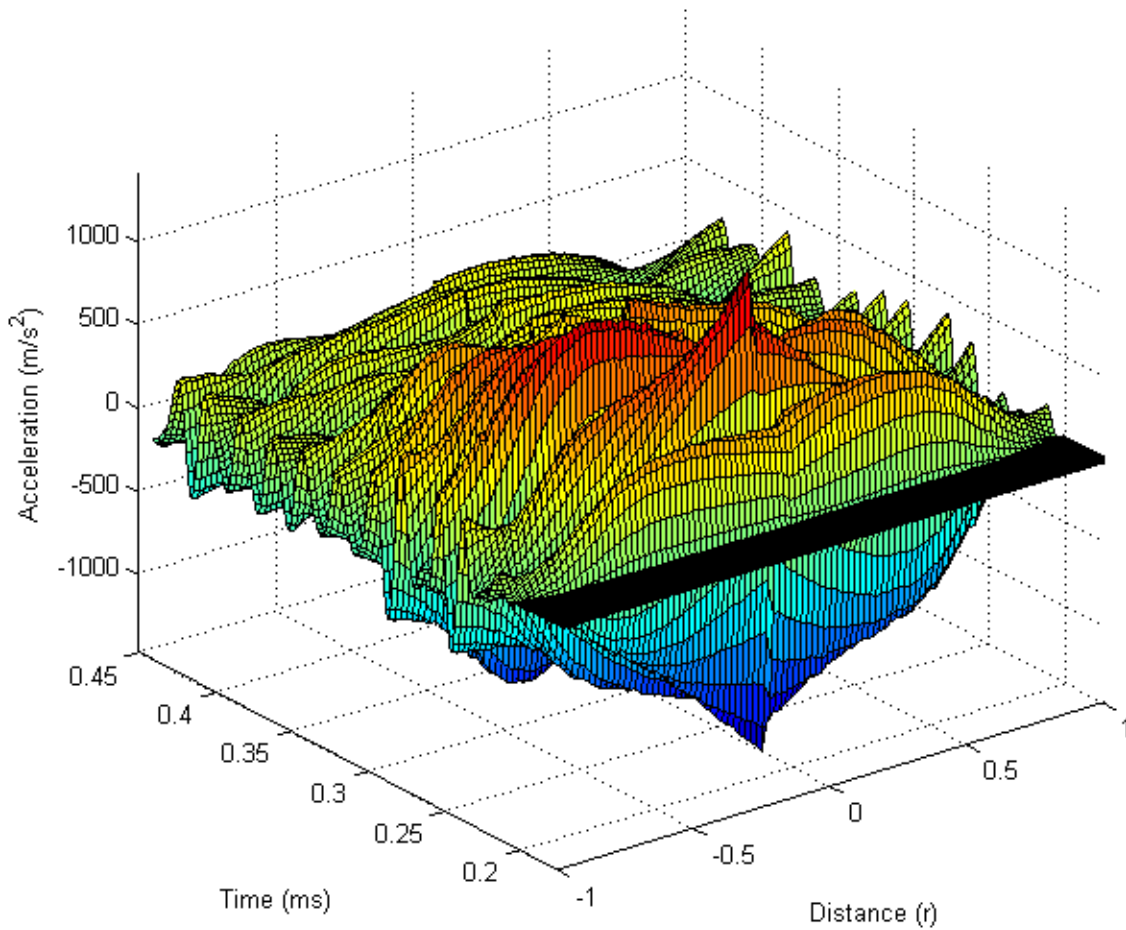


Figure B.25: Acceleration time history along the diameter of the transmitter under transient excitation of 125 Volt. The measurements at the center of the transmitter ($r=0$) corresponds to the scans at the edge of accelerometer A3, since center cannot be measured due to the attached accelerometer.

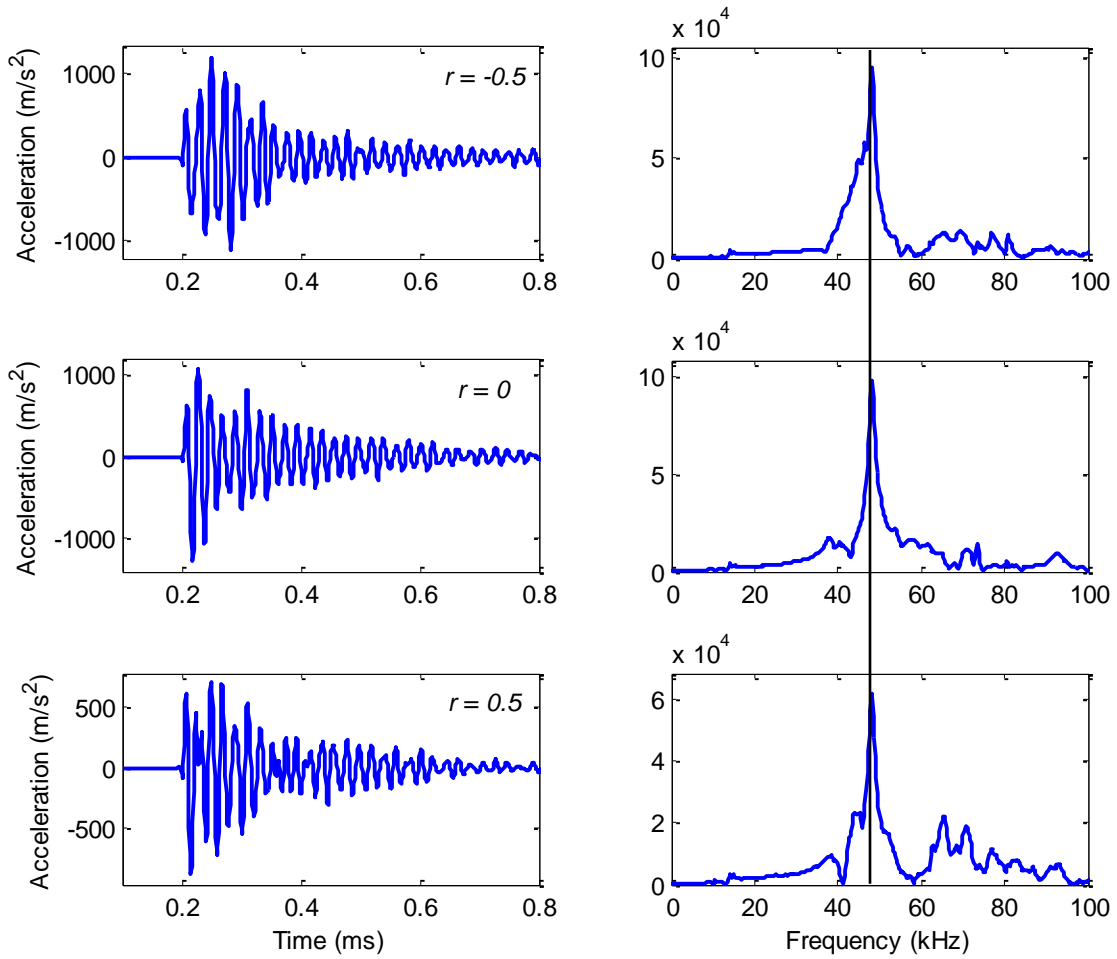


Figure B.26: Acceleration time histories and corresponding Fourier spectra at normalized radius of -0.5, 0 and 0.5 (Fig. B.25) respectively under transient excitation of 125 Volt for A3.

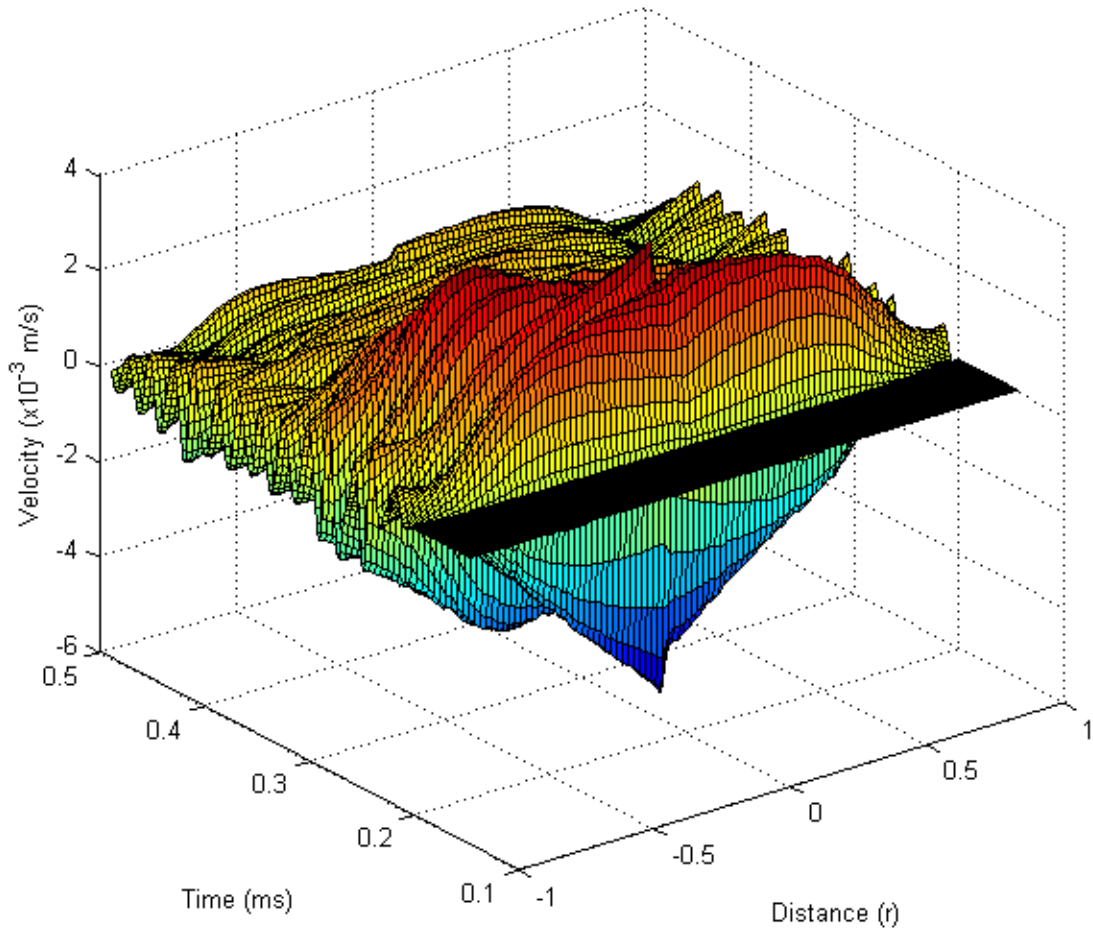


Figure B.27: Velocity time history along the diameter of the transmitter under transient excitation of 125 Volt. The measurements at the center of the transmitter ($r=0$) corresponds to the scans at the edge of accelerometer A3, since center cannot be measured due to the attached accelerometer.

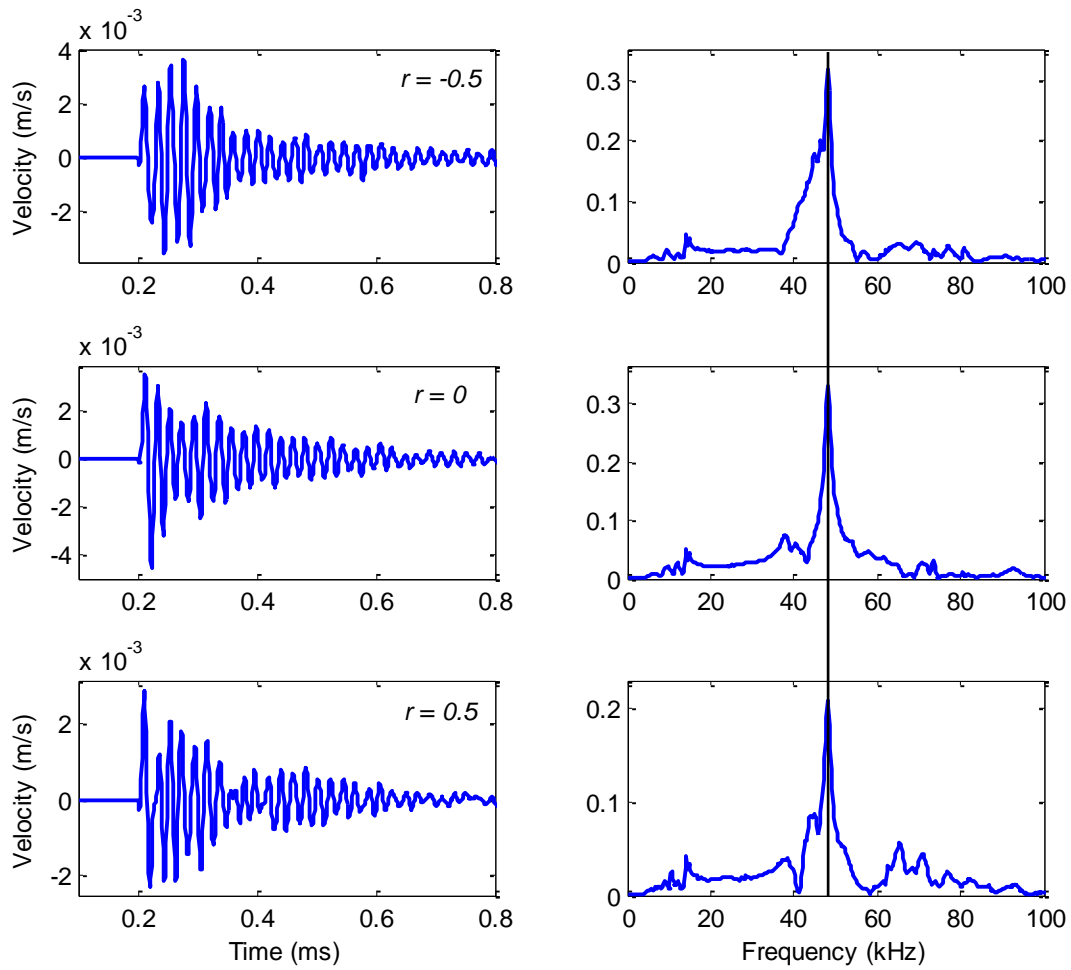


Figure B.28: Velocity time histories and corresponding Fourier spectra at normalized radius of -0.5, 0 and 0.5 (Fig. B.27) respectively under transient excitation of 125 Volt for A3.

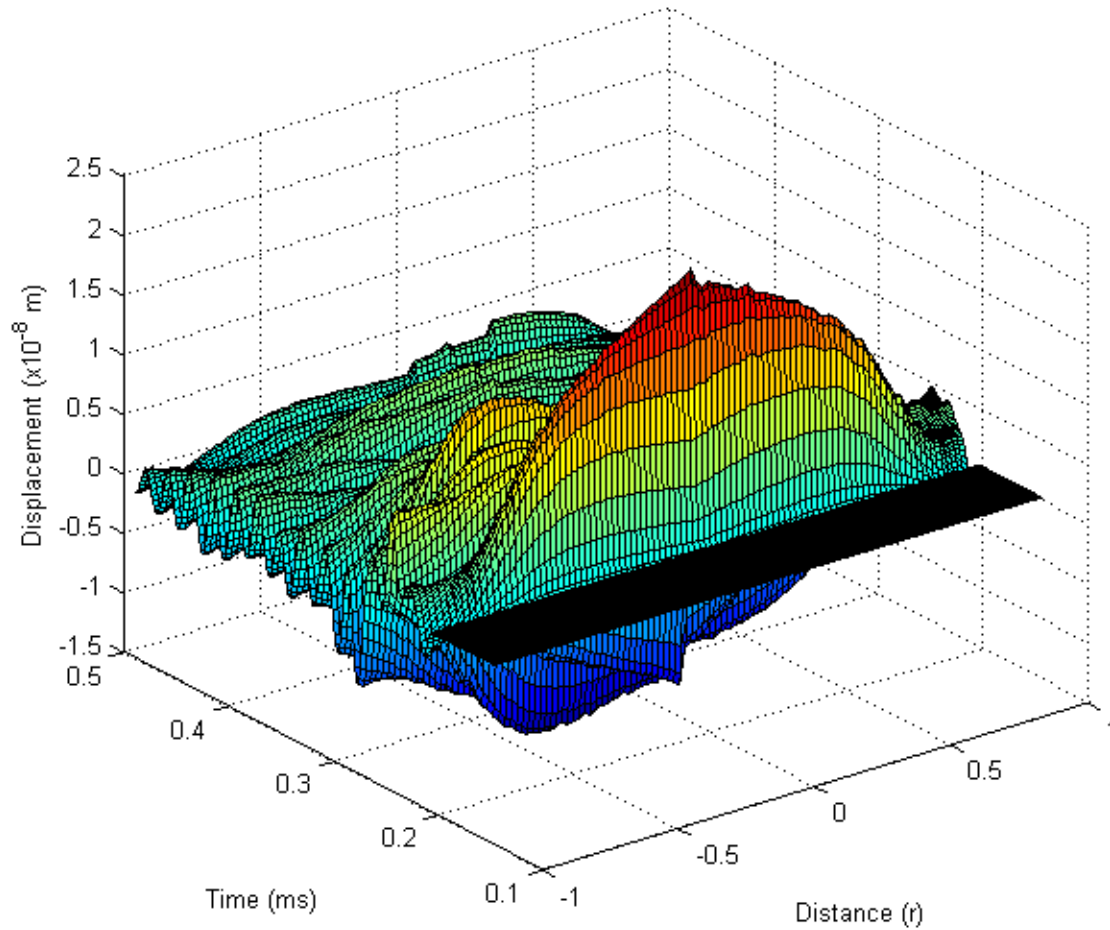


Figure B.29: Displacement time history along the diameter of the transmitter under transient excitation of 125 Volt. The measurements at the center of the transmitter ($r=0$) corresponds to the scans at the edge of accelerometer A3, since center cannot be measured due to the attached accelerometer.

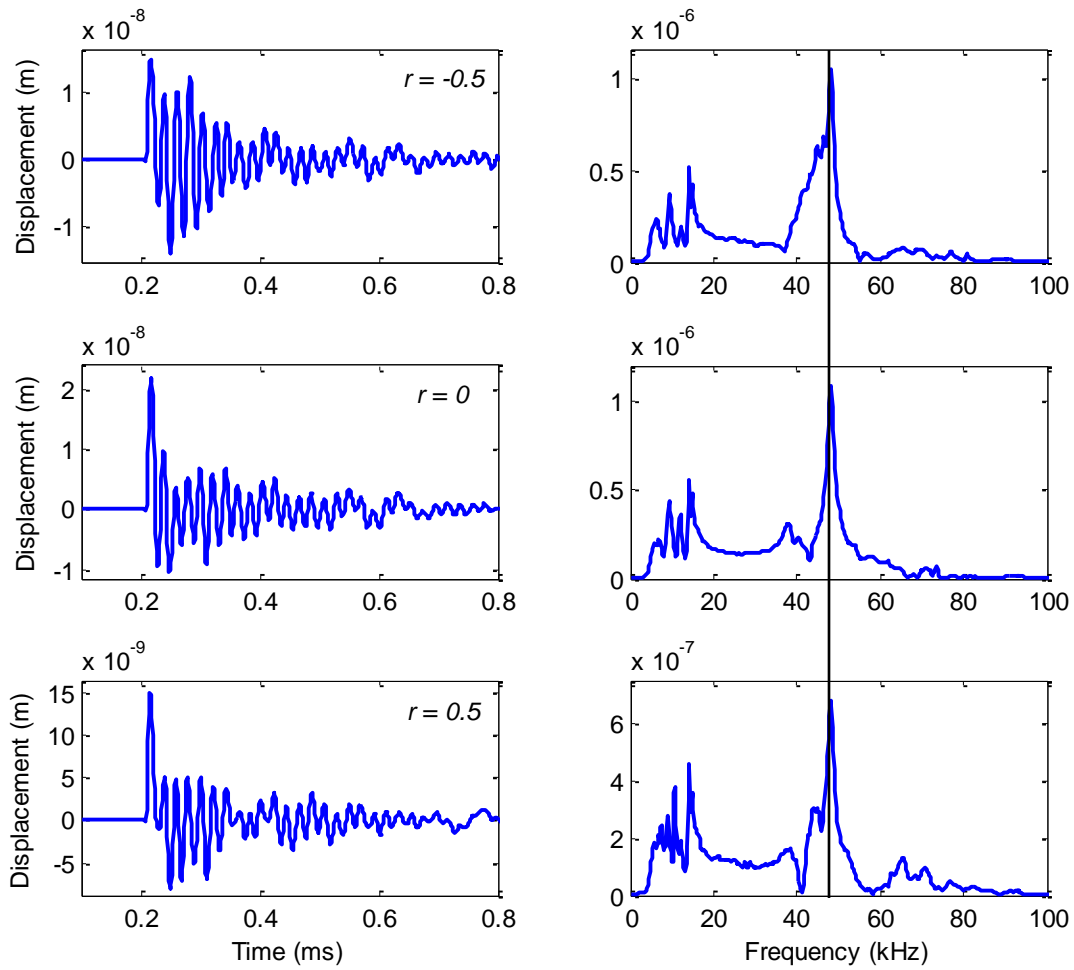


Figure B.30: Displacement time histories and corresponding Fourier spectra at normalized radius of -0.5, 0 and 0.5 (Fig. B.29) respectively under transient excitation of 125 Volt for A3.

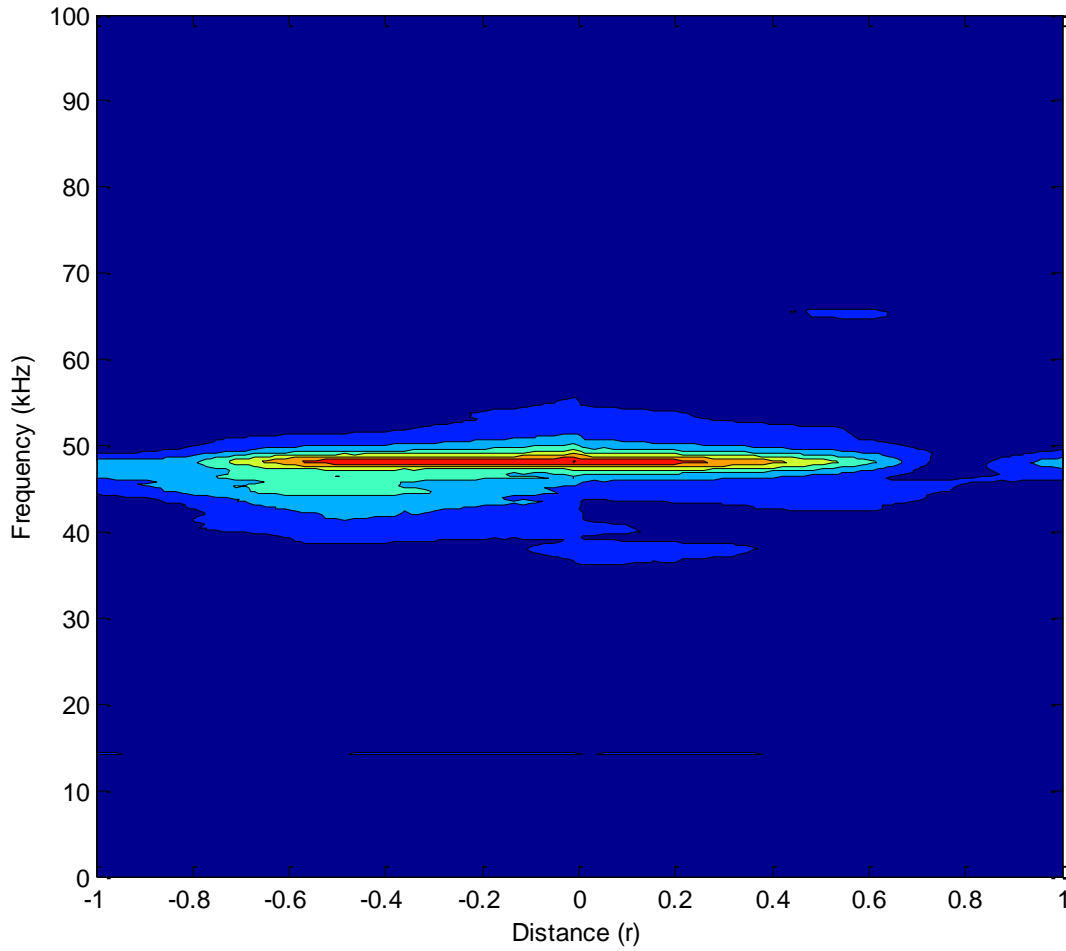


Figure B.31: Velocity Fourier spectra along the diameter of the transmitter under transient excitation of 125 Volt. The measurements at the center of the transmitter ($r=0$) corresponds to the scans at the edge of accelerometer A3, since center cannot be measured due to the attached accelerometer.

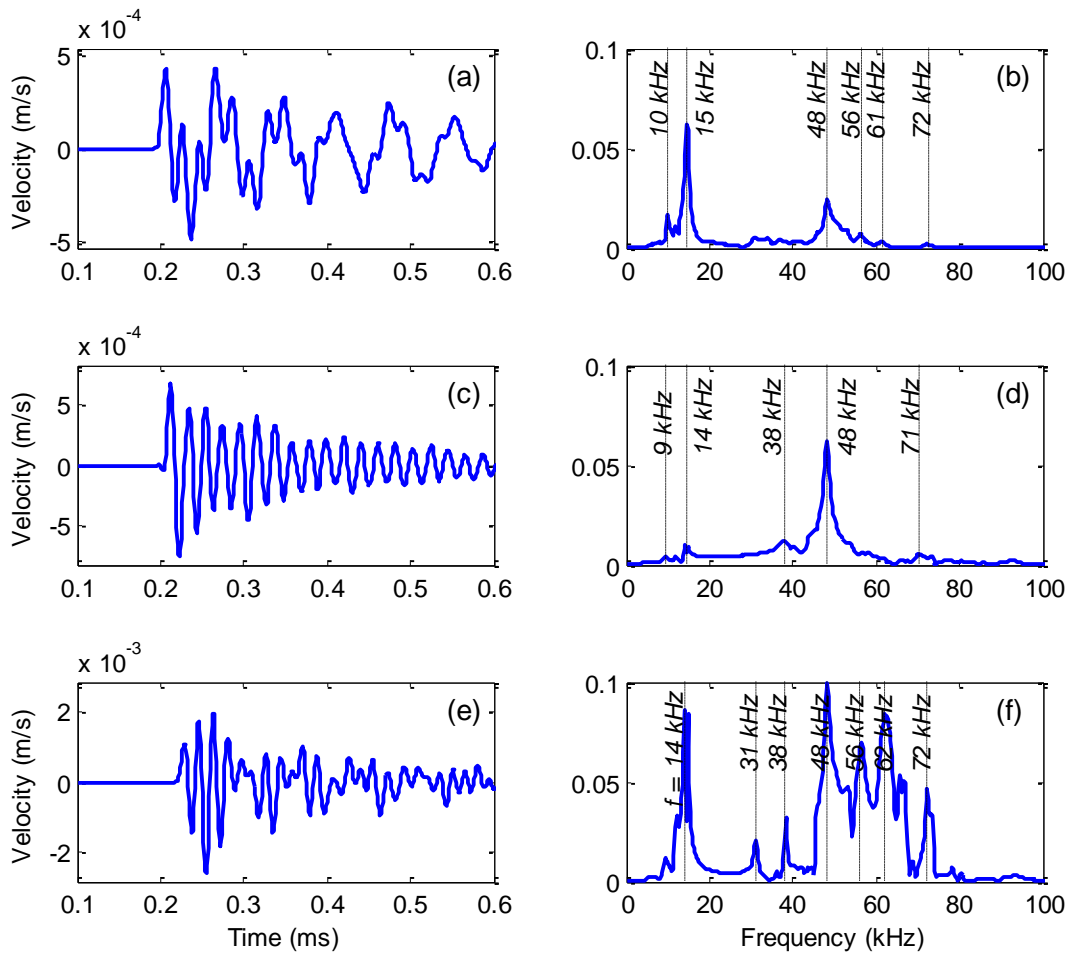


Figure B.32: Velocity time histories and Fourier spectra of (a,b) output, (c,d) input, and (e,f) vibration on the top of accelerometer A3. Input and top signals are divided by 5 ($125V/25V$) to ensure the same excitation voltage.

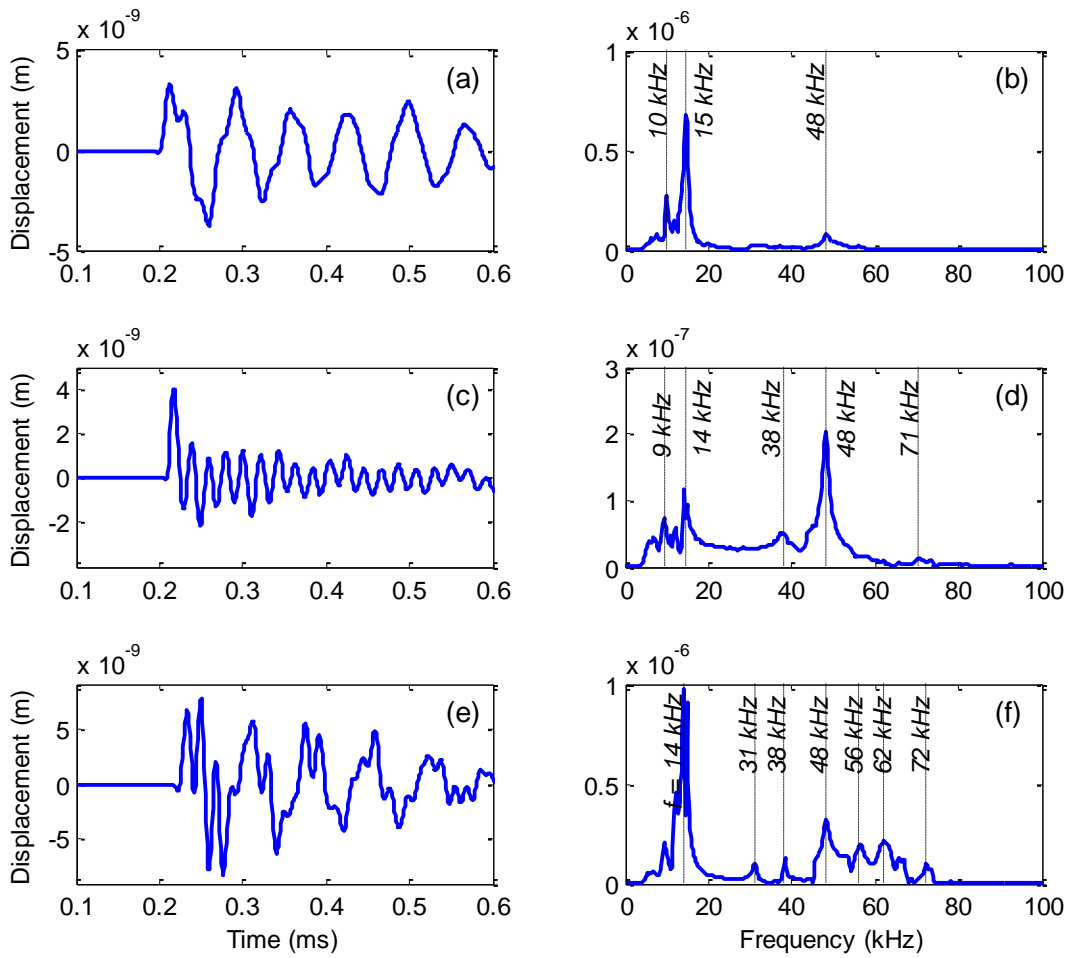


Figure B.33: Displacement time histories and Fourier spectra of (a,b) output, (c,d) input, and (e,f) vibration on the top of accelerometer A3. Input and top signals are divided by 5 ($125V/25V$) to ensure the same excitation voltage.

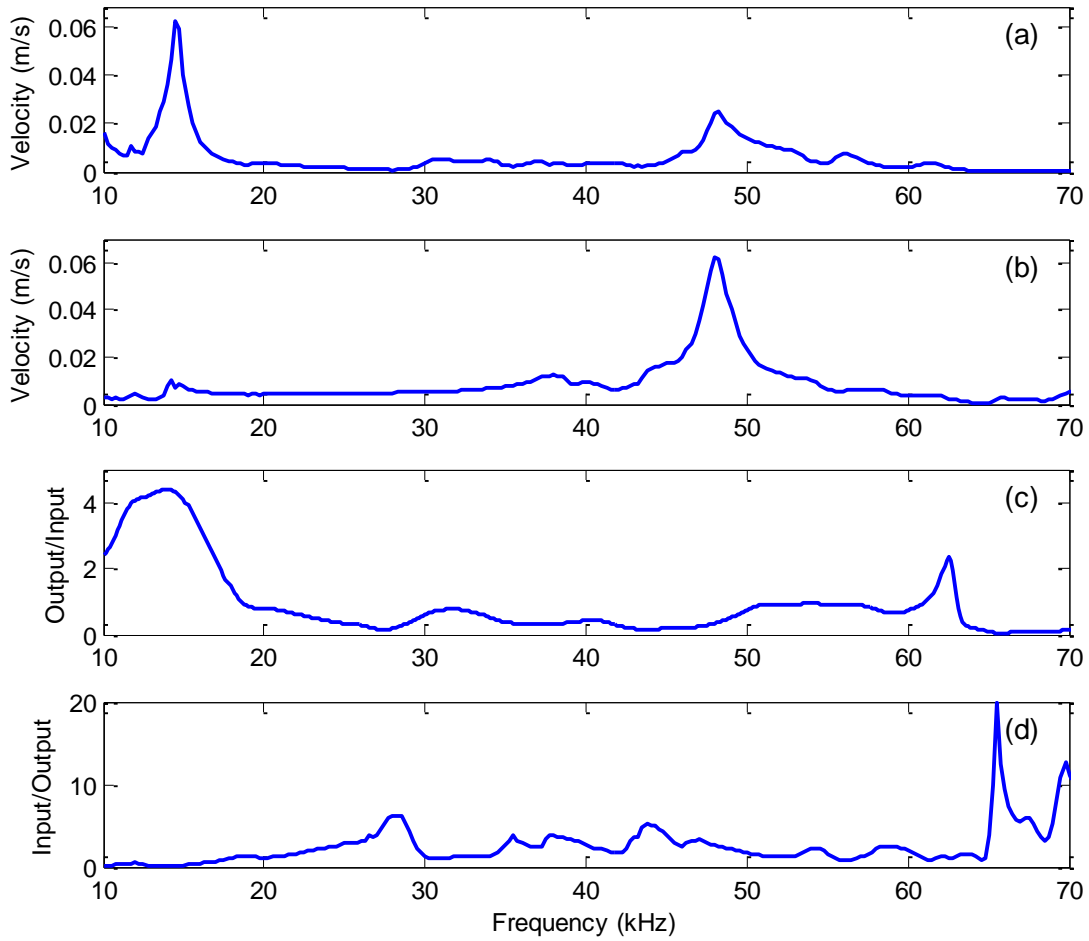


Figure B.34: (a) Input velocity, (b) Output velocity, (c) Frequency response function computed by taking the ratio of output over input, (d) Inverse FRF for A3.

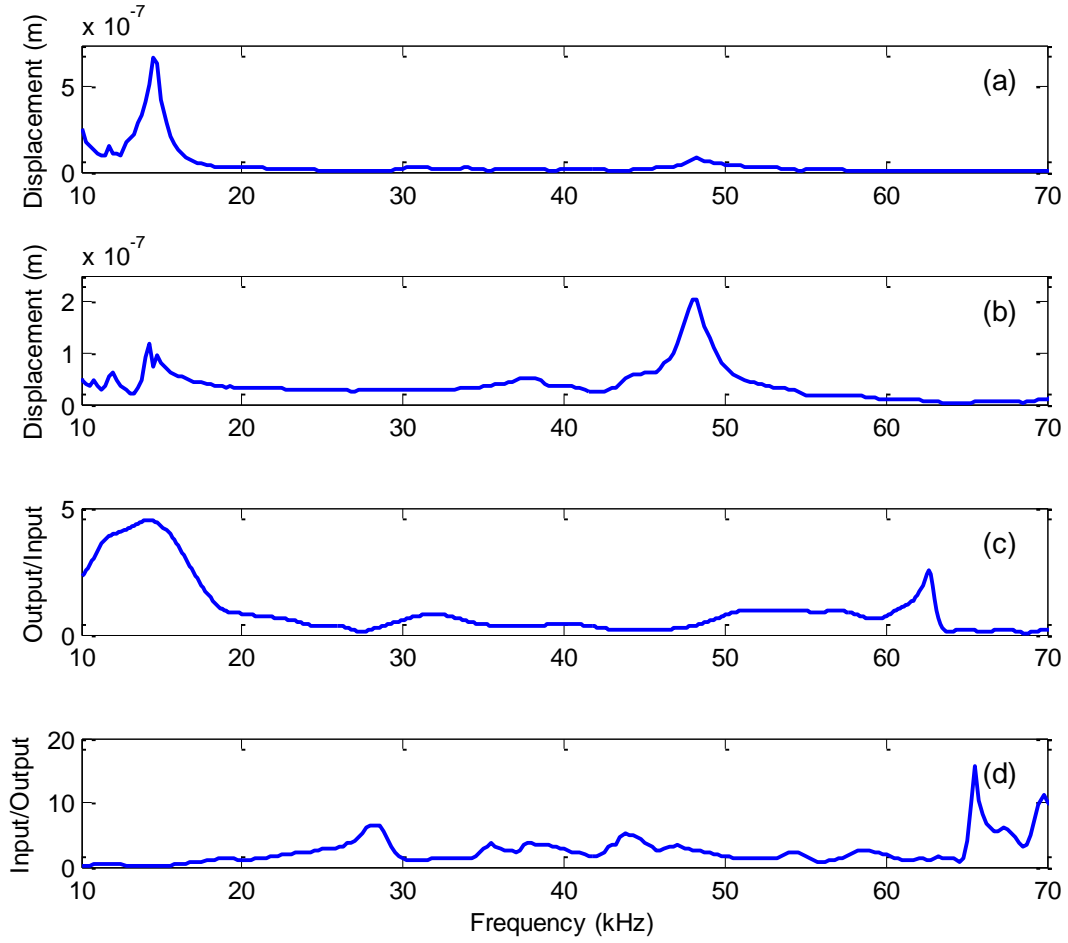


Figure B.35: (a) Input displacement, (b) Output displacement, (c) Frequency response function computed by taking the ratio of output over input, (d) Inverse FRF for A3.

Appendix C: Matlab Code for Signal Processing Procedure

```
% DEFINE PARAMETERS -----
% FILTERS -----
% WINDOWS -----
% ELIMINATE DC & GEO ATTENUATION and FILTER SIGNAL (OPTIONAL) -----
% COMPUTE VP & VR and PLOT TIME HISTORIES -----
% FOURIER SPECTRA -----
% ATTENUATION OF SPECTRAL AREA -----
% PHASE VELOCITY & 2D FFT -----
% PHASE VELOCITY from UNWRAPPED PHASE -----
% MATERIAL DAMPING based on WAVELET TRANSFORM -----
% DISCRETE WAVELET TRANSFORM -----
% NONLINEAR REGRESSION for ATTENUATION -----
% SAVE PARAMETERS -----

%function [] = Transit_1(no)
close all
%clearvars -except no
clear all
clc
% Type the test no
no1 = num2str(0); % Damage number
%no1 = num2str(no); % Damage number
no2 = 'A'; % Excitation type
no3 = num2str(1); % Source number
data = sprintf([no2 no3 '_' no1]);
load(strcat('C:\Users\askirlan\Desktop\Sandbox\Phase
III\Transient\Data\',no2,no3,'\ ',no2,no3,'\ ',no1, '.mat'));

%% DEFINE PARAMETERS -----
% Time and frequency array for the signals from oscilloscope
dt = 1e-6; % second
N = size(acc,1); % Number of data points
c = size(acc,2); % Number of receivers
t = dt:dt:(N*dt); % second
T = dt*N; % Total signal time
df = 1/(T-t(1)); % Hz
f = df:df:(N)*df; % Hz

% Distance and wanenumber array
x0 = 0.055; % m
dx = 0.025; % m
x = x0:dx:(x0+(c-1)*dx);

% Parameters for wavelet transform
Fc = 52000; % Central frequency (Hz)
Fb = 0.0000112; % Bandwith (modulation) parameter
a = 1; % Scale parameter
to = 2/Fc; % Default initial time (s)
b = t; % Shift time
Nw = round(N/10); % Size of signal to transform

% Parameters to compute material damping
```

```

siz = 7;           % Number of selected receivers
shift = c-siz+1;  % The first receiver of the array
mod = 8;          % How many times that # of receivers changes

% Other parameters
sc1 = 75;         % Scale distance for Time plots
sc2 = 35;         % Scale distance for FT plots
sc3 = 50;         % Scale distance for WT plots
Flim = 100;      % Max frequency limit for Fourier plots
avP = 1;         % Receivers that are avoided for VP calculation
avR1 = 1;        % The closer receivers that are avoided for VR
avR2 = 1;        % The further receivers that are avoided for VR
P1 = 0.0010;     % The normalized ampl. to pick the arrival of P-wave

Rmin1a = 0.25;   % The normalized acc. amp. to pick the pit of R-wave
Rmin1b = 0.25;   % The normalized acc. amp. pick the first pit of R-wave
Rmax1a = 0.25;   % The normalized acc. amp. to pick the peak of R-wave
Rmax1b = 0.25;   % The normalized acc. ampl. to pick the peak of R-wave

W1 = 0.25;       % The normalized ampl. to pick the first peak Wavelet
res_freq = Fc;   % Resonance freq of transmitter to compute damping based
                % on the Peak of R-wave in time domain
V1 = 2000;       % Assume velocity for window1
V2 = 1500;       % Assume velocity for window2
siz2 = c;        % Number of selected receivers to compute phase velocity
                % from unwrapped phase

% Switches
GEO = 1;         % Geometric Attenuation switch; '1' is for YES
FLTR = 0;        % Filter switch for damping calculations; '1' is for YES

%% FILTERS -----
% Define Butterworth Filter for Damping Calculation
% NOTE: Be careful with the max. value for freq. range 500 or 512 kHz
fmin = 3;        % kHz
fmax = 100;      % kHz
[bb,aa] = butter(6, [fmin/(max(f)/1000/2) fmax/(max(f)/1000/2)], 'bandpass');
h = dfilt.df1(bb,aa);
%fvtool(h)

%% WINDOWS -----
% Define Tukey (Tapered cosine) window for Vp and VR calculations
wr = 0.05;       % Taper slope
ww = 300;        % Width of window
wd = 60;         % Window delay
for k = 1:c
    n1(k) = round(x(k)/V1/dt)+wd;
    n2(k) = ww + n1(k);
end
for k = 1:c
    w_tukey = tukeywin(ww,wr);
    for j = 1:N
        if j <= n1(k) || j >= n2(k)
            win1(j,k) = 0;
        else win1(j,k) = w_tukey(j-n1(k));
        end
    end
end

```

```

    end
end

% Define Tukey (Tapered cosine) window for Permanent Window
wr = 0.05;      % Taper slope
ww = 1000;     % Width of window
wd = 0;        % Window delay
for k = 1:c
    n1(k) = round(x(k)/V1/dt)+wd;
    n2(k) = ww + n1(k);
end
for k = 1:c
    w_tukey3 = tukeywin(ww,wr);
    for j = 1:N
        if j <= n1(k) || j >= n2(k)
            win3(j,k) = 0;
        else win3(j,k) = w_tukey3(j-n1(k));
        end
    end
end

% Define Tukey (Tapered cosine) window for FFT
wr = 0.1;      % Taper slope
ww2 = 5;       % Additional width of window
wd = 100;      % Window delay
for k = 1:c
    n1(k) = round(x(k)/V2/dt)+wd;
    ww(k) = round(N/100+ww2*k); % Width of window
    n2(k) = ww(k) + n1(k);
end
for k = 1:c
    w_tukey1 = tukeywin(ww(k),wr);
    for j = 1:N
        if j <= n1(k) || j >= n2(k)
            win2(j,k) = 0;
        else win2(j,k) = w_tukey1(j-n1(k));
        end
    end
end

%% ELIMINATE DC & GEO ATTENUATION and FILTER SIGNAL (OPTIONAL) -----
% Eliminate DC component
for l = 1:c
    acc(:,l) = acc(:,l) - mean(acc(:,l));
end

% Filter signals using Butterworth filter
if FLTR == 1
    acc_f = filtfilt(bb,aa,acc);
else
    acc_f = acc;
end

% Eliminate geometric attenuation
if GEO == 1
    for k = 1:c

```

```

        acc_f(:,k) = (x(k)/x(1))^0.5*acc_f(:,k);
    end
end

% Permanent window
acc_f = acc_f.*win3;

%% COMPUTE VP & VR and PLOT TIME HISTORIES -----
% Normalize each time signal respect to maximum value of itself
for k = 1:c
    acc_n(:,k) = acc_f(:,k)/max(abs(acc_f(:,k)));
end

% Window signals
acc_nw1 = acc_n.*win1;

% Pick the arrival time for P-wave
for k = 1+avP:c-avP
    for j = 2:N
        if acc_nw1(j-1,k) < acc_nw1(j,k) && acc_nw1(j+1,k) < acc_nw1(j,k) &&
acc_nw1(j,k) >= P1
            A_P(k-avP) = abs(acc_f(j,k));
            T_P(k-avP) = j;
            break
        end
    end
end

% Compute the P-wave velocity
coef1 = polyfit(x(1+avP:c-avP),T_P,1);
fitT_P = polyval(coef1,x);
VP1 = abs(max(x)-min(x))/(abs(max(fitT_P)-min(fitT_P))*dt);

% Pick the 'first' pit amplitude and cell number for R-wave
for k = 1+avR1:c-avR2
    if k < 8
        Rmin = Rmin1a;
    else Rmin = Rmin1b;
    end
    for j = 2:N
        if acc_nw1(j-1,k) >= acc_nw1(j,k) && acc_nw1(j+1,k) >= acc_nw1(j,k)
&& abs(acc_nw1(j,k)) >= Rmin
            A_Rmin1(k-avR1) = abs(acc_f(j,k));
            T_Rmin1(k-avR1) = j;
            break
        end
    end
end

% Pick the 'first' peak amplitude and cell number for R-wave
for k = 1+avR1:c-avR2
    if k < 8
        Rmax = Rmax1a;
    else Rmax = Rmax1b;
    end
    for j = 2:N

```



```

        if acc_nw1(j-1,k) <= acc_nw1(j,k) && acc_nw1(j+1,k) <= acc_nw1(j,k)
&& acc_nw1(j,k) >= Rmax && T_Rmin1(k-avR1) < j
            A_Rmax1(k-avR1) = abs(acc_f(j,k));
            T_Rmax1(k-avR1) = j;
            break
        end
    end
end
end
% PTP value
A_R1 = A_Rmax1 + A_Rmin1;
T_R = (T_Rmax1 + T_Rmin1)/2;
% Compute the Rayleigh velocity
coef2 = polyfit(x(1+avR1:c-avR2),T_R,1);
fitT_R = polyval(coef2,x);
VR1 = abs(max(x)-min(x))/(abs(max(fitT_R)-min(fitT_R))*dt);

figure,
for k = 1:c
    plot(t*1000,acc_n(:,k)+sc1*x(k), 'Linewidth',2), hold on,
    plot(t*1000,win3(:,k)+sc1*x(k), 'Linewidth',2, 'Color', 'black'), hold on,
    % Mark the receiver no
    text(x(k), acc_n(1,1), num2str(k), ...
        'Units', 'normalized', 'Position', [0.01 k/c-0.025], 'EdgeColor', 'Red', ...
        'FontAngle', 'Italic', 'FontSize', 9, 'BackgroundColor', 'White');
end
plot(fitT_R*dt*1000, sc1*x, 'Linewidth', 2.5, 'Color', 'Black'), hold on,
plot(fitT_P*dt*1000, sc1*x, 'Linewidth', 2.5, 'Color', 'Black'),
xlim([0 1]), ylim([sc1*x(1)-1.2 sc1*x(c)+1.2]),
xlabel('Time (ms)'), ylabel('Distance to Source'), set(gca, 'YTickLabel', '')
% Mark the VP on the plot
text(x(1), fitT_P(1), [' V_P=', num2str(round(VP1)), ' m/s\rightarrow'], ...
'Units', 'normalized', 'Position', [0.07 0.9], 'EdgeColor', 'Red', 'FontAngle',
'Italic', 'FontWeight', 'Bold', 'FontSize', 10, 'BackgroundColor', 'White');
% Mark the VR1 on the plot
text(x(1), fitT_R(1), [' V_R=', num2str(round(VR1)), ' m/s\rightarrow'], ...
'Units', 'normalized', 'Position', [0.1 0.75], 'EdgeColor', 'Red', 'FontAngle',
'Italic', 'FontWeight', 'Bold', 'FontSize', 10, 'BackgroundColor', 'White');
set(gcf, 'Position', [512 50 650 500]); saveas(gcf, '01', 'fig'),

%% FOURIER SPECTRA -----
% Plot FFT for signals
ACC = abs(fft(acc_f));
for l = 1:c
    ACC_N(:,l) = ACC(:,l)/max(ACC(:,l));
end
figure,
for k = 1:c
    plot(f/1000, ACC_N(:,k)+sc2*x(k), 'Linewidth',2), hold on,
    % Mark the receiver no
    text(x(k), ACC_N(1,1), num2str(k), ...
        'Units', 'normalized', 'Position', [0.95 k/c-0.045], 'EdgeColor', 'Red', ...
        'FontAngle', 'Italic', 'FontSize', 9, 'BackgroundColor', 'White');
end
xlim([0 Flim]), ylim([sc2*x(1)-x(1) sc2*x(c)+1.1]),
xlabel('Frequency (kHz)'), ylabel('Distance to Source')
set(gca, 'YTickLabel', ''), set(gcf, 'Position', [512 50 650 500]);

```

```

title('Normalized Frequency Spectra'),saveas(gcf,'02','fig'),

% Normalized Contour plot of distance-frequency
figure
pcolor(f/1000, x, transpose(ACC_N));
xlabel('Frequency (kHz)'),ylabel('Distance (m)')
zlabel('Normalized Acceleration (m/s^2)'),xlim([0 Flim]), ylim([x(1) x(c)]),
shading interp,title('Normalized Frequency - Distance'),
set(gcf, 'Position', [512 50 650 500]);saveas(gcf,'03','fig'),

%% ATTENUATION OF SPECTRAL AREA -----
% Plot Windowed Normalized Time histories
acc_fw2 = acc_f; %.*win2;
figure,
for k = 1:c
    plot(t*1000,acc_fw2(:,k)/max(acc_fw2(:,k))+sc1*x(k), 'Linewidth',2), hold
on,
    plot(t*1000,win2(:,k)+sc1*x(k), 'Linewidth',2, 'Color','black'), hold on,
end
xlim([0 1]), ylim([sc1*x(1)-1 sc1*x(c)+2]),
xlabel('Time (ms)'), ylabel('Distance to Source')
set(gca, 'YTickLabel', '')
title('Windowed Normalized Time Histories'),
set(gcf, 'Position', [512 50 650 500]);
saveas(gcf,'04','fig'),
% Plot FFT of windowed signals
ACC1 = abs(fft(acc_fw2));
for l = 1:c
    ACC_N1(:,l) = ACC1(:,l)/max(ACC1(:,l));
end
figure,
for k = 1:c
    plot(f/1000,ACC_N1(:,k)+sc2*x(k), 'Linewidth',2), hold on,
    % Mark the receiver no
    text(x(k), ACC_N1(1,1),num2str(k),...
        'Units','normalized','Position',[0.95 k/c-0.045],'EdgeColor','Red',...
        'FontAngle','Italic','FontSize',9,'BackgroundColor','White');
end
xlim([0 Flim]), ylim([sc2*x(1)-x(1) sc2*x(c)+1.1]),
xlabel('Frequency (kHz)'), ylabel('Distance to Source')
set(gca, 'YTickLabel', ''),set(gcf, 'Position', [512 50 650 500]);
title('Normalized Frequency Spectra'), saveas(gcf,'05','fig'),

% 4 sets of receivers
hh(1) = 1; hh1(1) = c; % All receivers
hh(2) = 1; hh1(2) = round(c/2); % First half
hh(3) = 4; hh1(3) = 11; % Center portion
hh(4) = round(c/2)+1; hh1(4) = c;% Last half

% Attenuation coefficient for partial spectral areas
hhh = figure;
count = 0;
for df2 = 1:1; % kHz, spectral area resolution
    count = count+1;
    dfw(count) = df2;
endf1 = 100; % kHz, max frequency

```

```

fend = round(fend1*1000/df);
fwidth = round(df2*1000/df);
flim1 = 1:fwidth:fend;
flim1(1) = flim1(1)+1;
flim2 = flim1+fwidth-1;
flim2(1) = flim2(1)-1;
F_Area1 = zeros(fend,c,size(flim1,2));
Area_T = zeros(N/10,c);
for l = 1:size(flim1,2)
    for j = 1:c
        for k = flim1(1):flim2(1)
            F_Area1(k,j,l) = F_Area1(k-1,j,l)+(df/2)*(ACC1(k-1,j)+ACC1(k,j));
        end
    end
end

%Area(:, :, count) = sum(F_Area1,3);

% Select the spectral energy for each portion
for l = 1:size(flim1,2)
    for k = 1:c
        Area(l,k, count) = F_Area1(flim2(1),k,l);
    end
    Area_N(l, :, count) = Area(l, :, count)/max(Area(l, :, count));
end

% Compute alpha and R2
for j = 1:4
    for l = 1:size(flim1,2)
        coef3a = polyfit(x(hh(j):hh1(j)), log(Area(l, hh(j):hh1(j), count)), 1);
        alpha_FFT(j,l) = -coef3a(1);
        R1 = corrcoef(x(hh(j):hh1(j)), log(Area(l, hh(j):hh1(j), count)));
        R2_FFT(l, count, j) = R1(1,2)^2;
        freqq(1:size(flim2,2), count) = round((flim2-fwidth/2)*df/1000);
    end
end

% Attenuation coefficient for whole spectral area
for j = 1:c
    for k = 2:N/10
        Area_T(k,j) = Area_T(k-1,j)+(df/2)*(ACC1(k-1,j)+ACC1(k,j));
    end
end
for j = 1:4
    coef3_aa = polyfit(x(hh(j):hh1(j)), log(Area_T(N/10, hh(j):hh1(j))), 1);
    alpha_Area(j) = -coef3_aa(1);
    A1 = corrcoef(x(hh(j):hh1(j)), log(Area_T(N/10, hh(j):hh1(j))));
    R2_Area(j) = A1(1,2)^2;
end

figure,
Col = get(gca, 'Colororder');
col = zeros(14,3);
col(1:7,:) = Col(:, :);
col(8:14,:) = Col(:, :)/2;
for l = 1:3:size(flim1,2)

```

```

    plot(x*100,F_Area1(flim2(1),:,1)/max(F_Area1(flim2(1),:,1)),'+--
','displayname',...
    [sprintf('%1.0f',flim1(1)*df/1000),'-
',sprintf('%1.0f',flim2(1)*df/1000),'kHz'],'
\alpha=',sprintf('%1.2f',alpha_FFT(1,1))],'Linewidth',2,'MarkerSize',10);
%'Color',col(1,:));
    hold on;
end
plot(x*100,Area_T(N/10,)/max(Area_T(N/10,)),'+--','displayname',
[sprintf('%1.0f',0),'-',sprintf('%1.0f',fend1),'kHz'],' \alpha=',
sprintf('%1.2f',alpha_Area(1))],'Linewidth',2,'MarkerSize',10,'Color','Black'
); xlim([x(1)-dx x(c)+dx]*100), ylim([0 1.1]), legend('show'),
xlabel('Distance to Source (cm)'), ylabel('Normalized Spectral Area'),
set(gcf, 'Position', [512 50 650 500]);

% Plot Magtitudes (f-x)
figure
contourf(x*100,round((flim2-fwidth/2)*df/1000),Area_N(1:size((flim2-
fwidth/2),2),:,count)), hold on,
xlabel('Distance (cm)'), ylabel('Frequency (kHz)'),
%ylim([0 100]),
title('Attenuation'),
set(gcf, 'Position', [512 50 650 500]);
if df2 == 1
    saveas(gcf, '06', 'fig'),
end

% Plot R2 for frequency attenuations
figure(hhh);
for k = count
    plot(freqq(1:size(flim2,2),k),R2_FFT(1:size((flim2-
fwidth/2),2),k),'Color',col(k,:),'displayname',...
[sprintf('%1.0f',dfw(k)),' kHz']), hold on,
    xlabel('Frequency (kHz)'), ylabel('R^2'),
    %ylim([0 100]),
end
set(gcf, 'Position', [512 50 650 500]);
end
figure(hhh); legend('show'), saveas(gcf, '07', 'fig')

%% PHASE VELOCITY & 2D FFT -----
% 2D FFT
g = 8; % zero padding
% Zeropad in space and window it
acc_pad = zeros(N,g*c);
acc_pad(:,1:c) = acc_fw2(:,1:c);

% Distance and wavenumber array
xx = x0:dx:(x0+(g*c-1)*dx);
dk = 1/(xx(g*c)-x0+dx);
wn = 2*pi*(dk:dk:g*c*dk);

% 2D FFT
for m = 1:g*c-1
    accI(:,g*c+1-m) = acc_pad(:,m);
end

```

```

acc_2df = abs(fft2(accI));

% log does not provide a better exposition
%amp1 = 1; %amp2 = 5; %acc_2df = amp1*log(acc_2df+amp2);

% Normalize each row in matrix to expose maximums
for j = 1:N
    acc_2dfn(j,:) = acc_2df(j,:)/max(acc_2df(j,:));
end
for k = 1:g*c
    % acc_2dfn(:,k) = acc_2df(:,k)/max(acc_2df(:,k));
end
for j = 1:round(N/10)
    [peak,locs] = findpeaks(acc_2dfn(j,:), 'Npeaks',2, 'Minpeakheight',0.3);
    peaks(j,:) = peak;
    %peaks(j,2) = peak(1,2);
    loc(j,:) = locs;
    %loc(j,2) = locs(1,2);
end
% Pick two local maximum in each row
conter = 0;
for k = 1:2
    for j = 1:round(N/10)
        omegal(j,k) = 2*pi*j*df;
        wave_nol(j,k) = 2*pi*loc(j,k)*dk;
        vph(j,k) = omegal(j,k)/wave_nol(j,k);
        if 500 < vph(j,k) & vph(j,k) < 2000
            conter = conter+1;
            V_ph(conter,1) = vph(j,k);
            omega(conter,1) = omegal(j,k);
            wave_no(conter,1) = wave_nol(j,k);
        else
            end
        end
    end
end

% Pick the maximum in each row
conter = 0;
omegal = 0;
wave_nol = 0;
vph = 0;
for k = 1:g*c
    for j = 1:round(N/10)
        if acc_2dfn(j,k) == max(acc_2dfn(j,:))
            omegal = 2*pi*f(j);
            wave_nol = wn(k);
            vph = omegal/wave_nol;
            if 500 < vph & vph < 2000
                conter = conter+1;
                V_ph0(conter) = vph;
                omega0(conter) = omegal;
                wave_no0(conter) = wave_nol;
            end
        end
    end
end
end

```

```

% Plot f-k spectrum
figure
pcolor(wn,f/1000,acc_2dfn), hold on,
plot(wave_no(:,1),omega(:,1)/2/pi/1000,'o','Markersize',5,'Linewidth',1,'Color','Black'),hold on
plot(wave_no0,omega0/2/pi/1000,'o','Markersize',5,'Linewidth',1,'Color','Green'),
xlabel('Wave number (rad/m)'), ylabel('Frequency (kHz)'),
zlabel('Acceleration (m/s^2)'), ylim([0 60]), shading interp
set(gca,'CLim',[0.4 1]), title('Frequency - Wavenumber Plot'),
set(gcf,'Position',[512 50 650 500]); saveas(gcf,'08','fig'),

% Plot Dispersion Curve
figure
plot(omega/2/pi/1000,V_ph,'o','Markersize',5,'Linewidth',1,'Color','Black'),hold on,
plot(omega0/2/pi/1000,V_ph0,'o','Markersize',5,'Linewidth',1,'Color','Green')
xlim([0 60]), %ylim([600,1200]), xlabel('Frequency (kHz)'),ylabel('Phase Velocity (m/s)'),
title('Dispersion Curve'),
set(gcf,'Position',[512 50 650 300]); saveas(gcf,'09','fig'),

%% PHASE VELOCITY from UNWRAPPED PHASE -----
% Phase
for k = 1:c
    ph(:,k) = unwrap(angle(fft(acc_fw2(:,k))));
end

% Compute Phase Velocity for different numbers of shifted receivers and
% 'siz2' number of receivers are selected and moved "shift" times
% 'mod2' times the number of receivers in a set is changed
shift2 = c-siz2+1;
mod2 = c-siz2+1;
for n = 1:mod2
    for jk = 1:(shift2-n+1)
        for jx = 1:(siz2+n-1)
            ph1(jx,jk,n) = ph(round(res_freq/df),jx+jk-1); % Phase @ res_freq
            x1(jx,jk,n) = x(jx+jk-1);
        end
        % Compute R2
        R = corrcoef(x1(:,jk,n),ph1(:,jk,n));
        R2_W(jk,n) = R(1,2)^2;
    end
end

% Pick the set of receivers that provides the highest R2
for k = 1:shift2
    for l = 1:mod2
        if R2_W(k,l) == max(max(R2_W));
            shift_R2 = k;
            mod_R2 = l;
        end
    end
end

% Compute the phase velocity for all frequencies based on the selected receivers

```

```

% Vphase = w*x/phase
% "x/phase" is computed as the slope of curfitted line based on "siz2"
receivers
conter = 0;
for i = 1:1:round(2*res_freq/df)
    slope = polyfit(x(shift_R2:shift_R2+siz2+mod_R2-
2),ph(i,shift_R2:shift_R2+siz2+mod_R2-2),1);
    if slope == 0,
        slope = 1;
    end,
    vel(i) = -2*pi*i*df/slope(1);
    RR = corrcoef(x(shift_R2:shift_R2+siz2+mod_R2-
2),ph(i,shift_R2:shift_R2+siz2+mod_R2-2));
    RR2(i) = RR(1,2)^2;
    if slope<=0 & vel(i)<=VR1+100 & RR2(i)>=0.8
        conter = conter+1;
        V_ph2(conter) = vel(i);
        fr(conter) = i*df/1000;
        wk(conter) = 2*pi*fr(conter)*1000/V_ph2(conter);
    end
end

figure
subplot(2,1,1)
% Plot Dispersion Curve
plot(fr,V_ph2,'o','Linewidth',1),
xlim([0 120]), %ylim([600,1200]), ylabel('Phase Velocity (m/s)'),
title('a) Dispersion Curve, b) R2 values'),
% Plot R2
subplot(2,1,2)
plot(f(1:round(2*res_freq/df))/1000,RR2,'Linewidth',1),
xlim([0 120]), ylabel('R^2'), xlabel('Frequency (kHz)'),
% Mark the # of receivers and distance to source
annot = sprintf('Calculated based on %1.0f receivers located %1.2f cm from
the source', siz2+mod_R2-1, x(shift_R2)*100);
text(f(1), RR2(1), annot, 'Units','normalized','Position',[0.1 0.15],...
'EdgeColor','Red','FontAngle','Italic','FontSize',10)
set(gcf, 'Position', [512 50 650 500]); saveas(gcf,'10','fig'),

%% MATERIAL DAMPING based on WAVELET TRANSFORM -----
% Complex morlet function
cmor = exp(2*1i*pi*Fc*(t-to)).*exp(-((t-to).^2)/Fb^2);
cmor_F = abs(fft(cmor))/max(abs(fft(cmor)));

% Perform wavelet transform
v = zeros(Nw,c);
for l = 1:c
    v(1,l) = 0;
    for k = 1:Nw
        for i = 2:Nw
            v(i,l) = v(i-1,l) + 1/sqrt(a)*acc_f(i,l) .*...
            (exp(2*1i*pi*Fc*((t(i)-to-b(k))/a)) .* exp(-(((t(i)-to-
b(k))))/a).^2)/Fb^2));
        end
        WT(k,l) = v(i,l);
    end
end

```

```

end

% Pick the 'first' maximum amplitude and cell number
for k = 1:c
    % Normalize each wavelet signal respect to maximum value of itself
    WTN(:,k) = abs(WT(:,k))/max(abs(WT(:,k)));
    for j = 2:Nw
        if WTN(j-1,k) < WTN(j,k) && WTN(j+1,k) < WTN(j,k) && WTN(j,k)>W1
            W(k) = abs(WT(j,k));
            T_W(k) = j;
            break
        end
    end
end

% Compute the Rayleigh velocity
coef5 = polyfit(x(1:c),T_W(1:c),1);
fitT_W = polyval(coef5,x);
VR2(1) = abs(max(x)-min(x))/(abs(max(fitT_W)-min(fitT_W))*dt);
% First half receivers for R-wave
T_W_1 = T_W(1:7);
coef5_1 = polyfit(x(1:7),T_W_1,1);
fitT_W_1 = polyval(coef5_1,x(1:7));
VR2(2) = abs(x(7)-x(1))/(abs(max(fitT_W_1)-min(fitT_W_1))*dt);
% Middle receivers for R-wave
T_W_2 = T_W(4:11);
coef5_2 = polyfit(x(4:11),T_W_2,1);
fitT_W_2 = polyval(coef5_2,x(4:11));
VR2(3) = abs(x(11)-x(4))/(abs(max(fitT_W_2)-min(fitT_W_2))*dt);
% Last half receivers for R-wave
T_W_3 = T_W(8:14);
coef5_3 = polyfit(x(8:14),T_W_3,1);
fitT_W_3 = polyval(coef5_3,x(8:14));
VR2(4) = abs(x(14)-x(8))/(abs(max(fitT_W_3)-min(fitT_W_3))*dt);

% Phase and damped frequency
for k = 1:c
    phw(:,k) = unwrap(angle(WT(:,k)));
    % Take derivative of phase to compute damped frequency
    xx = dt:dt:t(Nw);
    yy(:,k) = spline(t(1:Nw),phw(:,k),xx);
    d_ph(:,k) = (1/(2*pi))*abs(diff(yy(:,k)))/dt;
end

% Pick the damped frequency at the arrival time
for k = 1:c
    d_freq(k) = d_ph(T_W(k),k);
end

% Normalize max. wavelet amplitudes respect to amplitude of damped
% frequency in Fourier spectrum of Morlet Wavelet
for k = 1:c
    W_N(k) = W(k)./cmor_F(round(d_freq(k)/df));
end

% Compute attenuation coefficient
for z = 1:4

```



```

% Curve fit
coef_WT = polyfit(x(hh(z):hh1(z)),log(W_N(hh(z):hh1(z))),1);
alpha_WT(1,z) = -coef_WT(1);
% R2 value
A1_WT = corrcoef(x(hh(z):hh1(z)),log(W_N(hh(z):hh1(z))));
R2_WT(1,z) = A1_WT(1,2)^2;
end

% Compute damping
for jx = 1:c
    dampW(jx) = alpha_WT(1,1)*1250/(2*pi*d_freq(jx));
end
% Take the average of damping for each location
mean_dampW = sum(dampW)/c;

% Compute material damping for the selected receivers
% "Siz" number of receivers are selected and moved "shift" times
% 'mod' times the number of receivers in a set is changed
for n = 1:mod
    for jk = 1:(shift-n+1)
        for jx = 1:(siz+n-1)
            W_N1(jx,jk,n) = W_N(jx+jk-1);           % Pick wavelet amplitudes
            d_freq1(jx,jk,n) = d_freq(jx+jk-1);     % Pick damped frequency
            x1(jx,jk,n) = x(jx+jk-1);               % Pick location
        end
        %Curve fit
        coef7 = polyfit(x1(1:siz+n-1,jk,n),log(W_N1(1:siz+n-1,jk,n)),1);
        fitW_N1(1:siz+n-1,jk,n) = polyval(coef7,x1(1:siz+n-1,jk,n));
        % R2 value
        r22 = corrcoef(x1(1:siz+n-1,jk,n),log(W_N1(1:siz+n-1,jk,n)));
        r2(jk,n) = r22(1,2)^2;
        % Attenuation coefficient
        alphaW1(jk,n) = -coef7(1);
        % Compute damping
        for jx = 1:siz+n-1
            dampW1(jx,jk,n) = alphaW1(jk,n)*1250/(2*pi*d_freq1(jx,jk,n));
        end
        % Take the average of damping for each location
        mean_dampW1(jk,n) = sum(dampW1(:,jk,n))/(siz+n-1);
        % Normalized dampings respect to VR for comperation to other data
sets
        N_dampW1(jk,n) = alphaW1(jk,n)*1208/(2*pi*res_freq); % Mutliplied to
VR=1208 m/s
    end
end

% Plot Wavelet amplitude vs shift time for all receivers
figure,
for k = 1:c
    plot(b(1:Nw)*1000,WTN(:,k)+sc3*x(k), 'Linewidth',2, 'Color','Black'), hold
on,
    % Mark the receiver no
    text(x(k), acc_n(1,1),num2str(k),...
'Units','normalized','Position',[0.01 k/c-0.03], 'EdgeColor','black',...
'FontAngle','Italic','FontSize',9, 'BackgroundColor','White');
end

```

```

plot(fitT_W*dt*1000,sc3*x,'Linewidth',2.5,'Color','Black'), hold on,
%plot(fitT_W_2*dt*1000,sc3*x(8:21),'Linewidth',2.5,'Color','Black'), hold on,
%plot(fitT_W_3*dt*1000,sc3*x(15:28),'Linewidth',2.5,'Color','Red'), hold on,
xlim([0 1]), ylim([sc3*x(1)-x(1) sc3*x(c)+1.1]),
xlabel('Time (ms)'), ylabel('Source Offset'), set(gca,'YTickLabel','')
% Mark the VR on the plot
text(x(1),fitT_W(1),[' V_R=', num2str(round(VR2(1))), ' m/s\rightarrow
'],'Units','normalized','Position',[0.05 0.75],'EdgeColor','Black',...
'FontAngle','Italic','FontWeight','Bold','FontSize',10,'BackgroundColor','White');
%title('Normalized Wavelet Amplitudes'),
set(gcf, 'Position', [512 50 650 500]); saveas(gcf,'11','fig'),

% Plot Maximum Wavelet and Local Dampings for all receivers
figure,
subplot(3,1,1)
plot(x*100,W_N,'--+', 'Linewidth',2, 'MarkerSize',10, 'Color', 'Black'),
ylim([0 max(W_N)+max(W_N)/10]), ylabel('Wavelet Amp')
subplot(3,1,2)
plot(x*100,d_freq/1000,'--+', 'Linewidth',2, 'MarkerSize',10, 'Color', 'Black'),
ylim([min(d_freq)/1000-5 max(d_freq)/1000+5]), ylabel('Damped Freq (kHz)'),
subplot(3,1,3)
for k = 1:c
    mean_damp(k) = mean_dampW;
end
plot(x*100,dampW*100,'--+', 'Linewidth',2, 'MarkerSize',10, 'Color', 'Black'),
hold on,
plot(x*100,mean_damp*100, 'Linewidth',2, 'Color', 'Black'),
ylim([min(dampW)*100-0.2 max(dampW)*100+0.2]),
xlabel('Distance to Source (cm)'), ylabel('Damping (%)'),
% Mark the mean damping on the plot
annot = sprintf('Mean damping = %3.2f', mean_damp(1)*100);
text(x(1), mean_damp(1)*100, annot, 'Units','normalized',...
'Position',[0.35 0.2],'EdgeColor','Black','FontAngle','Italic',...
'FontSize',10,'BackgroundColor','White')
subplot(3,1,1)
title('a) Maximum Wavelet Amplitude, b) Damped Frequency, c) Material Damping
Ratio'), set(gcf, 'Position', [512 50 650 500]); saveas(gcf,'12','fig'),

% Plot Dampings vs Distance to source for selected receivers
figure,
Col = get(gca, 'Colororder');
for n = 1:mod-1
    plot(x1(1,1:shift-n+1,n)*100,mean_dampW1(1:shift-n+1,n)*100,'-+',...
'Displayname',[num2str(siz+n-1), ' receivers'],'Linewidth',1,...
'MarkerSize',7, 'Color',Col(n,:)), hold on,
xlim([x(1)-0.01 max(max(x1(1, :, :)))+0.01]*100),
%ylim([min(min(mean_dampW1))*100-0.2 max(max(mean_dampW1))*100+1]),
end
legend('show'), legend('Location', 'NorthEast'), legend('boxoff'),
xlabel('Distance between the source and first receiver (cm)'),
ylabel('Material Damping (%)'), title('Material Damping vs. Source Offset'),
hold on, set(gcf, 'Position', [512 50 650 500]); saveas(gcf,'13','fig'),

% Plot R2 for each Dampings vs Distance to source for selected receivers
figure,

```

```

Col = get(gca, 'Colororder');
for n = 1:mod-1
    plot(x1(1,1:shift-n+1,n)*100,r2(1:shift-n+1,n), '-+', ...
        'Displayname', [num2str(siz+n-1), ' receivers'], 'Linewidth', 1, ...
        'MarkerSize', 7, 'Color', Col(n, :)), hold on,
    xlim([x(1)-0.01 max(max(x1(1, :, :))+0.01)*100],
        %ylim([min(min(mean_dampW1))*100-0.2 max(max(mean_dampW1))*100+1]),
end
legend('show'), legend('Location', 'NorthEast'), legend('boxoff'),
xlabel('Distance between the source and first receiver (cm)'),
ylabel('R^2'), title('R^2 vs. Source Offset'), hold on,
set(gcf, 'Position', [512 50 650 500]); saveas(gcf, '14', 'fig'),

%% DISCRETE WAVELET TRANSFORM -----
acc1 = acc(1:8192, :);
% Time and frequency array for the signals from oscilloscope
N1 = size(acc1, 1); % Number of data points
t1 = dt:dt:(N1*dt); % second
T1 = dt*N1; % Total signal time
df1 = 1/(T1-t1(1)); % Hz
f1 = df1:df1:(N1)*df1; % Hz

% Numbers of levels
lev = 6;
% Type of wavelet
wvlt = 'db18';
% Perform decomposition
[C,L] = wavedec(acc1(:,2), lev, wvlt);
% Extract the last level approximation coefficients
%CA3 = appcoef(C,L,wvlt,lev);
% Extract all detail coefficients
%[cD1,cD2,cD3,cD4,cD5,cD6,cD7,cD8,cD9] = detcoef(C,L,[1,2,3,4,5,6,7,8,9]);
% Reconstruct the last level approximation
%AA1 = zeros(10000,lev);
%AA1(:,lev) = wrcoef('a',C,L,wvlt,lev);
% Reconstruct the all level details
for k = 1:lev
    LEVEL(:,k) = wrcoef('d',C,L,wvlt,k);
end

figure,
for k = 1:lev
    plot(t1*1000, LEVEL(:,k)/max(LEVEL(:,k))+2.2*(lev+1-k), 'Linewidth', 2),
hold on,
    % Mark the level no
    text(k, LEVEL(1,1), ['Level ' num2str(lev+1-k)], ...
        'Units', 'normalized', 'Position', [0.01 k/(lev+0.25)-
0.05], 'EdgeColor', 'Red', ...
        'FontAngle', 'Italic', 'FontSize', 9, 'BackgroundColor', 'White');
end
xlim([0 1]), ylim([1 14.5]),
xlabel('Time (ms)'), ylabel('Decomposition Level')
set(gca, 'YTickLabel', ''), set(gcf, 'Position', [512 50 750 500]);
saveas(gcf, '15', 'fig'),

figure,

```

```

for k = 1:lev
    plot(f1/1000,abs(fft(LEVEL(:,k)))/max(abs(fft(LEVEL(:,k))))+1.1*(lev+1-
k), 'Linewidth',2), hold on,
    % Mark the level no
    text(k, LEVEL(1,1), ['Level ' num2str(lev+1-k)],...
    'Units','normalized','Position',[0.9 k/(lev+0.1)-
0.1], 'EdgeColor','Red',...
    'FontAngle','Italic','FontSize',9,'BackgroundColor','White');
end
xlim([0 500]), ylim([1.1 7.5]),
xlabel('Frequency (kHz)'), ylabel('Decomposition Level')
set(gca, 'YTickLabel',''), set(gcf, 'Position', [512 50 750 500]);
saveas(gcf, '16', 'fig'),

% Perform DWT for all receivers
for j = 1:c
    % Perform decomposition using
    [C,L] = wavedec(accl(:,j),lev,wvlt);
    % Reconstruct the all level details
    for k = 1:lev
        AA2(:,k) = wrcoef('d',C,L,wvlt,k);
        DWT(:,j,k) = AA2(:,k);
    end
end
figure,
for k = 1:c
    plot(t1*1000,DWT(:,k,4)/max(DWT(:,k,4))+2.2*k, 'Linewidth',2), hold on,
    % Mark the receiver no
    text(k, DWT(1,1),num2str(k),...
    'Units','normalized','Position',[0.01 k/c-0.025], 'EdgeColor','Red',...
    'FontAngle','Italic','FontSize',9,'BackgroundColor','White');
end
xlim([0 1]), ylim([1 32]), xlabel('Time (ms)'), ylabel('Distance to Source')
set(gca, 'YTickLabel',''), set(gcf, 'Position', [512 50 750 500]);
saveas(gcf, '17', 'fig'),

DWT_F = abs(fft(DWT));
figure,
for k = 1:c
    plot(f1/1000,abs(fft(DWT(:,k,4)))/max(abs(fft(DWT(:,k,4))))+1.1*k, 'Linewidth'
,2), hold on,
    % Mark the receiver no
    text(k, DWT(1,1),num2str(k),...
    'Units','normalized','Position',[0.01 k/c-0.035], 'EdgeColor','Red',...
    'FontAngle','Italic','FontSize',9,'BackgroundColor','White');
end
xlim([0 100]), ylim([1.1 16.5]), xlabel('Frequency (kHz)'), ylabel('Distance
to Source'), set(gca, 'YTickLabel',''), set(gcf, 'Position', [512 50 750 500]);
saveas(gcf, '18', 'fig'),

% Attenuation coefficient for whole spectral area
Area_DWT = zeros(N/10,c,lev);
for l = 1:lev
    for j = 1:c
        for k = 2:N/10

```

```

        Area_DWT(k,j,l) = Area_DWT(k-1,j,l)+(df/2)*(DWT_F(k-
1,j,l)+DWT_F(k,j,l));
    end
end
for z = 1:4
    coef_DWT =
polyfit(x(hh(z):hh1(z)),log(Area_DWT(N/10,hh(z):hh1(z),l)),1);
    alpha_DWT(z,l) = -coef_DWT(1);
    A1_DWT =
corrcoef(x(hh(z):hh1(z)),log(Area_DWT(N/10,hh(z):hh1(z),l)));
    R2_DWT(z,l) = A1_DWT(1,2)^2;
end
end

% Plot Attenuation trends
Col = get(gca,'Colororder');
figure,
for l = 2:lev-1
    plot(x*100,Area_DWT(N/10,:,l)/max(Area_DWT(N/10,:,l)),'+--
','displayname',...
        ['Level ',sprintf('%1.0f',l),' : ',sprintf('%1.0f',500/2^l)],'-
','sprintf('%1.0f',500/2^(l-1)),...
        ' kHz',' /
','\alpha=',sprintf('%1.2f',alpha_DWT(1,l))],'Linewidth',2,'MarkerSize',10,'C
olor',Col(1,:)); hold on;
end
xlim([x(1)-dx x(c)+dx]*100), ylim([0 1.02]), legend('show'),
xlabel('Distance to Source (cm)'), ylabel('Normalized Spectral Area'),
set(gcf, 'Position', [512 50 750 500]);saveas(gcf,'19','fig'),

%% SAVE PARAMETERS -----
% Magnitudes of receivers
par1 = zeros(c,4);
par1(:,1) = Area_T(N/10,:); % Total spectral area
par1(:,2) = Area(round(Fc/1000),:,1); % 52 kHz
par1(:,3) = W_N; % Wavelet magnitude normalized respect
to mag of damp. freq in morlet
par1(:,4) = Area_DWT(N/10,:,4); % DWT - Level 4 spectral area
% Velocity, Alpha amd Damping
par2 = zeros(4,4);
for j = 1:4
    par2(1,j) = VR2(j); % Rayleigh velocities from Wavelet Mag
    par2(2,j) = alpha_Area(1,j); % alpha for Whole Spectral Area
    par2(3,j) = alpha_FFT(j,round(Fc/1000)); % alpha for 52 kHz
    par2(4,j) = alpha_WT(1,j); % alpha for WT
end
% Alpha from DWT
par8 = alpha_DWT; % [4,6] alpha for 1-6 DWT levels
%Alpha for each frequency for 4 sets of receivers
par3 = alpha_FFT';
% Damping for Wavelet
par4 = mean_dampW1;
% Phase velocity for both cases
% 2DFFT maximum value
par5(:,1) = omega0/2/pi/1000; % kHz
par5(:,2) = V_ph0;

```

```

% 2DFFt two local maximums
par6(:,1) = omega/2/pi/1000; % kHz
par6(:,2) = V_ph;
% Unwrapped phase velocity
par7(:,1) = fr; % kHz
par7(:,2) = V_ph2;

% Save parameters
save(['C:\Users\askirlan\Desktop\Sandbox\Phase
III\Transient\Results\',no2,no3,'\ ',sprintf('%s','PAR1_ ',
data),'.mat'],'par1');
save(['C:\Users\askirlan\Desktop\Sandbox\Phase
III\Transient\Results\',no2,no3,'\ ',sprintf('%s','PAR2_ ',
data),'.mat'],'par2');
save(['C:\Users\askirlan\Desktop\Sandbox\Phase
III\Transient\Results\',no2,no3,'\ ',sprintf('%s','PAR3_ ',
data),'.mat'],'par3');
save(['C:\Users\askirlan\Desktop\Sandbox\Phase
III\Transient\Results\',no2,no3,'\ ',sprintf('%s','PAR4_ ',
data),'.mat'],'par4');
save(['C:\Users\askirlan\Desktop\Sandbox\Phase
III\Transient\Results\',no2,no3,'\ ',sprintf('%s','PAR5_ ',
data),'.mat'],'par5');
save(['C:\Users\askirlan\Desktop\Sandbox\Phase
III\Transient\Results\',no2,no3,'\ ',sprintf('%s','PAR6_ ',
data),'.mat'],'par6');
save(['C:\Users\askirlan\Desktop\Sandbox\Phase
III\Transient\Results\',no2,no3,'\ ',sprintf('%s','PAR7_ ',
data),'.mat'],'par7');
save(['C:\Users\askirlan\Desktop\Sandbox\Phase
III\Transient\Results\',no2,no3,'\ ',sprintf('%s','PAR8_ ',
data),'.mat'],'par8');

% Plot Attenuation trends
figure,
plot(x*100,par1(:,1)/max(par1(:,1)),'+--','displayname',['Area:
','\alpha=',sprintf('%1.2f',alpha_Area(1,1)),'
R^2=',sprintf('%1.2f',R2_Area(1,1))],...
'Linewidth',2,'MarkerSize',10,'Color','Black'); hold on;
plot(x*100,par1(:,2)/max(par1(:,2)),'+--','displayname',['52 kHz:
','\alpha=',sprintf('%1.2f',alpha_FFT(1,52)),'
R^2=',sprintf('%1.2f',R2_FFT(52,1,1))],...
'Linewidth',2,'MarkerSize',10,'Color','Red'); hold on;
plot(x*100,par1(:,4)/max(par1(:,4)),'+--','displayname',['DWT:
','\alpha=',sprintf('%1.2f',alpha_DWT(1,4)),'
R^2=',sprintf('%1.2f',R2_DWT(1,4))],...
'Linewidth',2,'MarkerSize',10,'Color','Green'); hold on;
plot(x*100,par1(:,3)/max(par1(:,3)),'+--','displayname',['WT:
','\alpha=',sprintf('%1.2f',alpha_WT(1,1)),'
R^2=',sprintf('%1.2f',R2_WT(1,1))],...
'Linewidth',2,'MarkerSize',10,'Color','Blue');
xlim([x(1)-dx x(c)+dx]*100), ylim([0 1.01]), legend('show'),
xlabel('Distance to Source (cm)'), ylabel('Normalized Quantity'),
set(gcf, 'Position', [512 50 750 500]); saveas(gcf,'20','fig'),

%% NONLINEAR REGRESSION for ATTENUATION -----

```

```

% Experimental data
test = par1(:,4)'/max(par1(:,4));
% Select model parameters
par_theo = 5;
% Select initial arbitrary parameters
par_init = par_theo*0.9;
% Write a function handle that represents the model
mdl = @(a,x) exp(-a*(x-x(1)));
%mdl = @(a,x) (x/x(1))^-0.5*exp(a(1))*(x-x(1));
% Generate model
attenuation = mdl(par_theo,x);

% Fit the model to data starting from the arbitrary guess
[par_est,resd,J,cov,mse] = nlinfit(x,test,mdl,par_init);
%[par_est,resd,J,cov,mse] =
nlinfit(x,test,mdl,par_init,statset('robust','on'));
sigma = sum(resd.^2)/size(resd,2);
% predictions and 95% confidence interval half-widths
[attenuation_est,delta] = nlpredci(mdl,x,par_est,resd,'covar',cov);
%[ypred,delta] = nlpredci(mdl,w,par_est,resd,'jacobian',J);
% 95% confidence intervals for par_est
ci = nlparci(par_est,resd,'Covar',cov);
%ci = nlparci(par_est,resd,'jacobian',J);
% R2 value
R22 = 1 - (sum(resd.^2))/sum((test-mean(test)).^2);

figure
plot(x*100,test,'o:','displayname','measured'), hold on
%plot(x*100,attenuation,'displayname','model','color','red'), hold on;
plot(x*100,attenuation_est,'+:','displayname','estimated','color','black','li
newwidth',2); hold on
%plot(x*100,attenuation_est+delta,':','color','black','linewidth',2)
%plot(x*100,attenuation_est-delta,':','color','black','linewidth',2)
% Mark the alpha
text('String',['\alpha =', sprintf(' %1.1f', par_est(1))
], 'Units', 'normalized', 'Position', [0.7 0.60], 'EdgeColor', 'Red', ...
'FontAngle', 'Italic', 'FontSize', 10, 'BackgroundColor', 'White');
xlim([x(1)*100-2 x(c)*100+2]), ylim([0 1.05])
xlabel('Distance (cm)'), ylabel('Normalized Spectral Area - DWT Level 4'),
legend('show'), legend('Location', 'northeast'), legend('boxoff')
saveas(gcf, '21', 'fig'),

```

Appendix D: Additional Figures for Section 6.4

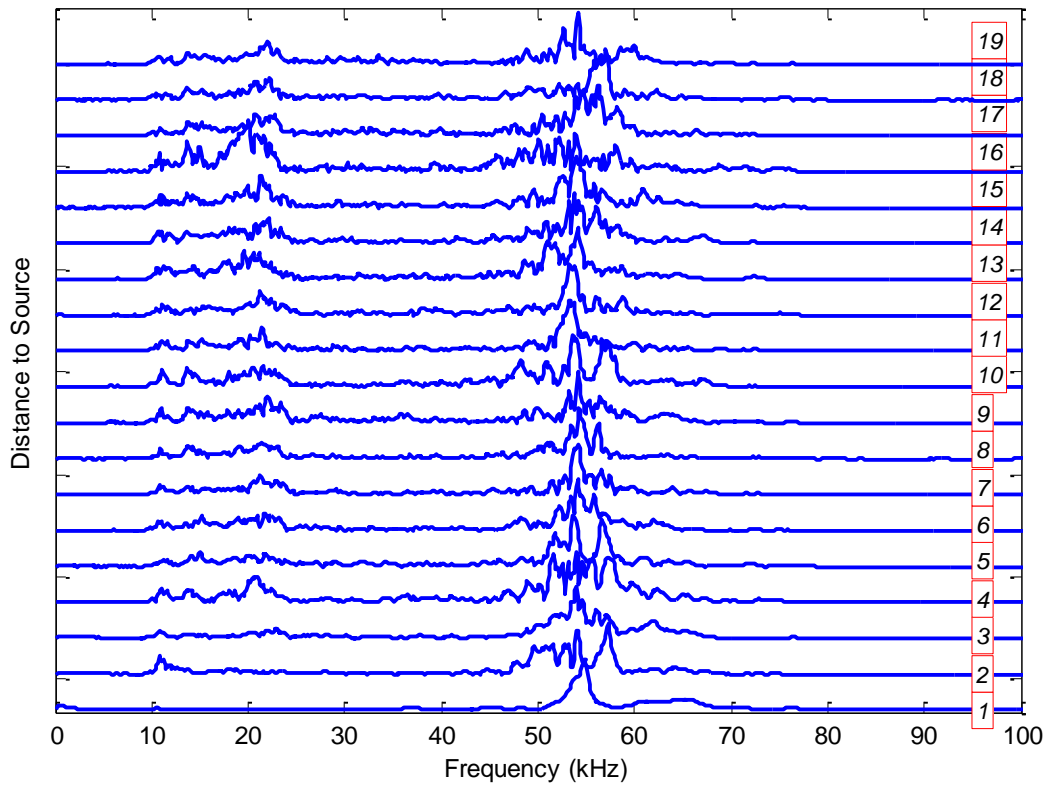
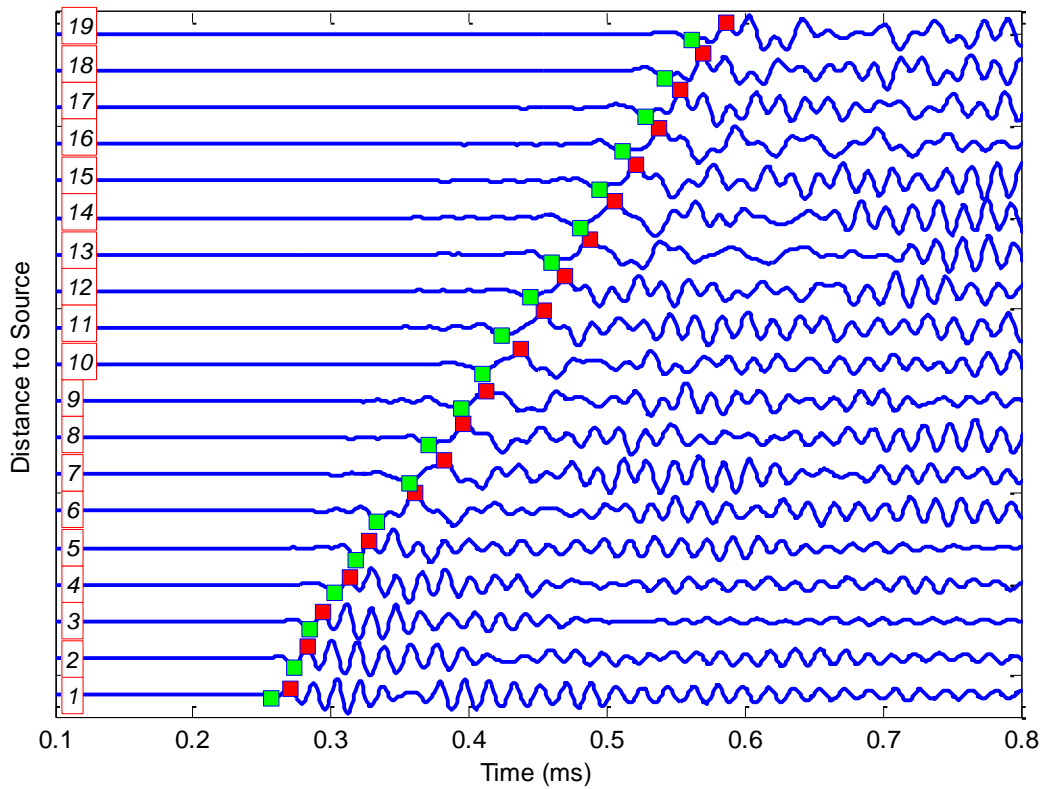


Figure D.1: Time histories and frequency spectra for Test1 (Adhesive).

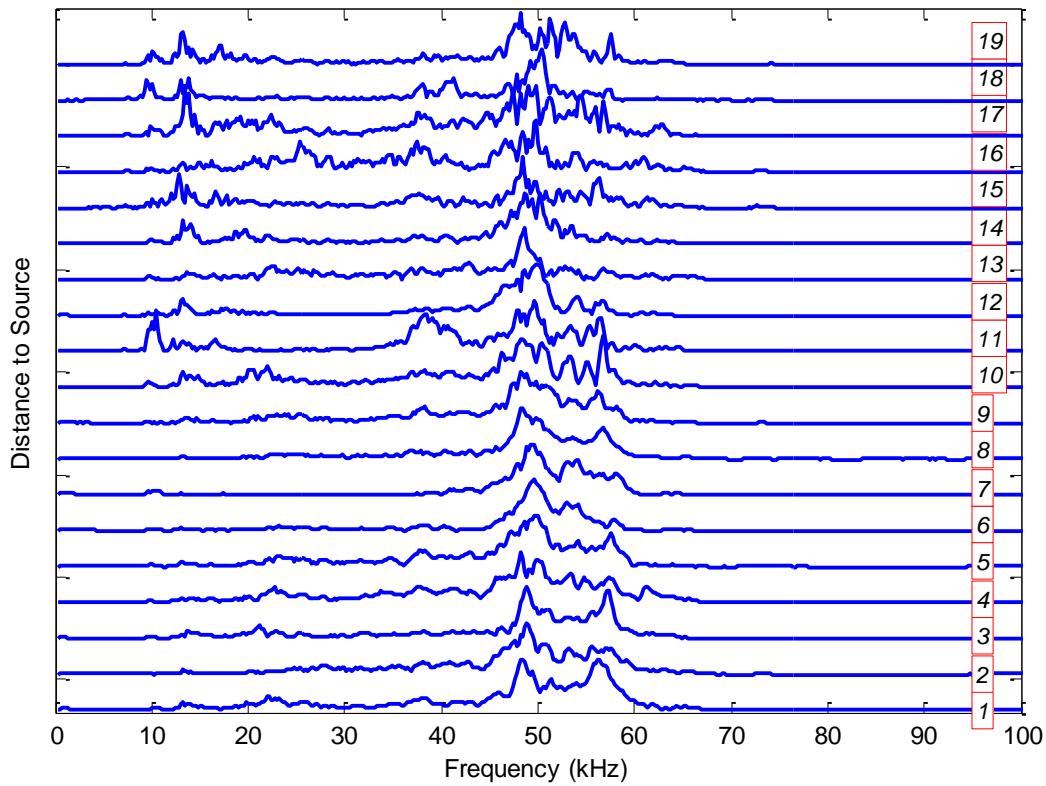
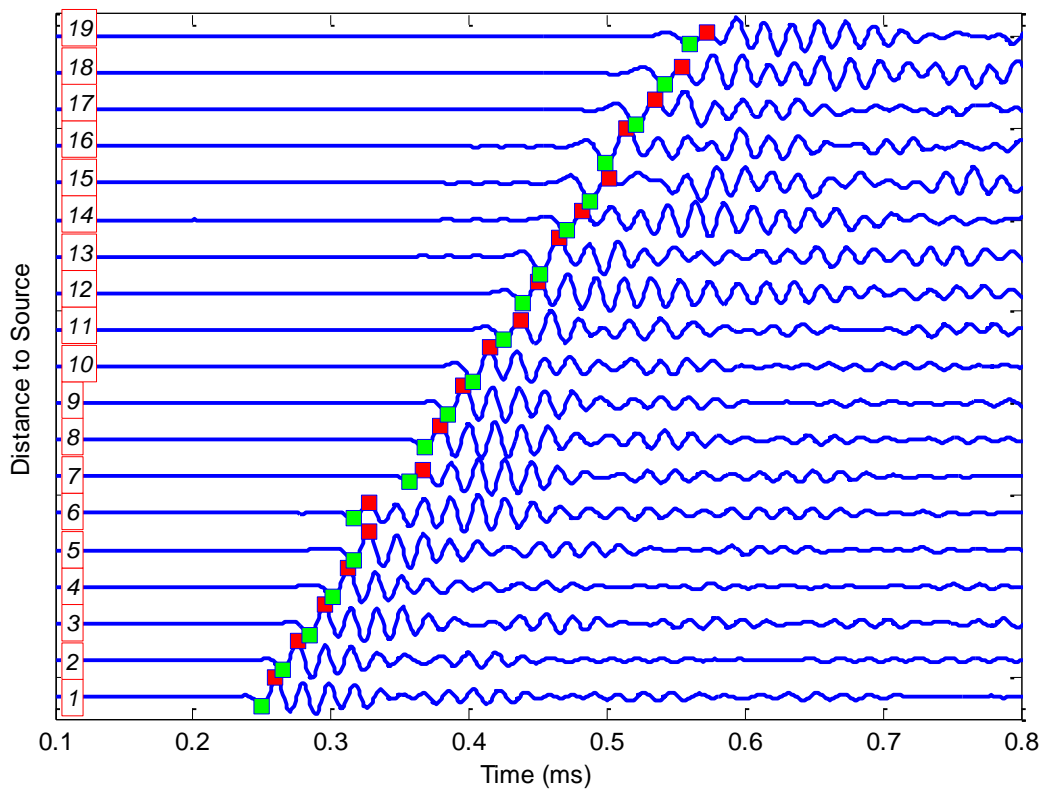


Figure D.2: Time histories and frequency spectra for Test2 (Embedded nuts).

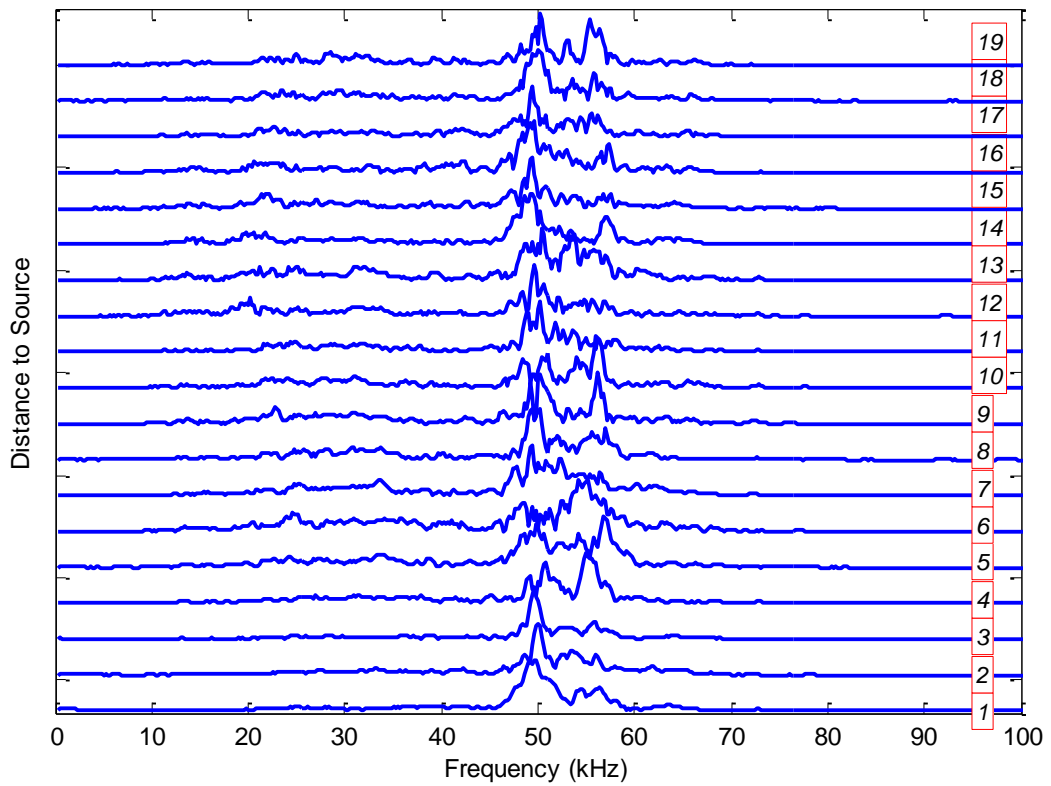
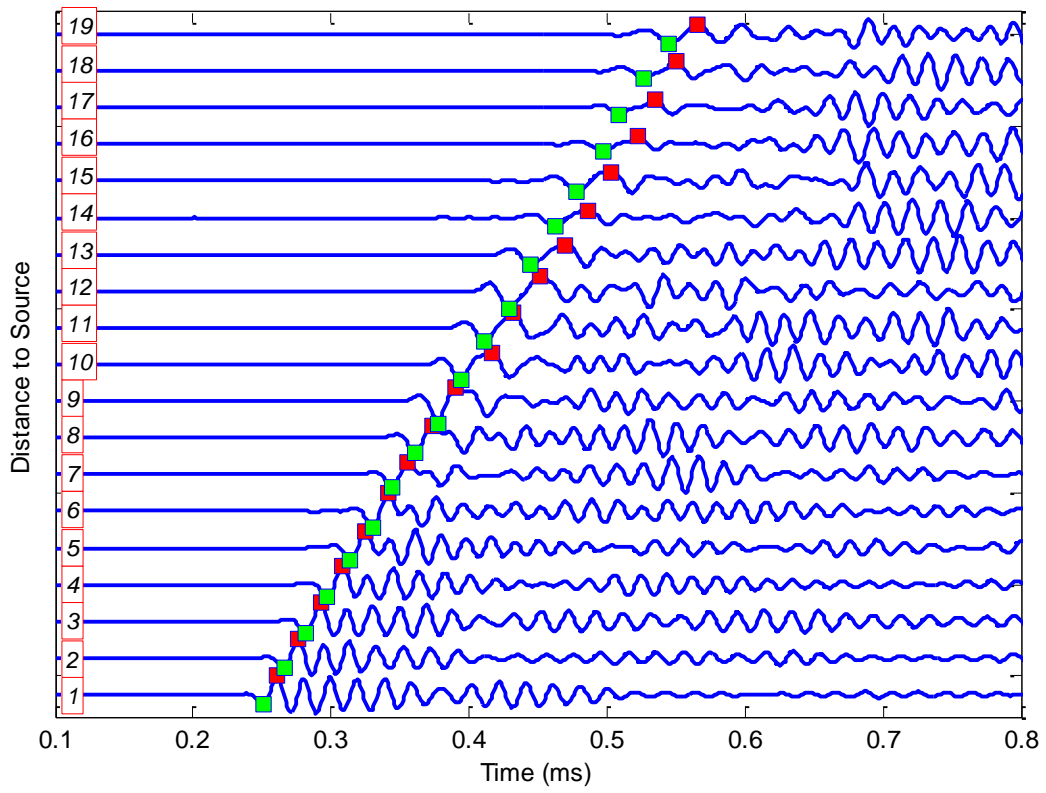


Figure D.3: Time histories and frequency spectra for Test3 (Epoxy strip).

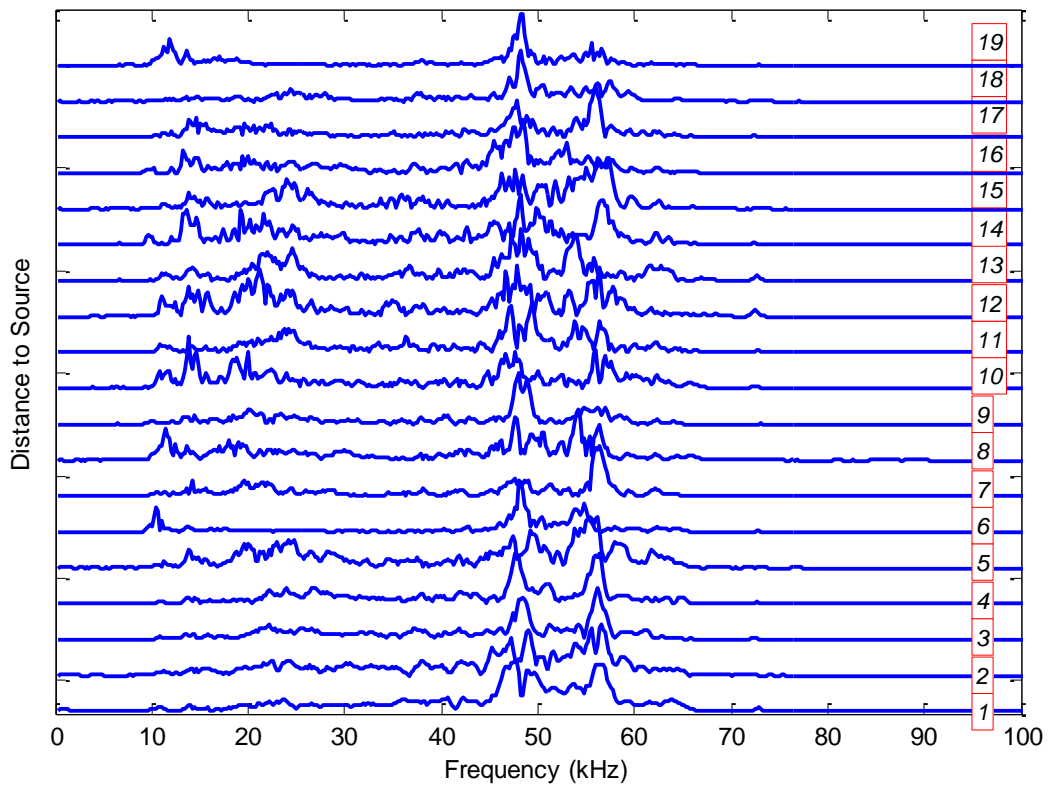
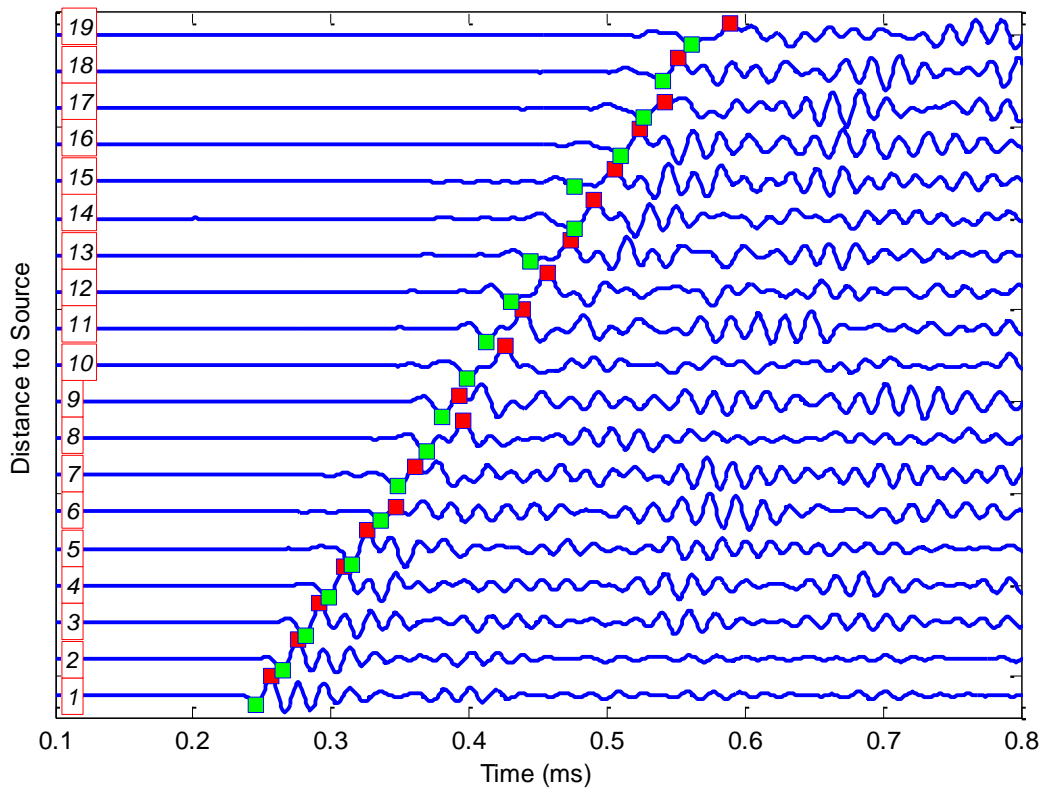


Figure D.4: Time histories and frequency spectra for Test4 (Discrete epoxy).

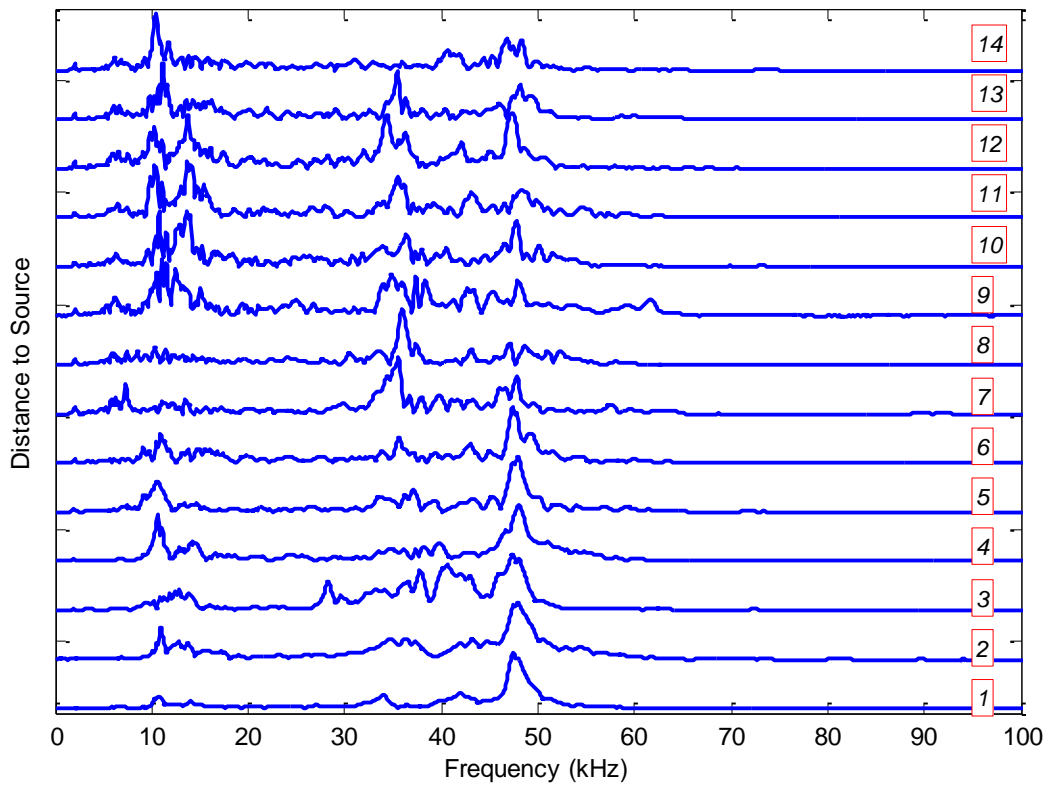
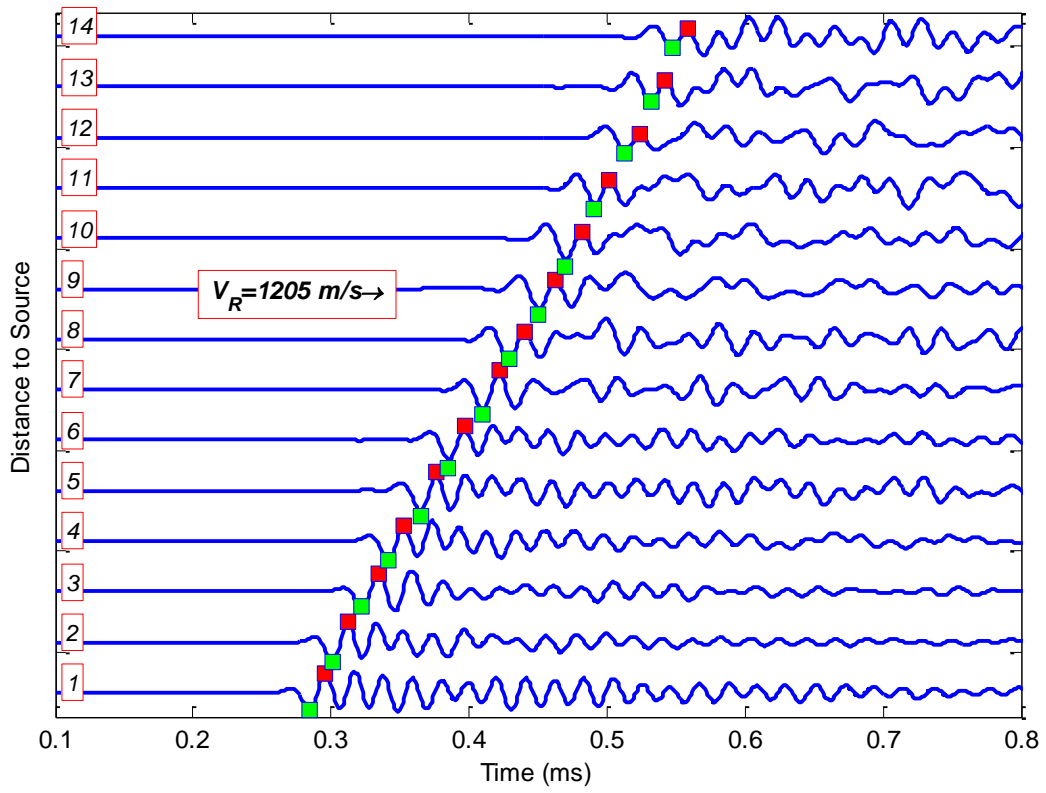


Figure D.5: Time histories and frequency spectra for Test5_S2 (All receiver array).

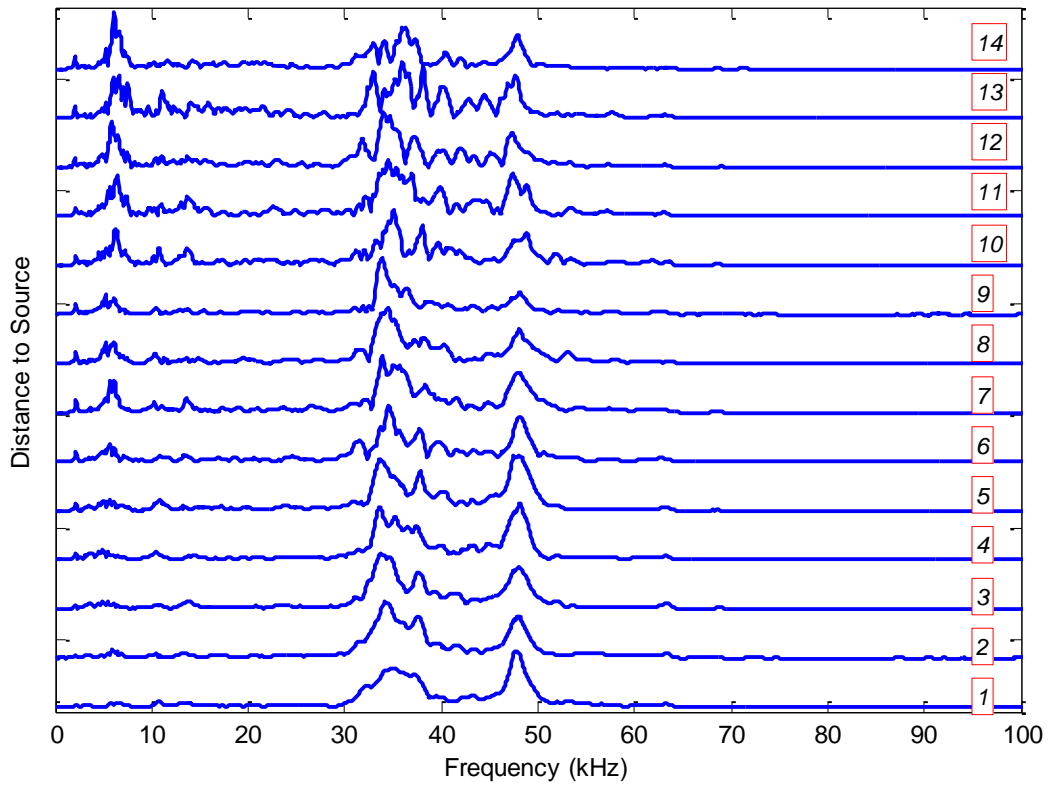
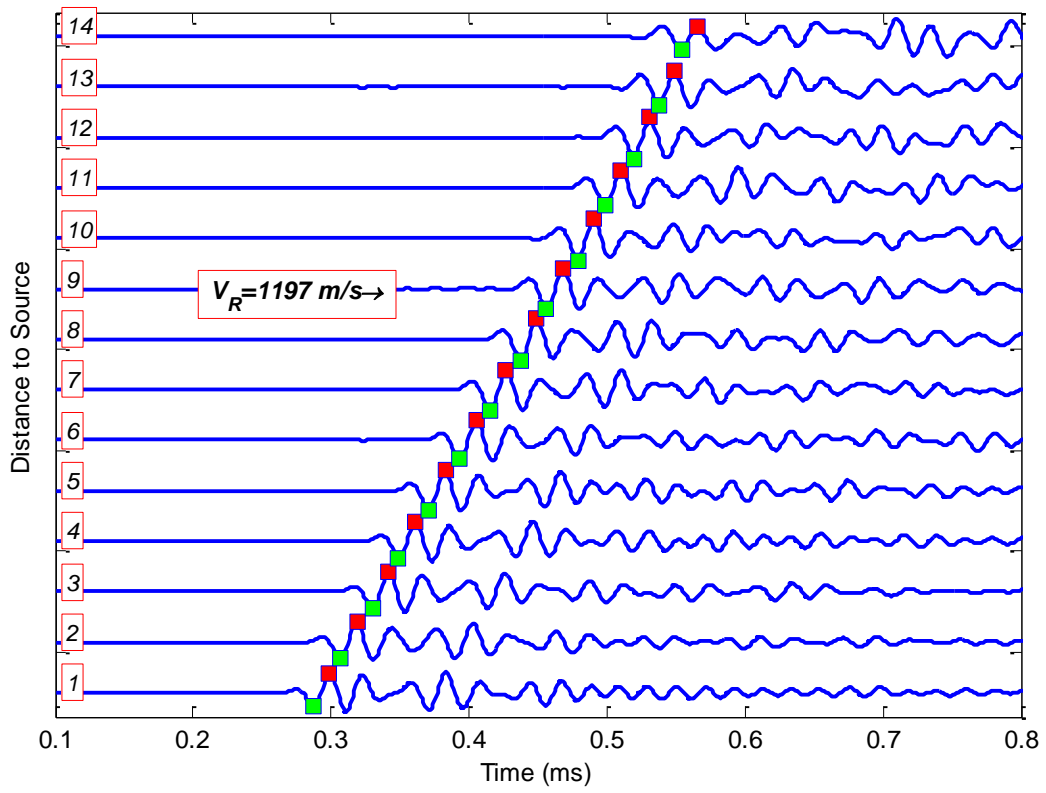


Figure D.6: Time histories and frequency spectra for Test6_S2 (The reference receiver).

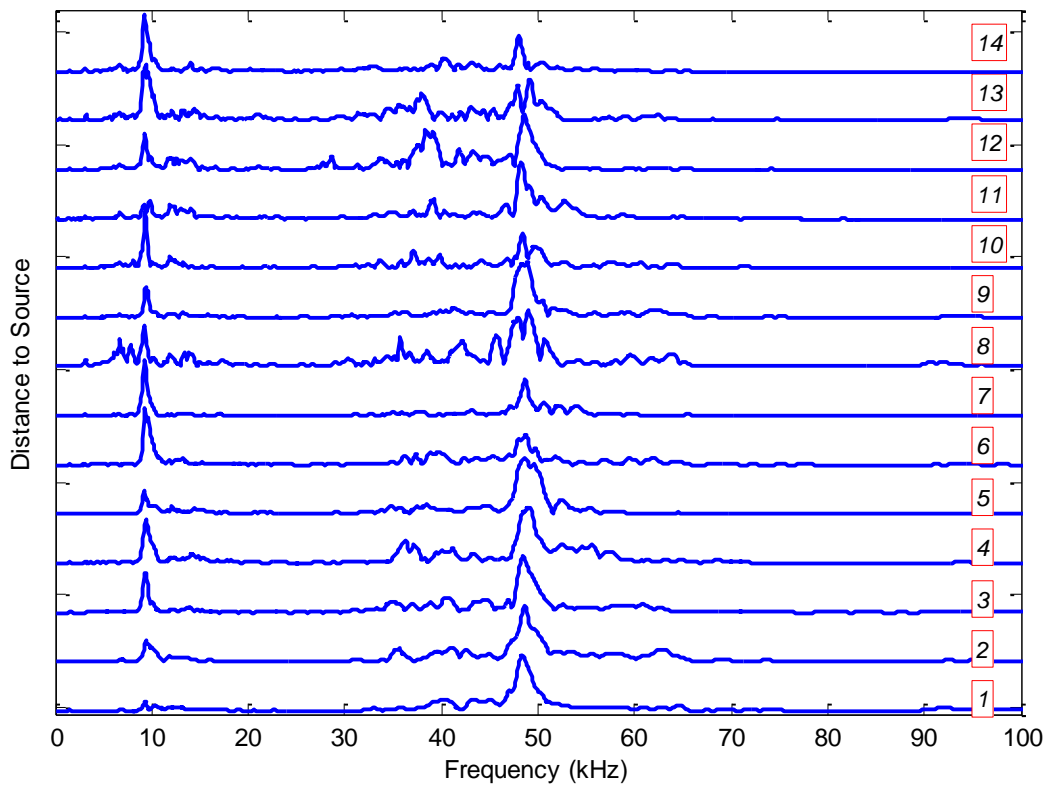
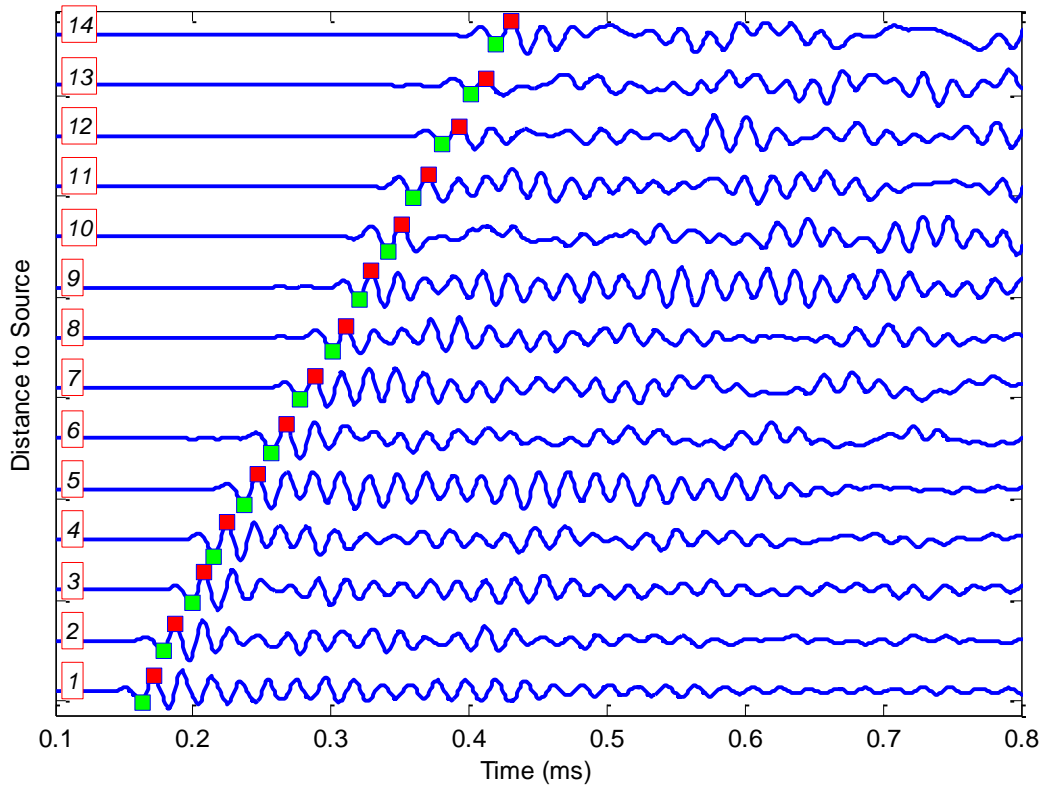


Figure D.7: Time histories and frequency spectra for Test5_S1 (Square pulse as excitation).

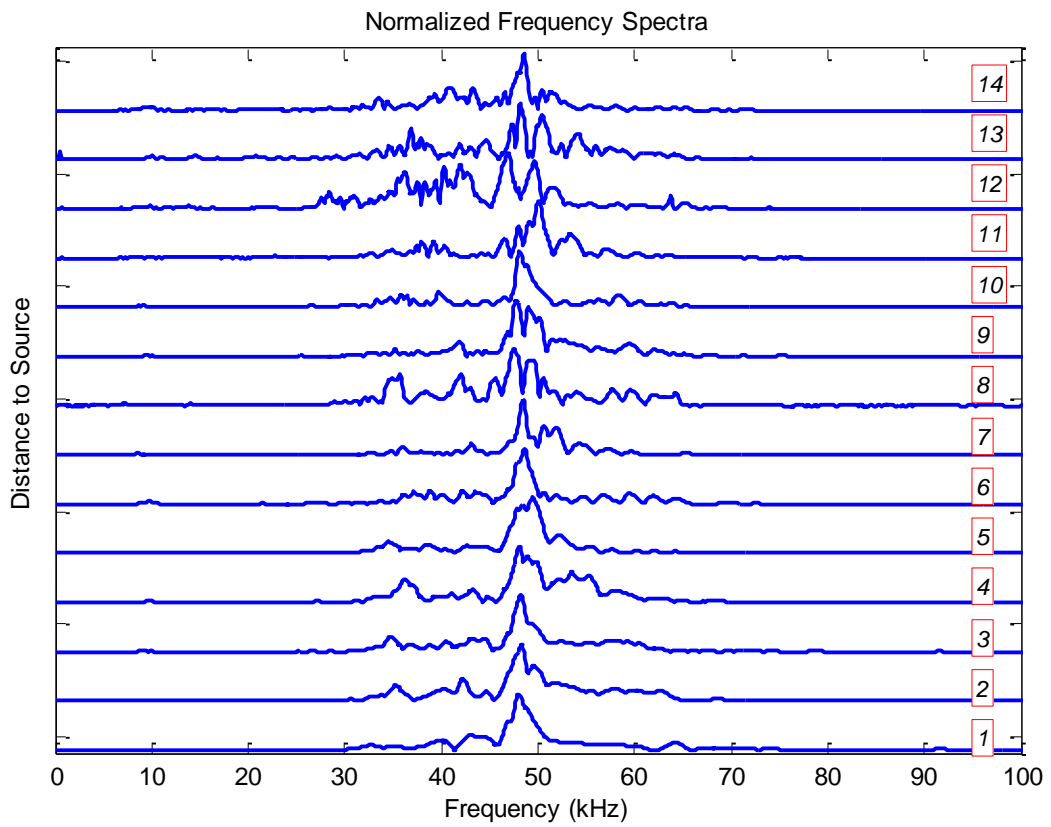
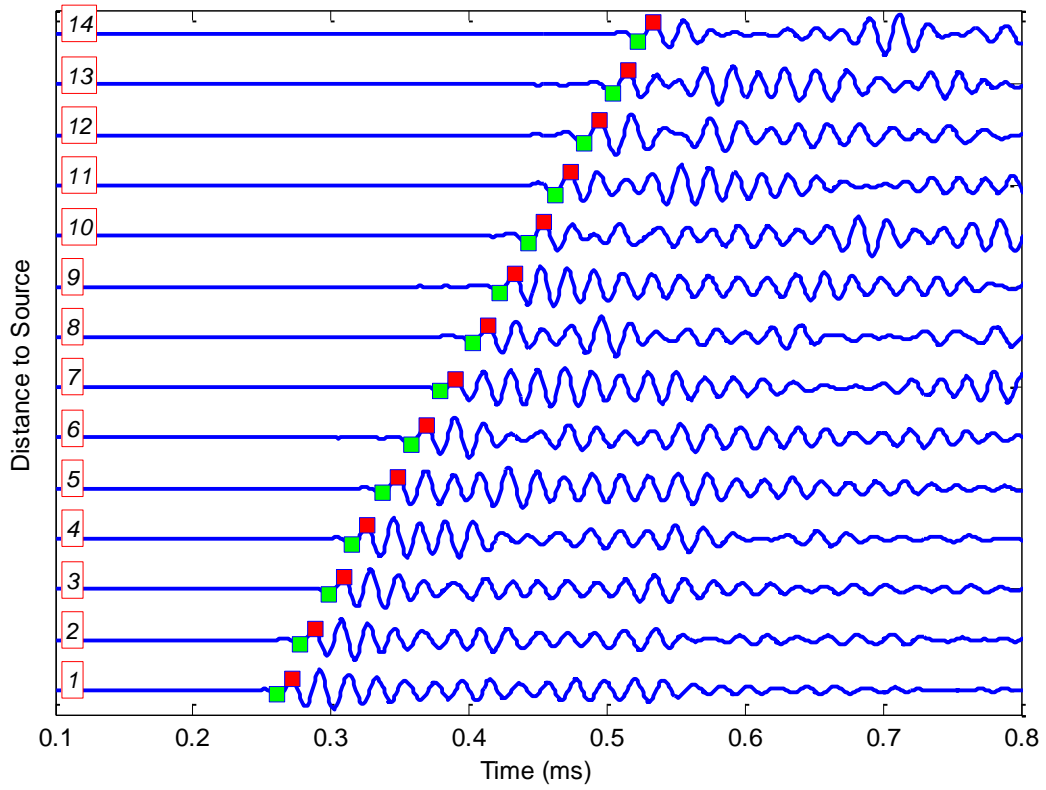


Figure D.8: Time histories and frequency spectra for Test7 (1 cycle 50 kHz sine as excitation).

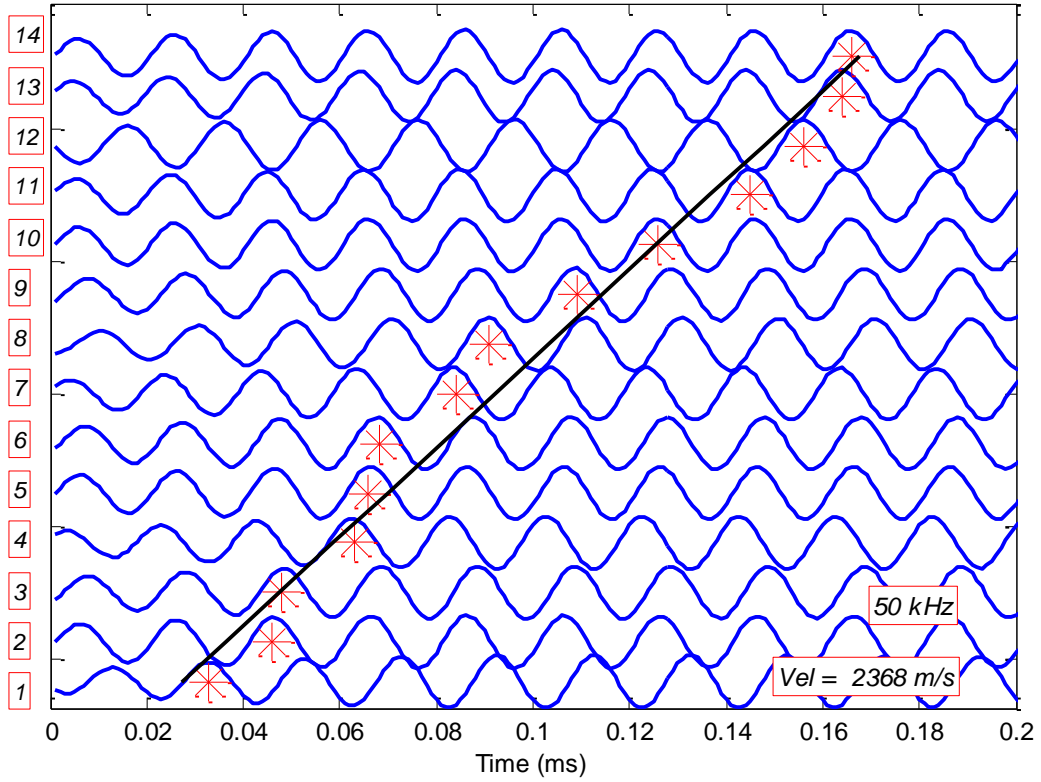


Figure D.9: Time histories for Test8 (Steady-state 50 kHz sine as excitation).

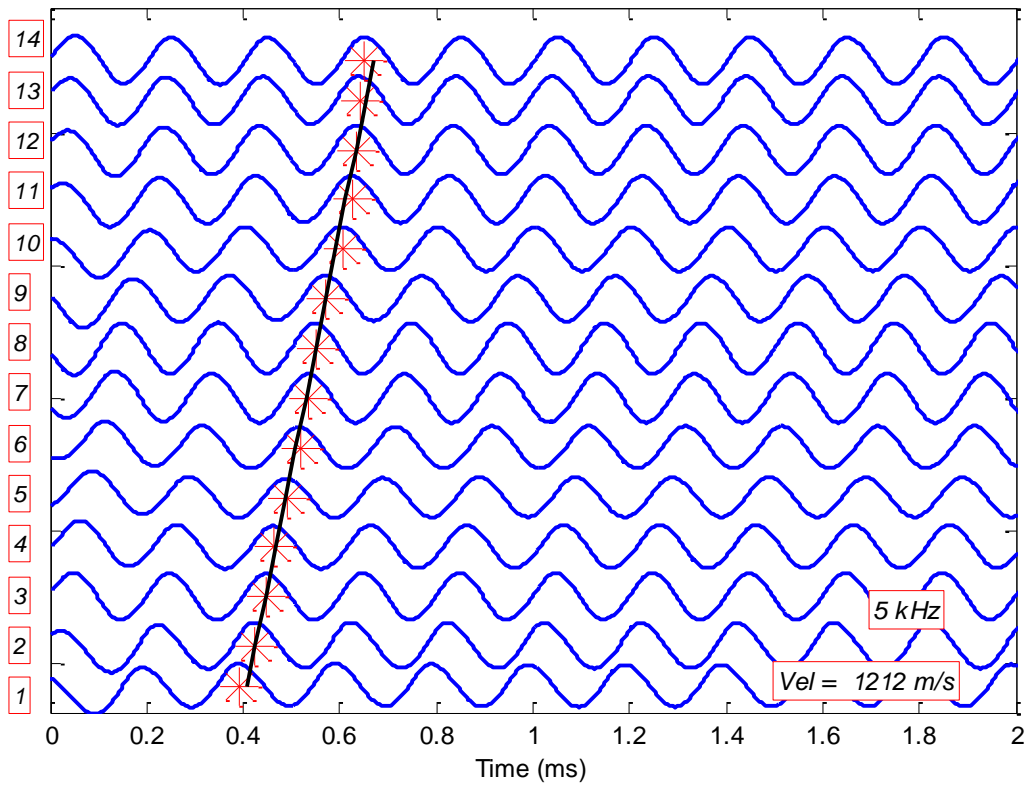


Figure D.10: Time histories for Test9 (Steady-state 5 kHz sine as excitation).